NASA/TM—1999–208798

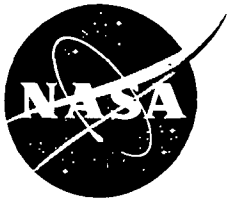

The Identification and Modeling of Visual Cue Usage in Manual Control Task Experiments

Barbara Townsend Sweet
Ames Research Center, Moffett Field, California

September 1999

The NASA STI Program Office ... in Profile

Since its founding, NASA has been dedicated to the advancement of aeronautics and space science. The NASA Scientific and Technical Information (STI) Program Office plays a key part in helping NASA maintain this important role.

The NASA STI Program Office is operated by Langley Research Center, the lead center for NASA's scientific and technical information. The NASA STI Program Office provides access to the NASA STI Database, the largest collection of aeronautical and space science STI in the world. The Program Office is also NASA's institutional mechanism for disseminating the results of its research and development activities. These results are published by NASA in the NASA STI Report Series, which includes the following report types:

- TECHNICAL PUBLICATION. Reports of completed research or a major significant phase of research that present the results of NASA programs and include extensive data or theoretical analysis. Includes compilations of significant scientific and technical data and information deemed to be of continuing reference value. NASA counterpart of peer-reviewed formal professional papers, but having less stringent limitations on manuscript length and extent of graphic presentations.

- TECHNICAL MEMORANDUM. Scientific and technical findings that are preliminary or of specialized interest, e.g., quick release reports, working papers, and bibliographies that contain minimal annotation. Does not contain extensive analysis.

- CONTRACTOR REPORT. Scientific and technical findings by NASA-sponsored contractors and grantees.

- CONFERENCE PUBLICATION. Collected papers from scientific and technical conferences, symposia, seminars, or other meetings sponsored or co-sponsored by NASA.

- SPECIAL PUBLICATION. Scientific, technical, or historical information from NASA programs, projects, and missions, often concerned with subjects having substantial public interest.

- TECHNICAL TRANSLATION. English-language translations of foreign scientific and technical material pertinent to NASA's mission.

Specialized services that complement the STI Program Office's diverse offerings include creating custom thesauri, building customized databases, organizing and publishing research results ... even providing videos.

For more information about the NASA STI Program Office, see the following:

- Access the NASA STI Program Home Page at ***http://www.sti.nasa.gov***

- E-mail your question via the Internet to help@sti.nasa.gov

- Fax your question to the NASA STI Help Desk at (301) 621-0134

- Telephone the NASA STI Help Desk at (301) 621-0390

- Write to:
  NASA STI Help Desk
  NASA Center for AeroSpace Information
  7121 Standard Drive
  Hanover, MD 21076-1320

NASA/TM—1999–208798

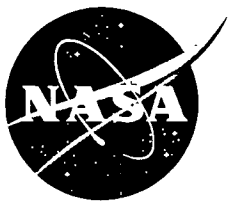

The Identification and Modeling of Visual Cue Usage in Manual Control Task Experiments

Barbara Townsend Sweet
Ames Research Center, Moffett Field, California

National Aeronautics and
Space Administration

Ames Research Center
Moffett Field, California 94035

September 1999

Available from:

NASA Center for AeroSpace Information
7121 Standard Drive
Hanover, MD 21076-1320
301-621-0390

National Technical Information Service
5285 Port Royal Road
Springfield, VA 22161
703-605-6000

Abstract

Many fields of endeavor require humans to conduct manual control tasks while viewing a perspective scene. Manual control refers to tasks in which continuous, or nearly continuous, control adjustments are required. Examples include flying an aircraft, driving a car, and riding a bicycle. Perspective scenes can arise through natural viewing of the world, simulation of a scene (as in flight simulators), or through imaging devices (such as the cameras on an unmanned aerospace vehicle).

Designers frequently have some degree of control over the content and characteristics of a perspective scene; airport designers can choose runway markings, vehicle designers can influence the size and shape of windows, as well as the location of the pilot, and simulator database designers can choose scene complexity and content. Little theoretical framework exists to help designers determine the answers to questions related to perspective scene content. An empirical approach is most commonly used to determine optimum perspective scene configurations.

The goal of the research effort described in this dissertation has been to provide a tool for modeling the characteristics of human operators conducting manual control tasks with perspective-scene viewing. This is done for the purpose of providing an algorithmic, as opposed to empirical, method for analyzing the effects of changing perspective scene content for closed-loop manual control tasks.

The dissertation contains the development of a model of manual control using a perspective scene, called the Visual Cue Control (VCC) Model. Two forms of model were developed: one model presumed that the operator obtained both position and velocity information from one visual cue, and the other model presumed that the operator used one visual cue for position, and another for velocity.

The models were compared and validated in two experiments. The results show that the two-cue VCC model accurately characterizes the output of the human operator with a variety of perspective scenes. The potential of using the model for visual cue identification was also investigated, with promising results. A third experiment was performed to compare perspective displays with more conventional display types.

Nomenclature

a_i	amplitude of ith component in Sum-of-Sines disturbance
$c\Theta$	cosine of Θ
$c\Phi$	cosine of Φ
$c\Psi$	cosine of Ψ
d_i	vector displacement of the ith feature in the image plane
$D(f)$	DTF coefficient of time sequence $\delta(n)$ at the normalized frequency f
D_X	scene feature longitudinal position
D_Y	scene feature lateral position
D_Z	scene feature vertical position
$E(\bullet)$	expected value of $\bullet$
f	normalized frequency (used in Discrete Fourier Transform)
F	focal length
j	square root of -1
J_p	fit quality index of model Y_p to measurement $\hat{Y}_p$
$J_{\theta 1}$	fit quality index of one-cue model $Y_{\theta 1}$ to measurement $\hat{Y}_\theta$
$J_{\theta 2}$	fit quality index of two-cue model $Y_{\theta 2}$ to measurement $\hat{Y}_\theta$
k_i	frequency specifier of ith component in Sum-of-Sines disturbance
K_p	gain parameter in Y_p model
K_α	sensitivity parameter of visual cue α in one-cue model $Y_{\theta 1}$
K_β	sensitivity parameter of visual cue β in two-cue model $Y_{\theta 2}$
K_γ	sensitivity parameter of visual cue γ in two-cue model $Y_{\theta 2}$
$K_{\lambda_\bullet}$	calculated sensitivity parameter of visual cue $\lambda_\bullet$
N	number of points in the time series used for Discrete Fourier Transforms
N_r	number of repetitions used to determine transfer function estimates
$P_{\delta\theta}$	percent of control (δ) power correlated with pitch attitude disturbance (q)
$P_{\delta x}$	percent of control (δ) power correlated with longitudinal disturbance (u)
q	pitch rate disturbance
$Q(f)$	DTF coefficient of time sequence $q(n)$ at the normalized frequency f

r	remnant
$\mathrm{RMS}_{\dot{x}}$	longitudinal velocity root mean square
RMS_x	longitudinal position root mean square
s	the Laplace Transform variable
$se_\bullet$	standard error of $\bullet$
$\mathrm{s}\Theta$	sine of Θ
$\mathrm{s}\Phi$	sine of Φ
$\mathrm{s}\Psi$	sine of Ψ
t	time
T	sampling interval
T_r	data run length
u	longitudinal acceleration disturbance
$U(f)$	DTF coefficient of time sequence $u(n)$ at the normalized frequency f
x	linearized longitudinal position
$X(f)$	DTF coefficient of time sequence $x(n)$ at the normalized frequency f
X	operator longitudinal position
Y	operator lateral position
Y_c	controlled element dynamics
Y_p	operator transfer function between control output and controlled state
$\hat{Y}_p$	experimentally measured operator transfer function between control output and longitudinal position
$Y_{\theta 1}$	one-cue operator transfer function between control output and pitch attitude
$Y_{\theta 2}$	two-cue operator transfer function between control output nd pitch attitude
$\hat{Y}_\theta$	experimentally measured operator transfer function between control output and pitch attitude
Z	operator vertical position

Greek:

α	visual cue for position and motion in one-cue model
β	visual cue for motion in two-cue model
γ	visual cue for position in two-cue model

δ	operator output (control)
ϵ	estimated transfer function measurement error
ζ_N	damping of neuromuscular dynamics in Y_p model
θ	linearized pitch attitude
Θ	pitch attitude
$\Theta(f)$	DTF coefficient of time sequence $\theta(n)$ at the normalized frequency f
$\lambda_\bullet$	linearized visual cue based on nonlinear visual cue $\Lambda_\bullet$
Λ	visual cue
$\Lambda_{\Delta h}$	visual cue based on the horizontal displacement between two features
$\Lambda_{\Delta v}$	visual cue based on the vertical displacement between two features
Λ_h	visual cue based on the horizontal displacement of a feature
Λ_s	visual cue based on the displacement of a feature along a line of splay
Λ_v	visual cue based on the vertical displacement of a feature
ρ_i	phase of ith component in Sum-of-Sines disturbance
$\sigma_\bullet$	standard deviation of $\bullet$
τ	time delay of human operator in Y_p model
ϕ_m	phase margin
ϕ_{yy}	power spectral density of $y(t)$
ϕ_{yz}	cross spectral density of $y(t)$ and $z(t)$
Φ	roll attitude
Ψ	heading
ω_c	crossover frequency
ω_s	sampling frequency
ω_L	lead equalization break frequency in Y_p model
ω_N	natural frequency of neuromuscular dynamics in Y_p model

Abbreviations:

CM	Crossover Model
dB	decibels
DFT	Discrete Fourier Transform
DTF	Discrete Transfer Function

OCM	Optimal Control Model
rad	radians
rms	root mean square
sec	seconds
VCC	Visual Cue Control

Contents

List of Figures

List of Tables

Chapter 1

Introduction

Little is known about how humans extract information from a perspective scene, particularly to perform closed-loop manual control tasks. Examples of perspective scenes include computer generated imagery (commonly used in simulators), camera images, and natural viewing of a scene (such as out of the window of an aircraft). Manual control refers to activities in which the human makes nearly continuous adjustments to a controlled element (e.g. aircraft) through a control inceptor (e.g. joystick), in order to produce some desired outcome (e.g. tracking or regulation).

Better understanding of how humans use information in a perspective scene can be important for several reasons. The content of a perspective scene is often a design choice. Airport and heliport markings constitute manipulation of perspective-scene content for real-world applications. Designers of simulators and associated databases for out-the-window scene generation make choices concerning scene content, complexity and update rate. And designers of unmanned aerospace vehicle (UAV) control systems have choices to make concerning the field of view, resolution, dynamic range, and update rates of imaging technologies. Currently, decisions related to perspective-scene content are frequently made with an empirical approach, in which multiple potential configurations are tested. Very little theoretical framework exists to enable designers to make informed *a priori* decisions in these types of applications.

The purpose of the research described herein was to advance the fundamental knowledge of this subject, and from there to develop a basic new tool to aid in the

design of the most cogent perspective-scene content. Specifically, this dissertation describes an experimental program in which a new methodology for modeling and identification of visual-cue usage in a manual control task was developed. Chapter 1 contains introductory information, including a review of relevant related work. Chapter 2 contains the derivation of two forms of a visual-cue-usage model. Chapters 3 and 4 describe two experiments that were conducted to identify and validate the most appropriate model. Chapter 5 describes an experiment in which the perspective display was compared with more conventional displays. Chapter 6 contains discussion of the results of the experiments, and some of the implications of these results. Chapter 7 contains conclusions from this research, a summary of the fundamental contributions it has made, and recommendations for future work.

1.1 Background

The work described in this dissertation, as well as the prior art, has relied heavily on two different disciplines. The first discipline is Psychophysics, which is the study of the mapping between physical stimuli and the psychological response to those stimuli. The second discipline is Manual Control, which is the study of human behavior when controlling a system that requires constant control inputs. Psychophysics is relevant because it has generated much understanding as well as mathematical models of perspective scene perception. Manual control is relevant because it provides a framework for analyzing the behavior of the human operator in performing a manual control task, given the information gleaned through visual perception of the perspective scene.

In the following sections, both Psychophysics and Manual Control will be discussed, and particularly relevant portions of each topic will be reviewed in detail. Then previous work that is considered relevant prior art will be discussed separately. The work that falls into this category has two distinct qualities; modeling of perspective-scene perception, and modeling of manual control based on the scene perception.

This chapter does not feature an extensive or inclusive review of displays, manual

control, or visual perception; for the most part, only the most directly relevant information from these topics is presented. Several sources are recommended if the reader wishes to obtain more extensive information. [1] contains an overview of research on the effects of control dynamics and display types on performance. [2] is a survey of research related to modeling of control behavior with various types of displays. [3] contains a summary of manual control models beyond the two models reviewed in this dissertation; [4] summarizes human supervisory control models. [5] contains an introductory overview of visual perception, while [6] is probably the best source of information on ecological psychophysics related to self-motion perception and control.

1.1.1 Ecological Psychophysics

Psychophysics as a discipline dates back more than 100 years. Just as engineering has evolved into several areas of specialization, psychophysics also has particular disciplines within it. Specifically, the work described in this thesis relies on the field of Visual Psychophysics, which is simply the study of the effect of light (the physical stimuli) on visual perception (the psychological response).

Several approaches to understanding and modeling visual perception have been advanced within the field of visual psychophysics. One such approach, often termed the "Information Processing" approach, encompasses empirical studies on the sensitivity of animals and humans to constrained stimuli, models to describe observed responses, and neurological studies to determine what functions the brain performs in visual perception. This approach has great relevance to a range of problems (such as image processing), but does little to describe how humans and animals draw upon this visual perception to perceive more about the complex world around them.

At the beginning of World War II, there was an intense interest in reducing the rate at which aviator candidates were washed out of the program. James J. Gibson, a perceptual psychologist drafted to serve in the war, was tasked with developing perceptual tests to administer to aviator candidates. The focus of Gibson's research effort quickly turned to depth and distance perception, which many believed to be critical to the landing task. However, none of the tests devised to measure these

perceptual capabilities proved to be successful in predicting a prospective pilot's capabilities. Work that Gibson performed in this area [7], coupled with research he had performed before and after the war, eventually lead to the development of a new theory of psychophysics which would become known as Ecological Psychophysics. Gibson advanced a set of hypotheses [8], which he called the " 'Ground Theory' of Space Perception". He described it as "the possibility that there is literally no such thing as a perception of space without the perception of a continuous background surface". The five initial hypotheses of this theory are presented below:

1. The elementary impressions of a visual world are those of surface and edge.

2. There is always some variable in stimulation (however difficult it may be to discover and isolate) which corresponds to a property of the spatial world.

3. The stimulus-variable within the retinal image to which a property of visual space corresponds need be only a correlate of that property, not a copy of it.

4. The inhomogeneities of the retinal image can be analyzed by the methods of number theory and modern geometry into a set of variables analogous to the variables of physical energy.

5. The problem of how we perceive the visual world can be divided into two problems to be considered separately: first, the perception of the substantial or spatial world, and, second, the perception of the world of useful and significant things to which we ordinarily attend.

This approach for understanding visual perception was quite different from the information processing approach taken by his predecessors. Most of the previous work had been done without taking the context of the perception into account; Gibson's approach made consideration of context an essential element in understanding perception. One central concept of this theory, best exemplified in hypotheses 2 and 3 above, is that we can find characteristics in the stimulation that correlate with some desired property of the spatial world. This concept was carried further by one of Gibson's students, Rik Warren. Warren developed a detailed mathematical description of the optical transformations occurring in rectilinear motion [9, 10]. Other

researchers (including Gibson) had developed expressions for optical invariants for various particular cases (such as constant-altitude flight); Warren's contribution was to formalize a more general description of the optical transformations for the purpose of determining potential optical invariants.

Much of the work done in ecological psychophysics has addressed human locomotion, both natural (e.g., walking, running) and vehicle-based. An excellent review of the relevant work related to human locomotion up to 1990 can be found in [6]. However, some researchers have focussed primarily on the optical information available for the more complex task[1] of flying an aircraft. One task that has received a great deal of attention is the approach to landing, particularly the problems of glidepath control and touchdown-point estimation. Gibson addressed this task in both his work for the Army and later work [11, 12]. Calvert was another researcher, working for the Royal Aircraft Establishment, who studied the approach-to-landing task [13, 14]. Both Gibson and Calvert approached this task from the standpoint of visual-cue identification (i.e. identifying patterns in the visual scene that would allow estimation of relevant parameters such as touchdown aimpoint).

Havron combined the optical information available in the landing scene with measurements of visual perceptual thresholds. In the summary of [15], he succinctly describes his approach:

> Formulae are presented which describe the apparent speeds of movement of ground objects during final approach. Next, human factors data are brought together to estimate perceptual thresholds for movement. Speeds of movement expressed as iso-velocity curves are then compared with perceptual thresholds of motion to evaluate the effectiveness of guidance that the apparent expansion pattern of earth can provide for touchdown point, heading and flare-out.

Naish [16] used a very similar approach to examine the geometrical properties of the runway outline projected onto the forward view. He developed predictions of the saliency of a number of visual cues based upon human perceptual thresholds. The

[1] Presumably more complex than walking or running

tasks he considered were related to lateral and vertical path positioning. Others have used more complex human perceptual models to examine the approach-to-landing task. Perrone applied models of slant misperception [17, 18] to the "black-hole" landing [19, 20]. This situation can occur at night when only the runway outline is illuminated. Galanis [21] developed a perceptual model for glideslope estimation in an impoverished scene, using a weighted average of the geometrical relations within the scene.

Another aviation-related task that has received much attention within the psychophysics community is altitude control. The literature in this area is quite extensive, and a thorough review is beyond the scope of this dissertation. Much of the relevant work in this area has been summarized in [6]. Owen [22], Johnson [23, 24], and Flach [25] have done empirical work based upon the functional optical invariant analysis techniques developed by Warren. While much of the prior work related to judgment of altitude has relied upon passive judgments, Johnson and Flach have focused more on the active-control paradigm. The basic experimental approach used by these researchers has been to 1) develop a candidate set of optical invariants to be evaluated, 2) design test stimuli with combinations of these optical invariants present, and 3) correlate the observed performance with the invariants. This approach has typically not included any modeling of the human operator's control behavior, with one exception. Johnson and Phatak used the results of one of these experiments [24] to demonstrate the efficacy of a combined manual control/perception model [26]; this is discussed further in Section 1.1.3.

Other researchers have expanded these methodologies further, applying optimal estimation theory to describe perspective scene viewing. This approach has been used to incorporate the effects of both perceptual thresholds and attention sharing. Since the researchers who have developed this approach have also considered closed-loop manual control, this work will be further discussed with the other prior art in section 1.1.3.

1.1.2 Human Operator Models

Human operator modeling started with Tustin in the late 1940's. In developing systems to aid gunners performing target tracking, Tustin discovered that the control behavior of the human could in many cases be modeled with simple linear servomechanisms [27]. Several models have since been developed to describe the strategy a human operator adopts in a closed-loop manual control task (a summary of human operator modeling for manual control tasks can be found in [3]). Two of these models will be briefly described.

Crossover Model

McRuer and several colleagues developed what they called the Crossover Model (CM) over a period of approximately 20 years; [28] contains a comprehensive summary. McRuer conducted extensive experiments with human operators controlling plants with varying dynamics, forcing functions, and differing levels of system complexity. The goal of this work was to understand and model the compensation that humans adopt in manual control tasks.

Conceptually, McRuer represented the human operator in a manual control system with components that were related to known processes and systems (Figure 1.1(a)). This conceptual model accounts for sensory processes (perception), equalization (control strategy), and the dynamics of the limb manipulating the controller. While useful for visualizing the human as a control element, this idealization is not particularly useful for measurement and model identification. The processes shown are known to be, in some situations, highly nonlinear, and the inner-loop states are, at best, difficult to measure.

The approach adopted by McRuer was to represent the output of the human operator with two components: 1) the component of the response that is linearly correlated with the forcing function, and 2) the remainder, termed the remnant. Figure 1.1(b) shows an equivalent block diagram of Figure 1.1(a), in which the output of the human operator is represented with these two components. The dynamics of the display (if any) are included with the controlled element dynamics as a single, linear,

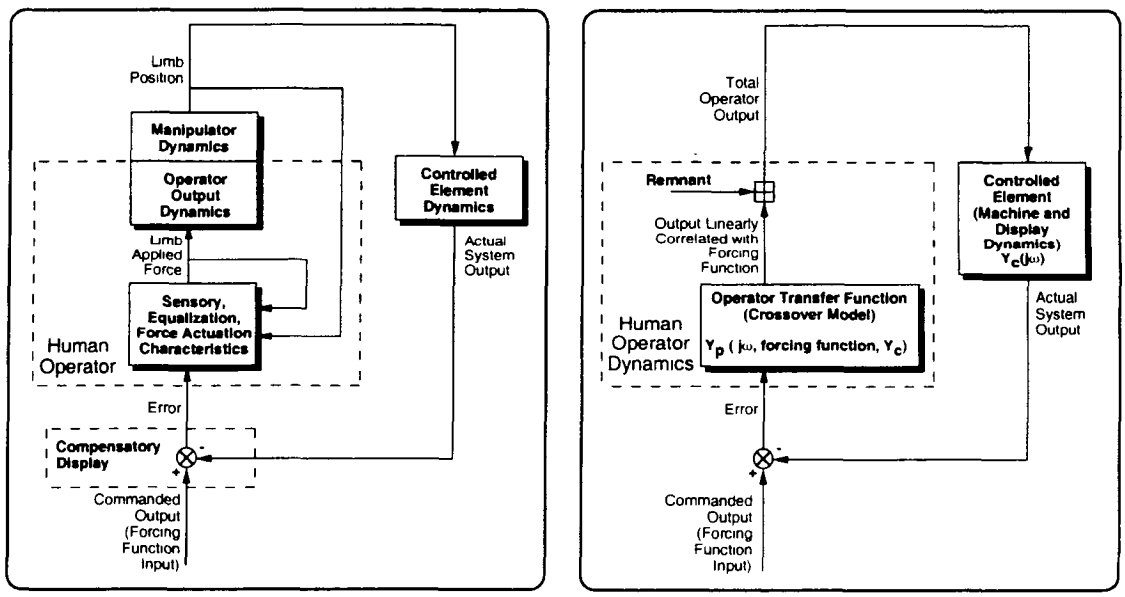

(a) Idealized manual control system using a compensatory display.

(b) Equivalent block diagram.

Figure 1.1: Two depictions of the human operator performing a compensatory task. The figure on the left (a) depicts an idealized block diagram of the system. The figure on the right (b) depicts an equivalent block diagram of the system, useful for measurement and identification.

constant coefficient element Y_c. The dynamic element Y_p is used to represent the linear compensation the human operator adopts. Factors that have been demonstrated to appreciably affect Y_p are the controlled element Y_c, the forcing function characteristics, and the frequency of the input.

McRuer found that the characteristics of Y_p tended to vary systematically as a function of these factors. He advanced a model for Y_p, that consists of two elements:

1. A general parameterized linear model form (a function of frequency, $j\omega$), and
2. A series of adjustment rules to set the model parameters for the particular situation

These adjustment rules account for the controlled element Y_c and the forcing function[2].

The first (and simplest) linear model form that was advanced from this effort specified that the human operator tended to adjust his or her compensation (Y_p), such that, in the input-frequency region of crossover (loop gain = 1), the combined open-loop transfer functions of the operator and controlled element (Y_c) had the form:

$$Y_p(s)Y_c(s) = \frac{\omega_c e^{-\tau s}}{s} \tag{1.1}$$

Equation 1.1 is the essence of the Crossover Model.

The crossover frequency ω_c is defined as the frequency at which the magnitude of the combined human operator and controlled element dynamics are equal to one; that is:

$$|Y_p(j\omega_c)Y_c(j\omega_c)| = 1 \tag{1.2}$$

The parameter τ in Equation 1.1 represents the human time delay, which is the lumped contribution of perceptual delays, neuromotor delays, and any other higher frequency lags. The adjustment rules for the selection of parameters will not be discussed here, but are available in [28].

[2] Y_p can also be time-varying, due to factors such as training (i.e. the process of skill acquisition constantly changes Y_p) and fatigue. These effects of these factors can (fortunately) typically be controlled through operator selection and training. The manipulator dynamics have been shown in most cases to cause second-order effects, and are typically not accounted for.

Further experimentation by McRuer and others yielded a more complex model form, called the Precision Model:

$$Y_p(s) = K_p e^{-\tau s}\left(\frac{T_L s+1}{T_I s+1}\right)\left(\frac{T_K s+1}{T'_K s+1}\right)\frac{1}{(T_{N_1} s+1)\left((\frac{s}{\omega_N})^2+\frac{2\zeta_N s}{\omega_N}+1\right)} \tag{1.3}$$

The terms T_L and T_I represent the basic lead and lag equalization capabilities the human provides. The terms T_K and T'_K represent a low-frequency lag-lead equalization that is sometimes observed called the low-frequency "phase droop". This typically appears when the forcing-function bandwidth increases. The terms T_{N_1}, ω_N, and ζ_N represent the neuromuscular dynamics. K_p represents the gain the operator adopts, and τ is a lumped time delay representing pure time delays in both the perceptual and neuromuscular systems. The Precision Model was developed specifically to allow precise fitting of data in frequency ranges well above and below the crossover frequency.

Although Equation 1.1 was termed the Crossover Model when it was first published, the term Crossover Model has become synonymous with the spectrum of models developed by McRuer and his colleagues. A modified Crossover Model as well as a form of the Precision Model are used in the analysis described in this dissertation.

Optimal Control Model

Another model that has been developed to model human compensation in closed-loop control is the Optimal Control Model (OCM). It had been noted by most researchers in human operator modeling that the compensation the human adopts is similar to the compensation that an experienced designer would put into an inanimate compensator element. Kleinman, Baron and Levison [29] used optimal-control techniques to develop a model of human compensation in manual control situations. One element of the model that sets it apart from the Crossover Model is the assumption that the human acts as an optimal estimator, reconstructing the system state from the observations.

Both types of model can achieve the same results: The dynamics represented in the precision model can usually be duplicated with the OCM with proper selection

of weighting matrices, noise covariances, and time delays. The choice of model to use often depends upon the desired result. The Crossover Model is better suited for parameter identification, but requires specifying the model structure explicitly. The OCM is more easily adapted to represent complex systems, and is particularly well suited to studying the effects of adjusting system characteristics. Both of these modeling approaches have been used to study manual control with perspective scene viewing; this work will be reviewed in the next section.

1.1.3 Prior Art

This subsection will discuss prior work that has the most direct relevance to the work described in the dissertation. The defining features of the work included in this section are 1) modeling of perception[3] of a perspective scene, and 2) modeling of closed-loop manual control using the perspective scene perception (as opposed to the explicit display of measured states). A common element of all of the work described in this section is to directly account for perspective scene viewing by modeling the perspective projection of the world into an image (or natural viewing).

The approach necessary to incorporate perceptual scene viewing with manual control was well understood by the developers of the manual control models. In 1974, McRuer demonstrated an understanding of this approach for modeling of manual control using visual scenes [30]:

> "The inputs sensed for VFR conditions are currently estimated on the basis of control needs (i.e., what feedback paths are necessary or desirable for the closed-loop system). The actual quantities perceived are likely to be linear combinations of these, with the weightings between the inputs fixed by the geometry and perspective rather than being independently adjustable by the pilot. These aspects of perception can have profound effects on the closed-loop analysis of various maneuvers (e.g., approach, landing, dive bombing, etc.)."

[3] In this context, perception is defined as the process by which a human operator obtains information, for the purpose of performing closed-loop manual control.

Baron [31] also suggested an approach to account for viewing of a perspective scene in closed-loop-control modeling with the human. The approach was to use the perspective transformations to identify the linearized components of each visual cue to construct the measurement matrix. Visual perception thresholds, where appropriate, were suggested to provide the observation noise covariance parameters. These measurements were then combined with human OCMs.

The first part of the following section reviews work in which the OCM has been used, as suggested by Baron, to model closed-loop manual control with natural scene viewing. The second part reviews work in which the Crossover Model is applied to model closed-loop manual control. The fundamental difference in these approaches is the philosophy of how the human applies the information: do humans do a reconstruction of the system state (including vehicle dynamics and disturbances), then use the reconstructed state to formulate a feedback solution? Or do humans find cues in the visual scene that correspond to the desired state, and use this cue directly in the feedback solution? The second view is the hypothesis embraced in this dissertation. As will be seen, relatively little work based on this second approach has been done previously. However, the work done with the OCM is highly relevant, since the process of constructing a "measurement" from the image or scene is quite similar in both approaches.

Optimal Control Model

Although the OCM for a human was developed after the Crossover Model was, it was the first model to be combined with perspective scene viewing. Grunwald and Merhav [32, 33] developed an optimal controller and estimator model of lateral control of a remotely piloted vehicle (RPV) using visual field cues. This model was validated and modified with the results from an experimental evaluation, and could generally be adjusted to provide good correspondence with the experimental data. Grunwald and other colleagues have conducted a series of design and evaluation efforts of combined perspective scenes and display symbology. In much of this work, Grunwald determines what essential control elements are present in the unaugmented perspective scene, and determines ways to improve closed-loop control either through

adding perspective scene elements (such as tunnel-in-the-sky displays), or presenting state information not available in the scene (such as accelerations) through predictor or other symbology. Grunwald and Merhav [34, 35] considered augmentations to the visual field cues for lateral control of an RPV. The tunnel-in-the-sky[4] display concept has been examined for helicopter approaches [39, 40], and aircraft approaches [41, 42, 43]. Negrin and Grunwald [44] developed a perspective cueing structure to aid helicopters performing shipboard landings using visual cue analysis. Grunwald and Kohn also investigated the role of different cueing elements in low-altitude visual flight [45, 46].

Wewerinke also applied optimal control modeling to examine the utility of a set of simplified visual cues for use in the approach-to-landing task [47, 48]. He later extended this analysis to the development of HUD symbology to augment the information available in the visual scene for both good and poor visibility conditions [49]. Both of these efforts included experimental validation of the model. Wewerinke used measured perceptual thresholds of particular visual cues to make *a priori* predictions of the observation noise covariance.

Baron, Lancroft, and Zacharias [50] developed an extensive OCM of the pilot in a simulator (which featured both a motion system and computer-generated visual images). The visual-scene-perception model accounted for several nonlinear processes: visual resolution, visual discrimination, quantization in the display (due to rasterization), and limitations to the field of view (FOV). Zacharias later extended several of the concepts introduced in this work into two different models of human visual scene perception. The first model, known as LINMOD, was used to describe visual perception of line segments [51]. The model was based upon the assumption that the operator could observe four aspects of a line segment; length, orientation, and 2-D location of the midpoint. The second model, TEXMOD, modeled perception of a visual flowfield, as is thought to be perceived when the operator is translating or rotating relative to the world [52, 53]. He later applied both of these models with

[4]While Grunwald was the first researcher to combine models of perspective scene viewing of tunnels with manual control models, numerous other researchers have examined the tunnel-in-the-sky concept. It was first studied by Wilckens [36]. Recent research efforts have included in-flight demonstration and evaluation by at least two research teams [37, 38].

OCMs to the altitude control task in low-level high-speed forward flight [54, 55]. An informative review of Zacharias' optimal-control modeling approach and experimental results can be found in [56].

Crossover Model

The first perceptual scene modeling combined with the Crossover Model was done by Johnson and Phatak [26]. They conducted an experiment in which altitude control with various types of ground textures was examined [24]. For one particular subject and ground texture, they showed that the operator's strategy could be closely modeled with a visual-cue model. This technique has the greatest similarity to the work described herein. The similarities include the use of sum-of-sines input signals for operator transfer function identification, linearization of perspective transformations for linearized visual-cue analysis, and preliminary identification of a visual cue based upon the transfer functions. In this dissertation, the experimental approach outlined by Johnson and Phatak is extended to identify multiple visual cues, with a much larger pool of operators and a larger number of visual scenes.

Mulder [57] has also combined Crossover Models with perspective scene viewing models. Mulder has studied the performance of subjects with various tunnel-in-the-sky symbologies, making *a priori* predictions on which tunnel display features would be susceptible to interference effects from combined lateral and longitudinal control tasks. Mulder used the Crossover Model to determine if any systematic changes in the pilot transfer function model parameters such as crossover frequency and phase margin occurred as a result of changing display conditions. This work did not include any identification of visual cues, or explicit modeling of visual-cue usage.

1.2 Objectives and Approach

There were three main objectives that motivated the work contained in this dissertation. They were:

- To develop a simple new model to characterize accurately manual control with perspective scene viewing.
- Validate the model with a variety of operators and conditions.
- Identify potential visual-cue combinations through application of the model to experimental data.

In this dissertation, a model that accounts for perspective scene viewing in a manual control task is developed. The model is termed the Visual Cue Control (VCC) model; it combines the previously described Crossover Model with a model of perspective scene viewing and visual cue selection. Two different forms of this model are developed and tested. One model form, termed the one-cue model, is based upon the assumption that the operator obtains both position and velocity from one visual cue on the perspective display. The other model, termed the two-cue model, is based upon the assumption that the operator uses one visual cue for position, and another for velocity. Both models incorporate the Crossover Model, and are partially described by the parameters in this model. The models can be differentiated from each other by an additional function which accounts for the perspective scene viewing. This function is characterized in the one-cue model by the specification of one additional parameter (called K_α); the two-cue model features two additional parameters (called K_β and K_γ).

The models are validated and compared by 1) experimentally measuring the transfer functions describing the human operator input/output characteristics, 2) fitting parameters of each model to the measurements. The resulting models are evaluated in two ways. First, the ability of each model form to fit the measurements is assessed. Then, the consistency of the identified parameters with the adjustment rules of the Crossover Model, and the expected values of the parameters from the perspective-scene characteristics, is assessed. In many cases, it will be shown that the identified parameters correspond to the values expected for particular visual cues.

The validation approach taken is quite similar to that described by Johnson and Phatak [26]. The present work departs from the previous work in two primary areas. First, the previous work applied to one operator in one condition. One objective

of the current work is to apply the model to a number of operators and a range of conditions. Second, the previous work identified only one cue being used; the present work expands the model to include two visual cues. It will be shown that the two-cue model is required to describe most of the experimental conditions.

1.3 Contributions

The unique contributions made with this work include:

- Development of a simple model which for the first time accurately characterizes human manual control through perspective scene viewing using a combination of cues, not just a single cue.
- Development of more-comprehensive knowledge through a more complete data set, with more statistical power, than the prior art.
- First detailed understanding through examination of visual cues, of the longitudinal position-control task using a perspective scene.
- An improved understanding of the differences and similarities between perspective and compensatory displays.
- Development of simplified parameter-identification procedures.
- Demonstration of a methodology to identify visual cues used in a manual control task.

Chapter 2

The Visual Cue Control Model

The purpose of the work described in this dissertation is to provide a better understanding of this process by which we use perspective scenes for manual control. Specifically, the goal is to model the input/output characteristics of the operator performing a manual-control task while viewing a perspective scene. This model, termed the Visual Cue Control (VCC) model, is based upon the hypothesis that the human operator finds visual cues that correspond to the desired state, and uses the cues in place of explicit state information (which is not available) to formulate a control strategy. The model of the process is created by combining the Crossover Model with a model of perspective-scene viewing and visual-cue selection.

Before proceeding into the model development, it is worthwhile focusing attention on a particularly important concept. The term "visual cue" is used extensively in this dissertation. *A visual cue is, in essence, any definable feature or characteristic of the visual scene.* Student pilots learn to use the position and orientation of the "line" made by the outside horizon, relative to the windscreen of the aircraft. The orientation of the line correlates with roll attitude, and the height of the horizon line in the windscreen correlates with pitch attitude. Likewise, the displacement of a distant feature relative to the centerline of the windscreen correlates with the heading. The horizon-line attitude references, and heading reference, are examples of visual cues useful for attitude determination.

Other cues can aid position determination. Consider the case of a hover. A feature

located in front of the operator would have a nominal position in the image. If the operator moved forward, the feature would move down in the image; if the operator moved back, the feature would move up. While the position of this feature in the image is certainly correlated with the horizontal position of the operator, changes in other vehicle states can also cause the feature to move in the image; specifically, the vertical position of the feature would be affected by both altitude and pitch in addition to horizontal position. Thus, in order to visually control longitudinal position using the feature as a reference, the operator needs to isolate the effects of the various degrees of freedom on the displacement of the feature in the image. This is obviously a task that can be accomplished; the goal of the present work is to provide a better understanding of how this is done.

As will be seen, this chapter contains the development of a model that is based upon the assumption that a separate visual cue is being used to detect motion. This concept defies easy description, but it can be likened to the use of peripheral vision to detect motion in some portion of the image. That is, the operator likely fixates on some feature of the image to provide a visual cue for good positional guidance, then uses motion of the entire image, or in a particular part of the image viewed in the periphery, as another visual cue.

These simple, qualitative descriptions will later be distilled into a set of very simple, quantitative models. These models will in no way capture the complexity or richness of the human perceptual process, but rather isolate the minimal elements necessary to describe the elements of the human operator being modelled (the input/output characteristics).

The modeling approach adopted is to modify the Crossover Model to directly account for the effects of perspective scene viewing. Figure 2.1(a)[1] depicts an operator performing a disturbance rejection task using a compensatory[2] display; Figure 2.1(b)

[1]The system depicted in Figure 2.1(a) is mathematically equivalent in form to Figure 1.1(a). The system shown in Figure 2.1(a) can be made equivalent to Figure 1.1(a) by 1) transforming the forcing function through the negative inverse of the controlled element, and 2) using it to replace the commanded state in Figure 1.1(a). This new representation is developed to correspond with the perspective-display-viewing condition.

[2]The term compensatory display is used even though there is no commanded input; in this case, the commanded input is zero, and the forcing function is being injected instead as a disturbance to

depicts the same task with a perspective display. With the compensatory display, the operator is viewing only direct measurements of the system output (i.e., controlled state). The perspective display, on the other hand, will generally be affected by *all* of the vehicle states, potentially even ones that are not being directly controlled. This is depicted in the figure with the injection of an additional disturbance as an uncontrolled state. Mathematically, the case of perspective-display viewing is fundamentally different in two ways: 1) the perspective display is affected by both controlled and uncontrolled states, and 2) the perspective display performs a nonlinear transformation on these states. The transformation typically couples the states to such an extent that there are rarely characteristics of the perspective scene that exhibit a one-to-one correspondence with a particular state.

Two different perspective-based model forms will be developed and tested in this dissertation. One model form, termed the one-cue model, will be based upon the assumption that the operator obtains both position and velocity from one visual cue on the perspective display. The other model form, termed the two-cue model, will be based upon the assumption that the operator uses one visual cue for position, and another for velocity. The one-cue and two-cue models take the form of parameterized transfer functions. Both model forms incorporate the Crossover Model, and are partially specified by the parameters of the Crossover model. The models differ from each other through an additional function, which is an outcome of the perspective display and visual-cue selection process: The one-cue model is specified by one additional parameter, and the two-cue model is specified by two additional parameters. These parameters are directly related to the visual cues.

Determination of which (if either) model form is accurate must be done experimentally. This experimental validation is done by fitting parameters of both models to measurements of the input/output characteristics of the human operator. As the models are based upon the Crossover model, one would expect the input/output characteristics to be sensitive to the same factors that have been shown to affect the Crossover Model parameters. Additionally, the human-operator characteristics should be sensitive to changes in the visual cue selected, and to characteristics of

---

the controlled element.

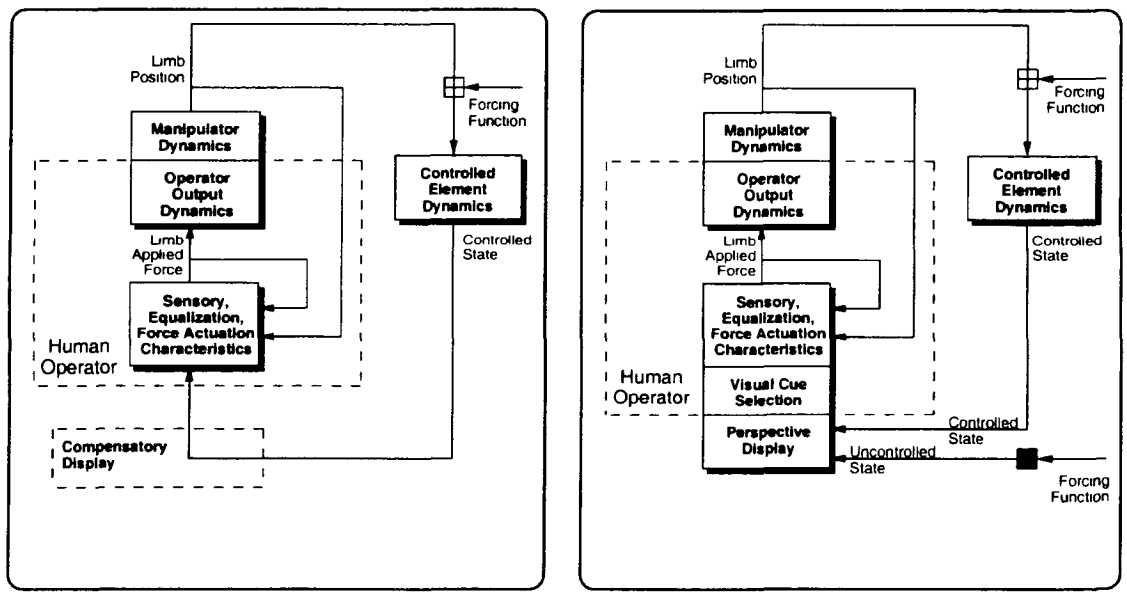

(a) Compensatory display

(b) Perspective display

Figure 2.1: Two idealized manual control systems, depicting a regulation task in the presence of disturbances. The figure on the left (a) depicts the operator presented with a compensatory display. The figure on the right (b) depicts the operator presented with a perspective display. The two forcing functions represent independent wind-gust disturbances.

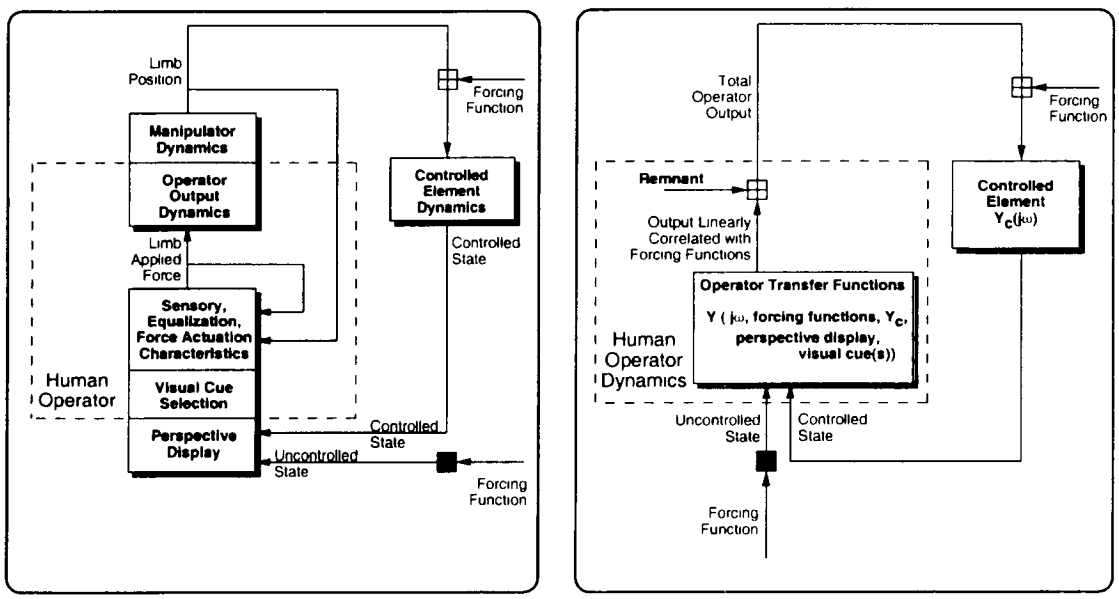

(a) Idealized manual control system using a perspective display.

(b) Equivalent block diagram.

Figure 2.2: Two depictions of the human operator performing a manual control task while viewing a perspective display.. The figure on the left (a) depicts an idealized block diagram of the system. The figure on the right (b) depicts an equivalent block diagram of the system, useful for measurement and identification.

the perspective display. Figure 2.2(a) shows the conceptual diagram of the VCC model, alongside an equivalent block diagram (Figure 2.2(b)) which illustrates the input/output function dependencies.

This chapter contains the development of the models and tools necessary to specify and validate the VCC model. Section 2.1 contains a description of the task that was used for model development and experimentation. Section 2.2 contains the derivation of a linearized model that accounts for the perspective display and visual-cue selection. In Section 2.3, this model is combined with the Crossover Model to create two different VCC model forms, the one-cue model and the two-cue model. Section 2.4 describes the measurement techniques used for experimental validation of the model forms. Section 2.5 contains an analysis of what parameter values are expected for a small subset of visual cues.

2.1 Task

The task considered here is an idealized hover of a helicopter-like vehicle, say, in the presence of disturbances (in Figure 1.1(a) or 1.1(b) this means commanding the output to be zero). The only degrees of freedom allowed were longitudinal motion and pitch; all other degrees of freedom were assumed held constant by other controls. The transfer functions representing the vehicle dynamics are taken to be:

$$x(s) = \frac{1}{s(s+0.2)}[\delta(s) + u(s)] \tag{2.1}$$

$$\theta(s) = \frac{1}{s}q(s) \tag{2.2}$$

δ is the joystick displacement, x is the longitudinal position in eyeheights[3], and θ is the pitch attitude in radians. In this task, θ and x were taken to be independent of each other. u is a disturbance to the longitudinal acceleration in units of eyeheights/sec^2, and q is a disturbance in pitch rate in units of rad/sec.

Operators were instructed that the vehicle they were controlling was not any real vehicle; the vehicle moved forward when the joystick moved forward, and aft when

[3]For a constant-altitude task, it is convenient to scale distances relative to the altitude, or height, of the eyepoint of the operator. This is discussed in more detail in Section 2.2.

the joystick moved aft. They were told that there would be longitudinal wind gusts as well as pitch disturbances, but the pitch did NOT affect the fore-aft motion, and they were NOT controlling pitch. Pitch and longitudinal motion were decoupled to facilitate visual-cue identification. The disturbances $q(s)$ in pitch rate and $u(s)$ in longitudinal acceleration (e.g., from the wind gusts) were each made up of a sum of 12 sines, with unique frequencies for each disturbance, to facilitate measurement of the operator response relative to the two degrees of freedom. Specific details of the disturbance spectrums, as well as the discrete transfer functions used to simulate the dynamics for Experiments 1 and 2, are contained in Sections D.1 and E.1 of Appendices D and E, respectively.

2.2 Perspective Visual Cue Selection Model

This section contains the development of a model to characterize the process of perspective-display viewing and visual-cue selection. This is done by defining a visual cue to be some characteristic of the perspective scene, and then determining the transformation between the relevant perspective-scene characteristics and the controlled and uncontrolled states, through the process of perspective projection.

The perspective projection process can occur through 1) natural viewing of a scene, 2) camera imaging, or 3) computer-generated imagery. It is the process by which the 3-D coordinates of world features are transformed into 2-D image coordinates [58]. These image coordinates can be on a display, as in the case of a camera image or computer-generated imagery, or with the proper projection parameters, on the human's retina. The current analysis will include only the case of Computer Generated Imagery (CGI). This implies that the surface onto which the image is projected is assumed to be flat (as in camera imagery or CGI) as opposed to curved (as with the retina).

The factors that affect the perspective projection are: 1) the locations of scene features, and 2) the location and orientation of the imaging device, and 3) the imaging device characteristics. The imaging device characteristics can include field of view and/or focal length, and are typically constant for a particular situation. The scene

features descriptions are typically available relative to a fixed, or world, coordinate system. Another coordinate system fixed in the vehicle being controlled is useful to describe the motion of the vehicle (in which the camera is located) relative to this fixed coordinate system. One coordinate system description which has been widely adopted in the field of aeronautical engineering is described by the Eulerian Angles [59].

In Appendix A, the general transformations between the position of scene features in world coordinates, position and orientation of the operator relative to the world coordinates, and the position of the feature in the image are derived. These relatively complex relationships, contained in Equations A.4 through A.6, are of course greatly simplified by taking into account the constraints of the task under consideration. This (purely geometrical) situation is represented in Figure 2.3. With these simplifications, the relationship defining the image-plane coordinates of a particular scene feature become:

$$y_i = -\frac{FD_Y}{((D_X - X)\mathrm{c}\Theta - \mathrm{s}\Theta)} \tag{2.3}$$

$$z_i = -\frac{F((D_X - X)\mathrm{s}\Theta + \mathrm{c}\Theta)}{((D_X - X)\mathrm{c}\Theta - \mathrm{s}\Theta)} \tag{2.4}$$

in which F is the focal length, X is the longitudinal position of the operator, D_X and D_Y are the longitudinal and lateral locations, respectively, of a scene feature. The expressions $\mathrm{s}\Theta$ and $\mathrm{c}\Theta$ denote the sine and cosine of Θ, respectively. For this task, the only degrees of freedom are longitudinal position and pitch attitude. Altitude is held constant, and the distances X, D_X and D_Y can be scaled in units of eyeheights, making $D_Z = 1$.

A visual cue is defined to be some function of the image-plane coordinates, which are in turn functions of the operator state and scene features. The visual cue Λ is represented as follows:

$$\Lambda = G_{\text{image}}(y_i, z_i) = G_{\text{world}}(X, \Theta, D_X, D_Y, F) \tag{2.5}$$

$G_{\text{image}}(\bullet)$ represents an arbitrary function of the image-plane coordinates (y_i, z_i). $G_{\text{world}}(\bullet)$ represents the same function but expressed in terms of the "world" characteristics, specifically the position and orientation of the operator (X, Θ), position

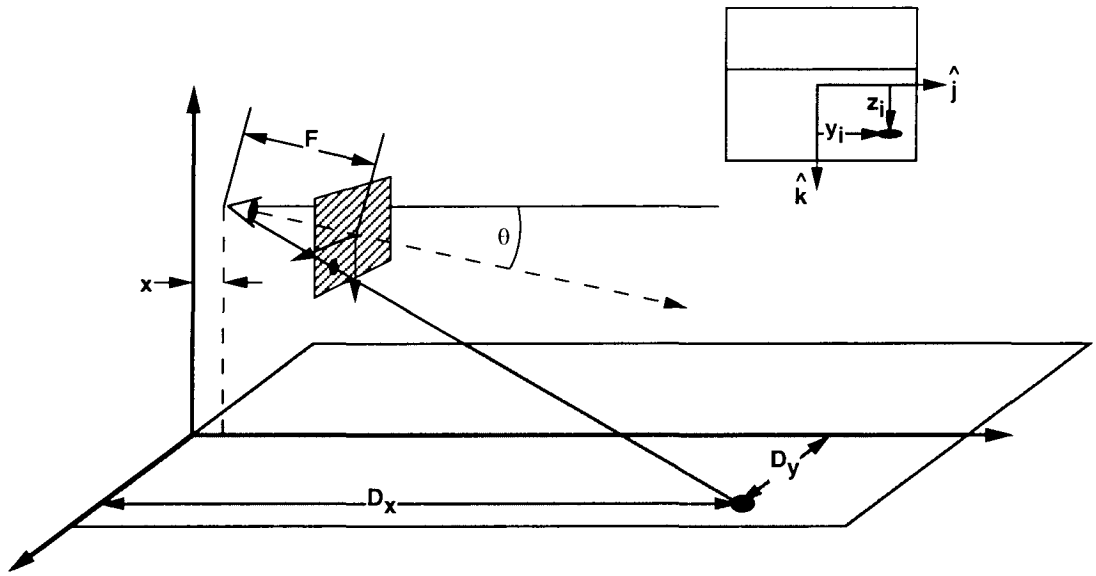

Figure 2.3: Perspective projection diagram for simplified hover task. The imaging device has a focal length F. The operator is located at a position X, with a pitch attitude Θ. The location of a particular feature being imaged is D_X, D_Y. The position of the feature in the image is denoted with y_i, z_i. All distances (X, D_X, D_Y) are scaled in units of eyeheights (the height of the eye above the groundplane). Equations 2.3 and 2.4 describe the relationship between the observer state (X, Θ), feature location (D_X, D_Y), focal length (F), and location of the feature *in the image* (y_i, z_i).

of the scene feature (D_X, D_Y), and focal length (F). It is obtained by substituting Equations 2.3 and 2.4 into $G_{\text{image}}(y_i, z_i)$. The parameters D_X, D_Y, and F are fixed for a particular feature and imaging geometry; the only variables are X and Θ.

The transformation between these variables, X and Θ, and the image-plane coordinates, y_i and z_i, is nonlinear, as can be seen by examining Equations 2.3 and 2.4. A linear relationship is desired for incorporation with the Crossover Model, since it is the linear input/output relationships of the human operator that are being modelled. A *linearized* visual cue λ, based on the visual-cue description Λ, is defined as:

$$\lambda = \left. \frac{d\Lambda}{\partial\Lambda/\partial X} \right|_{X=0,\Theta=0} \tag{2.6}$$

where

$$d\Lambda\Big|_{X=0,\Theta=0} = \left[\left. \frac{\partial\Lambda}{\partial X} \right|_{X=0,\Theta=0} \right] dX + \left[\left. \frac{\partial\Lambda}{\partial\Theta} \right|_{X=0,\Theta=0} \right] d\Theta \tag{2.7}$$

In this definition, the differential of Λ is *normalized* with $\partial\Lambda/\partial X$ to create one-to-one correspondence between the linearized cue λ and the longitudinal position. This was done to simplify incorporation into the Crossover Model. With this scaling, and substituting $x = dX$ and $\theta = d\Theta$, Equation 2.6 becomes:

$$\lambda = x + K_\lambda \theta \tag{2.8}$$

where

$$K_\lambda = \left. \frac{\partial\Lambda/\partial\Theta}{\partial\Lambda/\partial X} \right|_{X=0,\Theta=0} \tag{2.9}$$

This linearized visual cue λ is simply a linear combination of the states x and θ. The variable K_λ specifies the relative contributions of θ and x to the displacement of λ, and is determined by the function defining the cue, Λ.

This concept can be more easily understood by applying this derivation to an example. Figure 2.4 contains a diagram of a perspective scene, with an example visual cue Λ illustrated. In words, this cue is the vertical location, in image coordinates, of the dashed line on the image. This line, in world coordinates, is taken to be at a constant longitudinal position D_X.

In equation form, it can be expressed as:

$$\Lambda = z_i = -\frac{F((D_X - X)\mathrm{s}\Theta + \mathrm{c}\Theta)}{((D_X - X)\mathrm{c}\Theta - \mathrm{s}\Theta)} \tag{2.10}$$

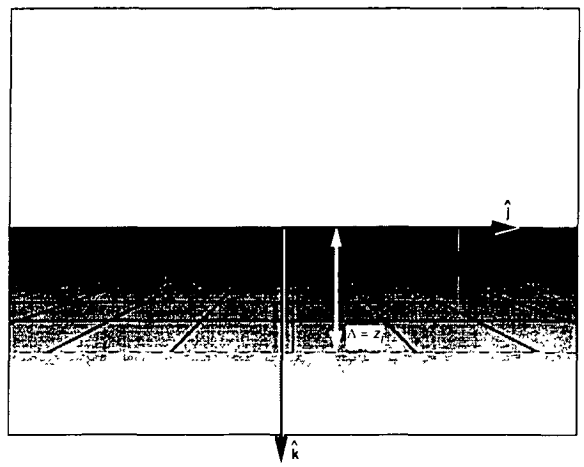

Figure 2.4: Visual cue used for example analysis. The cue consists of the vertical position of the feature (the line in the foreground) relative to the fixed image frame.

For this example cue that we have defined, we can calculate K_λ by: 1) taking the partial derivative of Λ, defined in Equation 2.10, with respect to X and Θ, 2) evaluating those derivatives at the linearization conditions, and 3) substituting them into Equation 2.9. The intermediate steps are not shown; the final result for this example cue is:

$$K_\lambda = 1 + D_X^2 \tag{2.11}$$

Expressions for K_λ for specific visual cues will be derived in Section 2.5.

The purpose of the preceding derivation was to develop a linearized model of a visual cue (λ), to be used as an input to an operator model. In the next section, one or more linearized visual cue models will be combined with the Crossover Model to provide models of manual control which account directly for perspective-scene viewing.

2.3 Visual Cue Control Model

This model is based on the hypothesis that the human operator finds visual cues that correspond to the desired state, and uses the cues in place of explicit state information (which is not available) to formulate a control strategy. Two forms of the model will

be developed; one in which one visual cue is used, and another in which two cues are used.

There is substantial psychophysical evidence that the human visual system has specialized structures to process motion in the visual stimulus [60]. Studies dating back more than 100 years have determined that the perception of motion is not just the perception of change of position over an interval of time, but appears to be highly specialized (and, fortunately, easily fooled, or we would not perceive television or movies as we do). The ability to sense static features (position) separately from moving features (motion) is assumed in the model.

In the model, the operator acts on information from both sensing systems. Two different forms of model are considered; one in which both the position and motion sensing system processes information from the same stimulus, and another in which the position and motion sensing system concurrently processes information from two different stimuli. The two model forms, and the expected transfer functions, are developed in the Sections 2.3.2 and 2.3.3.

While it is not possible to establish and define precisely what cues an operator is using, it *can* be determined, as a function of scene texture – as we shall see from experiments – how many cues are being used, and what texture features enable what level of control performance.

2.3.1 Crossover Model Predictions

Before considering the human operator response using a visual cue, it is worthwhile to review what the Crossover Model would predict for the human operator being presented with explicit state measurements[4]; refer to Figure 2.5. The controlled-element dynamics were defined in Equation 2.1. Specifically, $Y_c(s) = 1/s(s + 0.2)$. The Crossover Model predicts that the product of the controlled-element dynamics

[4]The VCC model described herein is based upon a manual control model for a compensatory task; this implies that only the error between the commanded and actual state is presented to the operator. It can be applied to this task when the "commanded" state is zero (or constant). The case in which some explicit or implicit dynamic commanded state is present would require application of pursuit models of manual control. This case would lead to the incorporation of a feed-forward element of the commanded state in the control strategy.

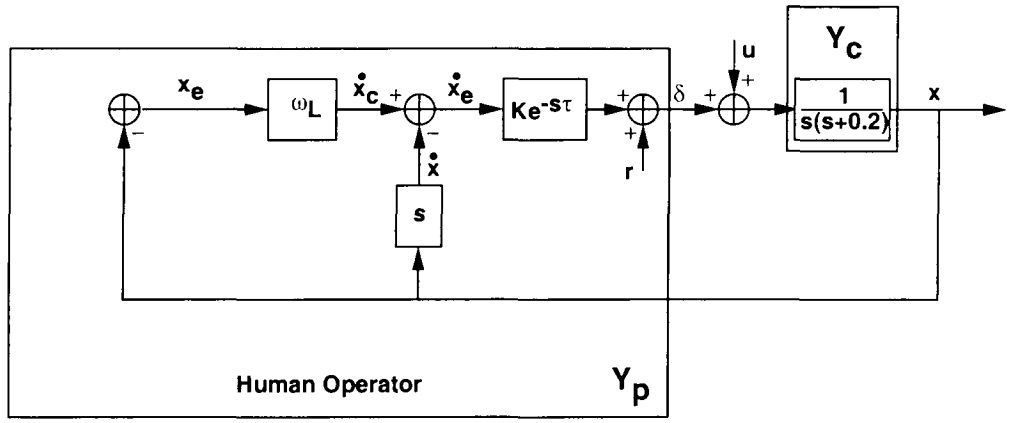

Figure 2.5: Block diagram of Crossover Model for current task, assuming explicit state measurement is available. Note that there is no "commanded" state x_c. For the disturbance rejection task considered here, the "command" is to remain stationary, or $x_c = 0$.

and human-operator compensation will be approximately:

$$Y_p(s)Y_c(s) = \frac{\omega_c e^{-\tau s}}{s} \tag{2.12}$$

in the frequency region of crossover. The crossover frequency ω_c is the frequency at which the open-loop transfer function $Y_p(s)Y_c(s)$ has a magnitude of one (Equation 1.2). It can be seen from inspection that when $s = j\omega_c$, the magnitude of $Y_p(s)Y_c(s)$ in Equation 2.12 becomes unity. Accounting for the fact that the human can probably not generate 5 seconds of lead compensation [1], one would expect the operator dynamics to take the approximate form:

$$Y_p(s) = \frac{\omega_c}{\omega_L} e^{-\tau s}(s + \omega_L) \tag{2.13}$$

where ω_L should occur at a frequency below crossover, and at or above 0.2 rad/sec ($0.2 < \omega_L < \omega_c$).

Figure 2.5 shows a schematic diagram of this assumed compensation strategy. The transfer function between the control and the state would be:

$$\delta(s) = -Y_p(s)x(s) + r(s) \tag{2.14}$$

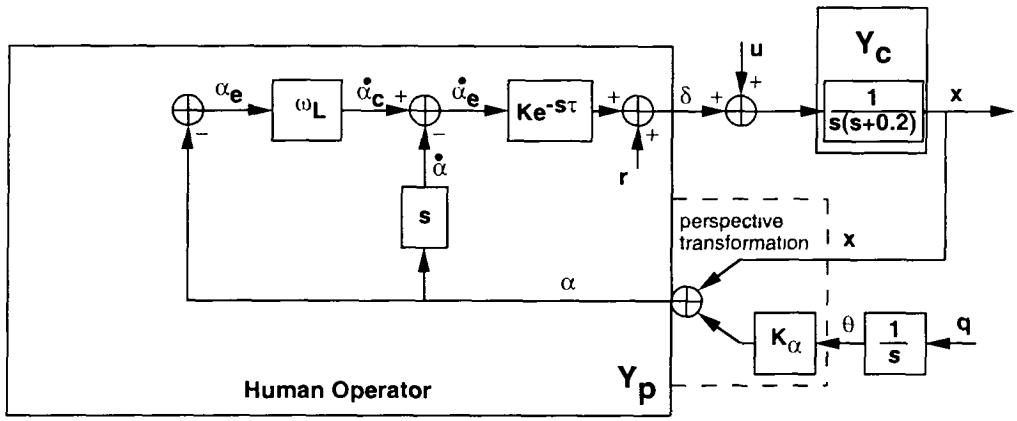

Figure 2.6: Block diagram of one-cue model for current task. The explicit state measurement shown in Figure 2.5 has been replaced with a visual cue, α. The visual cue the operator will in fact see in his view is represented as a sum of the state x and the pitch attitude θ multiplied by the factor K_α. K_α represents the relative contributions of θ and x to this particular cue; it is governed by the process of perspective projection. As in the case of explicit state measurement previously considered, the commanded visual-cue state is zero (i.e., "don't move").

Note that the term $r(s)$ is included in this transfer function and in the diagram; this represents remnant "injected" by the human operator into the control activity. Specifically, it is the control activity that is not linearly correlated with the input. This component of the control activity of the human will receive more attention in Section 2.4, in which measurement techniques will be discussed.

2.3.2 One-cue Model

We turn now to the case in which the explicit state information considered previously is replaced with a visual cue (α), which has presumeably been obtained from a perspective display (see Figure 2.6). The visual cue α is some characteristic or feature of the image, but as was shown in Equation 2.8, it can be expressed as a linear combination of the states x and θ:

$$\alpha(s) = x(s) + K_\alpha \theta(s) \tag{2.15}$$

The eye-brain system infers both α and its derivative from a perspective scene like Figure 2.4. The operator does not have any explicit measurement of the state x available in this case; instead, the operator selects a visual cue α which is correlated with x, and controls α directly.

The system of transfer functions relating control δ, longitudinal position x, and pitch attitude θ is:

$$\delta(s) = -Y_p(s)x(s) - Y_p(s)K_\alpha\theta(s) + r(s) \tag{2.16}$$

where $Y_p(s)$ is shown in the gray box in Figure 2.6. The only difference between this transfer function, and the one previously defined using the Crossover Model (Equation 2.14), is the addition of $\theta(s)$, which reduces the level of correlation between the visual cue α and the desired state[5]. Since the parameter K_α directly scales the magnitude of the disturbance (θ) being added to the system, one would expect the operator to choose a visual cue that minimizes the magnitude of K_α, so that the true position x dominates the cue.

2.3.3 Two-cue Model

We will now consider the case in which the operator is using two visual cues to accomplish the task (Figure 2.7). In this model, one visual cue (γ) is being used for position, and another cue (β) is used for motion, or velocity. γ and β are defined as:

$$\gamma(s) = x(s) + K_\gamma\theta(s) \tag{2.17}$$

$$\beta(s) = x(s) + K_\beta\theta(s) \tag{2.18}$$

In this case, the eye-brain system is inferring γ, and the derivative of β, from the perspective scene. These two cues could be likened to the position of a feature in the image (γ), and the motion of some portion of the image detected in the peripheral vision (β).

The transfer-function system relating δ, x, and θ for this case is:

$$\delta(s) = -Y_p(s)x(s) - Y_p(s)K_\beta\frac{(s + (K_\gamma/K_\beta)\omega_L)}{(s + \omega_L)}\theta(s) + r(s) \tag{2.19}$$

[5]In this case, θ is in fact independent of x, so it acts here as an independent disturbance.

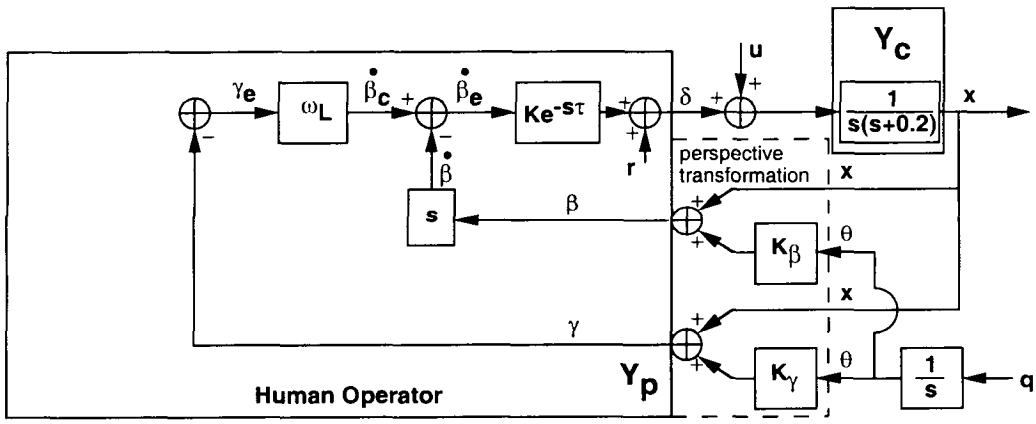

Figure 2.7: Block diagram of two-cue model for current task. The operator is now assumed to use one visual cue for position γ, and another for motion β. Note that the "differentiation" of the motion cue, β, occurs *inside* the operator; there is no direct display of motion in the perspective display. This motion cue is only derived through the perceptual process of the human. The presence of two separate cues, for motion and position, implies that the operator is concurrently attending to and using two sources of visual information. The commanded state, as in the previous cases, is to maintain the current visual-cue state (i.e., "don't move").

Mathematically, this differs from the one-cue model (Equation 2.16) through the addition of a lag-lead element multiplying $\theta(s)$ in the two-cue model (lag-lead for $K_\gamma > K_\beta$). The two models are otherwise identical. As was the case with the one-cue model, the terms K_β and K_γ are essentially gain terms which scale the disturbance source (θ) being added to the states; one would expect the operator to minimize K_β and K_γ when possible. Also note that this model reverts to the one-cue model form when K_β and K_γ are equal: $K_\beta = K_\gamma$.

2.4 Transfer-Function Measurements

Equations 2.16 and 2.19 describe models that represent the characteristics of the human operator. If the objective is to determine the functions and parameters in the models (Y_p, K_α, K_β, K_γ), the available experimental measurements must be related to these model functions. The Sum-of-Sines (SOS) technique has been used extensively in manual control to develop transfer functions from measurements. The basic steps are:

1. Design input signals that enable effective identification
2. Relate the cross spectral densities to model transfer functions
3. From time-history measurements, estimate pertinent cross spectral density ratios
4. Identify model parameters to fit the transfer functions

The last step in this process, identification of model parameters, will be discussed in the subsequent chapters. This is because the number of parameters used in the models varied with experimental treatments. In this section, the first three steps will be discussed. Much of the detail is included in the appendices to facilitate explanation.

2.4.1 SOS Input Signals

The first step, design of the input signals, is what sets SOS techniques apart from other transfer function measurement techniques. In this technique, multiple sine

functions, at different frequencies, are summed to create a random-appearing input signal. There are several advantages to using this type of input signal:

1. Signal power is concentrated in discrete frequencies, creating good signal-to-noise characteristics.

2. The random appearance of the signal prevents the operator from anticipating the input (which would elicit a predominantly open-loop, rather than closed-loop, control strategy).

3. The input signals can be designed to simplify the relationship between the cross spectral density estimates and the transfer functions. This is accomplished by creating independent signals, which act simultaneously on a system, and have no linear correlation with each other.

The design of the input signals involves specifying multiple parameters, including the run length, sampling intervals, and frequency components. Guidelines for proper selection of these parameters are presented in Section B.1 of Appendix B.

2.4.2 Transfer-Function Relationships

The second step of the process is to relate the cross spectral densities of system states to model functions. Figures 2.8 and 2.9 contain block diagrams for the purposes of identification for the one-cue and two-cue models, respectively. The terms u and q are the disturbances to the longitudinal acceleration and pitch rate, respectively. The term r is the remnant component of the human control output; it is that component which is not linearly correlated with the inputs to the operator.

For the one-cue model, the following relationships can be derived:

$$\delta = \frac{1}{1+Y_pY_c}[-Y_pY_cu - Y_pK_\alpha\theta + r] \tag{2.20}$$

$$x = \frac{1}{1+Y_pY_c}[Y_cu - Y_pY_cK_\alpha\theta + Y_cr] \tag{2.21}$$

$$\tag{2.22}$$

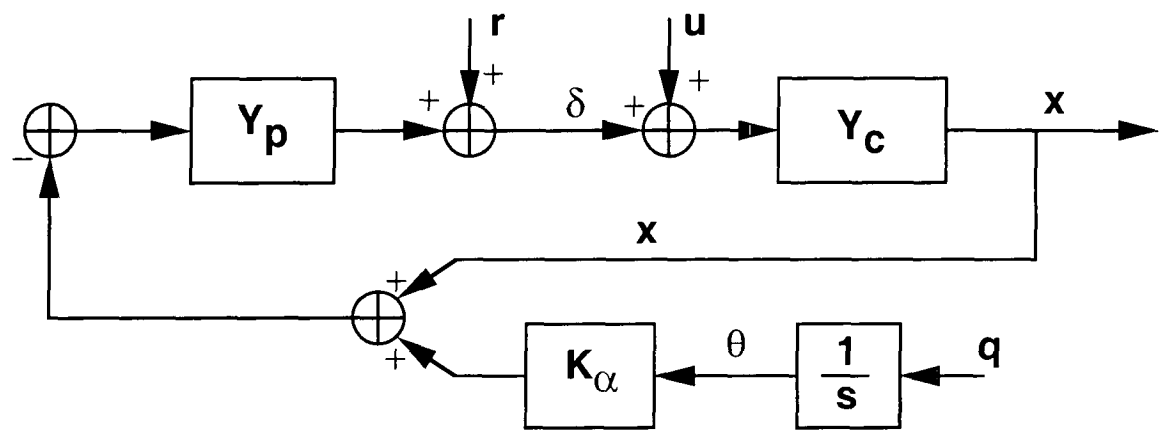

Figure 2.8: Block diagram of one-cue model used for transfer-function identification. The free parameters assumed in this model form are the parameters that specify the transfer function Y_p, and the visual-cue parameter K_α. K_α is related to the one visual cue that is used for both position and motion sensing. This realization is equivalent to that depicted in Figure 2.6.

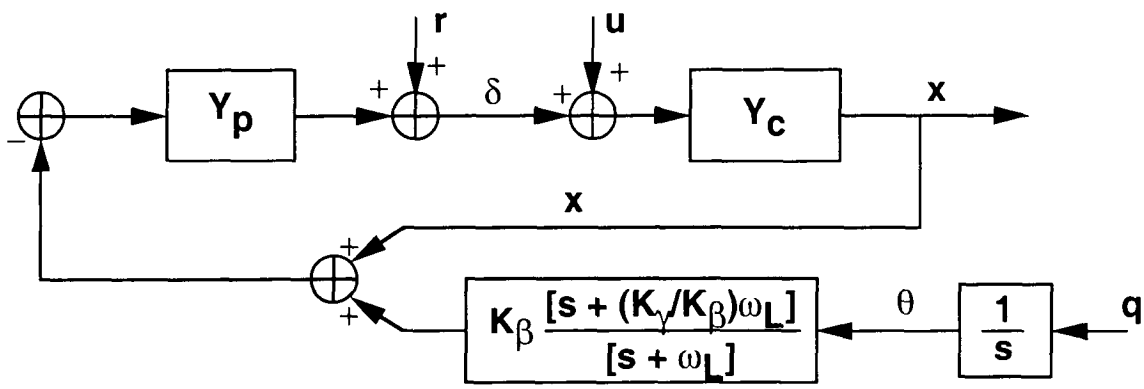

Figure 2.9: Block diagram of two-cue model used for transfer-function identification. The free parameters assumed in this model form are the parameters that specify the transfer function Y_p, and the visual-cue parameters K_β and K_γ. K_β is related to the visual cue for motion, K_γ relates to the cue for position. ω_L is one of the parameters of Y_p (not shown explicitly here), and defines the amount of lead the operator is generating. This realization is equivalent to that depicted in Figure 2.7.

The relationships of the ratios of power spectral densities and cross spectral densities are:

$$\frac{\phi_{\delta u}}{\phi_{xu}} = \frac{-Y_p Y_c \phi_{uu} - Y_p K_\alpha \phi_{\theta u} + \phi_{ru}}{Y_c \phi_{uu} - Y_p Y_c K_\alpha \phi_{\theta u} + Y_c \phi_{ru}} \tag{2.23}$$

$$\frac{\phi_{\delta q}}{\phi_{\theta q}} = \frac{1}{1 + Y_p Y_c} \frac{-Y_p Y_c \phi_{uq} - Y_p K_\alpha \phi_{\theta q} + \phi_{rq}}{\phi_{\theta q}} \tag{2.24}$$

No assumptions have been made about the input signals u and q up to this point. The SOS technique can be used to make u and q uncorrelated with each other. Specifically, for $\phi_{\theta u} = \phi_{uq} = 0$, the Equations 2.23 and 2.24 become:

$$\frac{\phi_{\delta u}}{\phi_{xu}} = \frac{Y_p Y_c \phi_{uu} + \phi_{ru}}{Y_c \phi_{uu} + Y_c \phi_{ru}} \tag{2.25}$$

$$\frac{\phi_{\delta q}}{\phi_{\theta q}} = \frac{1}{1 - Y_p Y_c} \frac{Y_p K_\alpha \phi_{\theta q} + \phi_{rq}}{\phi_{\theta q}} \tag{2.26}$$

If we further assume that the remnant noise source r is not correlated with the input signals q and u, making $\phi_{rq} = \phi_{ru} = 0$, the relationships become:

$$\frac{\phi_{\delta u}}{\phi_{xu}} = Y_p \tag{2.27}$$

$$\frac{\phi_{\delta q}}{\phi_{\theta q}} = \frac{Y_p K_\alpha}{1 - Y_p Y_c} \quad \text{(One-Cue)} \tag{2.28}$$

These relationships give us a direct method for determining the functions to describe Y_p and K_α. The two-cue case is quite simple to derive from this point. In the block diagrams, the only difference between the one-cue and two-cue models is that in the two-cue model, the term K_α present in the one-cue model is replaced with a more complex term. By substituting this term in for K_α, derivation of the two-cue case is trivial:

$$\frac{\phi_{\delta u}}{\phi_{xu}} = Y_p \tag{2.29}$$

$$\frac{\phi_{\delta q}}{\phi_{\theta q}} = \frac{Y_p K_\beta}{1 - Y_p Y_c} \frac{(s + \frac{K_\gamma}{K_\beta}\omega_L)}{(s + \omega_L)} \quad \text{(Two-Cue)} \tag{2.30}$$

2.4.3 Cross Spectral Density Estimates

Equations 2.27, 2.28, and 2.30 defined the relationships between the model functions, and particular power and cross spectral densities. The actual parameters measured

in an experimental run are time histories of δ, x, θ, q, and u. When using the SOS technique, the cross spectral density measurements can be approximated by products of the coefficients of the Discrete Fourier Transforms (DFTs) of the time signals [61]. The relationships are:

$$\phi_{\delta u}(f\omega_s) \approx \frac{1}{N} D(f)U(f)^* \tag{2.31}$$

$$\phi_{xu}(f\omega_s) \approx \frac{1}{N} X(f)U(f)^* \tag{2.32}$$

$$\phi_{\delta q}(f\omega_s) \approx \frac{1}{N} D(f)Q(f)^* \tag{2.33}$$

$$\phi_{\theta q}(f\omega_s) \approx \frac{1}{N} \Theta(f)Q(f)^* \tag{2.34}$$

where N is number of points in the time sequence, and $D(f)$, $U(f)$, $Q(f)$, and $\Theta(f)$ are the coefficients of the DFT of the respective time sequences. For a discrete sequence $x(n)$, $n = 0, 1, \ldots, N-1$, the DFT coefficient $X(f)$ is defined as:

$$X(f) = \sum_{n=0}^{N-1} x(n) exp(-j2\pi k \frac{n}{N}), \quad f = \frac{k}{N}, \quad k = 0, 1, \ldots, N-1 \tag{2.35}$$

The variable f is a "normalized" frequency which goes from values of zero to $N/(N-1)$. Note that the cross spectral densities have been expressed as a function of $f\omega_s$, which is a frequency related to the time domain (in rad/sec). ω_s is the sampling frequency, related to the sampling interval T:

$$\omega_s = \frac{1}{T} \tag{2.36}$$

We will now define new terms $\hat{Y}_p$ and $\hat{Y}_\theta$:

$$\hat{Y}_p(f\omega_s) = \frac{\overline{(D(f)U(f)^*)}}{\overline{(X(f)U(f)^*)}} \tag{2.37}$$

$$\hat{Y}_\theta(f\omega_s) = \frac{\overline{(D(f)Q(f)^*)}}{\overline{(\Theta(f)Q(f)^*)}} \tag{2.38}$$

From Equations 2.27, 2.28 and 2.30 above, we expect these quantities to be related to the models as follows:

$$\text{Both Models:} \quad \hat{Y}_p = Y_p \tag{2.39}$$

$$\text{One-Cue Model:} \quad \hat{Y}_\theta = Y_{\theta 1} \tag{2.40}$$

$$\text{Two-Cue Model:} \quad \hat{Y}_\theta = Y_{\theta 2} \tag{2.41}$$

where

$$Y_{\theta 1} = \frac{Y_p K_\alpha}{1 - Y_p Y_c} \tag{2.42}$$

$$Y_{\theta 2} = \frac{Y_p K_\beta}{1 - Y_p Y_c} \frac{(s + \frac{K_\gamma}{K_\beta}\omega_L)}{(s + \omega_L)} \tag{2.43}$$

To summarize, $\hat{Y}_p$ and $\hat{Y}_\theta$ are the ratios of the estimated power spectral density and cross spectral densities of specific time histories. Note that the measurements $\hat{Y}_p$ and $\hat{Y}_\theta$ are based upon ensemble averages of multiple time histories. This technique was developed by Levison [62], as were methods to estimate the standard error of the measurement. This is described in more detail in Section B.2 of Appendix B.

The techniques up to this point describe only how to inferrentially derive the transfer functions $\hat{Y}_p$ and $\hat{Y}_\theta$ from the available time histories. These transfer functions are related to the model parameters in the last step of the process. This process is described in detail in Section 3.2.2.

2.5 Parameters of the Visual Cue Control Model

Section 2.2 contained the development of a model of perspective-scene viewing and visual-cue selection. This model included a parameter (K_λ, Equation 2.9) which was a function of the particular visual cue selected. In this section, the expected values of that parameter, for a variety of potential visual cues, will be derived.

Prior to discussing particular cues, two concepts will be introduced that are relevant to the examination of all cues. The first concept is that of absolute versus relative cues. The second concept is that of choosing directional components.

2.5.1 Absolute versus Relative Displacement

Because the image surface is two-dimensional, displacements of scene features with respect to any reference should be described as a vector. Using the image-plane

coordinate system as the reference, we will denote the displacement of feature i to be (Figure 2.3):

$$d_i = y_i\hat{j} + z_i\hat{k} \tag{2.44}$$

This type of displacement, measured in the image-plane coordinate system, will be defined as an *absolute* displacement. It is also possible to consider the displacement between two features in the image. The vector displacement between the ith and jth features would be:

$$d_j - d_i = (y_j - y_i)\hat{j} + (z_j - z_i)\hat{k} \tag{2.45}$$

This type of displacement will be defined to be a *relative* displacement.

These displacements have been defined in terms of the image-plane coordinates. For later manipulations, it will be necessary to express these displacements in terms of the feature locations and operator location and orientation. Substituting Equations 2.3 and 2.4 into Equations 2.44 and 2.45 produces:

$$d_i = -F\left[\frac{D_{Y_i}}{((D_{X_i} - X)\mathrm{c}\Theta - \mathrm{s}\Theta)}\hat{j} + \frac{((D_{X_i} - X)\mathrm{s}\Theta + \mathrm{c}\Theta)}{((D_{X_i} - X)\mathrm{c}\Theta - \mathrm{s}\Theta)}\hat{k}\right] \tag{2.46}$$

$$\begin{aligned} d_j - d_i = F\Bigg[&\left\{\frac{D_{Y_i}}{((D_{X_i} - X)\mathrm{c}\Theta - \mathrm{s}\Theta)} - \frac{D_{Y_j}}{((D_{X_j} - X)\mathrm{c}\Theta - \mathrm{s}\Theta)}\right\}\hat{j} \\ &+ \left\{\frac{((D_{X_i} - X)\mathrm{s}\Theta + \mathrm{c}\Theta)}{((D_{X_i} - X)\mathrm{c}\Theta - \mathrm{s}\Theta)} - \frac{((D_{X_j} - X)\mathrm{s}\Theta + \mathrm{c}\Theta)}{((D_{X_j} - X)\mathrm{c}\Theta - \mathrm{s}\Theta)}\right\}\hat{k}\Bigg] \end{aligned} \tag{2.47}$$

Defining the vector displacement of a feature relative to the image-plane coordinate system is only one step in the definition of a visual cue. As used in the model, a visual cue is a scalar, not a vector, quantity. To convert these vector displacements to a scalar quantity for use as a visual cue, the concept of directional components is introduced.

2.5.2 Directional Components

The assumption is made that the operator is capable of attending to displacement that occurs in a particular direction or orientation. Indeed, often the motion can only be discerned in one direction (as in the case of a line, where motion along the line cannot be discerned; only motion perpendicular to the line can be detected). One probable

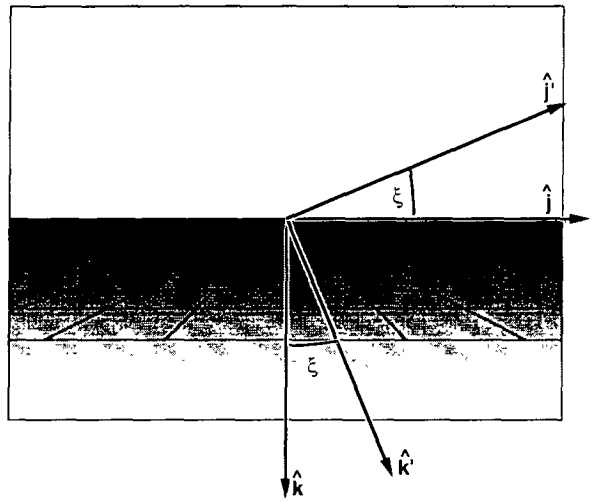

Figure 2.10: Coordinate system used to derive directional visual cues.

cue would be discerning displacement in the vertical or horizontal direction. In cases where the image has a sharp outer boundary (as in the frame of a monitor), this boundary can serve as a strong, fixed reference for the operator. In addition to vertical and horizontal components, the operator might be able to attend to displacement that occurs in the direction of a scene feature. One such feature might be along lines of splay[6]. Particularly in the case where the operator is viewing a scene through a non-rectangular window (as is the case with many vehicles), the operator might also attend to displacement or motion in a different direction than the image coordinate system derived here. In that case, we can express the absolute and relative displacements in terms of another coordinate system through a coordinate transformation.

A new coordinate system can be defined, $\hat{j}'$ and $\hat{k}'$ (Figure 2.10):

$$\hat{j}' = \hat{j}\cos(\xi) + \hat{k}\sin(\xi) \tag{2.48}$$

$$\hat{k}' = -\hat{j}\sin(\xi) + \hat{k}\cos(\xi) \tag{2.49}$$

Combining these definitions with the absolute and relative displacements derived

[6]A line of splay is a line parallel to the direction of motion. In the experiments done in this research the lines of splay are always longitudinal, which is the direction of motion.

above, we can express the displacements relative to the new coordinate system:

$$d_i = (y_i \cos(\xi) - z_i \sin(\xi))\hat{j}' + (y_i \sin(\xi) + z_i \cos(\xi))\hat{k}' \quad (2.50)$$

$$\begin{aligned} d_j - d_i = & ((y_j - y_i)\cos(\xi) - (z_j - z_i)\sin(\xi))\hat{j}' \\ & +((y_j - y_i)\sin(\xi) + (z_j - z_i)\cos(\xi))\hat{k}' \end{aligned} \quad (2.51)$$

These relationships can also be expressed in terms of the scene and operator variables as was done previously.

$$\begin{aligned} d_i = & -F\left[\left\{\frac{D_{Y_i}}{((D_{X_i} - X)\mathrm{c}\Theta - \mathrm{s}\Theta)}\cos(\xi)\right.\right. \\ & \left.-\frac{((D_{X_i} - X)\mathrm{s}\Theta + \mathrm{c}\Theta)}{((D_{X_i} - X)\mathrm{c}\Theta - \mathrm{s}\Theta)}\sin(\xi)\right\}\hat{j}' \\ & +\left\{\frac{D_{Y_i}}{((D_{X_i} - X)\mathrm{c}\Theta - \mathrm{s}\Theta)}\sin(\xi)\right. \\ & \left.\left.+\frac{((D_{X_i} - X)\mathrm{s}\Theta + \mathrm{c}\Theta)}{((D_{X_i} - X)\mathrm{c}\Theta - \mathrm{s}\Theta)}\cos(\xi)\right\}\hat{k}'\right] \end{aligned} \quad (2.52)$$

$$\begin{aligned} d_j - d_i = & F\left[\left\{\left(\frac{D_{Y_i}}{((D_{X_i} - X)\mathrm{c}\Theta - \mathrm{s}\Theta)} - \frac{D_{Y_j}}{((D_{X_j} - X)\mathrm{c}\Theta - \mathrm{s}\Theta)}\right)\cos(\xi)\right.\right. \\ & \left.-\left(\frac{((D_{X_i} - X)\mathrm{s}\Theta + \mathrm{c}\Theta)}{((D_{X_i} - X)\mathrm{c}\Theta - \mathrm{s}\Theta)} - \frac{((D_{X_j} - X)\mathrm{s}\Theta + \mathrm{c}\Theta)}{((D_{X_j} - X)\mathrm{c}\Theta - \mathrm{s}\Theta)}\right)\sin(\xi)\right\}\hat{j}' \\ & +\left\{\left(\frac{D_{Y_i}}{((D_{X_i} - X)\mathrm{c}\Theta - \mathrm{s}\Theta)} - \frac{D_{Y_j}}{((D_{X_j} - X)\mathrm{c}\Theta - \mathrm{s}\Theta)}\right)\sin(\xi)\right. \\ & \left.\left.+\left(\frac{((D_{X_i} - X)\mathrm{s}\Theta + \mathrm{c}\Theta)}{((D_{X_i} - X)\mathrm{c}\Theta - \mathrm{s}\Theta)} - \frac{((D_{X_j} - X)\mathrm{s}\Theta + \mathrm{c}\Theta)}{((D_{X_j} - X)\mathrm{c}\Theta - \mathrm{s}\Theta)}\right)\cos(\xi)\right\}\hat{k}'\right] \end{aligned} \quad (2.53)$$

To examine cues that are relative to lines of splay, it is necessary to determine the coordinate transformation. Defining the angle a splay line at D_Y makes with the vertical to be ξ, the sine and cosine will be:

$$\sin(\xi) = \frac{D_Y \mathrm{c}\Theta}{\sqrt{{D_Y}^2 \mathrm{c}^2\Theta + 1}} \quad (2.54)$$

$$\cos(\xi) = \frac{1}{\sqrt{{D_Y}^2 \mathrm{c}^2\Theta + 1}} \quad (2.55)$$

For relatively small values of Θ, this angle will essentially be fixed for a particular line. That is, the angle of a particular line of splay (located at a lateral displacement D_Y, in the above equation) will remain fixed.

2.5.3 Illustrative Examples

These concepts will now be applied to the derivation of several possible cues for the current task. The desired quantity is the relationship K_λ, which determines the relative contributions of longitudinal displacement and pitch displacement to the visual cue displacement. Five different types of cues will be defined, and an expression for K_λ will be developed for each one. Examples of each type of cue are shown in Figure 2.11.

Absolute Vertical Displacement (Λ_v)

This cue is equivalent to the operator attending to the absolute vertical displacement of a feature in the image. The value of this displacement will be determined from the component of absolute displacement in the $\hat{k}$ direction of Equation 2.46 (which is equivalent to z_i).

$$\Lambda_v = -F\frac{((D_{X_i} - X)\mathrm{s}\Theta + \mathrm{c}\Theta)}{((D_{X_i} - X)\mathrm{c}\Theta - \mathrm{s}\Theta)} \tag{2.56}$$

The value of K_λ is defined as:

$$K_\lambda = \frac{\partial\Lambda/\partial\Theta}{\partial\Lambda/\partial X} \tag{2.57}$$

From the previous definition of Λ_v, we can compute:

$$\frac{\partial\Lambda_v}{\partial X} = F\left[\frac{\mathrm{s}\Theta}{[(D_{X_i} - X)\mathrm{c}\Theta - \mathrm{s}\Theta]} - \frac{\mathrm{c}\Theta[(D_{X_i} - X)\mathrm{s}\Theta + \mathrm{c}\Theta]}{[(D_{X_i} - X)\mathrm{c}\Theta - \mathrm{s}\Theta]^2}\right] \tag{2.58}$$

$$\frac{\partial\Lambda_v}{\partial\Theta} = -F\left[1 + \frac{[(D_{X_i} - X)\mathrm{s}\Theta + \mathrm{c}\Theta]^2}{[(D_{X_i} - X)\mathrm{c}\Theta - \mathrm{s}\Theta]^2}\right] \tag{2.59}$$

Evaluating at the linearization conditions of $X = 0$ and $\Theta = 0$, we have:

$$\left.\frac{\partial\Lambda_v}{\partial X}\right|_{X=0,\Theta=0} = -\frac{F}{D_{X_i}^2} \tag{2.60}$$

$$\left.\frac{\partial\Lambda_v}{\partial\Theta}\right|_{X=0,\Theta=0} = -F\left[1 + \frac{1}{D_{X_i}^2}\right] \tag{2.61}$$

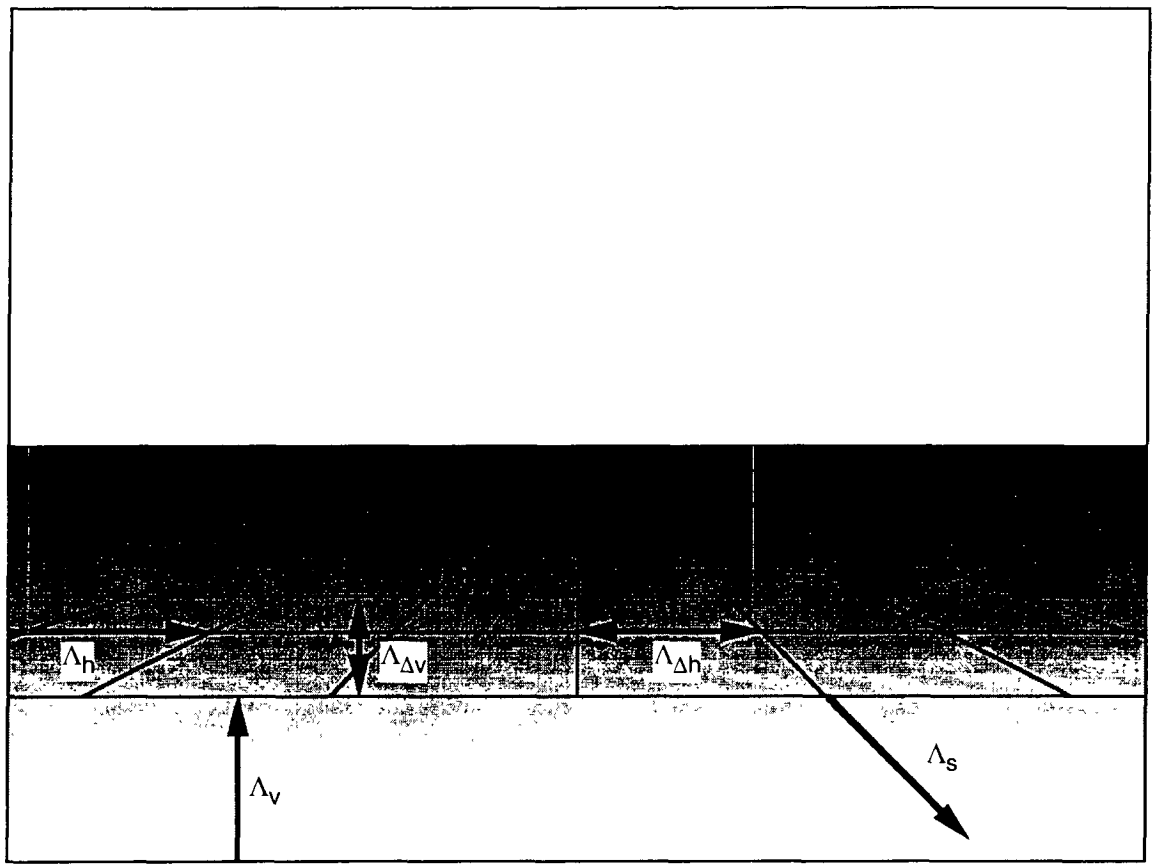

Figure 2.11: Examples of potential visual cues. Cues can be defined as the position of a feature, or the displacement between two features. Potential features include lines, and junctions of lines (such as grid intersections). The displacement of a line whose endpoints lie outside of the frame of the image can only be observed perpendicular to the line, and thus the direction in which displacement or motion can be detected is constrained. Particular points, such as formed by grid intersections, can apparently be displaced or have motion which is unconstrained. The subscripts h and Δh refer to visual cues formed by *horizontal* judgements made in the image plane; it can be the horizontal displacement between two features ($\Lambda_{\Delta h}$), or the absolute horizontal displacement of a feature in the image (Λ_h). The subscripts v and Δv refer to *vertical* judgements, such as the absolute vertical position of a line, or the vertical displacement between two features (Λ_v and $\Lambda_{\Delta v}$, respectively). The s subscript refers to judgements in displacement or motion of a feature that are made relative to the direction of a line of splay (Λ_s), and is thus highly dependent on the location of the feature in the image (since the angles of lines of splay vary as a function of their location in the image.)

Correspondingly, K_λ for this cue is:

$$K_{\lambda_v} = D_{X_i}^2 + 1 \tag{2.62}$$

Note that D_{X_i} is the longitudinal position of the feature relative to the operator. As the feature gets farther from the operator, K_{λ_v} gets larger rapidly. If the goal of the operator is to choose the lowest possible value of K_λ, for this visual cue one would expect the operator to use the closest feature available.

In the remaining derivations, the expressions for $d\Lambda$ are presented for $X = 0$ and $\Theta = 0$; the intermediate derivation steps are omitted.

Absolute Horizontal Displacement (Λ_h)

This cue is equivalent to the operator attending to the absolute horizontal displacement of a feature in the image. The value of this displacement will be determined from the component of absolute displacement in the $\hat{j}$ direction of Equation 2.46 (equivalent to y_i).

$$\Lambda_h = -F\frac{D_{Y_i}}{((D_{X_i} - X)\mathrm{c}\Theta - \mathrm{s}\Theta)} \tag{2.63}$$

The differential of this cue is:

$$d\Lambda_h\Big|_{X=0,\Theta=0} = -F\frac{D_{Y_i}}{{D_{X_i}}^2}dX - F\frac{D_{Y_i}}{{D_{X_i}}^2}d\Theta \tag{2.64}$$

For this cue, the value of K_λ at any location in the image is:

$$K_{\lambda_h} = 1 \tag{2.65}$$

Relative Vertical Displacement ($\Lambda_{\Delta v}$)

With this cue, the assumption is made that the operator can perceive the vertical component of the relative displacement of features located at longitudinal positions D_{X_i} and D_{X_j}.

$$\Lambda_{\Delta v} = F\left[\frac{((D_{X_i} - X)\mathrm{s}\Theta + \mathrm{c}\Theta)}{((D_{X_i} - X)\mathrm{c}\Theta - \mathrm{s}\Theta)} - \frac{((D_{X_j} - X)\mathrm{s}\Theta + \mathrm{c}\Theta)}{((D_{X_j} - X)\mathrm{c}\Theta - \mathrm{s}\Theta)}\right] \tag{2.66}$$

The differential is:

$$d\Lambda_{\Delta v}\Big|_{X=0,\Theta=0} = F\Big[\frac{1}{{D_{X_i}}^2} - \frac{1}{{D_{X_i}}^2}\Big]dX + F\Big[\frac{1}{{D_{X_i}}^2} - \frac{1}{{D_{X_i}}^2}\Big]d\Theta \tag{2.67}$$

For this cue, the value of K_λ is:

$$K_{\lambda_{\Delta v}} = 1 \tag{2.68}$$

$K_{\lambda_{\Delta v}}$ is not dependent on the features chosen for reference. An example of this cue would be if the operator were attending to the displacement between the horizon and the baseline.

Relative Horizontal Displacement ($\Lambda_{\Delta h}$)

With this cue, the assumption is made that the operator can track magnitude of the horizontal component of the relative displacement of features located at lateral positions D_{Y_i} and D_{Y_j}.

$$\Lambda_{\Delta h} = F\left[\frac{D_{Y_i}}{((D_{X_i} - X)\mathrm{c}\Theta - \mathrm{s}\Theta)} - \frac{D_{Y_j}}{((D_{X_j} - X)\mathrm{c}\Theta - \mathrm{s}\Theta)}\right] \tag{2.69}$$

The differential is:

$$d\Lambda_{\Delta h}\Big|_{X=0,\Theta=0} = F\Big[\frac{D_{Y_i}}{{D_{X_i}}^2} - \frac{D_{Y_j}}{{D_{X_j}}^2}\Big]dX + F\Big[\frac{D_{Y_i}}{{D_{X_i}}^2} - \frac{D_{Y_j}}{{D_{X_j}}^2}\Big]d\Theta \tag{2.70}$$

For this cue, the value of K_λ is:

$$K_{\lambda_{\Delta h}} = 1 \tag{2.71}$$

Again, K_λ is unity, regardless of the features chosen for reference. An example of this cue would be if the operator were attending the displacement between two points on the baseline.

Displacement Aligned with Splay Line (Λ_s)

To determine the component of displacement that is aligned with the splay line, the $\hat{k}'$ component of d_i in Equation 2.46 is combined with Equations 2.54 and 2.55. As derived here, this is an absolute cue, since it is based on the component of the absolute displacement d_i that is parallel to the line of splay. In practice, to use this absolute

cue, the operator would need to remember the original position of d_i in the image plane, derive the displacement from it, then determine the component of displacement along the nearest line of splay. While this does not seem practical for position sensing, it is plausible that the operator can sense the motion of this cue: that is, the operator could sense the component of motion of the point parallel to the line of splay near (or on) which it lies. The expression for this cue is:

$$\begin{aligned}\Lambda_s &= -F\left\{\frac{D_{Y_i}}{((D_{X_i}-X)\mathrm{c}\Theta-\mathrm{s}\Theta)}\frac{D_{Y_i}\mathrm{c}\Theta}{\sqrt{{D_{Y_i}}^2\mathrm{c}^2\Theta+1}}\right. \\ &\quad \left.+\frac{((D_{X_i}-X)\mathrm{s}\Theta+\mathrm{c}\Theta)}{((D_{X_i}-X)\mathrm{c}\Theta-\mathrm{s}\Theta)}\frac{1}{\sqrt{{D_{Y_i}}^2\mathrm{c}^2\Theta+1}}\right\} \end{aligned} \tag{2.72}$$

The differential of this cue is:

$$d\Lambda_s\Big|_{X=0,\Theta=0} = -F\frac{({D_{Y_i}}^2+1)}{{D_{X_i}}^2\sqrt{{D_{Y_i}}^2+1}}dX - F\frac{({D_{Y_i}}^2+1)+{D_{X_i}}^2}{{D_{X_i}}^2\sqrt{{D_{Y_i}}^2+1}}d\Theta \tag{2.73}$$

The value of K_λ will be:

$$K_{\lambda_s} = \frac{{D_{Y_i}}^2+{D_{X_i}}^2+1}{{D_{Y_i}}^2+1} \tag{2.74}$$

The sensitivity of this cue varies as a function of location in the image. Transforming the expression back into image coordinates can be done by recognizing that for $X=0$ and $\Theta=0$, the relationship between screen coordinates (y_i, z_i) and feature coordinates (D_X, D_Y) is:

$$y_i = -F\frac{D_Y}{D_X} \tag{2.75}$$

$$z_i = -F\frac{1}{D_X} \tag{2.76}$$

Substituting these expressions for D_Y and D_X back into Equation 2.74 will provide an expression for K_{λ_s} that is a function of screen coordinates, y_i and z_i, and focal length F:

$$K_{\lambda_s} = 1+\frac{F^2}{y_i^2+z_i^2} \tag{2.77}$$

When lines of constant K_{λ_s} are plotted as a function of image coordinates, it can be seen that the isolines of K_{λ_s} are concentric circles radiating out from the image

Cue (λ)	K_λ
λ_v	$D_X^2 + 1$
$\lambda_{\Delta v}$	1
λ_h	1
$\lambda_{\Delta h}$	1
λ_s	$\frac{D_Y^2 + D_X^2 + 1}{D_Y^2 + 1}$

Table 2.1: Expressions for K_λ for proposed visual cues

center, with K_{λ_s} getting smaller as the distance from the image center increases. Also note the effect of the focal length. As the focal length increases (assuming fixed image size, or maximum values for y_i and z_i), the value of K_{λ_s} increases. This is equivalent to the case of a telephoto lens, that subtends a relatively small field of view. This would be like looking though a straw at the horizon; very little image motion results from longitudinal motion, and a great deal results from pitch motion. With a very small focal length (e.g., a wide-angle lense), K_{λ_s} decreases. This case would result in much more overall image motion resulting from longitudinal motion, except for those parts of the image that are insensitive to longitudinal motion. It can be seen that at the very center of the image ($y_i = z_i = 0$), K_{λ_s} becomes infinite; this is because all of the image motion results from pitch and none results from longitudinal motion.

The expressions for K_λ for each type of proposed cue are presented in Table 2.1. The actual values of K_λ for particular texture types will be considered in Chapters 3 and 4.

This chapter contained the derivation of visual cue models, transfer function measurement methodologies, and characteristics of visual cues. The next two chapters contain descriptions of two experiments performed to validate the models derived in this chapter, and to show how to estimate the values of their constants.

Chapter 3

Experiment 1

The previous chapter contained the derivation of two forms of the VCC model. The primary purpose of this experiment was to determine if the VCC model could represent the input/output relationships of the human operator performing a manual control task using a perspective display. In particular, which form of the model (one-cue or two-cue) was superior? A second goal was to determine if systematic variations in the task variables could produce systematic variations in the control strategy and/or performance. To determine this, variations were introduced in both the nature of the disturbances perturbing the system, and to the content of the perspective scenes. The purpose of testing with systematic variations was to facilitate development of the model under a variety of conditions.

The data analysis of the experimental results includes both Analysis of Variance (ANOVA) and individual modeling. The ANOVA was performed to assess the degree to which variations in the task variables produced variations in the control strategy and performance. The individual modeling consisted of fitting parameters of both of the VCC model forms (one-cue and two-cue) to experimentally derived transfer functions.

The results of this experiment will show that both forms of the VCC model provide good representations of the input/output characteristics of the operator in the majority of cases. However, high variances in the transfer function measurement prevented conclusive determination of which model form was superior (for this reason, a

second experiment, Experiment 2, was developed to focus on this issue, as Chapter 4 will describe). The variations in the task variables did produce measurable effects in the control strategy and performance.

A description of the experimental protocol is provided in Section 3.1. Section 3.2 contains the experimental results from both the ANOVA analyses and the individual modeling, and Section 3.3 contains discussion of those results.

3.1 Protocol

3.1.1 Participants

Six participants were used. They were recruited from a contractor pool at Ames Research Center. All were male flight instructors, with experience ranging from 270 to 620 total flight hours.

3.1.2 Apparatus

A simulation was developed on a Silicon Graphics Indigo II Extreme. Control inputs were supplied with the 3-axis joystick in a B&G Systems Flybox. The color monitor had a 19-inch diagonal screen, with resolution of 1024 vertical and 1280 horizontal pixels. Operators were seated approximately 20 inches from the display. This resulted in approximately 30 vertical by 37.5 horizontal degrees of visual angle subtended by the display. The simulation had a 33.3 Hz update rate (from a .03 second sampling interval), and the monitor refreshed at a rate of 72 Hz noninterlaced. The joystick information was updated at the simulation update rate of 33.3 Hz.

The dynamics of the vehicle were described in Section 2.1. The actual discrete transfer functions used, as well as the disturbance dynamics, are presented in Section D.1 of Appendix D.

3.1.3 Scene

Modifications to the visual scene were done by applying different types of patterns to a simulated ground plane; these pattern types are referred to as textures. In this experiment, four textures were presented, shown in Figure 3.1. The texture types were; 1) Grid (G), 2) Parallel ($\parallel$), 3) Perpendicular ($\perp$), and 4) Line (L). All of the textures featured a line on the ground plane, referred to as the baseline (perpendicular to the ostensible direction of motion of the operator), located 3 eyeheights in front of the operator. In the Grid texture, lines both perpendicular and parallel to the direction of motion of the operator were present (this included the baseline). In the Parallel texture, the parallel lines and the baseline were present. In the Perpendicular texture, only the perpendicular lines were present (including the baseline). In the Line texture, only the baseline was present. The lines perpendicular to the direction of motion were spaced at 0.5 eyeheight intervals; the lines parallel were spaced at 0.78 eyeheight intervals.

All scenes were rendered with a 60-degree vertical field of view, which resulted in a 75 degree horizontal field of view. This represents approximately a 2-to-1 ratio between the field of view displayed and the actual viewing angle of the display. Although significantly non-conformal, the large field of view is fairly consistent with the large fields of view typically available on flight vehicles (particularly the horizontal field of view). The operator of an unmanned aerospace vehicle (UAV) can be presented with a similar situation; the image from a camera with a wide-angle lens can be displayed on a monitor that actually fills a much smaller visual angle than the visual angle subtended with the camera.

The ground plane was linearly shaded from light to dark from a position directly under the operator to a distance of 15 eyeheights in front. The dark color was maintained from that location to the horizon. This was done to minimize the effects of aliasing in the lines distant to the operator. As in one-dimensional signal processing, aliasing in an image occurs when the frequency content of the image is higher than the Nyquist frequency (half of the sampling frequency). Specifically, near the horizon, the distance between individual lines becomes less than one pixel, which is a higher spatial frequency than the display can support. In concrete terms, the aliasing makes

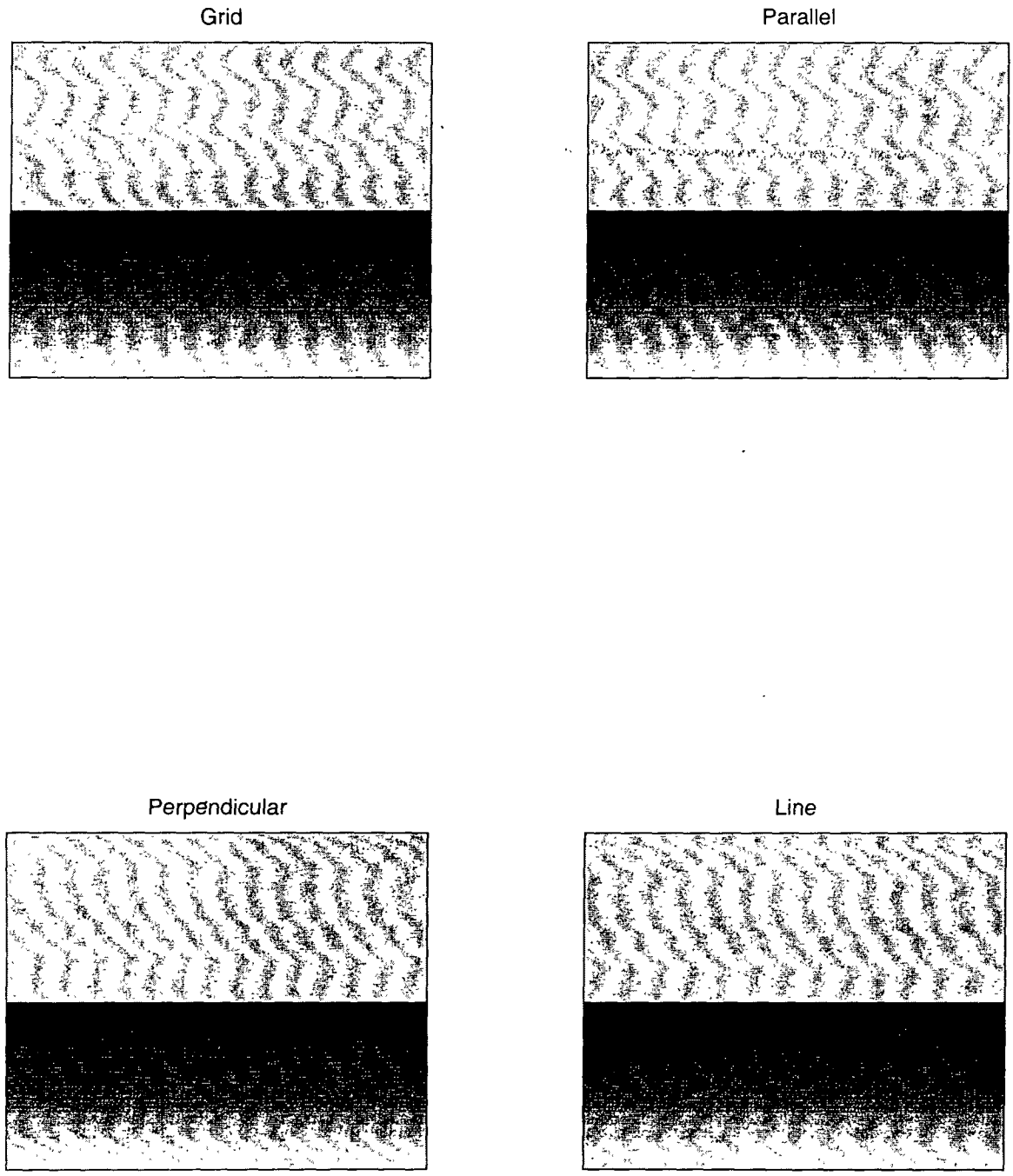

Figure 3.1: The four texture patterns used in Experiment 1.

the lines in the vicinity of the horizon seem to flicker, and a particular line will move up and down one pixel in a way that is not related to the motion. The distance of 15 eyeheights was chosen to correspond to the distance at which the visual angle subtended between two lines perpendicular to the line of sight would correspond to less than two pixels. The graphical rendering was done with no hardware anti-aliasing, and the lines were all one pixel wide. There was also no depth cueing enabled. Thus, the operator could not get any position information from the perspective thickening of the lines as they grew closer, or from changes in contrast due to distance.

Visual-Cue Characteristics

As will be seen, the results of the experiment include the derivation of parameters that are related to the characteristics of visual cues in the scene. Therefore, in order to compare the measured values of the parameters with the available visual cues, it is necessary to determine what the theoretical values of those parameters would be for particular cues. Five potentially available cues were discussed in Section 2.5.3; expressions for the value of K_λ were derived for each of these cues, shown in Table 2.1. Examples of the visual cues were also shown graphically in Figure 2.11. Only two of the visual cues proposed, λ_s and λ_v, are a function of the scene features used to derive the cue. For the four texture conditions used in this experiment, the available ranges of K_λ are derived.

The cue λ_v is defined as the absolute vertical displacement of a scene feature. The fixed reference point that the displacement is measured relative to can be any landmark fixed relative to the image. One of the most likely references would be the bottom edge of the display; the example demonstrated in Figure 2.11 was the displacement of the baseline (in the image) relative to the bottom of the display.

The expression (Equation 2.62) for K_{λ_v} is:

$$K_{\lambda_v} = D_X^2 + 1 \tag{3.1}$$

D_X is the longitudinal displacement of a feature (the feature being used for the cue) relative to the operator. For this task, the closest feature is the baseline, located 3 eyeheights in front of the operator. The subsequent lines are spaced at intervals of .5

	Texture			
Cue	Grid	Line	Parallel	Perpendicular
λ_v	≥ 10	10	10	≥ 10
λ_{Δ_v}	1	1	1	1
λ_h	1	—	1	—
$\lambda_{\Delta h}$	1	—	1	—
λ_s	≥ 2.8	—	3.6, 6.6 or 10	—

Table 3.1: Values of K_λ for proposed visual cues in Experiment 1. These cues are depicted visually in Figure 2.11.

eyeheights, up to a distance of 15 eyeheights from the operator. Accounting for this, the minimum obtainable value of K_{λ_v} would be 10. In the Grid and Perpendicular textures, intermediate values of K_{λ_v} would exist (K_{λ_v} = 13.25, 17.0, etc.). In the Parallel and Line textures, only the baseline is available to base this visual cue on, therefore $K_{\lambda_v} = 10$.

The other cue that varies as a function of scene features is λ_s. This cue was defined as the *component along a line of splay* of the absolute displacement of a scene feature. The expression (Equation 2.74) for K_{λ_s} is:

$$K_{\lambda_s} = \frac{D_Y^2 + D_X^2 + 1}{D_Y^2 + D_X^2} \tag{3.2}$$

D_X and D_Y define the longitudinal and lateral position of the feature (relative to the operator) used for the visual cue. Since the Perpendicular and Line textures do not have any features that exhibit lateral movement, this cue is not available in these textures. In the Grid texture, it can be shown that the minimum obtainable value of K_{λ_s} is 2.8. In the Parallel texture, there are a limited number of features for which this cue is available; specifically, the intersections of the baseline and the lines of splay. For this texture, the minimum obtainable value for K_{λ_s} is 3.6.

Table 3.1 presents theoretically obtainable values of K_λ for each of the visual cue and texture combinations. It was discussed previously that the operator could minimize the effect of the pitch-attitude disturbance by minimizing K_λ when possible. From this visual cue analysis, one would expect the operator to use one of the three

cues that yield $K_\lambda = 1$ whenever possible. It should also be noted that in all of the texture conditions, there is one cue available that yields $K_\lambda = 1$, namely $\lambda_{\Delta v}$. This cue is potentially available, in all of the textures, through sensing of the distance between the horizon and the baseline.

3.1.4 Task

As was previously described in Section 2.1, the objective was to maintain a constant position in the presence of disturbances. The operator was verbally instructed to keep the longitudinal position fixed at the position at the start of the trial (which was the same for all trials). The operator was informed that he could control only longitudinal position, and not pitch, and that both pitch and position would be subject to disturbances. Operators were also instructed to develop their control strategies during the training runs; once data runs were begun, they were instructed to maintain a consistent control strategy for a particular texture.

3.1.5 Procedure

Each operator participated for one day. The experimental protocol consisted of a block of training runs and two blocks of data runs. The data-run blocks were identical to each other except for the randomized phase angles used to initialize the disturbances. In both the training and data blocks, six experimental conditions were tested on each of the six operators; the conditions are enumerated below.

1. Grid, no pitch (G/0)
2. Line, no pitch (L/0)
3. Grid, with pitch (G/1)
4. Line, with pitch (L/1)
5. Parallel, with pitch ($\|$/1)
6. Perpendicular, with pitch ($\perp$/1)

Operator	Condition					
1	L/0	G/1	∥/1	L/1	G/0	⊥/1
2	L/1	⊥/1	G/0	L/0	∥/1	G/1
3	G/1	L/0	∥/1	G/0	L/1	⊥/1
4	G/0	⊥/1	L/1	G/1	∥/1	L/0
5	∥/1	L/0	G/1	⊥/1	L/1	G/0
6	⊥/1	G/0	L/1	∥/1	G/1	L/0

Table 3.2: Experiment 1 presentation order by operator. The first character denotes the texture type; the second character denotes if the pitch disturbance was present (1) or absent (0).

Each operator was given a different presentation order for the conditions. In the training block, operators were given six sequential training runs in each of the six conditions, for a total of 36 training runs. In the data blocks, the operator was given one training run and then three data runs for each condition. The order of presentation (shown in Table 3.2) remained fixed for the training run and both data runs.

Each data run lasted a total of 4 minutes, 10 seconds. Training runs lasted 55 seconds. Both data and training runs were initiated by the operator by using the mouse button. During the first five seconds, there was no activity in the display, and an auditory signal was given at one-second intervals. For the next five seconds, the display and control became active, and the disturbances ramped linearly from zero to full intensity. The simulation proceeded with full-strength disturbances for the remaining time (4 minutes for data runs, 45 seconds for training runs). Following this, the operators received feedback after both training and data runs on their performance; the feedback consisted of a single value derived by summing the root mean square (rms) velocity (in eyeheights/sec) and rms longitudinal position (in eyeheights) from the training run.

3.1.6 Experiment Design

The design consists of two nested factorials: a 6 x 2 x 2 with repetitions, textures (Grid and Line), and pitch disturbance (with and without) as factors, and a 6 x 4 with repetitions and texture types (Grid, Parallel, Perpendicular, and Line) as factors (pitch disturbance was always present). The dependent variables included: the percent of control (δ) power correlated with pitch disturbance (q); percent of control power correlated with longitudinal disturbance (u); longitudinal velocity rms; and longitudinal position rms. To simplify later discussion, the following symbols are introduced to identify these four dependent variables:

$P_{\delta\theta}$: % of control (δ) power correlated with the pitch disturbance (q)
$P_{\delta x}$: % of control (δ) power correlated with the longitudinal disturbance (u)
RMS_x: longitudinal velocity rms
RMS_x: longitudinal position rms

3.2 Results

3.2.1 Analysis of Variance (ANOVA)

An Analysis of Variance (ANOVA) was conducted for each of the two factorials; 1) a 2×2 factorial analysis with texture (Grid vs Line) and pitch disturbance (present vs absent) as factors[1]; and 2) a one-way ANOVA examining the effects of the four textures with the pitch disturbance present. The ANOVA assesses the probability that observed differences in dependent measures across conditions are due to random variation. This is done via a comparison of differences between conditions to variability within conditions. Measuring performance for all conditions in a single group of participants (i.e., a within-subject design) is generally more powerful than having

[1]Factor is another name for independent variable. The term "$n \times m$" factorial denotes a design in which two factors are varied; n levels within the first factor, and m levels within the second factor. In this 2 × 2 factorial, two pitch disturbance levels (present and absent), and two scene textures (Grid and Line) were considered. Repetition is not considered a factor of theoretical interest in this study. Rather, multiple samples were taken for each pitch disturbance × scene texture condition to provide additional statistical power.

Symbol	Meaning	Probability of Chance Occurrance
+	statistically significant	$p \leq 0.05$
$_+$	marginally significant	$0.05 < p \leq 0.10$
0	not statistically significant	$0.10 < p$

Table 3.3: Summary of statistical significance terminology

different participants in each condition (i.e., a between-subjects design) since the impact of individual differences is mitigated. Differences that would occur by chance less than 5% of the time are considered statistically significant (i.e., p < 0.05). An effect or interaction is considered to be marginal if the probability of it occurring by chance is between 5% and 10%. Rather than present the numerical values for each analysis factor, the results are summarized in tables, in which "+" represents a probability of chance occurrence less than 5% (statistically significant),"$_+$" is a probability between 5% and 10% (marginal), and "0" represents 10% or greater probability of chance occurrence (i.e., a null or nonsignificant finding). These relationships are shown in Table 3.3.

The dependent measures examined in both factorial analyses were: the percent of control power correlated with the pitch disturbance ($P_{\delta\theta}$); percent of control power correlated with the longitudinal disturbance ($P_{\delta x}$); longitudinal velocity rms ($\text{RMS}_{\dot{x}}$); and longitudinal position rms (RMS_x).

The 2×2 ANOVA results comparing the effects of texture (Grid vs Line) and pitch disturbance (present vs absent) are shown in Table 3.4 and Figure 3.2. These results indicate the pitch disturbance has a much greater effect when the operator is using the Line texture than when he is using the Grid. $P_{\delta\theta}$ without the pitch disturbance present simply represents the remnant that is present at the frequencies that are later used to inject the pitch disturbance. When the disturbance is present, $P_{\delta\theta}$ barely increases with the Grid texture, but increases significantly with the Line texture. This increase in $P_{\delta\theta}$ is accompanied by almost a one-to-one drop in $P_{\delta x}$. Not surprisingly, both the outcome variables $\text{RMS}_{\dot{x}}$ and RMS_x are increased with the Line texture when the pitch disturbance is present; this is an expected outcome from

	Factor		
Measurement	Pitch disturbance	Texture	Dist/Text Interaction
$P_{\delta\theta}$	+	+	+
$P_{\delta x}$	0	+	$_+$
RMS_x	+	$_+$	+
$\mathrm{RMS}_{\dot{x}}$	+	0	$_+$

Table 3.4: Statistical significance for the 2×2 Analysis of Variance (textures × pitch disturbance) from Experiment 1. "+" indicates statistical significance, "$_+$" indicates marginal significance, and "0" indicates lack of statistical significance.

injecting a disturbance into the control.

The results of the one-way ANOVA, examining the effect of texture alone (pitch disturbance present), are presented in Table 3.5 and Figure 3.3. In this case, the texture had a significant effect on $P_{\delta\theta}$; it increased in the order of Grid, Parallel, Perpendicular, and Line textures. $P_{\delta x}$ had a corresponding drop, similar to that observed in the 2×2 ANOVA. $\mathrm{RMS}_{\dot{x}}$ and RMS_x increased from the Grid to the Line texture, although these measurements were nearly identical for the Perpendicular and Parallel textures, even though the Parallel texture is associated with a lower amount of pitch activity in the control. The reason no effect is observed in RMS_x and $\mathrm{RMS}_{\dot{x}}$ is probably because the operators occasionally "lost" the baseline reference by moving too far forward. When this happened with the Parallel texture, there were no positional or motion cues available, and the operator would have to adopt an open-loop control strategy to move back enough to engage the reference. With the Perpendicular texture, the operator would at least have some motion cues from the other lines, and could reengage the baseline reference more easily. This tendency probably negated any favorable effect on RMS_x or $\mathrm{RMS}_{\dot{x}}$ due to the reduced pitch disturbance feedthrough with the Parallel texture.

The numerical values of the means and standard errors for both analyses, as well as the actual values used to determine statistical significance, are contained in Section D.2 of Appendix D.

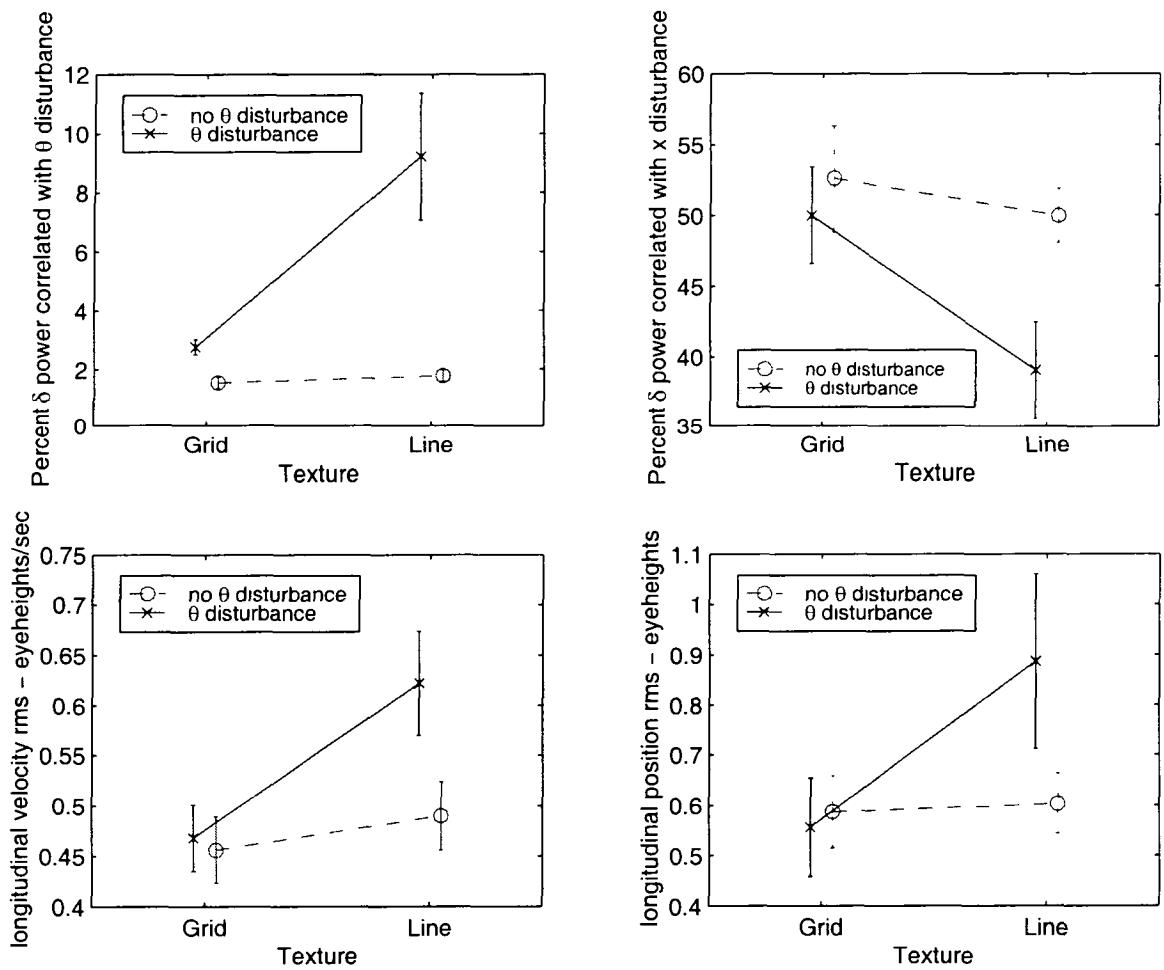

Figure 3.2: Analysis of Variance (ANOVA) results for effect of texture and pitch disturbance in Experiment 1. Operating with the cue gleaned from the Grid texture is significantly better than with the Line-texture cue when there is an uncontrolled pitch motion present. (Otherwise, the Line-texture cue is probably about as good as the Grid-texture cue.) That is, getting higher rms errors and using more control power to respond to the pitch disturbance both indicate poorer performance.

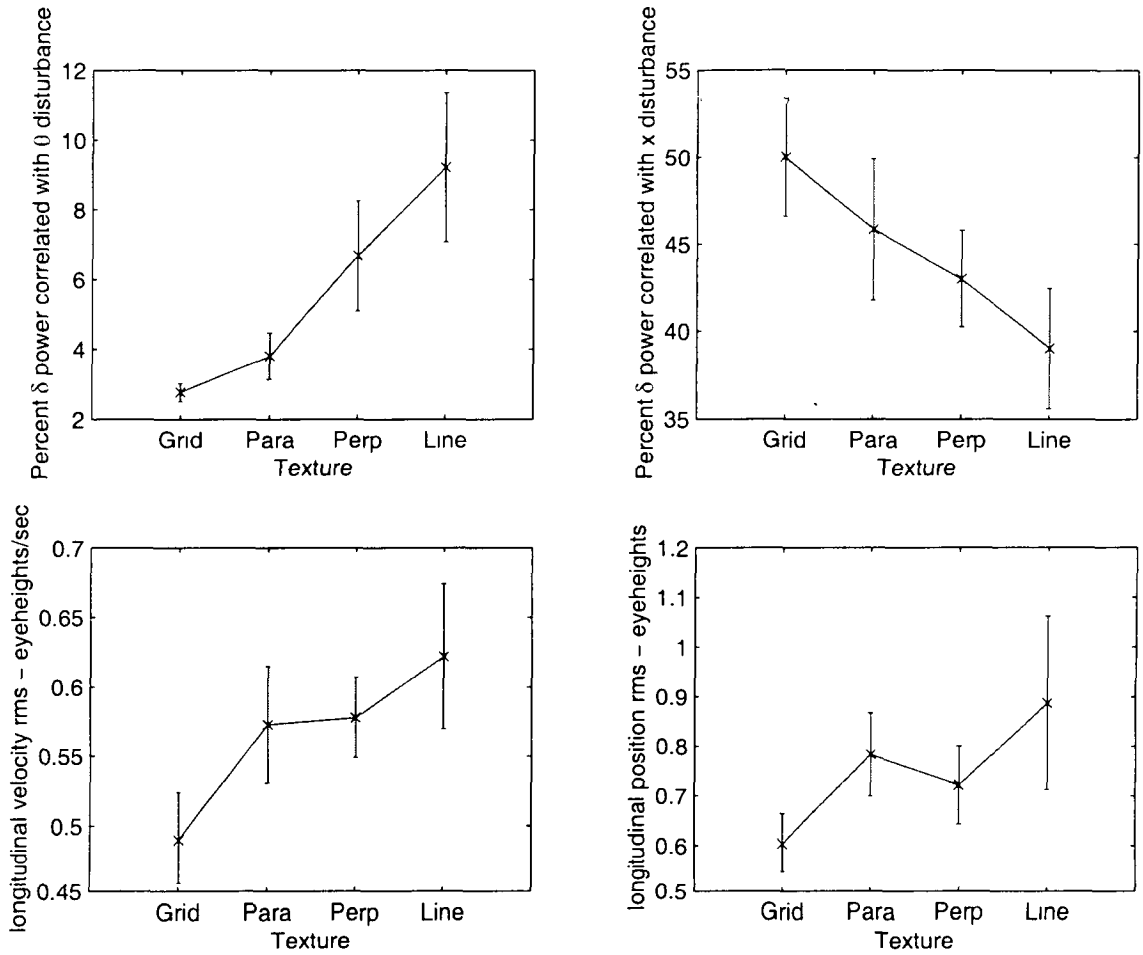

Figure 3.3: Analysis of Variance (ANOVA) results for effect of texture with pitch disturbance present in Experiment 1. The Parallel texture is associated with better pitch disturbance rejection (lower $P_{\delta\theta}$) than the Perpendicular texture, but not as good as the Grid. The lack of effect on the outcome variables, RMS_x and $\mathrm{RMS}_{\dot{x}}$ is likely due to a tendancy for operators to "lose" usable visual reference with the Parallel texture, when the one line in the foreground would disappear out of sight when the operator moved too far forward.

	Factor
Measurement	Texture
$P_{\delta\theta}$	+
$P_{\delta x}$	+
RMS_x	+
RMS_x	+

Table 3.5: Statistical significance for the one-way Analysis of Variance (effect of texture) from Experiment 1. The "+'s" indicates that the date about the effect of texture is statistically significant for all of these dependent measures.

3.2.2 Individual Models

The spectral density measurements $\hat{Y}_p$ and $\hat{Y}_\theta$ (defined in Equations 2.37 and 2.38, respectively) were derived for each operator and condition using the techniques described in [62], also summarized in Appendix B. $\hat{Y}_p$ is the ratio between the control activity δ and longitudinal position x (the portion of it that is linearly correlated with the longitudinal acceleration disturbance); its units are stick displacement/eyeheight. $\hat{Y}_\theta$ is the ratio between the control activity and pitch attitude θ (the portion which is linearly correlated with the pitch rate disturbance); it is expressed in units of stick displacement/rad. These ratios are complex relationships which describe the gain and phase relationships between the input signals (x and θ) to the operator and his control output (δ). Each operator completed six data runs in each condition[2]. The spectral density measurements were based on the five time histories (of six taken) that exhibited the lowest velocity and position rms. This was done to eliminate those data runs in which the operators occasionally lost visual references. Although theoretically possible for one data run to have the highest velocity rms and another to have the highest position rms, this never occurred in practice; in every case, the data run with the highest position rms was also associated with the highest velocity rms.

[2]The cases in which the pitch disturbance is not present were not included in the individual model fitting. The lack of a pitch disturbance makes it impossible to identify which visual cue is being used. This is because the measurement $\hat{Y}_\theta$ is used to derive the parameters (K_α, K_β, and K_γ) which are related to the perspective display and visual cue selection. The term "all conditions" should be taken to mean those conditions in which the pitch disturbance was present.

The relationships between the model parameters and the measurements are derived in Equations 2.39 through 2.43. In practice, it can be quite difficult to identify the model parameters that best correspond to frequency-domain measurements. Several approaches are possible. In one approach, the parameters of Y_p, $Y_{\theta 1}$ and $Y_{\theta 2}$ that provide best fits to the measurements $\hat{Y}_p$ and $\hat{Y}_\theta$ can be determined through some type of parameter optimization. This is an iterative, numerical search of some type, and in this case would involve the determination of four or five parameters to fit 20 data points. The time required to apply this to all of the measurements (six operators in four conditions yielded 24 individual sets of parameters to be identified) became prohibitive.

It is also possible to find parameters of a discrete transfer function that best fit the time-sampled data using non-iterative methods; however, this technique tends to fit only the largest-magnitude portions of the response, neglecting the smaller-magnitude responses. Since the magnitude of different frequency components can vary appreciably, this approach does not yield very good correspondence with frequency-domain measurements.

A third approach was developed, in which a discrete transfer function (DTF) identification process was modified to provide a fit that corresponds closely to the frequency-domain fit. This technique is described in detail in Appendix C. This approach was combined with parameter optimization to provide parameter estimates for the measurements available.

The model-fitting procedure used is as follows:

1. The parameters of Y_p that best fit the measurement $\hat{Y}_p$ were determined. The form of Y_p (e.g. order of numerator and denominator) was chosen to provide a reasonable fit to $\hat{Y}_p$ with the minimum number of parameters. The modified DTF identification process described in Section C.1 of Appendix C was used for this parameter identification.

2. Using the identified parameters of Y_p:

   (a) For the one-cue model: the free parameter of $Y_{\theta 1}$ (K_α) to best fit the measurement $\hat{Y}_\theta$ was determined.

(b) For the two-cue model: the free parameters of $Y_{\theta 2}$ (K_β and K_γ) to best fit the measurement $\hat{Y}_\theta$ were determined.

The grid search technique described in Section C.2 of Appendix C was used for the identification of these parameters.

The reason for using the two different techniques is related to the number of parameters to be identified, as well as the variances of the measurements involved. The modified DTF technique involves a weighted least-squares solution, with the inverse of the measurement magnitude partially determining the weights. When the data exhibits large variances, some of the measurements can have a disproportionate effect on the parameters. However, the level of complexity of the solution increases very slightly with increasing numbers of parameters. It is ideally suited to cases with low variances, in which the number of parameters make numerical solution techniques particularly cumbersome.

The measurement $\hat{Y}_p$ typically had low variances associated with it; the standard errors for all conditions, operators, and frequency measurements are shown in Figure 3.4. The methodology for deriving the standard errors is described in Section B.2 of Appendix B. For the data generated in this experiment, the model Y_p had three free parameters (this will be described in more detail below). These two factors (low standard errors and larger number of parameters) made the modified DTF identification method ideal for this data set.

The measurement $\hat{Y}_\theta$, which is associated with one or two parameters, had relatively high standard errors (Figure 3.5). The high variances, and low number of parameters to be identified, justified use of the slower parameter-optimization techniques for fitting to the $\hat{Y}_\theta$ measurement.

The actual numerical values for all of the identified parameters, for all operators and conditions, are presented in Section D.3 of Appendix D. In addition to the model parameters, a fit quality index, J, is reported to help assess the quality of the fit for each condition; it is defined in Equation C.10. Lower values of J indicate better fits. The terms J_p, $J_{\theta 1}$, and $J_{\theta 2}$ refer to the fit quality indices for the models Y_p, $Y_{\theta 1}$, and $Y_{\theta 2}$, respectively. As this data is quite extensive, only a subset will be presented in

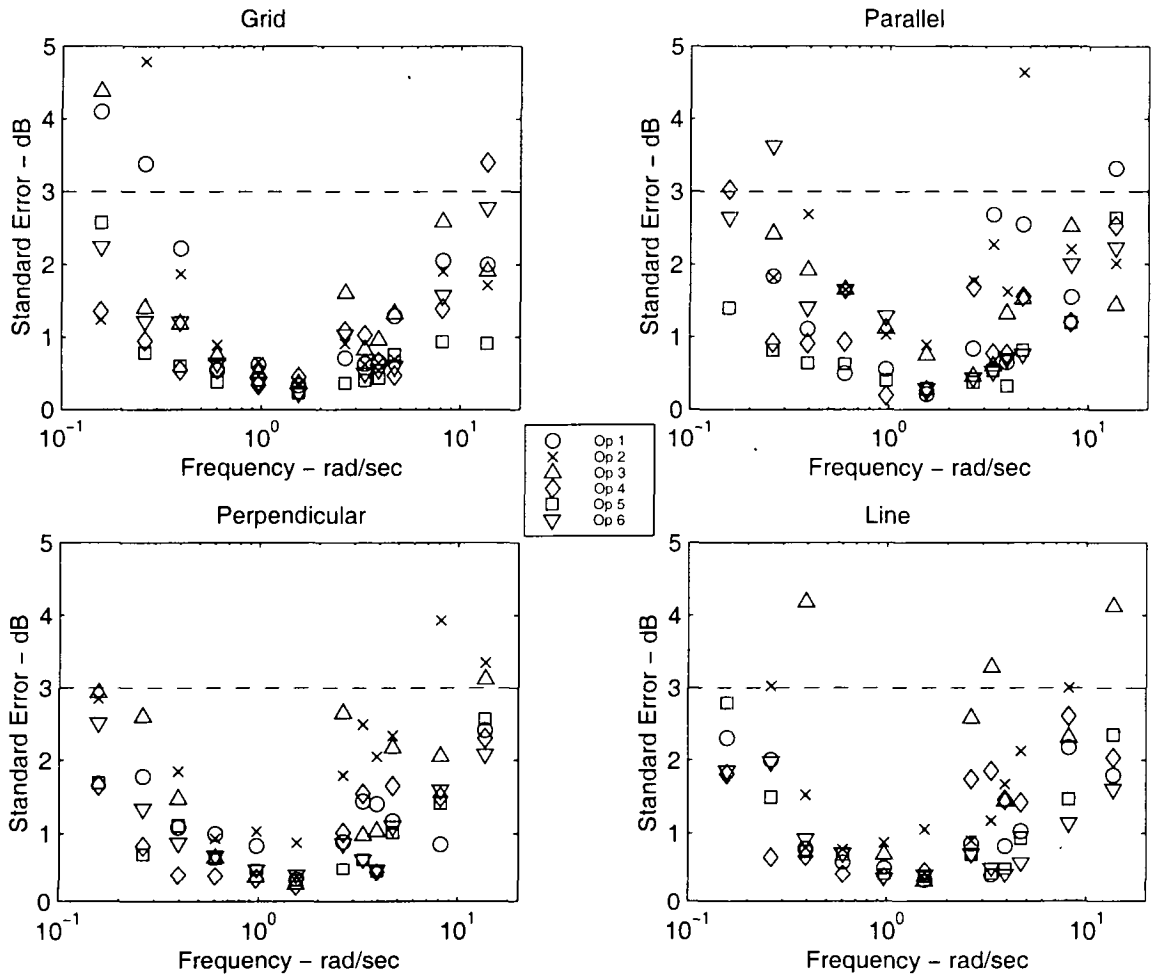

Figure 3.4: Standard error estimates of $\hat{Y}_p$, as a function of input frequency, for all operators and conditions in Experiment 1. The standard error is related to the standard deviation for this data by $se = \sigma/\sqrt{5}$ (the measurements are ensemble averages from five repetitions). The technique used to determine the standard error is described in Section B.2. A value of 3 dB is commonly used in manual control research as the cutoff point for the maximum acceptable standard error; a dashed line is shown as a reference at this 3 dB point.

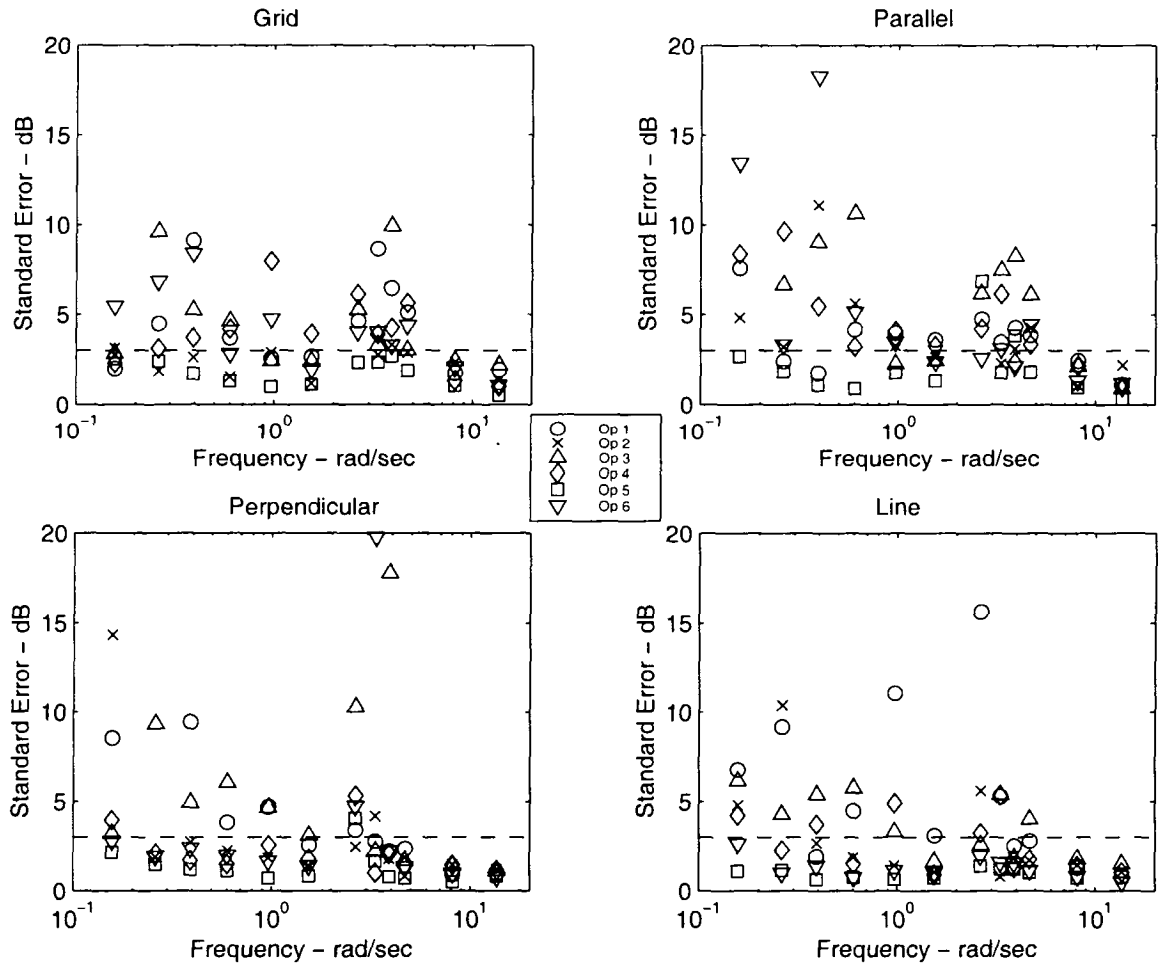

Figure 3.5: Standard error estimates of $\hat{Y}_\theta$, as a function of frequency, for all operators and conditions in Experiment 1. The standard error is related to the standard deviation for this data by $se = \sigma/\sqrt{5}$ (the measurements are ensemble averages from five repetitions). The technique used to determine the standard error is described in Section B.2. A value of 3 dB is commonly used in manual control research as the cutoff point for the maximum acceptable standard error; a dashed line is shown as a reference at this 3 dB point.

figure form in the body of this chapter. What follows are the most relevant results of the model fitting to the measurements $\hat{Y}_p$ and $\hat{Y}_\theta$.

As suggested by Equation 2.13, the simplest form of Y_p that consistently fit the data was:

$$Y_p(s) = K_p e^{-\tau s}(s + \omega_L) \tag{3.3}$$

The measurements from the highest two frequencies (at approximately 8 and 13 rad/sec) were not used for the parameter fitting. Initial attempts at parameter fitting revealed a systematic error in the fit at these frequencies. Closer examination of the data revealed that, at these two frequencies, the culprit was a pixel-jumping phenomenon: the effect of the longitudinal position disturbance on the visual cues was extremely small (less than one pixel peak-to-peak). The effect of the pitch disturbance at these frequencies was still quite noticeable, approximately five pixels peak-to-peak. In the other frequency ranges, the effects of both disturbances were easily observable. Therefore, the parameter fitting was constrained to the first ten frequency points. The actual plots of the measurements and model fits, for all conditions and operators, are contained in Figures D.1 through D.24 in Section D.4 of Appendix D.

The derived values for K_p, τ, and ω_L, as well as the index of fit quality J_p, are presented in Table D.8. Overall, there appeared to be very little if any systematic variation in these parameters due to the manipulation in texture. However, systematic variations are not easily seen in these parameters because of the way in which the parameters interact with each other. In manual control, it is common practice to examine the characteristics of the product of the operator compensation (Y_p) and the controlled element dynamics (Y_c). In particular, the variables of interest are the crossover frequency ω_c and phase margin ϕ_m. Figure 3.6 shows the open-loop frequency response of the nominal Crossover Model (Equation 1.1) with the crossover frequency and the phase margin identified. The crossover frequency ω_c and phase margin ϕ_m are defined as follows:

$$|Y_p(j\omega_c)Y_c(j\omega_c)| = 1 \tag{3.4}$$

$$180^\circ + \angle(Y_p(j\omega_c)Y_c(j\omega_c)) = \phi_m \tag{3.5}$$

The crossover frequency is the frequency at which the magnitude of the open-loop

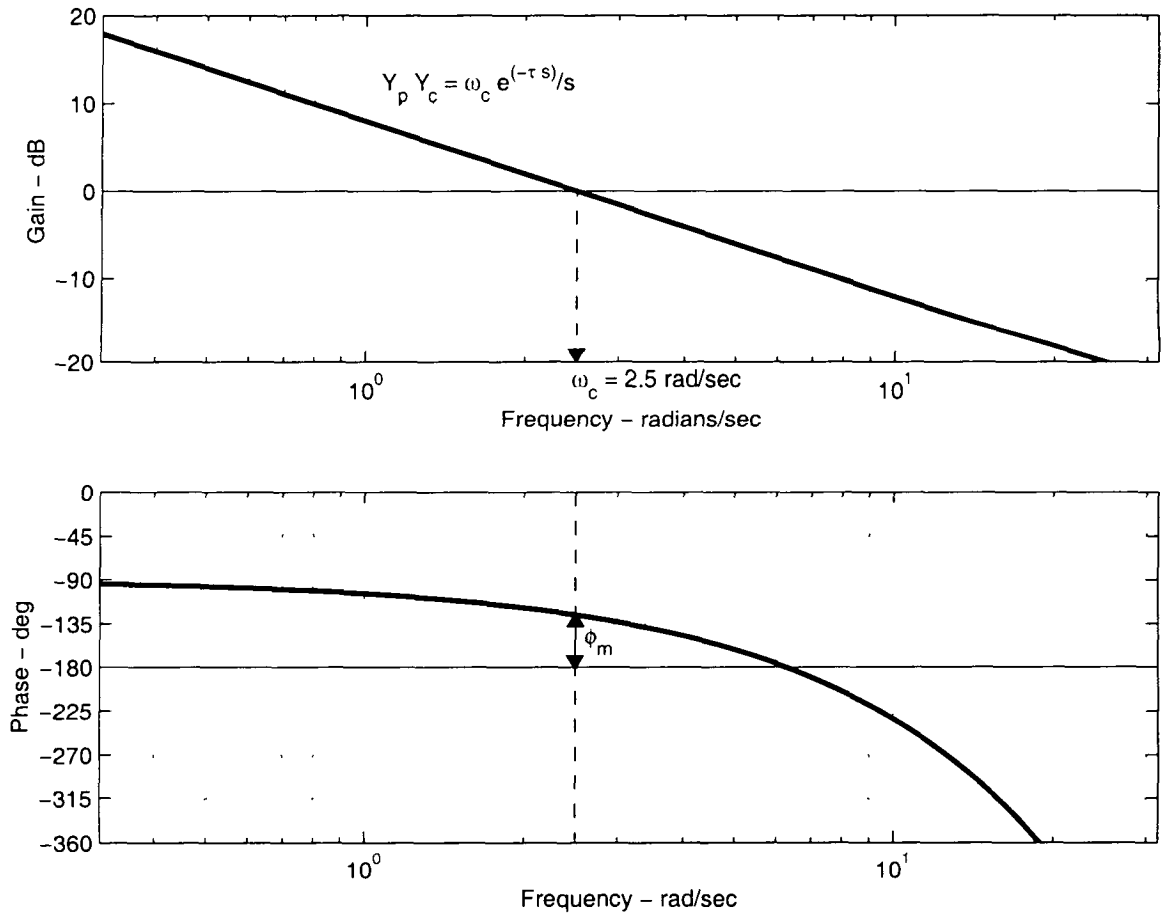

Figure 3.6: Example Crossover Model frequency-response plot showing crossover frequency ω_c and phase margin ϕ_m. The open-loop frequency response of $Y_p(s)Y_c(s) = 2.5e^{-.25s}/s$ is shown.

transfer function is unity. The phase margin is the amount of phase in excess of -180 degrees of the open-loop transfer function evaluated at the crossover frequency. The crossover frequency determines the bandwidth of the system, or the frequency above which tracking performance starts to degrade. The phase margin is a measure of the stability of the closed-loop system. When the phase margin approaches zero, slight uncertainties in the plant dynamics or variations in loop gain can create unstable closed-loop characteristics.

Crossover frequency and phase margin were derived for all operators and conditions; they are presented in Table D.9 and Figure 3.7. As can be readily seen, there is far more individual difference between operators than between texture conditions. There does appear to be some systematic variation in the crossover frequency with texture type, although it is still small in relation to the individual differences. Generally, for a particular operator, the highest crossover frequencies were observed with the Grid texture, and the lowest with the Line texture. The higher crossover frequency implies that the operator is responding over an effectively higher bandwidth with the Grid texture than the Line texture; this is one likely cause of the improved performance shown in Figure 3.3. The qualitative difference between the displays is that the Grid texture has far more available visual cues than the Line texture; the Parallel and Perpendicular textures have more cues than the Line, but less than the Grid. The level of redundancy of available cue sources in the different textures could be responsible for the observed performance effects. Unlike the crossover frequency, the phase margin does not appear to have any systematic variation with texture condition[3], implying that the stability of the closed-loop system was not affected by texture type.

The amount of lead developed by the operators, defined by $1/\omega_L$, also seemed to vary as a function of texture. This is shown in Figure 3.9. The Grid and Parallel textures were associated with the lowest values of ω_L (most lead generation) for most operators, and the Line texture had the highest values.

The function Y_p is related to how the operator responds to the relevant longitudinal

[3]Although it does vary sharply and conformally with ω_c achieved, i.e., with the aggressiveness of the individual operator. See Figure 3.8.

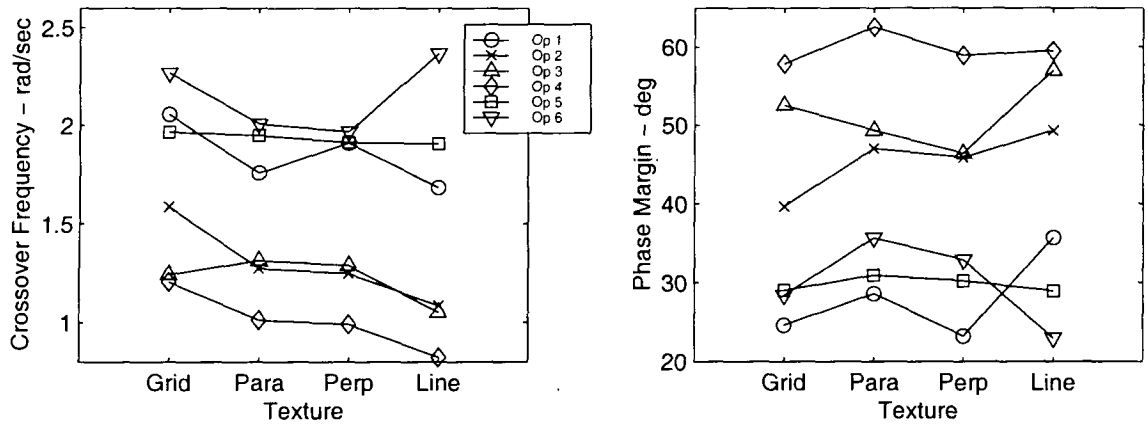

Figure 3.7: Crossover frequency and phase margin for all operators and conditions in Experiment 1.

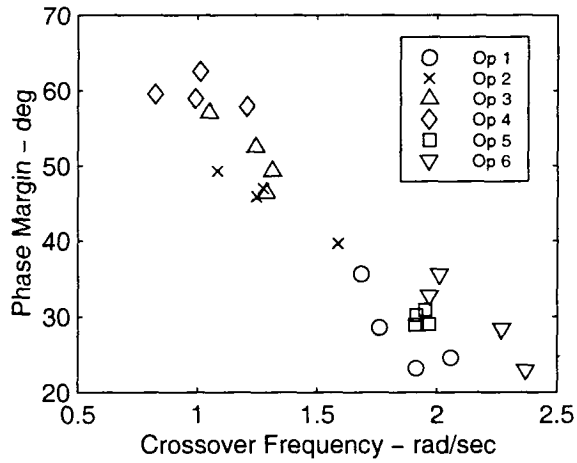

Figure 3.8: Crossover frequency versus phase margin for all operators and conditions in Experiment 1. Note that operators 4, 5, and 6 were the most "aggressive", achieving the highest crossover frequencies and lowest phase margins. Operators 1, 2, and 3 were more comfortable adopting a less aggressive control strategy, with more phase margin.

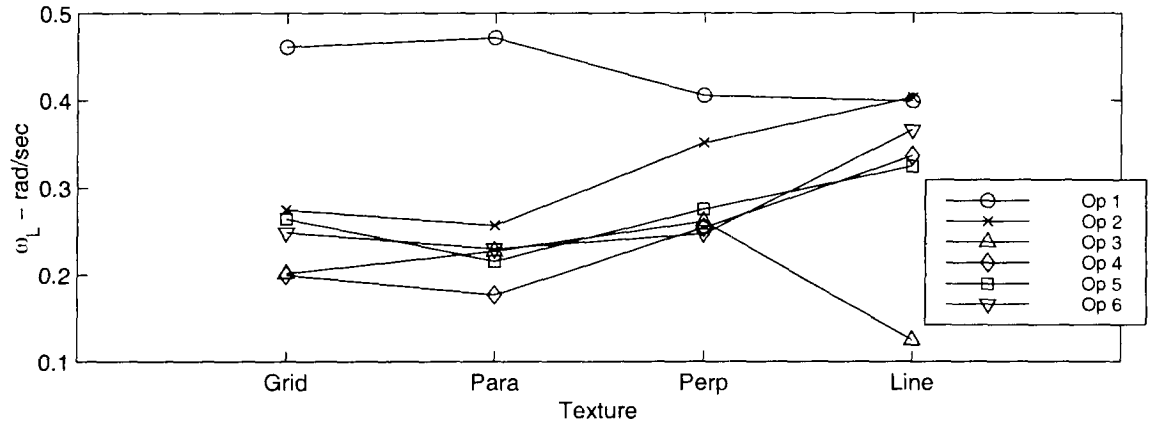

Figure 3.9: Lead break frequency ω_L for all operators and conditions in Experiment 1. Most of the operators using the Grid and Parallel textures demonstrate the ability to generate more lead in their control strategy (incorporate more velocity feedback) than when using the Perpendicular or Line textures.

position variable x, and by itself, does nothing to determine how visual cues were used. The operator response to the irrelevant variable θ, modeled by $Y_{\theta 1}$ or $Y_{\theta 2}$, relates to the visual cue being used. To review, $Y_{\theta 1}$ is the visual-cue model based upon one cue for both motion and position sensing; it is defined through the previously identified parameters of Y_p, as well as the additional parameter K_α. $Y_{\theta 2}$ is the visual-cue model incorporating one cue for motion, and another cue for position. This model is defined by the parameters of Y_p, and the parameters K_β (for motion sensing) and K_γ (for position sensing). The parameters of Y_p are completely determined through the spectral density measurement $\hat{Y}_p$; therefore, the only degrees of freedom remaining to fit the spectral density measurement $\hat{Y}_\theta$ are K_α for the one-cue model $Y_{\theta 1}$, and K_β and K_γ for the two-cue model $Y_{\theta 2}$.

The parameters K_α, K_β and K_γ were chosen as described previously and in Appendix C, to fit the measurement $\hat{Y}_\theta$. The fit quality index $J_{\theta 1}$ and parameter K_α, for all operators and conditions, are contained in Table D.10. $J_{\theta 2}$, $J_{\theta 2}/J_{\theta 1}$, K_β, and K_γ for all operators and conditions are contained in Table D.11. The identified parameters of K_α, K_β and K_γ are shown in Figure 3.10. The theoretical values expected for the visual cues analyzed in Section 2.5 are also included in this figure. Note that the

identified values of the parameters generally fall within the expected range of values from the theoretical visual cue analysis (Table 3.1).

The one-cue and two-cue models are compared in two ways. The first way is to determine how similar the parameters of the two-cue model are to the parameter of the one-cue model. It was previously noted that the two-cue model becomes equivalent to the one-cue model when the parameters K_β and K_γ are identical to each other, or when $K_\beta = K_\gamma$. Figure 3.11 shows the ratio K_β/K_γ for all operators and conditions. In many cases, particularly with the Grid and Parallel textures, operators appear to be using two cues (since the ratio is well below unity). The operators using the Line texture, however, appear to be using one cue.

This ratio K_β/K_γ alone does not conclusively indicate that the operator is using two cue sources. The one-cue model has one free parameter, while the two-cue model has two free parameters. A model-fitting procedure will always "use" a free parameter when available to achieve the best fit, even though it could be fitting a relatively high-variance datum. In addition to checking the ratio K_β/K_γ, it also is prudent to examine how much the additional parameter improved the quality of the fit. Figure 3.12 shows the ratio of the fit-quality parameters $J_{\theta 2}$ and $J_{\theta 1}$. It is difficult to quantify a number for this ratio that corresponds to the case when the one-cue strategy is adequate to describe the data, but some estimates can be made. There are twenty data points (ten complex measurements) being fit. If we assume that the additional parameter on average will provide a one-in-twenty improvement to the fit, an average improvement in the performance index of 5% might be expected. Therefore, if the *one-cue* model is adequate, one might still expect that, on average, the ratio of $J_{\theta 2}/J_{\theta 1}$ would be approximately .95. A confidence interval of three times this, or in this case 15% improvement, might be used to determine when the two-cue model is clearly more representative. These intervals are included in Figure 3.12; as can be seen, in many cases, particularly for the Parallel and Grid textures, the ratio is at and below 0.85. Many other cases fall between the two intervals. While this data does not conclusively support the two-cue model, there is evidence that the two-cue model is required to adequately describe several of the cases. The fact that in many cases, the one-cue model appears to adequately describe the data, does not prove that a one-cue strategy

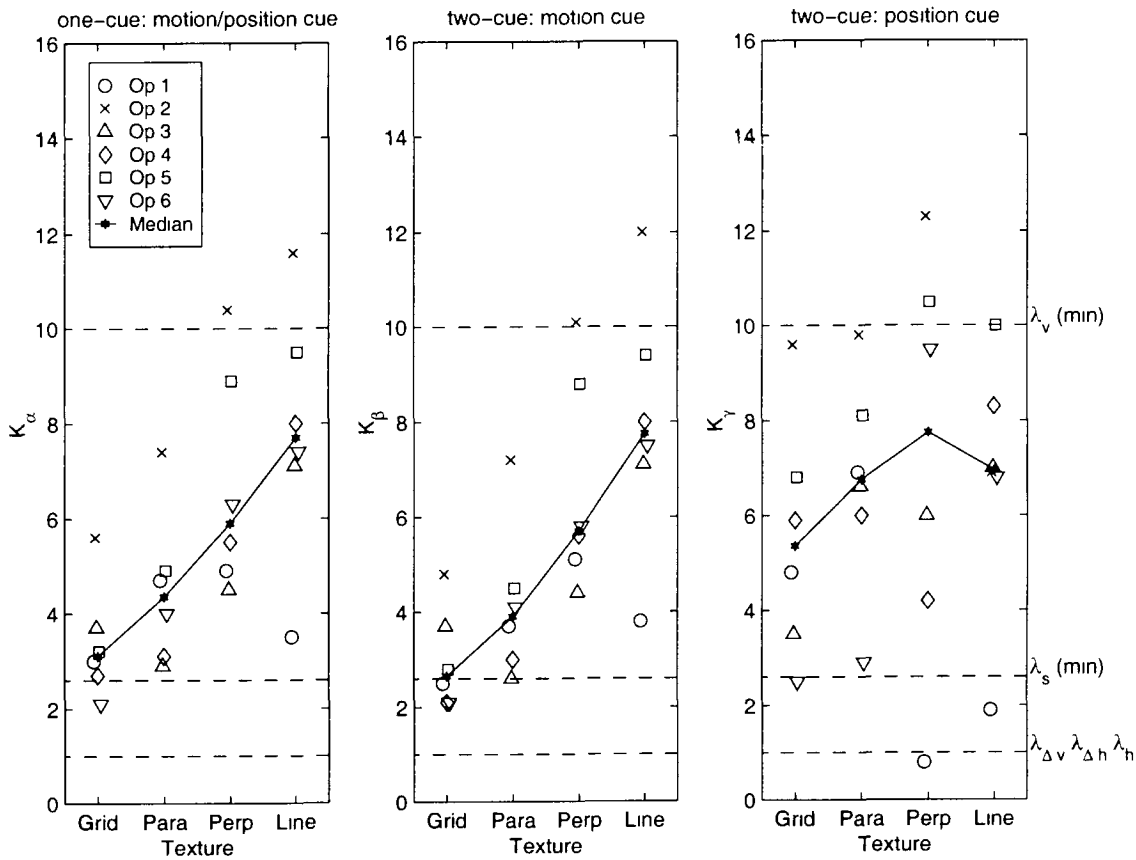

Figure 3.10: Identified parameters K_α (left), K_β (middle), and K_γ (right) for all operators and conditions in Experiment 1. K_α is the parameter in the one-cue model that corresponds to the sensitivity of the visual cue used for both position and motion; refer to Figure 2.6 and Equation 2.42. K_β is the parameter in the two-cue model for the sensitivity of the visual cue used for motion sensing; K_γ is the parameter for the position visual cue. Refer to Figure 2.7 and Equation 2.43 for the two-cue model. Dashed lines on the plot (and labeled in the right margin) indicate the predicted values of these parameters for the potential visual cues examined (refer to Table 3.1). Examples of the visual cues are shown in Figure 2.11. To review, λ_s refers to displacements or motions along the lines of splay, λ_h and $\lambda_{\Delta h}$ are horizontal components of motion or displacement of features (absolute and relative respectively), and λ_v and $\lambda_{\Delta v}$ are vertical components.

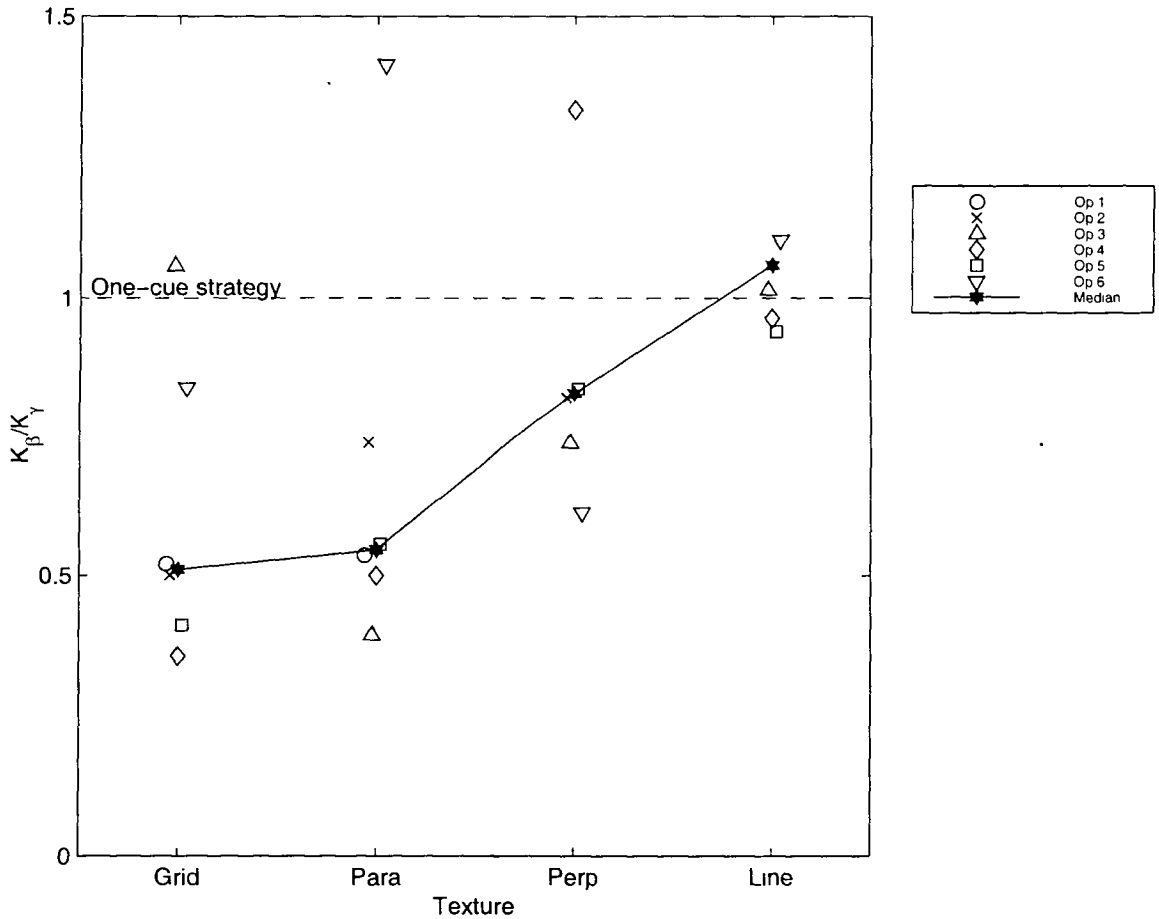

Figure 3.11: The ratio K_β/K_γ from Experiment 1 for all operators and conditions. K_β and K_γ are the motion and position visual cue sensitivities, respectively, in the two-cue model. The two-cue model becomes equivalent to the one-cue model (in which one visual cue is used for both position and motion sensing) when the ratio K_β/K_γ is unity. The data is strongly supportive of the two-cue model, rather than the one-cue model, when this ratio is well above or below unity, as it is, except for the pure line texture.

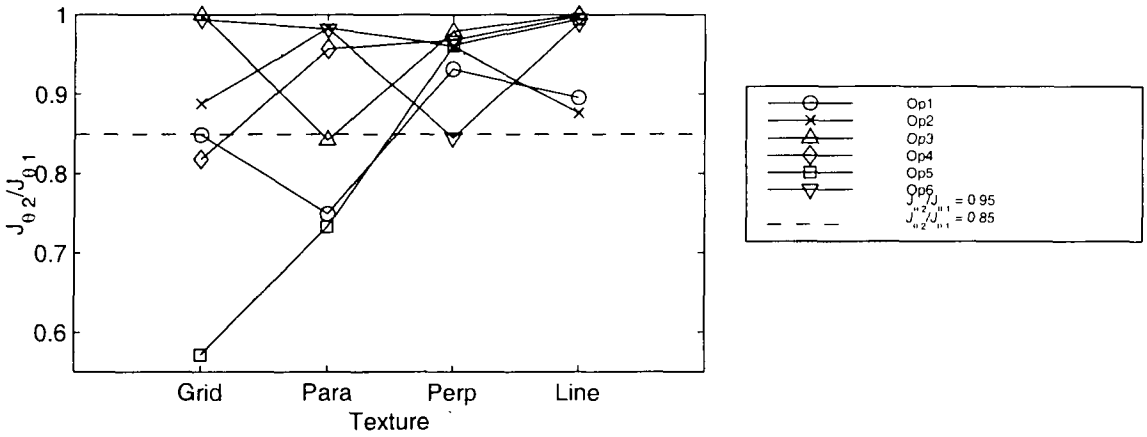

Figure 3.12: The ratio of the fit quality indices $J_{\theta 2}/J_{\theta 1}$, for the two-cue versus one-cue model fits, for all operators and conditions for Experiment 1. Lower values of J indicate a better fit. In those instances when the ratio $J_{\theta 2}/J_{\theta 1}$ is significantly below unity, the two-cue model provides a significantly better fit to the data than the one-cue model. The dotted line at 0.95 shows the level of improvement in the ratio that might be expected from chance with the addition of one parameter to the model (going from one-cue to two-cue); the dashed line at 0.85 shows three times this level.

is being used; it is also possible that the variances prevent discrimination of the two models. The structural difference between the two models is a lag-lead element in the vicinity of the lead break frequency ω_L. This lag-lead network has the form:

$$LL(s) = \frac{s + (K_\gamma/K_\beta)\omega_L}{s + \omega_L} \tag{3.6}$$

For this data set, the values of ω_L are in the range of 0.2 to 1.0 rad/sec, while the ratio of K_β/K_γ tends to be in the vicinity of 0.5 to 1.0. This would put the frequency range in which one would "see" the effects of the lag-lead network to be in the range of 0.2 to 2.0 rad/sec, with most of the cases falling into the range of 0.5 to 1.0 rad/sec. As was pointed out before, the data in this area tended to have high variances (see Figure 3.5). Since the fitting procedure as well as the fit quality index J uses the inverse of variance, the fitting of high-variance data can create a very modest improvement in $J_{\theta 2}$ relative to $J_{\theta 1}$. Although the fitting procedure identifies values of K_β and K_γ that are quite different, the improved fit has very little effect on the fit-quality index due to the high variances of the points that were improved.

It can be seen from referring to Figure 3.10 that the values derived for K_α tended to be quite close to K_β, rather than being some median value between K_β and K_γ. This is a predictable result for two reasons. The first reason is that the majority of the data points are above the frequency region in which the lag-lead network exerts it's influence; above this frequency, K_β is the parameter that determines the fit. Since more than half of the points are more strongly influenced by K_β, the one-cue fit would tend to identify values of K_α closer to K_β than K_γ. The second factor is that the fit was influenced by the variances; the frequency region above the influence of the lag-lead network was typified by lower variances than the data within the frequency region of the lag-lead network. This would also tend to favor identification of values of K_α that are closer to K_β than K_γ.

3.3 Discussion

The two objectives of this experiment were: 1) to determine if the operator's strategy could be modeled with either form of the VCC model, and 2) to determine if measurable differences in the operator strategies would result from manipulation of the perspective scene elements.

The second objective has been demonstrated with the ANOVA analysis results. The manipulation of the scene elements produced statistically significant effects on the control activity (percent of control correlated with pitch disturbance and with longitudinal disturbance), as well as the position and velocity rms.

The first objective has been partially met; although the models show good correspondence with the data in many cases, it is impossible to determine from this data set whether the two-cue model is more representative than the one-cue model. In several cases, the two-cue model is clearly superior, but in the majority of the cases the improvement in the fit achieved with the two-cue model is not appreciably better than what would be expected from chance. A factor that could be responsible for the difficulty in differentiating the acceptability of the models was the high variances associated with the $\hat{Y}_\theta$ measurement. This will be addressed in Experiment 2, described in the next chapter.

An encouraging result from the individual modeling was that the parameters derived for the visual-cue sensitivities (K_α, K_β, K_γ) generally fell into the range expected from the theoretical analysis of the visual cues. Specifically, many operators achieved values of K_α and K_β that were close to the predicted value for the cue related to the line of splay (λ_s). This would be achieved if the operator were capable of attending to displacement or motion of a particular feature *along* the lines of splay at the lower, outer corners of the display. Additionally, the values of K_γ achieved for many operators, particularly with the Perpendicular and Line textures, were close to the expected value if they used the line closest to the operator as a position reference (λ_v). This lends support to the validity of the modeling approach. It also suggests the possibility that this methodology could support the identification of particular visual cues being used for a task. This is feasible because the identified parameters K_α, K_β, and K_γ can be directly related to the visual cue or cues being used, through the model of perspective projection and visual cue selection.

The potential for visual cue identification suggested additional changes in Experiment 2. A fundamental characteristic differentiates the Grid and Parallel textures from the Perpendicular and Line textures. The Grid and Parallel textures have individual points (from the grid intersections) that can create arbitrary two-dimensional motion in the image. They also have lines of splay. It was realized after-the-fact that this experimental treatment did not allow any differentiation between the effects of lines of splay, and individual points. This is potentially an important factor, since one of the theoretical visual cues was based on the hypothesis that motion directed along a line of splay was being detected. Additionally, the identified parameters for K_β in several cases were quite close to the theoretical predictions for using this cue (λ_s). Experiment 2, then, will be seen to include modifications to allow differentiation between the contribution of lines of splay and individual points.

Chapter 4

Experiment 2

The results of Experiment 1 demonstrated that:

1. The input/output characteristics could be accurately represented with either form of the VCC model (both the one-cue and two-cue).

2. Manipulation of the task variables could produce measurable effects on the control strategy and performance.

What the experiment failed to demonstrate was which form of VCC model, one-cue or two-cue, was a superior representation of the task. This failure could be attributed to high variances in the measurements of one of the transfer functions, $\hat{Y}_\theta$ (the control output of the operator due to pitch attitude). Another factor which could not be discriminated from the Experiment 1 results was the potential effects of lines of splay in the display versus individual points.

These factors and others were addressed in Experiment 2. Efforts were made to reduce the measurement variance. Individual points were added to some of the perspective scene textures, to differentiate the effects of the lines of splay and individual points. This experiment also provided an opportunity to rectify some inadvertent errors that had occurred in Experiment 1. The uneven lateral and longitudinal spacing of the grid lines in Experiment 1 was the result of a coding error; this was corrected in Experiment 2. Another problem addressed in Experiment 2 was the unequal effect of the longitudinal and pitch disturbances at the highest frequencies.

The goal of Experiment 2 was to:

1. Determine which form of the VCC model, the one-cue or two-cue, was most representative of the operator's control strategy.

2. Determine what effect, if any, lines of splay in the display have on the control strategy.

3. Investigate the potential of the model to provide a methodology for visual cue identification.

In summary, Experiment 2 duplicated much of the Experiment 1 design, with the changes and modifications described above. The results will show that the two-cue model is necessary to represent the task for nearly all of the conditions tested. They will also show that the presence of lines of splay have a slight, but statistically significant, effect on the control activity and the velocity rms. Conditions with the lines of splay were associated with control power with more correlation to the longitudinal disturbance, and less correlation with the pitch disturbance, than those conditions without lines of splay. The lines of splay were also associated with lower levels of velocity rms. The model appears to provide a preliminary basis for visual cue identification; in many cases the parameters identified in the models corresponded closely to the available visual cues.

A description of the experimental protocol for Experiment 2 is provided in Section 4.1. Section 4.2 contains the experimental results from both the ANOVA analyses and the individual modeling, and Section 4.3 contains discussion of those results.

4.1 Protocol

4.1.1 Participants

Ten participants were used. They were recruited from a contractor pool at Ames Research Center. All were male general aviation pilots, with experience ranging from 135 to 1600 total flight hours. The study design required a total of eight participants;

the data from two of the ten participants were not included in the data analysis of this study. One of these participants was dropped from analysis because he had participated in Experiment 1. Another was replaced when he was unable to comply with the test instructions (this is described further in Section 4.2.2). None of the eight participants used for the data analysis presented in this chapter participated in Experiment 1.

4.1.2 Apparatus

A different apparatus was used in Experiment 2 than had been used in Experiment 1. The simulation was hosted on a different computer, a Silicon Graphics Octane. The Octane offered better update rates and a potential for more complex graphics than the original host computer. On this new platform, the simulation updated at the monitor refresh rate of 72 Hz, increased from the previous update rate of 33.3 Hz. A new joystick was also employed on this apparatus. In Experiment 1, the operators used a device called a Flybox, which is a device holding not only the joystick, but also buttons and throttle-type levers. Operators were required to hold the flybox on their lap in the first experiment. For this experiment, a B&G Systems JF3 3-axis joystick was mounted onto the table holding the computer and monitor. This new apparatus was much more comfortable to use than the Experiment 1 apparatus, particularly for long-duration runs. The joystick inputs were collected at the simulation update rate of 72 Hz.

A different monitor was used in Experiment 2, but it was the same size and at the same position relative to the operator. As in Experiment 1, the color monitor had a 21-inch diagonal screen, with resolution of 1024 vertical and 1280 horizontal pixels. Operators were seated approximately 20 inches from the display. This resulted in approximately 30 vertical by 37.5 horizontal degrees of visual angle subtended by the display.

The dynamics of the vehicle were described in Section 2.1. The actual discrete transfer functions used, as well as the disturbance dynamics, are presented in Section E.1 of Appendix E.

4.1.3 Scene

The textures used in this task are shown in Figure 4.1. The basic four ground texture types used in Experiment 1 were used in Experiment 2, combined with random placements of dots. The vertical and horizontal grid spacings were set to 0.5 eyeheights each. The dots were uniformly distributed, at the same average density of the grid intersections (i.e. 4 per square eyeheight).

As was done in Experiment 1, the ground plane was linearly shaded from light to dark from a position directly under the operator to a distance of 15 eyeheights in front. The dark color was maintained from that location to the horizon. The graphical rendering was done with no anti-aliasing, and the lines were all one-pixel wide. The points in the random dot fields were square, 3 pixels on a side. There was also no depth cueing enabled. Thus, the operator could not get any position information from the perspective thickening of the lines as they grew closer, or from changes in contrast due to distance. The dots also did not change in size due to distance.

Visual-Cue Characteristics

As was done in Experiment 1, the theoretical values of the visual cue parameters were derived for each texture and dot combination tested. The analysis of visual-cue characteristics is identical to that done for Experiment 1, described in Section 3.1.3. Differences relative to the Experiment 1 analysis are as follows:

1. The decreased horizontal spacing of the lines of splay result in slightly lower obtainable values for λ_s in both the Grid and Parallel textures in than Experiment 1.

2. The dots are assumed to be, on average, optimally placed to allow best possible cueing. This means, for example, that the minimum obtainable value for $K_{\lambda s}$ is assumed for all of the conditions with dots (even though in some particular cases this might not be true due to the random placements)

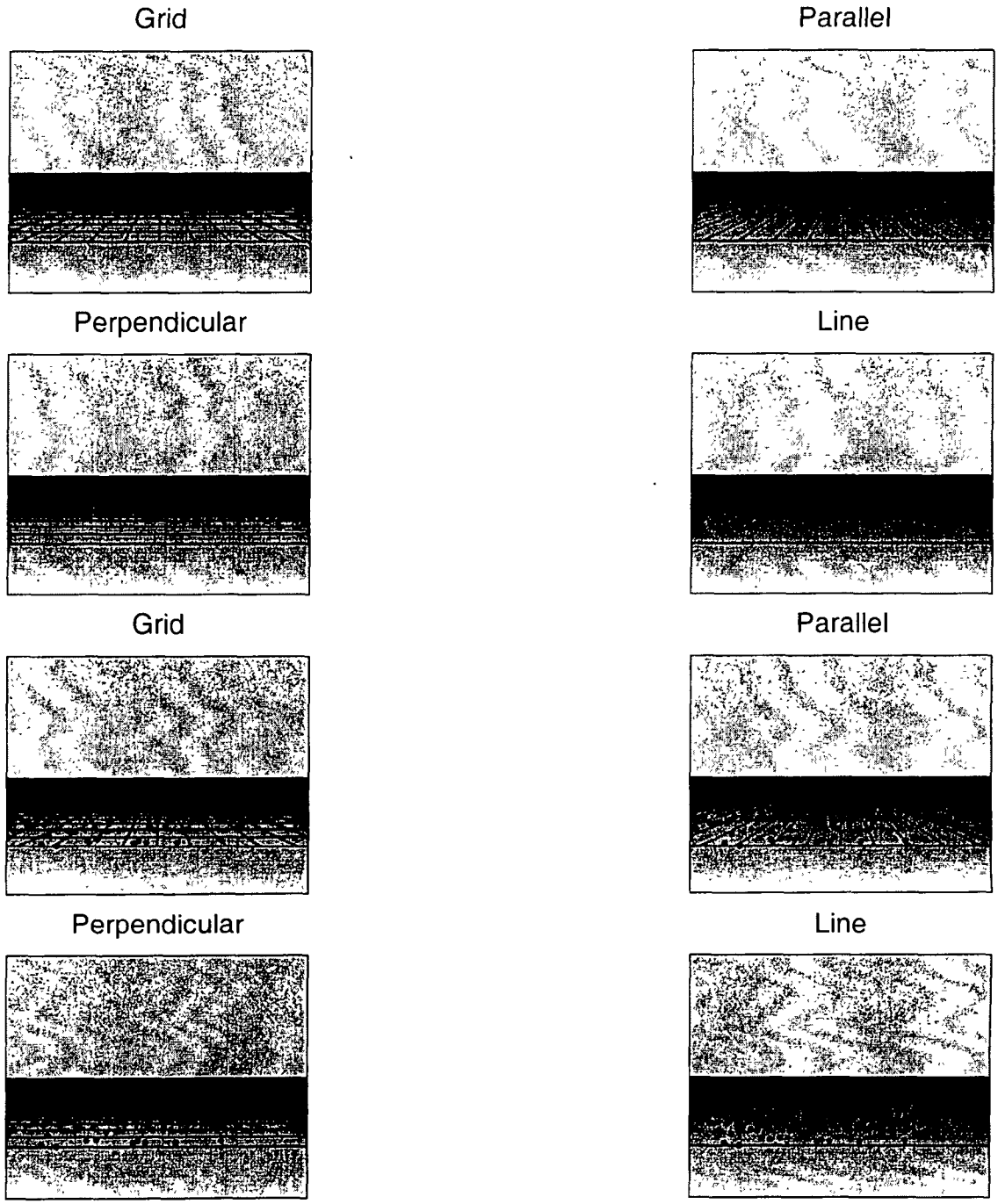

Figure 4.1: The eight texture and dot combinations used in Experiment 2. The top four textures are without dots; the bottom four textures are with dots.

	Texture							
	Without Dots				With Dots			
Cue	Grid	Line	Para	Perp	Grid	Line	Para	Perp
λ_v	≥ 10	10	10	≥ 10	≥ 10	≥ 10	≥ 10	≥ 10
λ_{Δ_v}	1	1	1	1	1	1	1	1
λ_h	1	—	1	—	1	1	1	1
$\lambda_{\Delta h}$	1	—	1	—	1	1	1	1
λ_s	≥ 2.6	—	≥ 2.8	—	≥ 2.6	≥ 2.6	≥ 2.6	≥ 2.6

Table 4.1: Values of K_λ for proposed visual cues in Experiment 2. These cues are depicted visually in Figure 2.11.

The obtainable values for each texture and dot combination of the five potential visual cues is shown in Table 4.1

4.1.4 Task

The task objectives were identical to those of the Experiment 1 task, although the disturbance characteristics were modified. In order to better standardize task performance, written instructions were provided to the participants. The written instructions are shown in Section E.2 of Appendix E.

4.1.5 Procedure

Each operator participated for a total of three days (compared to one day in Experiment 1). On the first day, the operator received training runs in each of the eight conditions. If the average of the operators top five scores[1] (of eight) in all conditions was 1.4 or less, they completed the remaining test protocol which consisted of two days of data runs. The conditions on each of the days were identical, with the exception of the randomized phase angles of the disturbance input components and dot patterns. The data runs were broken into two days to allow an acceptable total time on task; completing the data runs in one day would have required the operator to

[1]The score was the summation of the position and velocity rms over the duration of the run.

Operator	Condition							
1	G/—	‖/:	⊥/—	L/:	‖/—	G/:	L/—	⊥/:
2	‖/—	G/:	L/—	⊥/:	G/—	‖/:	⊥/—	L/:
3	⊥/—	L/:	G/—	‖/:	L/—	⊥/:	‖/—	G/:
4	L/—	⊥/:	‖/—	G/:	⊥/—	L/:	G/—	‖/:
5	G/:	‖/—	⊥/:	L/—	‖/:	G/—	L/:	⊥/—
6	‖/:	G/—	L/:	⊥/—	G/:	‖/—	⊥/:	L/—
7	⊥/:	L/—	G/:	‖/—	L/:	⊥/—	‖/:	G/—
8	L/:	⊥/—	‖/:	G/—	⊥/:	L/—	G/:	‖/—

Table 4.2: Experiment 2 presentation order by operator. The first character in the condition (G, ‖, ⊥, or L) designates the type of line texture (Grid, Parallel, Perpendicular, or Line). The second character, — or :, designates whether dots are absent (—) or present (:).

stay for approximately nine hours.

The experimental protocol consisted of a block of training runs and two blocks of data runs. The data-run blocks were identical to each other except for the randomized phase angles and dot patterns. In both the training and data blocks, eight experimental conditions were tested on each of the eight operators. The conditions consisted of the four textures (Grid, Parallel, Perpendicular, and Line), each with dots present or absent.

Each operator was given a different presentation order for the conditions. In the training block, operators were given eight sequential training runs in each of the eight conditions, for a total of 64 training runs. In the data blocks, the operator was given one training run and then four data runs for each condition. For each operator, the order of presentation (shown in Table 4.2) was identical for the training run and both data runs.

Each data run lasted a total of 4 minutes, 5 seconds. Training runs lasted 60 seconds. Both data and training runs were initiated by the operator by pressing a trigger switch on the joystick. During the first five seconds, the disturbances ramped linearly from zero to full intensity. The simulation proceeded with full-strength disturbances for the remaining time (4 minutes for data runs, 55 seconds for training

runs). Following this, the operators received feedback after both training and data runs on their performance; the feedback consisted of a single value derived by summing the rms velocity and rms position from the run (expressed in eyeheights/sec and eyeheights, respectively).

4.1.6 Experiment Design

The design consists of one factorial, 8 x 4 x 2 with repetitions, line textures (Grid, Parallel, Perpendicular, and Line), and dots (with and without) as factors. The dependent variables included percent control power correlated with pitch disturbance ($P_{\delta\theta}$), percent control power correlated with longitudinal disturbance ($P_{\delta x}$), rms velocity ($\mathrm{RMS}_{\dot{x}}$), and rms position error (RMS_{x}).

4.2 Results

4.2.1 Analysis of Variance (ANOVA)

A 4 × 2 (texture × dots) within subjects Analysis of Variance (ANOVA) was conducted. The same variables used in Experiment 1 were considered: $P_{\delta\theta}$, $P_{\delta x}$, RMS_{x}, and $\mathrm{RMS}_{\dot{x}}$. The results are shown in Figure 4.2, and the statistical significance of each factor and interaction is summarized in Table 4.3. The results without the dots are quite similar to those in Experiment 1, as would be expected. With the dots present, the effect of texture on all of the outcome variables was significantly reduced. The Grid, Parallel, and Perpendicular textures with the dots all exhibited similar values of $P_{\delta x}$, $\mathrm{RMS}_{\dot{x}}$, and RMS_{x}. Only the Line texture appears to be significantly different, and even that effect is much less than that observed without the dots. With the dots present, there appears to be a slight difference in $P_{\delta\theta}$ between textures with lines of splay (Grid and Parallel) and those without (Line and Perpendicular).

One of the purposes for adding dots to the ground texture patterns in Experiment 2 was to help differentiate the contribution of lines of splay from that of individual points. An Analysis of Variance was conducted between two particular texture conditions; the parallel texture with dots, and the line texture with dots. The results

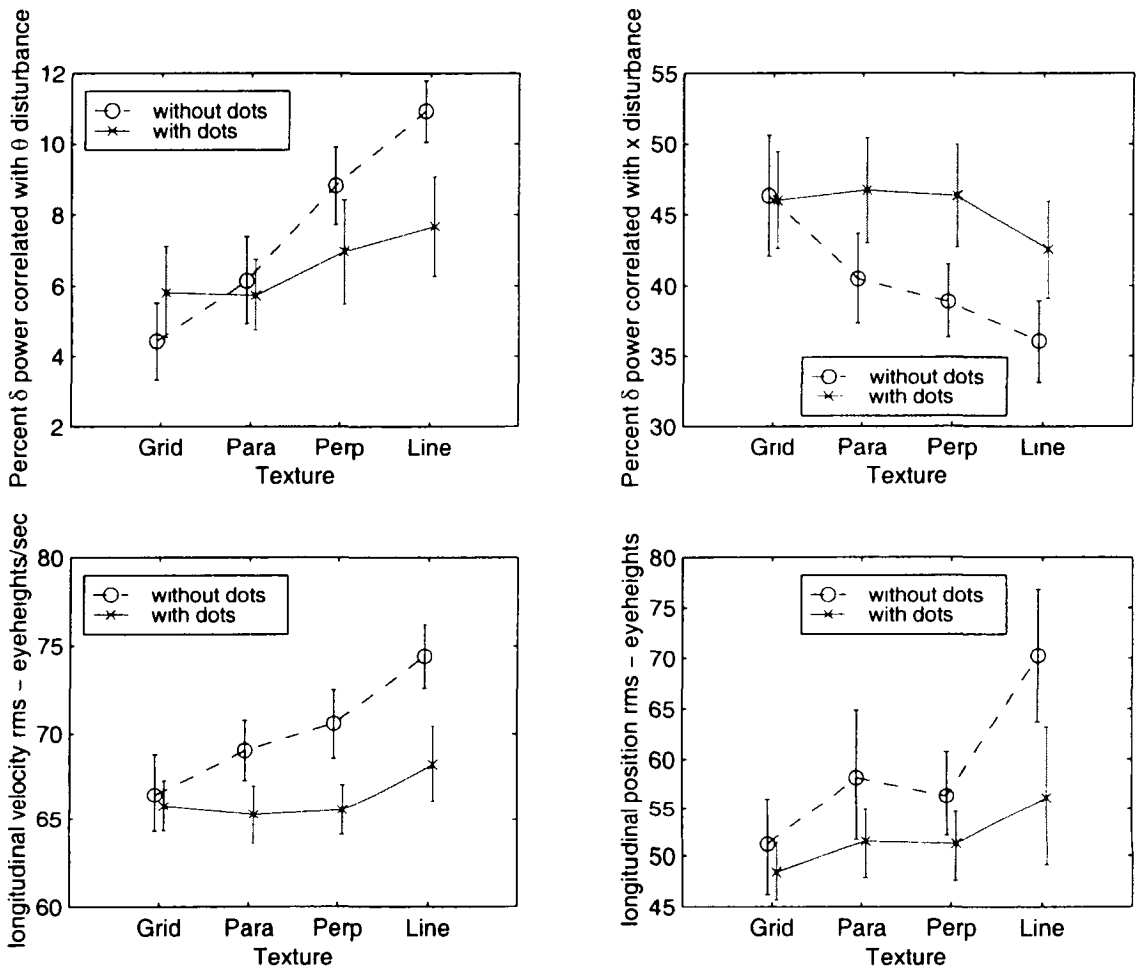

Figure 4.2: Analysis of Variance (ANOVA) results for effect of texture and dots in Experiment 2. The effects on the outcome variables from the differences in texture was generally much less when the dots were present than when they were not.

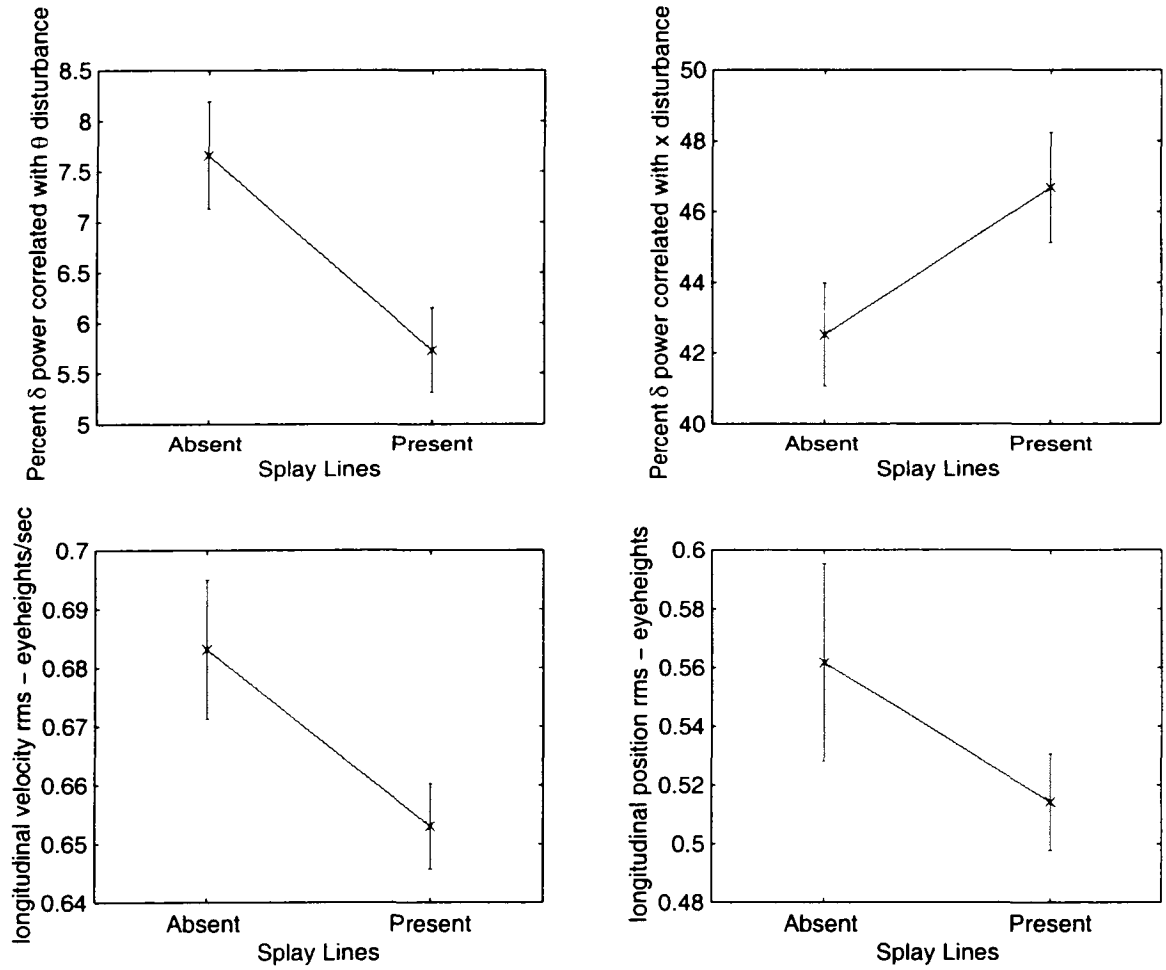

Figure 4.3: Analysis of Variance (ANOVA) results for effect of lines of splay in Experiment 2. Dots were present in all of the conditions included in this analysis. The splay-present condition consisted parallel texture with dots; the splay-absent condition consisted of the line texture with dots. The effect of the lines of splay on the position rms was *not* statistically significant; the effects on the other outcome variables (velocity rms, control power correlated with θ disturbance, control power correlated with x disturbance) were statistically significant.

	Factor		
Measurement	Texture	Dots	Text/Dots Interaction
$P_{\delta\theta}$	+	0	+
$P_{\delta x}$	+	+	+
RMS_x	+	+	0
RMS_x	+	+	0

Table 4.3: Statistical significance for the 4×2 Analysis of Variance (texture × dots) from Experiment 2. The presence of the dots significantly reduces the effects of texture, which is clearly observed when the dots are not present. "+" indicates statistical significance, "0" indicates lack of statistical significance. For this factorial analysis, none of the effects or interactions had marginal statistical significance.

are shown in Figure 4.3. The only difference between these two conditions is the presence of the lines of splay. The analysis revealed a significant effect on both $P_{\delta\theta}$ and $P_{\delta x}$: The presence of the lines of splay was associated with higher levels of control power correlated with the relevant disturbance ($P_{\delta x}$), and lower levels of control power correlated with the irrelevant disturbance ($P_{\delta\theta}$). There was also a marginal effect on the velocity rms, RMS_x: It was slightly lower when the lines of splay were present. The effect of lines of splay on the position rms (RMS_x) was not statistically significant. The results are shown in Figure 4.3.

The numerical values for means and standard errors, as well as the values used to determine statistical significance, are contained in Section E.3 of Appendix E.

4.2.2 Individual Models

Measurements of $\hat{Y}_p$ and $\hat{Y}_\theta$ were made using the technique described in [62] and Appendix B. Each operator completed a total of eight data runs in each condition; for the transfer-function measurements, the six time histories exhibiting the lowest velocity and position rms were used. Although a total of ten operators completed the test protocol, the results of only eight were used for the ANOVA, and are discussed here. One operator was replaced when he volunteered that he had adopted a new control strategy midway through the data runs; since this was not consistent with the

test instructions, his data were not included in the analysis. Another operator was replaced because he had participated in Experiment 1. It was initially thought that some of the participants from Experiment 1 would have to be used, simply because of a shortage of participants. This proved not to be the case. When it became feasible to run only naive participants that had not participated in Experiment 1, this participant was replaced in the data analysis with another, naive, participant. The data from these two (replaced) participants are not included here.

The parameter identification techniques used were identical to those used on the Experiment 1 data, described in Section 3.2.2, with the exception of the model form used for Y_p. The plots of the measurements and model fits for all operators and conditions are shown in Figures E.1 through E.64 of Section E.5 in Appendix E. The simplest form of model Y_p found to correspond well with the measurement $\hat{Y}_p$ was:

$$Y_p = K_p e^{-\tau s} \frac{(s + \omega_L)}{(s^2/\omega_N^2 + 2\zeta_N s/\omega_N + 1)} \tag{4.1}$$

The inclusion of the two highest-frequency data points (at approximately 8 and 13 rad/sec) made it necessary to include a second-order term in the denominator, to represent the neuromuscular dynamics. As can be seen from Table E.8, this term was typified by values of ω_N in the range of 5 to 10 rad/sec, with ζ_N varying from 0.3 to 0.7. This representation for Y_p, and the previously defined structures for $Y_{\theta 1}$ and $Y_{\theta 2}$ (Equations 2.42 and 2.43, respectively), generally provided good fits to the data. The measurements $\hat{Y}_p$ and $\hat{Y}_\theta$ had considerably lower variances overall than those obtained in Experiment 1. The standard error estimates for $\hat{Y}_p$ and $\hat{Y}_\theta$, for all operators and conditions, are shown in Figures 4.4 and 4.5, respectively. The reduced variances were probably due to several factors, including 1) increased simulation update rate, 2) pre-screening participants for a minimum level of performance, and 3) spreading the training and data collection over several days (reducing the effects of fatigue).

As was the case in Experiment 1, the parameter data is quite extensive. It is presented in it's entirety in Section E.4 of Appendix E. Only a subset of this data will be presented in figure form within this chapter. First, the parameters identified for Y_p will be discussed. The fit quality index J_p, and parameters K_p and ω_L are contained in Table E.7 in Appendix E. The parameters τ, ω_N and ζ_N are in Table E.8; the

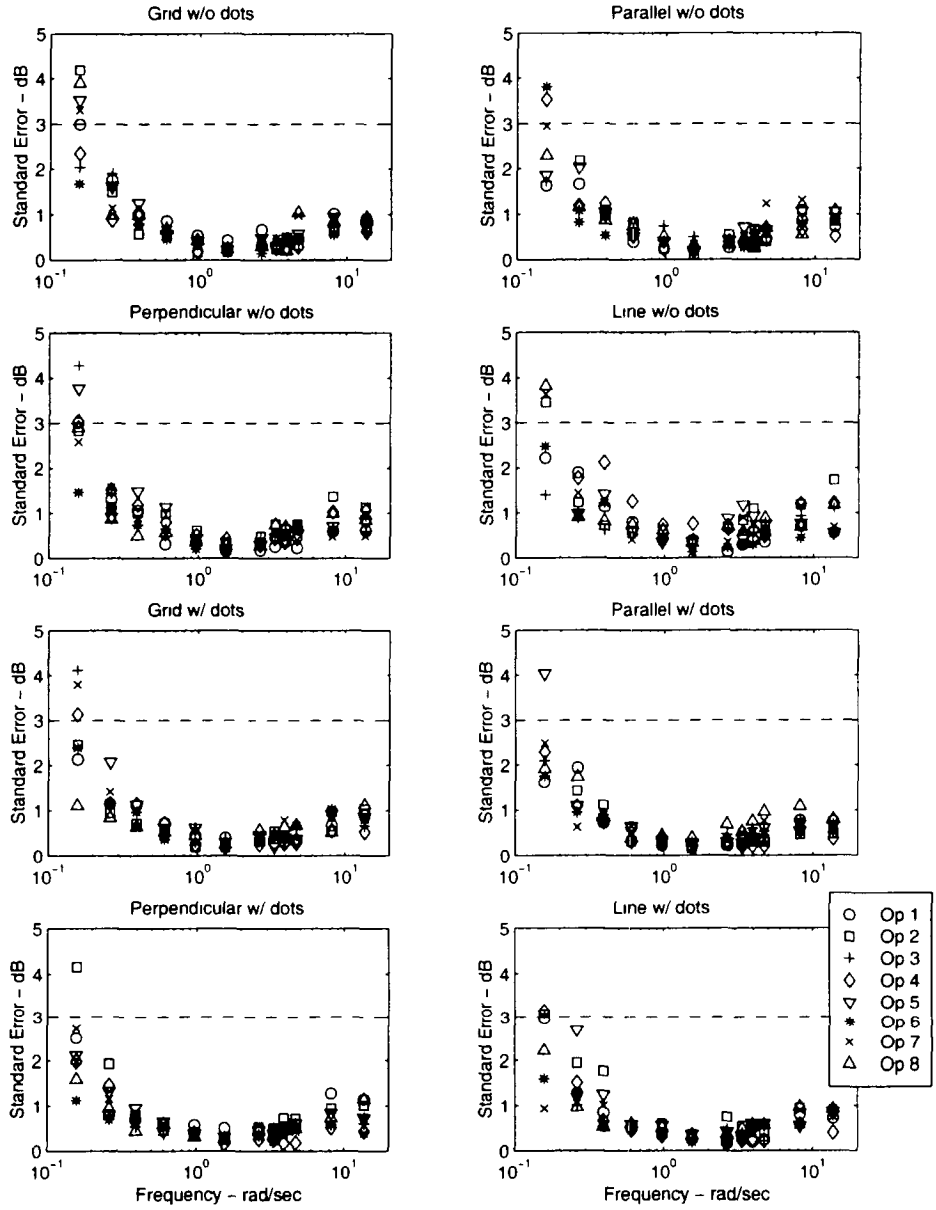

Figure 4.4: Standard error estimates of $\hat{Y}_p$, as a function of frequency, for all operators and conditions in Experiment 2. The standard error is related to the standard deviation for this data by $se = \sigma/\sqrt{6}$ (the measurements are ensemble averages from six repetitions). The technique used to determine the standard error is described in Section B.2. A value of 3 dB is commonly used in manual control research as the cutoff point for the maximum acceptable standard error; a dashed line is shown as a reference at this 3 dB point. These variances represent a significant improvement from Experiment 1 (Figure 3.4).

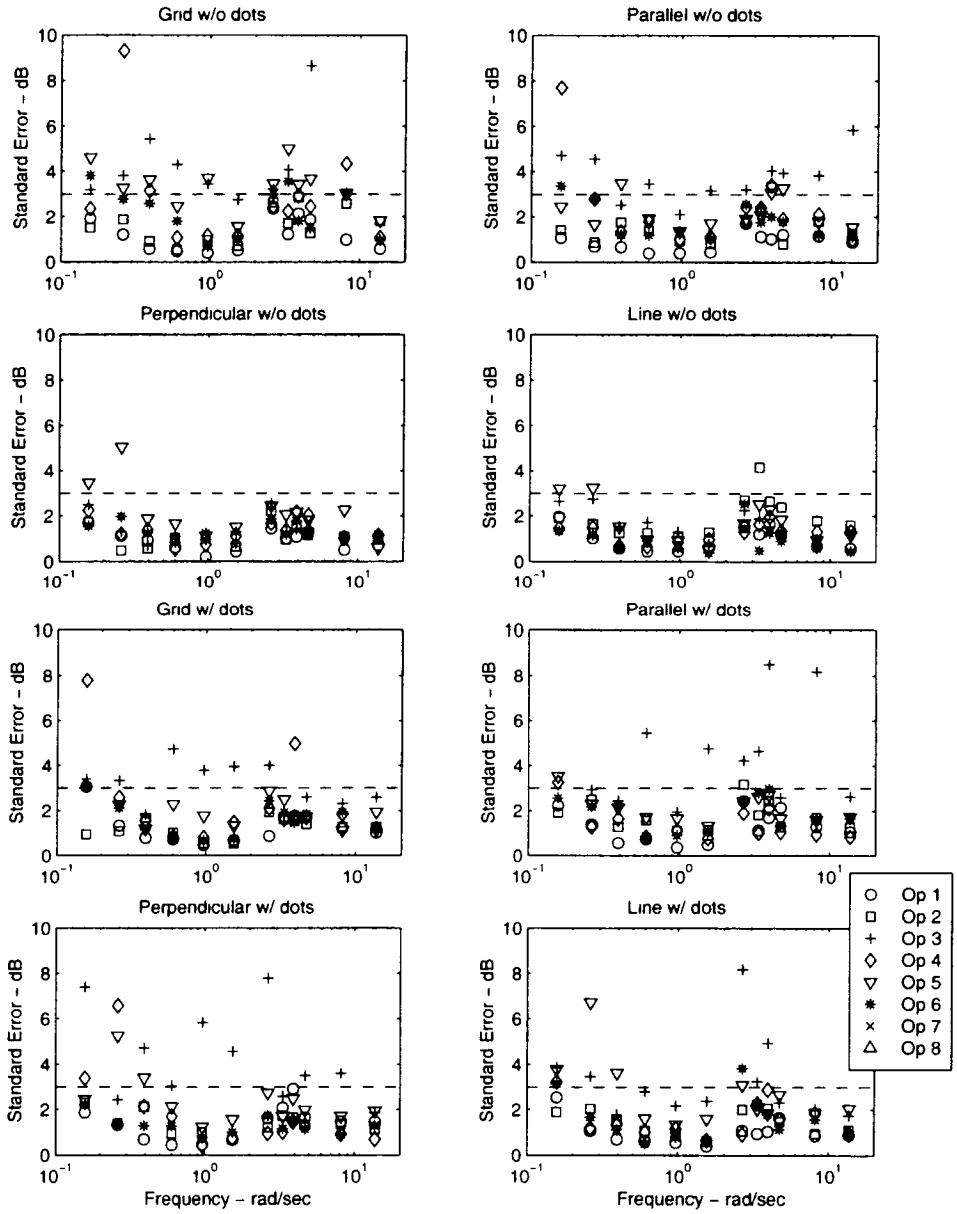

Figure 4.5: Standard error estimates of $\hat{Y}_\theta$, as a function of input frequency, for all operators and conditions in Experiment 2. The standard error is related to the standard deviation for this data by $se = \sigma/\sqrt{6}$ (the measurements are ensemble averages from six repetitions). The technique used to determine the standard error is described in Section B.2. A value of 3 dB is commonly used in manual control research as the cutoff point for the maximum acceptable standard error; a dashed line is shown as a reference at this 3 dB point. These variances also represent a significant improvement from Experiment 1 (Figure 3.5).

crossover frequency ω_c and phase margin ϕ_m of the combined function $Y_p Y_c$ are shown in Table E.9.

Overall, the parameters of Y_p showed little variation with texture. As was the case in Experiment 1, the crossover frequency was somewhat affected by the texture for particular operators, although the variation between operators was of a greater magnitude. The crossover frequency and phase margin for all operators and conditions are shown in Figure 4.6. In Experiment 1, there appeared to be some effect of texture on the crossover frequency. In this experiment, there appears to be a similar effect for the conditions without the dots, although the individual differences between operators is typically greater than the variation within a particular operator. There appears to be no effect in the cases with the dots. The crossover frequency of the loop indicates the bandwidth of effective response; higher crossover frequencies are associated with better closed-loop tracking performance (assuming adequate phase margin). The trends observed in the crossover frequencies are consistent with the ANOVA results in figure 4.2; the "denser" textures (more potential cues) are associated with both higher crossover frequencies and lower rms errors. In the textures without the dots, the texture with the most cues (Grid) has the highest crossover frequency and lowest rms values; the texture with the least cues (Line) is generally associated with the lowest crossover frequencies and highest rms values.

In Experiment 1, there appeared to be little variation in phase margin with texture, which implies that the textures had no effect on the stability of the closed-loop human/vehicle system. The results of this experiment were quite similar, with the possible exception of the Line texture without dots. There was a modest increase in phase margin (5 to 10 degrees) with this condition, relative to the other conditions, for several of the operators. However, in all conditions, the phase margin was adequate to provide good closed-loop stability (no values below 20 degrees were observed). The tendency to increase phase margin in that particular condition could be an attempt of the operator to account for uncertainty in the visual cues.

In Experiment 1, it appeared that the amount of lead the operators were generating was possibly affected by the texture. The effect is not present in the Experiment 2 results. The lead break frequency ω_L for all operators and conditions is shown

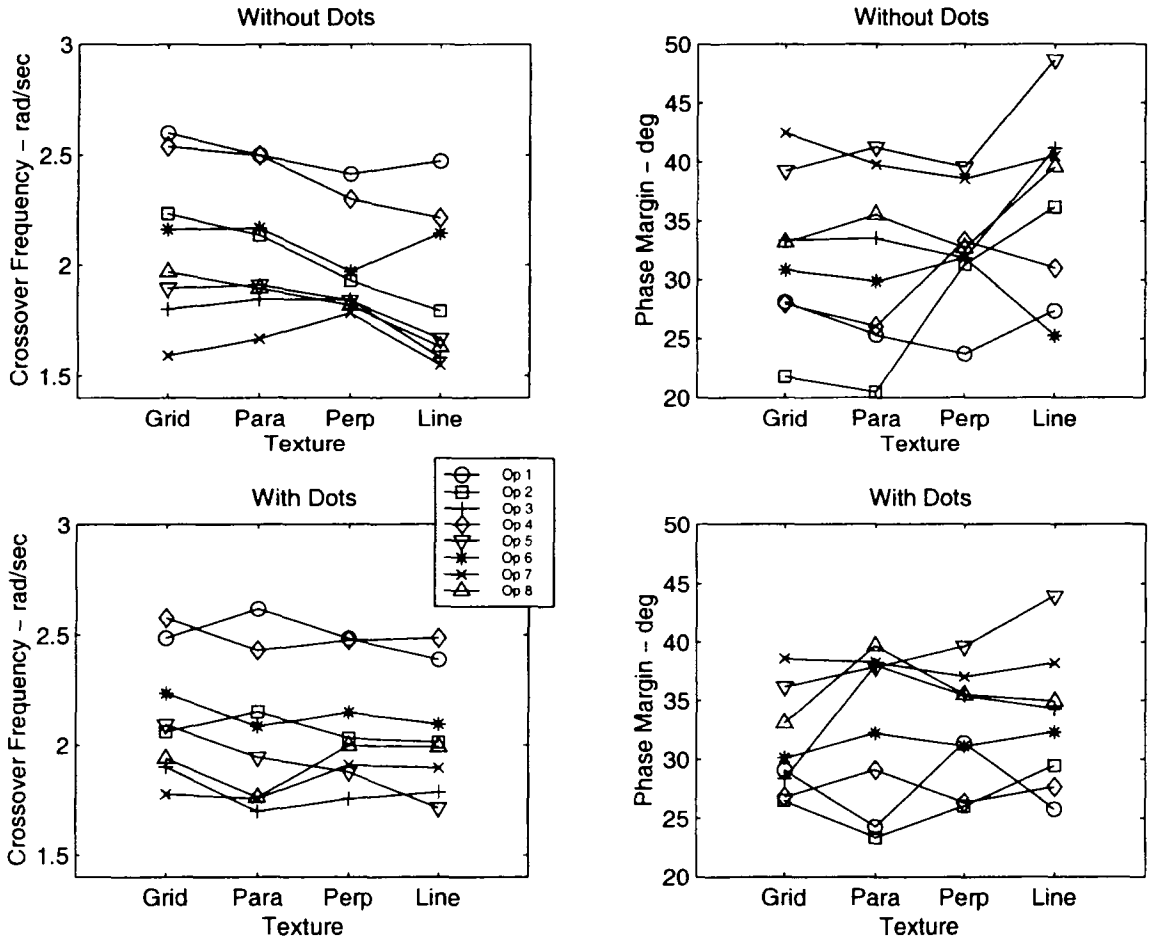

Figure 4.6: Crossover frequency and phase margin for all operators and conditions in Experiment 2. When the dots *are not* present, the crossover frequency varies as a function of scene complexity (higher crossover frequencies with the Grid Texture, lower with the Line texture. When the dots *are* present, there is little if any effect of texture on crossover frequency. Phase margins do not appear to vary within operators as a function of texture, with the exception of the Line texture without dots: This texture is associated with an increase in phase margin with most of the operators.

in Figure 4.7. There are at least two possibilities; one is that the effect observed in Experiment 1 was solely due to chance; without standard error measurements on the parameters, this is difficult to assess. Another possibility is that the modification to the disturbance signal done in Experiment 2 produced a change in strategy that canceled this effect. One characteristic that has been observed in human operator modeling is that as the bandwidth of the disturbance signal increases, an effect known as low-frequency phase droop occurs [28]. When this happens, the phase generated by the human operator at the low frequencies (generally less than 1 rad/sec) decreases noticeably. The bandwidth of the longitudinal disturbance was effectively increased in Experiment 2 (relative to Experiment 1) by increasing the power at the highest frequencies. This increase in bandwidth of the disturbance is another possible explanation for the effect disappearing.

Although not shown graphically here, there was essentially no effect on the neuromuscular parameters ω_N and ζ_N as a function of texture. This can easily be verified by reviewing the data contained in Table E.8.

Now attention will be turned to the identification of parameters to fit the measurement $\hat{Y}_\theta$. The identified parameter K_α and fit quality index $J_{\theta 1}$ for the one-cue model, for all operators and conditions, is shown in Table E.10. The parameters K_β, K_γ, and fit quality index $J_{\theta 2}$ of the two-cue model, for all operators and conditions, are shown in Table E.11. The parameters K_α, K_β, and K_γ, for the conditions without and with dots, are shown in Figures 4.8 and 4.9 respectively.

It was hoped that this experiment would allow a more conclusive determination of whether the one-cue or two-cue model was more appropriate. As in the previous experiment, two different comparisons were done to aid this determination. One was to test the similarities of the model parameters by examining the ratio K_β/K_γ; values of this ratio near unity indicate relatively little difference between the one-cue and two-cue models. This ratio is shown for the conditions without and with dots in Figures 4.10 and 4.11, respectively.

In nearly all cases, this ratio is well below unity, which would indicate that the two-cue model is potentially more descriptive of the data. Moreover, with the dots, this ratio is consistently and significantly below unity, indicating that the two-cue

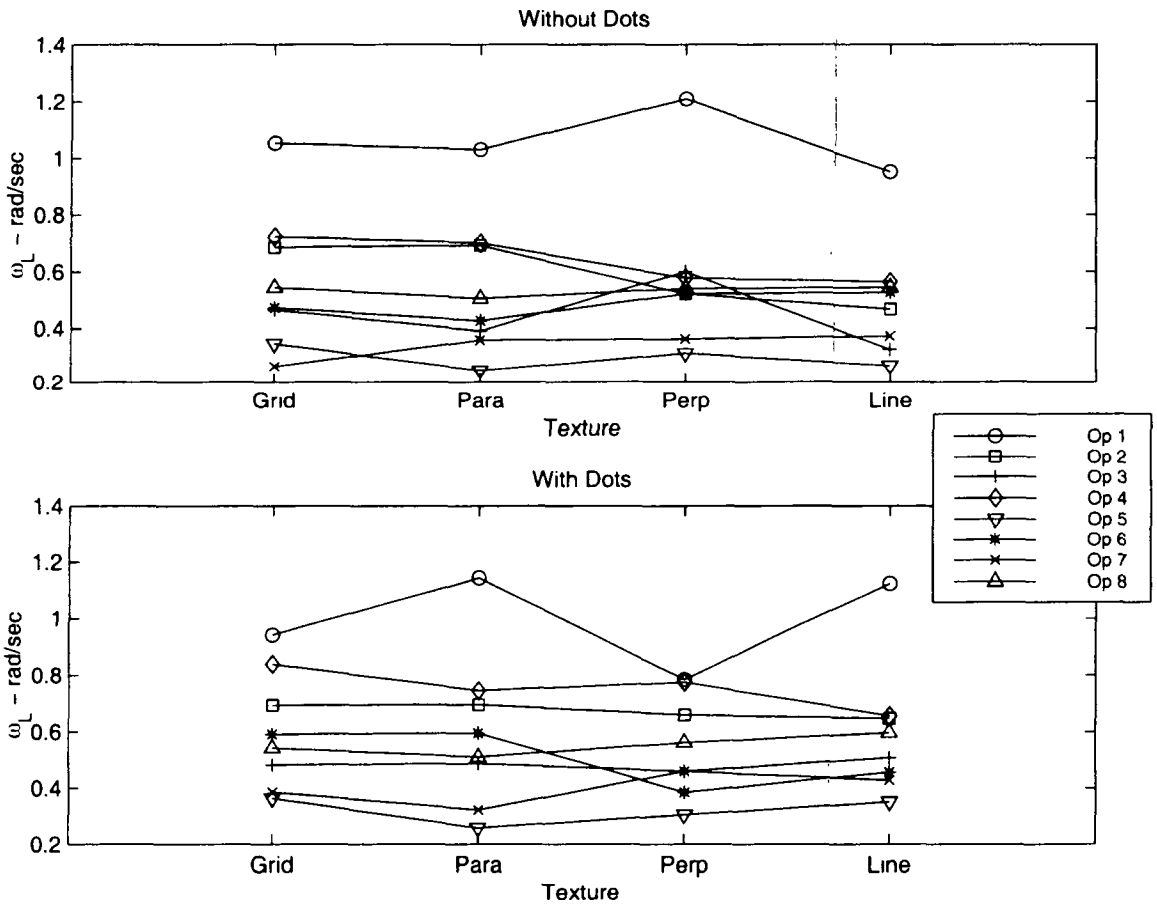

Figure 4.7: Lead break frequency ω_L for all operators and conditions in Experiment 2. In Experiment 1, the Grid and Parallel textures were associated with better lead generation (lower ω_L) than the Perpendicular and Line textures. That effect does not appear in the Experiment 2 results. A likely cause is the increase of the forcing-function bandwidth between Experiment 1 and Experiment 2.

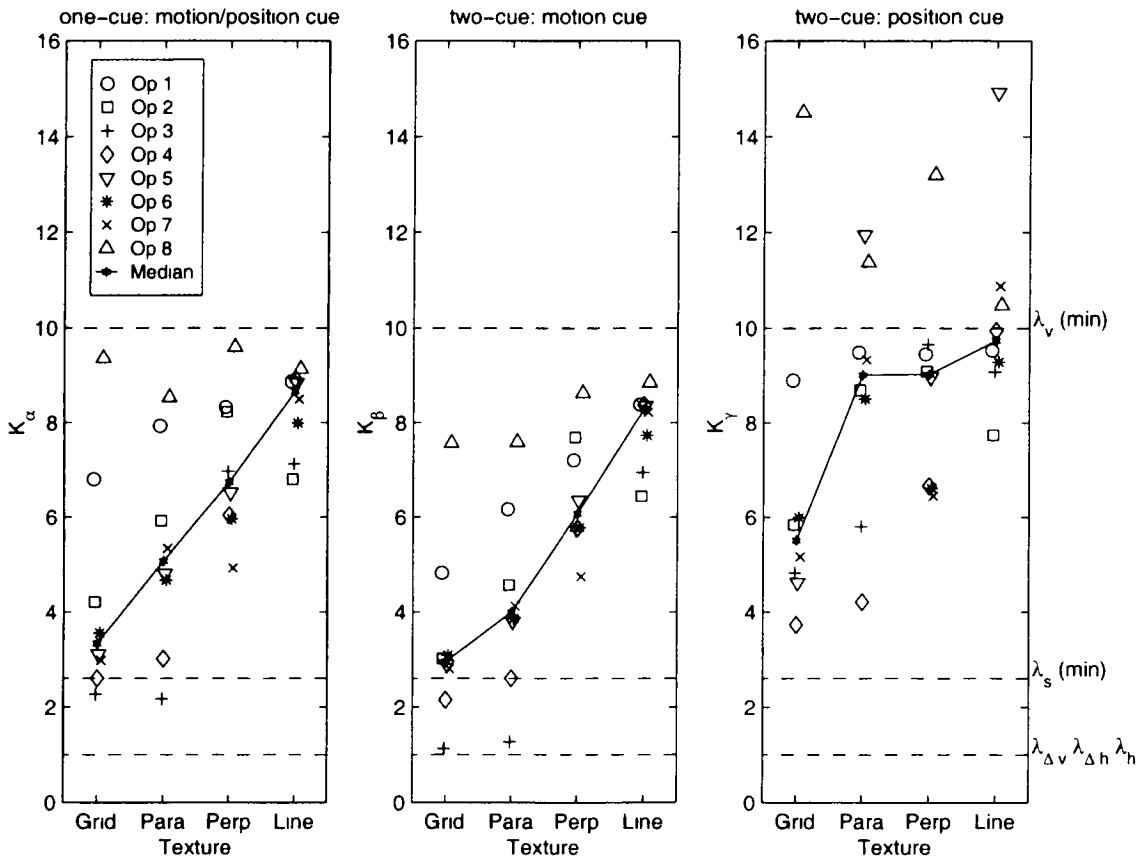

Figure 4.8: Identified parameters K_α (left), K_β (middle), and K_γ (right) for all operators, in texture conditions *without dots* in Experiment 2. K_α is the parameter in the one-cue model that corresponds to the sensitivity of the visual cue used for both position and motion; refer to Figure 2.6 and Equation 2.42. K_β is the parameter in the two-cue model for the sensitivity of the visual cue used for motion sensing; K_γ is the parameter for the position visual cue. Refer to Figure 2.7 and Equation 2.43 for the two-cue model. Dashed lines on the plot (and labeled in the right margin) indicate the predicted values of these parameters for the potential visual cues examined (refer to Table 4.1). Examples of the visual cues are shown in Figure 2.11. To review, λ_s refers to displacements or motions along the lines of splay, λ_h and $\lambda_{\Delta h}$ are horizontal components of motion or displacement of features (absolute and relative respectively), and λ_v and $\lambda_{\Delta v}$ are vertical components.

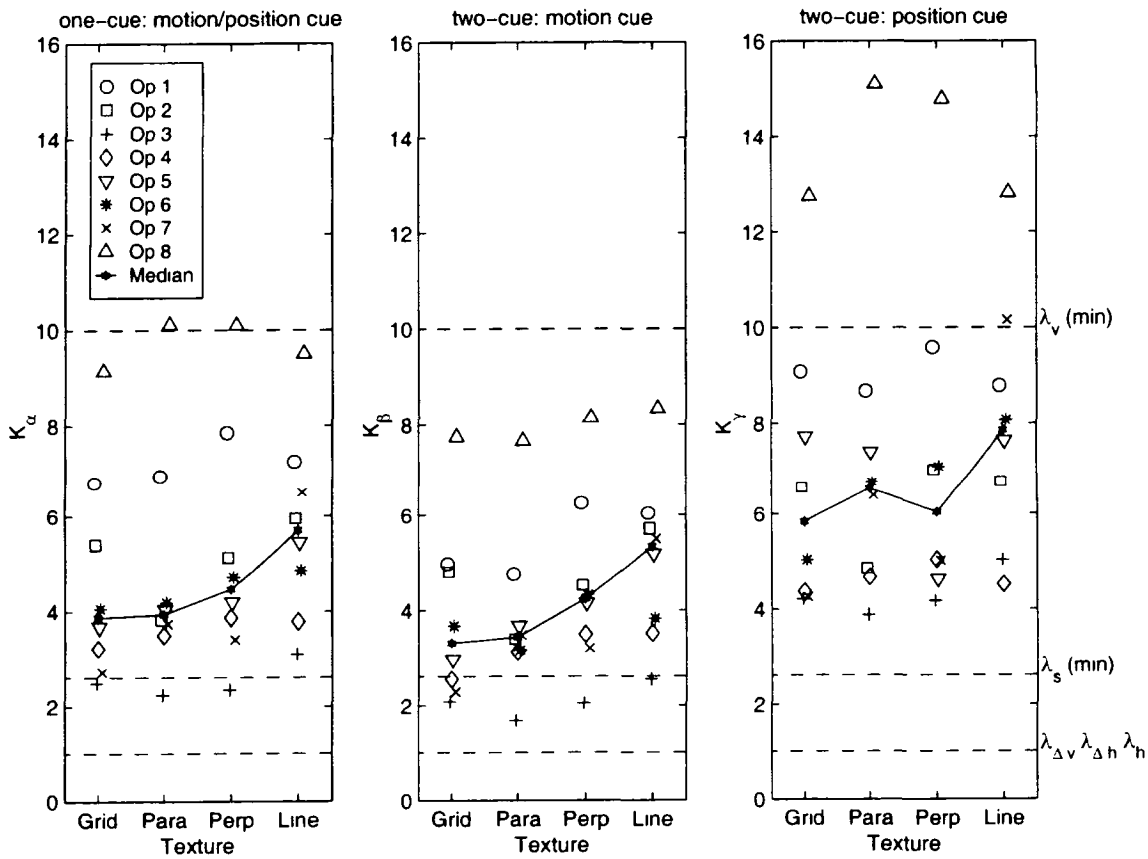

Figure 4.9: Identified parameters K_α (left), K_β (middle), and K_γ (right) for all operators, in texture conditions *with dots* in Experiment 2. K_α is the parameter in the one-cue model that corresponds to the sensitivity of the visual cue used for both position and motion; refer to Figure 2.6 and Equation 2.42. K_β is the parameter in the two-cue model for the sensitivity of the visual cue used for motion sensing; K_γ is the parameter for the position visual cue. Refer to Figure 2.7 and Equation 2.43 for the two-cue model. Dashed lines on the plot (and labeled in the right margin) indicate the predicted values of these parameters for the potential visual cues examined (refer to Table 4.1). Examples of the visual cues are shown in Figure 2.11. To review, λ_s refers to displacements or motions along the lines of splay, λ_h and $\lambda_{\Delta h}$ are horizontal components of motion or displacement of features (absolute and relative respectively), and λ_v and $\lambda_{\Delta v}$ are vertical components.

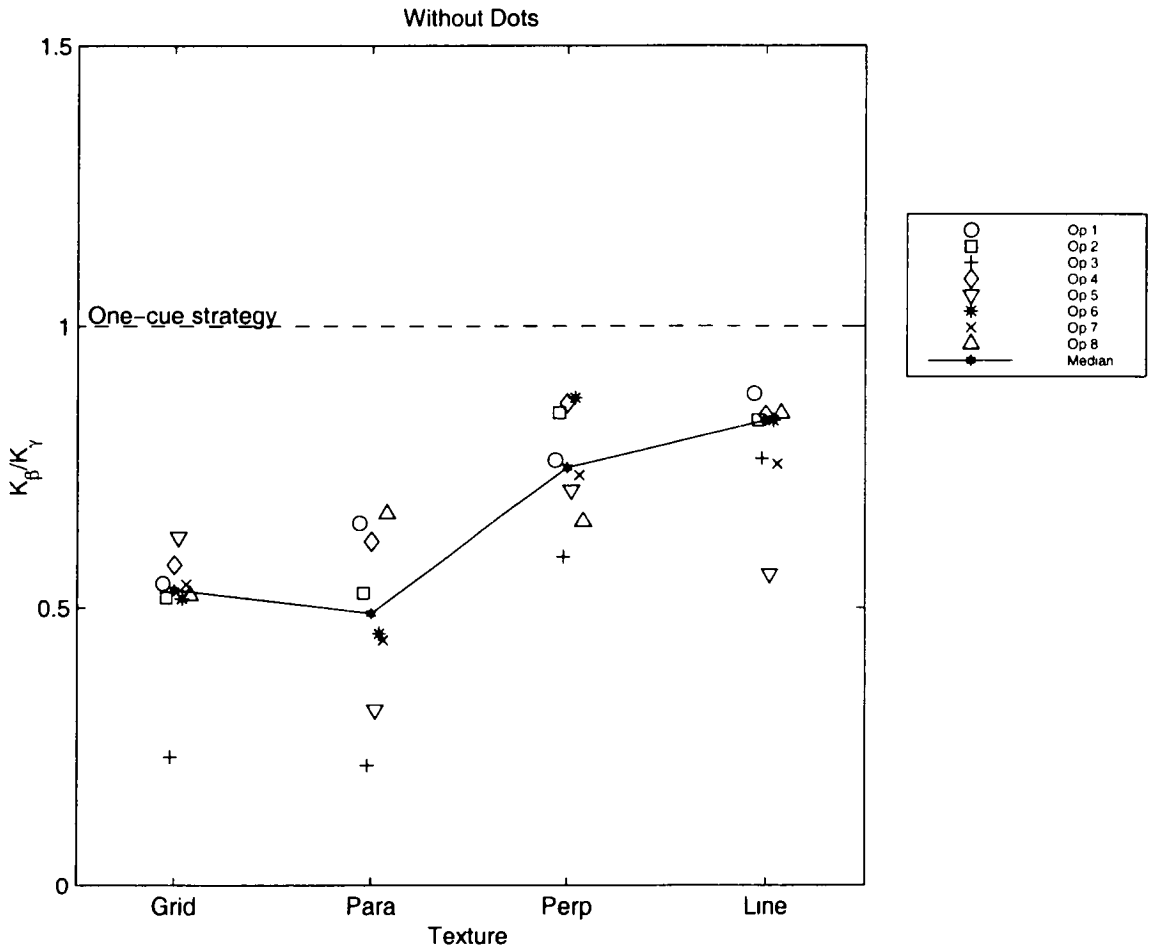

Figure 4.10: The ratio K_β/K_γ from Experiment 2 for all operators, in texture conditions *without dots*. K_β and K_γ are the motion and position visual cue sensitivities, respectively, in the two-cue model. The two-cue model becomes equivalent to the one-cue model (in which one visual cue is used for both position and motion sensing) when the ratio K_β/K_γ is unity. The data is strongly supportive of the two-cue model, rather than the one-cue model, when this ratio is well above or below unity, which it is in all cases here.

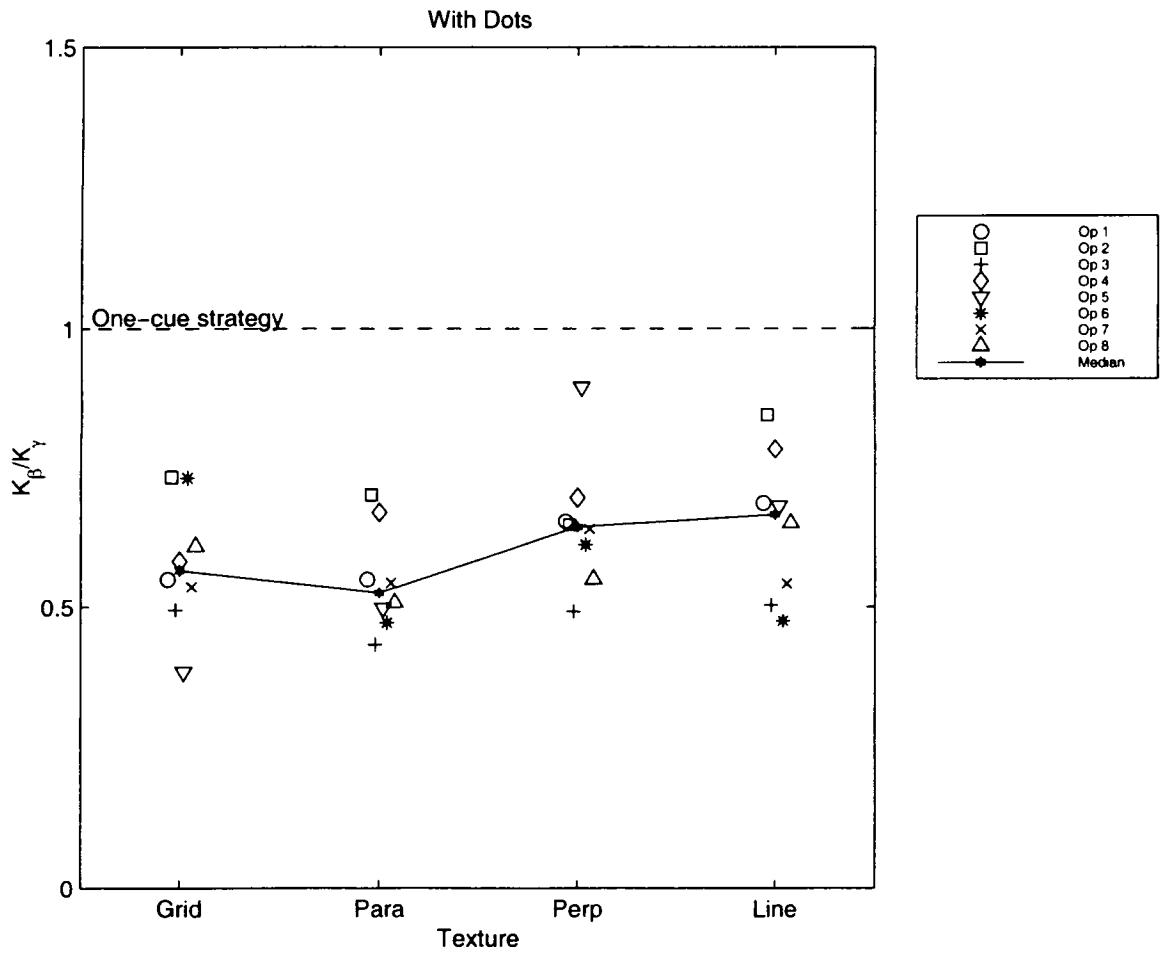

Figure 4.11: The ratio K_β/K_γ from Experiment 2 for all operators, in texture conditions *with dots*. K_β and K_γ are the motion and position visual cue sensitivities, respectively, in the two-cue model. The two-cue model becomes equivalent to the one-cue model (in which one visual cue is used for both position and motion sensing) when the ratio K_β/K_γ is unity. The data is strongly supportive of the two-cue model, rather than the one-cue model, when this ratio is well above or below unity, which it is in all cases here.

model is particularly descriptive of this condition. However, this analysis needs to be augmented with a check of the fit quality improvement, between the one-cue model and the two-cue model, to determine that the difference in parameters was not due to chance variations in the data. This is done by examining the ratio of the fit quality parameters for the two-cue and one-cue models, specifically $J_{\theta 2}/J_{\theta 1}$. This ratio is shown in Figure 4.12. In Experiment 1, it was hypothesized that the addition of a parameter would on average provide a one-in-twenty improvement to the index, based upon twenty data points. For this case, 24 data points (12 complex measurements) are being fit, so on average a 1 in 24 improvement (or 4.2%) might be expected. Setting a threshold of three times this for acceptance of the two-cue model requires a 12.5% improvement, or a ratio of $J_{\theta 2}/J_{\theta 1}$ less than 0.875. These two values are included in Figure 4.12. As can be seen, in nearly all of the cases, the two-cue model provides a significant improvement in the fit. Two conditions that are notable exceptions are the Perpendicular and Line textures without the dots; the models for the majority of the operators in these cases to not meet the "acceptance" threshold for the two-cue model.

Overall, the models provided extremely good correspondence with the data. Figure 4.13 shows the magnitude (in dB) of the measurement divided by the model ($\hat{Y}_p/Y_p$ and $\hat{Y}_\theta/Y_{\theta 2}$) for every operator, condition, and frequency. A common cutoff value in manual control research for acceptable levels of variance is 3 dB; the number of points that fit within this 3 dB limit was computed and is displayed on the plot. For the fit to $\hat{Y}_p$, the five parameters defining the model Y_p provided fits within 3 dB for nearly 98% of the data points. For the fit to $\hat{Y}_\theta$, the two parameters in the two cue model $Y_{\theta 2}$ provided fits within 3 dB for 86% of the data points.

Figure 4.14 shows the phase difference that occurs between the measurements and model for all operators and conditions. A systematic failure of the model to accurately represent the phase of the highest frequency component of $\hat{Y}_\theta$ is apparent. The clear trend is that the measurement exhibits less phase delay than the model in nearly every case. Several attempts were made to account for this in the modeling procedure, including reducing the time delay associated with the Y_θ modeling (relative to the time delay in the Y_p model); none was successful. Because this frequency point

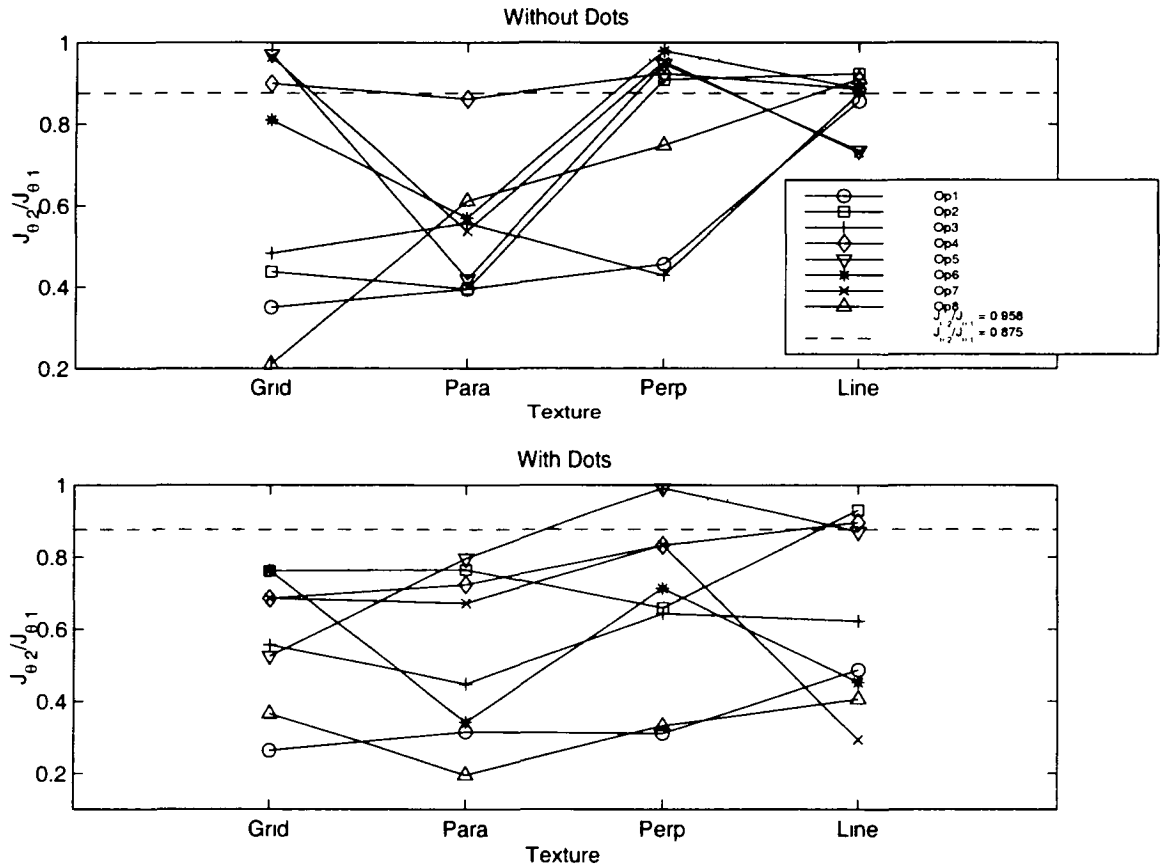

Figure 4.12: The ratio of the fit quality indices $J_{\theta 2}/J_{\theta 1}$, for the two-cue versus one-cue model fits,for all operators and conditions for Experiment 2. Lower values of J indicate a better fit. The two-cue model provides a substantially better fit in nearly all cases. The fit improvement using the two-cue model is also uniformly better in the conditions with the dots. The dotted line at 0.958 shows the level of improvement in the ratio that might be expected from chance with the addition of one parameter to the model (going from one-cue to two-cue); the dashed line at 0.875 shows three times this level.

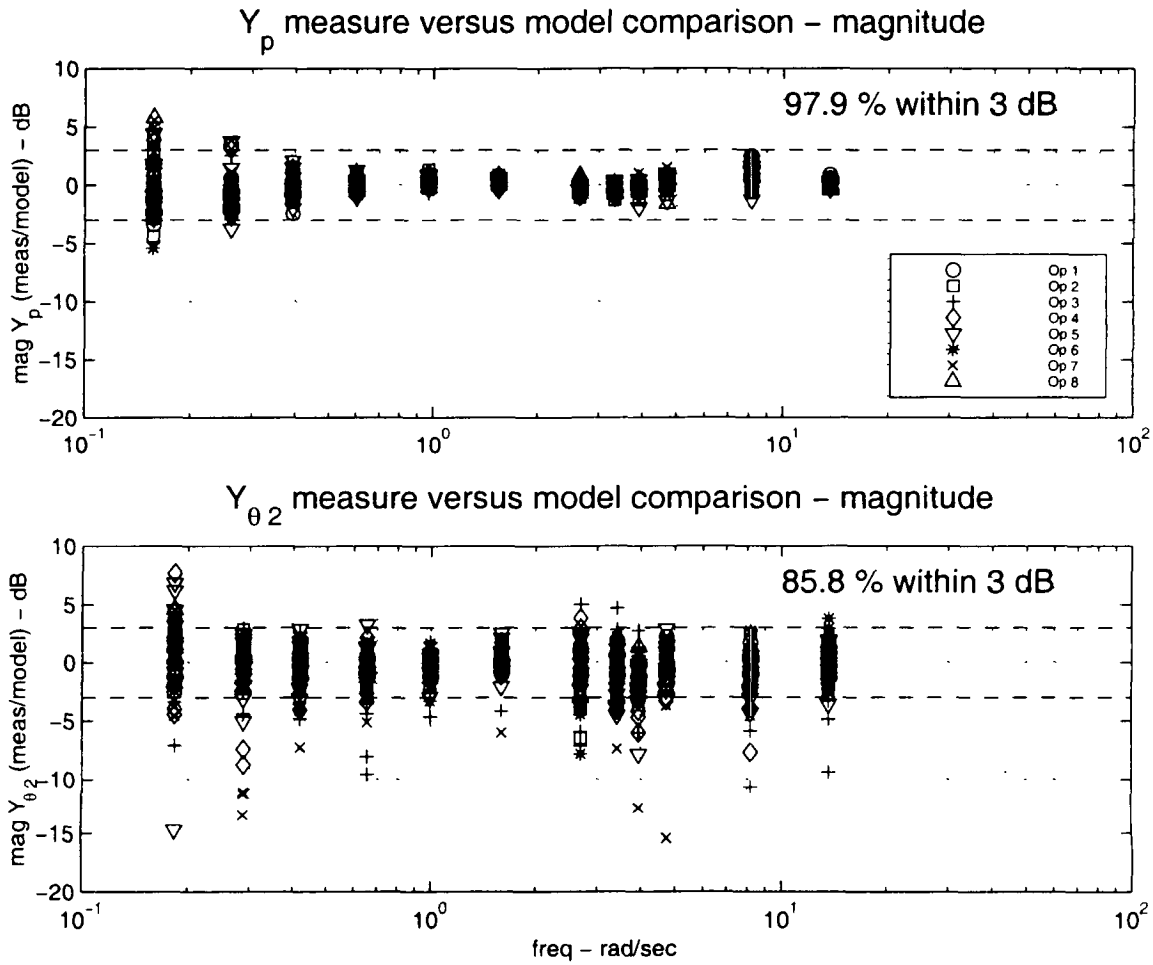

Figure 4.13: Magnitude of the ratio of measurement to model fit, in dB, for all conditions, operators, and frequencies for Experiment 2. $\hat{Y}_p/Y_p$ (top) and $\hat{Y}_\theta/Y_{\theta 2}$ (bottom). These data do indeed show a high quality of fit.

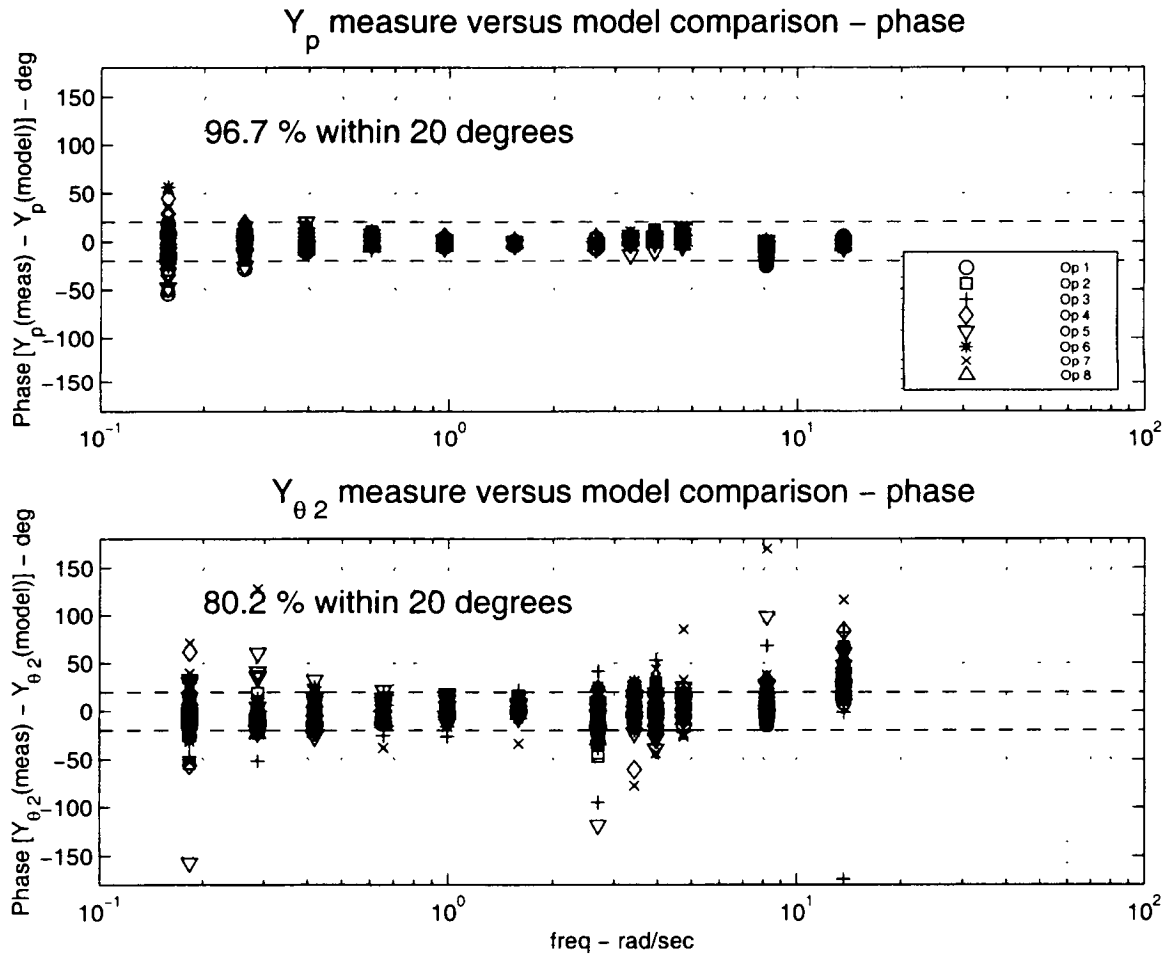

Figure 4.14: Phase of the ratio of measurement to model fit, in radians, for all conditions, operators, and frequencies for Experiment 2. $\hat{Y}_p/Y_p$ (top) and $\hat{Y}_\theta/Y_{\theta 2}$ (bottom). Again, a high quality of fit is shown.

is well above crossover, this error in the model has little effect on the closed-loop characteristics of the combined operator-vehicle system. Although this is an intriguing finding, no additional effort was expended to model this observed characteristic.

The range of actual values derived for K_β and K_γ generally corresponded with the range of potential values from the visual cue analysis: nominal values from the analysis are shown in the figures. One interesting difference relative to Experiment 1 is that it appeared that some operators were achieving values closer to the best achievable value of one. Operator 3 achieved values of K_β near unity with the Grid and Parallel textures without dots, and between unity and 2.6 for all of the textures with the dots. When this operator was questioned about his strategy, he indicated that he had in fact used one of these optimal visual cues, λ_h. This operator controlled the *lateral* displacement of a feature (either a grid intersection or a dot) close to the edge of the display, deliberately neglecting the vertical motion. This cue would ideally provide a value of unity for K_β. It is interesting that he did *not* achieve this value for the position cue parameter K_γ; this is perhaps due to the fact that the operator indicated that he still occasionally referenced the position of the baseline from the bottom of the display (λ_v), which would yield a value of 10 if used exclusively. This self-reported strategy is consistent with the identified parameters, if we consider that the ideal cue λ_h was used for primarily for motion sensing, and a combination of λ_v and λ_h was used for position sensing.

4.3 Discussion

The goals from this experiment were to: 1) determine which form of the VCC model, the one-cue or two-cue, is most representative of the operator's control strategy, 2) determine what effect, if any, lines of splay in the display have on the control strategy, and 3) investigate the potential of the model to provide a methodology for visual cue identification. These goals have been met. The two-cue form of the VCC model has been shown to accurately characterize the data in a large number of cases: Reduced measurement variances in the transfer functions $\hat{Y}_p$ and $\hat{Y}_\theta$ made it possible to differentiate the effects of the models enough to conclusively show the superiority

of the two-cue form.

The lines of splay have been shown to have a slight, but measurable and statistically significant improvement, on the control activity ($P_{\delta\theta}$, $P_{\delta x}$) and the velocity rms (RMS_x). The presence of lines of splay is associated with lower levels of power in the control correlated with θ, and higher levels correlated with x. Lower levels of velocity rms were demonstrated when the lines of splay were present. The presence of the lines of splay apparently provide visual information that helps the operator to distinguish the effects of pitch from the effects of longitudinal displacement.

This model shows great potential as a methodology for the identification of visual cues. The identified model parameters (K_β and K_γ) correspond closely with the theoretical values for particular visual cues. Specifically, most of the operators achieved values of K_β (the motion cue parameter) that were in the vicinity of the values expected if they were sensing the motion directed along a line of splay (λ_s). One operator, who achieved values for this parameter below that expected for this cue, indicated that he was using a cue that would provide a lower value of K_β (λ_h, from controlling the lateral position of a feature). And also, notably, this particular operator's values of K_β increased dramatically when operating in the texture conditions that lacked this particular cue (Perpendicular and Line without dots). Values of K_γ, the position cue, did not have as strong a correspondence with a particular visual cue, but instead tended to rest between the values of two cues. This could be explained with an attention-sharing strategy between the position of the baseline (λ_v) and another more optimal cue that might be difficult to use for absolute position judgements (such as λ_s, or displacement oriented along a line of splay).

One more question arose at the completion of this experiment: How, if at all, is our perception of desired states through a perspective scene different from the case in which that state is directly displayed? This question was the target of the last experiment, described in the following chapter.

Chapter 5

Experiment 3

The objective of performing Experiment 3 was to gain a better understanding of the differences and similarities between perspective and compensatory displays. A compensatory display is one in which the error information is presented directly to the operator (through, for example, the displacement of an indicator from a null position).

In the VCC model development contained in Chapter 2, two fundamental differences were identified between compensatory and perspective displays:

1. The perspective display is (potentially) affected by other vehicle states than the ones being controlled.

2. The perspective display performs a nonlinear transformation on both the controlled and uncontrolled states, through the process of perspective projection.

In Experiment 3, these differences are compared and controlled. Compensatory displays were developed in which the actual state (longitudinal position) was directly displayed. In some conditions, this state went through the same nonlinear transformation of the perspective-projection process before being displayed. The perspective display was also compared with and without the pitch disturbance present. In this way, the effects of these three interacting factors could be examined: perspective vs compensatory, linear vs nonlinear state transformation, disturbance vs no disturbance.

In some of the compensatory displays, a rate bar was incorporated to provide additional motion cueing to operators. This was done to help offset an anticipated improvement in motion sensing by the operators using the perspective display.

The data analysis consisted of both Analysis of Variance and individual modeling of the control activity, as was done in the two previous experiments. Because a number of the conditions did not have the pitch disturbance present[1], visual cue modeling was not performed (since the model is based on parameters that fit the measurement $\hat{Y}_\theta$, which is not available when there is no pitch disturbance present). Only the control strategy to the relevant state was modelled (Y_p).

The results will show that:

1. The effect of the nonlinear transformation of the state (due to perspective projection) is minimal.

2. The effect of uncontrolled states on the perspective displays is to reduce performance, compared with the compensatory display. The Grid display is associated with much smaller decrements in performance than the Line display.

3. The compensatory displays are associated with better position rms than the perspective displays; this is likely due to the lack of a null indicator on the perspective displays.

The rate bar was not associated with any better levels of performance as had been anticipated; the likely reason is that the velocity was not filtered before being displayed. Had this been done, the compensatory performance might have been substantially better: one potentially valuable result was unfortunately missed. Even so, we learned some very valuable things.

A description of the experimental protocol for Experiment 3 is provided in Section 5.1. Section 5.2 contains the experimental results from both the Analysis of Variance and the individual modeling, and Section 5.3 contains discussion of those results.

[1]In particular, none of the compensatory display conditions had the pitch disturbance present, since only longitudinal position was presented.

5.1 Protocol

5.1.1 Participants

Six participants were used, all of whom had participated in Experiment 2. The data from two of these participants had not been used for the Analysis of Variance and individual modeling analysis in Experiment 2. One operator was not included because he had participated in Experiment 1, and the decision was made to use all naive participants in Experiment 2 to remove any potential for bias due to previous experience with the displays. It was believed that this would not be a factor in Experiment 3 since any training or recency effects should have averaged out between the operators due to the extensive exposure of all the operators.

The second operator was removed from the Experiment 2 analysis because he volunteered that he had changed his strategy midway through the data runs. This was not believed to be a factor that would prevent his participation in the third experiment, since the strategy change reported was specifically a visual cue that would be optimal with the pitch disturbance present. Since the disturbance was not present in the third experiment, it was believed that he would be a reliable participant in this experiment.

5.1.2 Apparatus

The test apparatus was identical to that used in Experiment 2, described in Section 4.1.2.

5.1.3 Scene

Four new displays were developed, identified as compensatory displays. The compensatory display elements are shown in Figure 5.1. The four displays were made from combining two conditions: 1) with and without rate bar, and 2) linear and non-linear state scaling. The purpose of the nonlinear scaling in the compensatory displays was to replicate the nonlinear transformation that occurs through perspective projection, so that the two conditions are the same in that respect. Details of the scaling are

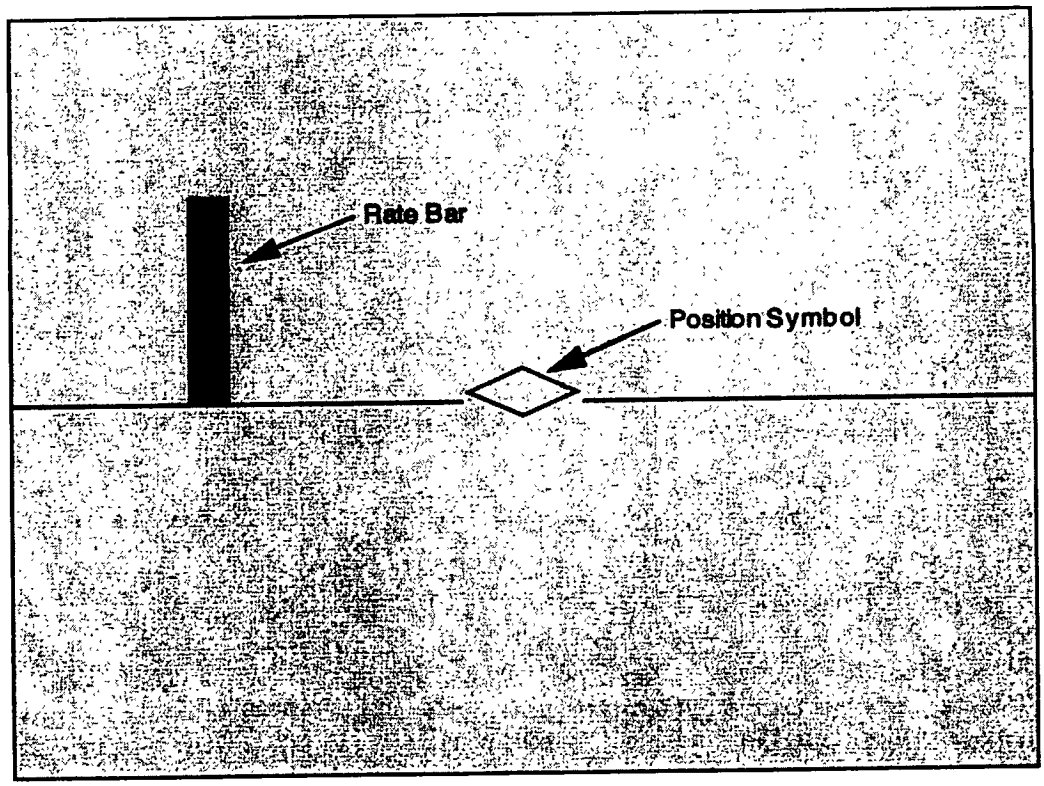

Figure 5.1: Compensatory display format used in Experiment 3. This format is one of many that could have been chosen, and is simply a first point of comparison.

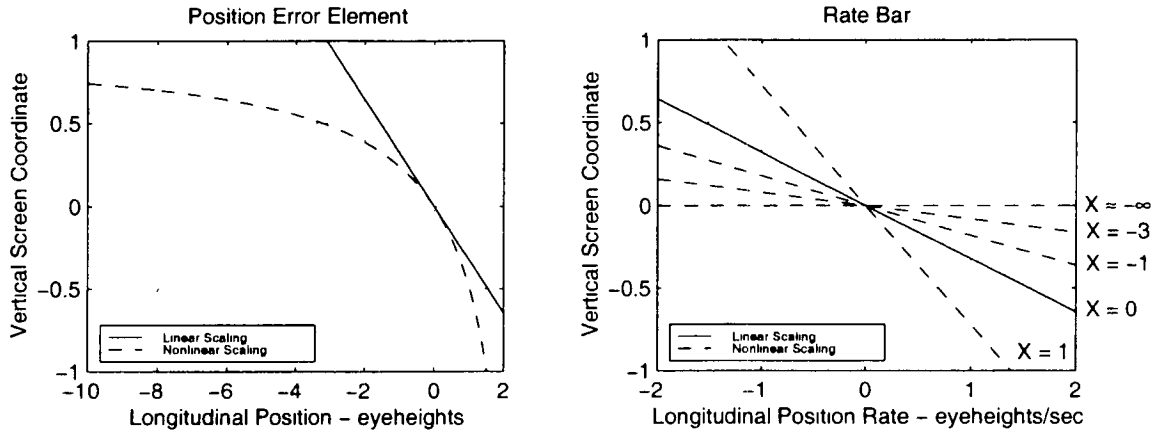

Figure 5.2: Linear and nonlinear scaling of position and rate information in the compensatory displays of Experiment 3. Position error element scaling is on the left; rate bar scaling is on the right. Displacement is presented in screen coordinates, with full scale deflections of ± 1. Note that the nonlinear rate bar scaling is a function of both longitudinal position rate and longitudinal position (x).

presented in Section F.2 of Appendix F; the relationship between the linear and nonlinear scaling is shown in Figure 5.2. The figure on the left shows the linear and nonlinear scaling of the position error element. The figure on the right shows the linear and nonlinear scaling of the rate bar, which is also a function of longitudinal position (labeled "$x = \ldots$" in the figure).

The effect of the nonlinear scaling was to replicate the motion of the baseline in the perspective displays. This scaling produces some interesting artifacts when large displacements in longitudinal position occur. One such artifact is a virtual "horizon" formed when the operator moves very far backward from the starting position. In a perspective scene, if the operator moves a great distance backward, the original reference point will move eventually to the horizon, and will not appear to move as the operator moves farther backward. This can be seen in the nonlinear position error element in Figure 5.2: the position goes to an asymptotic value (corresponding to the horizon in the perspective projection). The fact that a feature far distant from the operator will not appear to move regardless of the operator motion can be seen in the nonlinear rate-bar scaling. As longitudinal position (x) becomes more negative, meaning the original position is in front of the operator, the rate-bar scaling reduces.

As the longitudinal displacement increases, the motion of the rate bar drops to zero (in the figure, where $x \approx -\infty$). This is consistent with a perspective display, in which the horizon does not appear to move as a function of longitudinal position change.

Two other displays were also tested: the perspective displays with the Grid and Line textures (without dots) tested in Experiment 2. This made a total of six display conditions; two perspective, and four compensatory.

5.1.4 Task

The task was similar to Experiment 2, although no pitch disturbance was present. The task instructions given to participants are shown in Section F.2 of Appendix F.

5.1.5 Procedure

Each operator participated for a total of two days. In this experiment, there was concern that the compensatory displays would be particularly difficult to use for long periods of time. The primary purpose of this experiment was to determine if the ANOVA analysis revealed any differences between the displays, and the secondary purpose was to examine the operator transfer functions for any changes due to the experimental manipulations. Since visual cue modeling was *not* being performed, it was not necessary to conduct as many long (four minute) data runs. A smaller number of long data runs was believed to be sufficient to achieve a reliable estimate of $\hat{Y}_p$, since in the earlier experiments the variances on the $\hat{Y}_p$ measurements tended to be much smaller than the variances on Y_θ. Although a smaller number of long data runs was believed to be sufficient for transfer function measurement, it was thought that more data runs might be required to show statistical significance of any observed effects in the ANOVA analysis. A number of shorter data runs were also incorporated, with the goal of improving the ANOVA results.

As was done in Experiment 2, written instructions were provided to the operators; they are shown in Section F.2 of Appendix F. On day one, participants were provided with eight one-minute familiarization runs in each of the compensatory display conditions. The feedback was identical to that received in Experiment 2; a sum of

the velocity and position rms was displayed as a score. The additional familiarization runs with the compensatory displays were given to remove any bias that the operators might have due to additional time already spent using the perspective displays.

Following the compensatory familiarization runs, the operators were given five one-minute training runs in each of the six experimental conditions. The order of presentation varied with the operator, as shown in Table 5.1. Then a total of 15 one-minute data runs were completed in each of the conditions. The data runs were collected in blocks of five per condition, just as in the previous training runs.

On day two, the participants were asked to complete a total of four four-minute data runs in each of the six conditions, with the same order of presentation used on the first day. The data runs were grouped in sets of two per condition, with one one-minute training run before each two data runs.

The six conditions tested, with shortened identifiers, are below:

1. Perspective Grid (G)
2. Perspective Line (L)
3. Compensatory w/o rate bar, linear scaling (C)
4. Compensatory w/ rate bar, linear scaling (CR)
5. Compensatory w/o rate bar, nonlinear scaling (C*)
6. Compensatory w/ rate bar, nonlinear scaling (CR*)

5.2 Results

5.2.1 Analysis of Variance (ANOVA)

The outcome variables examined were the position rms error (RMS_x) and velocity rms ($RMS_{\dot{x}}$). Several combinations of factorials were analyzed, including as factors:

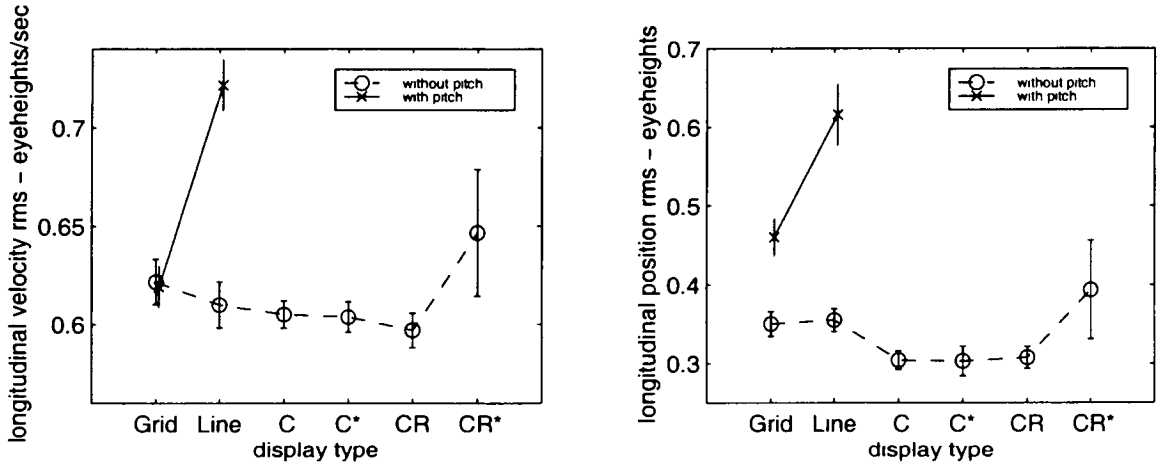

Figure 5.3: Mean velocity rms (left), and mean position rms (right), for all operators, as a function of display type and disturbance condition in Experiment 3. Standard error bars are shown. The two perspective displays are the Grid and Line displays. The four compensatory displays are: linear scale (C), nonlinear scale (C*), linear scale with rate bar (CR), and nonlinear scale with rate bar (CR*). Items to note are that the performance is not improved with the rate bar (displays CR and CR*); in fact, the display with the rate bar and nonlinear scaling (CR*) is associated with the highest rms of the no-pitch-disturbance conditions. This was due to large excursions on two trials. The failure of the rate bar to improve performance is likely due to a lack of filtering of the velocity before displaying. When the pitch disturbance is *not present*, the only observable difference between the compensatory displays and perspective displays that with the perspective display there is a larger position rms; this is likely due to the lack of an explicit null indicator on the perspective displays. When the pitch display *is present*, the performance with the Line perspective display shows much larger values in both position and velocity rms than with the compensatory display. With the Grid perspective display, the velocity rms is unaffected by the presence of the pitch disturbance, but the position rms is larger than with compensatory display, albeit to a lesser extent than with the Line perspective display. It is expected also that the performance with compensatory display would be better still with a good rate display – perhaps substantially so.

Operator	Condition					
1	CR	C*	G	CR*	C	L
2	CR*	C	L	CR	C*	G
3	C	G	CR*	C*	L	CR
4	C*	L	CR	C	G	CR*
5	G	CR	C*	L	CR*	C
6	L	CR*	C	G	CR	C*

Table 5.1: Experiment 3 presentation order by operator. (G) and (L) denote the perspective Grid and Line conditions. (C) and (CR) denote the Compensatory and Compensatory with Rate Bar displays, respectively, both with linear error scaling. (C*) and (CR*) denote the compensatory and compensatory with rate bar displays, respectively, using nonlinear scaling of the error.

presence or absence of the rate bar, perspective versus compensatory, linear versus nonlinear scaling, pitch disturbance absent versus present[2].

Overall, the different conditions did not yield any statistically significant differences from each other. Mean velocity and position rms, for all operators and displays, are shown in Figure 5.3. Particular findings to note were that:

1. There was no difference between the compensatory displays using linear and nonlinear scaling.

2. For the particular (noisy) rate display used, the rate bar did not improve performance[3].

3. When the pitch disturbance was *not present*:

   (a) There was no difference between the Grid and Line perspective displays.

   (b) The only significant difference between the perspective and compensatory

[2]The comparison of the pitch-disturbance-present condition, for the Grid and Line displays, was done using data from Experiment 2.

[3]This result is in direct contradiction of a large body of work in rate augmentation of displays, and should not be considered to be of any significance, given the noisy character of the rate display used. This is addressed further in Section 5.3.

displays was in position rms, which was higher with the perspective displays. This is most likely due to the fact that with the perspective displays, operators need to control position from a remembered position; there is no null indicator on the display. With the compensatory display, an explicit null indicator is present, creating improved position rms performance. Velocity rms was not appreciably different between the displays.

4. When the pitch disturbance was *present*:

   (a) The velocity rms using the Grid display was *not* affected; the Line display was associated with a large increase in velocity rms compared to the Line display without the pitch disturbance.

   (b) The position rms was increased with both perspective displays; the Line display was associated with a much larger increase than the Grid display.

These results presented are based upon analysis of the long data runs collected in Day 2 of the experiment. The inclusion of the additional short data runs did not appear to appreciably affect the ANOVA analysis results.

5.2.2 Individual Models

Measurements of $\hat{Y}_p$ were made using the technique described in [62] and Appendix B. All of the four long data runs taken in each condition were used to formulate the measurement. As was noted previously, the visual cue modeling (fitting of models to $\hat{Y}_\theta$) was not possible with this experiment due to the fact that no pitch disturbance was present. Therefore, the only individual models that can be examined are the models fitting to $\hat{Y}_p$.

As in Experiment 2, the form of the model Y_p that best fit the measurement $\hat{Y}_p$ was:

$$Y_p = K_p e^{-\tau s} \frac{(s + \omega_L)}{(s^2/\omega_N^2 + 2\zeta_N s/\omega_N + 1)} \tag{5.1}$$

The parameters of this model were fit using the modified DTF technique described in Section C.1 of Appendix C. Because all of the participants had also participated

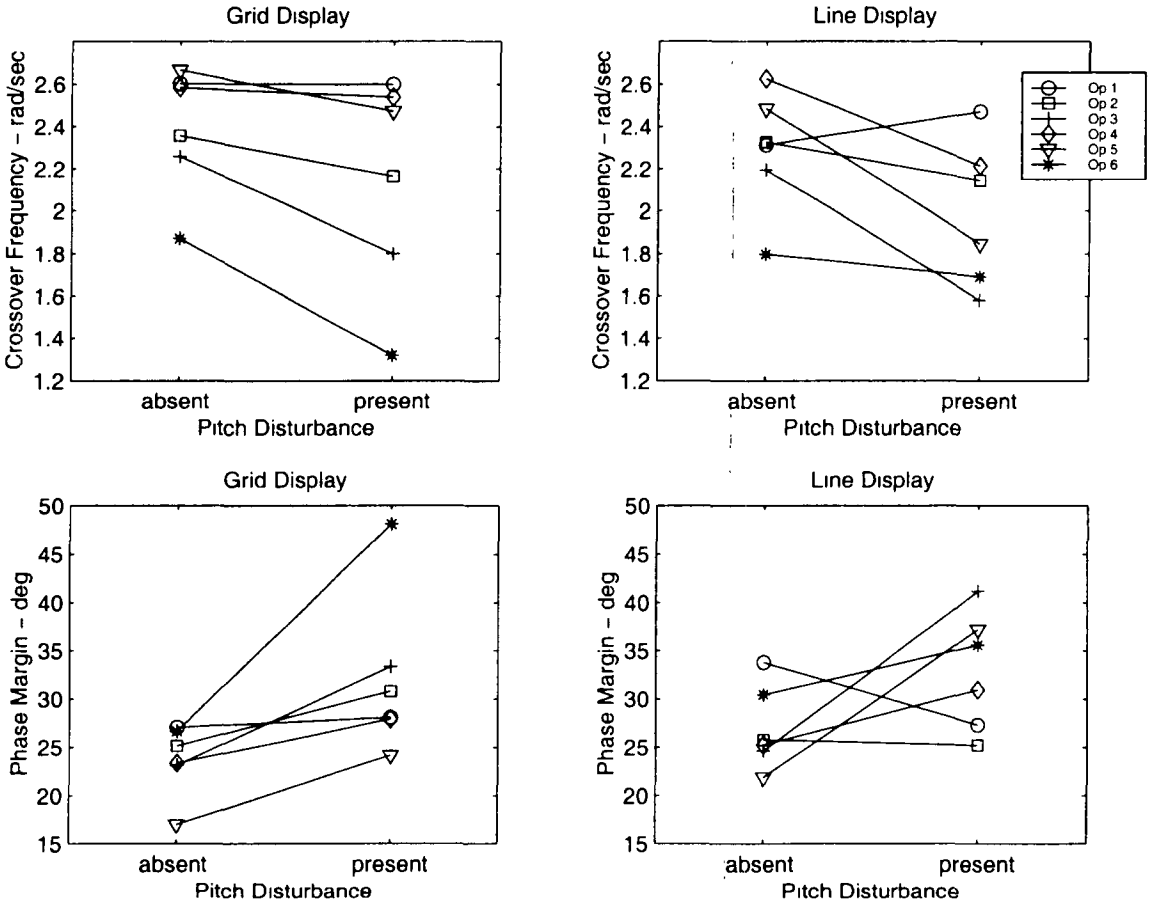

Figure 5.4: Crossover frequency and phase margin as a function of pitch disturbance and texture, for the perspective displays, for all operators in Experiment 3. The disturbance-present condition is based on data collected during Experiment 2. When the pitch disturbance was present, the crossover frequency decreased with the majority of operators, on both display types (Grid and Line). The decrease in crossover frequency, signifying a lower loop gain, is a likely factor in the increased position and velocity rms observed in Figure 5.3. Phase margin increased for most operators, with both display types, when the pitch disturbance was present. The increase in phase margin indicates a tendancy of the operators to be less aggressive, probably due to the uncertainty introduced with the disturbance.

in Experiment 2, it is possible not only to do comparisons between the displays in Experiment 3, but also between conditions in Experiment 2 and 3. In Experiment 2, all of the experimental conditions were done *with* the pitch disturbance present. In Experiment 3, there was no pitch disturbance. Therefore, it is possible to compare the effect on the pilot model parameters, with and without the pitch disturbance present, for the Grid and Line texture displays (these are the only two display/texture types used in both experiments). The plots of the measurements and model fits for all conditions and operators discussed in this section are contained in Figure F.1 through F.48 in Section F.4 of Appendix F.

The effect of the disturbance is most easily seen in the crossover frequency and phase margins, shown in Figure 5.4. With both the Grid and Line textures, the crossover frequency decreased, and the phase margin increased, for nearly all operators, when the disturbance was present.

When the pitch disturbance was not present, there was little effect of display type on the crossover frequency or phase margin. Figure 5.5 shows the identified crossover frequency and phase margin for all displays and operators for the condition when the pitch disturbance is not present. As can be seen, the only fairly consistent effect is that the phase margin increases slightly with the perspective Line display relative to the other displays. Also, it appears that for some operators, the compensatory display with the rate bar and linear scaling was associated with somewhat higher crossover frequencies. The identified model parameters of Y_p, as well as the crossover frequency and phase margin, for all of the conditions in Experiment 3 and the two conditions used for comparison from Experiment 2, are presented in Section F.3 in Appendix F.

5.3 Discussion

Two particular differences between compensatory and perspective displays were controlled and compared in this experiment: 1) the effect of disturbances, and 2) the nonlinear transformation of the state. The second factor, the nonlinear transformation through perspective projection, did not produce any measurable effect in either

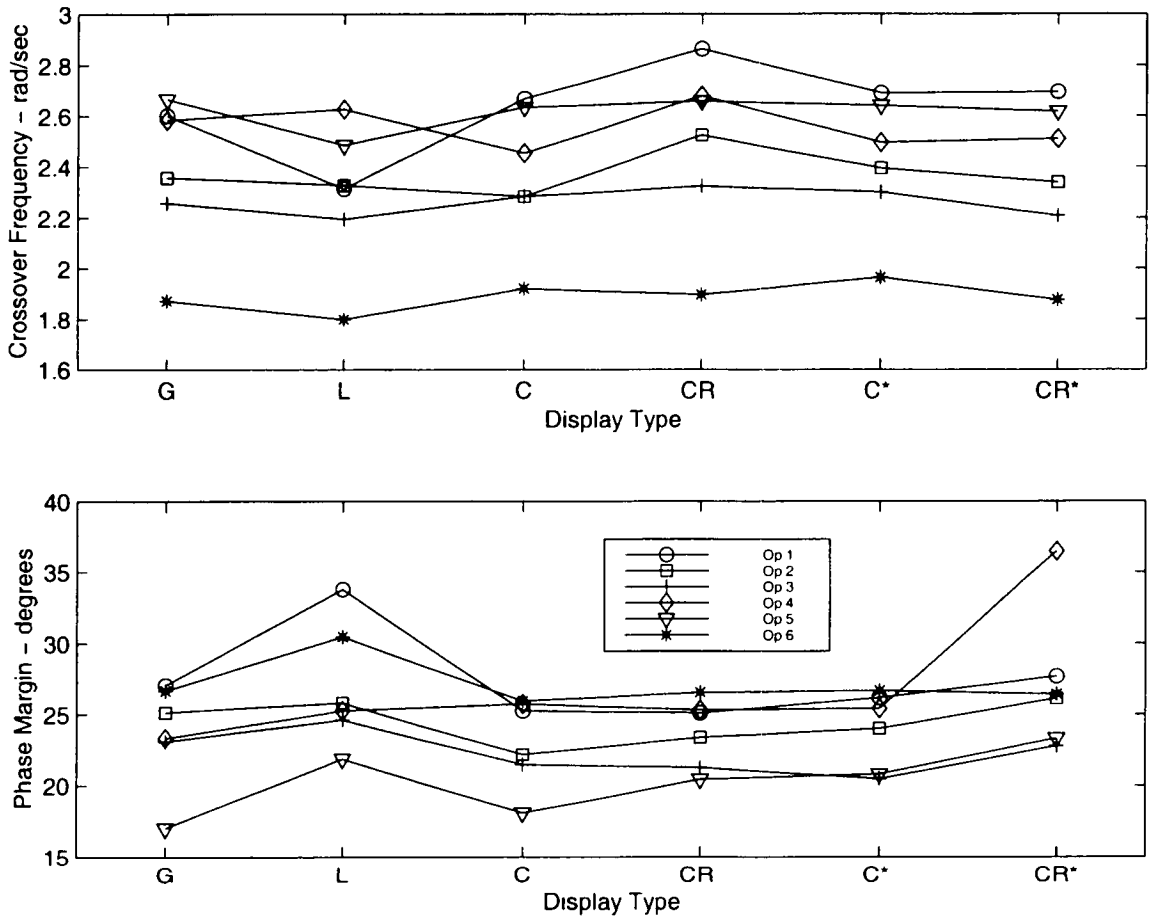

Figure 5.5: Crossover frequency and phase margin as a function of display type for all operators in Experiment 3. Pitch disturbance is not present in any of the conditions. There is minimal variation in these parameters as a function of display type, although the Line display is associated with somewhat higher phase margin and lower crossover frequency. The compensatory display with rate bar, using nonlinear scaling, was associated with an increase in phase margin for most operators - this is consistent with the observation of most operators that the rather noisy rate bar provided was distracting as opposed to helpful.

the Analysis of Variance or the individual modeling: There was effectively no difference between the linear and nonlinear compensatory displays. This is no doubt largely because operators were capable of controlling the state to a degree of accuracy which kept the transformation in a linear range a majority of the time.

The effect of disturbance through uncontrolled states, which affect a perspective display but not a compensatory display, was noticeable and adverse. The performance decrement with the Grid display due to the disturbance was much less than with the Line display, but still substantial.

Even when the pitch disturbance was not present, the perspective displays were associated with higher values of position rms than the compensatory displays: *This is a significant result of the research.* The higher position rms performance with the perspective displays is most likely due to the fact that the operators were required to remember the null position[4] (because of the lack of a fixed reference). This difference might have been still larger if the compensatory display had also included a well-filtered (less noisy) rate display.

Indeed, much of the previous work in display design and augmentation has shown that displaying rate information generally aids the operator in performing manual control tasks [37, 63, 42, 64, 65, 35, 1]. This was not the case in this experiment. Here, most operators felt that the rate bar they were given either did not help their performance, or actually hindered it. The lack of observed effect in the Analysis of Variance supports this subjective opinion. Several operators indicated that is was not helpful, since they could not differentiate between the "bad" velocity occurring from a disturbance, and the "good" velocity occurring because of an aggressive control strategy. Another factor that likely made the rate bar difficult to use was the fact that it was "raw" velocity, with no filtering. Typically, rate elements incorporated in displays have some degree of filtering before presentation. The lack of filtering led, in this case, to an extremely active rate bar; in fact, the periodic nature of the highest frequency component of the disturbance was clearly visible. Since this disturbance was well above the crossover frequency (13 rad/sec), and therefore well outside of

[4]Pilots sometimes use references in the vicinity of the windscreen, such as a particular rivet, as a null indicator for the horizon line.

the ability of the operator to control, it represented a fairly spurious source of data that could not be effectively incorporated in the control strategy. The rate bar was initially incorporated to determine if it might offset any improved rate sensing with the perspective displays. What was learned instead was that the presentation of rate information cannot be usefully done without considerable care.

Chapter 6

Discussion

The results of the Analysis of Variance (ANOVA) in the three experiments showed that manipulation of the scene content could produce measurable, statistically significant effects on the outcome variables studied. This was considered to be an important prerequisite to the individual modeling. The goal of this work was to develop a visual cue model that could account for observed effects; the modeling becomes little more than an academic exercise if the effects being modeled could easily have occurred by chance.

The two-cue form of the VCC model, validated with the Experiment 2 data, has been shown to characterize the data very accurately. The number of model parameters is very small relative to the number of data points; in Experiment 2, only five parameters were necessary to accurately model the control response to the longitudinal disturbance (consisting of 24 data points). Two parameters were required to characterize the control response to the pitch disturbance, also fitting 24 data points. This highly accurate model is based upon the simple hypothesis that the operator chooses visual cues in the image and controls them directly, as opposed to performing a full reconstruction of the vehicle state. It is a direct validation of Gibson's " 'Ground Theory' of Space Perception" [8], particularly two of the five postulates:

1. There is always some variable in stimulation (however difficult it may be to discover and isolate) which corresponds to a property of the spatial world.

2. The stimulus-variable within the retinal image to which a property of visual space corresponds need be only a correlate of that property, not a copy of it.

An interesting characteristic of the model is that: 1) operators appear to derive motion and position from two different sources[1], and 2) the motion source is associated with superior disturbance rejection relative to the position cue. This second characteristic is potentially important since it might be linked with human perceptual capabilities. The human visual motion processing system requires the stimulus to have certain characteristics before "apparent motion" results, or a perception of motion. Specific conditions that can make apparent motion disappear are update rates that are too slow, or too much movement of a feature between updates. Current visual flight simulation applications tend to favor highly accurate scene content, often with the tradeoff of lower update rates. Little attention is paid to whether the normal scene motion at these update rates can still stimulate motion detection in the entire image. Some researchers have proposed modifying visual scene simulation to take better advantage of human visual motion perception capabilities, potentially at no computational cost [66, 67]. Nakayama [68] has proposed tuning of the update rate and scene complexity to be more compatible with visual motion processing capabilities. High scene complexity is not necessary when the image is moving quickly, because we are sensitive to only the lowest spatial frequency components when the temporal frequency is high. However, update rate needs to be high enough to prevent loss of "apparent motion" which occurs when features move too far spatially between updates.

It is difficult to generalize these findings to visual cue requirements of fixed-wing aircraft, because of their requirement for constant forward speed, but some of the results can be related to helicopter visual cue requirements. Roger Hoh [69] conducted a study in which he manipulated the available visual cues in helicopter hovering maneuvers by limiting both field of view and level of scene detail. This study was done in actual helicopters using outside visual references. Field of view manipulation

[1]Grunwald and Merhav [33] also discovered that a two-cue model best represented the case of unconstrained viewing in a lateral vehicular control paradigm. The two cues were related to near and far distances, but in terms of the state information provided, one cue provided more motion information than the other.

was done by draping cloth panels with cutouts in front of the evaluation pilot (a safety pilot had an unrestricted field of view). The scene detail manipulation was accomplished through the use of special goggles, which would "fog" the scene and obscure the fine details (called microtexture) in the environment, without reducing the ability to perceive outlines of large objects. Some of Hoh's findings are very consistent with the results of the current experiments. One very interesting finding was that the pilots felt that the attitude cues were significantly reduced with the lenses fogged than with the lenses clear. This was counter to the expectations of the experimenter, since the horizon was *clearly* visible with the lenses fogged, and the position of the horizon in the image has a one-to-one correspondence with pitch angle (neglecting motions related to the lateral degrees of freedom). Hoh states:

> "From this data it appears that pilots utilize information in the near field on an equal level, or even more than the distant horizon for attitude information in low speed and hover."

He goes on to state that operational experience in flight simulators seemed to support this conclusion, with inadvertently large pitch excursions being reported in simulators (even simulators with good motion fidelity).

This outcome is consistent with the experimental results in this dissertation. In Experiments 1 and 2, it was found that the presence or absence of scene detail, through grid intersections or dots, was associated with much better rejection of the pitch motion from the longitudinal motion. The theoretical visual cue analysis also reveals that the most effective differentiation of pitch from longitudinal motion is from the near-field cues, specifically the lower outer corners of the display. It is possible that the very features that enable *rejection* of pitch could also enable the *detection* of pitch. In Hoh's study, the lack of cues in the most critical part of the image, from the lack of microtexture, could explain the observed effects.

In Experiment 2, the presence of lines of splay was shown to have a statistically significant effect on the amount of control activity correlated with the irrelevant disturbance. This is interesting because of the relative lack of motion of the lines of splay; the angles the lines make (in the image plane) remain essentially fixed (pitch

has a second order effect on this angle). The angle of splay lines has been proposed and studied numerous times as an altitude cue ([25] is a recent example), but in the case of changing altitude, the angle of the line correlates with altitude. In this case, it is possible that these lines provide a fixed reference to help differentiate the sources of image feature motion; motion directed along a line of splay is correlated with longitudinal position. This finding could have implications for both simulator visual scene design and airport markings.

We might expect that, through trial and error, that many current practices are in fact optimal. An interesting example relates to heliport markings. Public-use heliports have a large "H" on the landing surface [70]. If lines of splay and discrete points are essential elements in a visual display to differentiate longitudinal and pitch motions, the letter "H" is probably the best letter in the english alphabet to be used for heliport marking. It provides lines of splay (from the two vertical elements), and discrete points (from the intersections of the horizontal element and ends of the vertical elements). The letters "I" and "T" would not provide lines of splay, only a centerline reference. Other letters like "E", "F" and "L" could provide some references, but the lack of symmetry would probably not be ideal for lateral guidance.

It is doubtful that such markings would affect the hovering performance of an experienced pilot when numerous visual cues are available (as in the case of clear visibility and adequate microtexture). Helicopters are routinely hovered without notations or markings on the ground. However, such markings could become more important in reduced visual conditions when, as simulated in Hoh's study, the microtexture becomes less visible. The results of Experiment 2 showed that even an impoverished scene (i.e., the Parallel texture without dots) can be used to achieve performance that is comparable to a much more detailed scene (i.e., the Grids, and all scenes with dots), provided that the impoverished scene has usable and advantageous cues available (i.e., λ_s, or motion oriented along a line of splay). Specifically, for the position control case, that means lines of splay and individual points (or intersections) at the lower, outer corner of the display or windscreen. The Parallel texture provided relatively few cues, but they were ideally located to provide accurate detection of lateral motion. The simple "H" marking on a heliport could provide guidance that is

optimal for such a simple cueing element.

The results of Experiment 3 comparing perspective scenes with compensatory displays show that in some ways, operators can achieve performance with a perspective scene that is similar to what can be achieved with explicit state presentation (velocity rms). The lack of a null indicator on a perspective scene does degrade position control relative to conformal display usage. These results should only be generalized to cases in which the operator is capable of controlling the desired state within a region that produces quasi-linear motion of the perspective-scene elements. This is a factor under the control of the designer through choice of the scene content (location of relevant cues) and imaging geometry (field of view).

The results from Experiment 3 should not be generalized to support the use of compensatory displays (in lieu of perspective scenes or displays) in all cases where state measurements are available. This study examined only the case in which one state was being displayed and controlled; it did not address at all the issue of integrating information from different states into one display. There is extensive evidence that when multiple states are being controlled simultaneously, the natural integration that occurs in a perspective scene is superior to most compensatory displays, in spite of the coupling of states occurring through perspective projection. Helicopter control during approach and landing is one example. Helicopters with no stability augmentation (which typically possess unstable open-loop dynamics) are routinely flown and landed in visual conditions. Studies indicate that augmentation to the control system is required to accomplish this when only compensatory displays showing attitude and flight path error are available [65, 71]. Further improvements in performance and workload occur when additional augmentation is performed on the control system and/or the display. Typical display augmentation includes the addition of predictor or flight director elements (which integrate attitude, position, rate and/or acceleration information).

The results of these experiments alone, and the resulting models, would appear to be relevant to only this application (or closely related ones, as in the helicopter examples given above). However, the visual cue analysis method, and modeling technique

developed here, have extremely wide potentials for application. The basic methodologies can be applied to any quasi-static control task using a perspective scene.

In order to fully apply this methodology with a wider variety of vehicle dynamics, disturbances, and scenes, a better understanding of what cues the operator is capable of attending to, and in what circumstances, is necessary. In the first two experiments, there was a particular cue that was available in all of the perspective scenes: the vertical distance between the horizon and a feature in the foreground ($\lambda_{\Delta v}$). This cue would have provided the best possible disturbance rejection, yet the evidence suggests that none of the operators used the cue effectively. By applying this analysis method to a variety of tasks and scenes, an inventory of usable and unusable visual cue sources can be developed. A particularly interesting area to examine would be the interference effects, if any, on visual cue perception with both lateral and longitudinal motions. Many studies have shown that in the case where the vehicle dynamics are relatively uncoupled (e.g., when lateral and longitudinal modes of motion are not coupled) that there is little interference from controlling both axes simultaneously. It would be particularly interesting and useful to understand the perceptual characteristics underlying this.

This method has been used to "identify" particular visual cues, but the identification can only be done by process of elimination to some extent: only one parameter actually specifies the cue, and it is possible that two different cue sources can share the same parameter. This was in fact the case with the three "optimal" cues λ_h (lateral position), $\lambda_{\Delta h}$ (relative lateral spacing), and $\lambda_{\Delta v}$ (relative vertical spacing), which all had characteristic parameters of unity. The hypothesis that $\lambda_{\Delta v}$ was not being used by anyone was determined through process of elimination; in the scenes where that cue was the only one present that would produce a value of unity, nobody achieved parameter values near unity. It is possible that this method could be extended to provide more definitive identification of cues through injection of additional disturbance sources. Each degree of freedom has a different effect on the perspective projection transformations, and the identification of individual parameters for each disturbance source might be consistent with only a particular cue. However, this approach would have some fundamental limitations: the current method relies on spectral separation

of the disturbances, and it would be difficult to add more than one or two additional disturbance sources with zero correlation. However, even adding one additional source could produce an enormous benefit.

The results of this effort have significant implications for a number of topics. We have control over visual scene content in a number of manual control applications. In vehicle design, we can choose the size and shape of the windows. Actual scene features for vehicle control are also selectable to some extent; runway markings and lane markings are two examples relevant to aircraft and automobiles. In synthetic scene generation, we have some control and choice over update rate and scene complexity, as well as display resolution. Designers of remotely-operated systems and vehicles can have some control over the display resolution, update rate, dynamic range (number of grayscale values, for example), and field of view. Evaluation of these factors in the design process has typically been done empirically; this methodology offers an algorithmic approach for evaluating the potential effects of perspective-scene manipulation, and validating the results.

Chapter 7

Contributions and Conclusions

7.1 Summary of Contributions

The unique contributions of the work described in this dissertation were listed in Section 1.3. Conclusions of the research, relevant to these contributions, are presented below.

- Development of a simple model which for the first time accurately characterizes human manual control through perspective scene viewing using a combination of cues.

The two-cue form of the VCC model developed in this dissertation demonstrates a high level of ability to match the measured input/output characteristics of humans performing manual control tasks using perspective displays. The fits to the data are consistently good with a limited number of parameters. The form of model for Y_p (the operator transfer function between position and control output) used in Experiment 2 featured five parameters (K_x, τ, ω_L, ω_N, ζ_N), which for each particular condition (operator $\times$ texture) were chosen to fit 24 data points (12 complex measurements). For each of the 64 conditions, this model provided a fit that was within 3 dB of the measurements with over 97% of the data points.

The extensive body of past work in manual control would predict the results for the Y_p model fits; the models used were consistent with known characteristics of human

manual control. What is notable about this new model is the high quality of fit achieved on $\hat{Y}_\theta$ (the measured operator transfer function between pitch attitude and control output). The two-cue model has two free parameters (K_β and K_γ); the other parameters of Y_p are set based upon the $\hat{Y}_p$ measurement. With the parameters of Y_p having been set with a different measurement ($\hat{Y}_p$), and the additional two parameters of the two-cue models, high degrees of fit accuracy were achieved to the 24 data points in the $\hat{Y}_\theta$ measurement. Specifically, in Experiment 2, the two parameters of the two-cue model provided fits within 3 dB of the measurements for over 84% of the data points. Thus, this simplified model accurately characterized perspective display usage in this manual control task.

Most of the textures clearly elicited a two-cue response from the human operator. The motion cue response also tended to have reduced disturbance content compared with the position cue ($K_\beta < K_\gamma$). If, in fact, this motion-cue response is due to specialized human motion perception, this leads to predictions that could be made concerning when the human motion perception would not be excited by the stimuli. Reductions in update rate, for example, could degrade the human motion-processing capability to the extent that the performance is no better than the position sensing. This methodology could help guide visual scene database designers making tradeoffs between scene complexity and update rate. In cases where scene complexity must be sacrificed to allow sufficient update rates, it should be possible to identify those portions of the image in which the benefits of scene detail are minimal.

- Development of more comprehensive knowledge through a more complete data set, with more statistical power, than the prior art.

The results of Experiment 1 did not allow determination of the most appropriate model (one-cue versus two-cue) due to high variances. In Experiment 2, efforts to reduce the amount of measurement variance in the control response to pitch attitude were successful: The reduction in variance produced definitive evidence that the operator was using two different cue sources. In some conditions, the amount of power in the control that was correlated with the pitch attitude disturbance was as low as 3%. It is a notable achievement that the measurement variances achieved fo

this variable were generally below 3 dB, often below 1 dB.

Analysis of Variance (ANOVA) results also confirm that manipulation of task variables could create measurable differences in the outcome variables. Probabilities of chance occurence in Experiment 2, on those results found to be statistically significant, were typically well below the 5% threshold. The consistency of the ANOVA findings lends additional credibility to the VCC model, since it shows that the task variables that are predicted to change the input/output relationships of the operator are producing statistically significant effects on both the characteristics of the operator output ($P_{\delta\theta}$, $P_{\delta x}$) and the performance (RMS_x, $\mathrm{RMS}_{\dot{x}}$).

- First detailed understanding through examination of visual cues, of the longitudinal position control task using a perspective scene.

It is apparent that the hovering control of a helicopter-like vehicle, through a perspective display, can be strongly affected by the characteristics of the scene. Redundancy of available cues appears to be important, although it was shown that even a relatively sparse display (the parallel texture) could produce very similar performance to a richer display (grid, dots), if that sparse display had optimal cues available. The available cues in this sparse display were limited to the position of the baseline, and the intersections of the baseline with the lines-of-splay. The optimal cues in this display are likely the presence of discrete points at the lower outer corners of the display, which allow better differentiation of longitudinal motion (which occurs along lines of splay) from pitch motion (which is primarily up and down).

- An improved understanding of the differences and similarities between perspective and compensatory displays.

Two main effects have been considered as differences between the perspective and compensatory displays. The first effect was the fact that a single state could be isolated and displayed on a compensatory display, while a perspective display is (typically) subject to effects from multiple states. The second factor is the nonlinear scaling of states that occur in the perspective display through perspective projection. These effects were isolated and studied. It appears that:

1. With a perspective display (unlike with a compensatory one), the coupling of states can adversely affect performance because it is (usually) impossible to find a visual cue that correlates perfectly with the desired state.

2. The nonlinear scaling has a minimal effect (given that the perturbations remain small).

3. Lack of a null indicator on a perspective display, as opposed to a compensatory display, has an adverse effect on performance.

It has already been noted that in some cases where multiple states are being displayed and controlled, that the perspective display can be superior to the compensatory display. That case was *not* examined in the current work, and these findings (particularly regarding the superiority of the compensatory display) are not generalizable to these cases.

- Development of simplified parameter identification procedures.

The large number of operators and conditions necessitated the development of streamlined parameter identification procedures. In Experiment 1, this new procedure was used to fit three parameters to 24 measurements[1]. In Experiment 2, five parameters were fit to 64 measurements, and in Experiment 3, five parameters were fit to 36 measurements. The fact that the resulting models exhibited a high degree of correspondence with the measurements is a validation of the method's effectiveness.

- Demonstration of a methodology to identify visual cues used in a manual control task.

The new modeling and identification technique described herein provides measurable quantities that can be related to the probability that the operator is using a particular visual cue. This technique has been used to determine when an optimal visual cue is not usable for closed-loop control, at least not to the degree of accuracy that could

[1]The term measurement here describes the transfer function measurement as a function of frequency; in Experiment 1, a single measurement consisted of ten complex values. In Experiments 2 and 3, each measurement consisted of 12 complex values.

be theoretically obtainable. This optimal visual cue was the distance, in the image, between the horizon line and the line in the foreground; none of the operators was capable of using this cue, although most of them indicated an awareness that keeping this distance fixed would be an effective control strategy. In general, the parameters derived for the motion cue were consistent with a strategy of sensing motion directed along the lines of splay (λ_s). The one operator who demonstrated better values of this parameter than are obtainable with λ_s indicated verbally that he had used another cue (horizontal displacement of features in the display) which would account for the lower values. Further work is required to fully realize the potential of this technique for identifying visual cues: This will be discussed in the following section.

7.2 Recommendations for Future Work

The work described in this dissertation provides a framework for modeling the use of perspective displays in manual control tasks. It also provides a potential methodology for identification of visual cues used in perspective displays. However, much work is still required to fully realize the potential of the model contained herein. The current research has shown that the parameters of the VCC model are consistent with particular visual cues, but definitive identification is impossible because of the existance of multiple cues with similar parameters. By incorporating one or more additional disturbance states, it should be possible to create a unique mapping between the parameters and particular visual cues, which would potentially enable definitive visual cue identification.

First and foremost, the model must be validated in a variety of conditions. The original Crossover Model consisted of both a parameterized model form, and a set of adjustment rules of the parameters, which varied as a function of the task variables. *The two-cue VCC model developed in the present research can be likened to and works closely with the parameterized model form of the Crossover Model, and the adjustment rules from this experiment are consistent with the available visual cues.* A basic set of adjustment rules based upon the ability of the human to perceive and use particular cues, and the likely effect of the vehicle degrees of freedom, needs to be developed.

Task variables that need to be studied include the imaging characteristics (field-of-view, resolution, update rate), scene content, controlled element dynamics, and forcing functions.

The VCC model currently does not incorporate the possibility of either an explicitly or implicitly generated commanded state. This would require incorporation of pursuit models of manual control, and depending on the situation, potentially even preview models (in which the operator sees not only current commanded state, but future commanded state).

The only degrees of freedom considered in this work were longitudinal position and pitch attitude. All of the vehicle states couple together in the process of perspective projection, but we can easily disambiguate some of these states visually (roll from pitch, for example). We need to develop a better understanding of the process by which we decouple states that are affecting particular visual cues.

This model did not incorporate any effects of perceptual thresholds. There are two factors that could affect a person's choice of visual cue, one of which has not been considered here. It was assumed that the operator would, when possible, choose a visual cue with the least "contamination" from the disturbance state θ. That is not the same as picking a cue that has the greatest sensitivity to the controlled state. The potential exists, in the equations of perspective projection, for the location in the image of maximum sensitivity to the relevant state to be different than the location at which the lowest amount of "contamination" from other states occurs. Both factors need to be considered, because the simplistic strategy of choosing a cue for which the "contamination" is minimized could also result in a cue for which the sensitivity to the relevant state is unacceptably close to perceptual thresholds.

Another potential area of improvement to this technique is the incorporation of eye-tracking. Eye-tracking alone cannot determine what information the human operator is using, for at least two reasons. First, the receptor field of the eyes is quite large (more than 180 degrees field-of-view for binocular viewing), so knowing the fixation point just determines the source of the highest-resolution information. Second, knowing where the eyes are fixated does not determine what judgment the person is making (i.e., determining the absolute position of a feature, or the relative distance

between two features). However, the eye movements could help to reduce the potential set of visual cues to be considered, since some might be shown to be outside of the required resolution range to be usable (due to the filtering that occurs in the eye). Another useful benefit of eye-movement measurement could be to refine the two-cue processing model. Certain types of eye movements are linked with motion perception, and study of eye movements could help to determine when motion processing is being optimally stimulated.

Many areas of research and design could benefit from the analysis methodology developed here. Training could include learning to attend to and perceive the most important visual cues for control. Decisions concerning field-of-view (for natural viewing or camera images) could be influenced by an analysis of the scene content and vehicle dynamics. Accident investigations in which loss of visual references is thought to be a factor could potentially benefit from this analysis technique. Simulator design can be influenced by determining tradeoffs of factors such as resolution, update rate, and time delays.

The research described in this disseration provides a fundamental improvement in our understanding and modeling of perspective display usage. While much work remains to be done, the current results provide a foundation for the development of new tools for the design and analysis of perspective scene usage in manual control tasks.

Appendix A

Perspective Projection Transformation

In order to analyze the relationship between vehicle states and image motion, it is necessary to determine the transformation which occurs between the state of the vehicle, the location of an object in the world, and the location of the object in the image plane.

Figure A.1 defines the geometry of the imaging situation analyzed here. The perspective projective transform defines the position of an object D in the image plane, (y_i, z_i), to be [58]:

$$\begin{Bmatrix} y_i \\ z_i \\ 1 \end{Bmatrix} = \begin{bmatrix} 0 & 1 & 0 & 0 \\ 0 & 0 & 1 & 0 \\ -1/F & 0 & 0 & 1 \end{bmatrix} \begin{Bmatrix} w\ x_D \\ w\ y_D \\ w\ z_D \\ w \end{Bmatrix} \tag{A.1}$$

The parameter w is an arbitrary scale factor which is not equal to zero. The value F is the distance between the center of projection P and the image plane; it would be related to focal length of a camera. The coordinates x_D, y_D, z_D are the position of the feature D relative to the image plane coordinate system, $\mathbf{i}, \mathbf{j}, \mathbf{k}$. Since the position of D and the center of projection P are typically expressed relative to another, earth-fixed coordinate system, a transformation is necessary.

$$x_D\mathbf{i} + y_D\mathbf{j} + z_D\mathbf{k} = F\mathbf{i} - \mathbf{P} + \mathbf{D} \tag{A.2}$$

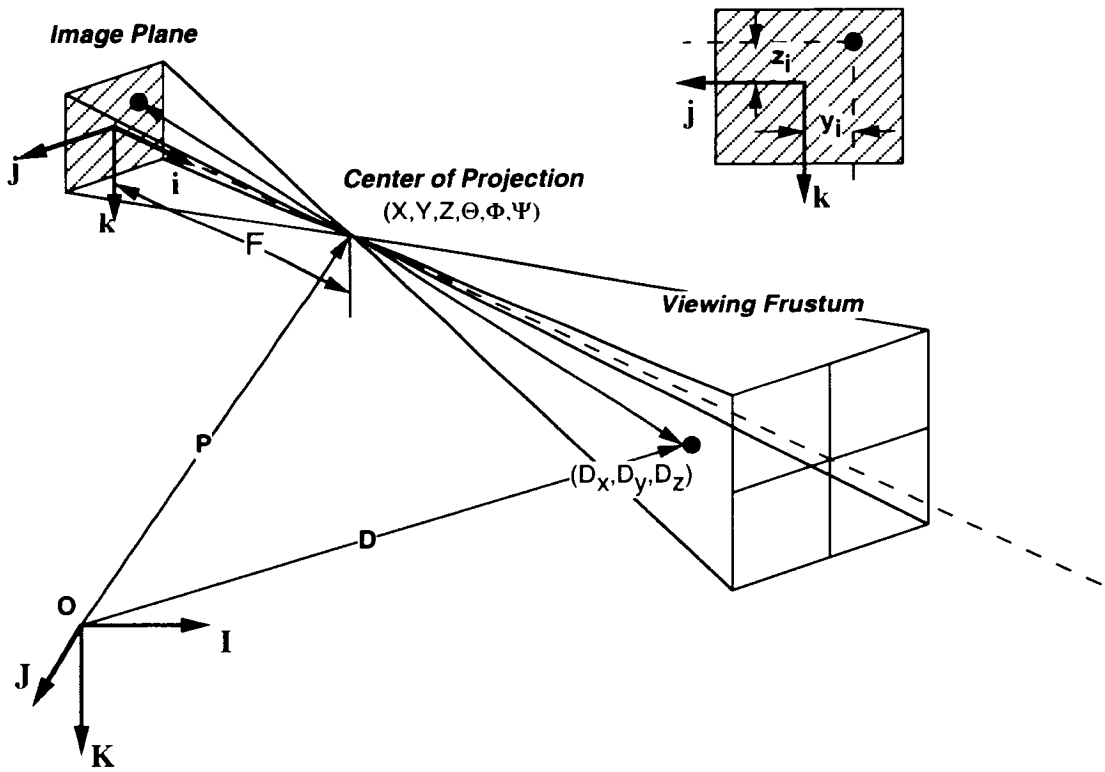

Figure A.1: Perspective projection transform geometry diagram.

P and **D** are the positions of points P and D relative to the coordinate system **I**, **J**, **K**. The transformation between the two coordinate systems, using Eulerian angles [59], is:

$$\begin{Bmatrix} \mathbf{i} \\ \mathbf{j} \\ \mathbf{k} \end{Bmatrix} = \begin{bmatrix} \mathrm{c}\Psi\mathrm{c}\Theta & \mathrm{s}\Psi\mathrm{c}\Theta & -\mathrm{s}\Theta \\ -\mathrm{s}\Psi\mathrm{c}\Phi + \mathrm{c}\Psi\mathrm{s}\Theta\mathrm{s}\Phi & \mathrm{c}\Psi\mathrm{c}\Phi + \mathrm{s}\Psi\mathrm{s}\Theta\mathrm{s}\Phi & \mathrm{c}\Theta\mathrm{s}\Phi \\ \mathrm{s}\Psi\mathrm{s}\Phi + \mathrm{c}\Psi\mathrm{s}\Theta\mathrm{c}\Phi & -\mathrm{c}\Psi\mathrm{s}\Phi + \mathrm{s}\Psi\mathrm{s}\Theta\mathrm{c}\Phi & \mathrm{c}\Theta\mathrm{c}\Phi \end{bmatrix} \begin{Bmatrix} \mathbf{I} \\ \mathbf{J} \\ \mathbf{K} \end{Bmatrix} \tag{A.3}$$

The resulting transformation between world displacements P and D to image plane coordinates (y_i, z_i) is:

$$\begin{aligned} y_i &= w((D_X - X)(-\mathrm{s}\Psi\mathrm{c}\Phi + \mathrm{c}\Psi\mathrm{s}\Theta\mathrm{s}\Phi) \\ &\quad +(D_Y - Y)(\mathrm{c}\Psi\mathrm{c}\Phi + \mathrm{s}\Psi\mathrm{s}\Theta\mathrm{s}\Phi) + (D_Z - Z)\mathrm{c}\Theta\mathrm{s}\Phi) \qquad \text{(A.4)} \\ z_i &= w((D_X - X)(\mathrm{s}\Psi\mathrm{s}\Phi + \mathrm{c}\Psi\mathrm{s}\Theta\mathrm{c}\Phi) \\ &\quad +(D_Y - Y)(-\mathrm{c}\Psi\mathrm{s}\Phi + \mathrm{s}\Psi\mathrm{s}\Theta\mathrm{c}\Phi) + (D_Z - Z)\mathrm{c}\Theta\mathrm{c}\Phi) \qquad \text{(A.5)} \\ w &= \frac{-F}{(D_X - X)\mathrm{c}\Psi\mathrm{c}\Theta + (D_Y - Y)\mathrm{s}\Psi\mathrm{c}\Theta - (D_Z - Z)\mathrm{s}\Theta} \qquad \text{(A.6)} \end{aligned}$$

Appendix B

Transfer Function Measurement Techniques

B.1 Sum-of-Sines Technique

The Sum-of-Sines (SOS) technique has been used extensively for human operator transfer function measurement [72]. It is particularly well suited for situations in which the inputs and/or disturbances are variables under the control of the experiment designer. The SOS technique calls for inputs and disturbances which are sums of multiple sine functions, each at a different fundamental frequency and phase. Although the resulting signal has a completely random appearance to a human operator, the characteristic of the signal lends itself to analysis using frequency based methods.

In Section 2.4, it was stipulated that the disturbance functions u and q were not correlated. This is done by making each signal from sums of sines of different fundamental frequencies from each other. The exact composition of these signals used for the experiments is described further in Sections D.1 and E.1. Now some practical guidelines and limitations of the SOS technique will be discussed. Specifically, the particular elements which must be carefully chosen are the sampling interval, the run length, and the frequencies used to make up the SOS signals.

B.1.1 Sampling Interval

The sampling interval T limits the bandwidth of the maximum frequency which can be identified; the bandwidth will be the Nyquist frequency, or $1/2T$. For example, with a sampling interval of 0.03 seconds, the Nyquist frequency is 16.6 Hz. The sampling frequency needs to be set high enough that it is at least two times above the expected bandwidth of the system (including disturbances) to be identified; otherwise, the frequency content of the signal which is above the Nyquist frequency will be aliased into lower frequencies during processing, producing an erroneous measurement.

B.1.2 Run Length

One requirement for the run length is that it be long enough to allow identification of the lowest frequency content of the input signal. Common practice in human modeling is to measure frequencies as low as 0.15 rad/sec; one cycle at this frequency takes approximately 42 seconds. Another common practice is to allow at least 4 or 5 repetitions of the lowest frequency within a data run; five repetitions of this frequency requires approximately 210 seconds, or 3.5 minutes.

Another requirement, which is perhaps obvious but should be stated, is that the run length (time elapsed) should be an integer multiple of the sampling interval. This is usually a natural consequence of digital simulation, but is included here for completeness.

Commonly, the Discrete Fourier Transform is used develop cross spectral density estimates from the time histories of the state. Although it was not done in this dissertation, choosing the run length such that the number of samples is a power of 2 will allow great computational advantages in data analysis (much more efficient algorithms exist for DFT when the length of the sequence is a power of 2).

B.1.3 Frequency Components

The frequency components of the SOS signal should all be multiples of the period established by the total run length. This is easily accomplished by specifying discrete

values of frequencies which are *available* to form the SOS signal (designated ω_k):

$$\omega_k = \frac{2\pi k}{T_r}, \quad k = 1, 2, 3, \ldots, T_r \tag{B.1}$$

where T_r is the data run length in seconds.

McRuer's recommendations [30] for input signals for human operator transfer function identification are to pick approximately 12 frequencies, equally spaced logarithmically from approximately 0.15 to 15 rad/sec. The magnitudes of the different frequency components can have noticeable effects on the operator strategy, and must be chosen carefully; a thorough treatment of this subject is beyond the scope of this section. More detailed guidelines concerning the choice of input signals frequencies and magnitudes can be found in [30].

B.1.4 Minimizing Errors from Nonlinearities

The guidelines noted above would theoretically work for any linear system identification, but in fact the system we are identifying, the human operator, does exhibit nonlinear characteristics. We can take one additional precaution to assure that these nonlinearities do not adversely affect accurate modeling of the linear characteristics.

A linear system acting upon a sine wave signal, with a fundamental frequency of ω_f, for example, will produce an output which only possesses that fundamental frequency. However, a nonlinear system acting on this signal would produce output not only at that fundamental frequency (ω_f), but also at harmonics of the frequency ($2\omega_f$, $3\omega_f$, etc.) [72]. We can minimize the effects of nonlinearities on the measurements by ensuring that measurements at each frequency are not affected by harmonics from other frequencies.

This can be prevented by choosing frequency components that are not harmonics of each other. This is easily done at the higher frequencies by choosing only prime numbers for the value of k in Equation B.1. At the very lowest frequencies, this is not always possible because of the relatively small number of primes, but at these frequencies, there are no inputs at the frequencies below that should be causing harmonics.

B.2 Estimation of $\hat{Y}_p$ and $\hat{Y}_\theta$

In section 2.4.2, equations relating the components of the one-cue model and the system state power and cross spectral densities were developed. These equations are repeated here, originally Equations 2.25 and 2.26:

$$\frac{\phi_{\delta u}}{\phi_{xu}} = \frac{Y_p Y_c \phi_{uu} + \phi_{ru}}{Y_c \phi_{uu} + Y_c \phi_{ru}} \tag{B.2}$$

$$\frac{\phi_{\delta q}}{\phi_{\theta q}} = \frac{1}{1 - Y_p Y_c} \frac{Y_p K_\alpha \phi_{\theta q} + \phi_{rq}}{\phi_{\theta q}} \tag{B.3}$$

These equations are based on the assumption that the input signals u and q are uncorrelated. Both of these equations include some correlation between the inputs and the remnant term r. The assumption was further made, in Section 2.4.2, that the correlation between this remnant and the inputs is also zero. While this assumption is valid in a statistical sense, meaning that the expected value should be zero, it is unlikely that zero correlation will occur in a particular experimental run.

The potential effect of this noise on model function estimates can easily be seen. The Discrete Fourier Transform (Equation 2.35) coefficients are used to estimate the cross spectral density measurements (reference Equations 2.31 through 2.34). For a *single* experimental run, the estimate of the cross spectral density $\phi_{\delta u}/\phi_{xu}$ would be:

$$\frac{\phi_{\delta u}}{\phi_{xu}} \approx \frac{D(f)U(f)^*}{X(f)U(f)^*} = \frac{D(f)}{X(f)} \tag{B.4}$$

With a measurement based upon a single experimental run, $V(f)$ has no effect. This measurement can be shown to have the following relationship with the model:

$$\frac{D(f)}{X(f)} = \frac{Y_p Y_c u + r}{Y_c u + Y_c r} \tag{B.5}$$

This would be an accurate representation of the model Y_p only if the magnitude of r is small. A common modeling error reported by novice modelers is the unwitting identification of the inverse plant dynamics when the noise magnitude becomes large. For $r >> u$, we have:

$$\frac{D(f)}{X(f)} = \frac{r}{Y_c r} \approx \frac{1}{Y_c} \tag{B.6}$$

Averaging can be used to improve these estimates of cross-spectral densities. Levison [62] recommended averaging the products of the DFT coefficients before taking the ratio:

$$\hat{Y}_p = \frac{\overline{D(f)U(f)^*}}{\overline{X(f)U(f)^*}} \tag{B.7}$$

$$\hat{Y}_\theta = \frac{\overline{D(f)Q(f)^*}}{\overline{\Theta(f)Q(f)^*}} \tag{B.8}$$

The primary assumption enabling this is that the processes described by Y_p and Y_θ are statistically stationary. From these ensemble averages, Levison also developed relationships for estimating the variances of these estimates. That derivation is presented here in its entirety. First, it is worthwhile to quickly review the assumptions made concerning the characteristics of the remnant. Levison makes the assumption that the remnant is a zero-mean Gaussian process whose real and imaginary Fourier coefficients have zero cross-correlation, zero covariance across frequency and replication, and equal autocovariances. It is referred to as a "stationary incoherent" process, implying the the remnant power is statistically constant, and the phase is randomly distributed between 0 and 2π across frequencies and replications.

One is interested in knowing the variance of the estimate of $\hat{Y}_p$. The estimate $\hat{Y}_p$, and the correct or true value, Y_{p_o}, can be expressed with the following relationship:

$$\hat{Y}_p = Y_{p_o}(1+\epsilon) \tag{B.9}$$

The term ϵ represents a measurement error. We are interested in estimating variance in this measurement, specifically how much this estimate varies from the correct value. The estimate of the variance is [73]:

$$\sigma_\epsilon^2 = \frac{N_r}{N_r - 1} E(|\hat{Y}_p - Y_{p_o}|^2) \tag{B.10}$$

where $E(\bullet)$ is the expected value, or mean of $(\bullet)$, and N_r is the number of samples used to derive the estimate. To simplify further analysis, the following definitions are made:

$$D' \equiv D(f)V(f)^* \tag{B.11}$$

$$X' \equiv X(f)V(f)^* \tag{B.12}$$

Using a similar notation as was used in Equation B.9, these terms can be broken into their "true" values and measurement error:

$$D' = D'_o + \tilde{D}' \tag{B.13}$$

$$X' = X'_o + \tilde{X}' \tag{B.14}$$

In these equations, D'_o and X'_o represent the true values, and $\tilde{D}'$ and $\tilde{X}'$ represent the measurement errors. $\hat{Y}_p$ can be written as:

$$\hat{Y}_p = \frac{D'_o + \tilde{D}'}{X'_o + \tilde{X}'} \tag{B.15}$$

If D'_o and X'_o are the "true" values, one can also write:

$$\hat{Y}_p = Y_{p_o} \frac{1 + \tilde{D}'/D'_o}{1 + \tilde{X}'/X'_o} \tag{B.16}$$

If one assumes that the measurement error $\tilde{X}'$ is small[1] relative to X'_o, making $\tilde{X}'/X'_o << 1$, one can approximate this expression as:

$$\hat{Y}_p = Y_{p_o}\left(1 + \frac{\tilde{D}'}{D'_o} - \frac{\tilde{X}'}{X'_o}\right) \tag{B.17}$$

The measurement error term ϵ is thus identified as:

$$\epsilon = \frac{\tilde{D}'}{D'_o} - \frac{\tilde{X}'}{X'_o} \tag{B.18}$$

By solving Equations B.13 and B.14 for $\tilde{D}'$ and $\tilde{X}'$, and substituting into Equation B.18, the expression for ϵ becomes:

$$\epsilon = \frac{D'}{D'_o} - \frac{X'}{X'_o} \tag{B.19}$$

The variance of ϵ can then be expressed as:

$$\sigma_\epsilon^2 = \frac{N_r}{N_r - 1} E\left(\left(\frac{D'}{D'_o} - \frac{X'}{X'_o}\right)\left(\frac{D'^*}{D'^*_o} - \frac{X'^*}{X'^*_o}\right)\right) \tag{B.20}$$

[1]This is not the same as assuming that the magnitude of the remnant is small. X' is an ensemble average of multiple measurements. The assumption is that the phase of the remnant is uniformly distributed from 0 to 2π, which makes the expected value of this measurement error zero. This assumption becomes more accurate as more measurements are used to form the ensemble average of X'.

The expected value of the terms such as $D'D'^*$ can be estimated through ensemble averaging of the experimentally derived values (remember that $D' = D(f)V(f)^*$). The expected values of the terms such as $D'_oD'^*_o$ should in fact be equivalent to the expected value of D', squared. With these substitutions, one can write:

$$\sigma_\epsilon^2 = \frac{N_r}{N_r - 1}\left[\frac{\overline{(D'D'^*)}}{(\overline{D'}\,\overline{D'^*})} + \frac{\overline{(X'X'^*)}}{(\overline{X'}\,\overline{X'^*})} - 2Re\left(\frac{\overline{(D'X'^*)}}{(\overline{D'}\,\overline{X'^*})}\right)\right] \tag{B.21}$$

This standard error is a quantity that relates to the standard error of the estimate of the *complex* quantity $\hat{Y}_p$. A common method used to examine the characteristics of frequency domain transfer functions is to derive two scalar parameters which together specify the function: gain and phase. Levison developed an expression to help relate the standard error estimate to these two characteristics. Defining A and B to represent the real and imaginary parts of ϵ, Equation B.9 can be expressed as:

$$\hat{Y}_p = Y_{p_o}(1 + A + jB) \tag{B.22}$$

The gain G of this quantity is defined as:

$$\begin{aligned} G &= 10\mathrm{Log}_{10}(\hat{Y}_p\hat{Y}_p^*) = 4.34\mathrm{Ln}(\hat{Y}_p\hat{Y}_p^*) && \text{(B.23)} \\ &= G_o + G_e && \text{(B.24)} \end{aligned}$$

where

$$\begin{aligned} G_o &= 10\mathrm{Log}_{10}(Y_{p_o}) && \text{(B.25)} \\ G_e &= 4.34\mathrm{Ln}(1 + 2A + A^2 + B^2) && \text{(B.26)} \end{aligned}$$

G_e represents the error in the measurement of the the "true" gain, G_o. Expressing the natural logarithm with the series expansion $\mathrm{Ln}(1 + x) = x - x^2/2 + x^3/3 - \ldots$, and dropping powers higher than 2, the expression for G_e can be written as:

$$G_e = 4.34(2A + B^2 - A^2) \tag{B.27}$$

Since A and B are the real and imaginary components of ϵ, and ϵ is assumed to have a uniform phase distribution, the expected value of the quantity $A^2 - B^2$ is zero.

Further noting that the expected value of A is half of the expected magnitude-squared of ϵ, we can obtain for the variance of G_e:

$$\sigma_G^2 = 2(4.34)^2\sigma_\epsilon^2 \tag{B.28}$$

$$\sigma_G = 6.14\sigma_\epsilon \tag{B.29}$$

Now the expression for the variance in the phase will be developed. The phase shift of $\hat{Y}_p$ can be expressed as:

$$\phi_e = \tan\left[\frac{B}{1+A}\right] \tag{B.30}$$

For $A, B << 1$, this becomes:

$$\phi_e = B(1 - A + A^2) \tag{B.31}$$

$$\sigma_\phi^2 = E\Big(B^2(1 - A + A^2)^2\Big) \tag{B.32}$$

The expected values of all the terms in the above equation are zero[2] with the exception of B^2; thus

$$\sigma_\phi^2 = E(B^2) = \frac{1}{2}E(\epsilon^2) = \frac{\sigma_\epsilon^2}{2} \tag{B.33}$$

The standard deviation terms derived here, σ_ϵ, σ_G, and σ_ϕ are representative of the sample variances, which reflect the trial-to-trial variations expected. However, we are more interested in knowing the variance in our estimate of the mean values; this term is known as the standard error. For any of the standard deviation terms used, the relationship of the standard error (denoted se) to the standard deviation (denoted σ) for N_r samples is [73]:

$$se = \sqrt{\frac{\sigma^2}{N_r}} \tag{B.34}$$

[2]Because the remnant is assumed to be uniformly distributed in phase between 0 and 2π, expected values of any terms containing products of A and B will be zero.

Appendix C

Model Fitting Technique

C.1 Time History Fit Technique for Y_p

Assume that a measurement vector $H(\omega)$ is available. The free parameters u of a model $Y_p(u,\omega)$ are sought to minimize differences between the model and the measurement. To obtain best fit in the frequency domain, it makes sense to actually minimize the difference of the ratio from 1, or $Y_p/H - 1$. Selection of parameters u to accomplish this cannot be done analytically; a numerical approach is necessary. However, a closed-loop, non-numerical approximation can be obtained through discrete approximation techniques.

As described in [74], a discrete transfer function can be obtained through least-squares methodology. The discrete transfer function can be transformed to an equivalent frequency domain function through a w-transform [75]. The generalized transfer function of the form:

$$Y_p(s) = \frac{e^{-\tau s}(c_n s^n + c_{n-1}s^{n-1} \ldots c_1 s + c_0)}{d_n s^n + d_{n-1}s^{n-1} \ldots d_1 s + d_0} \tag{C.1}$$

can be represented with a discrete transfer function:

$$Y_p(z) = \frac{z^{-p}(b_1 z^{-1} + b_2 z^{-2} \ldots + b_n z^{-n})}{1 - a_1 z^{-1} - a_2 z^{-2} - \ldots - a_m z^{-m}} \tag{C.2}$$

If, for example, the transfer function $Y_p(z)$ is meant to represent a transfer function

δ/x, the corresponding difference equation would be:

$$\delta_{k+1} = \delta_k a_1 + \delta_{k-1} a_2 + \ldots + \delta_{k-m+1} a_m + x_{k-p} b_1 + x_{k-p-1} b_2 + \ldots + x_{k-p-n} b_n \quad \text{(C.3)}$$

Given a measured time history $\delta(t)$, $x(t)$, taken at time increments T, a matrix can be formed to generate a least-squares solution for the discrete transfer function parameters a_i and b_i.

$$\begin{Bmatrix} \delta_{k+1} \\ \delta_k \\ \vdots \end{Bmatrix} = \begin{bmatrix} \delta_k & \delta_{k-1} & \cdots & x_{k-p} & x_{k-p-1} & \cdots \\ \delta_{k-1} & \delta_{k-2} & \cdots & x_{k-p-1} & x_{k-p-2} & \cdots \\ \vdots & \vdots & \ddots & \vdots & \vdots & \ddots \end{bmatrix} \begin{Bmatrix} a_1 \\ a_2 \\ \vdots \\ b_1 \\ b_2 \\ \vdots \end{Bmatrix} \quad \text{(C.4)}$$

The parameter vectors a and b can be determined from a least-squares fit of time history data. The resulting discrete transfer function can be converted to a continuous transfer function via the w-transform:

$$z = \frac{1 + \mathrm{w}T/2}{1 - \mathrm{w}T/2} \quad \text{(C.5)}$$

After substituting this relationship into Equation C.2, the w-plane transfer function $Y_p(\mathrm{w})$ can be used to approximate the s-plane transfer function $Y_p(s)$. The quality of the fit can be evaluated through a correlation coefficient, which would have a value of unity for a perfect model. If Δ' is the measured output vector, and Δ is the modeled output vector, the correlation coefficient R^2 is defined as:

$$R^2 = 1 - \left[\sum(\Delta_k - \Delta_k')^2\right] / \sum(\Delta_k)^2 \quad \text{(C.6)}$$

This same technique can be used to find a best fit to the frequency domain measurements H by reconstructing a time history from the frequency measurements. Given a complex measurement H_i taken at frequency ω_i with magnitude A_i and phase ϕ_i, an input-output time history can be constructed. If the input is assumed to be

$$x(t)_i = \sin(\omega_i t) \quad \text{(C.7)}$$

The output corresponding to this measurement would be

$$\delta(t)_i = A_i \sin(\omega_i t + \phi_i) \tag{C.8}$$

This pseudo-time-history can then be used to construct a matrix as in Equation C.4 to perform a least-squares solution for the vectors a and b. The term above can be used to form a fit corresponding to one measurement point; the entire measurement vector can be fit by concatenating the input-output matrices together. In order to keep the highest magnitude measurements from influencing the fit disproportionately, all the components are weighted with the inverse of the measurement amplitude. It is also possible to weight with the inverse of the variance to put greater emphasis on fitting the low-frequency points.

The time granularity with which one reconstructs the input-output vectors is not limited to the time interval upon which the original measurement was based; it is possible to simulate a smaller sampling interval in order to estimate the time delay more accurately. However, the size of the matrix to be inverted scales with the inverse of the sampling interval chosen. For a time vector that spans the measurement interval, this can be quite large. Another limitation is that it is *not* equivalent to fitting in the frequency domain. However, it will come much closer to a frequency domain fit than standard time-domain fitting techniques, and it is an analytical solution as opposed to numerical.

This technique was used to fit the model parameters of Y_p to the measurement $\hat{Y}_p$. Each measurement was inversely weighted with the magnitude of the measurement and the standard error. For Experiment 1, the time delay τ was varied in .01 second steps to determine the best fit using the correlation coefficient R^2. For Experiments 2 and 3, τ was varied in increments of 1/72 sec.

C.2 Grid-Search Fit Technique for $Y_{\theta 1}$ and $Y_{\theta 2}$

In the case of the fit to the measurement $\hat{Y}_\theta$, a smaller number of parameters needed to be fitted, making a numerical technique practical. The performance index J was used to evaluate the one-cue and two-cue model fits, respectively. If we assume that

the measured frequency response vector is $\hat{H}$, and the modeled vector is H, and the standard error vector is σ, the equations defining the performance index J are:

$$R_i = \frac{\hat{H}_i}{H_i} \tag{C.9}$$

$$J = \sum_{i=1}^{I} \left[\frac{\log(R_i)}{\sigma_i} \frac{\log(R_i^*)}{\sigma_i} \right] \tag{C.10}$$

H_i, $\hat{H}_i$ and σ_i denote the ith elements of the vectors H, $\hat{H}$, and σ, respectively. The model parameters to fit H_θ were derived through a grid search technique to minimize the performance index J.

Appendix D

Experiment 1 Appendix

D.1 Vehicle Dynamic Simulation

$$\begin{Bmatrix} \ddot{x} \\ \dot{x} \\ \dot{\theta} \end{Bmatrix} = \begin{bmatrix} -0.2 & 0 & 0 \\ 1 & 0 & 0 \\ 0 & 0 & 0 \end{bmatrix} \begin{Bmatrix} \dot{x} \\ x \\ \theta \end{Bmatrix} + \begin{bmatrix} 1 & 1 & 0 \\ 0 & 0 & 0 \\ 0 & 0 & 0.033 \end{bmatrix} \begin{Bmatrix} \delta \\ u \\ q \end{Bmatrix} \tag{D.1}$$

The position x is in units of eyeheights. The angle θ is expressed in radians. This state-space equation was converted to discrete form for real-time simulation with a sampling interval of 0.03 seconds, using the first-order hold [75]. The resulting discrete state-space equations were:

$$\begin{Bmatrix} \dot{x}_{k+1} \\ x_{k+1} \\ \theta_{k+1} \end{Bmatrix} = \begin{bmatrix} 0.9940 & 0 & 0 \\ 0.0299 & 1 & 0 \\ 0 & 0 & 1 \end{bmatrix} \begin{Bmatrix} \dot{x}_k \\ x_k \\ \theta_k \end{Bmatrix} + \begin{bmatrix} 0.0299 & 0.0299 & 0 \\ 0.00045 & 0.00045 & 0 \\ 0 & 0 & .001 \end{bmatrix} \begin{Bmatrix} \delta_k \\ u_k \\ q_k \end{Bmatrix} \tag{D.2}$$

The control input of the operator is δ; the maximum range achievable was from -4 to 4. The disturbances u and q had the following form as a function of time (t):

$$u(t) = \sum_{i=1}^{12} D \frac{a_i 2\pi k_i}{240} \cos\left(\frac{2\pi k_i}{240} t + \rho_i\right) \tag{D.3}$$

$$q(t) = \sum_{i=1}^{12} D \frac{a_i 2\pi k_i}{240} \cos\left(\frac{2\pi k_i}{240} t + \rho_i\right) \tag{D.4}$$

x disturbance (u)				θ disturbance (q)			
i	a_i	k_i	ω_i (rad/sec)	i	a_i	k_i	ω_i (rad/sec)
1	.5	6	.16	1	.5	7	.18
2	.5	10	.26	2	.5	11	.28
3	.5	15	.39	3	.5	16	.42
4	.5	23	.60	4	.5	25	.65
5	.5	37	.97	5	.5	38	.99
6	.5	59	1.54	6	.5	61	1.60
7	.05	101	2.64	7	.05	103	2.70
8	.05	127	3.32	8	.05	131	3.43
9	.05	149	3.90	9	.05	151	3.95
10	.05	179	4.69	10	.05	181	4.74
11	.05	311	8.14	11	.05	313	8.19
12	.05	521	13.64	12	.05	523	13.69

Table D.1: Experiment 1 disturbance spectra magnitudes and frequencies.

The actual values of a, k and resulting frequencies ($\omega = 2\pi k/240$) are shown in Table D.1 for the two disturbance spectra. D was set to a value of .7.

The phase offsets (ρ_i) for each repetition and disturbance (q and u) were precomputed with a random number generator, randomly distributed from -π to π. These angles used for each repetition are shown in Table D.2 (u) and D.3 (q).

The design of the disturbance spectra is in accordance with guidelines supplied in [30] for pilot frequency response identification. Most of the points are logarithmically spaced between .15 and 15 rad/sec. Two additional points were added in the range between 1.6 and 4.7 Hz to better capture the response in this region.

D.2 ANOVA results summary

D.2.1 2×2 Factorial

In the main body of the report, only figures depicting the means and standard errors of the dependent measures are presented, with tables summarizing the degree of statistical significance. The actual values for statistical significance are shown in

	Repetition					
i	1	2	3	4	5	6
1	-2.88	2.59	1.78	0.97	0.16	-0.66
2	2.10	0.46	-1.18	-2.83	1.81	0.17
3	0.41	0.34	0.26	0.19	0.11	0.04
4	-1.96	1.15	-2.02	1.09	-2.08	1.03
5	1.57	0.80	0.02	-0.75	-1.53	-2.30
6	-0.93	-1.53	-2.13	-2.72	2.96	2.37
7	-2.31	0.20	2.72	-1.05	1.46	-2.31
8	2.83	0.05	-2.74	0.76	-2.03	1.47
9	0.53	-1.10	-2.74	1.91	0.27	-1.37
10	1.93	2.50	3.07	-2.64	-2.07	-1.50
11	0.77	1.81	2.86	-2.38	-1.34	-0.29
12	-3.10	-0.20	2.70	-0.69	2.21	-1.17

Table D.2: Experiment 1 phase angles ρ_i used to define disturbance u per repetition.

	Repetition					
i	1	2	3	4	5	6
1	-0.29	-2.14	2.29	0.43	-1.43	3.00
2	-1.03	1.89	-1.46	1.46	-1.90	1.03
3	-3.13	-1.77	-0.42	0.94	2.30	-2.63
4	3.08	0.70	-1.67	2.23	-0.14	-2.52
5	-0.84	3.06	0.68	-1.70	2.21	-0.17
6	0.46	1.84	-3.06	-1.68	-0.30	1.08
7	-2.74	2.31	1.08	-0.15	-1.38	-2.61
8	-2.18	0.19	2.56	-1.36	1.01	-2.91
9	-1.78	2.25	-0.01	-2.27	1.76	-0.50
10	-2.26	-1.90	-1.54	-1.18	-0.81	-0.45
11	-1.82	-1.18	-0.55	0.09	0.72	1.35
12	0.46	1.61	2.76	-2.38	-1.23	-0.09

Table D.3: Experiment 1 phase angles ρ_i used to define disturbance q per repetition.

		$P_{\delta\theta}$		$P_{\delta x}$		$\mathrm{RMS}_{\dot{x}}$		RMS_{x}	
Texture	Noise	mean	SE	mean	SE	mean	SE	mean	SE
Grid	absent	1.54	0.19	52.59	3.76	0.456	0.033	0.587	0.072
Grid	present	2.76	0.26	50.00	3.40	0.490	0.034	0.603	0.060
Line	absent	1.78	0.20	49.97	1.92	0.468	0.033	0.556	0.098
Line	present	9.21	2.15	39.04	3.44	0.622	0.052	0.887	0.175

Table D.4: Means and Standard Errors for $P_{\delta\theta}$, $P_{\delta x}$, RMS_{x} and RMS_{x} for the 2 × 2 (disturbance × texture) ANOVA in Experiment 1.

	Factor					
Measurement	Pitch disturbance		Texture		Dist/Text Interaction	
	F(1,5)	p	F(1,5)	p	F(1,5)	p
$P_{\delta\theta}$	14.54	0.012	9.96	0.025	9.47	0.028
$P_{\delta x}$	16.95	0.009	4.06	0.101	6.07	0.057
$\mathrm{RMS}_{\dot{x}}$	10.53	0.002	5.74	0.062	9.59	0.027
RMS_{x}	10.53	0.023	2.75	0.158	7.42	0.042

Table D.5: F-test and probabilities for statistical analysis of the 2 × 2 (disturbance × texture) ANOVA in Experiment 1.

Table D.5. The numerical values for means and standard errors for $P_{\delta\theta}$, $P_{\delta x}$, $\mathrm{RMS}_{\dot{x}}$ and RMS_{x} are shown in Table D.4.

D.2.2 One-way Factorial

The actual values for statistical significance of the one-way ANOVA are shown in Table D.7. The numerical values for means and standard errors for $P_{\delta\theta}$, $P_{\delta x}$, RMS_{x} and RMS_{x} are shown in Table D.6.

	$P_{\delta\theta}$		$P_{\delta x}$		RMS_x		RMS_x	
Texture	mean	SE	mean	SE	mean	SE	mean	SE
Grid	2.76	0.26	50.00	3.40	0.490	0.034	0.603	0.060
Parallel	3.80	0.66	45.85	4.06	0.573	0.042	0.783	0.084
Perpendicular	6.67	1.59	43.02	2.78	0.578	0.029	0.721	0.079
Line	9.21	2.15	39.04	3.44	0.622	0.052	0.887	0.175

Table D.6: Means and Standard Errors for $P_{\delta\theta}$, $P_{\delta x}$, RMS_x and RMS_x for the one-way (texture) ANOVA in Experiment 1 .

Measurement	Factor	
Measurement	Texture	
	F(3,15)	p
$P_{\delta\theta}$	9.44	0.001
$P_{\delta x}$	3.37	0.047
$\mathrm{RMS}_{\dot{x}}$	5.61	0.009
RMS_x	3.50	0.042

Table D.7: F-test and probabilities for statistical analysis of the one-way (texture) ANOVA in Experiment 1.

	K_p				J_p			
	Condition (Texture)				Condition (Texture)			
Obs.	3 (G)	4 (L)	5 (‖)	6 (⊥)	3 (G)	4 (L)	5 (‖)	6 (⊥)
1	2.02	1.71	1.88	1.65	19.2	19.3	17.3	33.3
2	1.58	1.26	1.22	1.03	40.6	13.6	7.0	18.9
3	1.24	1.31	1.28	1.06	39.6	20.7	33.1	12.8
4	1.21	1.02	0.98	0.78	77.7	52.2	57.6	15.1
5	1.96	1.95	1.90	1.89	62.1	49.7	37.2	35.7
6	2.26	2.01	1.96	2.35	53.3	33.4	36.0	34.3
	τ (sec)				ω_L (rad/sec)			
	Condition (Texture)				Condition (Texture)			
Obs.	3 (G)	4 (L)	5 (‖)	6 (⊥)	3 (G)	4 (L)	5 (‖)	6 (⊥)
1	0.48	0.51	0.54	0.48	0.46	0.47	0.41	0.40
2	0.51	0.54	0.51	0.48	0.27	0.26	0.35	0.40
3	0.51	0.51	0.54	0.60	0.20	0.23	0.26	0.12
4	0.45	0.48	0.48	0.45	0.20	0.18	0.25	0.34
5	0.51	0.51	0.51	0.51	0.26	0.22	0.28	0.32
6	0.45	0.45	0.48	0.45	0.25	0.23	0.25	0.37

Table D.8: Y_p parameters K_p, ω_L, and τ, and model fit index J_p from Experiment 1.

D.3 Individual Model Parameter Summary

Y_p model parameters K_p, ω_L, τ, and fit quality index J_p are presented in Table D.8. The crossover frequency ω_c and phase margin ϕ_m of Y_pY_c are in Table D.9. $Y_{\theta 1}$ parameter K_α, and fit quality index $J_{\theta 1}$ are in Table D.10. $Y_{\theta 2}$ parameters K_β and K_γ, fit quality index $J_{\theta 2}$, and the ratio $J_{\theta 2}/J_{\theta 1}$ are in Table D.11.

	ω_c (rad/sec)				ϕ_m (deg)			
	Condition (Texture)				Condition (Texture)			
Obs.	3 (G)	4 (L)	5 ($\|\|$)	6 ($\perp$)	3 (G)	4 (L)	5 ($\|\|$)	6 ($\perp$)
1	2.06	1.76	1.91	1.68	24.6	28.6	23.2	35.7
2	1.59	1.27	1.25	1.08	39.6	47.0	45.9	49.3
3	1.24	1.31	1.29	1.05	52.5	49.3	46.4	57.0
4	1.21	1.01	0.99	0.82	57.9	62.6	58.9	59.5
5	1.97	1.95	1.91	1.91	29.0	30.9	30.2	28.9
6	2.27	2.01	1.97	2.37	28.4	35.6	32.8	23.0

Table D.9: Crossover frequency and phase margin of $Y_p Y_c$ from Experiment 1.

	K_α				$J_{\theta 1}$			
	Condition (Texture)				Condition (Texture)			
Obs.	3 (G)	4 (L)	5 ($\|\|$)	6 ($\perp$)	3 (G)	4 (L)	5 ($\|\|$)	6 ($\perp$)
1	3.0	4.7	4.9	3.5	19.5	17.9	43.7	27.3
2	5.6	7.4	10.4	11.6	25.5	17.1	14.0	17.8
3	3.7	2.9	4.5	7.1	21.6	16.0	14.0	20.6
4	2.7	3.1	5.5	8.0	33.2	26.1	18.8	14.4
5	3.2	4.9	8.9	9.5	50.1	19.0	28.8	67.5
6	2.1	4.0	6.3	7.4	9.9	8.5	26.4	42.4

Table D.10: Y_{θ_1} parameter K_α, and model fit index $J_{\theta 1}$ from Experiment 1.

	$J_{\theta 2}$				$J_{\theta 2}/J_{\theta 1}$			
	Condition (Texture)				Condition (Texture)			
Obs.	3 (G)	4 (L)	5 ($\|\|$)	6 ($\perp$)	3 (G)	4 (L)	5 ($\|\|$)	6 ($\perp$)
1	16.6	13.4	40.7	24.5	0.85	0.75	0.93	0.90
2	22.6	16.8	13.4	15.6	0.89	0.98	0.96	0.88
3	21.6	13.5	13.7	20.6	1.00	0.84	0.98	1.00
4	27.2	25.0	18.2	14.3	0.82	0.96	0.97	1.00
5	28.6	13.9	27.7	67.1	0.57	0.73	0.96	0.99
6	9.9	8.3	22.3	41.9	0.99	0.98	0.85	0.99
	K_β				K_γ			
	Condition (Texture)				Condition (Texture)			
Obs.	3 (G)	4 (L)	5 ($\|\|$)	6 ($\perp$)	3 (G)	4 (L)	5 ($\|\|$)	6 ($\perp$)
1	2.5	3.7	5.1	3.8	4.8	6.9	0.8	1.9
2	4.8	7.2	10.1	12.0	9.6	9.8	12.3	6.9
3	3.7	2.6	4.4	7.1	3.5	6.6	6.0	7.0
4	2.1	3.0	5.6	8.0	5.9	6.0	4.2	8.3
5	2.8	4.5	8.8	9.4	6.8	8.1	10.5	10.0
6	2.1	4.1	5.8	7.5	2.5	2.9	9.5	6.8

Table D.11: Y_{θ_2} parameters K_β and K_γ, model fit index $J_{\theta 2}$, and model fit ratio $J_{\theta 2}/J_{\theta 1}$ from Experiment 1.

D.4 Individual Model Fit Plots

The model fits are shown in the following figures (Figures D.1 through D.24).

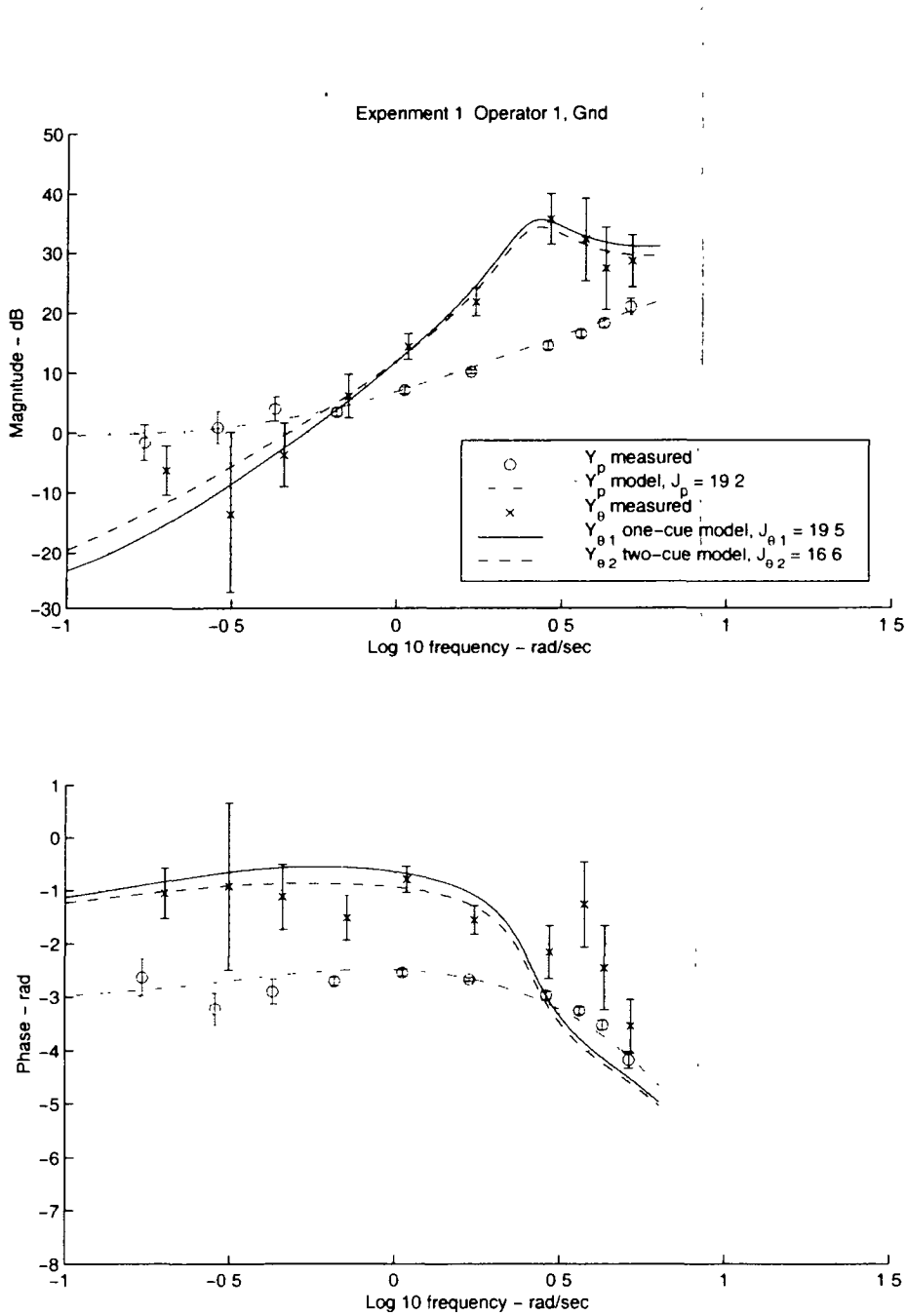

Figure D.1: Experiment 1 model fit results for Operator 1, Grid Texture.

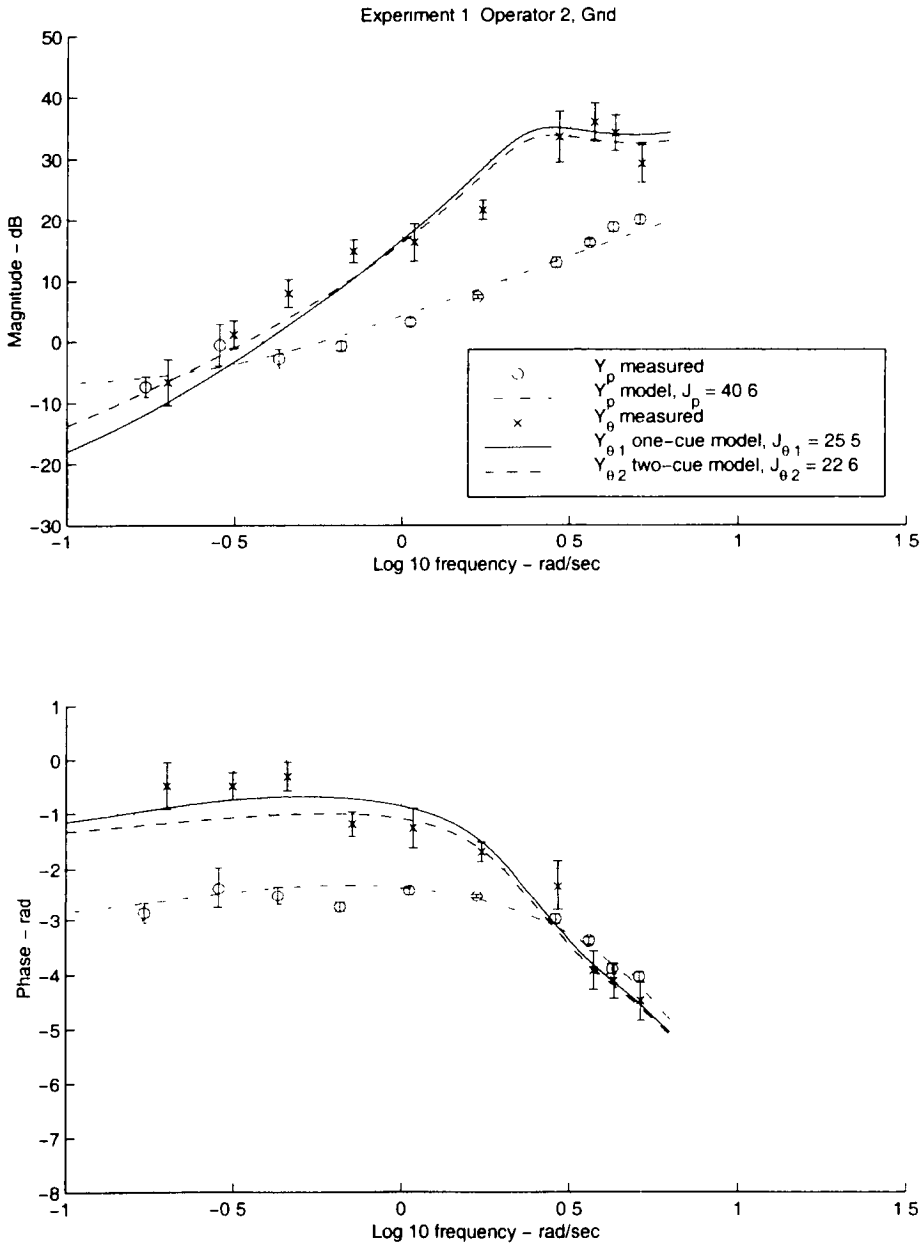

Figure D.2: Experiment 1 model fit results for Operator 2, Grid Texture.

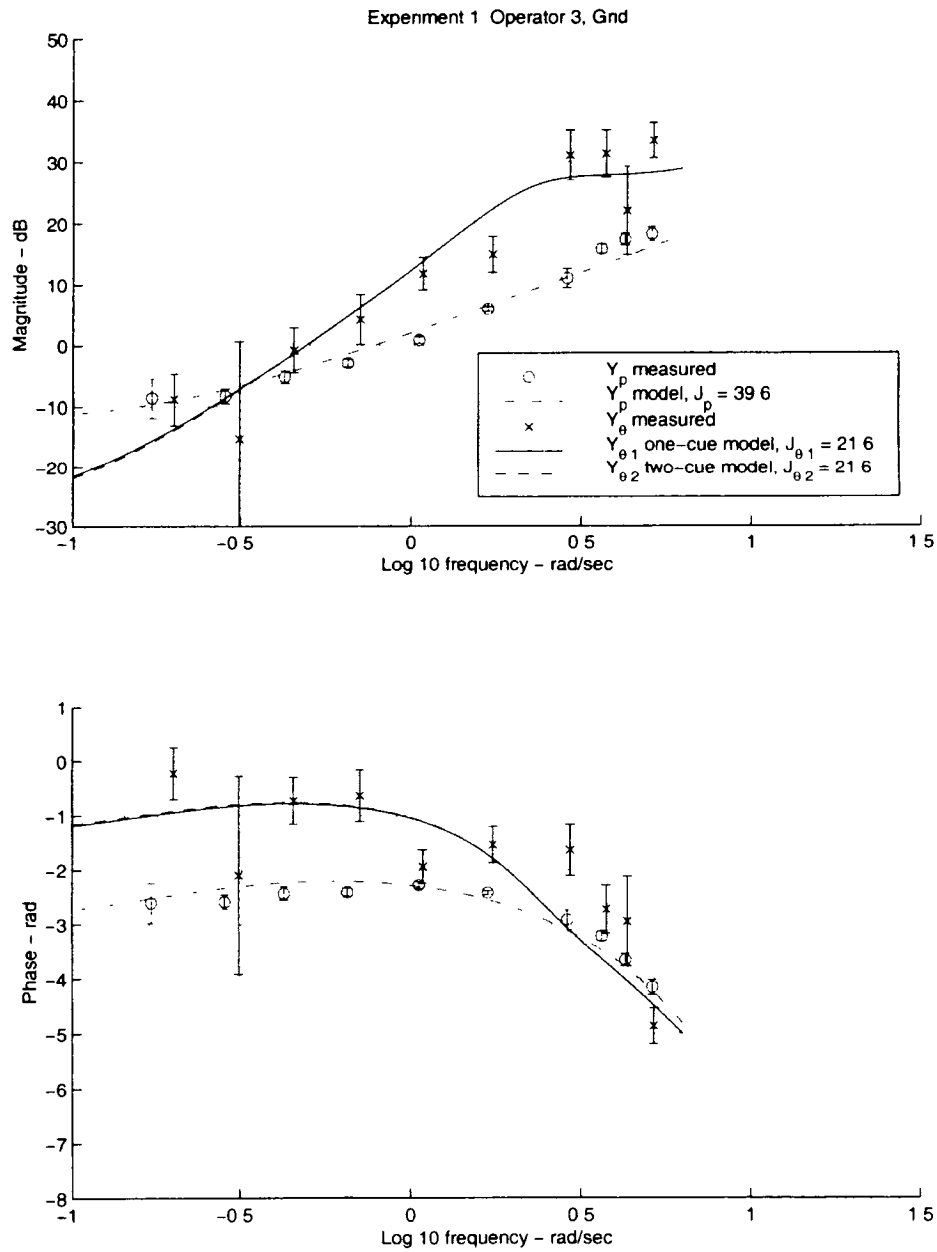

Figure D.3: Experiment 1 model fit results for Operator 3, Grid Texture.

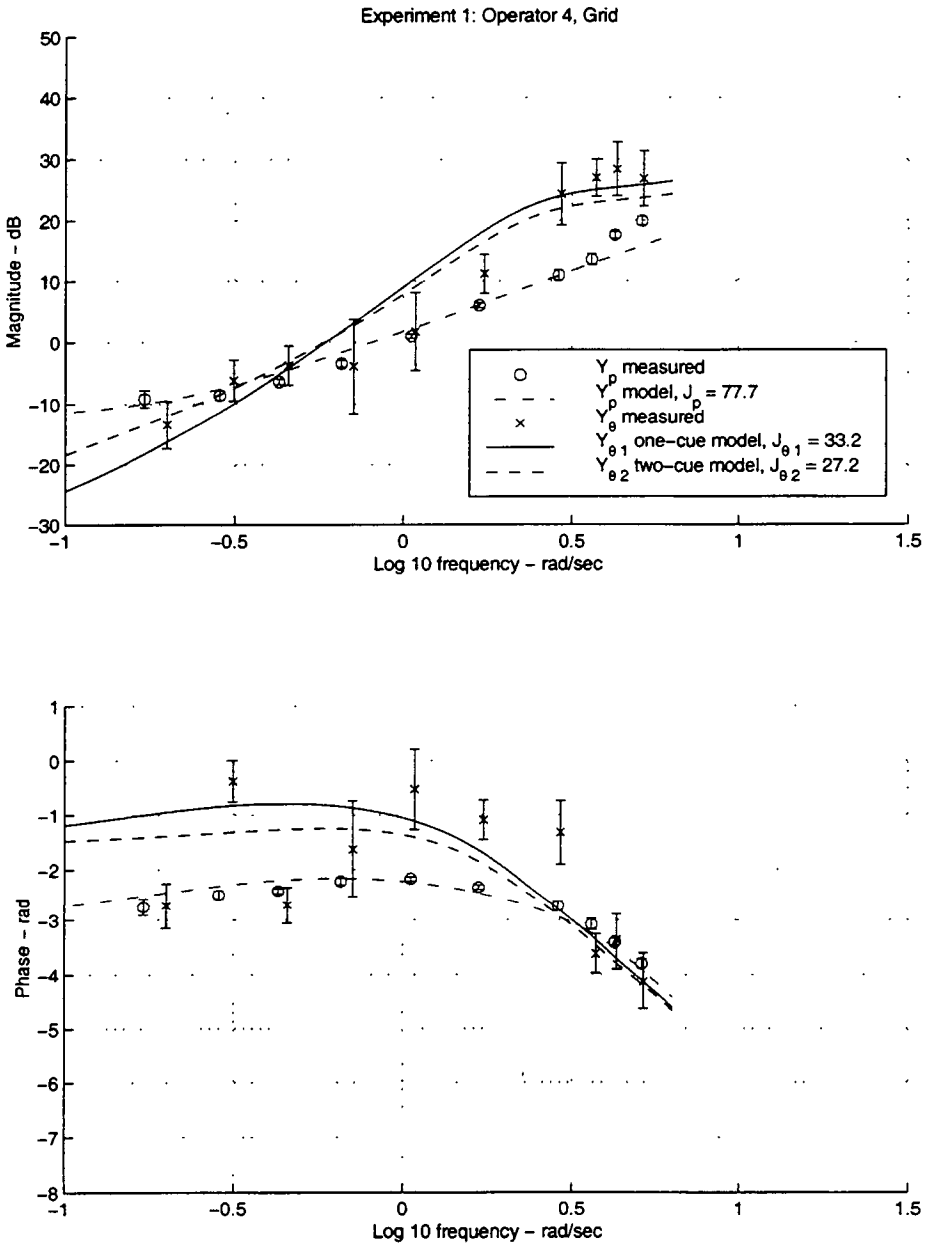

Figure D.4: Experiment 1 model fit results for Operator 4, Grid Texture.

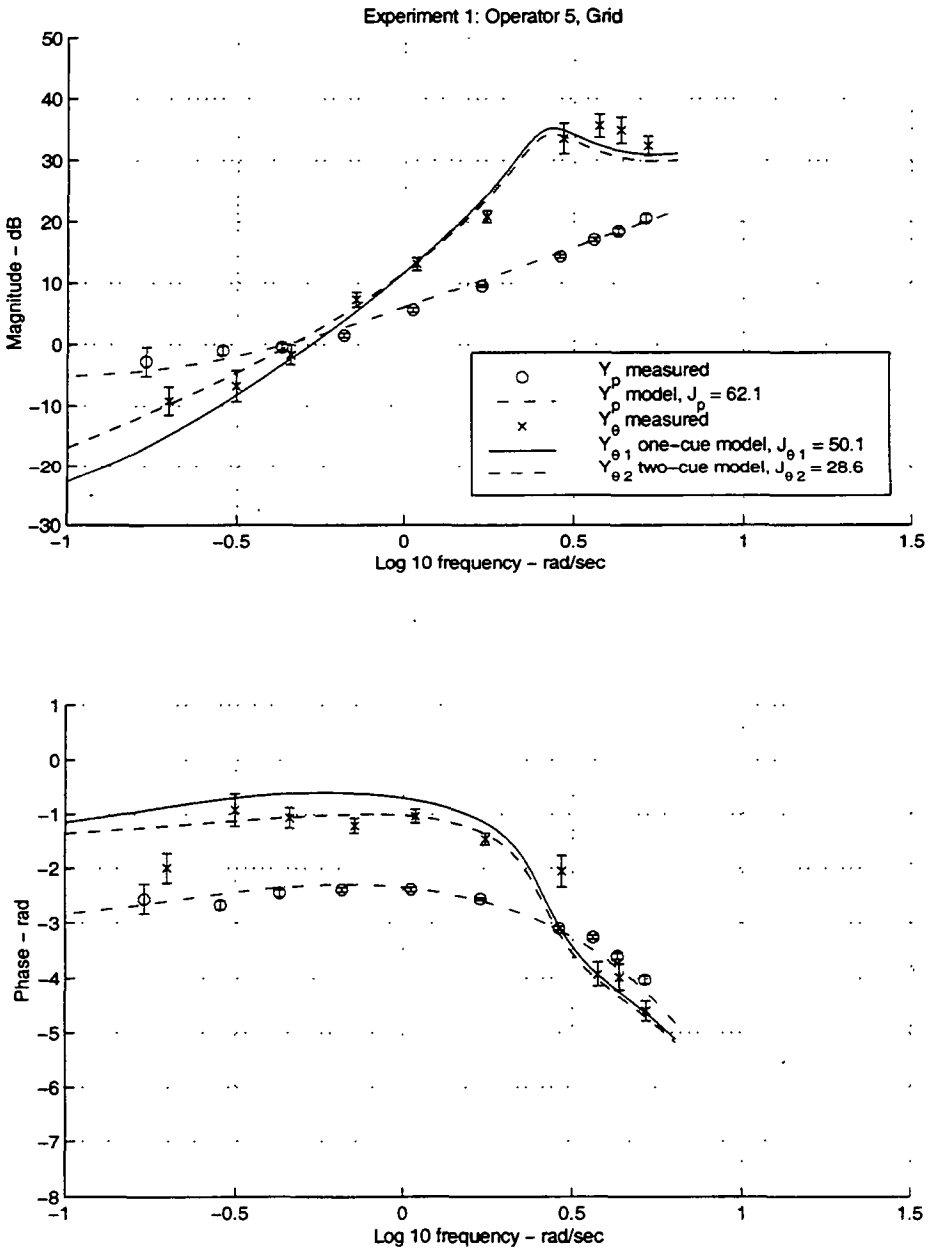

Figure D.5: Experiment 1 model fit results for Operator 5, Grid Texture.

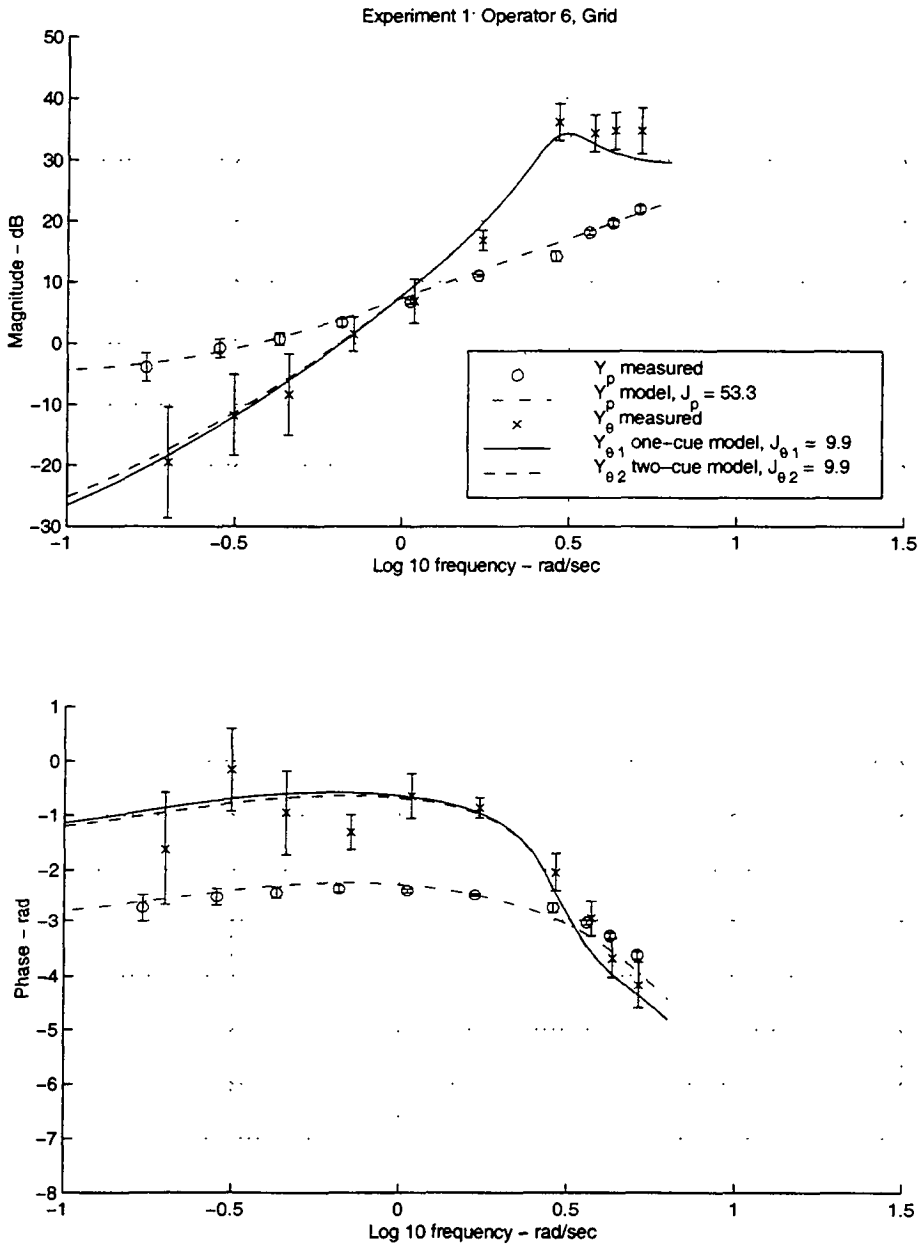

Figure D.6: Experiment 1 model fit results for Operator 6, Grid Texture.

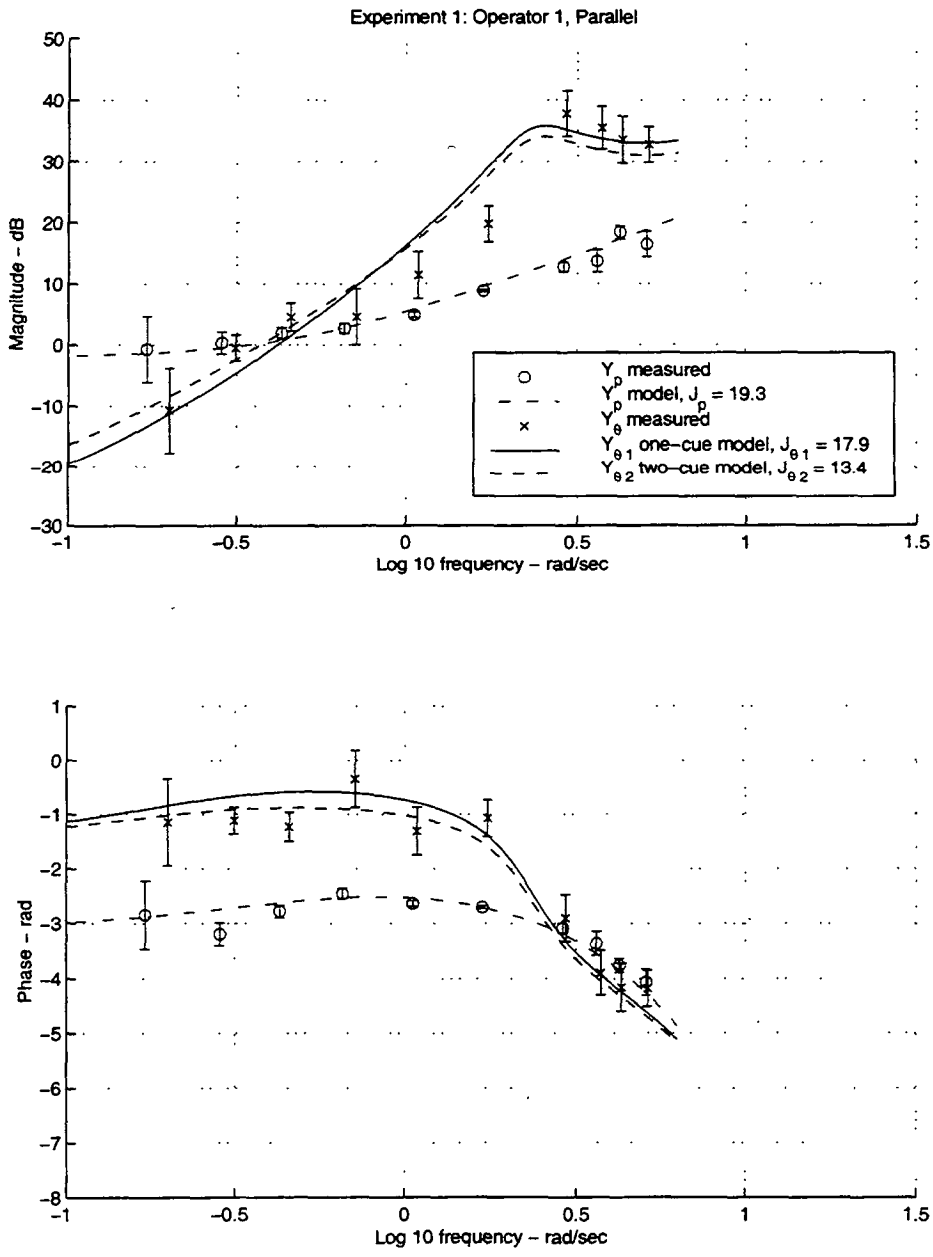

Figure D.7: Experiment 1 model fit results for Operator 1, Parallel Texture.

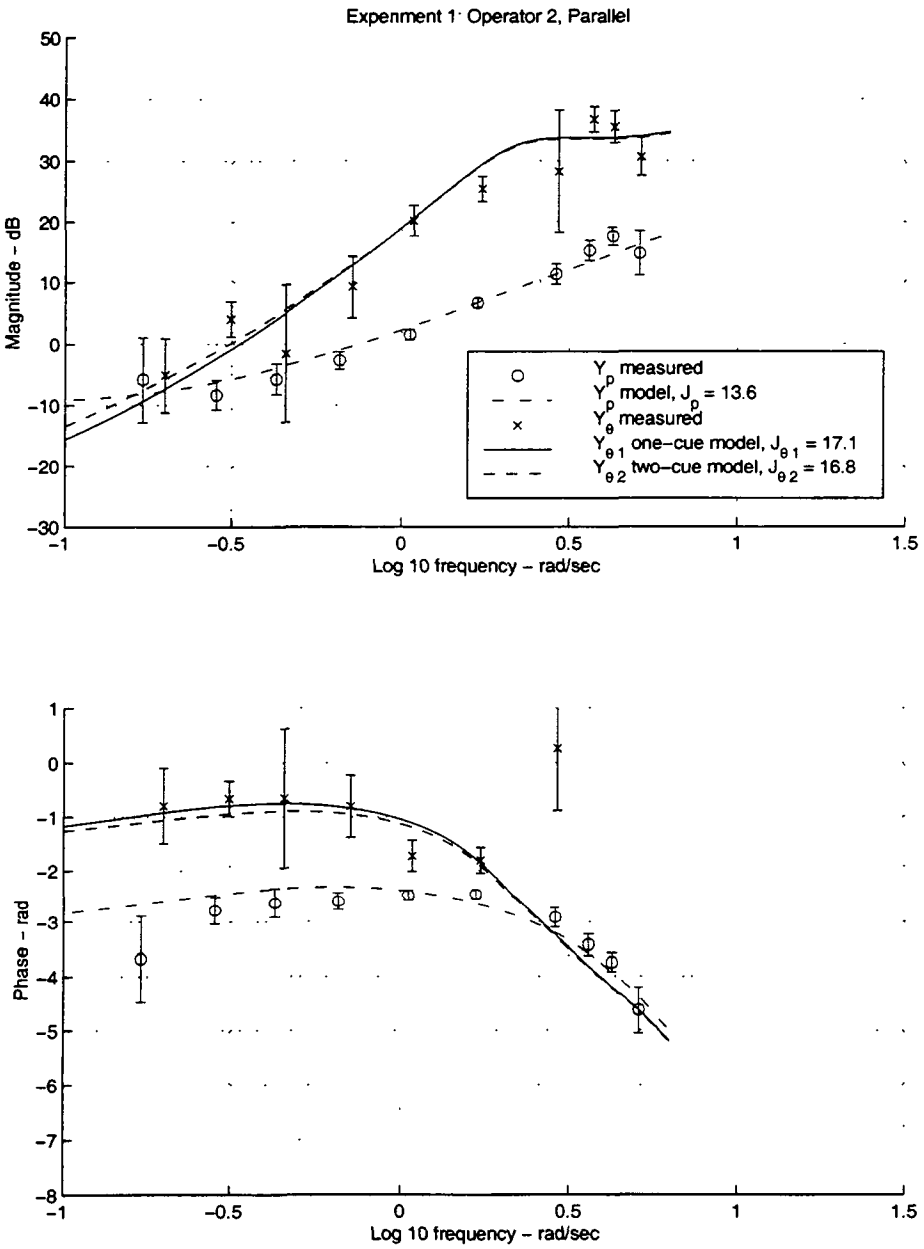

Figure D.8: Experiment 1 model fit results for Operator 2, Parallel Texture.

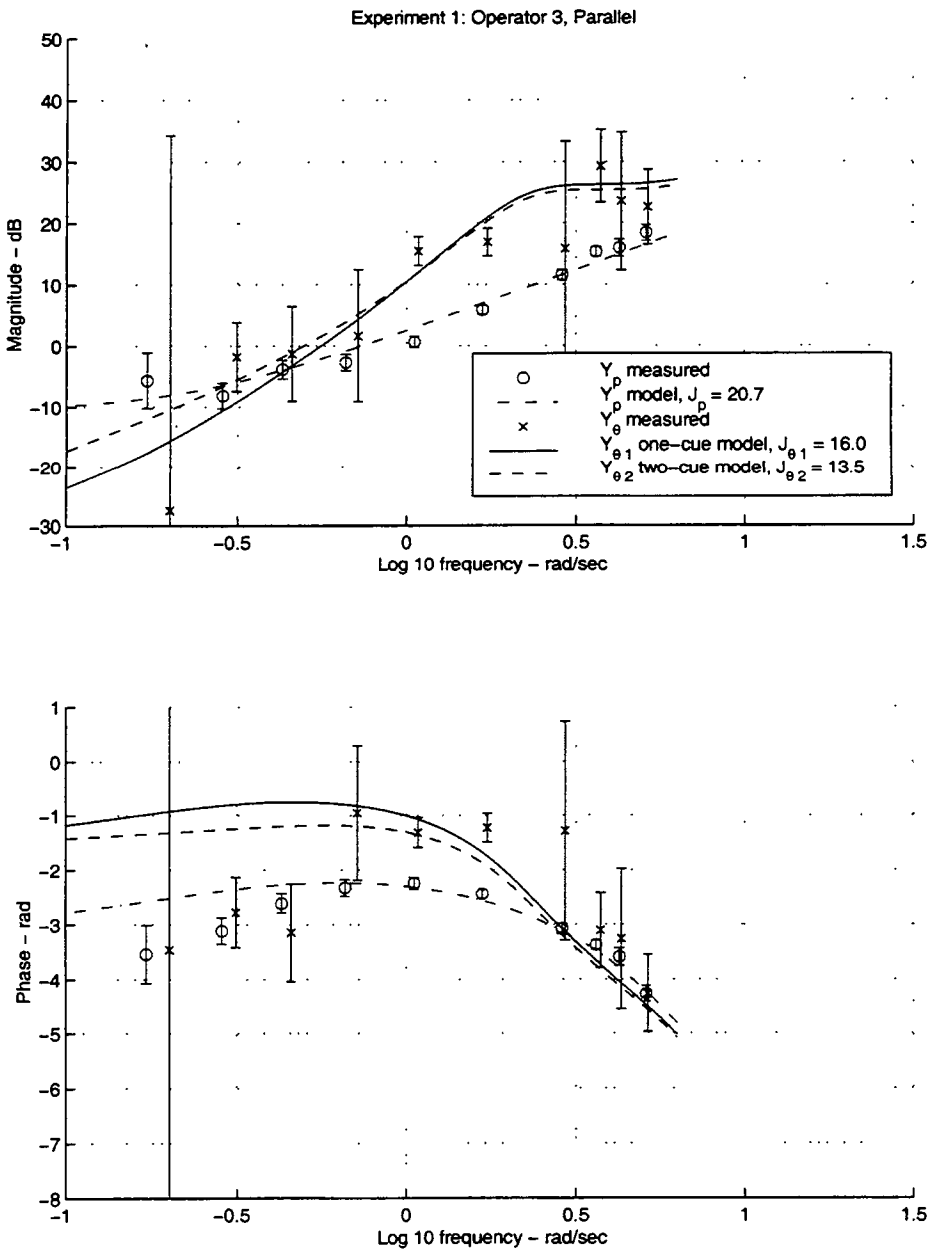

Figure D.9: Experiment 1 model fit results for Operator 3, Parallel Texture.

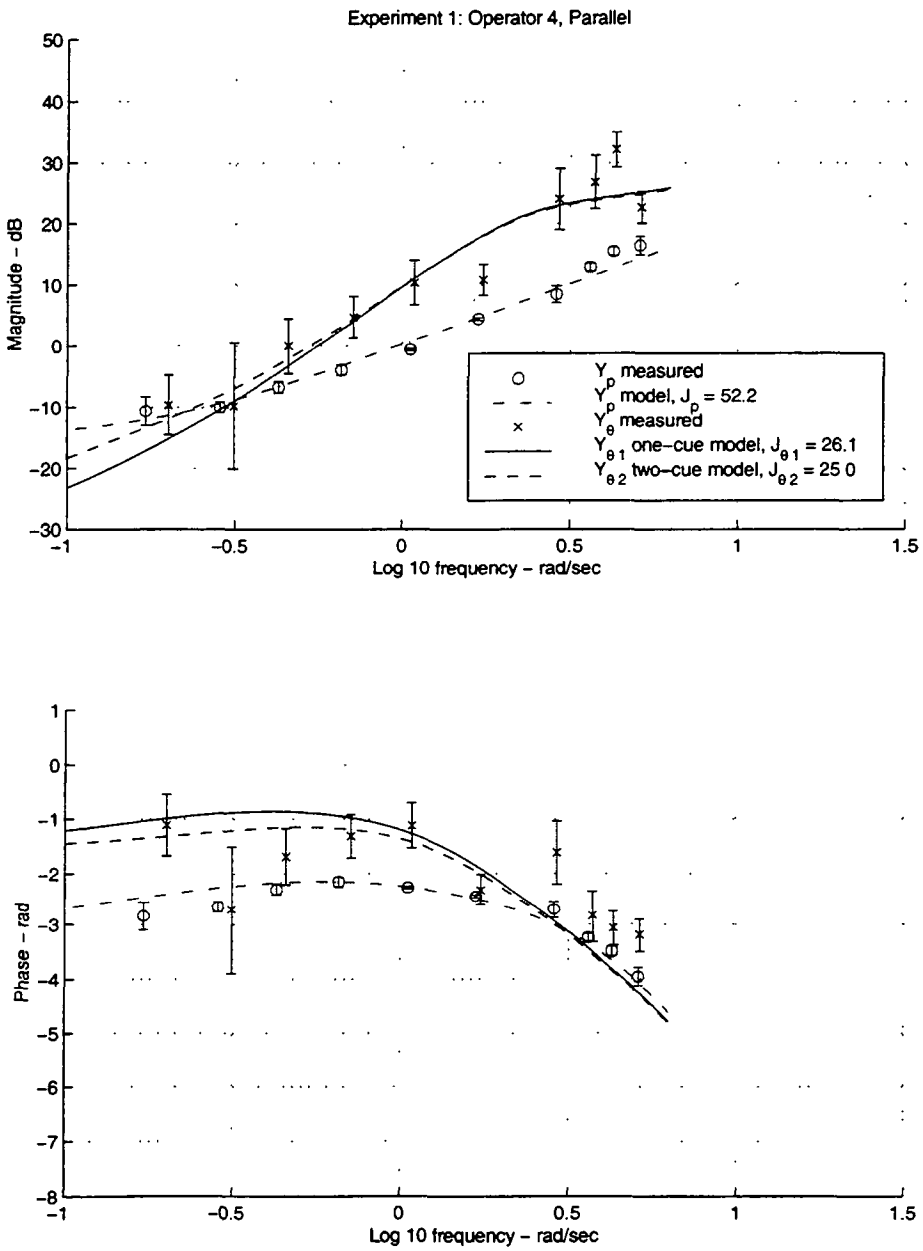

Figure D.10: Experiment 1 model fit results for Operator 4, Parallel Texture.

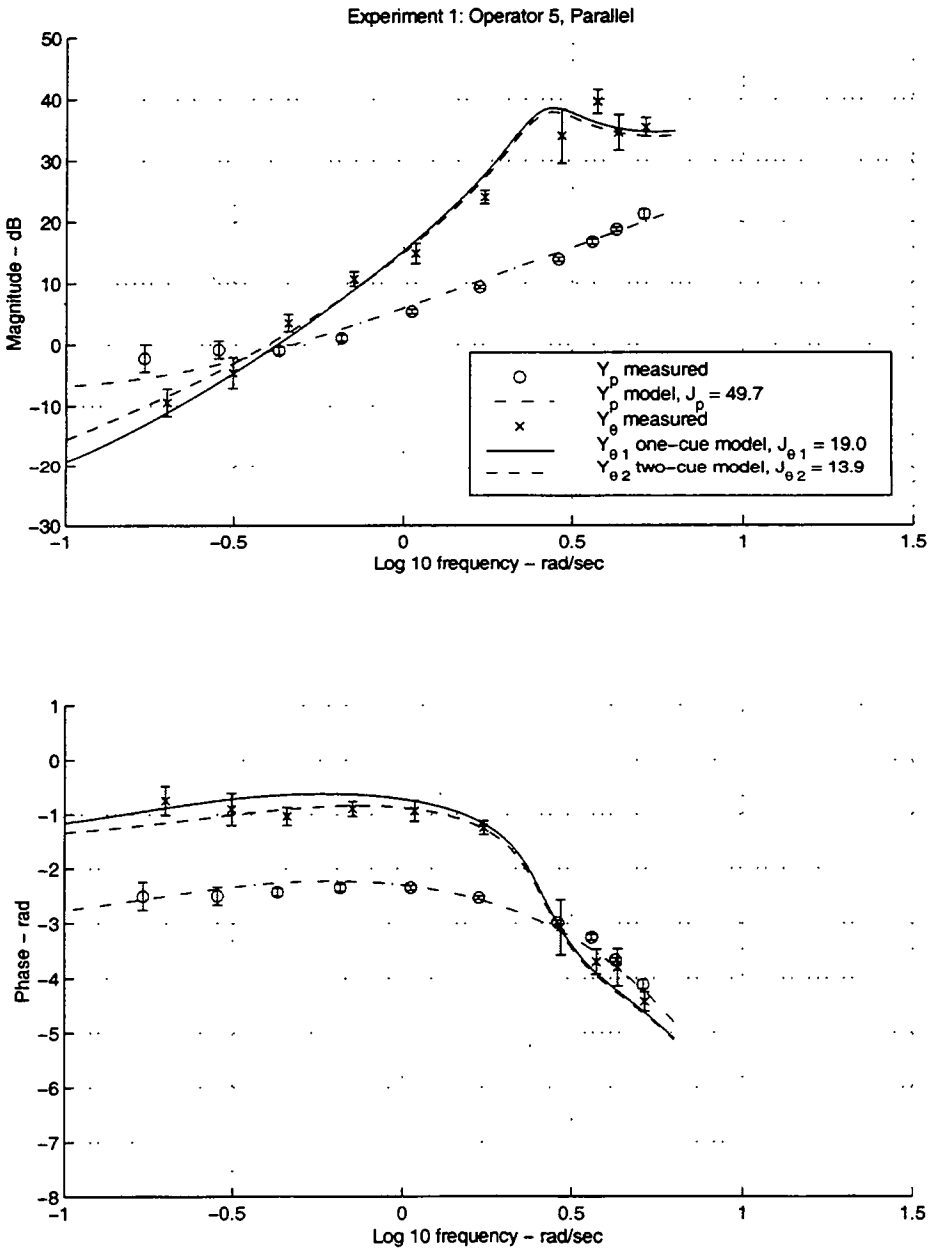

Figure D.11: Experiment 1 model fit results for Operator 5, Parallel Texture.

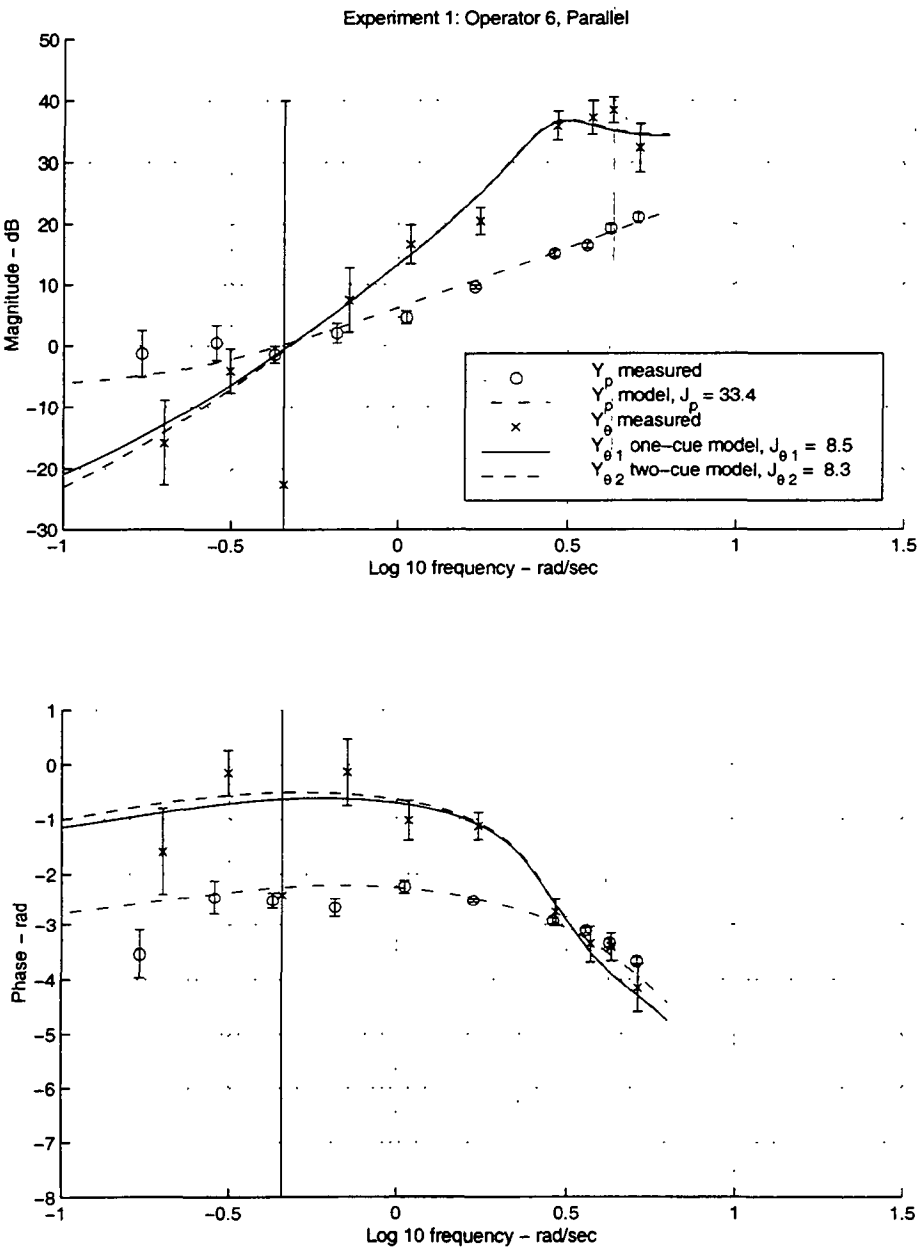

Figure D.12: Experiment 1 model fit results for Operator 6, Parallel Texture.

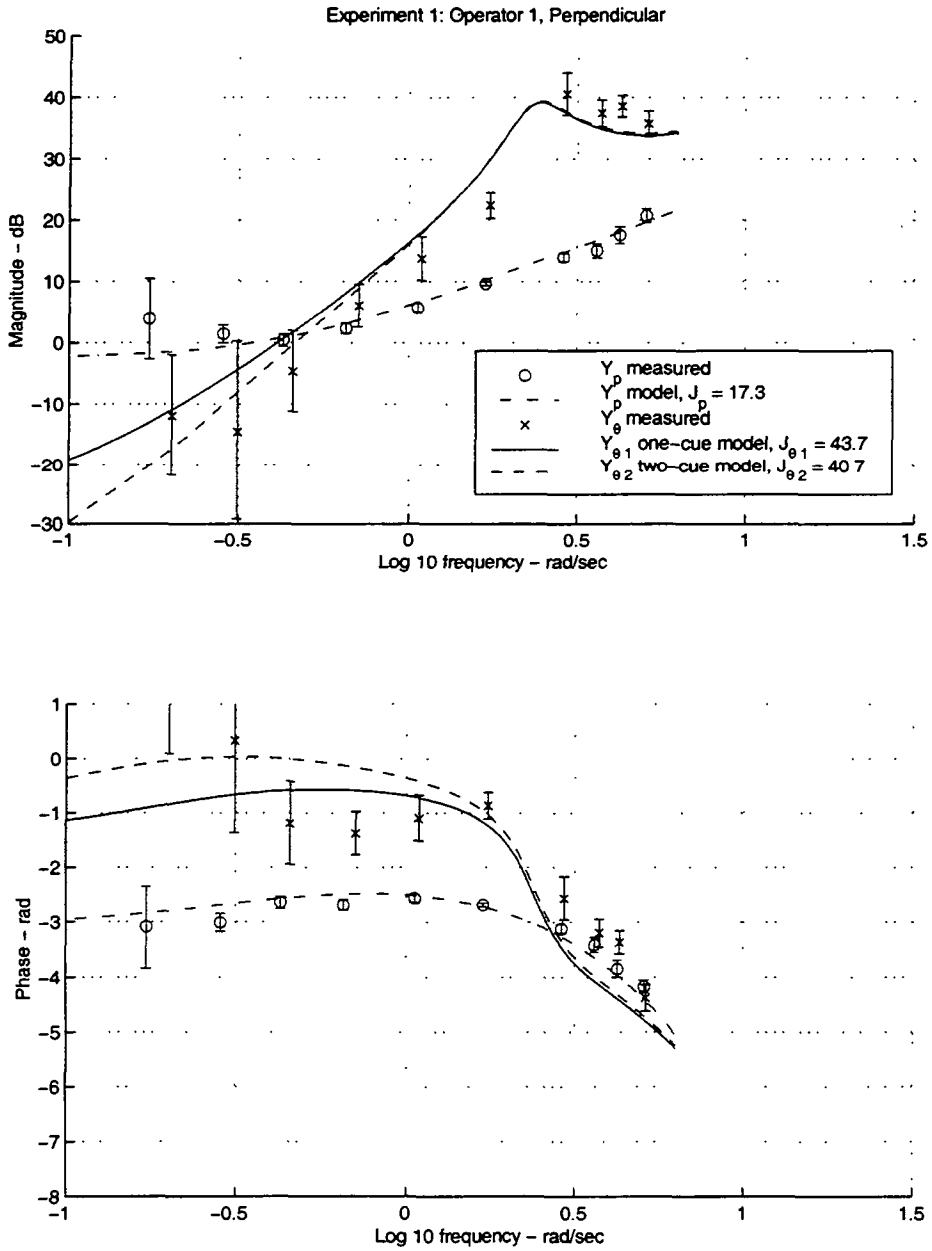

Figure D.13: Experiment 1 model fit results for Operator 1, Perpendicular Texture.

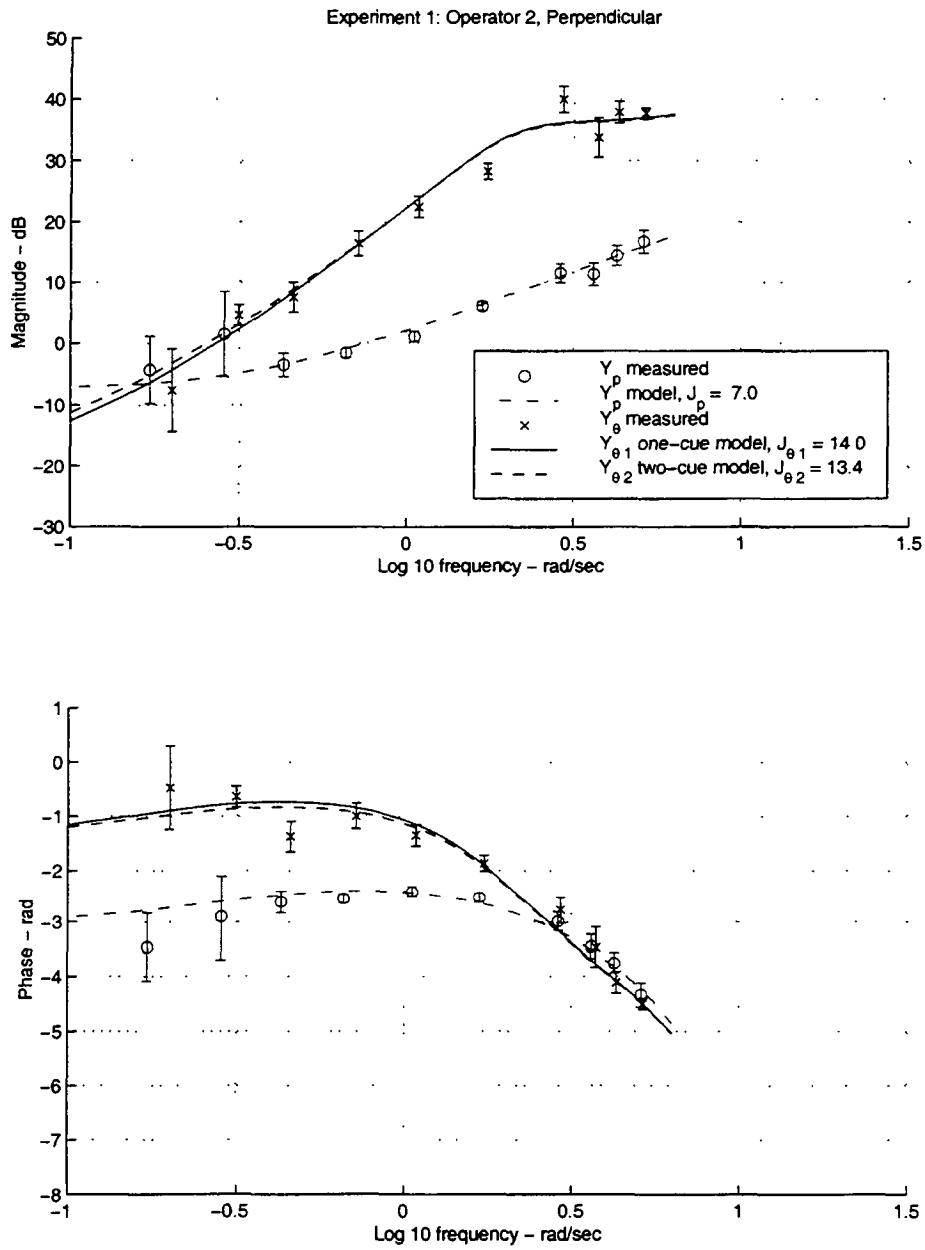

Figure D.14: Experiment 1 model fit results for Operator 2, Perpendicular Texture.

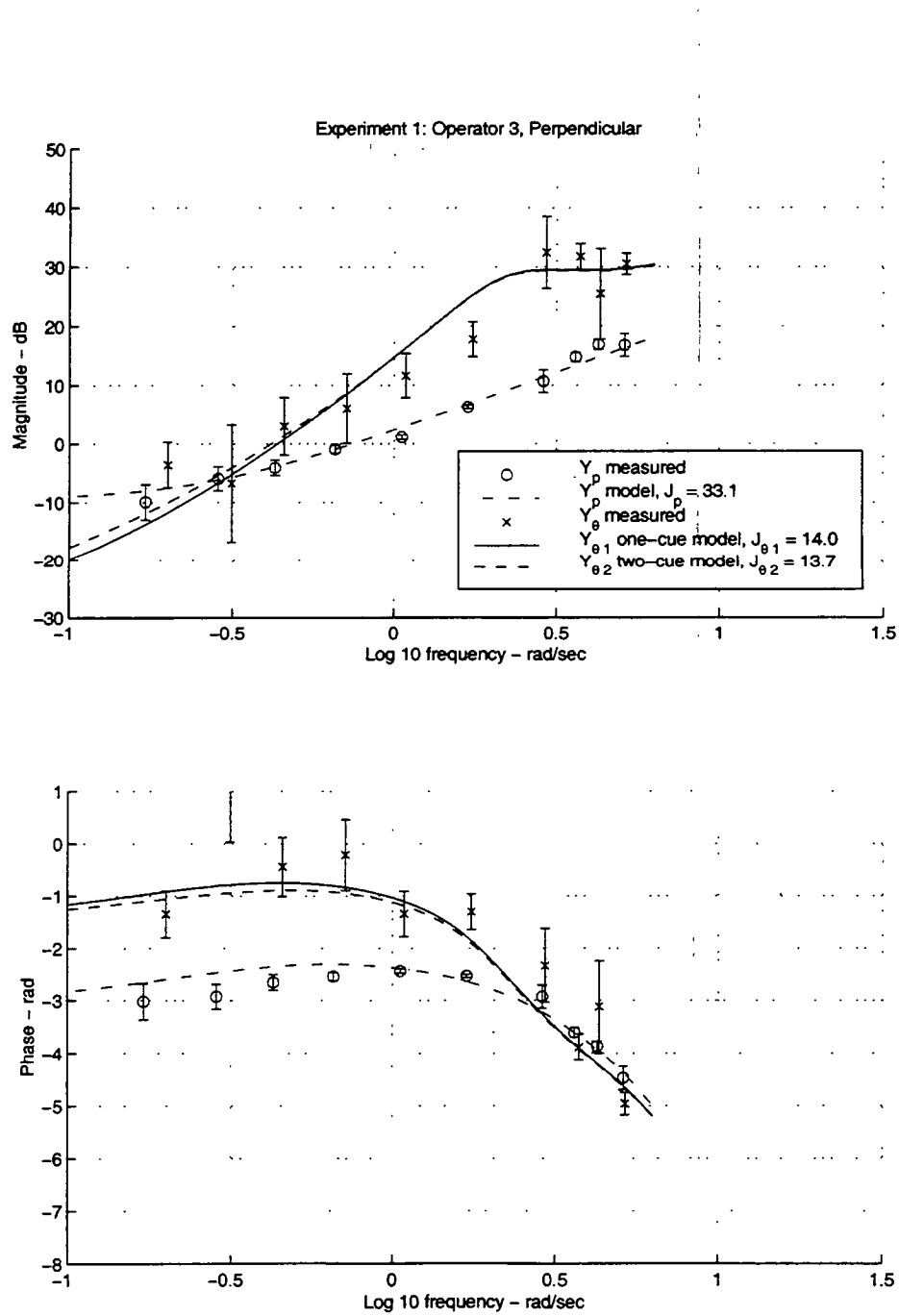

Figure D.15: Experiment 1 model fit results for Operator 3, Perpendicular Texture.

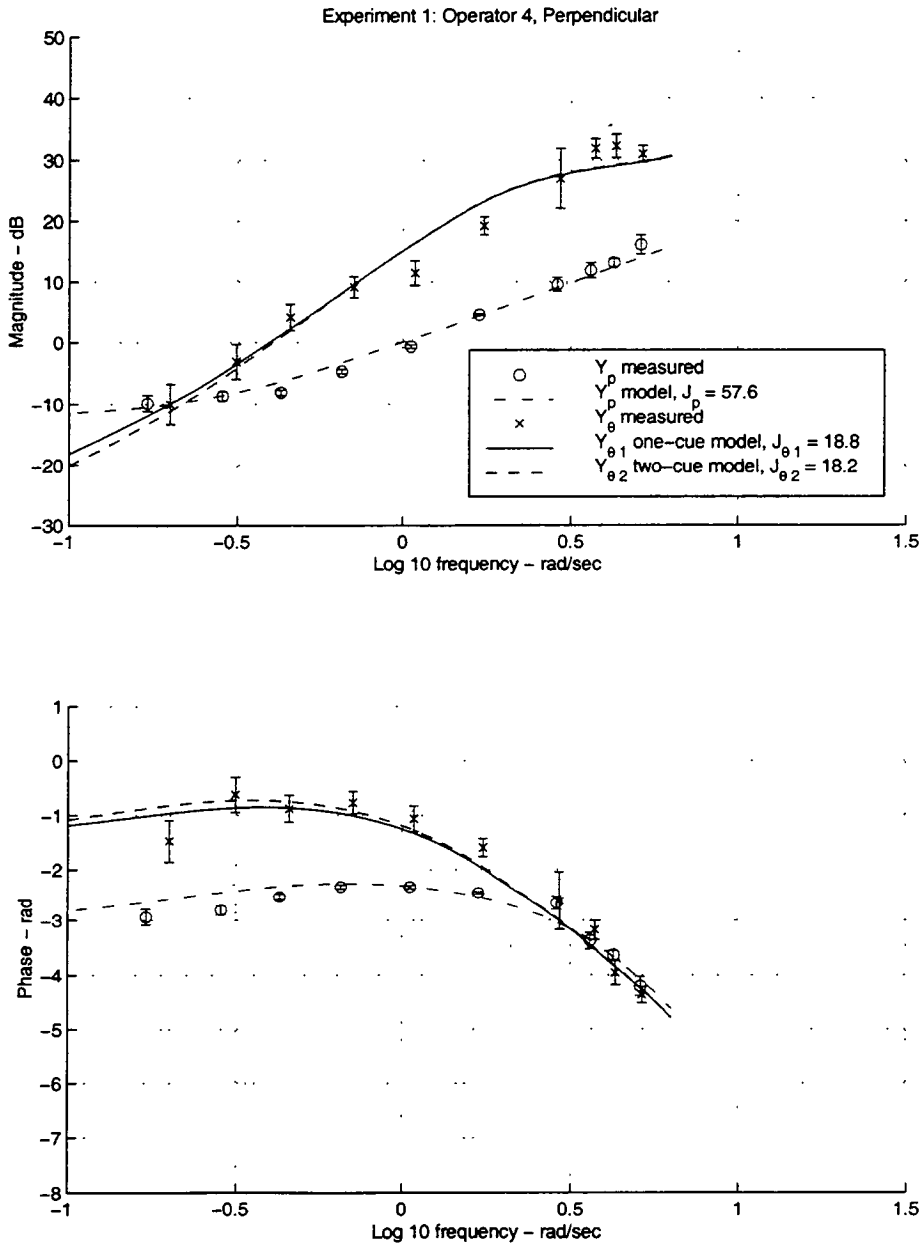

Figure D.16: Experiment 1 model fit results for Operator 4, Perpendicular Texture.

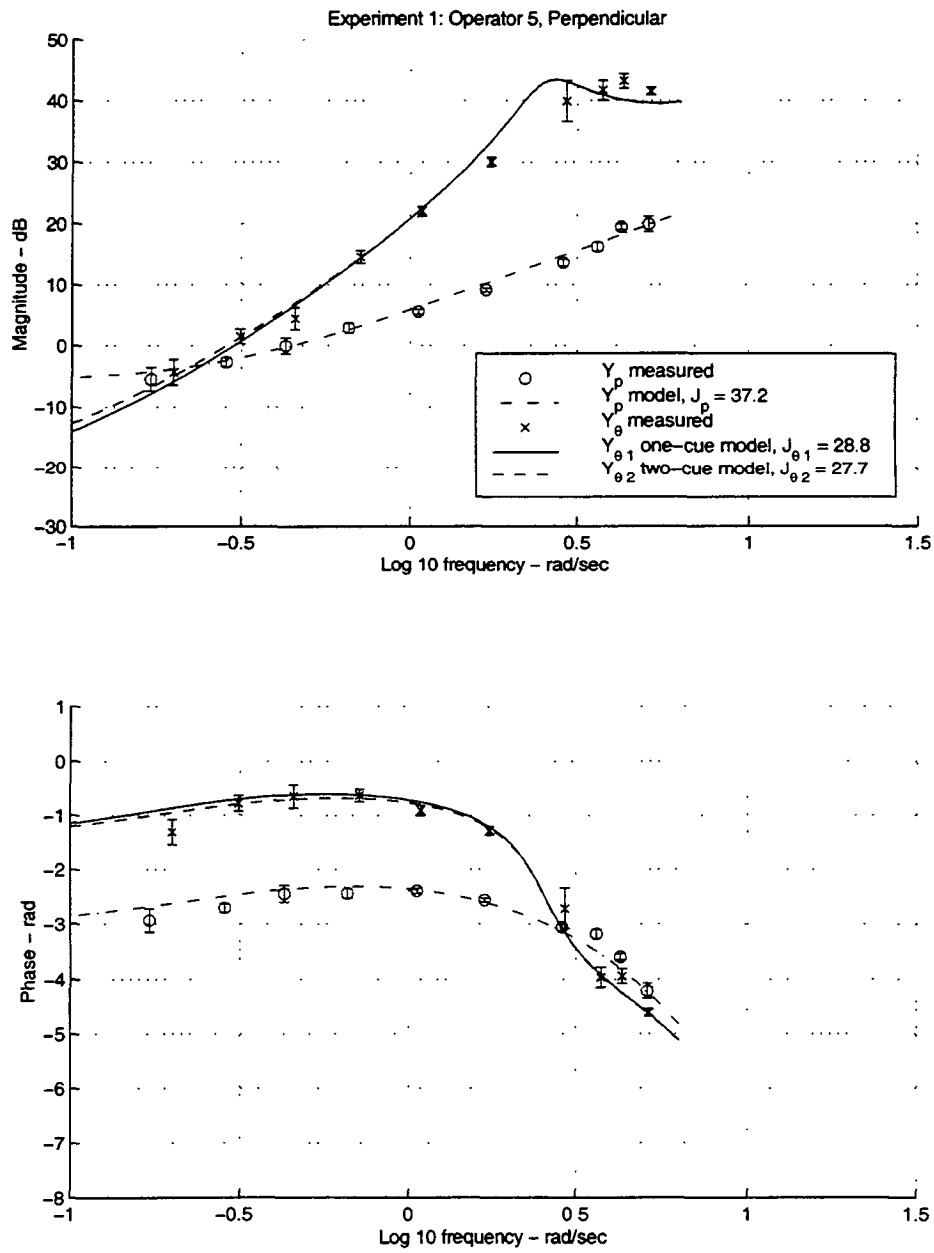

Figure D.17: Experiment 1 model fit results for Operator 5, Perpendicular Texture.

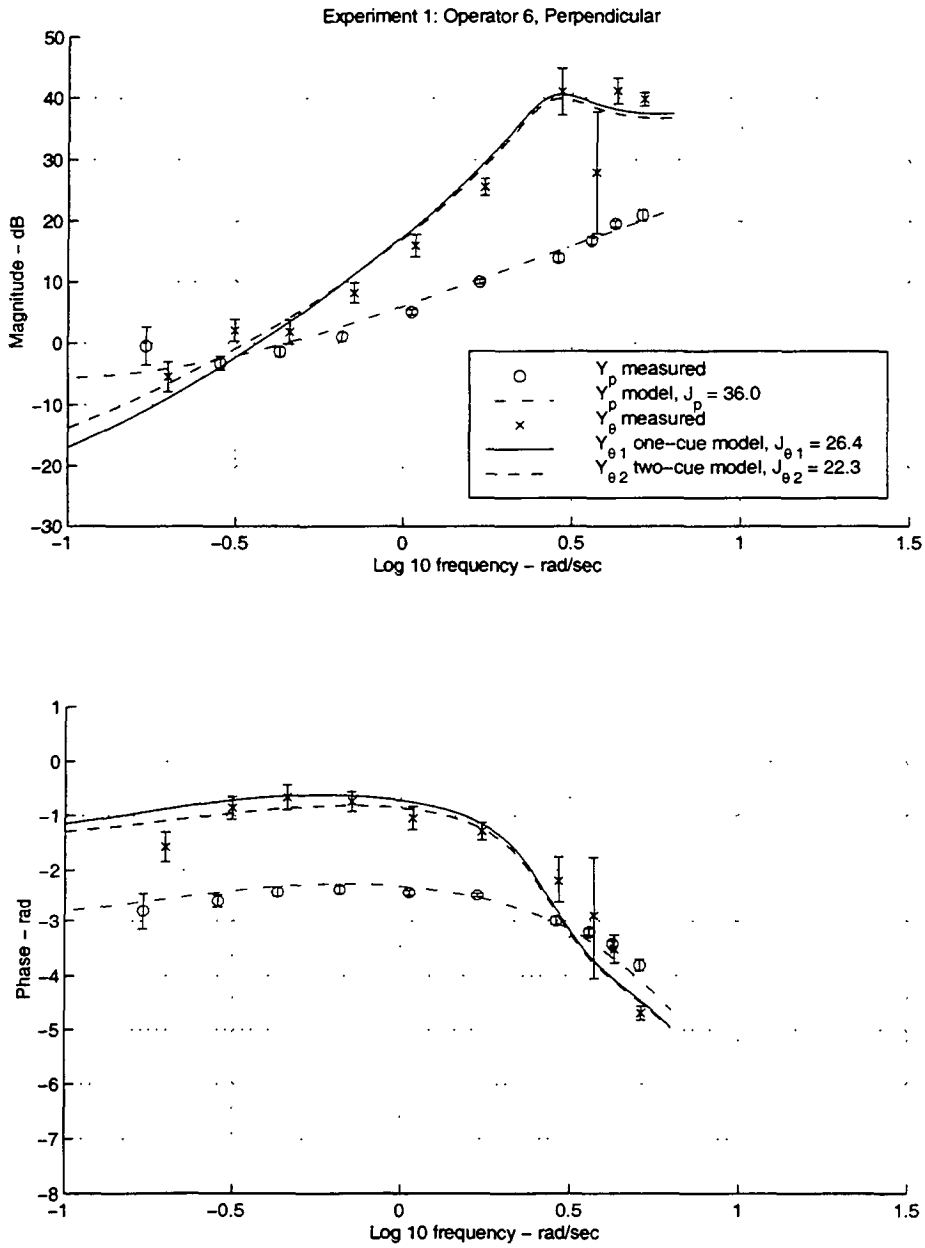

Figure D.18: Experiment 1 model fit results for Operator 6, Perpendicular Texture.

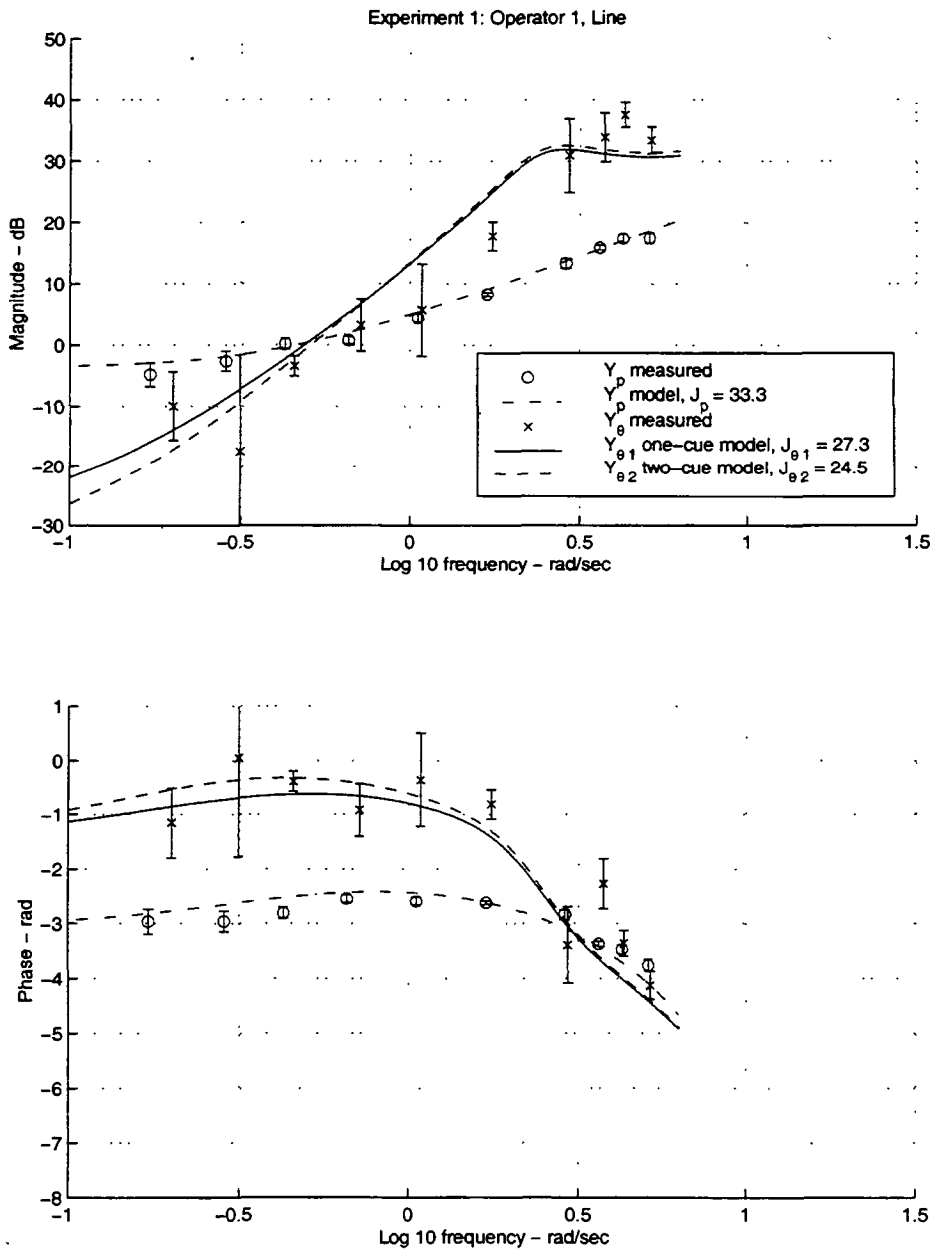

Figure D.19: Experiment 1 model fit results for Operator 1, Line Texture.

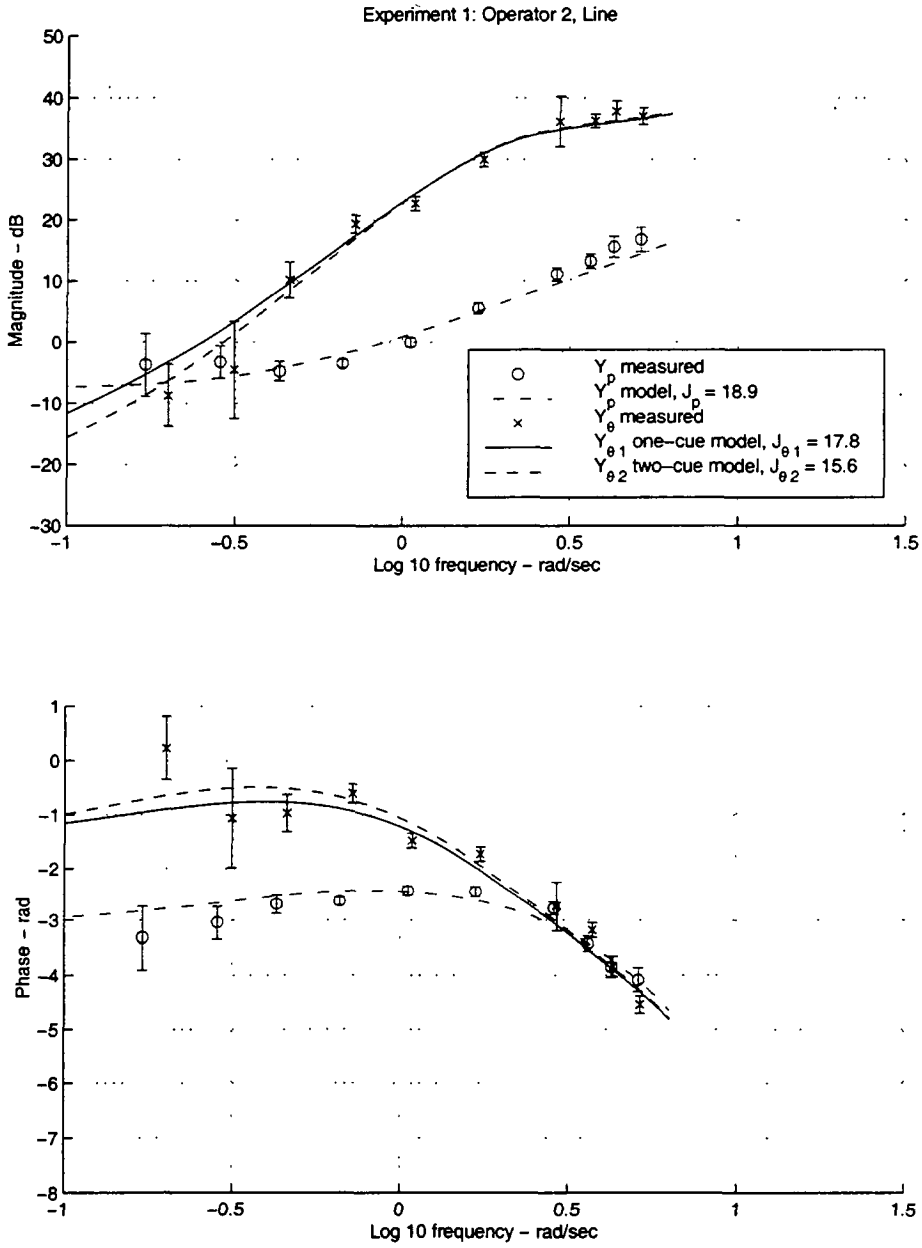

Figure D.20: Experiment 1 model fit results for Operator 2, Line Texture.

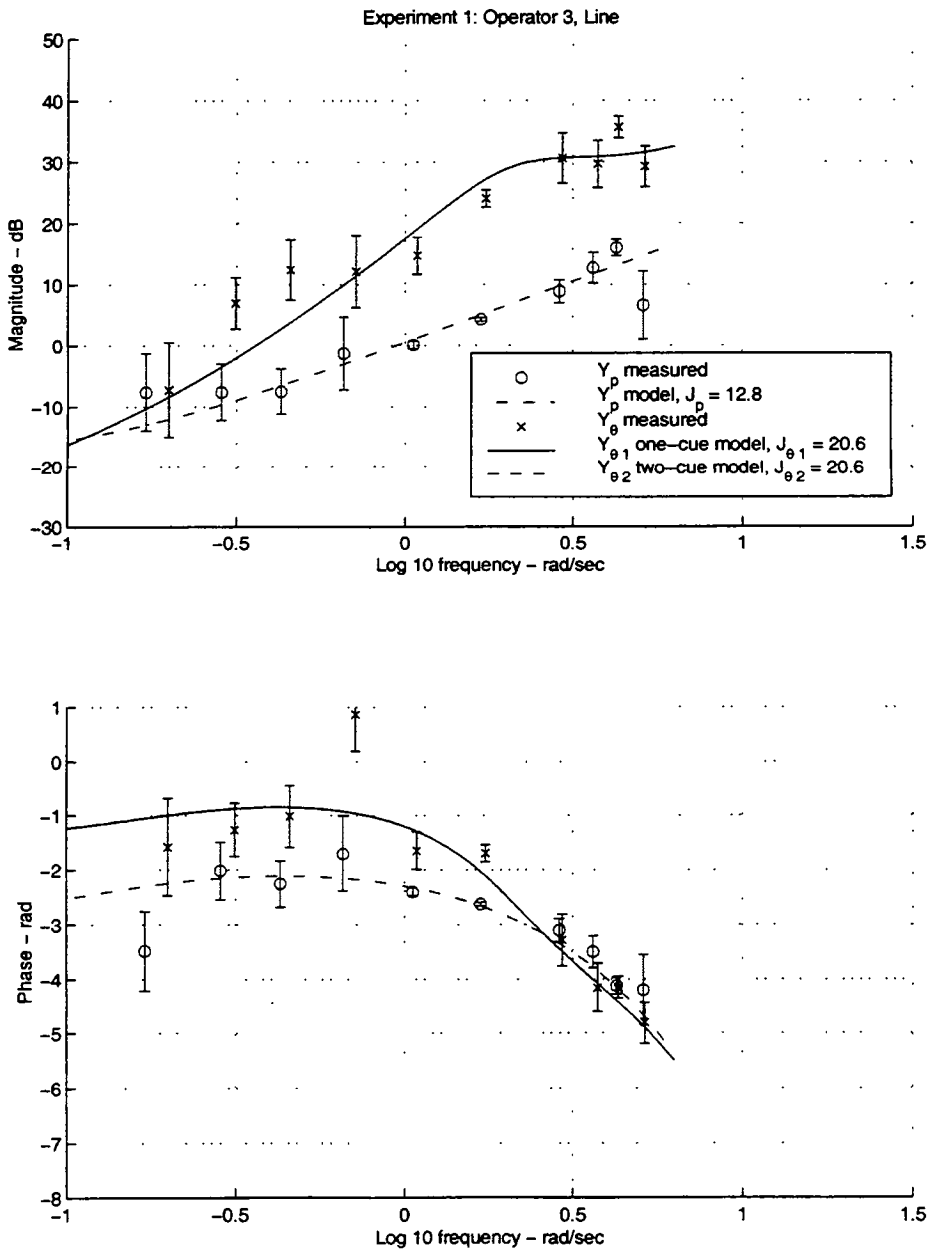

Figure D.21: Experiment 1 model fit results for Operator 3, Line Texture.

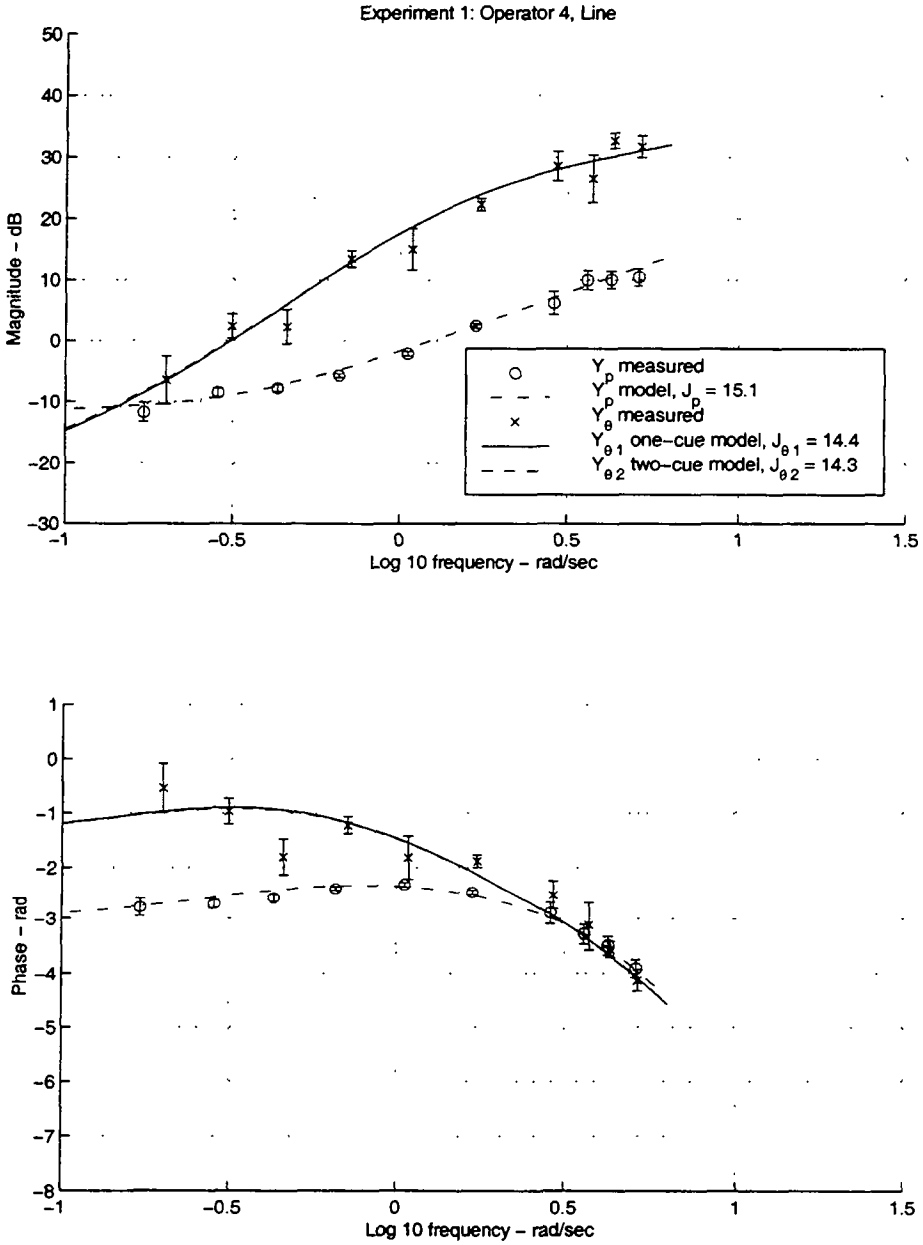

Figure D.22: Experiment 1 model fit results for Operator 4, Line Texture.

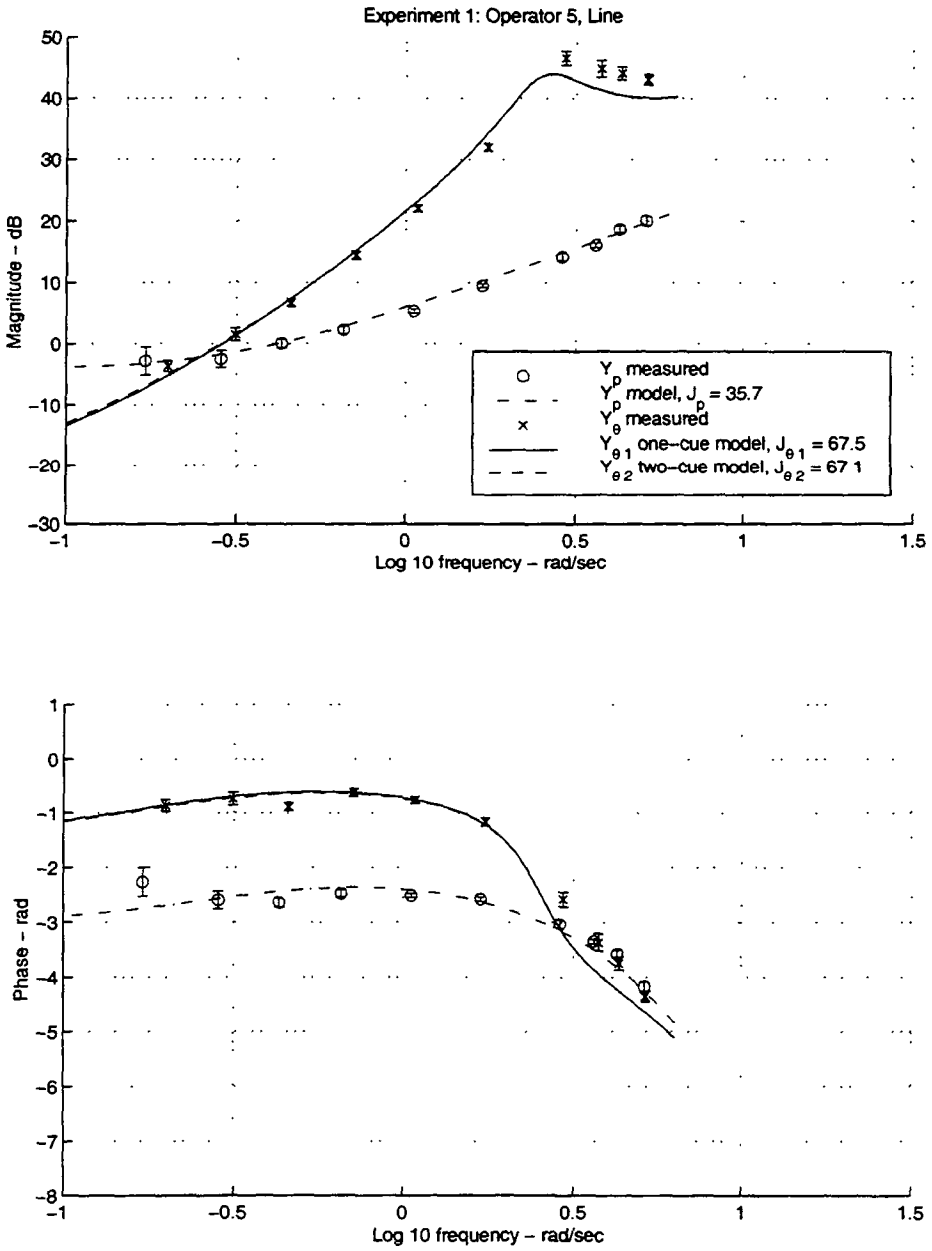

Figure D.23: Experiment 1 model fit results for Operator 5, Line Texture.

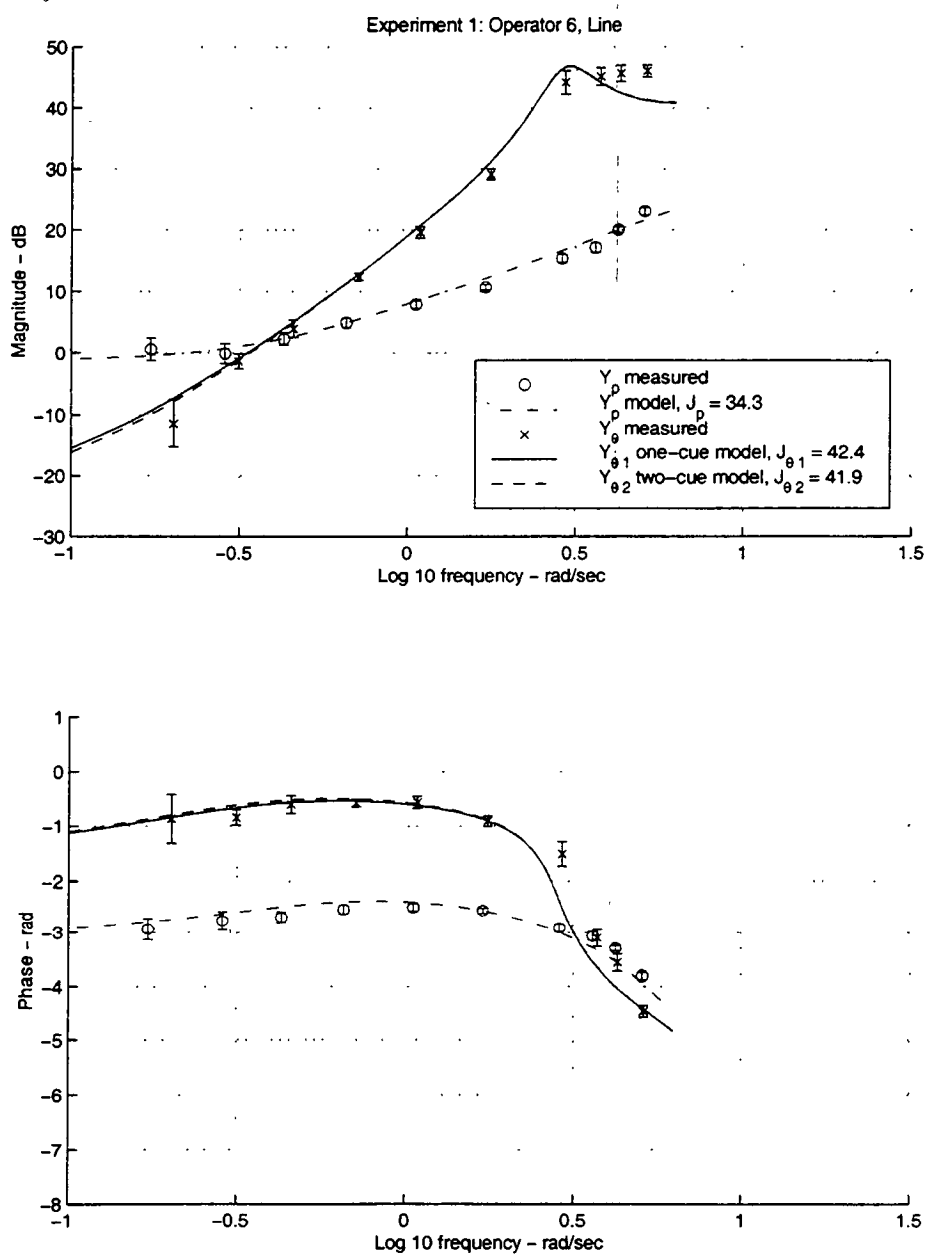

Figure D.24: Experiment 1 model fit results for Operator 6, Line Texture.

Appendix E

Experiment 2 Appendix

E.1 Vehicle Dynamic Simulation

$$\begin{Bmatrix} \ddot{x} \\ \dot{x} \\ \dot{\theta} \end{Bmatrix} = \begin{bmatrix} -.2 & 0 & 0 \\ 1 & 0 & 0 \\ 0 & 0 & 0 \end{bmatrix} \begin{Bmatrix} \dot{x} \\ x \\ \theta \end{Bmatrix} + \begin{bmatrix} 1 & 1 & 0 \\ 0 & 0 & 0 \\ 0 & 0 & .1 \end{bmatrix} \begin{Bmatrix} \delta \\ u \\ q \end{Bmatrix} \tag{E.1}$$

The position x is in units of eyeheights. The angle θ is expressed in radians. This state-space equation was converted to discrete form for real-time simulation with a sampling interval of 0.01389 seconds, using the first-order hold [75]. The resulting discrete state-space equations were:

$$\begin{Bmatrix} \dot{x}_{k+1} \\ x_{k+1} \\ \theta_{k+1} \end{Bmatrix} = \begin{bmatrix} 0.9972 & 0 & 0 \\ 0.01387 & 1 & 0 \\ 0 & 0 & 1 \end{bmatrix} \begin{Bmatrix} \dot{x}_k \\ x_k \\ \theta_k \end{Bmatrix} + \begin{bmatrix} 0.01387 & 0.01387 & 0 \\ 0.00009636 & 0.00009636 & 0 \\ 0 & 0 & 0.01389 \end{bmatrix} \begin{Bmatrix} \delta_k \\ u_k \\ q_k \end{Bmatrix} \tag{E.2}$$

The control input of the operator is δ; the maximum range achievable was from -10 to 10. The disturbances u and q had the following form as a function of time (t):

$$u(t) = \sum_{i=1}^{12} D \frac{a_i 2\pi k_i}{240} \cos\left(\frac{2\pi k_i}{240} t + \rho_i\right) \tag{E.3}$$

x disturbance (u)				θ disturbance (q)			
i	a_i	k_i	ω_i (rad/sec)	i	a_i	k_i	ω_i (rad/sec)
1	3	6	.16	1	1	7	.18
2	3	10	.26	2	1	11	.28
3	3	15	.39	3	1	16	.42
4	3	23	.60	4	1	25	.65
5	3	37	.97	5	1	38	.99
6	3	59	1.54	6	1	61	1.60
7	.529	101	2.64	7	.2	103	2.70
8	.665	127	3.32	8	.2	131	3.43
9	.708	149	3.90	9	.2	151	3.95
10	.937	179	4.69	10	.2	181	4.74
11	1.63	311	8.14	11	.2	313	8.19
12	2.73	521	13.64	12	.2	523	13.69

Table E.1: Experiment 2 disturbance spectra magnitudes and frequencies.

$$q(t) = \sum_{i=1}^{12} D\frac{a_i 2\pi k_i}{240}\cos(\frac{2\pi k_i}{240}t + \rho_i) \tag{E.4}$$

The actual values of a, k and resulting frequencies ($\omega = 2\pi k/240$) are shown in Table E.1 for the two disturbance spectra. D was set to a value of .125.

The phase offsets (ρ_i) for each repetition and disturbance (q and u) were precomputed with a random number generator, randomly distributed from -π to π. These angles used for each repetition are shown in Table E.2 (u) and E.3 (q).

The magnitudes of the disturbance components were modified from the Experiment 1 conditions to remedy a problem which was observed. The u disturbance is transformed into longitudinal position through approximately a double integrator, and the q dynamics are transformed into pitch attitude through a single integrator. In the first experiment, this resulted in less than one pixel peak-to-peak displacement to any of the visual cues due to the longitudinal disturbance at the two highest frequency points. In this experiment, for the last six frequency points (2.6 rad/sec and above), the magnitude of the u disturbance was made proportional to frequency (as opposed to constant, as was done in Experiment 1).

	Repetition							
i	1	2	3	4	5	6	7	8
1	0.26	-0.55	-1.36	-2.17	-2.99	2.49	1.67	0.86
2	-1.04	-2.68	1.96	0.32	-1.33	-2.97	1.67	0.02
3	-2.73	-2.80	-2.88	-2.95	-3.03	-3.10	3.11	3.03
4	1.18	-1.99	1.12	-2.05	1.06	-2.11	1.01	-2.17
5	-1.57	-2.34	-3.12	2.39	1.61	0.84	0.06	-0.71
6	2.21	1.61	1.01	0.42	-0.18	-0.77	-1.37	-1.96
7	0.83	-2.94	-0.42	2.09	-1.68	0.83	-2.94	-0.42
8	-0.31	-3.10	0.40	-2.38	1.11	-1.67	1.82	-0.96
9	-2.61	2.04	0.40	-1.23	-2.87	1.78	0.14	-1.50
10	-1.22	-0.64	-0.07	0.50	1.07	1.64	2.21	2.78
11	-2.37	-1.33	-0.29	0.76	1.80	2.85	-2.39	-1.35
12	0.04	2.94	-0.44	2.45	-0.93	1.97	-1.42	1.48

Table E.2: Experiment 2 phase angles ρ_i used to define disturbance u per repetition.

	Repetition							
i	1	2	3	4	5	6	7	8
1	2.86	1.00	-0.86	-2.71	1.71	-0.14	-2.00	2.43
2	2.11	-1.25	1.68	-1.68	1.24	-2.11	0.81	-2.55
3	0.01	1.37	2.73	-2.20	-0.84	0.51	1.87	-3.06
4	-0.06	-2.44	1.47	-0.91	3.00	0.62	-1.76	2.15
5	2.30	-0.08	-2.46	1.44	-0.94	2.97	0.59	-1.79
6	-2.68	-1.30	0.08	1.46	2.84	-2.06	-0.68	0.70
7	0.40	-0.83	-2.06	2.99	1.76	0.53	-0.70	-1.94
8	0.96	-2.95	-0.58	1.78	-2.13	0.24	2.60	-1.31
9	1.36	-0.90	3.13	0.87	-1.38	2.64	0.39	-1.87
10	0.88	1.24	1.60	1.97	2.33	2.69	3.05	-2.87
11	1.33	1.96	2.59	-3.06	-2.42	-1.79	-1.15	-0.52
12	-2.68	-1.53	-0.39	0.76	1.91	3.06	-2.08	-0.93

Table E.3: Experiment 2 phase angles ρ_i used to define disturbance q per repetition.

E.2 Task Instructions

The written instructions provided to participants are shown below. In addition to the written instructions, on the first day (training) participants were also given a demonstration of the task with all of the test conditions.

E.2.1 Training Instructions

Perspective Displays for Position Control

Thank you for agreeing to participate in this study. The objective of the study is to determine what features of a perspective scene are useful for position control.

You will be asked to perform a task with a variety of perspective displays. The task will be to maintain your position fixed despite wind disturbances. The vehicle you are controlling is not an airplane, or a helicopter, or any real vehicle. It hovers above the ground at a constant altitude, and you can make it move forward by moving the stick forward, and backward by moving the stick backward. The vehicle also pitches up and down randomly, but you cannot control this motion and the pitching does NOT affect the fore-aft position. The vehicle does not move side-to-side, nor does it roll or yaw. The only motions it can do are fore-aft, and pitch.

You will be given an opportunity to train on all of the display conditions. A total of eight one-minute training runs will be given for each of the eight conditions (a total of 64 training runs). A score will be assigned to each run which is a combination of your position error and velocity. A smaller score is better. After each condition, you will be required to take a four-minute break. You are also encouraged to take breaks of whatever duration you wish between runs, in order to alleviate the discomfort which can occur from sitting in a fixed position for a prolonged period of time.

The results of the training sessions will be analyzed to determine if you meet the criteria for the follow-on experiments.

E.2.2 Data Run Instructions

Perspective Displays for Position Control

Phase II

Thank you for participating in the second phase of this study. The objective of the study is to determine what features of a perspective scene are useful for position control.

The task is identical to the one performed in the training conditions, but will involve longer run times. You are asked to control position as accurately as possible. As described below, you are required to take breaks from the task at particular times. You are also encouraged to take breaks as frequently as necessary to maintain performance on the task.

This portion of the experiment will require two days to complete. On each day, you will be asked to perform the position control task with the same eight displays you encountered in the training conditions. For each condition, you will receive one one-minute training run, then four four-minute data runs. A score will be assigned to each run which is a combination of your position error and velocity. A smaller score is better. For training scores, your performance relative to your previous training scores will be shown. For data runs, your performance relative to other subjects data run scores (if available) will be shown. Training runs can be visually discriminated from data runs by the color of the ground plane. Training runs feature a brown ground plane; data runs feature a green ground plane.

After each condition (one training and four data runs), you will be required to take a four minute break. You will complete four conditions in the morning, and four conditions in the afternoon. You will be required to take a lunch break of at least 30 minutes. The experiment is identical on both days. The purpose of the repetition is to allow averaging of the data.

		$P_{\delta\theta}$		$P_{\delta x}$		$\mathrm{RMS}_{\dot{x}}$		RMS_{x}	
LineTexture	Dots	Mean	SE	Mean	SE	Mean	SE	Mean	SE
Grid (G)	absent	4.42	1.09	46.31	4.29	0.667	.023	0.511	.049
Grid (G)	present	5.81	1.28	46.00	3.42	0.658	.016	0.485	.028
Para ($\parallel$)	absent	6.14	1.23	40.47	3.16	0.691	.017	0.582	.066
Para ($\parallel$)	present	5.73	1.00	46.68	3.75	0.653	.018	0.514	.035
Perp ($\perp$)	absent	8.81	1.10	38.88	2.59	0.706	.020	0.564	.044
Perp ($\perp$)	present	6.94	1.47	46.30	3.65	0.656	.015	0.512	.035
Line (L)	absent	10.92	.87	36.04	2.91	0.744	.018	0.702	.066
Line (L)	present	7.66	1.39	42.52	3.42	0.683	.021	0.562	.070

Table E.4: Means and Standard Errors for $P_{\delta\theta}$, $P_{\delta x}$, $\mathrm{RMS}_{\dot{x}}$, and RMS_{x} from the 4×2 (texture $\times$ dots)ANOVA in Experiment 2.

> For a given type of display, use a consistent strategy. Once you have started the data runs (green ground plane), dont experiment with your strategy (for example, the aggressiveness of control movements).

E.3 ANOVA results summary

In the main body of the report, only figures depicting the means and standard errors of the dependent measures are presented, with tables summarizing the degree of statistical significance. The actual values for statistical significance are shown in Table E.5. The numerical values for means and standard errors for $P_{\delta\theta}$, $P_{\delta x}$, $\mathrm{RMS}_{\dot{x}}$ and RMS_{x} are shown in Table E.4.

	Factor					
Measurement	Texture		Dots		Text/Dots Interaction	
	F(3,21)	p	F(1,7)	p	F(3,21)	p
$P_{\delta\theta}$	38.85	< 0.0005	2.14	0.188	6.483	0.003
$P_{\delta x}$	10.832	< 0.0005	42.5	<0.0005	4.169	.018
$\mathrm{RMS}_{\dot{x}}$	11.256	< 0.0005	122.15	< 0.0005	2.10	0.131
RMS_{x}	5.368	0.007	18.651	0.003	2.33	0.103

Table E.5: F-test and probabilities for statistical analysis of the 4 × 2 (texture × dots) ANOVA in Experiment 2.

	Factor	
Measurement	Splay	
	F(1,7)	p
$P_{\delta\theta}$	12.972	0.009
$P_{\delta x}$	8.071	0.025
$\mathrm{RMS}_{\dot{x}}$	5.032	0.060
RMS_{x}	0.749	0.415

Table E.6: F-test and probabilities for statistical analysis of one-way (splay effects) ANOVA in Experiment 2.

E.4 Individual Model Parameter Summary

Y_p model parameters K_p, ω_L, and fit quality index J_p are presented in Table E.7; the parameters τ, ω_N and ζ_N are shown in Table E.8. The crossover frequency ω_c and phase margin ϕ_m of Y_pY_c are in Table E.9. $Y_{\theta 1}$ parameter K_α, and fit quality index $J_{\theta 1}$ are in Table E.10. $Y_{\theta 2}$ parameters K_β and K_γ, and fit quality index $J_{\theta 2}$ are in Table E.11. The ratios K_β/K_γ and $J_{\theta 2}/J_{\theta 1}$ are in Table E.12.

	J_p							
	Without Dots				With Dots			
Obs.	G	$\parallel$	$\perp$	L	G	$\parallel$	$\perp$	L
1	17.9	23.1	34.8	36.6	28.4	22.4	14.1	28.5
2	51.2	23.6	18.6	9.4	31.9	44.1	16.0	18.8
3	11.4	11.2	19.3	14.3	12.3	14.4	21.9	17.0
4	39.6	28.4	9.3	6.5	32.9	35.0	48.6	40.1
5	14.7	18.4	39.1	21.9	12.4	17.1	13.5	21.5
6	18.5	20.5	27.0	55.8	13.0	12.6	39.8	22.3
7	15.5	11.8	34.5	15.9	17.0	14.9	31.1	19.1
8	10.0	17.6	12.2	10.5	25.0	8.6	19.3	6.3
	K_p							
	Without Dots				With Dots			
Obs.	G	$\parallel$	$\perp$	L	G	$\parallel$	$\perp$	L
1	2.29	2.24	2.09	2.23	2.21	2.30	2.28	2.09
2	2.04	1.97	1.77	1.67	1.88	1.97	1.85	1.80
3	1.69	1.74	1.70	1.54	1.83	1.59	1.66	1.67
4	2.35	2.37	2.19	2.16	2.39	2.28	2.33	2.38
5	1.78	1.82	1.74	1.57	1.98	1.88	1.80	1.61
6	2.12	2.14	1.88	2.13	2.12	2.02	2.12	2.06
7	1.49	1.55	1.64	1.45	1.64	1.64	1.74	1.76
8	1.74	1.69	1.63	1.45	1.74	1.60	1.77	1.78
	ω_L, rad/sec							
	Without Dots				With Dots			
Obs.	G	$\parallel$	$\perp$	L	G	$\parallel$	$\perp$	L
1	1.05	1.03	1.21	0.95	0.94	1.14	0.78	1.12
2	0.68	0.69	0.52	0.47	0.69	0.69	0.66	0.65
3	0.46	0.39	0.60	0.32	0.48	0.49	0.46	0.51
4	0.72	0.70	0.58	0.56	0.84	0.74	0.77	0.66
5	0.35	0.25	0.31	0.27	0.36	0.26	0.31	0.35
6	0.47	0.43	0.52	0.53	0.59	0.59	0.38	0.45
7	0.26	0.36	0.36	0.37	0.39	0.32	0.46	0.43
8	0.54	0.50	0.54	0.54	0.54	0.51	0.56	0.60

Table E.7: Y_p parameters K_p and ω_L, and model fit index J_p from Experiment 2.

	τ, sec							
	Without Dots				With Dots			
Obs.	G	$\parallel$	$\perp$	L	G	$\parallel$	$\perp$	L
1	0.21	0.22	0.21	0.22	0.22	0.21	0.22	0.21
2	0.24	0.24	0.24	0.24	0.24	0.24	0.24	0.24
3	0.25	0.25	0.24	0.24	0.25	0.24	0.24	0.24
4	0.22	0.24	0.22	0.24	0.22	0.22	0.22	0.24
5	0.28	0.28	0.28	0.28	0.28	0.28	0.28	0.28
6	0.24	0.25	0.22	0.22	0.22	0.25	0.24	0.25
7	0.28	0.26	0.25	0.25	0.25	0.26	0.24	0.24
8	0.25	0.25	0.26	0.25	0.25	0.25	0.24	0.24
	ω_N, rad/sec							
	Without Dots				With Dots			
Obs.	G	$\parallel$	$\perp$	L	G	$\parallel$	$\perp$	L
1	9.7	10.0	9.3	9.9	9.2	9.8	9.8	9.2
2	6.0	5.7	5.4	5.5	6.2	6.0	5.7	5.7
3	5.5	5.3	5.9	5.3	5.8	5.8	5.5	5.6
4	8.8	9.6	9.0	9.8	10.2	9.7	9.6	10.2
5	6.4	6.7	6.2	6.2	7.6	6.7	6.9	6.4
6	8.0	7.9	6.3	6.7	7.5	10.7	7.3	8.7
7	4.8	5.0	5.1	4.7	5.2	5.1	5.6	5.8
8	5.4	5.3	5.3	5.1	5.5	5.8	5.7	6.1
	ζ_N							
	Without Dots				With Dots			
Obs.	G	$\parallel$	$\perp$	L	G	$\parallel$	$\perp$	L
1	0.37	0.47	0.47	0.46	0.37	0.44	0.43	0.46
2	0.54	0.59	0.51	0.52	0.54	0.55	0.53	0.46
3	0.55	0.55	0.54	0.64	0.65	0.54	0.57	0.56
4	0.50	0.58	0.57	0.72	0.52	0.56	0.61	0.61
5	0.43	0.46	0.47	0.37	0.46	0.54	0.51	0.41
6	0.70	0.69	0.61	0.75	0.59	0.73	0.70	0.72
7	0.47	0.47	0.46	0.51	0.46	0.48	0.44	0.47
8	0.39	0.39	0.44	0.37	0.42	0.40	0.38	0.40

Table E.8: Y_p parameters τ, ω_N, and ζ_N from Experiment 2.

	ω_c, rad/sec							
	Without Dots				With Dots			
Obs.	G	$\parallel$	$\perp$	L	G	$\parallel$	$\perp$	L
1	2.60	2.50	2.41	2.47	2.49	2.62	2.48	2.39
2	2.23	2.14	1.93	1.79	2.06	2.15	2.03	2.01
3	1.80	1.84	1.84	1.58	1.90	1.70	1.76	1.79
4	2.54	2.50	2.30	2.21	2.58	2.43	2.48	2.49
5	1.90	1.91	1.84	1.67	2.09	1.94	1.88	1.71
6	2.16	2.17	1.97	2.14	2.23	2.08	2.15	2.09
7	1.59	1.67	1.78	1.55	1.78	1.76	1.91	1.90
8	1.97	1.89	1.82	1.63	1.94	1.76	2.00	1.99
	ϕ_m, deg							
	Without Dots				With Dots			
Obs.	G	$\parallel$	$\perp$	L	G	$\parallel$	$\perp$	L
1	28.1	25.3	23.7	27.3	29.1	24.3	31.4	25.8
2	21.8	20.5	31.3	36.2	26.5	23.3	26.0	29.5
3	33.4	33.5	31.8	41.2	28.4	38.0	35.4	34.3
4	27.9	26.0	33.3	31.0	26.8	29.1	26.3	27.6
5	39.3	41.3	39.6	48.6	36.2	37.9	39.6	43.9
6	30.8	29.9	31.8	25.2	30.1	32.2	31.1	32.3
7	42.5	39.8	38.6	40.5	38.6	38.3	37.0	38.2
8	33.2	35.5	32.7	39.6	33.1	39.7	35.5	34.9

Table E.9: Crossover frequency and phase margin of Y_pY_c from Experiment 2.

	$J_{\theta 1}$							
	Without Dots				With Dots			
Obs.	G	$\parallel$	$\perp$	L	G	$\parallel$	$\perp$	L
1	125.8	79.9	56.7	25.9	71.0	91.2	42.4	55.1
2	78.4	55.6	47.9	16.6	49.9	25.4	40.7	25.9
3	22.6	44.3	47.5	11.7	15.2	10.4	12.9	17.1
4	112.9	70.9	22.7	21.6	55.4	47.5	89.9	43.6
5	48.4	42.2	42.9	34.8	43.4	28.1	15.9	12.7
6	95.9	63.0	49.4	52.2	30.4	46.9	39.7	105.0
7	70.4	38.9	47.0	10.5	13.1	12.2	23.2	35.8
8	97.4	55.0	54.3	22.7	52.8	68.5	66.8	48.7
	K_α							
	Without Dots				With Dots			
Obs.	G	$\parallel$	$\perp$	L	G	$\parallel$	$\perp$	L
1	6.81	7.93	8.33	8.87	6.78	6.93	7.85	7.24
2	4.21	5.92	8.23	6.81	5.42	3.83	5.15	5.94
3	2.27	2.17	6.97	7.13	2.48	2.24	2.34	3.10
4	2.60	3.02	6.04	8.92	3.23	3.51	3.87	3.79
5	3.11	4.81	6.52	8.84	3.69	4.04	4.19	5.46
6	3.56	4.67	5.96	7.99	4.06	4.19	4.73	4.87
7	2.98	5.34	4.93	8.50	2.72	3.74	3.42	6.54
8	9.36	8.54	9.60	9.13	9.14	10.11	10.10	9.51

Table E.10: Y_{θ_1} parameter K_α, and model fit index $J_{\theta 1}$ from Experiment 2.

	$J_{\theta 2}$							
	Without Dots				With Dots			
Obs.	G	$\parallel$	$\perp$	L	G	$\parallel$	$\perp$	L
1	43.9	31.5	25.9	22.2	18.7	28.6	13.1	26.8
2	34.3	22.0	43.5	15.3	38.0	19.4	26.8	24.0
3	10.9	24.7	20.3	10.2	8.5	4.7	8.3	10.7
4	101.4	61.0	20.9	19.1	37.9	34.3	74.7	39.0
5	47.0	17.7	40.6	25.5	22.7	22.4	15.7	11.0
6	77.7	35.9	48.4	46.3	23.2	16.0	28.3	47.4
7	67.9	20.9	44.7	7.7	9.0	8.2	19.3	10.5
8	20.4	33.6	40.6	20.6	19.3	13.4	22.1	19.8
	K_β							
	Without Dots				With Dots			
Obs.	G	$\parallel$	$\perp$	L	G	$\parallel$	$\perp$	L
1	4.83	6.17	7.21	8.39	4.99	4.77	6.26	6.03
2	3.02	4.57	7.69	6.45	4.82	3.41	4.53	5.71
3	1.13	1.27	5.71	6.95	2.08	1.68	2.05	2.54
4	2.15	2.60	5.76	8.38	2.54	3.13	3.51	3.53
5	2.89	3.80	6.36	8.36	2.97	3.68	4.15	5.20
6	3.09	3.86	5.78	7.73	3.68	3.17	4.32	3.83
7	2.80	4.12	4.75	8.22	2.28	3.49	3.21	5.51
8	7.57	7.59	8.63	8.85	7.75	7.66	8.14	8.33
	K_γ							
	Without Dots				With Dots			
Obs.	G	$\parallel$	$\perp$	L	G	$\parallel$	$\perp$	L
1	8.89	9.49	9.45	9.53	9.08	8.68	9.59	8.79
2	5.84	8.69	9.08	7.74	6.60	4.87	7.01	6.74
3	4.83	5.80	9.66	9.07	4.21	3.88	4.17	5.05
4	3.73	4.21	6.67	9.95	4.37	4.68	5.05	4.52
5	4.62	11.94	8.96	14.93	7.72	7.40	4.63	7.64
6	5.99	8.51	6.62	9.28	5.05	6.73	7.08	8.07
7	5.17	9.33	6.45	10.87	4.25	6.42	5.03	10.16
8	14.51	11.37	13.21	10.47	12.75	15.10	14.78	12.82

Table E.11: Y_{θ_2} parameters K_β and K_γ, and model fit index $J_{\theta 2}$ from Experiment 2.

	$J_{\theta 2}/J_{\theta 1}$							
	Without Dots				With Dots			
Obs.	G	$\parallel$	$\perp$	L	G	$\parallel$	$\perp$	L
1	0.35	0.39	0.46	0.86	0.26	0.31	0.31	0.49
2	0.44	0.39	0.91	0.92	0.76	0.76	0.66	0.93
3	0.48	0.56	0.43	0.87	0.56	0.45	0.64	0.62
4	0.90	0.86	0.92	0.88	0.68	0.72	0.83	0.89
5	0.97	0.42	0.95	0.73	0.52	0.80	0.99	0.87
6	0.81	0.57	0.98	0.89	0.76	0.34	0.71	0.45
7	0.96	0.54	0.95	0.73	0.68	0.67	0.83	0.29
8	0.21	0.61	0.75	0.91	0.37	0.20	0.33	0.41
	K_β/K_γ							
	Without Dots				With Dots			
Obs.	G	$\parallel$	$\perp$	L	G	$\parallel$	$\perp$	L
1	0.54	0.65	0.76	0.88	0.55	0.55	0.65	0.69
2	0.52	0.53	0.85	0.83	0.73	0.70	0.65	0.85
3	0.23	0.22	0.59	0.77	0.49	0.43	0.49	0.50
4	0.58	0.62	0.86	0.84	0.58	0.67	0.70	0.78
5	0.63	0.32	0.71	0.56	0.38	0.50	0.90	0.68
6	0.52	0.45	0.87	0.83	0.73	0.47	0.61	0.47
7	0.54	0.44	0.74	0.76	0.54	0.54	0.64	0.54
8	0.52	0.67	0.65	0.85	0.61	0.51	0.55	0.65

Table E.12: Model fit index ratio $J_{\theta 2}/J_{\theta 1}$, and gain ratio K_β/K_γ to compare the one-cue and two-cue model fits from Experiment 2.

E.5 Individual Model Fit Plots

The model fits are shown in the following figures (Figures E.1 through E.64).

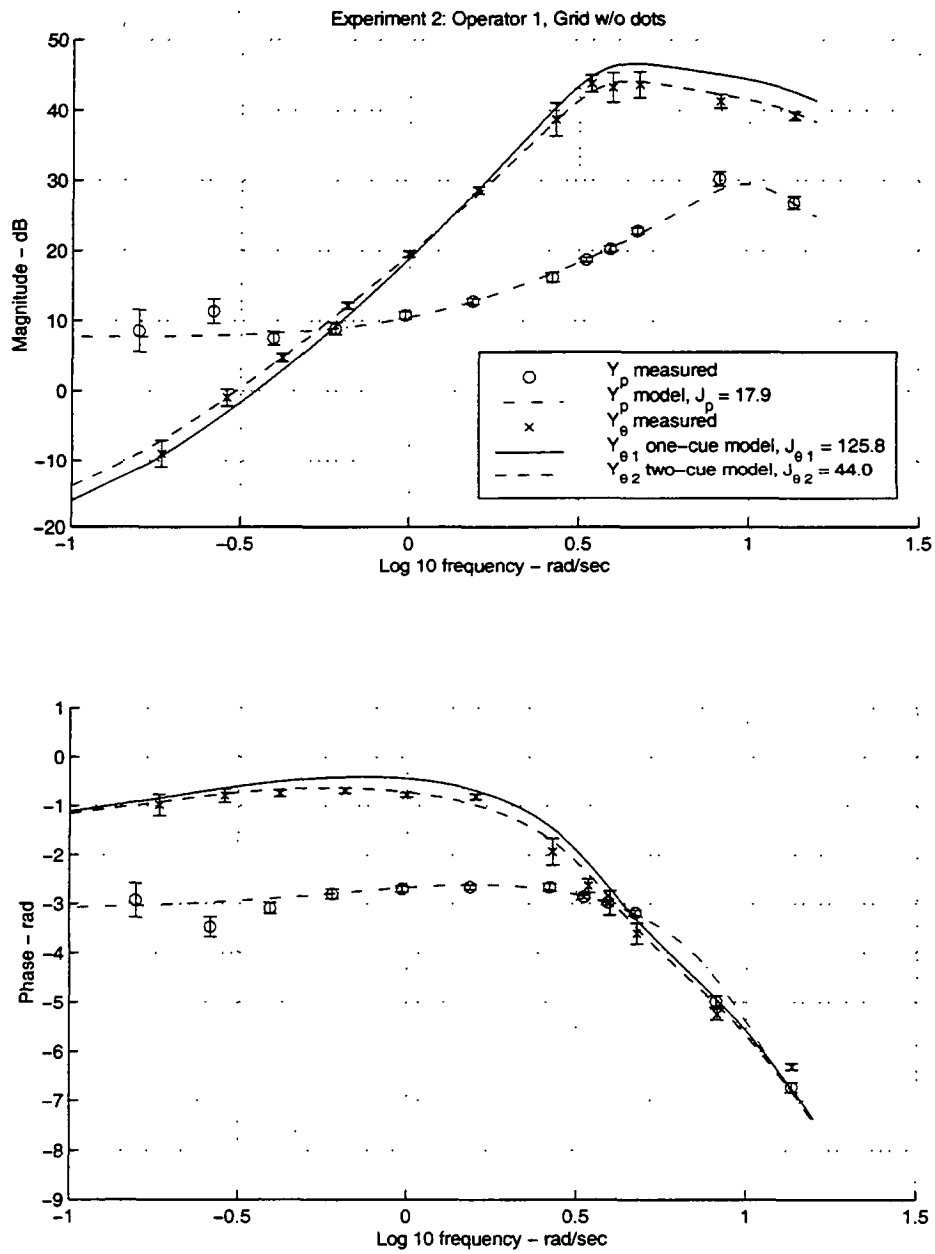

Figure E.1: Experiment 2 model fit results for Operator 1, Grid Texture w/o dots.

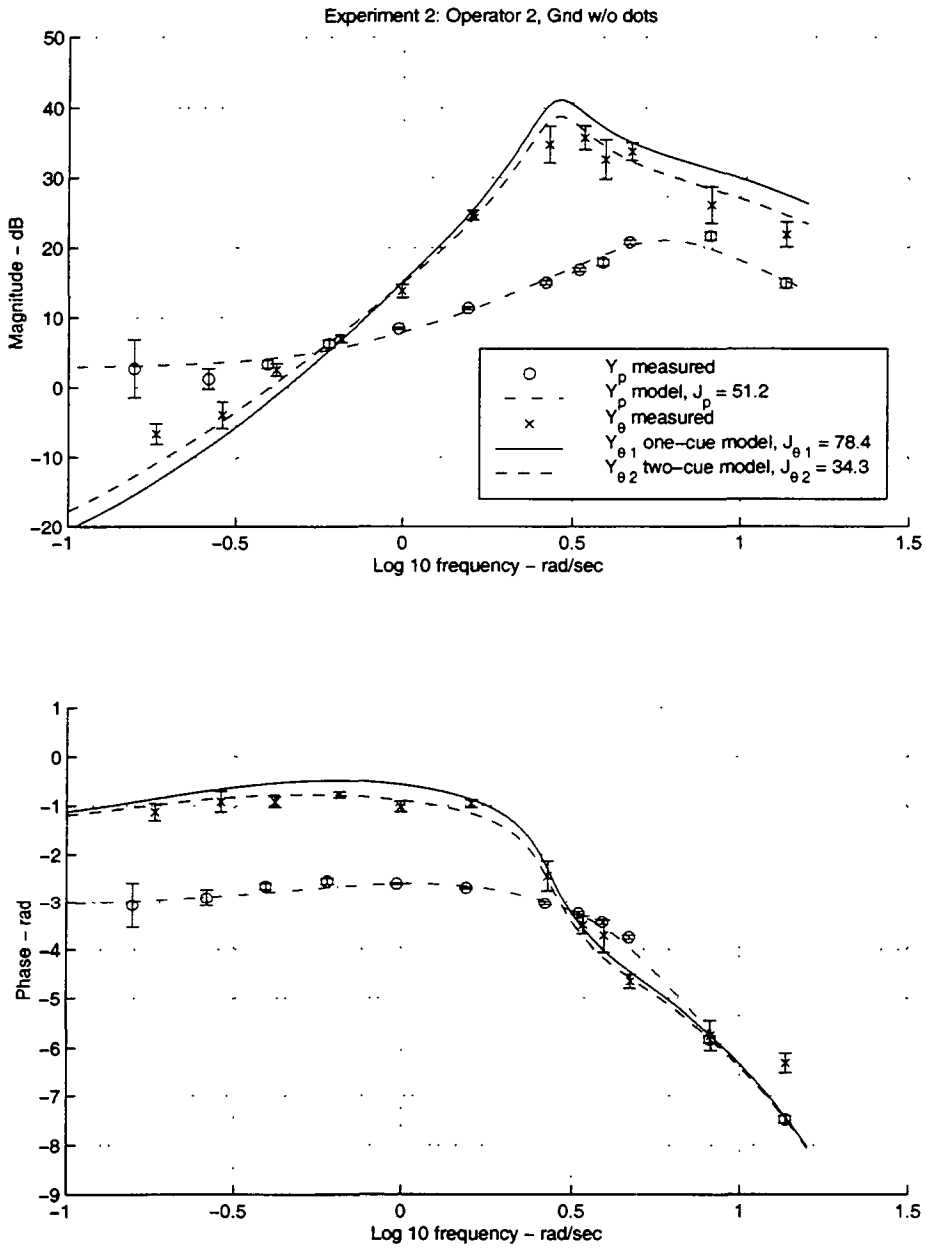

Figure E.2: Experiment 2 model fit results for Operator 2, Grid Texture w/o dots.

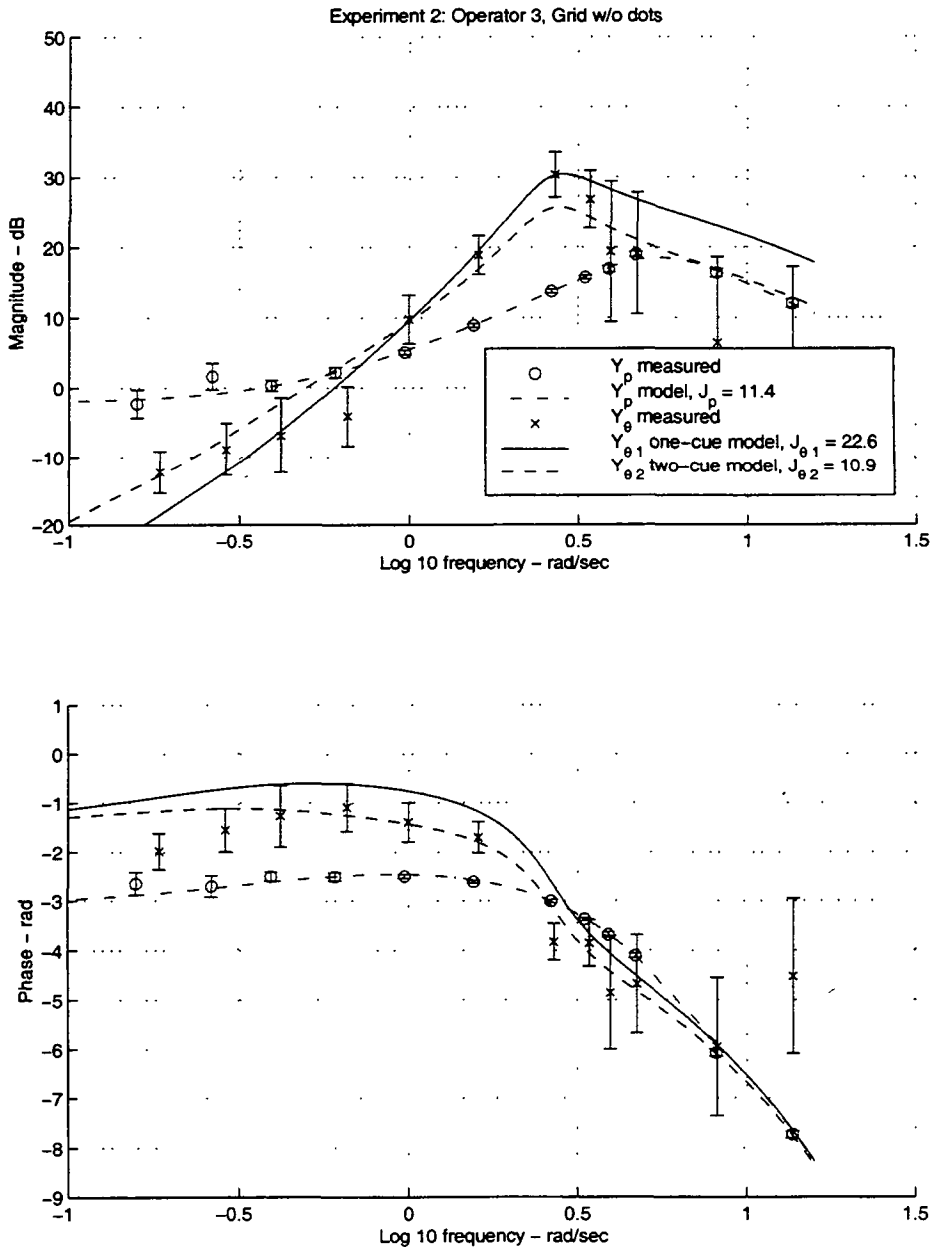

Figure E.3: Experiment 2 model fit results for Operator 3, Grid Texture w/o dots.

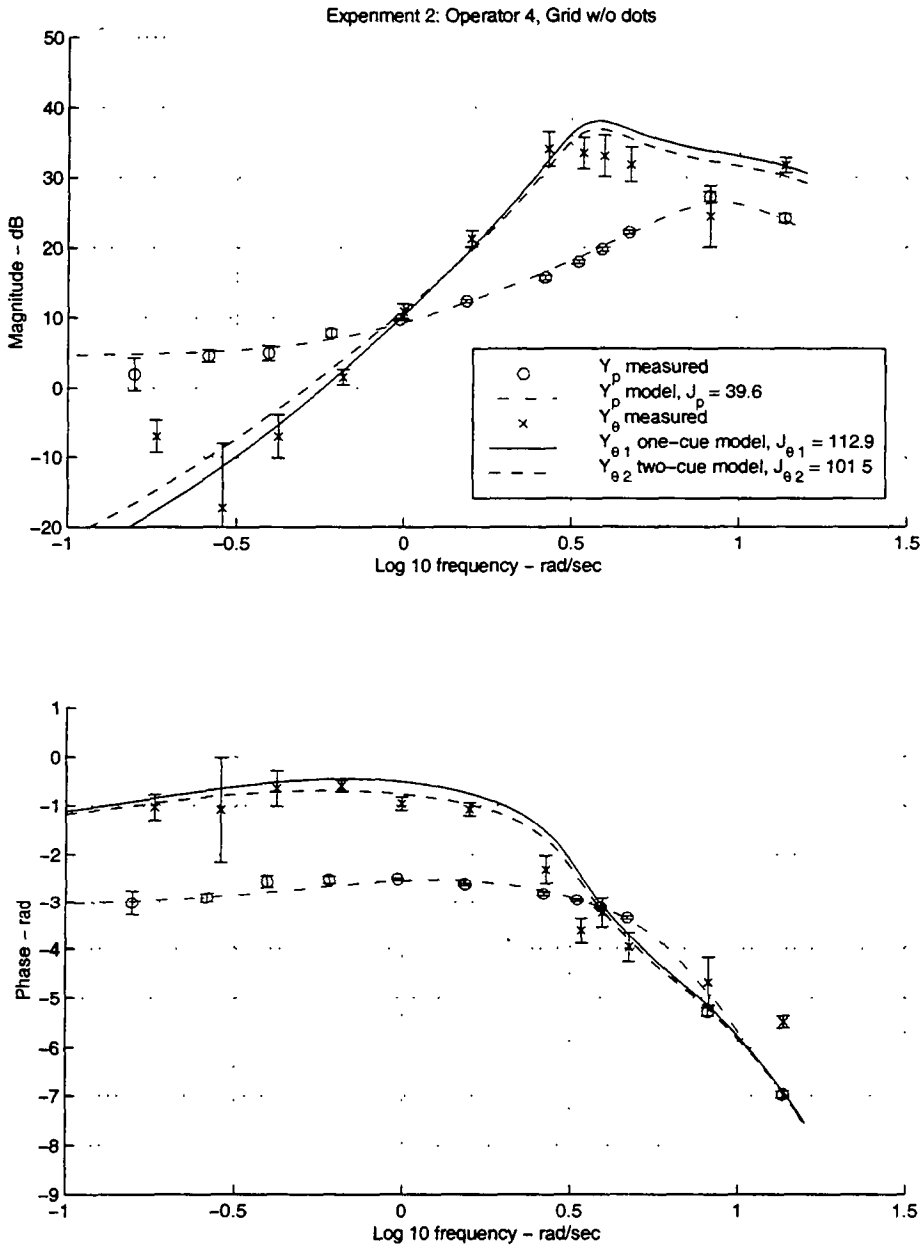

Figure E.4: Experiment 2 model fit results for Operator 4, Grid Texture w/o dots.

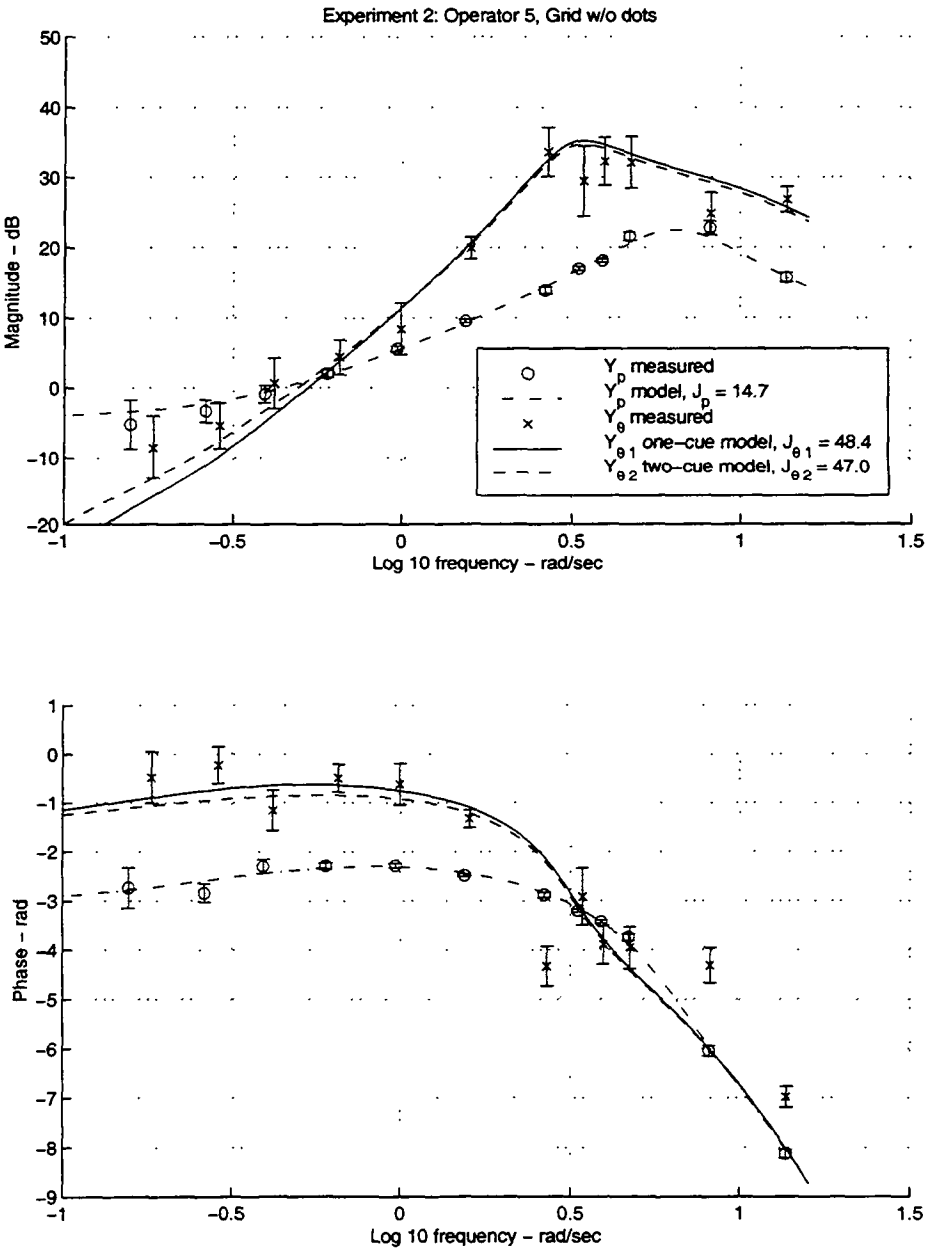

Figure E.5: Experiment 2 model fit results for Operator 5, Grid Texture w/o dots.

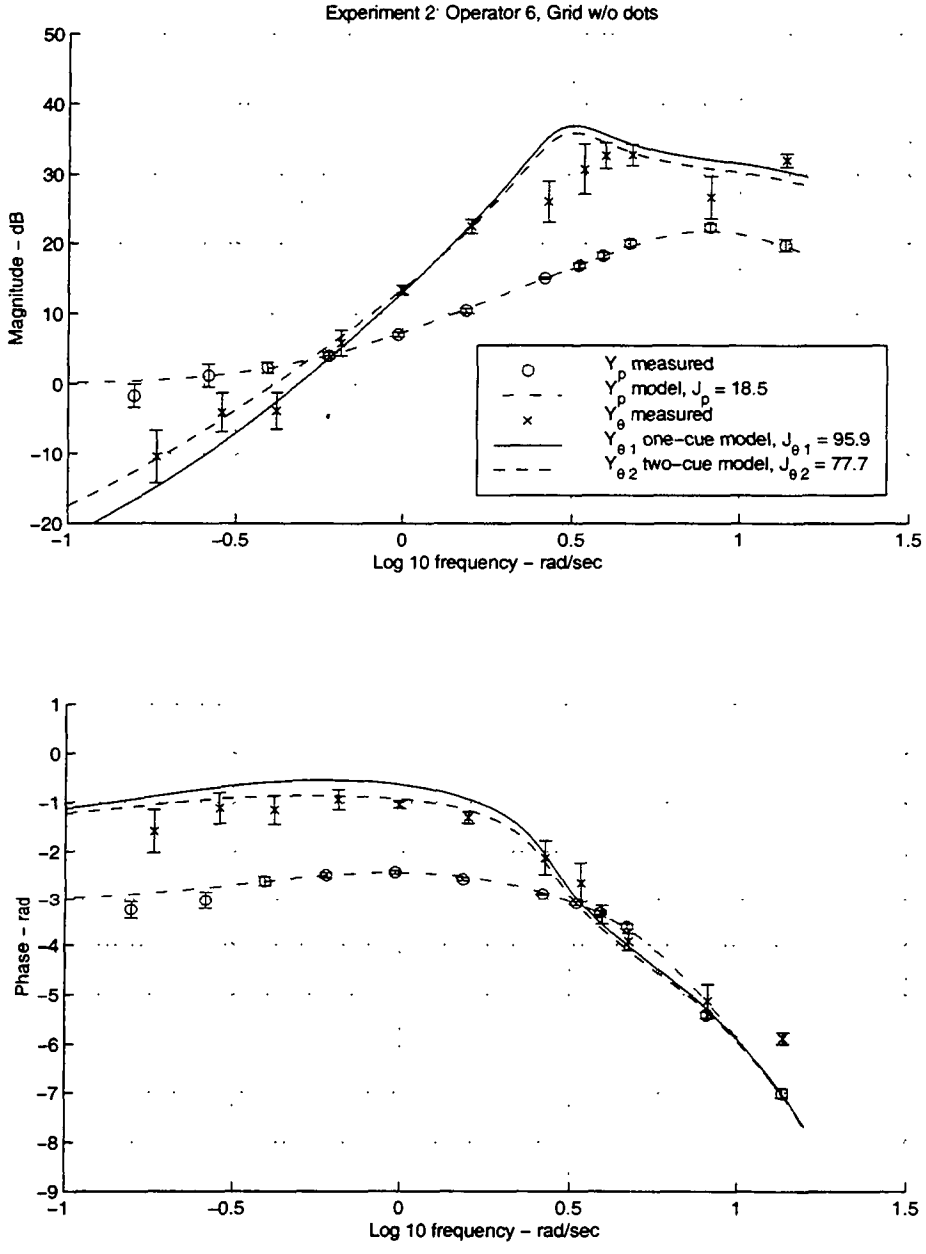

Figure E.6: Experiment 2 model fit results for Operator 6, Grid Texture w/o dots.

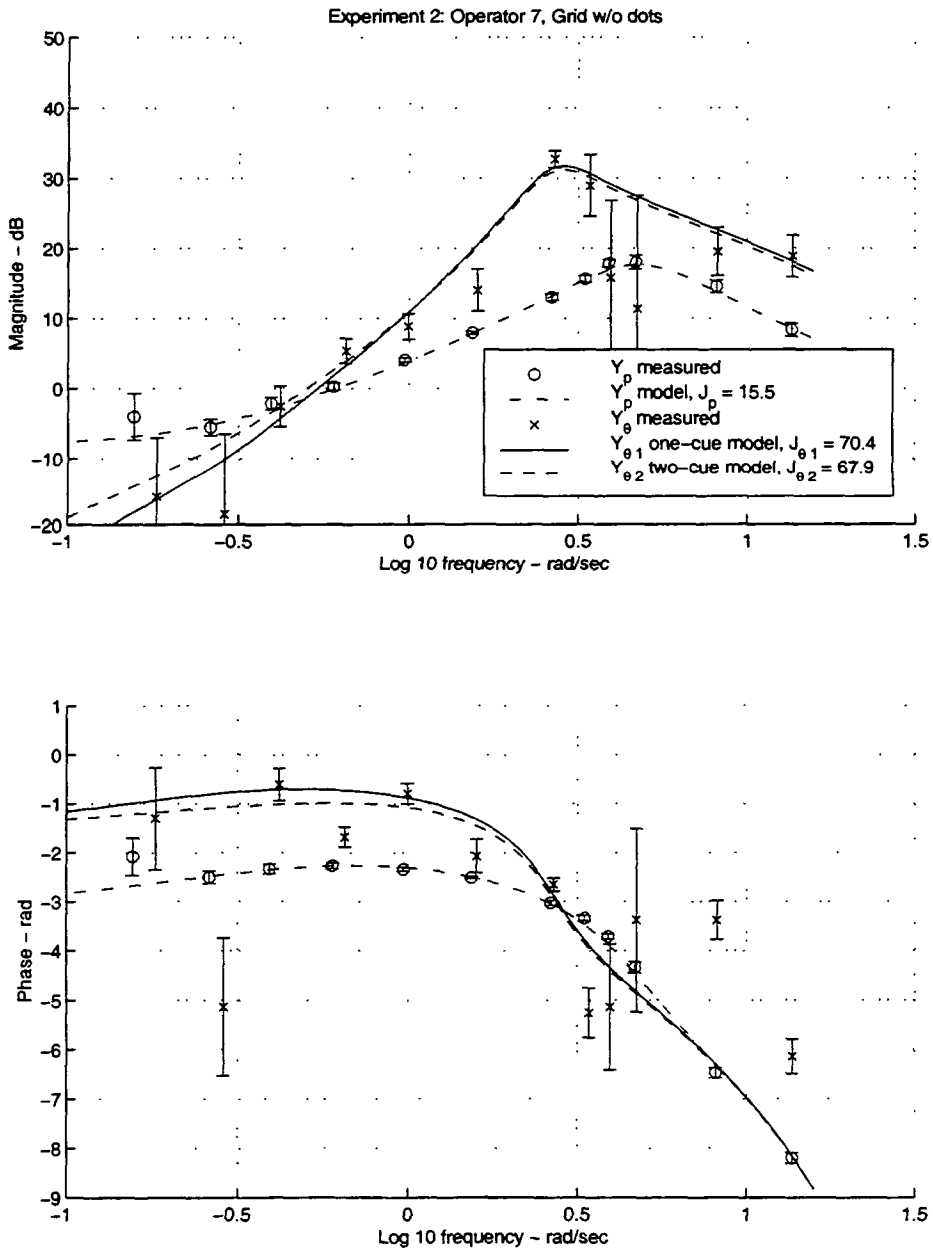

Figure E.7: Experiment 2 model fit results for Operator 7, Grid Texture w/o dots.

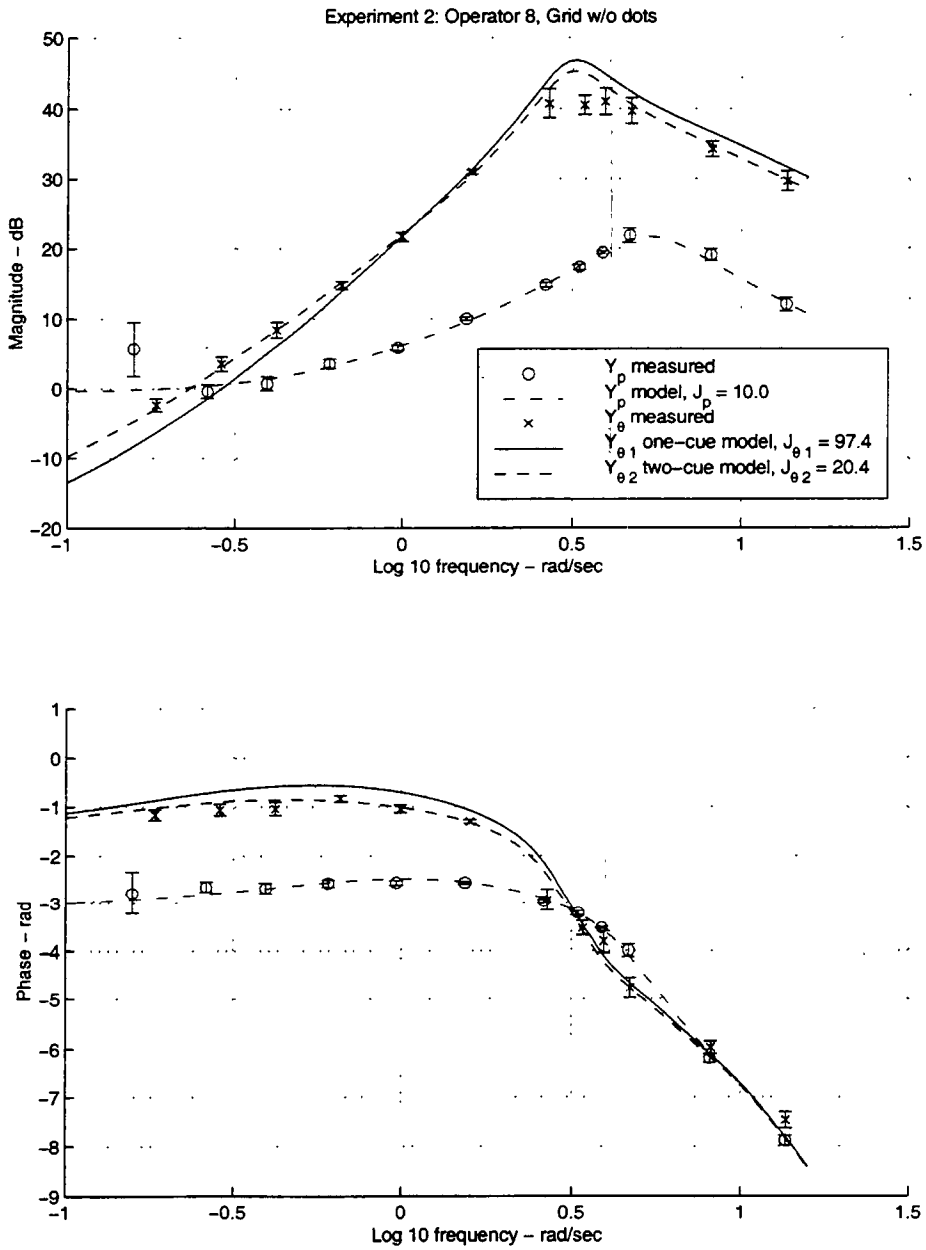

Figure E.8: Experiment 2 model fit results for Operator 8, Grid Texture w/o dots.

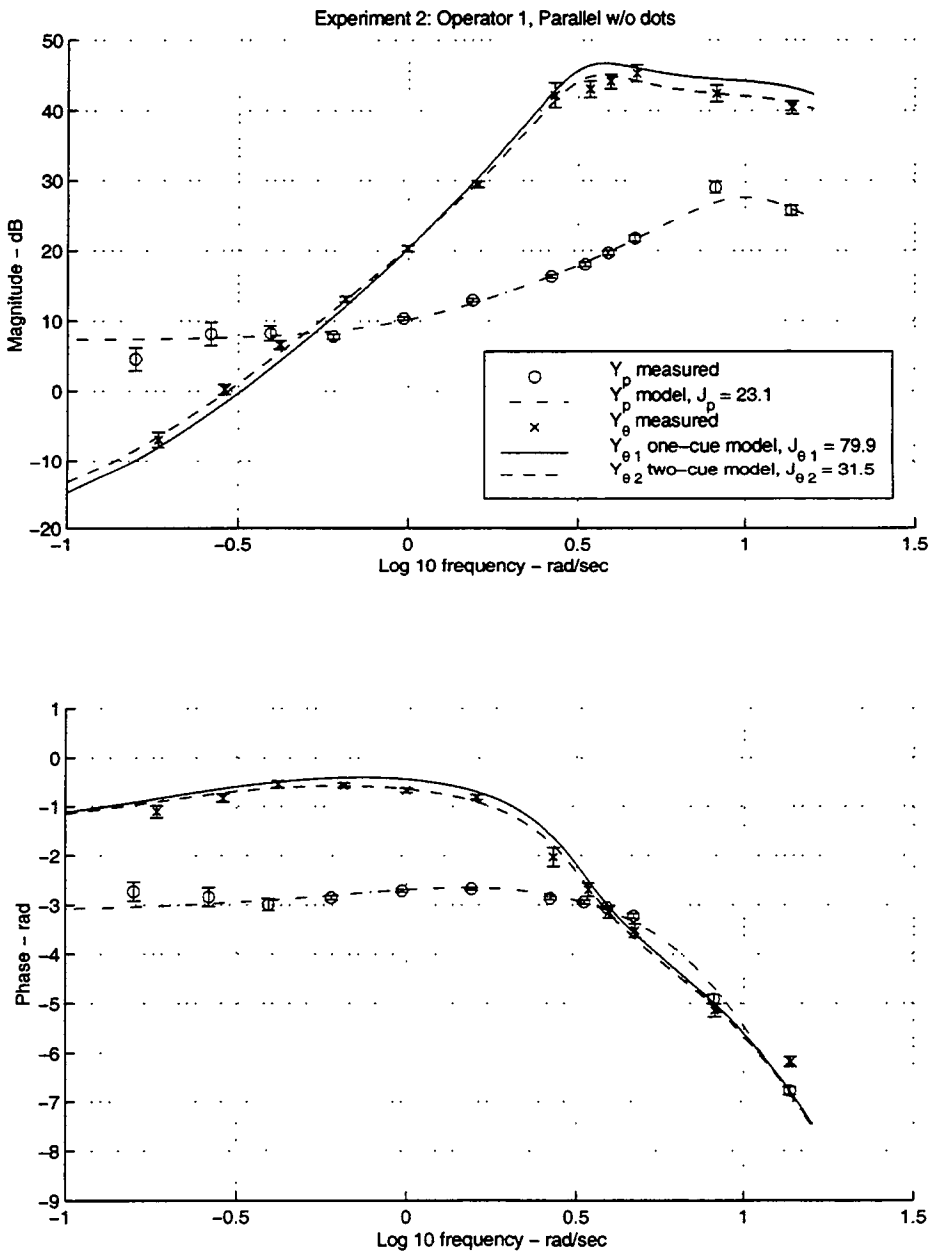

Figure E.9: Experiment 2 model fit results for Operator 1, Parallel Texture w/o dots.

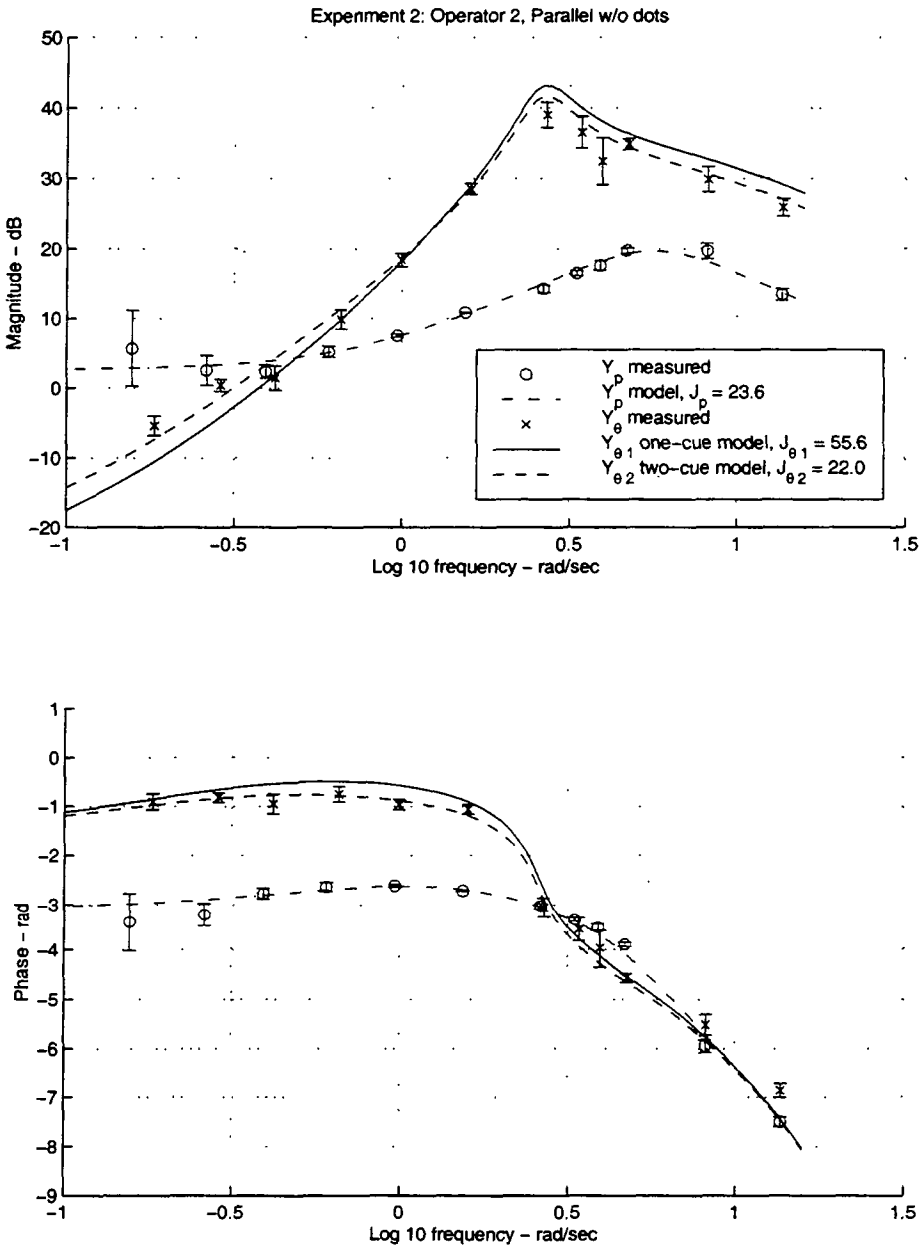

Figure E.10: Experiment 2 model fit results for Operator 2, Parallel Texture w/o dots.

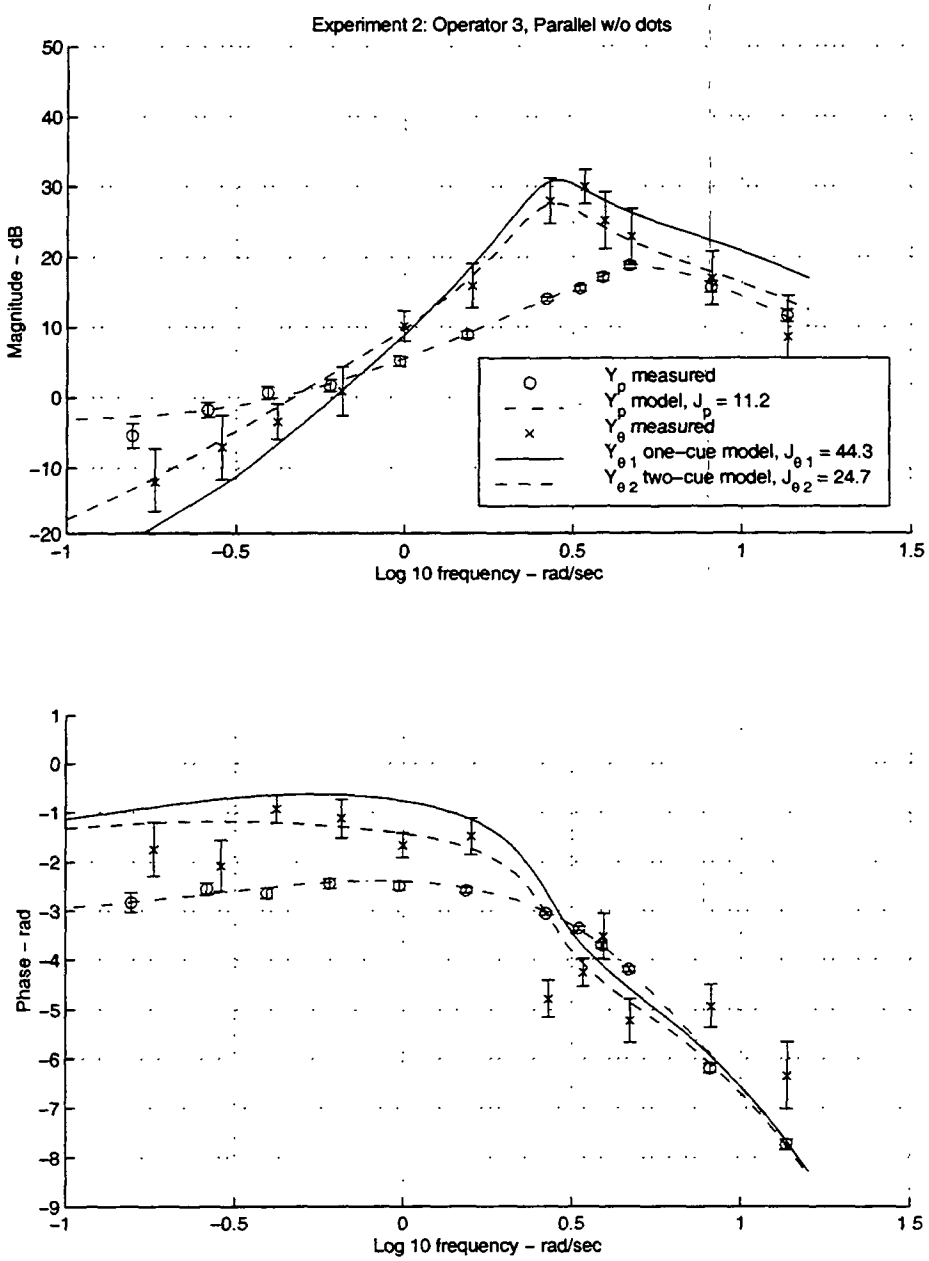

Figure E.11: Experiment 2 model fit results for Operator 3, Parallel Texture w/o dots.

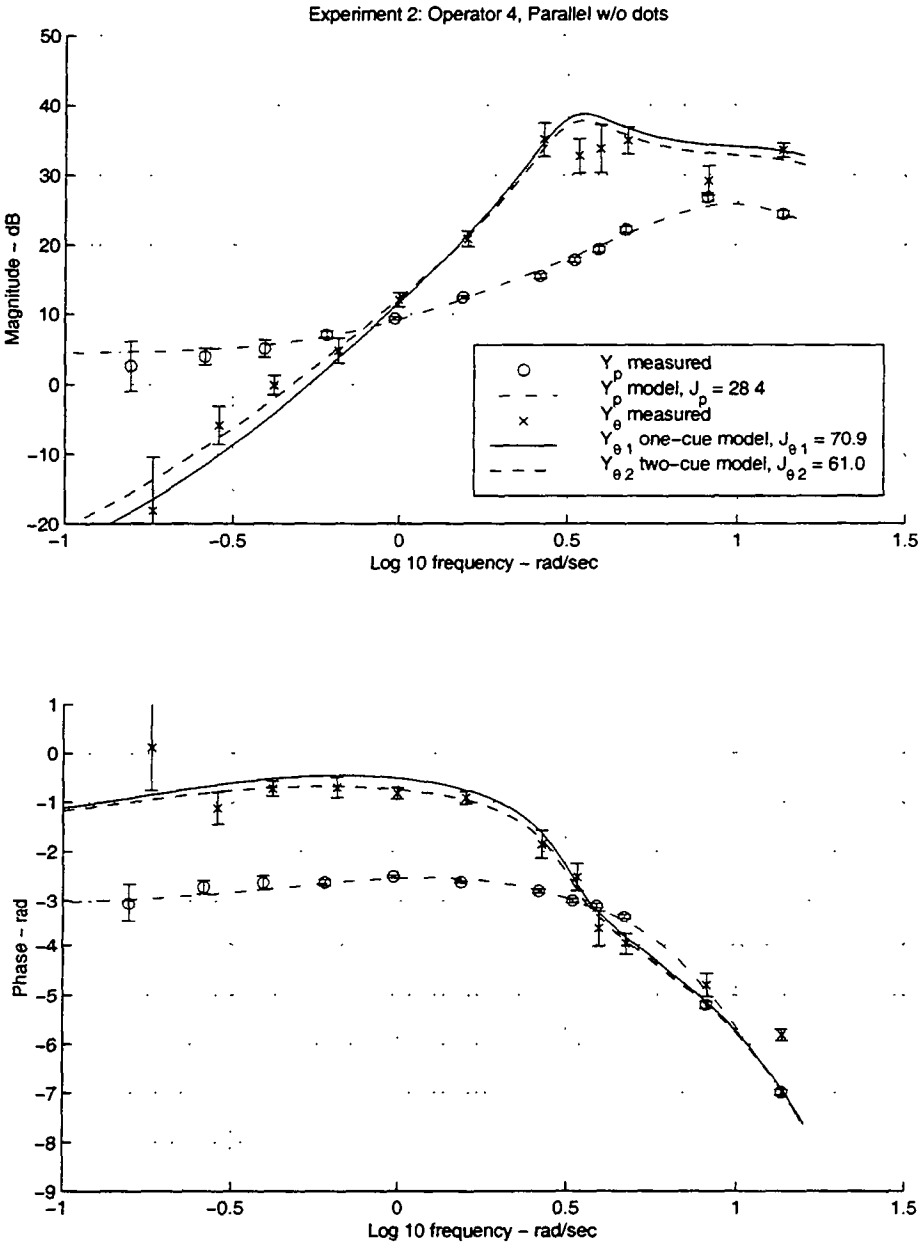

Figure E.12: Experiment 2 model fit results for Operator 4, Parallel Texture w/o dots.

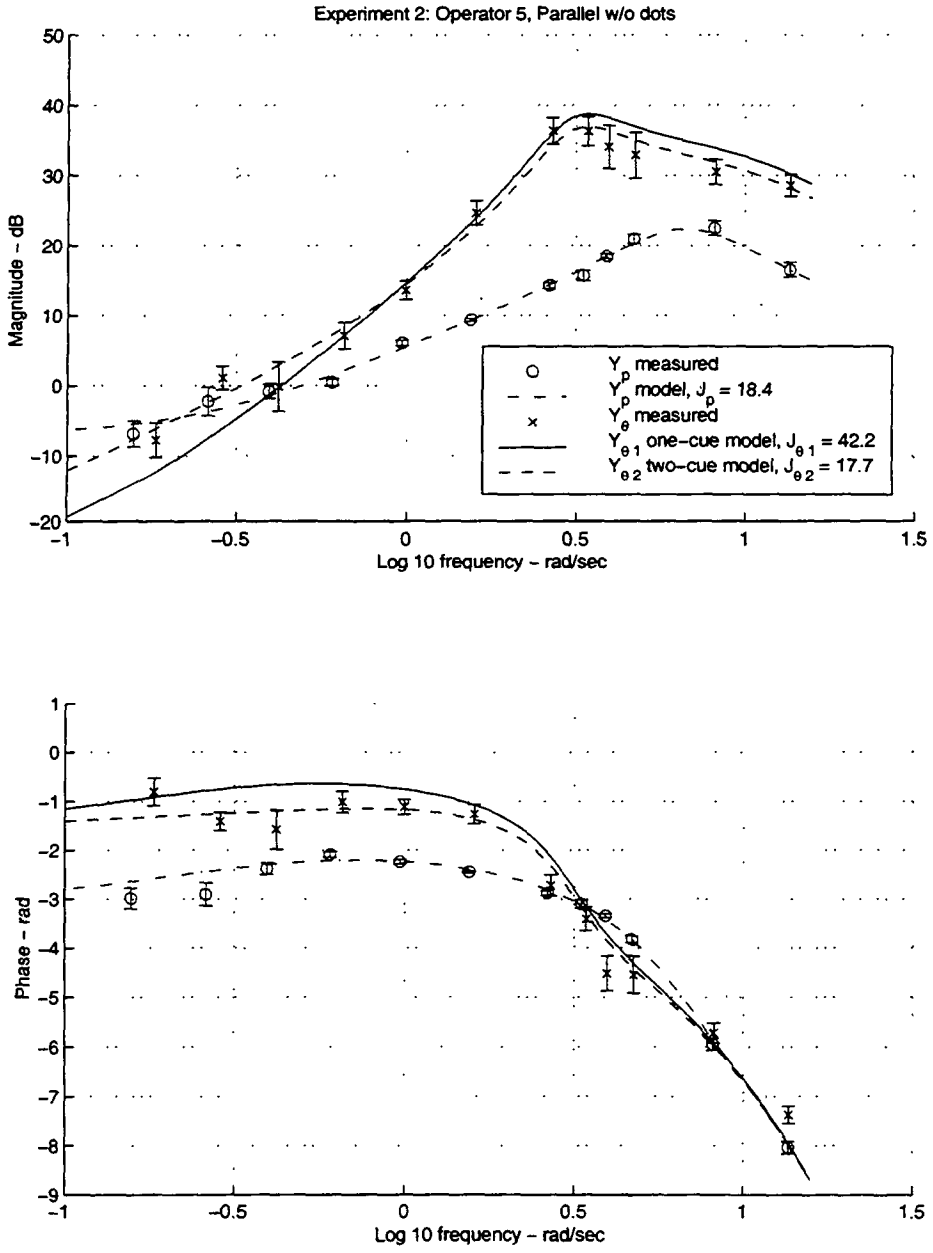

Figure E.13: Experiment 2 model fit results for Operator 5, Parallel Texture w/o dots.

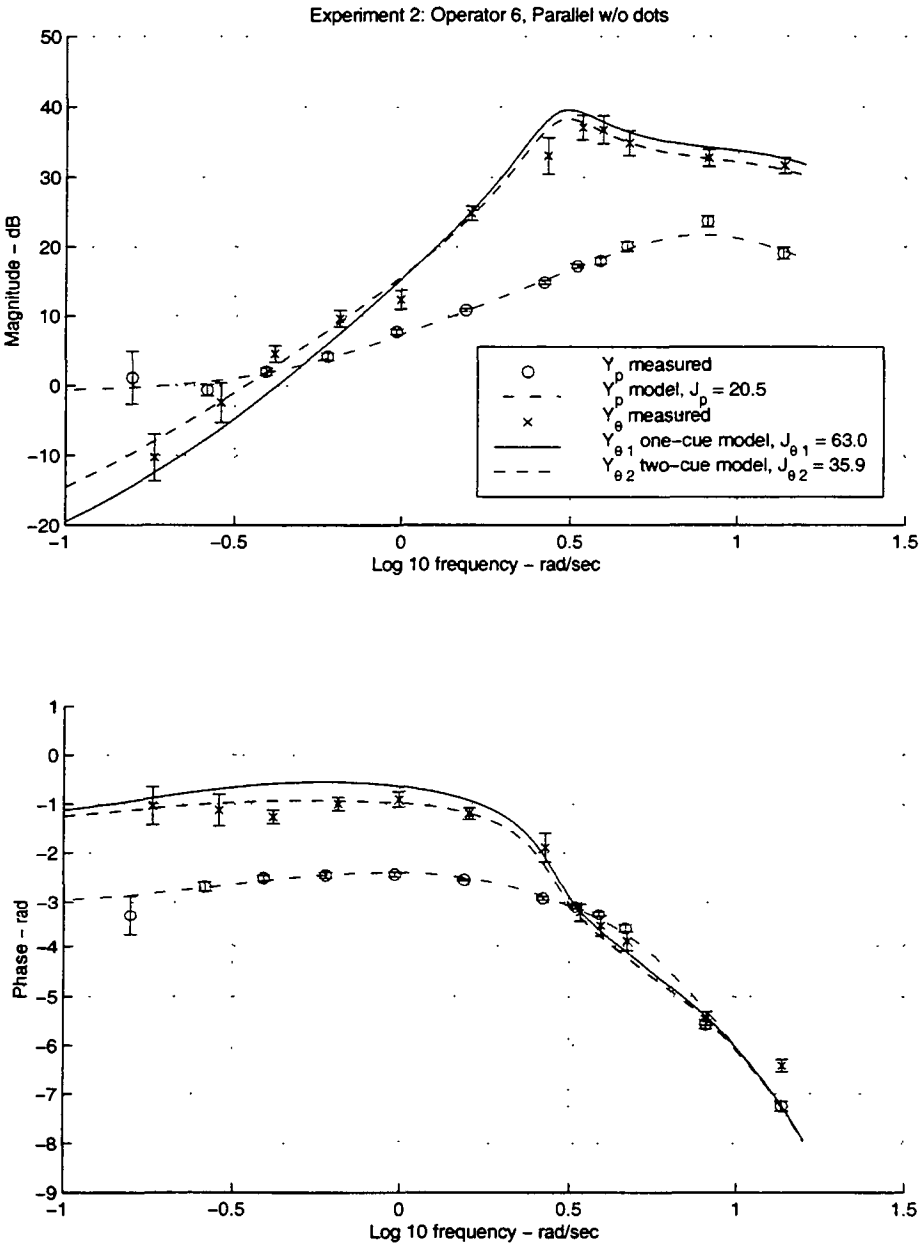

Figure E.14: Experiment 2 model fit results for Operator 6, Parallel Texture w/o dots.

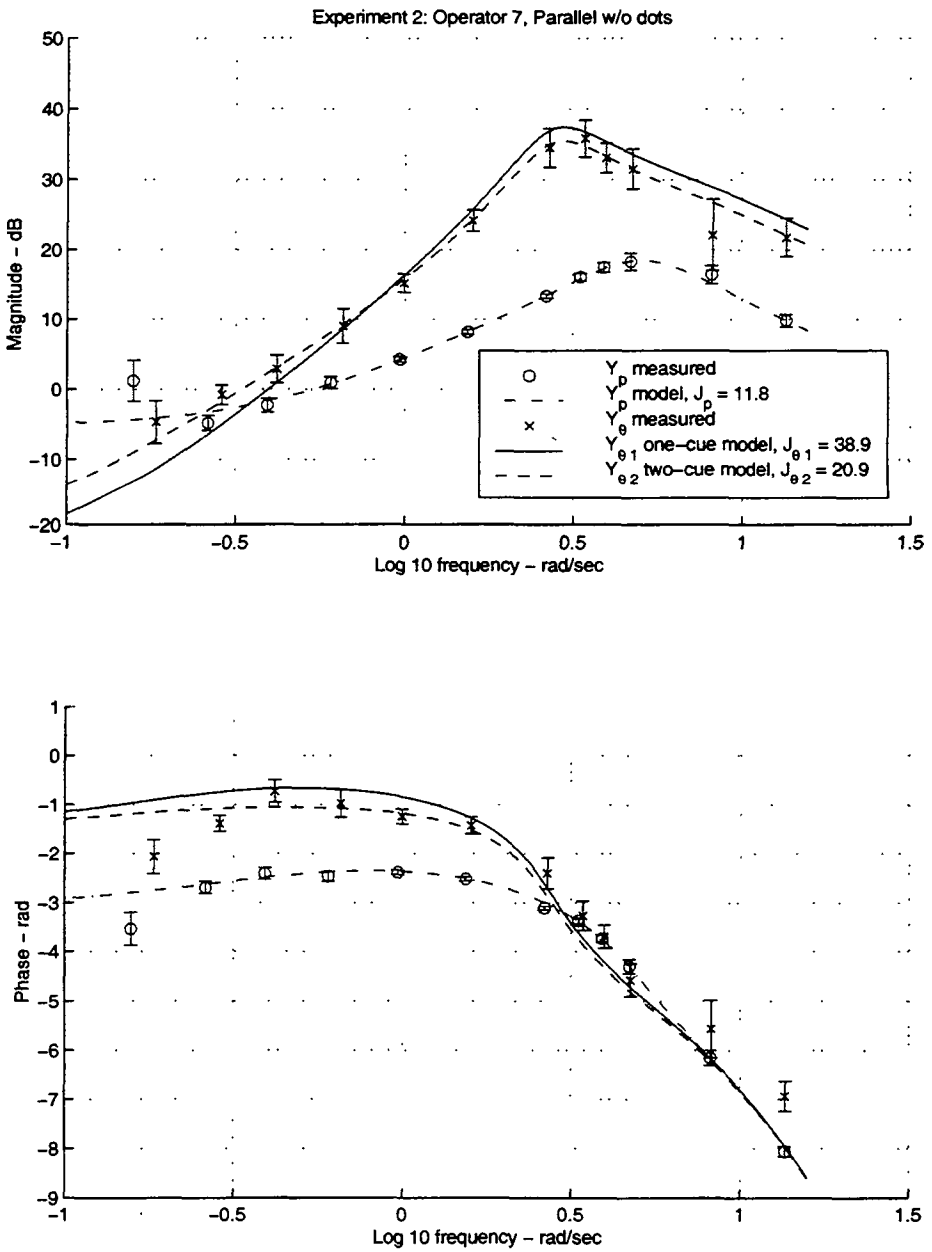

Figure E.15: Experiment 2 model fit results for Operator 7, Parallel Texture w/o dots.

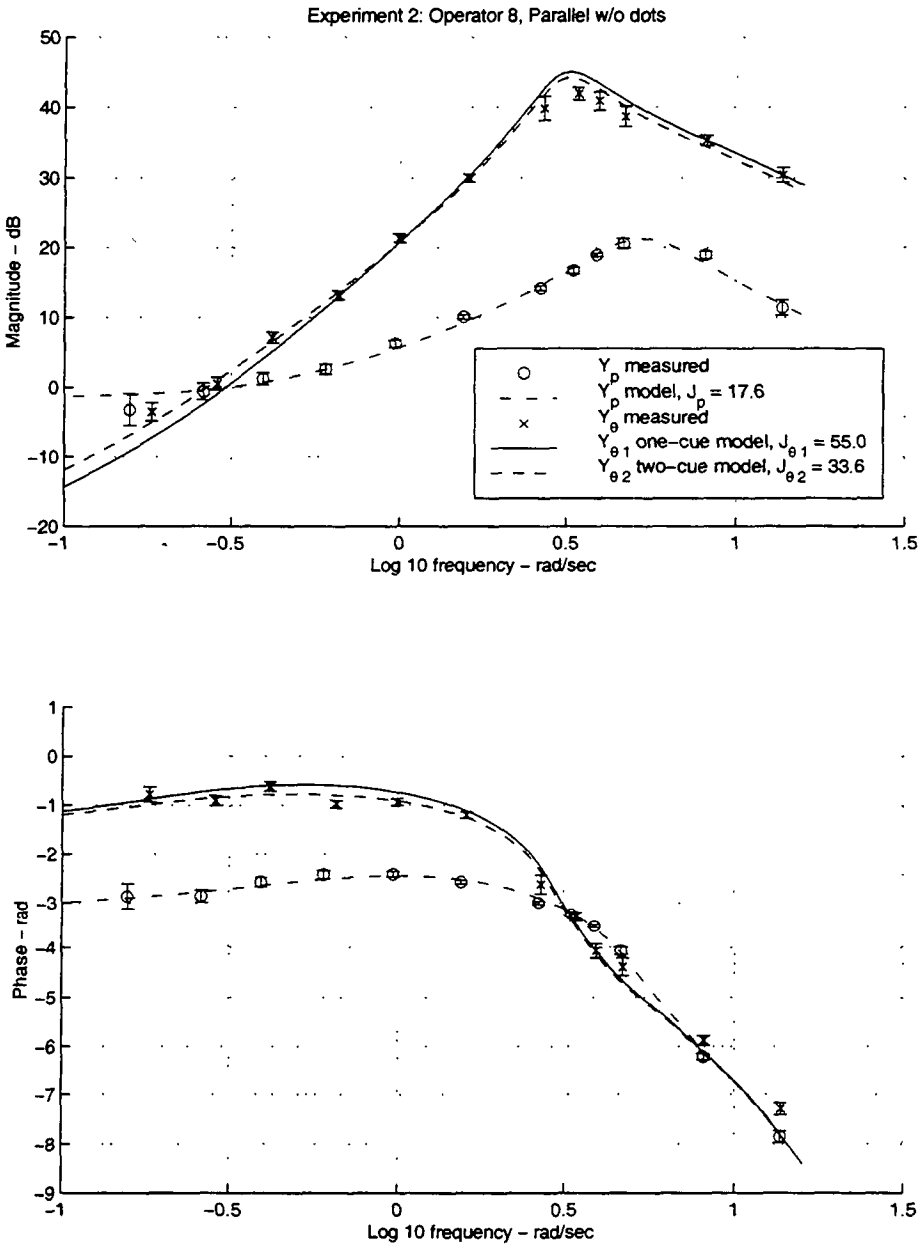

Figure E.16: Experiment 2 model fit results for Operator 8, Parallel Texture w/o dots.

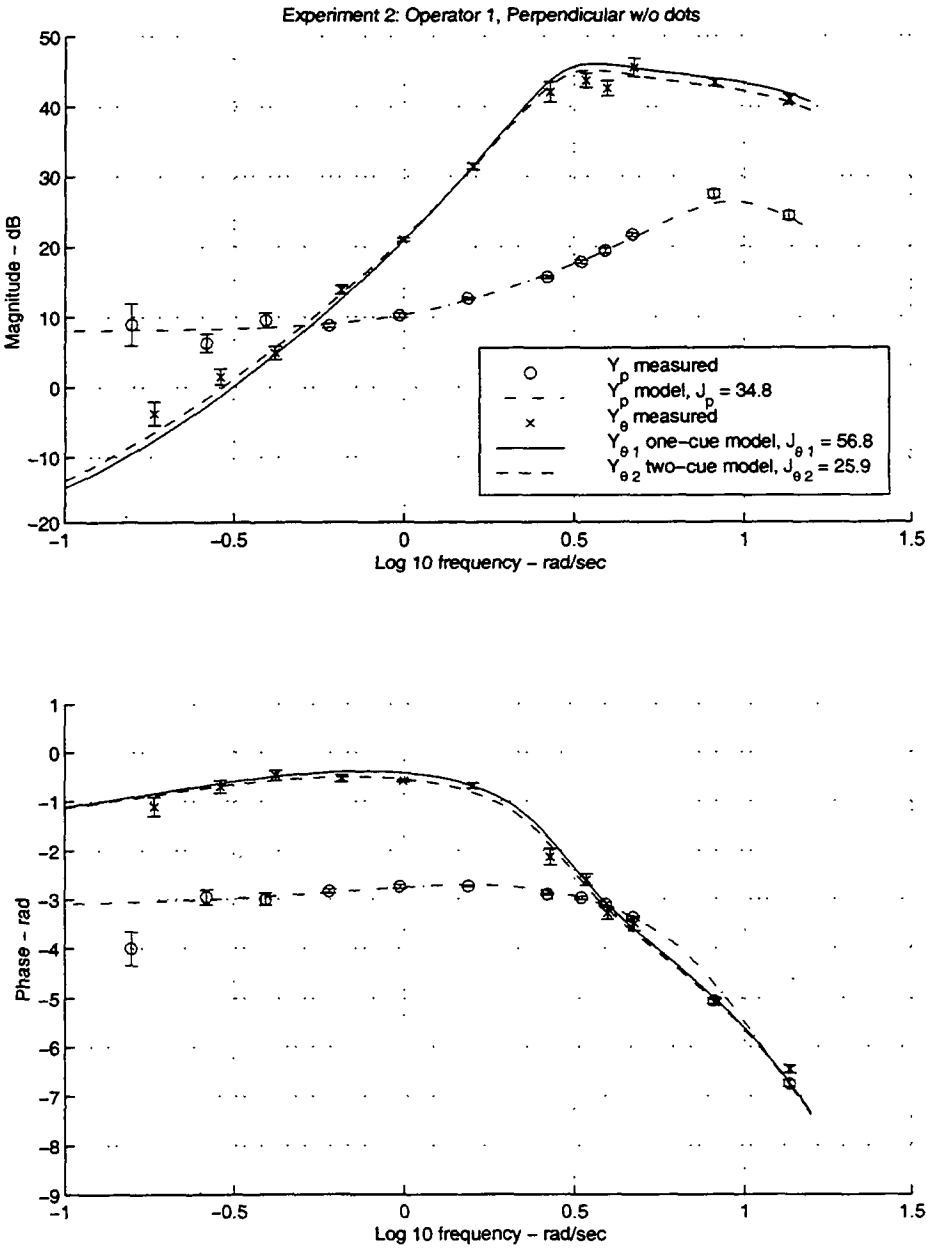

Figure E.17: Experiment 2 model fit results for Operator 1, Perpendicular Texture w/o dots.

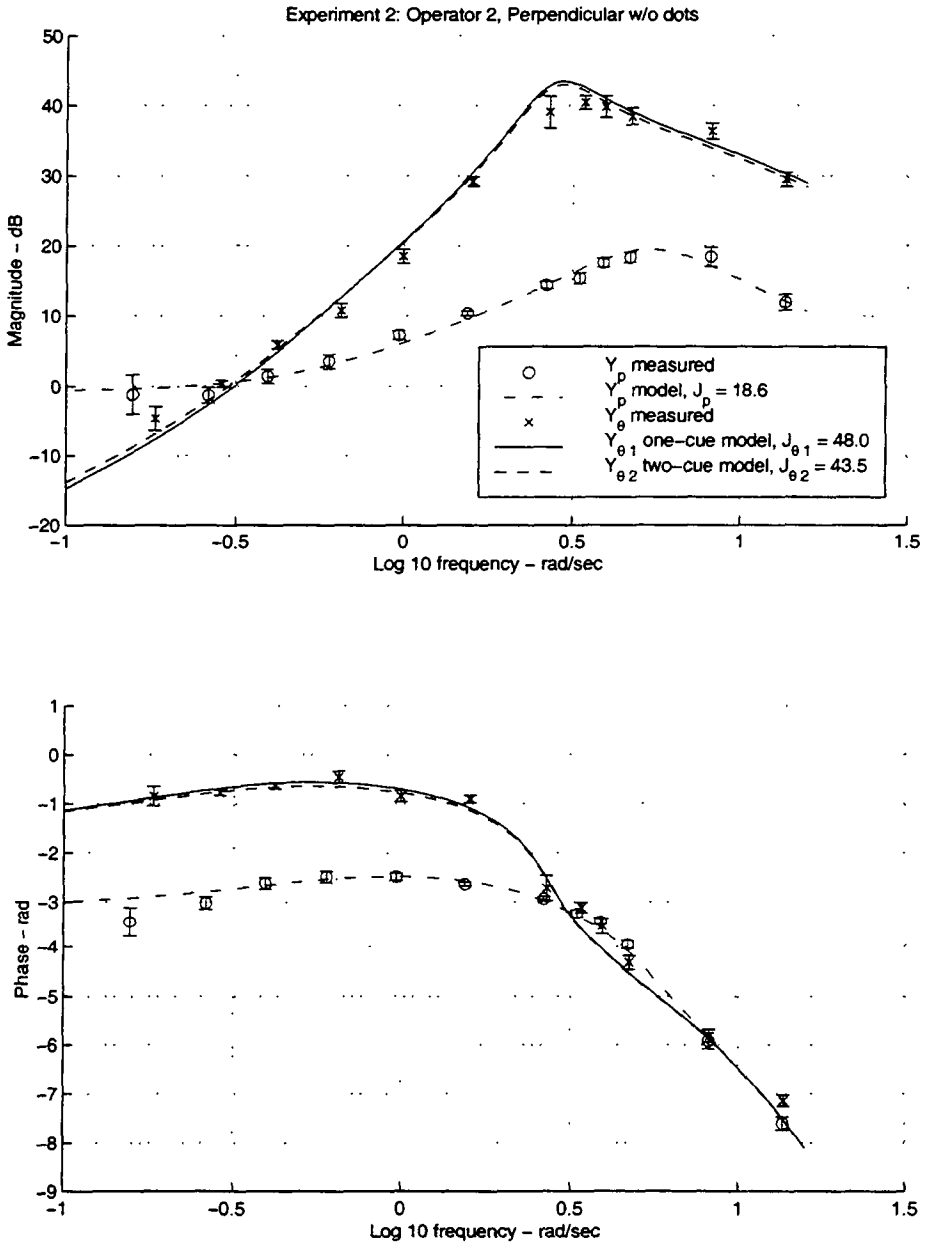

Figure E.18: Experiment 2 model fit results for Operator 2, Perpendicular Texture w/o dots.

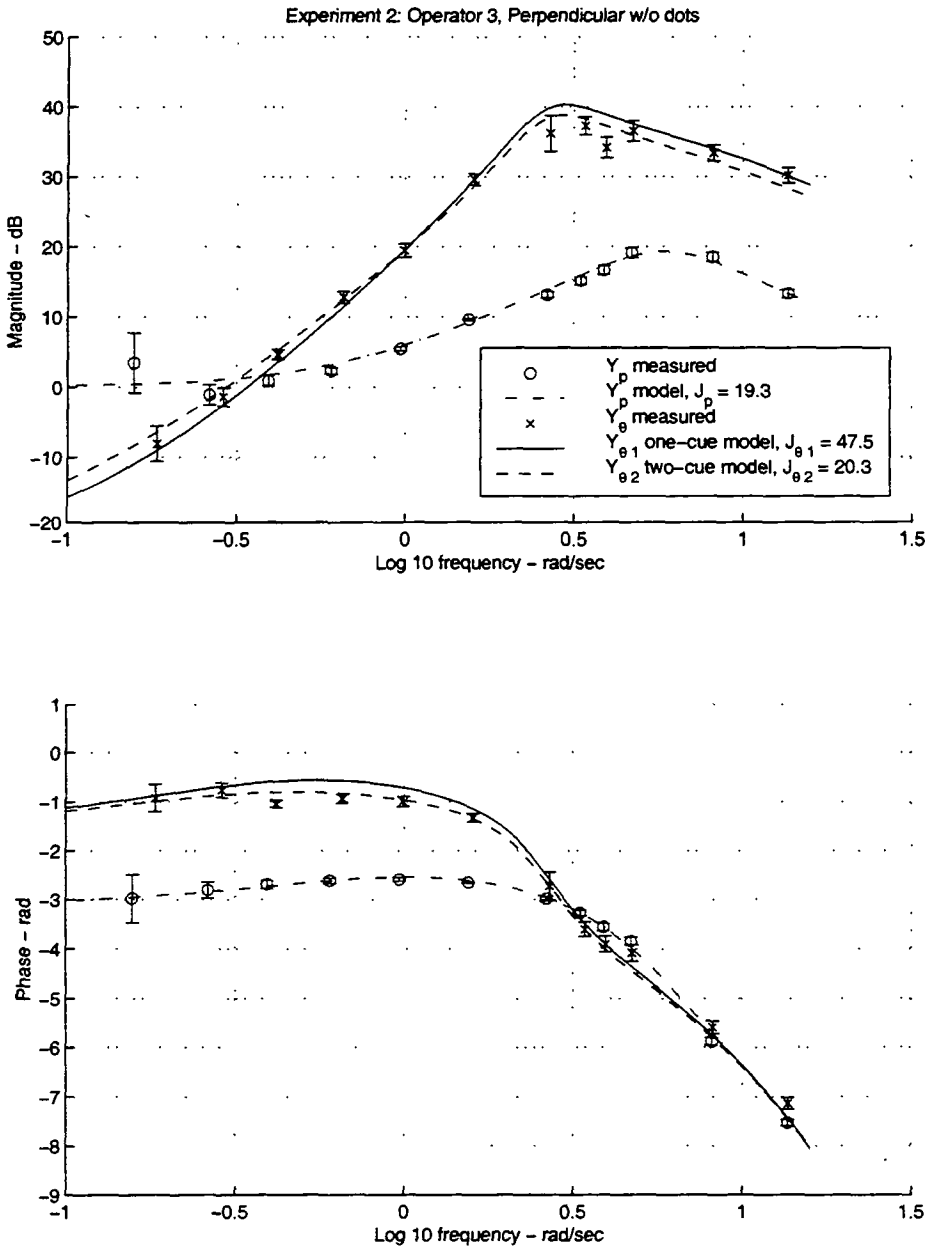

Figure E.19: Experiment 2 model fit results for Operator 3, Perpendicular Texture w/o. dots.

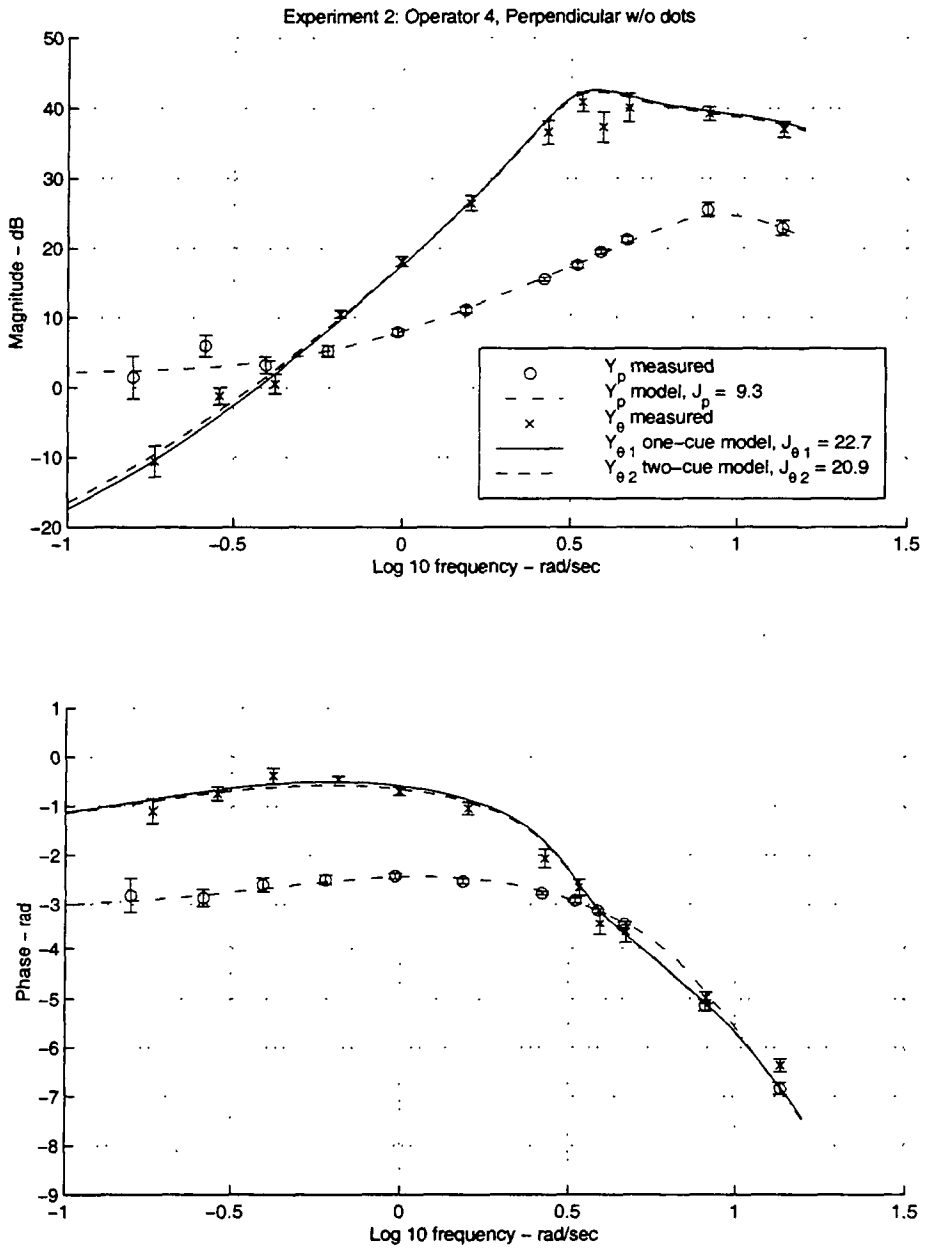

Figure E.20: Experiment 2 model fit results for Operator 4, Perpendicular Texture w/o dots.

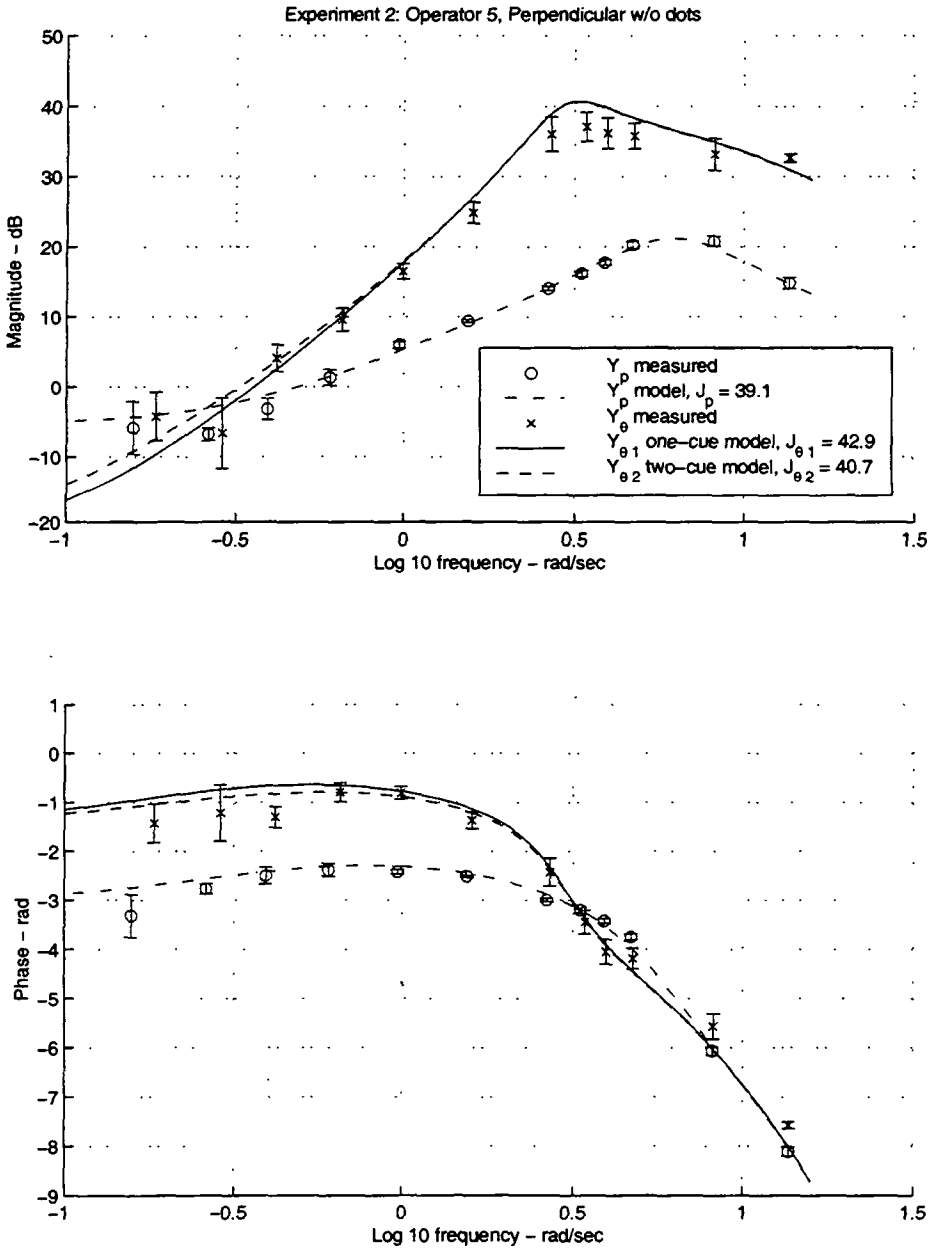

Figure E.21: Experiment 2 model fit results for Operator 5, Perpendicular Texture w/o dots.

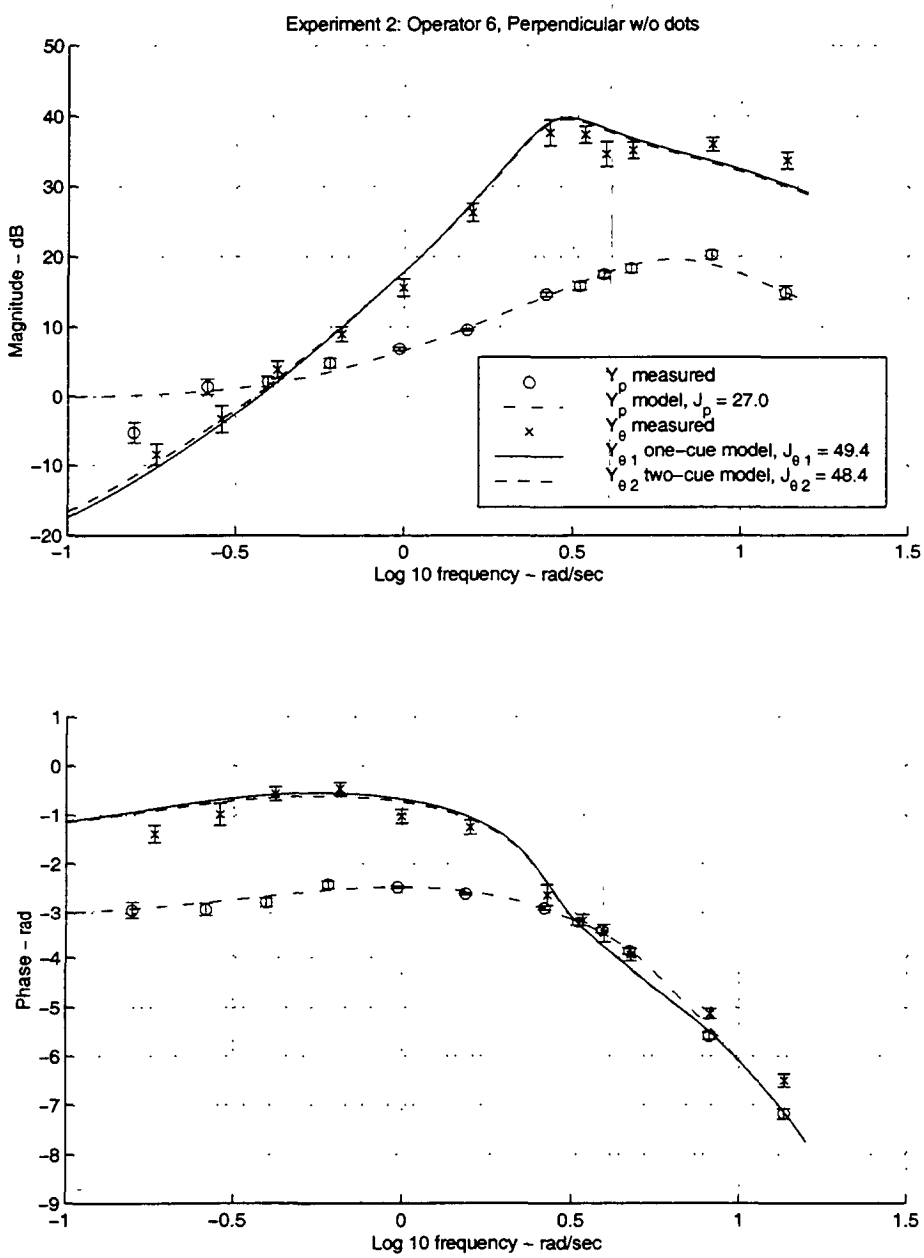

Figure E.22: Experiment 2 model fit results for Operator 6, Perpendicular Texture w/o dots.

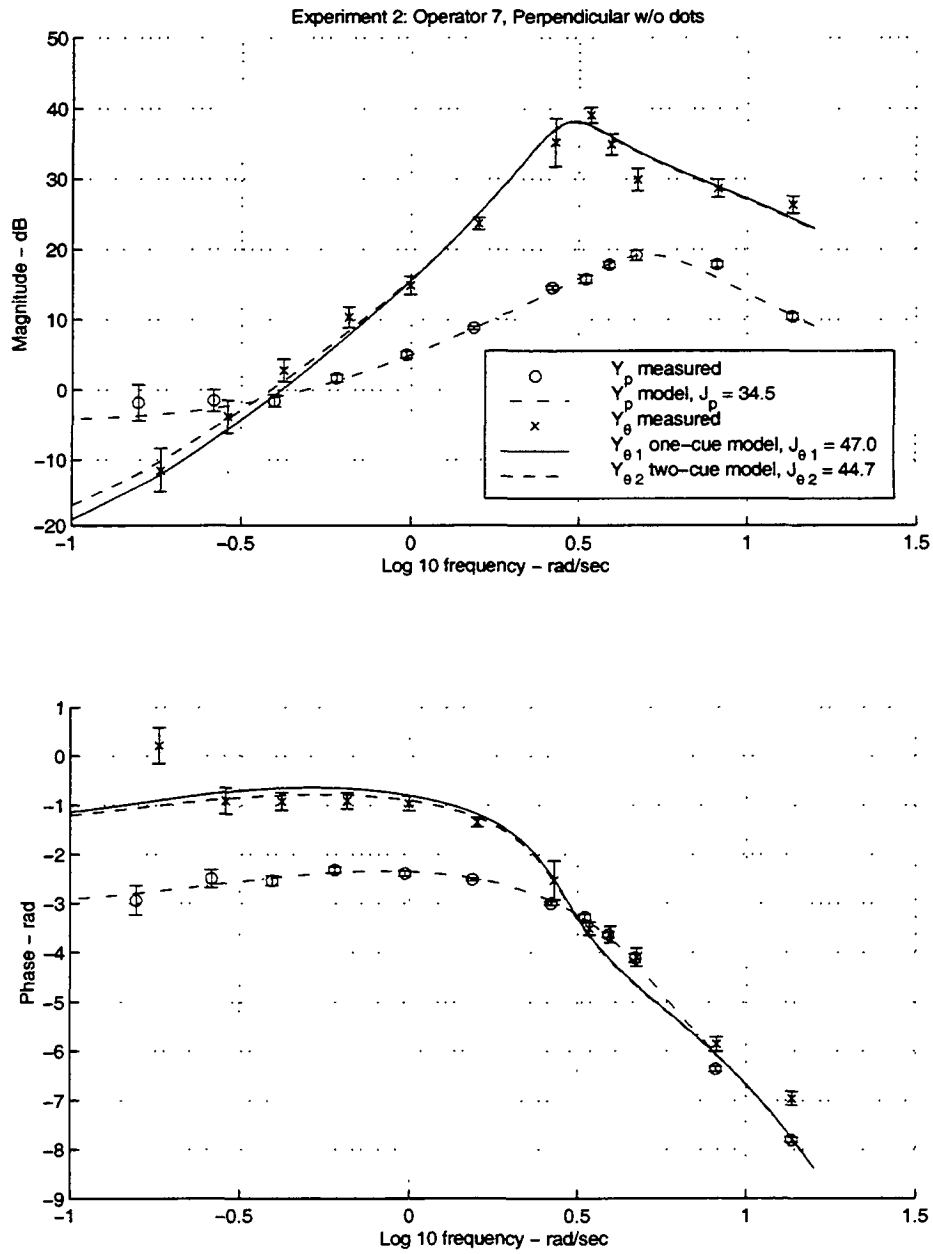

Figure E.23: Experiment 2 model fit results for Operator 7, Perpendicular Texture w/o dots.

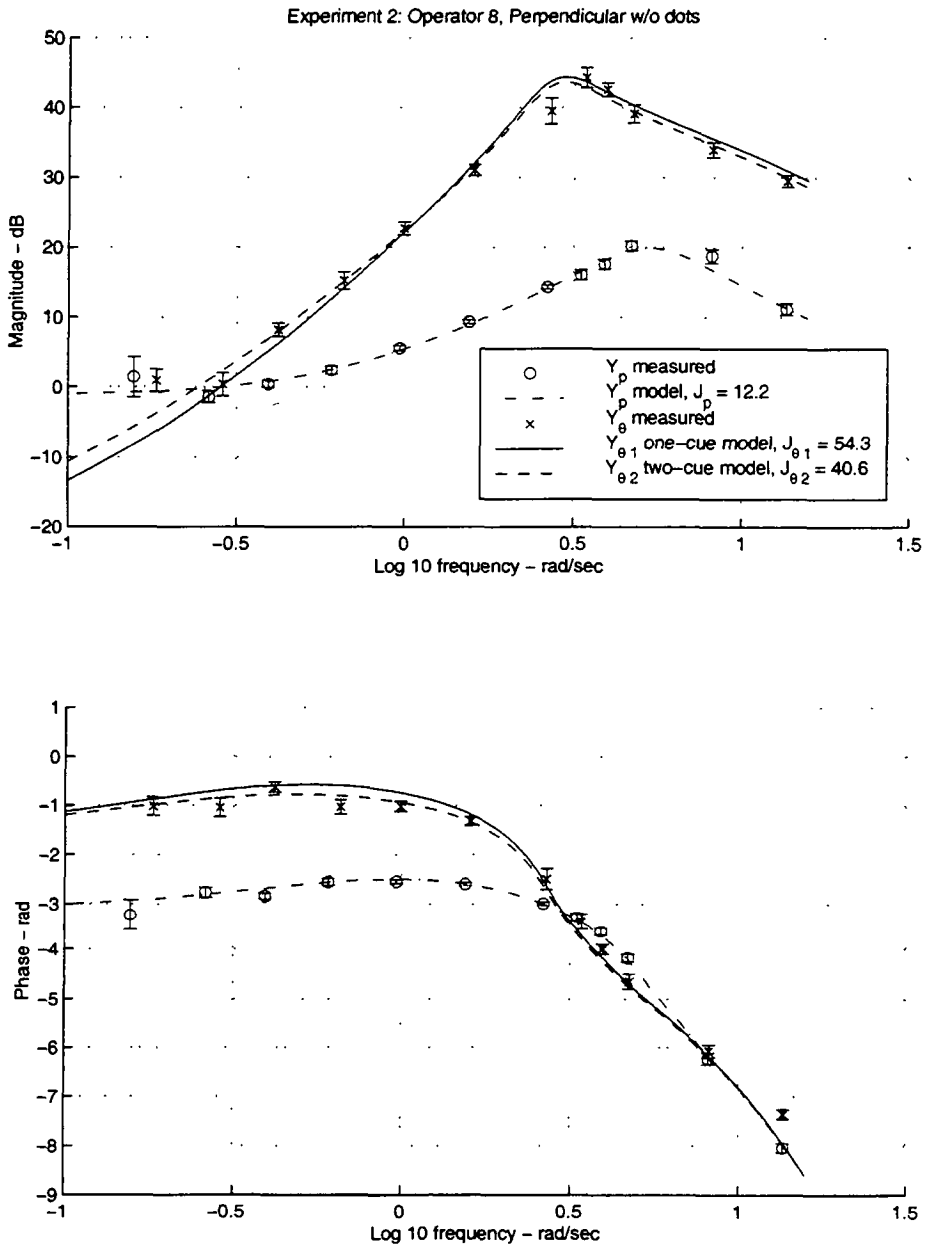

Figure E.24: Experiment 2 model fit results for Operator 8, Perpendicular Texture w/o dots.

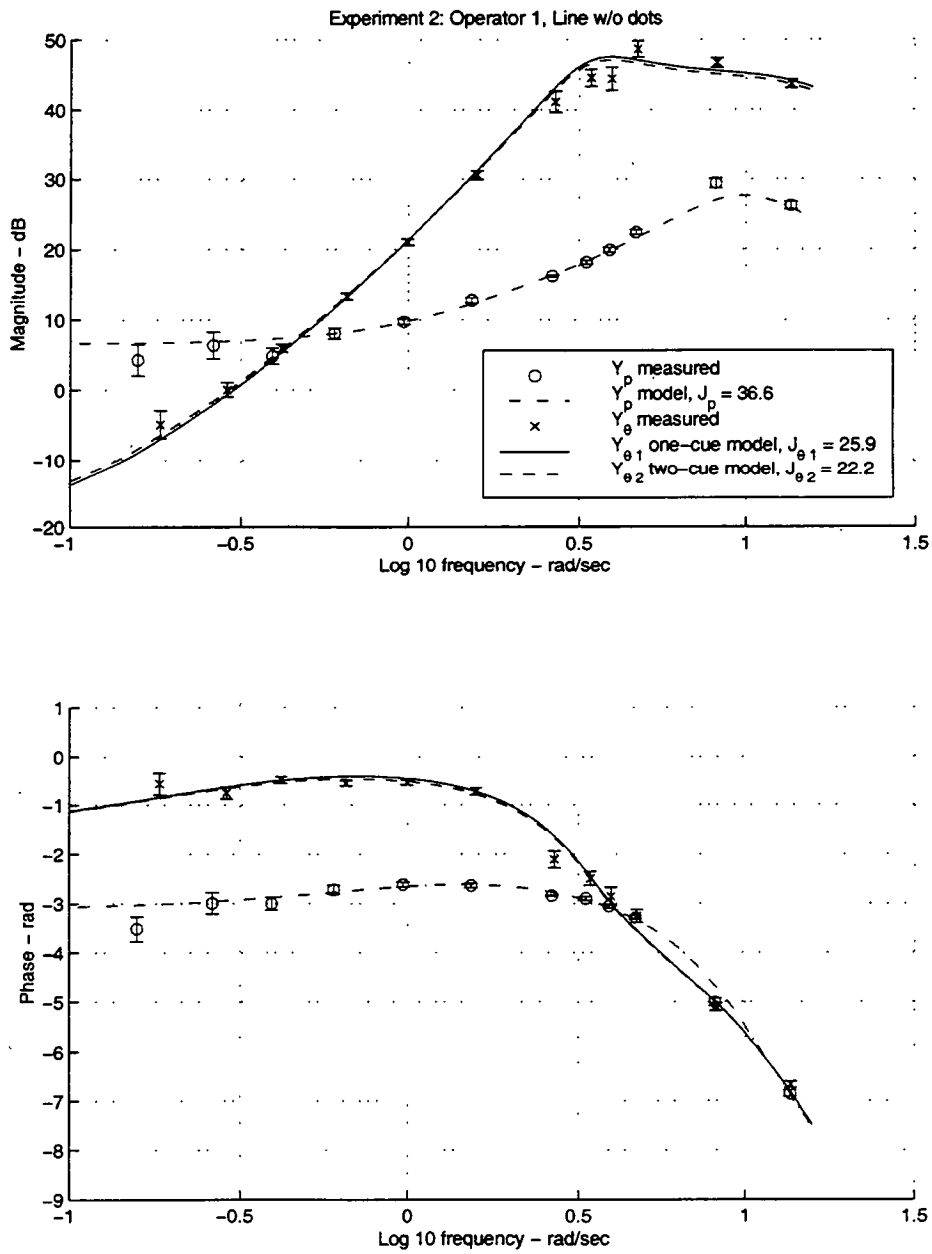

Figure E.25: Experiment 2 model fit results for Operator 1, Line Texture w/o dots.

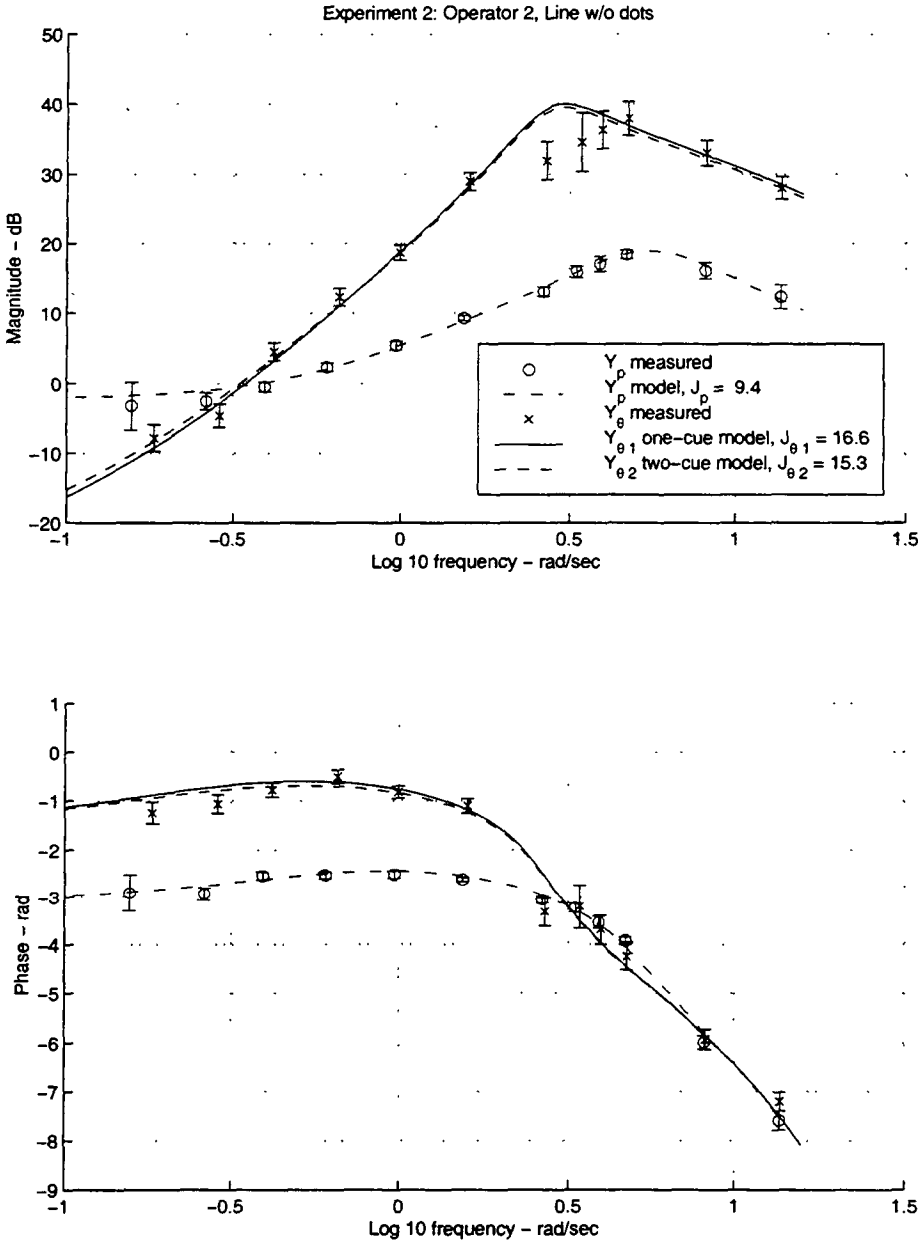

Figure E.26: Experiment 2 model fit results for Operator 2, Line Texture w/o dots.

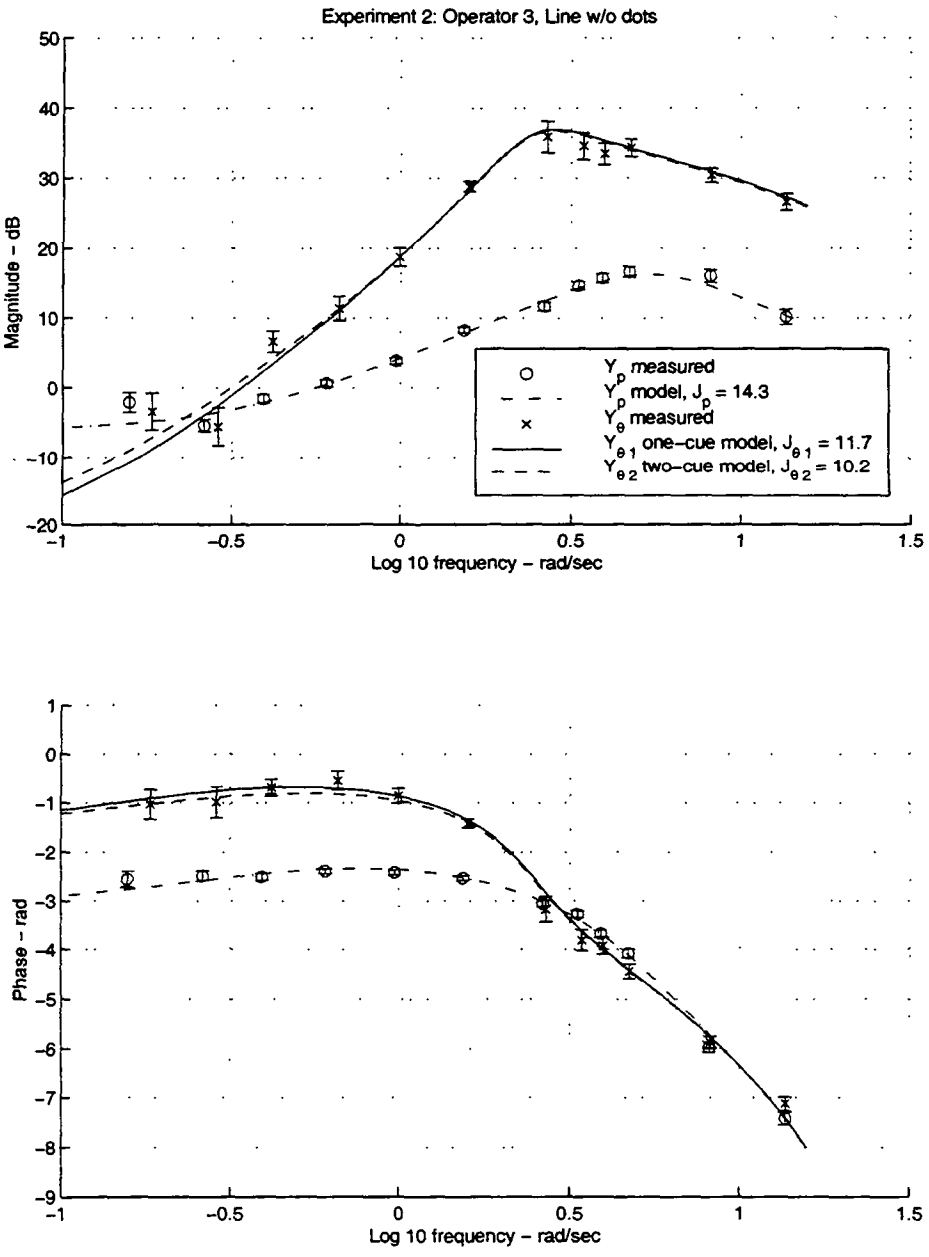

Figure E.27: Experiment 2 model fit results for Operator 3, Line Texture w/o dots.

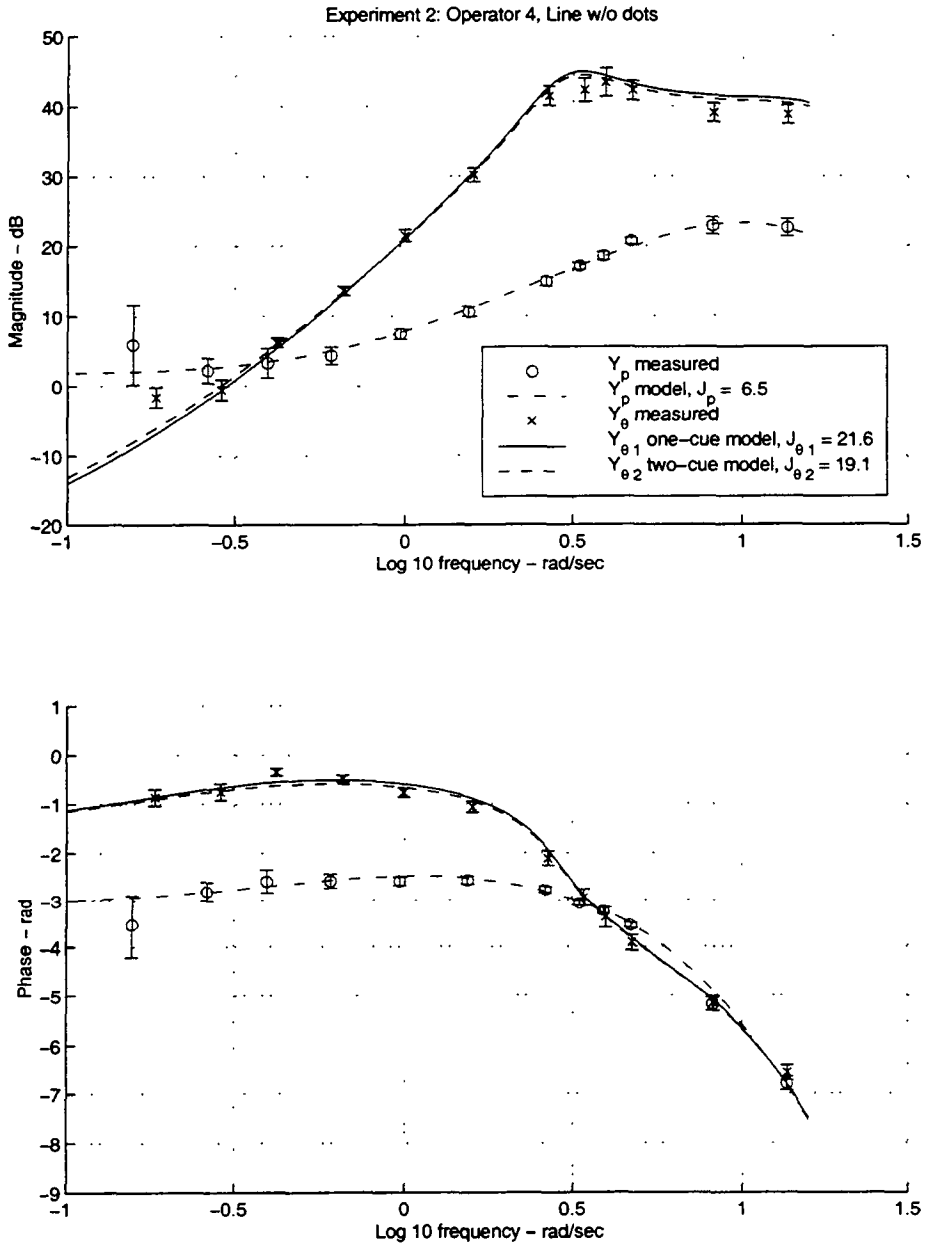

Figure E.28: Experiment 2 model fit results for Operator 4, Line Texture w/o dots.

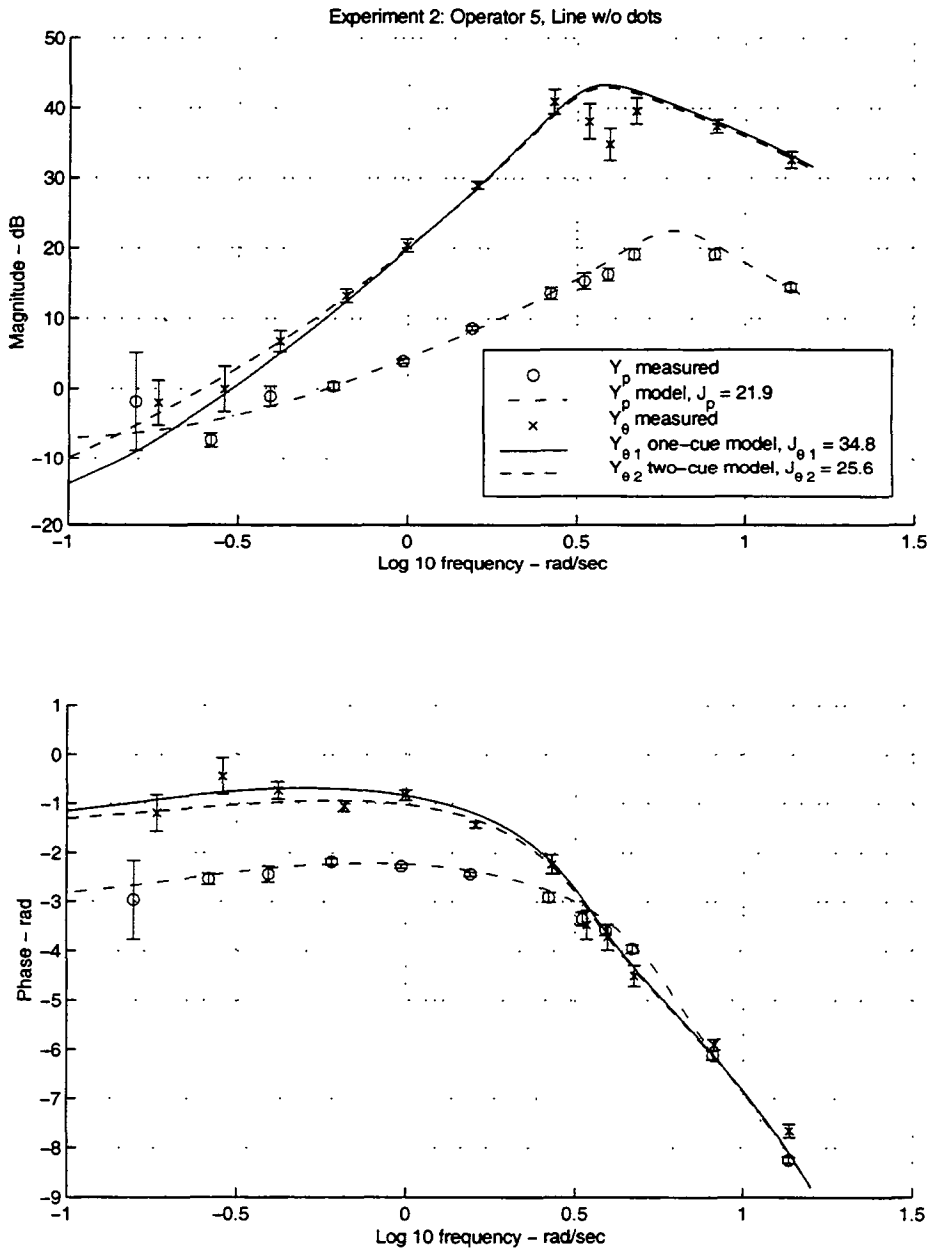

Figure E.29: Experiment 2 model fit results for Operator 5, Line Texture w/o dots.

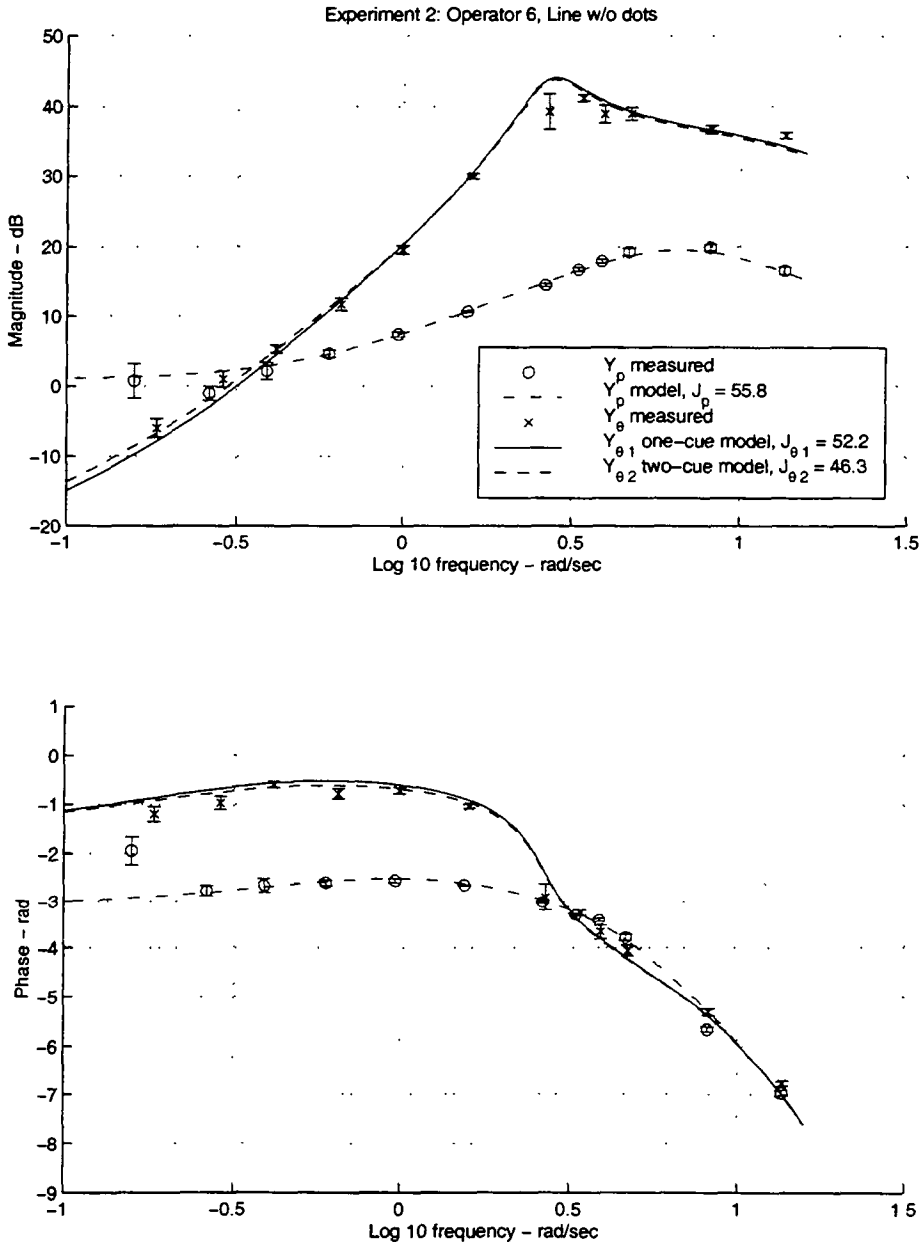

Figure E.30: Experiment 2 model fit results for Operator 6, Line Texture w/o dots.

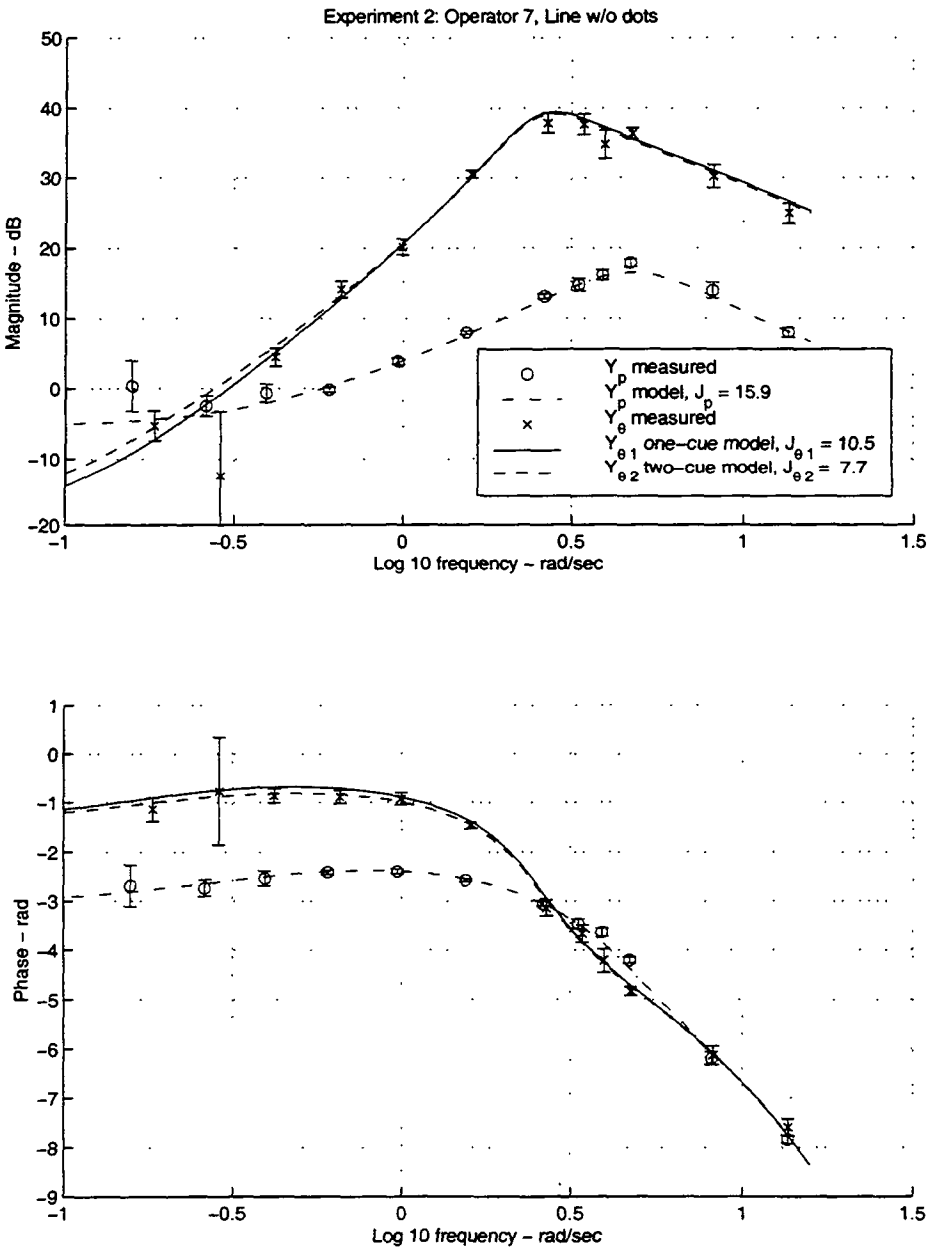

Figure E.31: Experiment 2 model fit results for Operator 7, Line Texture w/o dots.

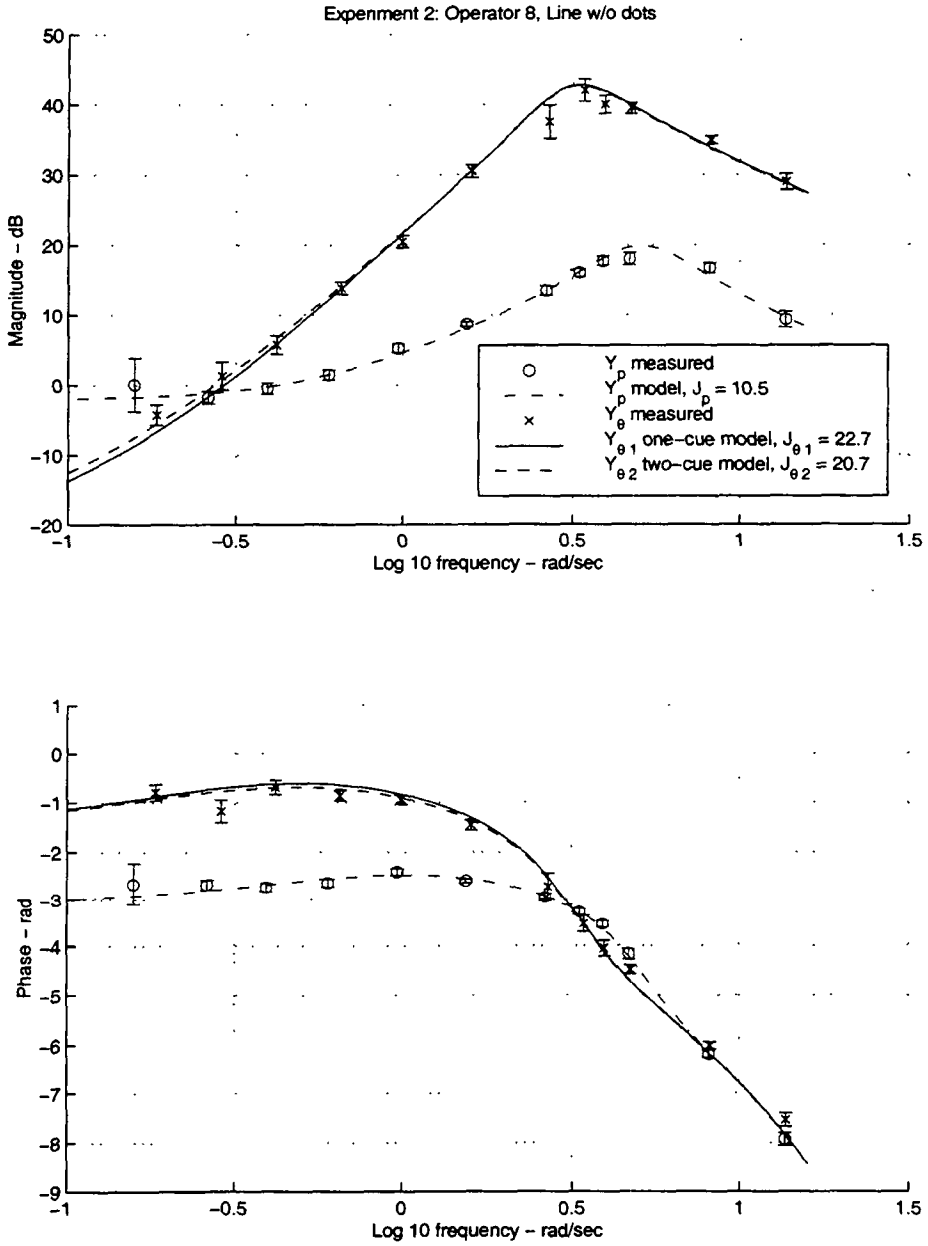

Figure E.32: Experiment 2 model fit results for Operator 8, Line Texture w/o dots.

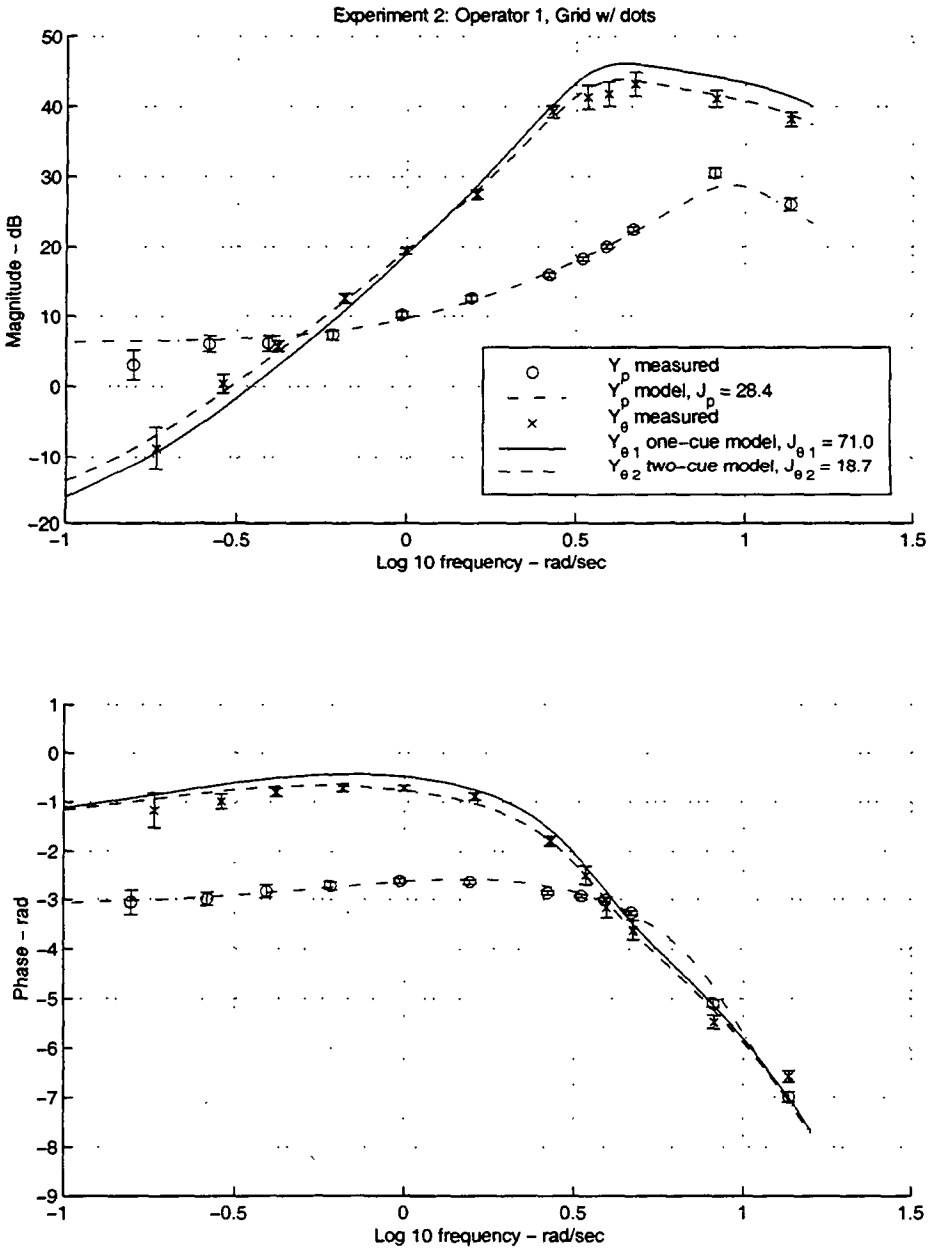

Figure E.33: Experiment 2 model fit results for Operator 1, Grid Texture w/dots.

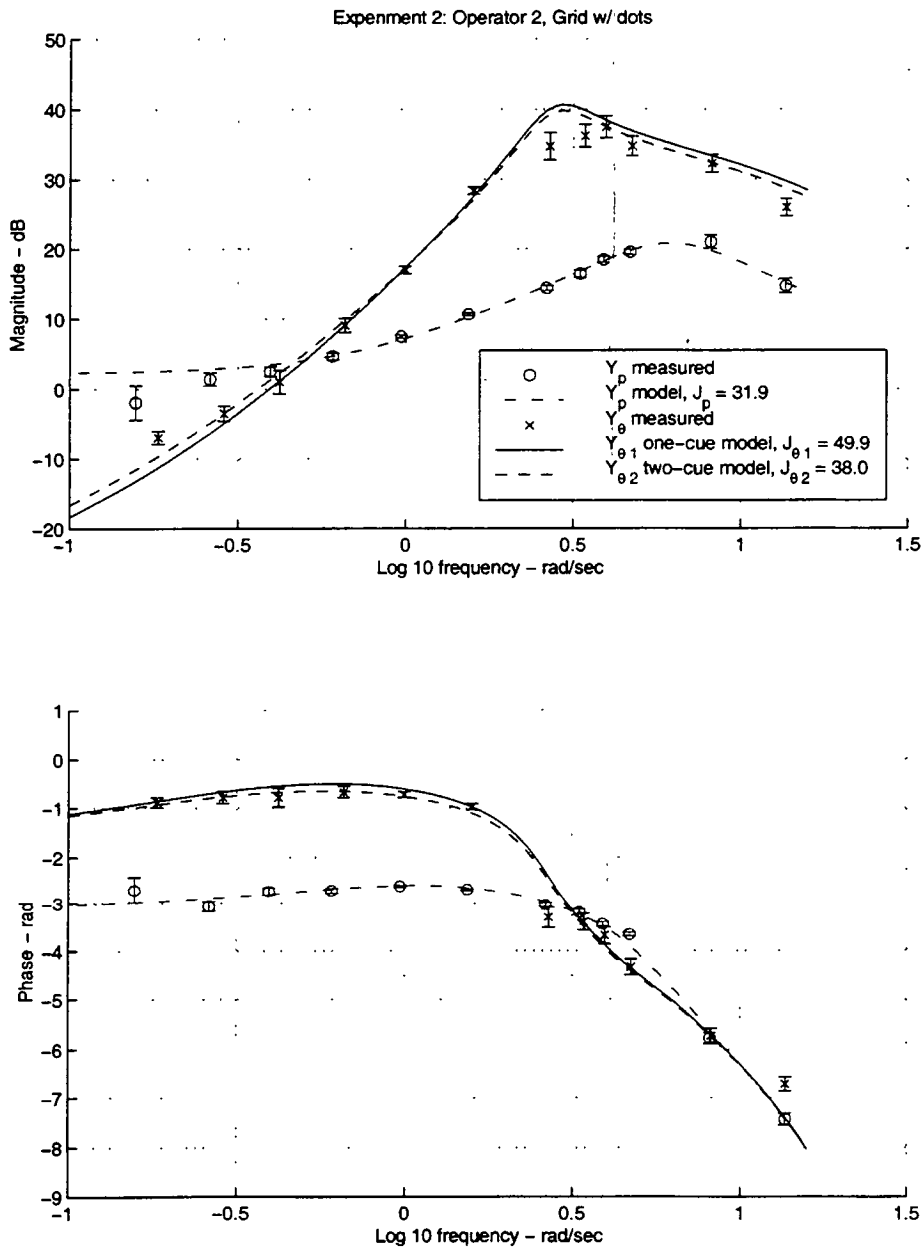

Figure E.34: Experiment 2 model fit results for Operator 2, Grid Texture w/dots.

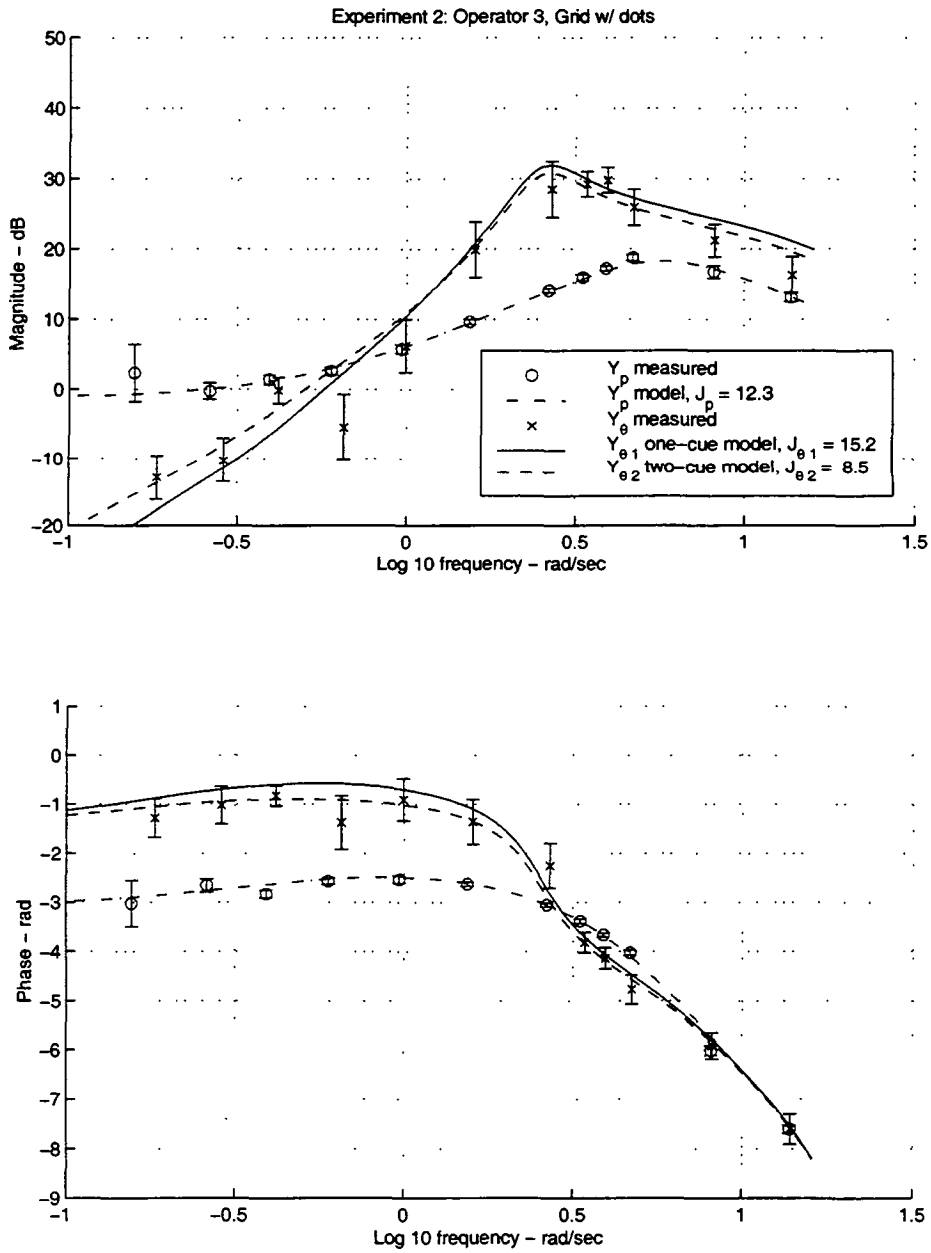

Figure E.35: Experiment 2 model fit results for Operator 3, Grid Texture w/dots.

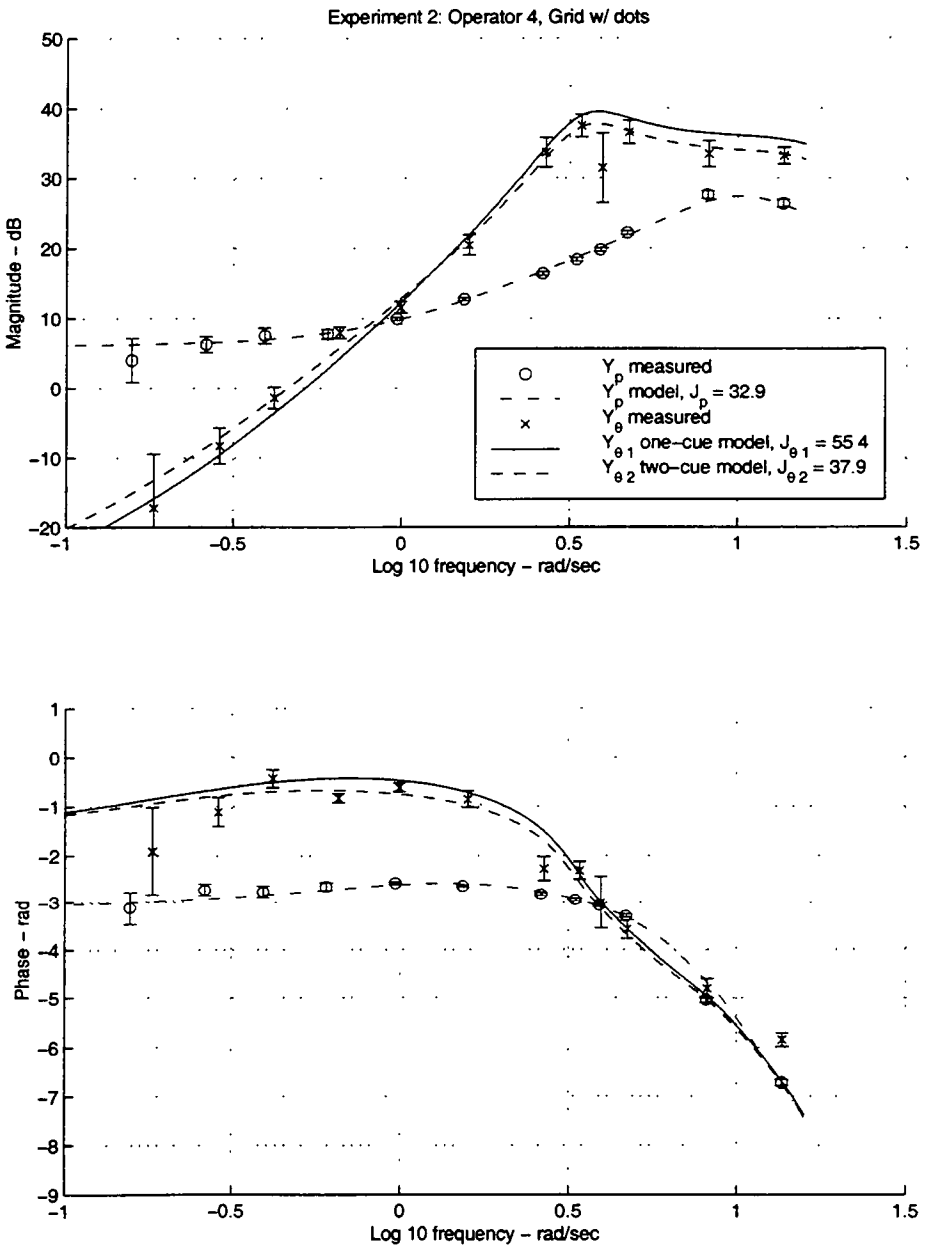

Figure E.36: Experiment 2 model fit results for Operator 4, Grid Texture w/dots.

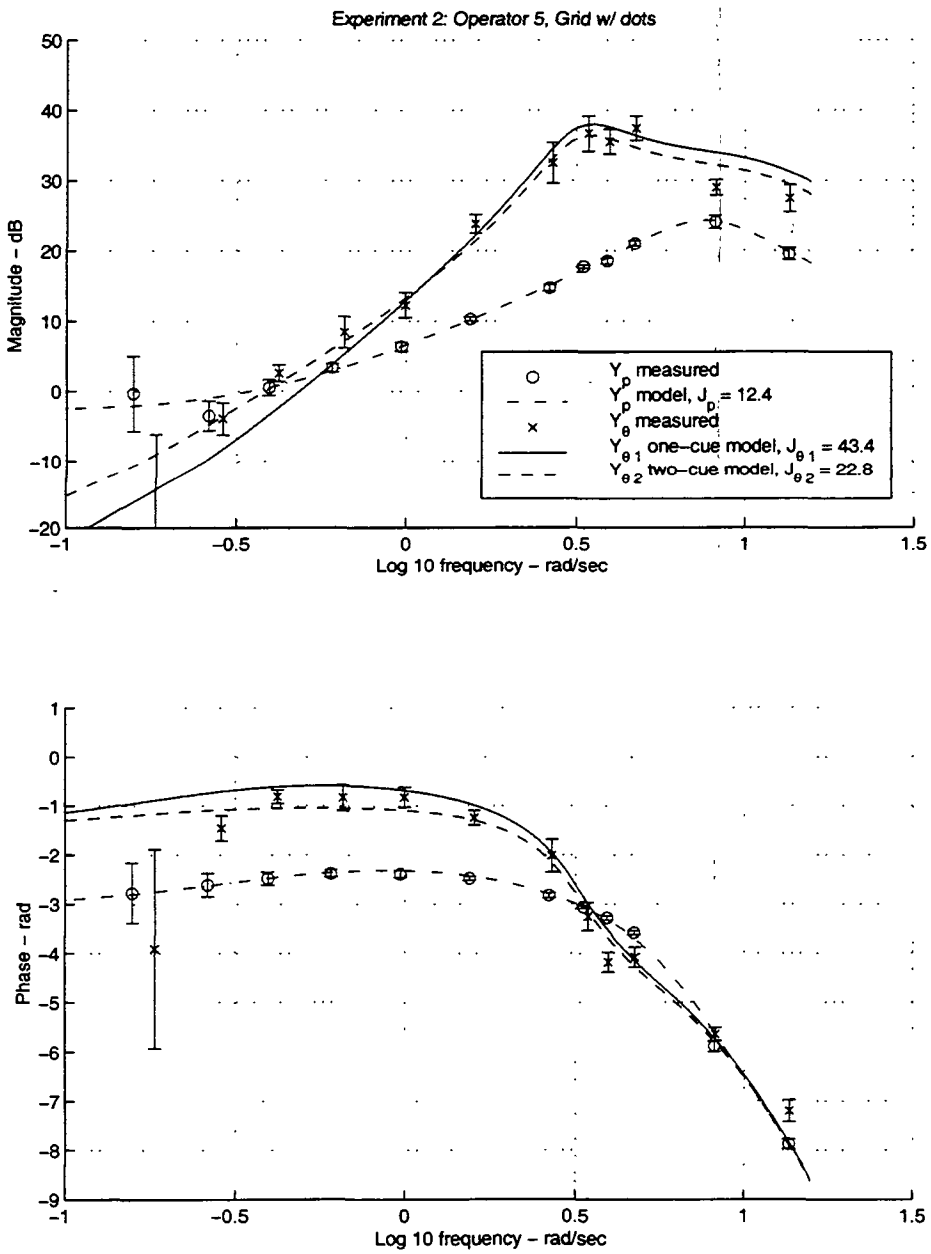

Figure E.37: Experiment 2 model fit results for Operator 5, Grid Texture w/dots.

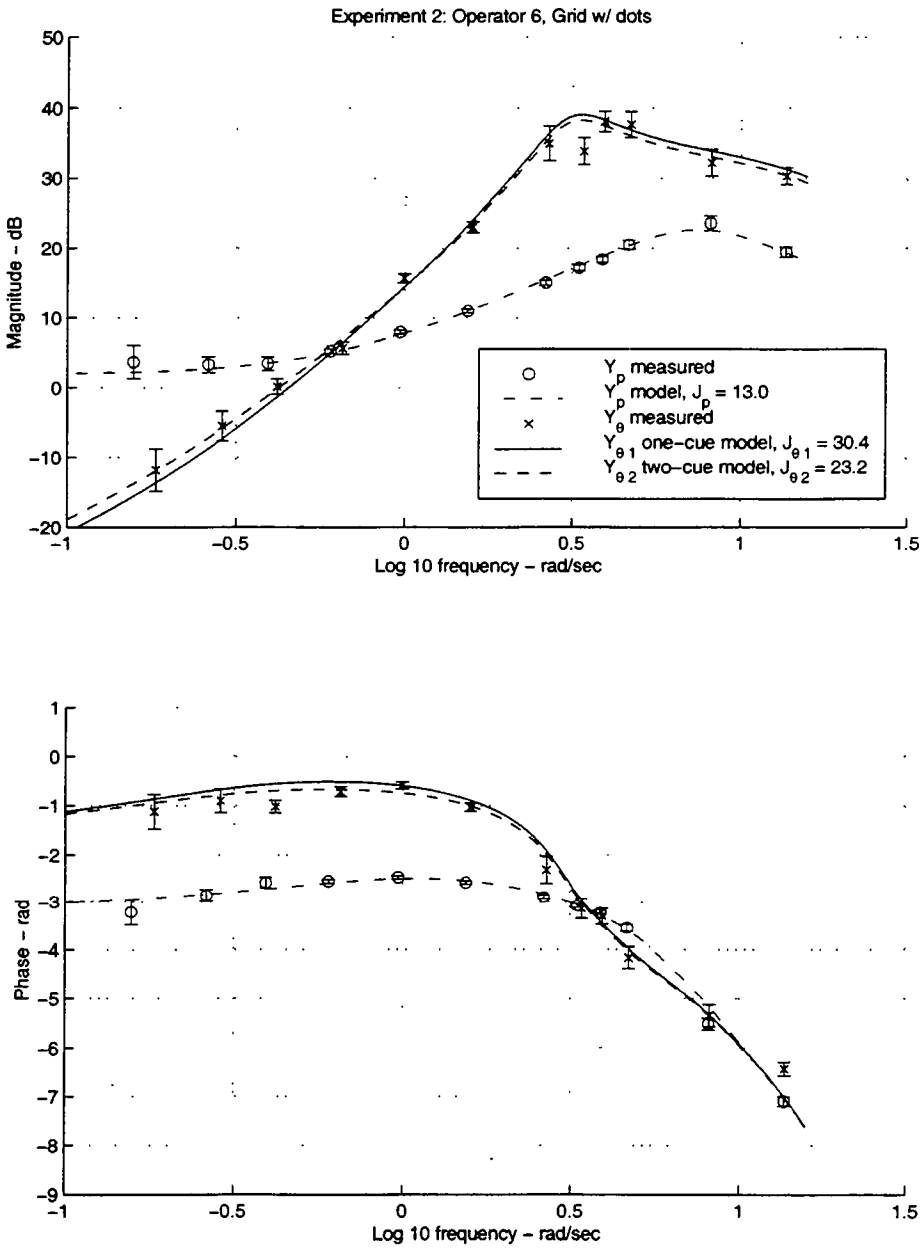

Figure E.38: Experiment 2 model fit results for Operator 6, Grid Texture w/dots.

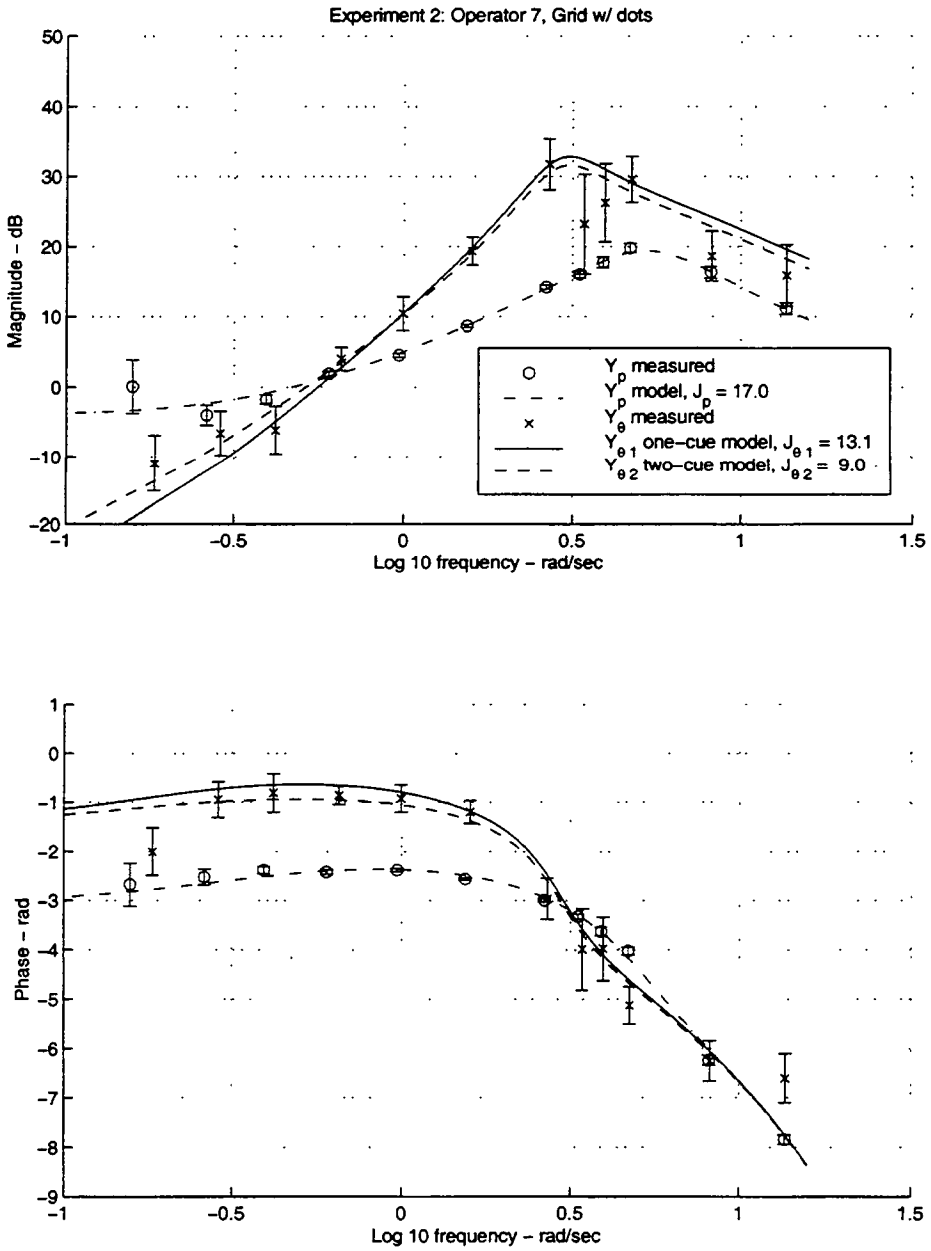

Figure E.39: Experiment 2 model fit results for Operator 7, Grid Texture w/dots.

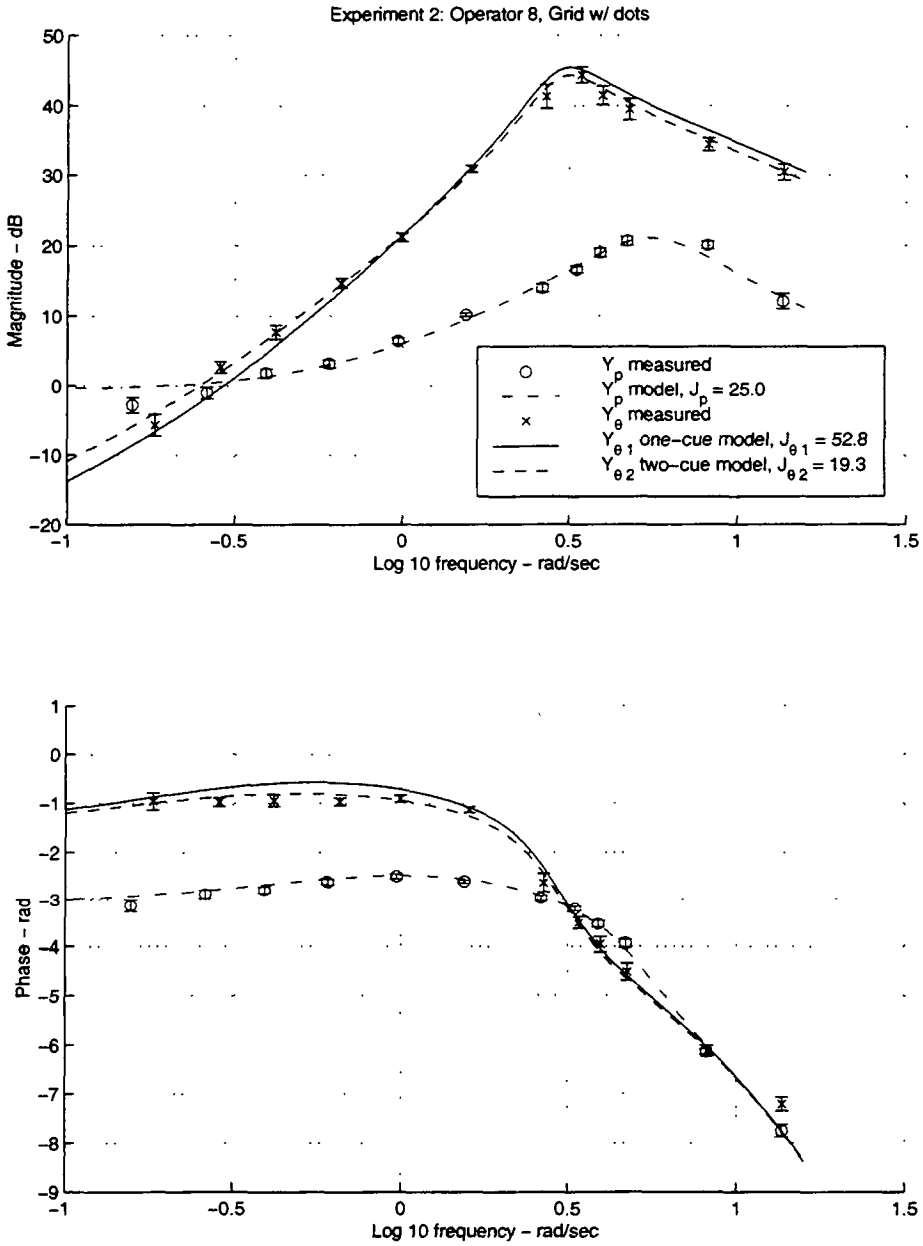

Figure E.40: Experiment 2 model fit results for Operator 8, Grid Texture w/dots.

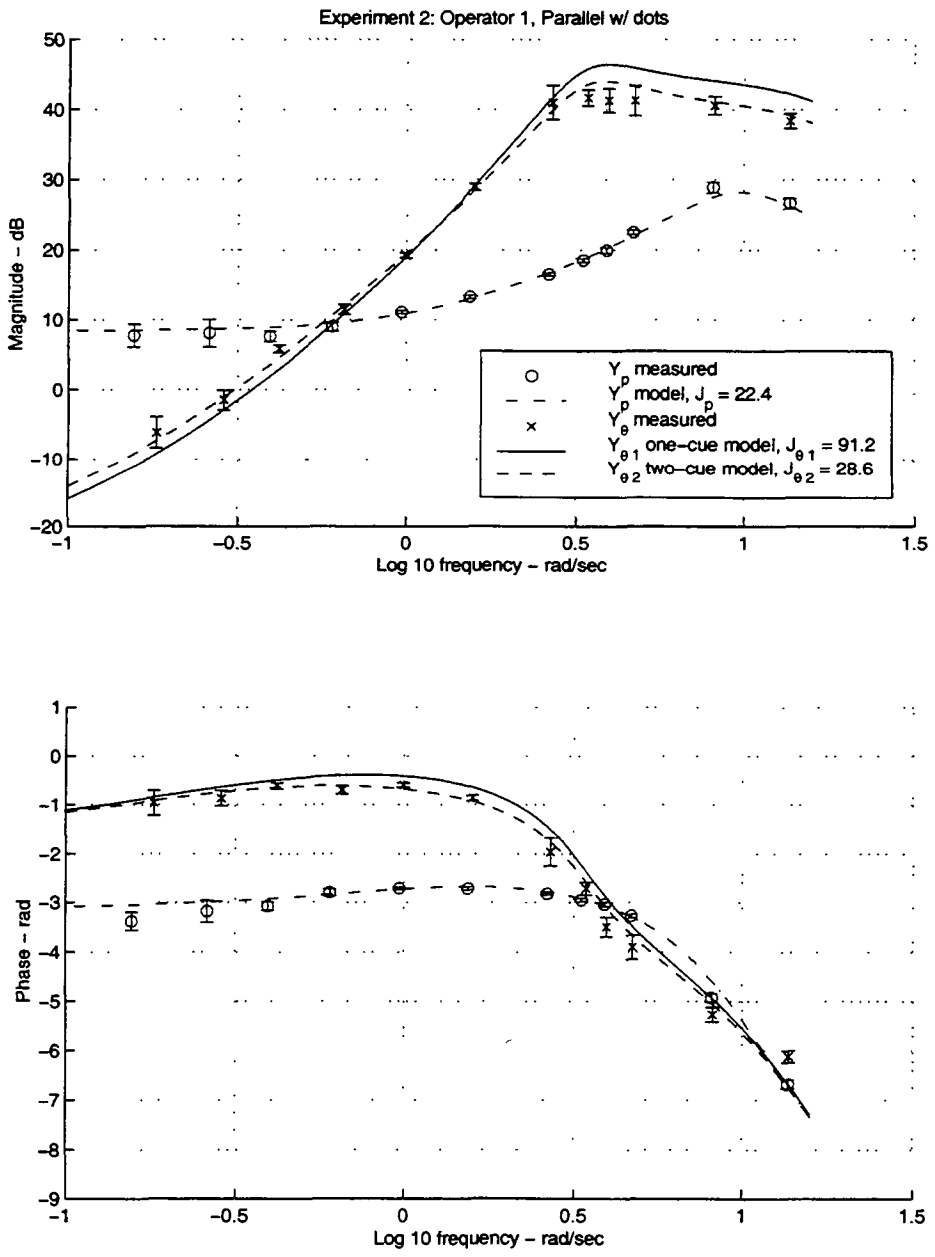

Figure E.41: Experiment 2 model fit results for Operator 1, Parallel Texture w/dots.

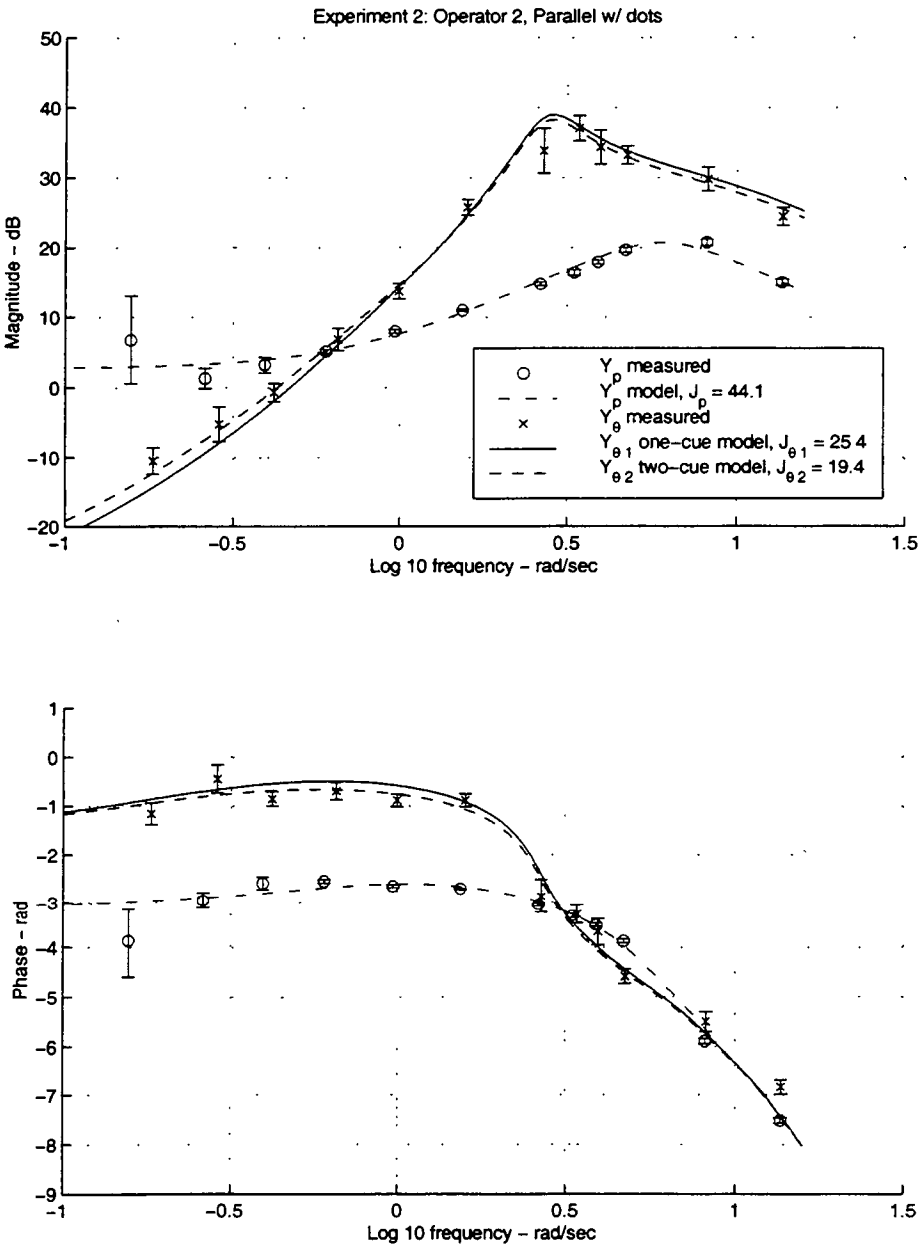

Figure E.42: Experiment 2 model fit results for Operator 2, Parallel Texture w/dots.

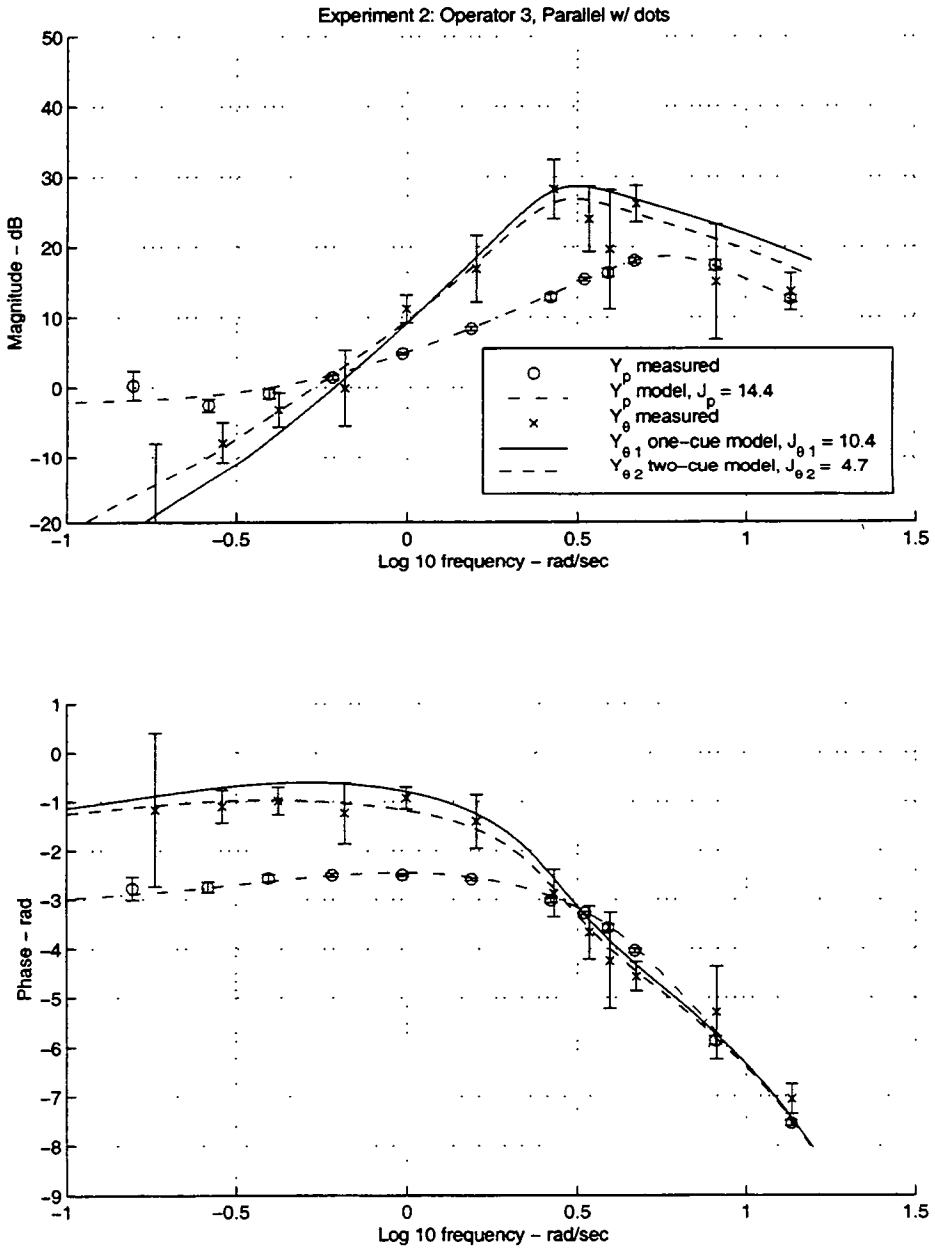

Figure E.43: Experiment 2 model fit results for Operator 3, Parallel Texture w/dots.

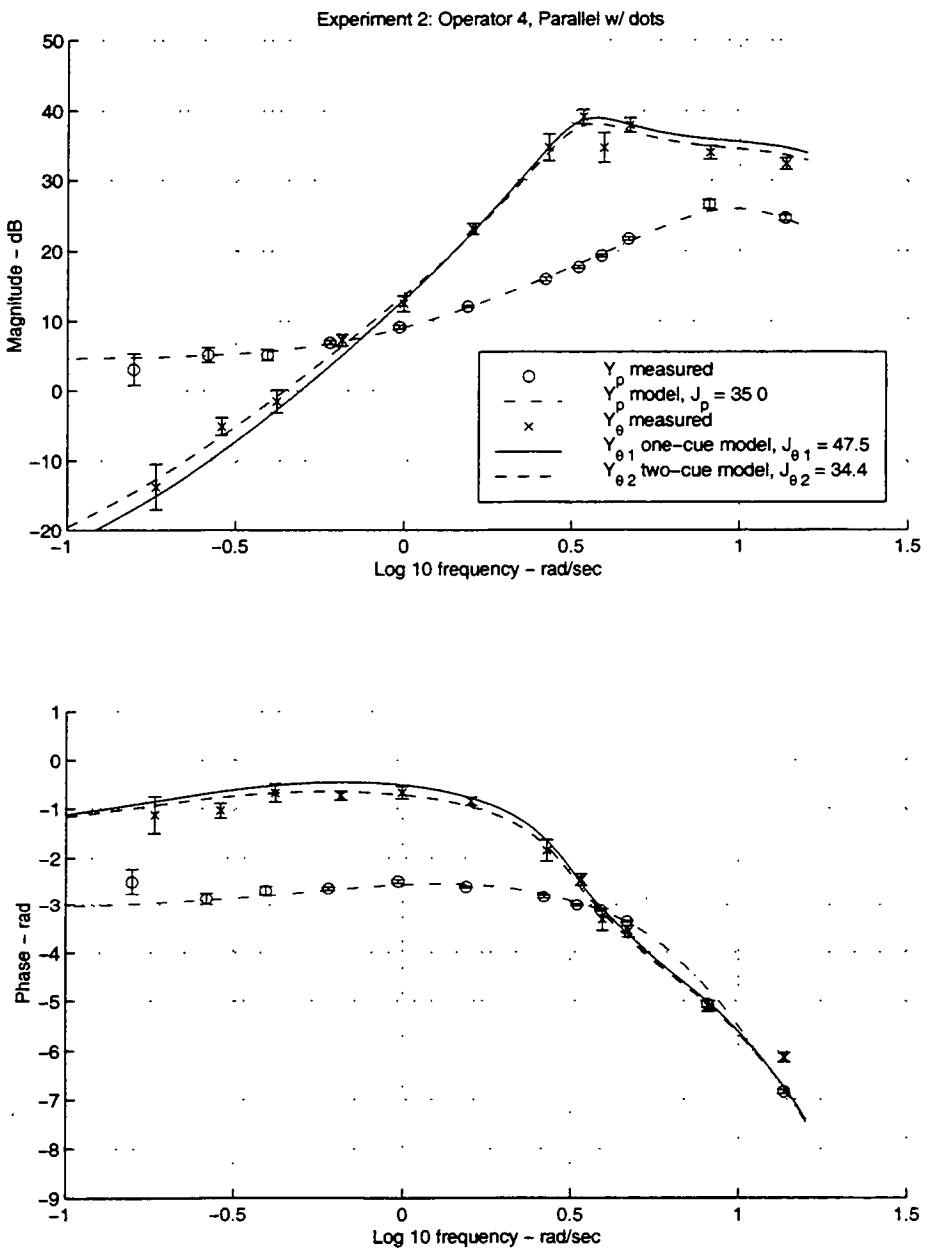

Figure E.44: Experiment 2 model fit results for Operator 4, Parallel Texture w/dots.

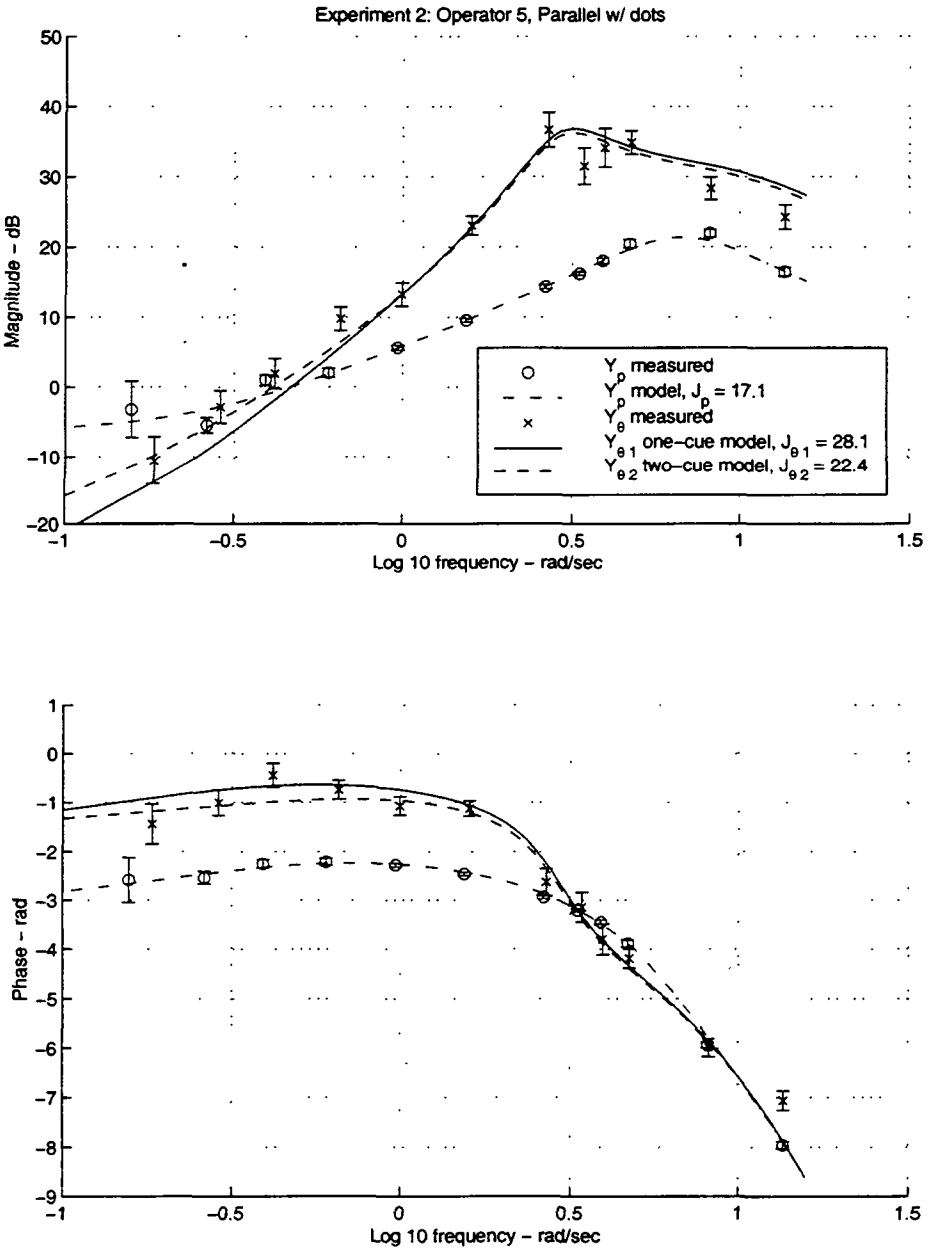

Figure E.45: Experiment 2 model fit results for Operator 5, Parallel Texture w/dots.

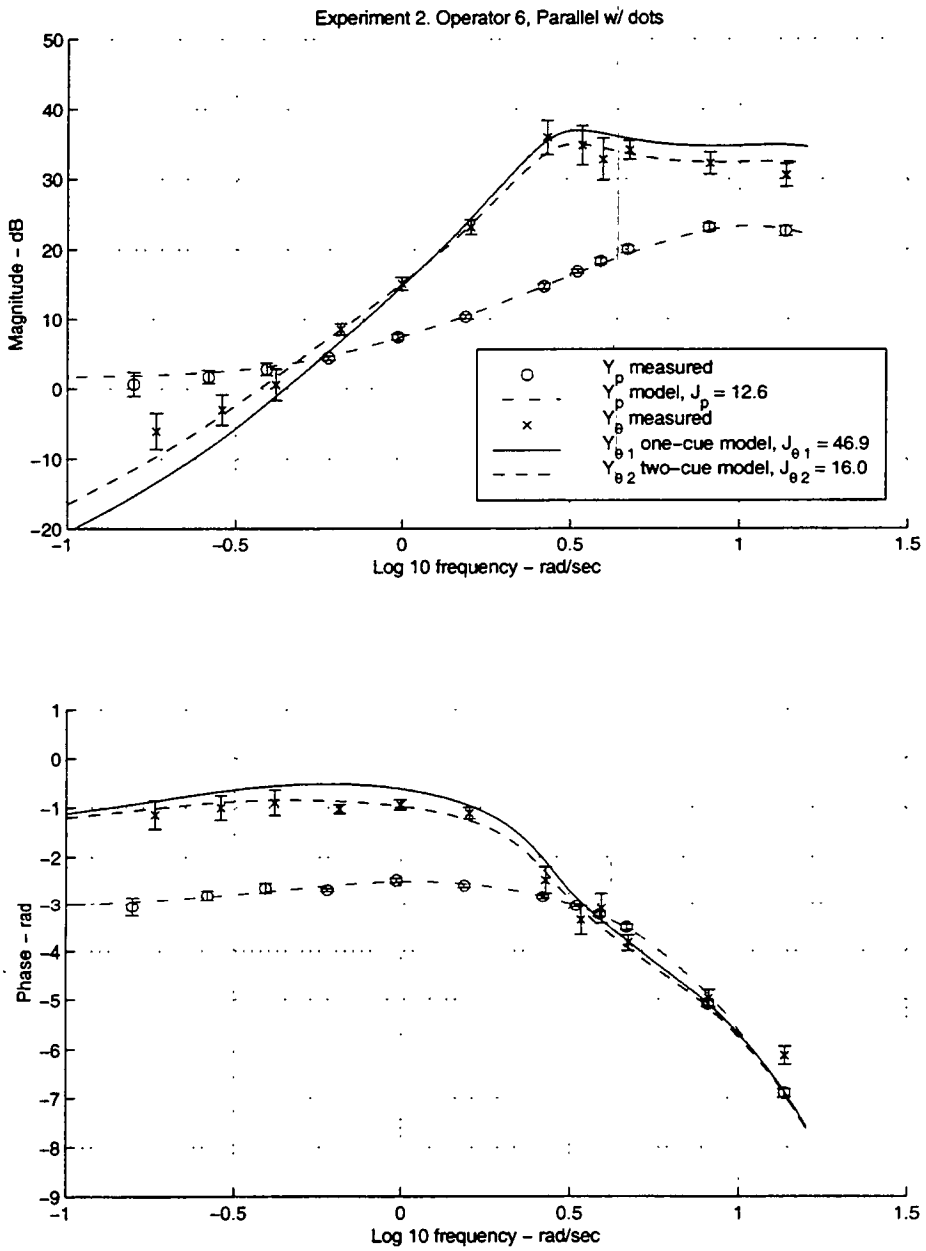

Figure E.46: Experiment 2 model fit results for Operator 6, Parallel Texture w/dots.

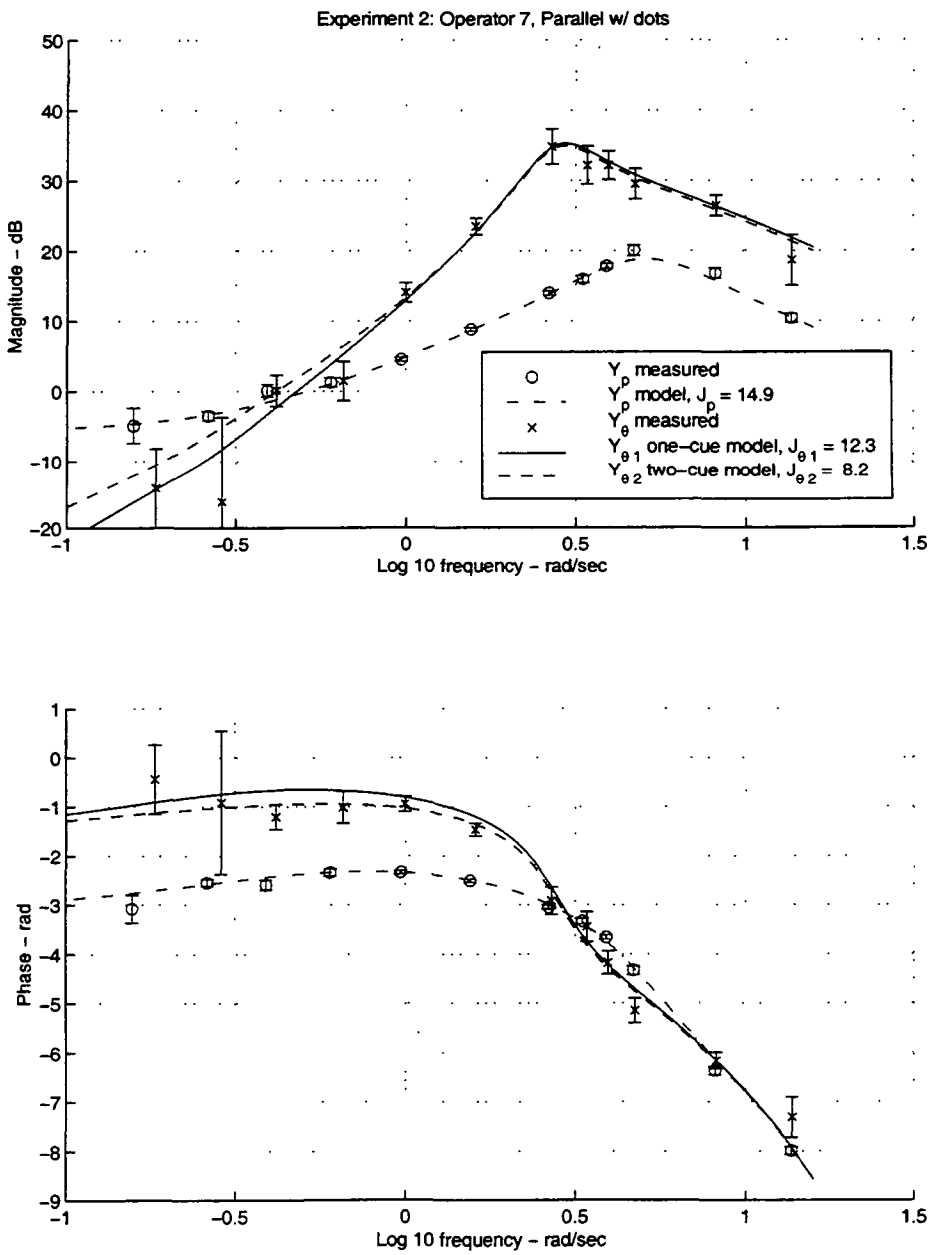

Figure E.47: Experiment 2 model fit results for Operator 7, Parallel Texture w/dots.

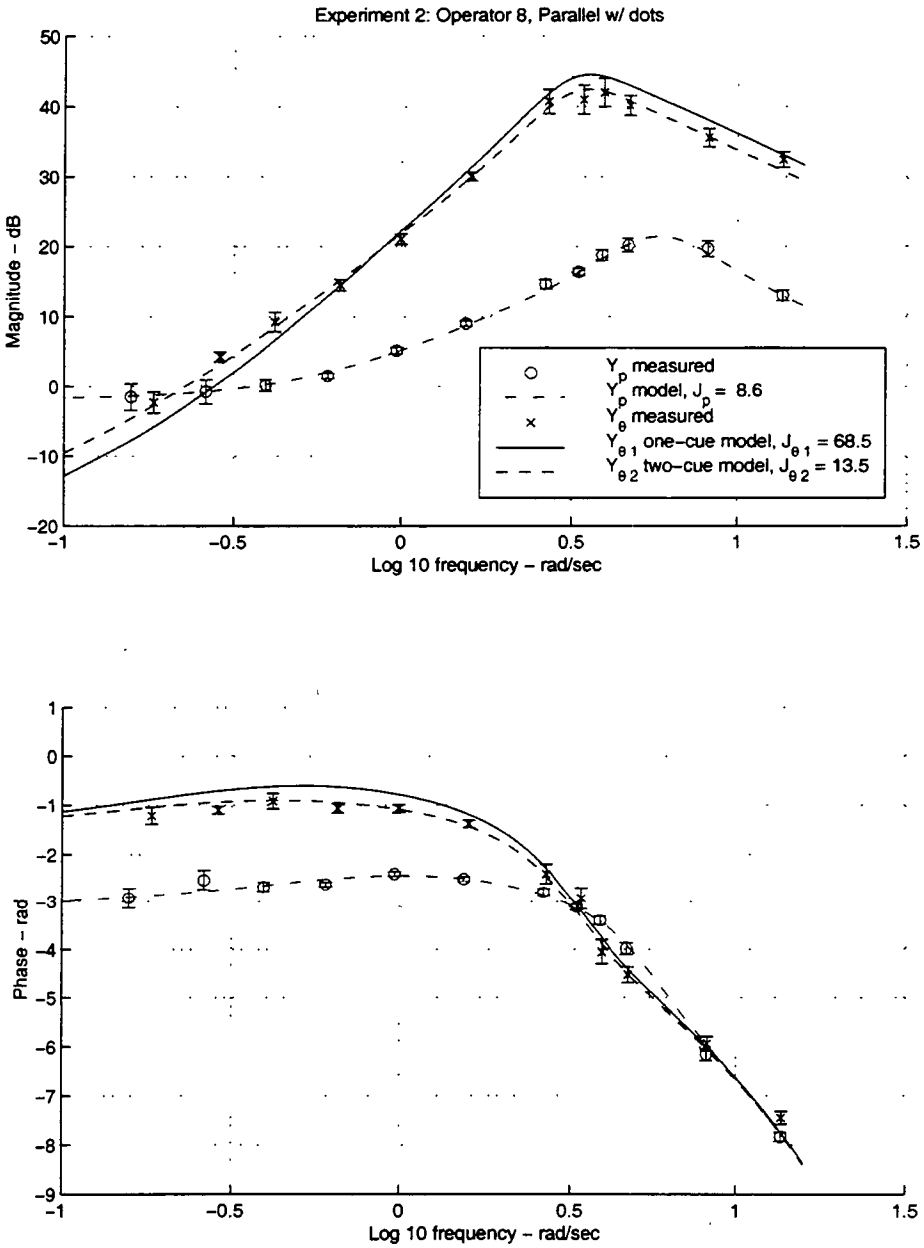

Figure E.48: Experiment 2 model fit results for Operator 8, Parallel Texture w/dots.

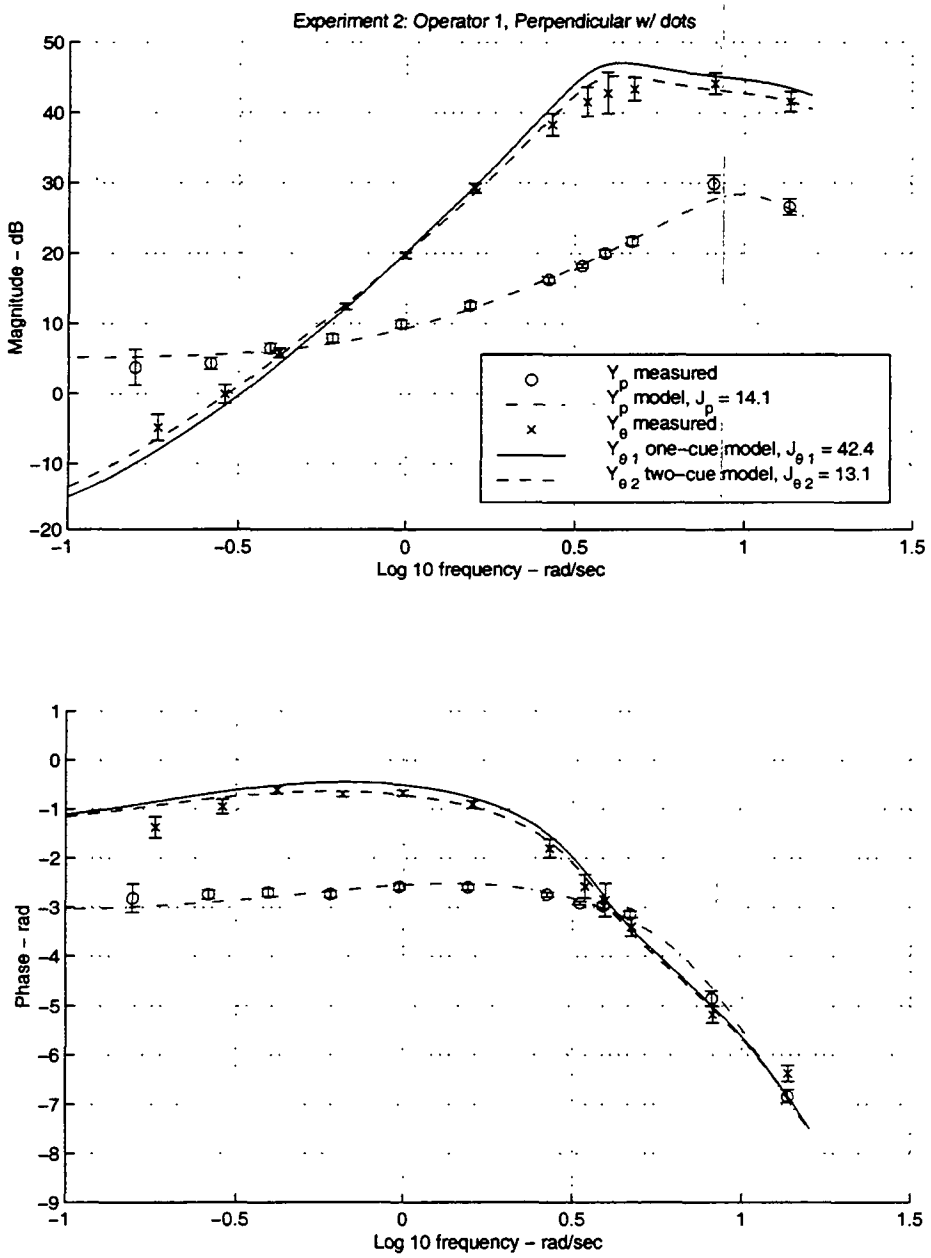

Figure E.49: Experiment 2 model fit results for Operator 1, Perpendicular Texture w/dots.

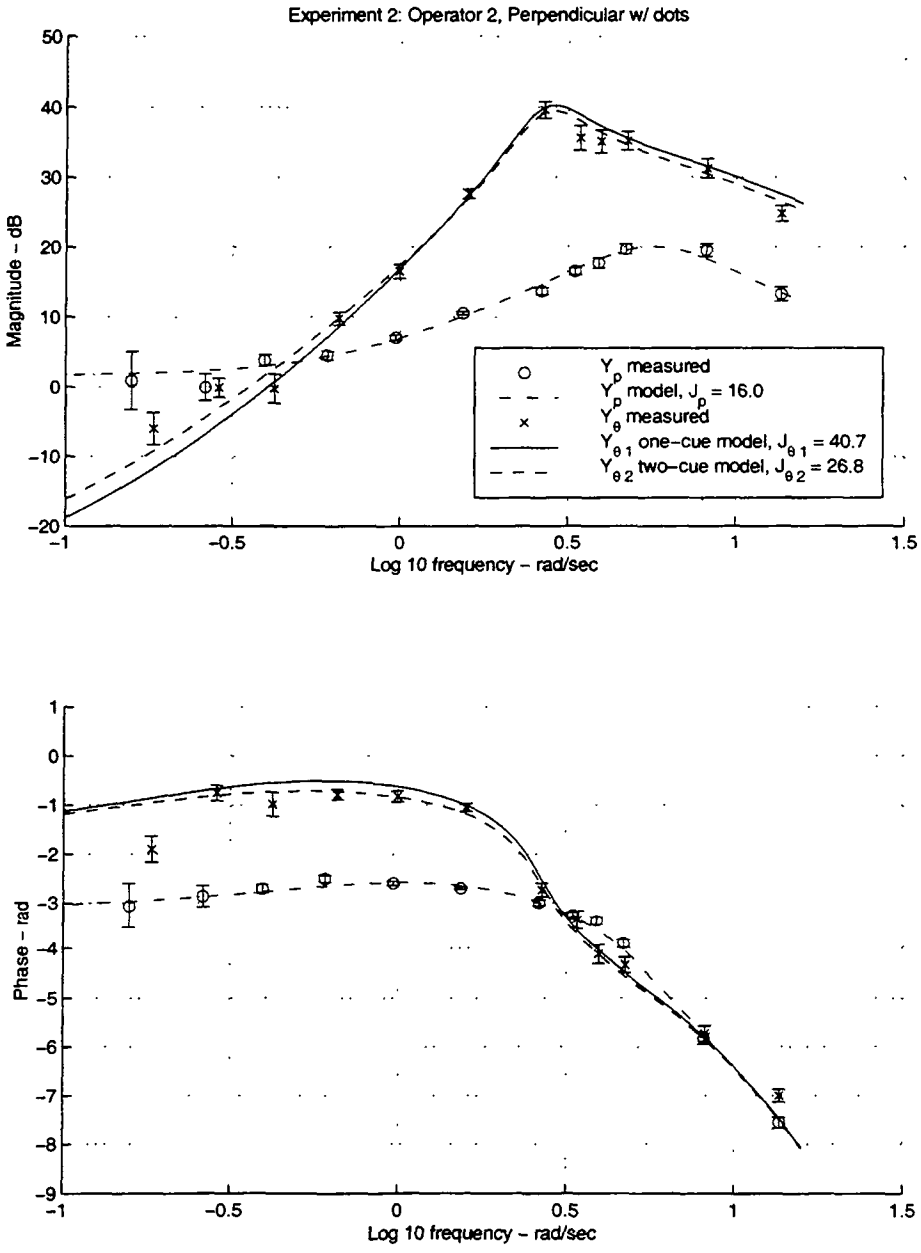

Figure E.50: Experiment 2 model fit results for Operator 2, Perpendicular Texture w/dots.

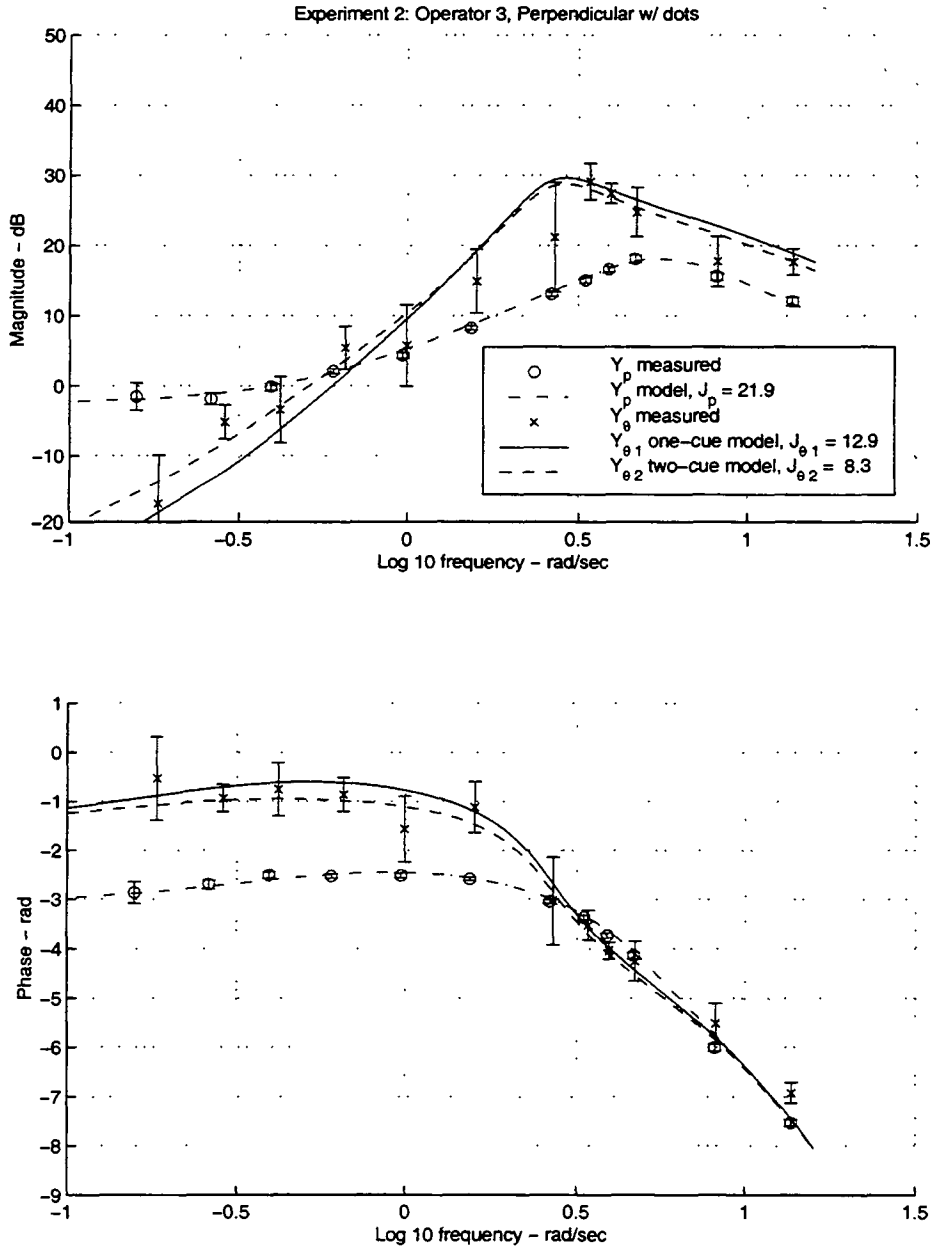

Figure E.51: Experiment 2 model fit results for Operator 3, Perpendicular Texture w/dots.

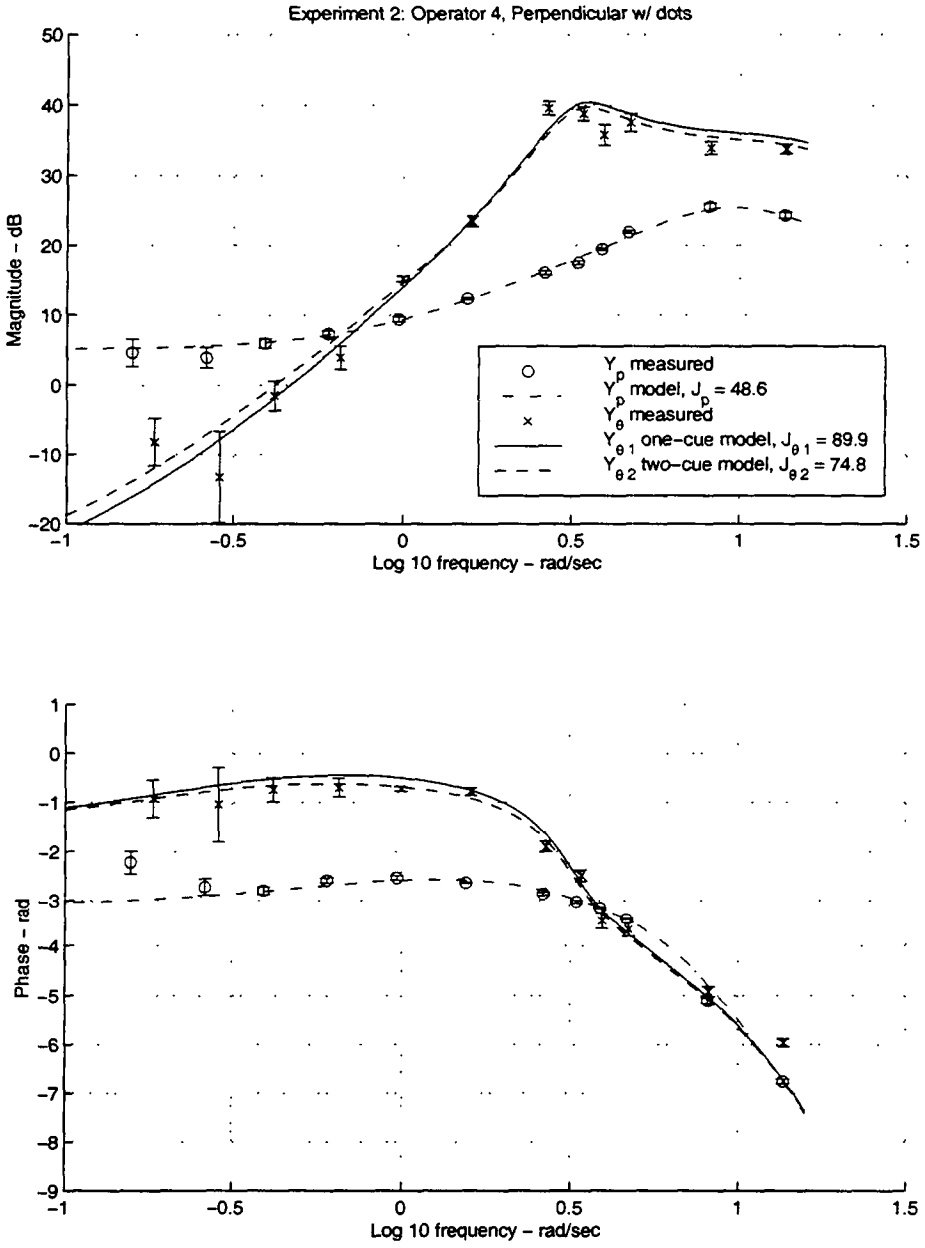

Figure E.52: Experiment 2 model fit results for Operator 4, Perpendicular Texture w/dots.

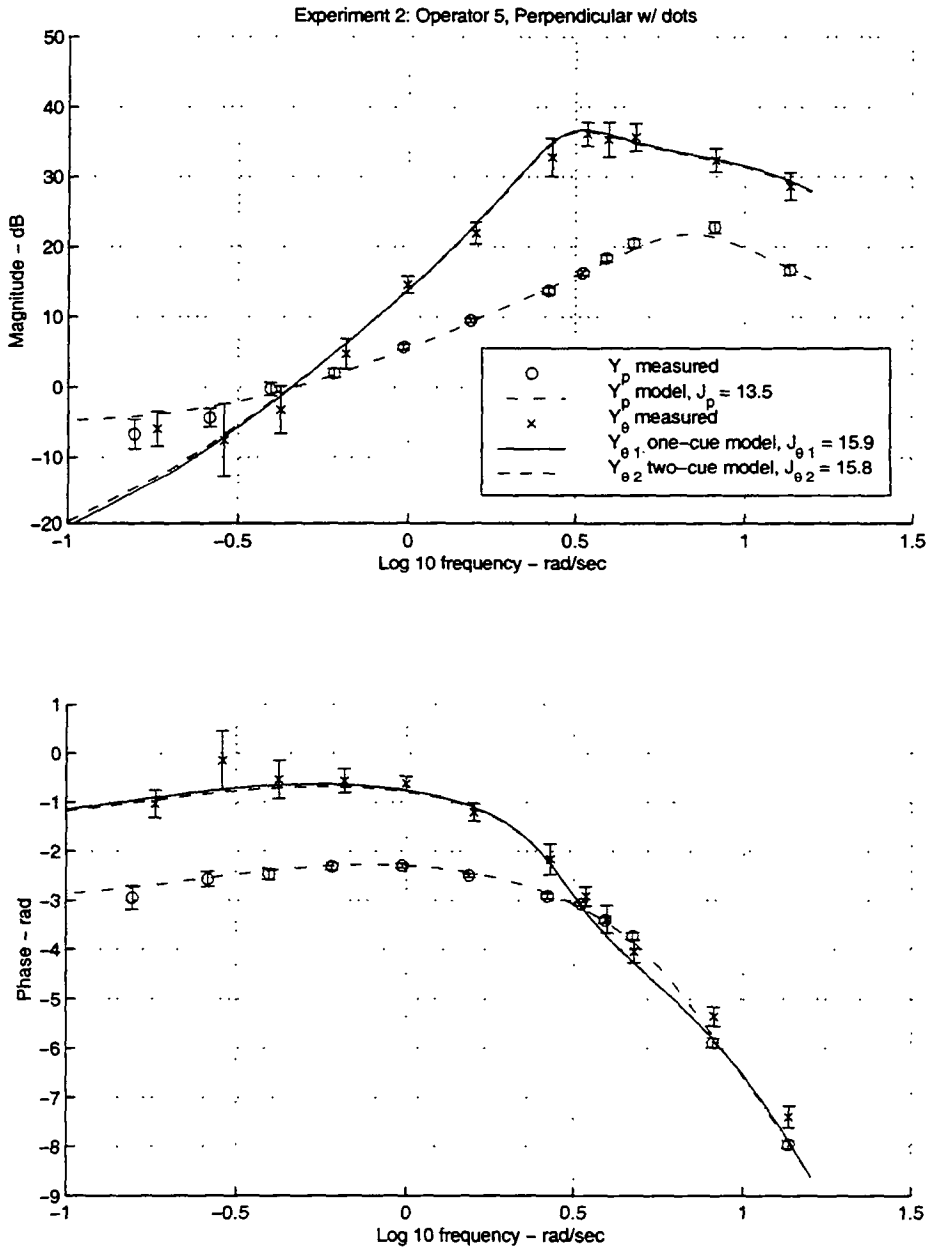

Figure E.53: Experiment 2 model fit results for Operator 5, Perpendicular Texture w/dots.

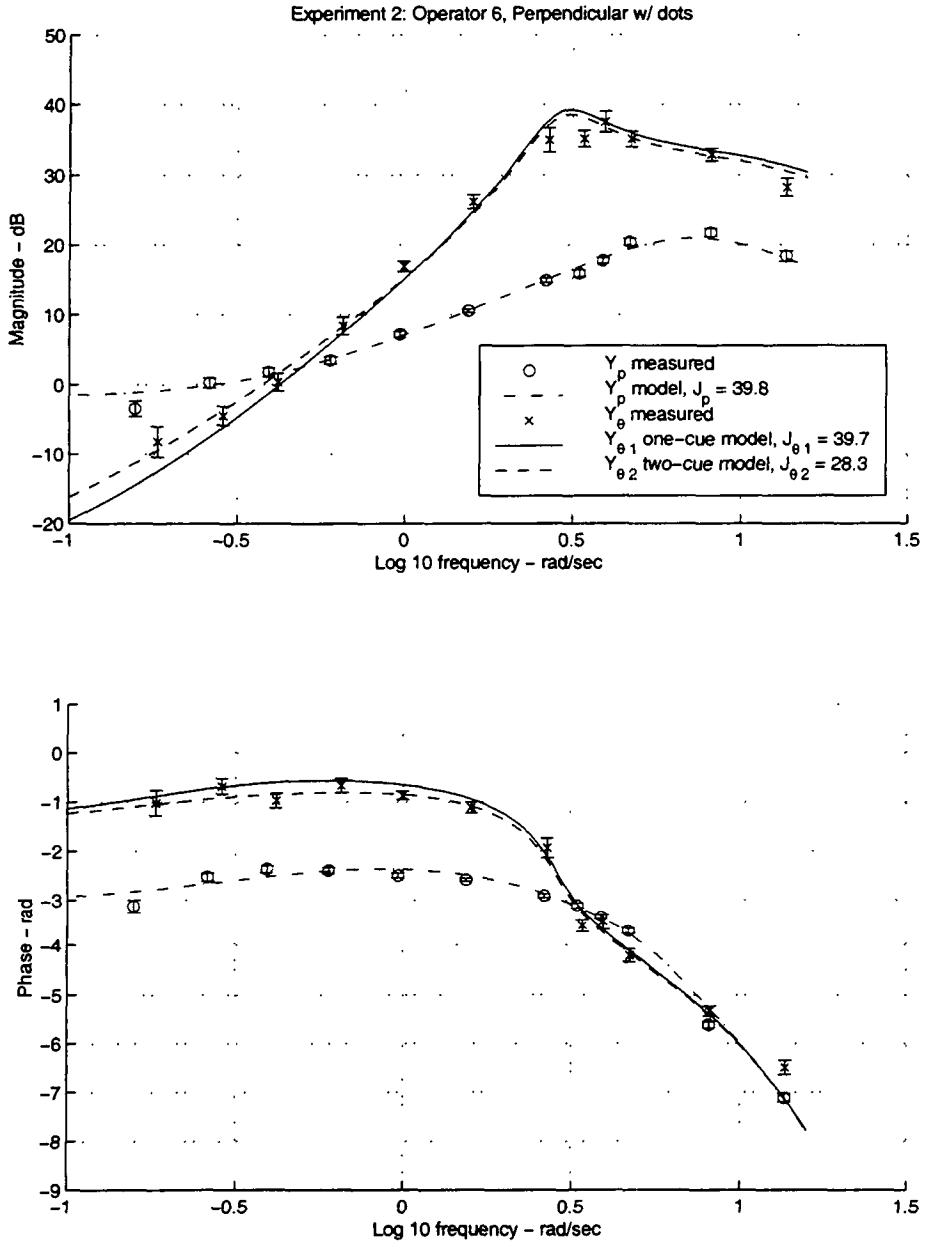

Figure E.54: Experiment 2 model fit results for Operator 6, Perpendicular Texture w/dots.

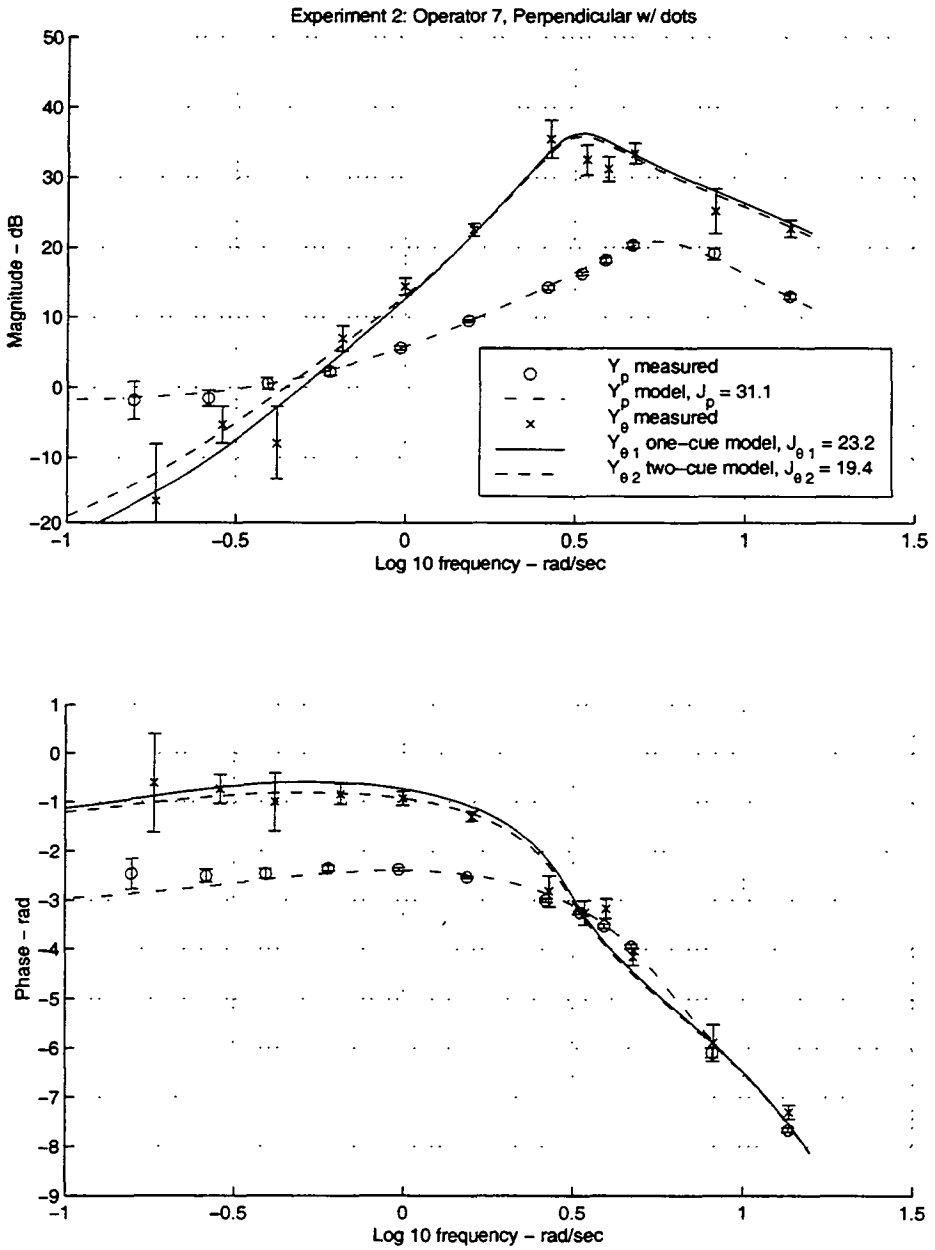

Figure E.55: Experiment 2 model fit results for Operator 7, Perpendicular Texture w/dots.

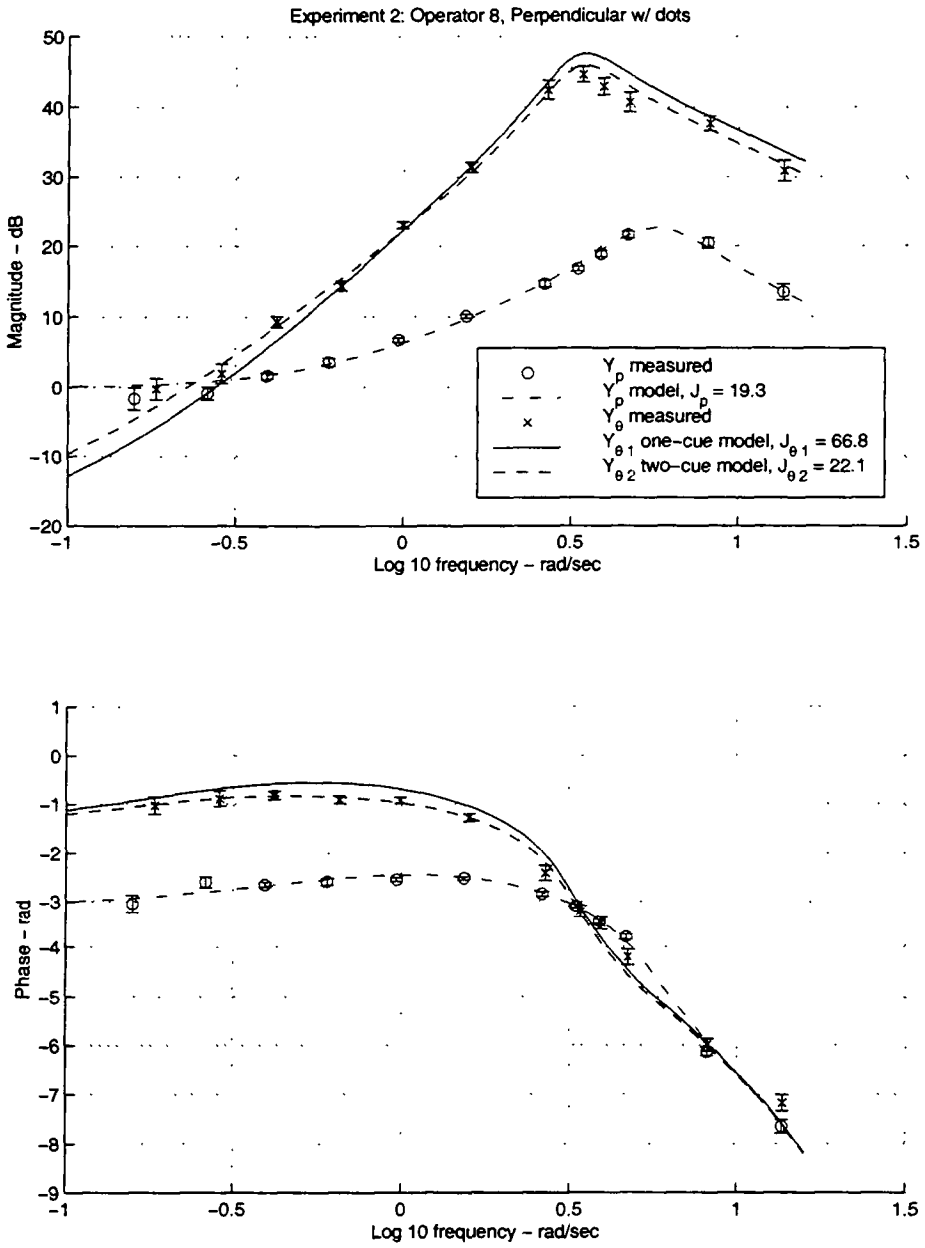

Figure E.56: Experiment 2 model fit results for Operator 8, Perpendicular Texture w/dots.

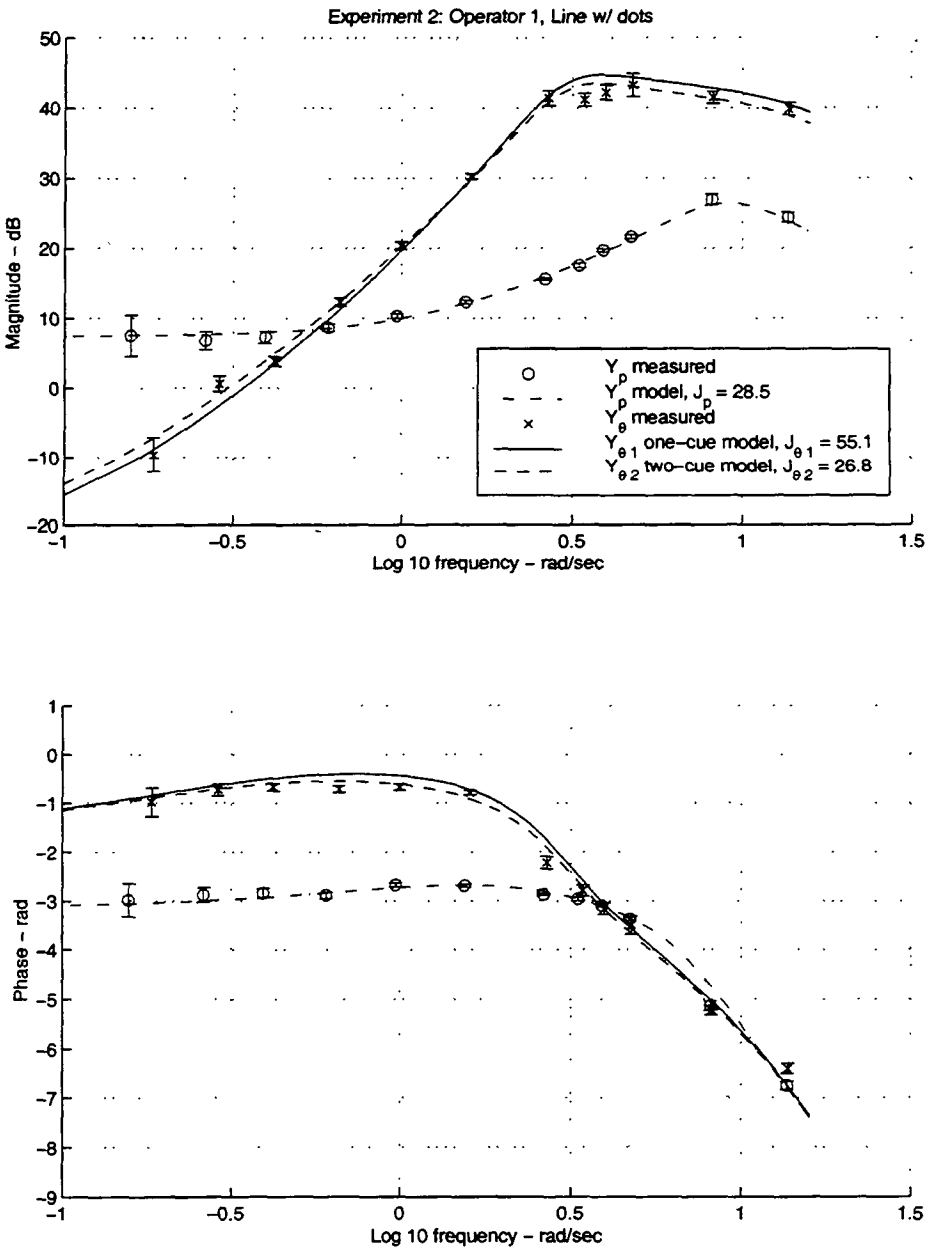

Figure E.57: Experiment 2 model fit results for Operator 1, Line Texture w/dots.

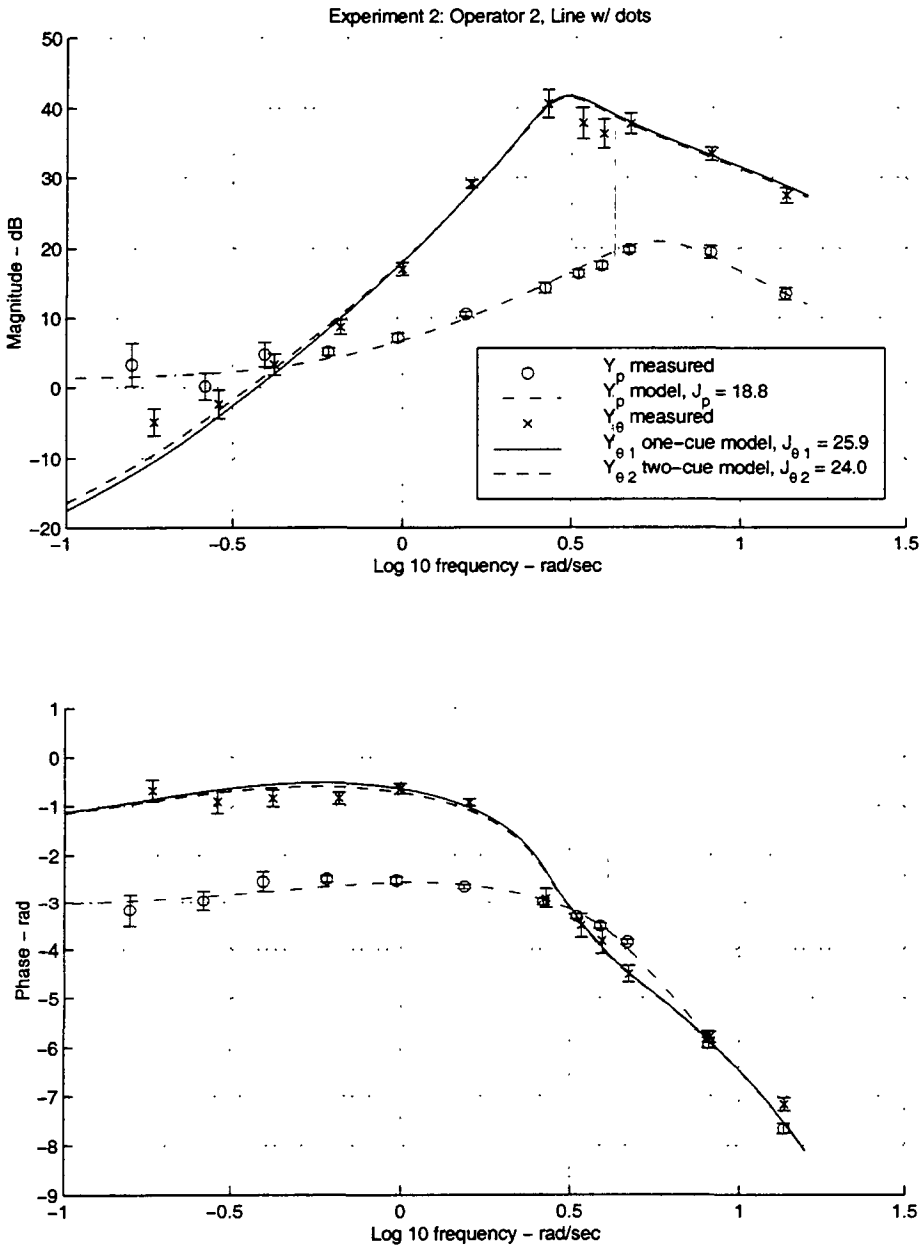

Figure E.58: Experiment 2 model fit results for Operator 2, Line Texture w/dots.

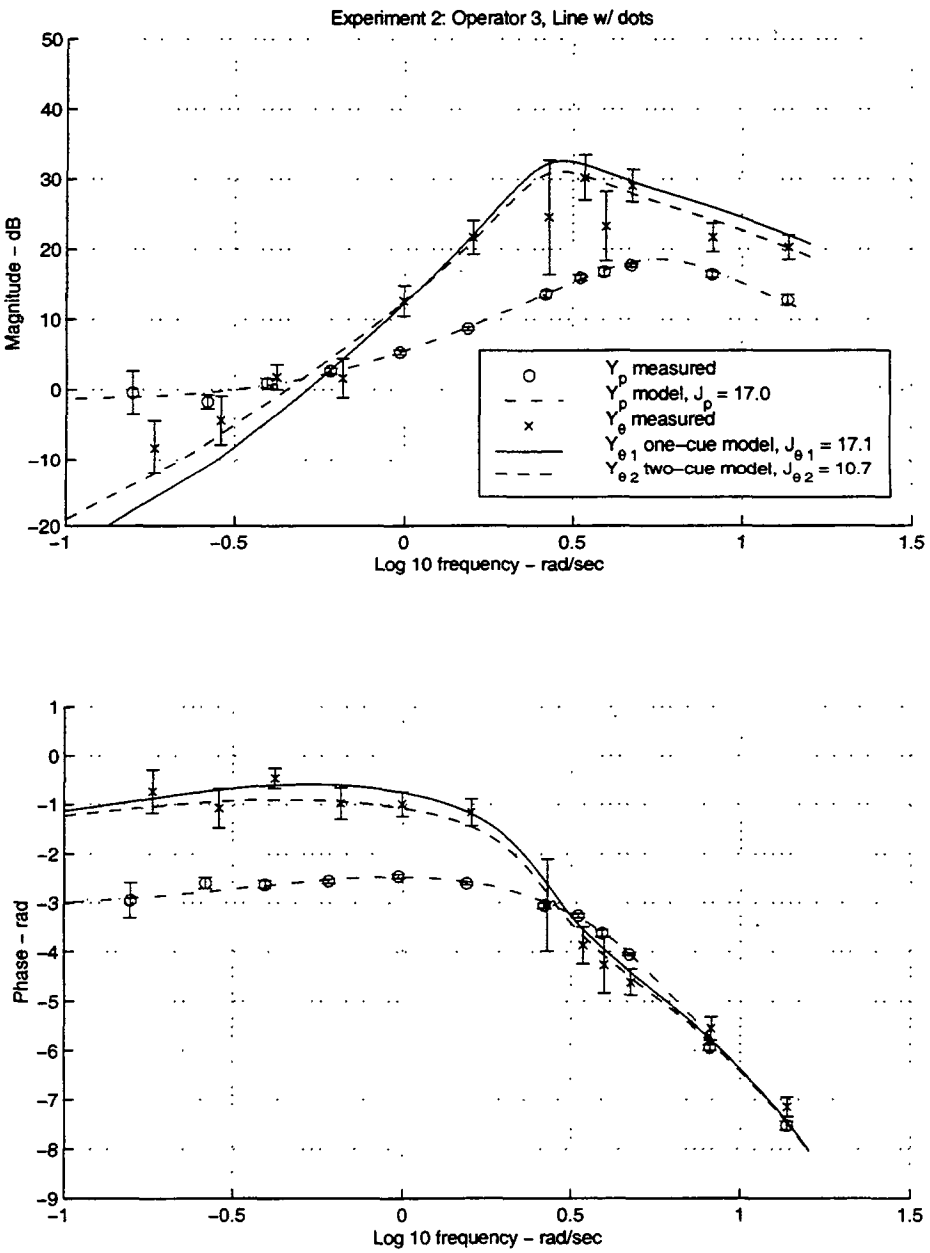

Figure E.59: Experiment 2 model fit results for Operator 3, Line Texture w/dots.

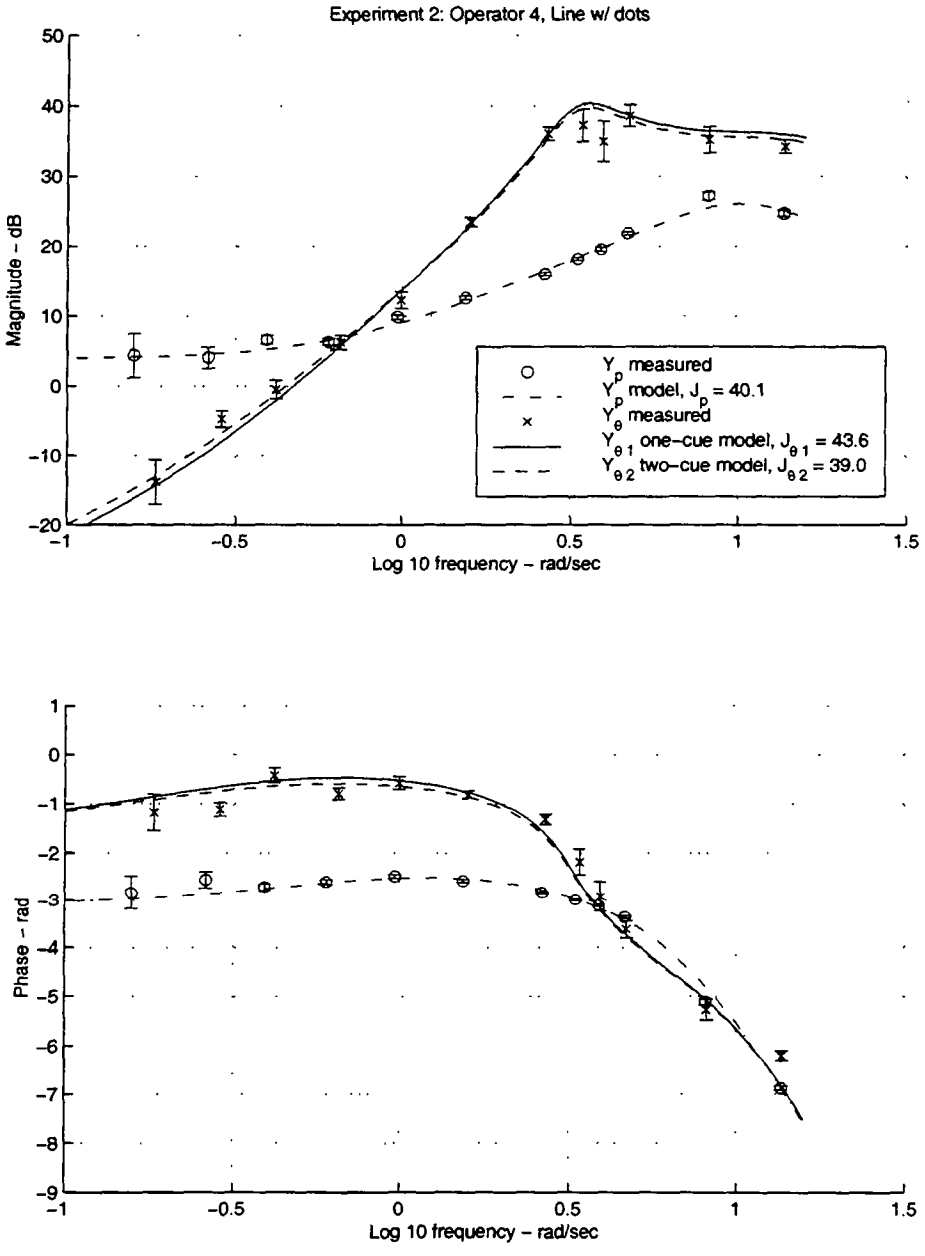

Figure E.60: Experiment 2 model fit results for Operator 4, Line Texture w/dots.

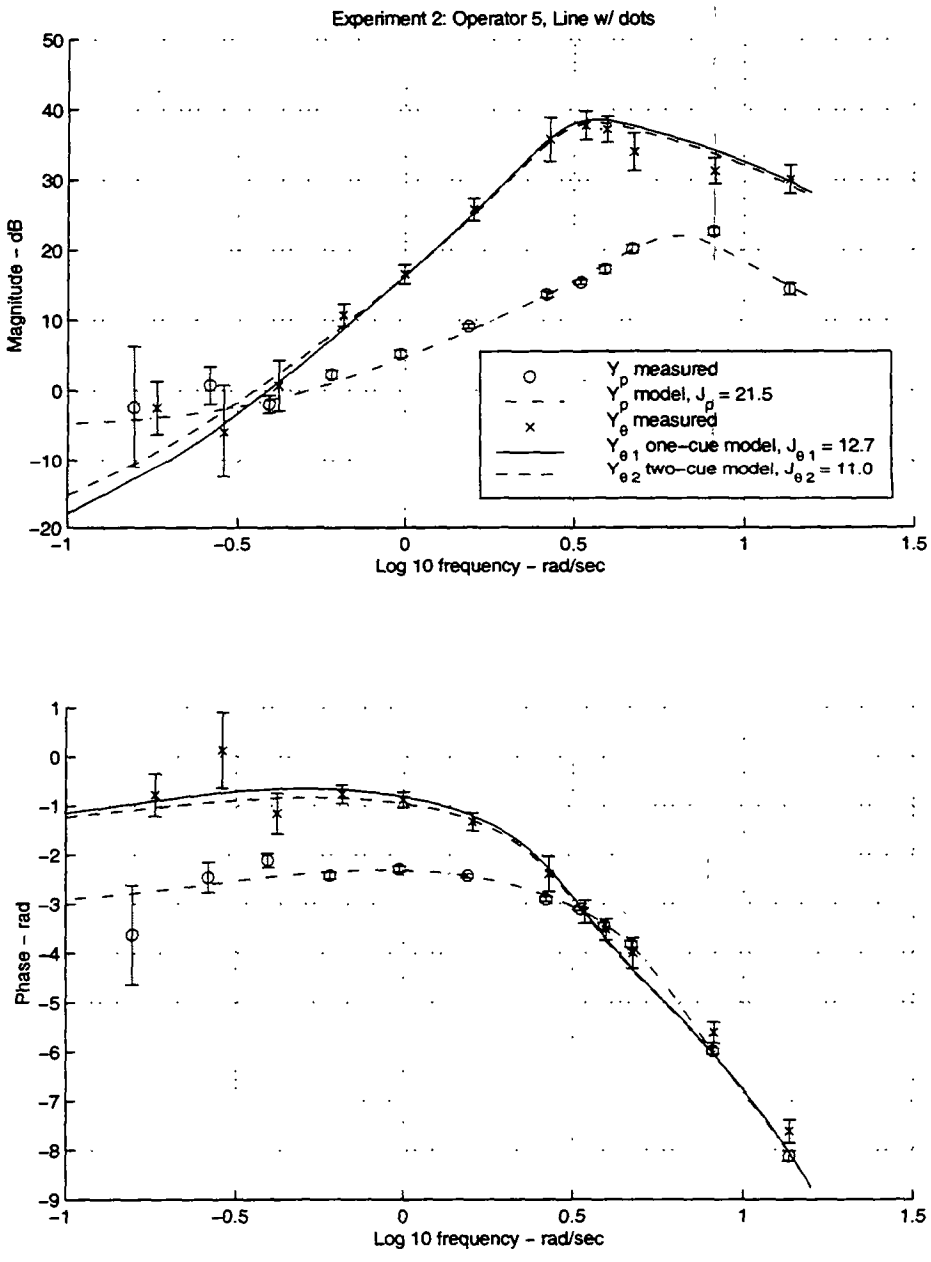

Figure E.61: Experiment 2 model fit results for Operator 5, Line Texture w/dots.

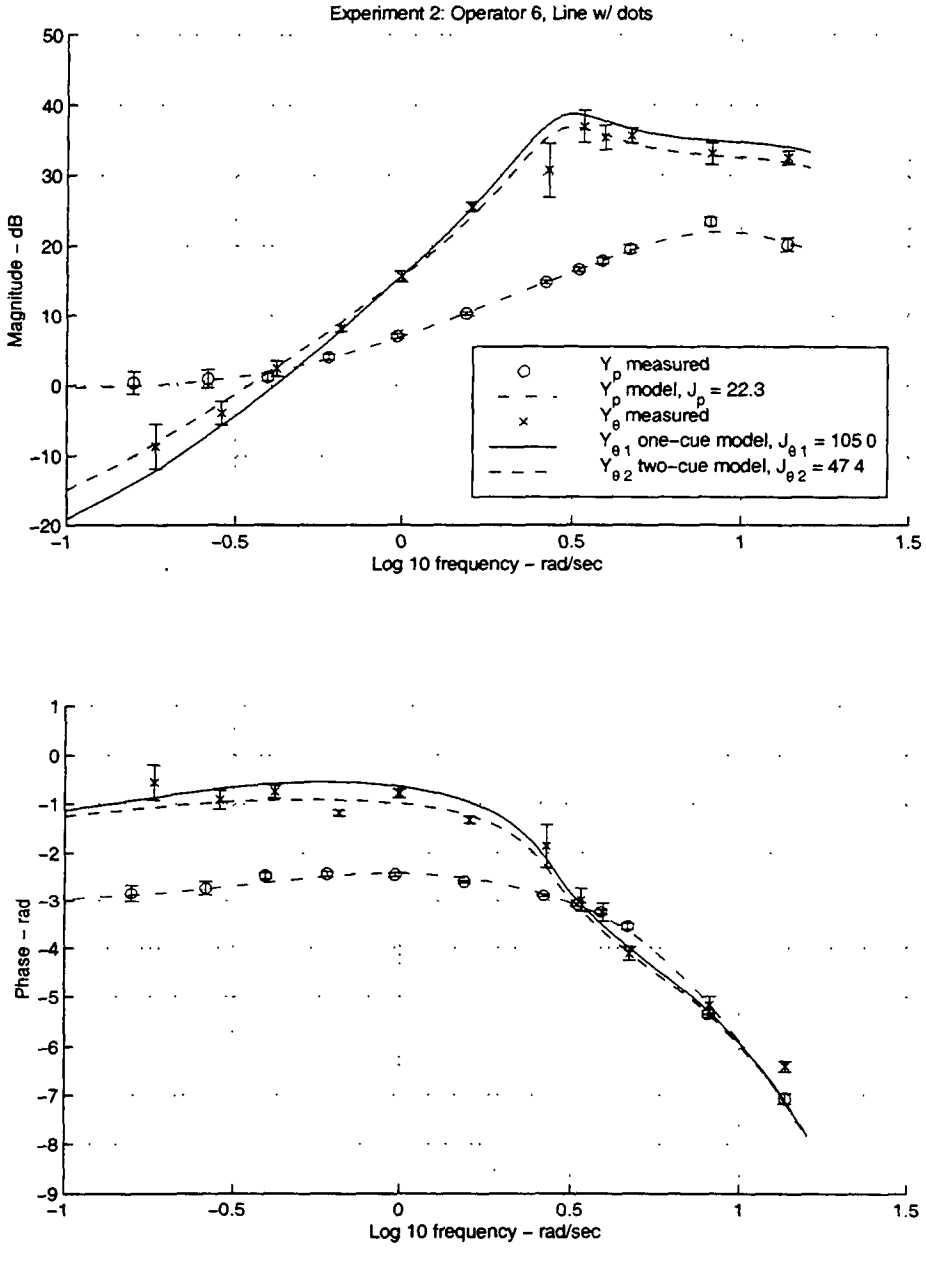

Figure E.62: Experiment 2 model fit results for Operator 6, Line Texture w/dots.

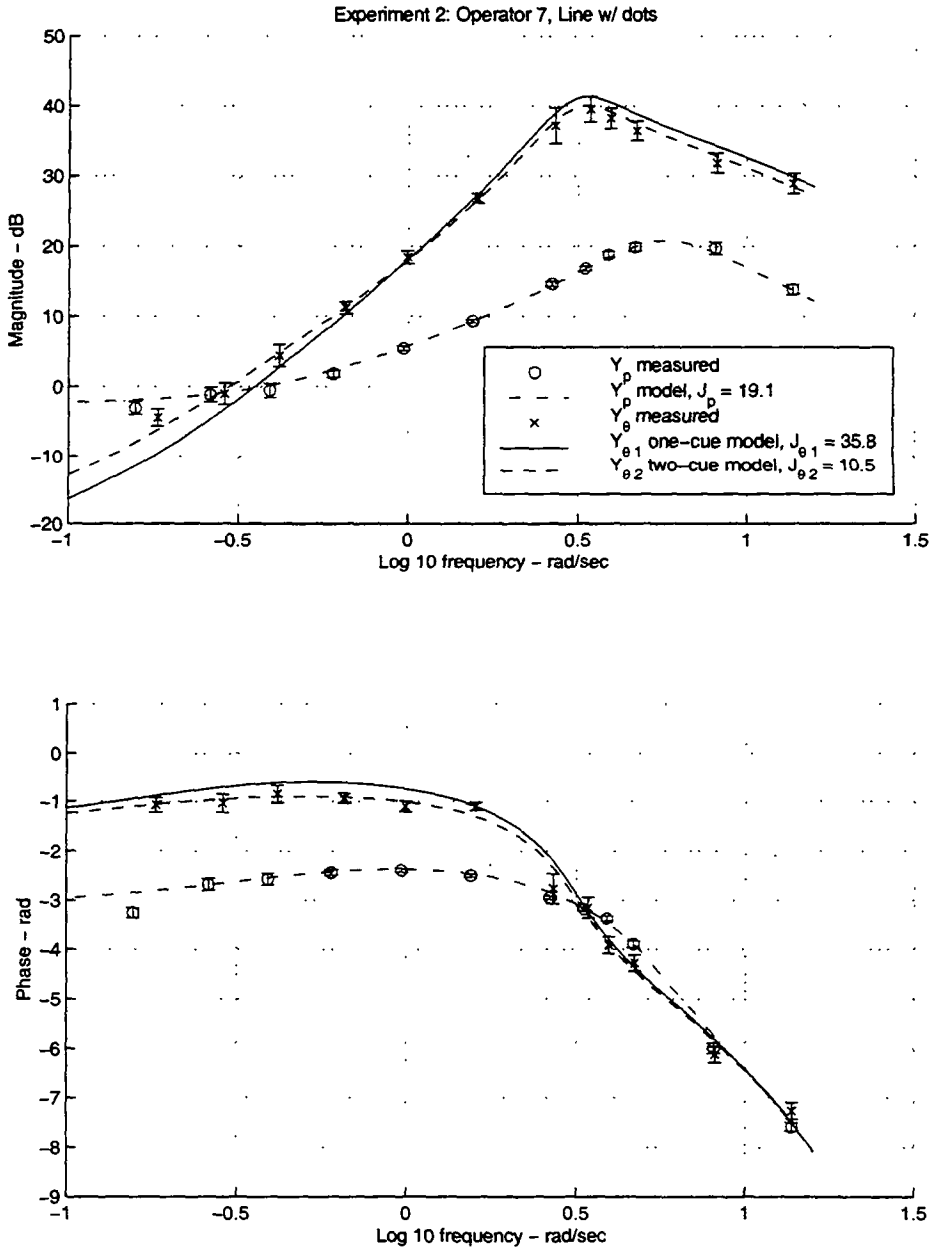

Figure E.63: Experiment 2 model fit results for Operator 7, Line Texture w/dots.

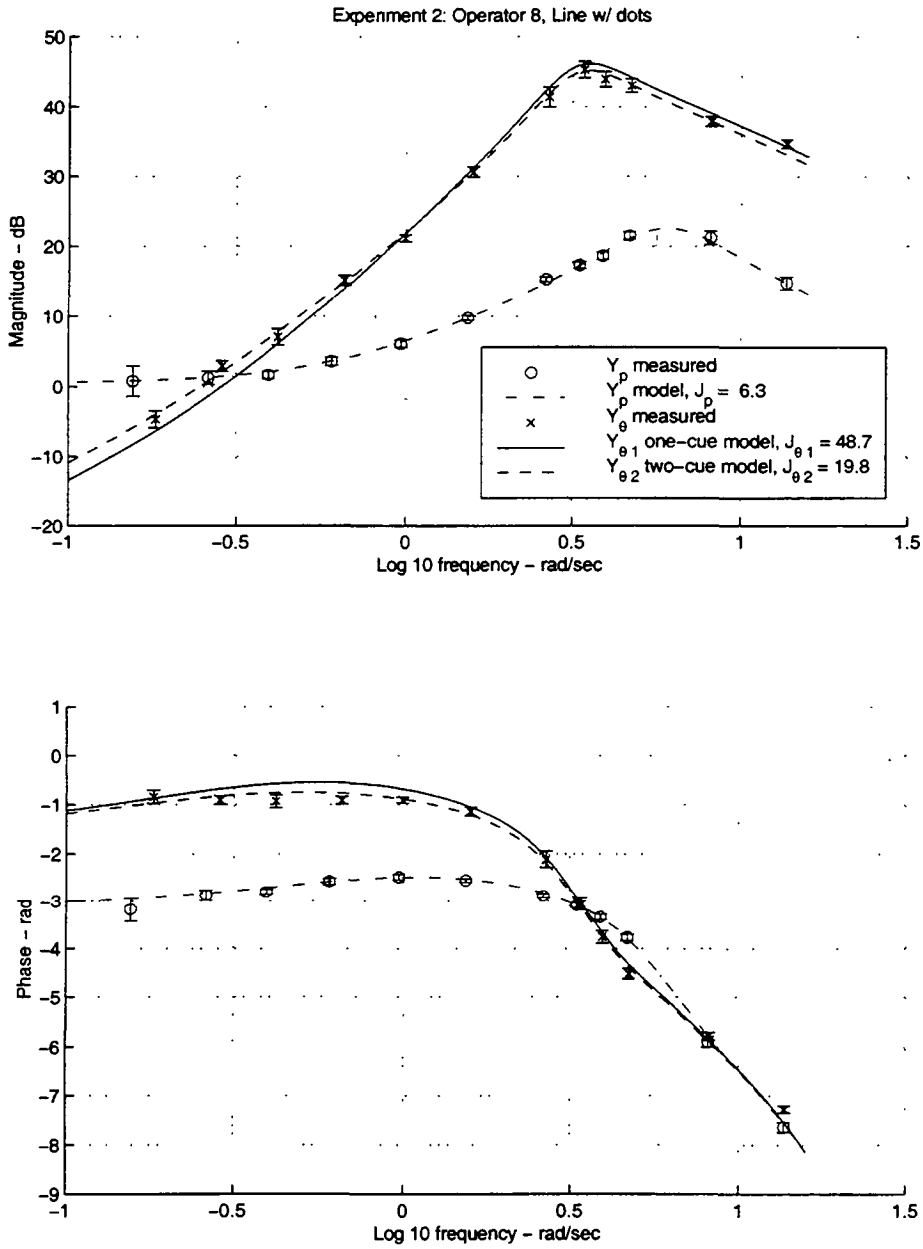

Figure E.64: Experiment 2 model fit results for Operator 8, Line Texture w/dots.

Appendix F

Experiment 3 Appendix

F.1 Display Characteristics and Dynamics

The vehicle dynamics were identical to those described in Section E.1 of Appendix E, with the exception that the pitch disturbance was set to zero. The Grid and Line displays were generated through the perspective projection process instantiated in the hardware of the SGI computer system; however, the process is described by the Equations A.4 through A.6 in Appendix A. Several checks were made in the development of the software to assure that the graphical rendering being done in the computer hardware was consistent with these equations.

The compensatory and compensatory with rate bar (C and CR, respectively) displays were rendered by making the displacement of the position error element linearly proportional to the longitudinal position error, and displacement of the rate bar linearly proportional to the longitudinal velocity. The constant of proportionality was derived to make the sensitivity of the position error element identical to the sensitivity of the baseline on the Grid and Line displays.

The relationship between the vertical screen coordinate of the feature located at (D_X, D_Y, D_Z), viewed from an operator location of $(X, 0, Z)$, is:

$$z_i = \frac{-F(D_Z - Z)}{(D_X - X)} \tag{F.1}$$

The factor F is the focal length of the camera; for the purposes of this experiment,

it can be chosen to scale the image coordinates to some useful system. This will be done later in the derivation.

For the perspective displays (Grid and Line), with the feature being the baseline, located at $D_X = D_{BL}$ and $D_Z = 0$, viewed from the longitudinal position X and a constant altitude $Z = 1$, the equation for z_i becomes:

$$\text{Perspective Scaling (G and L):} \quad z_i = -\frac{F}{(D_{BL} - X)} \tag{F.2}$$

What we are trying to control between the compensatory and perspective displays is the sensitivity of the error element; therefore, we want to keep the derivative with respect to the position error fixed. For the perspective display, this is:

$$\left.\frac{dz_i}{dX}\right|_{X=0} = \frac{-F}{D_{BL}^2} \tag{F.3}$$

We want to display the error in the compensatory displays such that this sensitivity will be the same. It can be shown that this can be accomplished by rendering the error element in the scene at a longitudinal distance of $D_X = D_{BL}^2$ eyeheights, with the altitude term as follows:

$$\text{Linear Scaling (C and CR):} \quad D_Z = X \tag{F.4}$$

$$\text{Nonlinear Scaling (C* and CR*):} \quad D_Z = -FD_{BL}^2\left[\frac{1}{(D_{BL} - X)} - \frac{1}{D_{BL}}\right] \tag{F.5}$$

Substituting these terms into Equation F.1 will yield:

$$\text{Linear Scaling:} \quad z_i = -F\frac{X}{(D_{BL}^2)} \tag{F.6}$$

$$\text{Nonlinear Scaling:} \quad z_i = -F\left[\frac{1}{(D_{BL} - X)} - \frac{1}{D_{BL}}\right] \tag{F.7}$$

Differentiating with respect to X will yield:

$$\text{Linear Scaling (C and CR):} \quad \left.\frac{dz_i}{dX}\right|_{X=0} = -\frac{F}{D_{BL}^2} \tag{F.8}$$

$$\text{Nonlinear Scaling (C* and CR*):} \quad \left.\frac{dz_i}{dX}\right|_{X=0} = -\frac{F}{D_{BL}^2} \tag{F.9}$$

Thus, the sensitivity of all display elements at the nominal condition of $X = 0$ is identical.

While it made sense to scale the sensitivity of the position error element in this way, there was no similar justification to be made concerning the scaling of the rate bar element. Without any specific quantifiable term which was being matched, the only guidelines for scaling the rate bar were to make sure that it was easily above threshold, but not going outside of the field of view. The scaling used for the rate bar was:

$$\text{Linear Scaling (CR):} \quad D_Z = \dot{X} \tag{F.10}$$

$$\text{Nonlinear Scaling (CR*):} \quad D_Z = D_{BL}^2 \frac{\dot{X}}{(D_{BL} - X)^2} \tag{F.11}$$

These terms are difficult to understand without putting them in the context of the display. For this experiment, the vertical field of view was 60 degrees, and the number of pixels in the vertical direction is 1024. We can choose the focal length to make the scaling of the image coordinate z_i correspond to pixels. For this case, the focal length will be:

$$F = \frac{(1024/2)}{\tan(30\,\text{deg})} = 886.81 \text{ pixels/eyeheight} \tag{F.12}$$

With this focal length definition, we can now investigate the sensitivity of both the error terms and the rate bar in pixels per unit of eyeheight motion.

For the position error term:

$$\frac{dz_i}{dX} = \frac{-F}{D_{BL}^2} = 98.5 \text{ pixels/eyeheight} \tag{F.13}$$

For the rate bar term:

$$\frac{dz_i}{d\dot{X}} = \frac{-F}{D_{BL}^2} = 98.5 \text{ pixels/eyeheight/sec} \tag{F.14}$$

To better put this in context, means and standard errors of rms position and velocity values from Experiment 2 are shown in table E.4 in Appendix E. From the tables, it can be seen that the rms values of both position and velocity tend to be less than .8 eyeheights for position, and .7 eyeheights/sec for velocity. With the scaling shown, and with a total pixel height of 1024 pixels, this would yield less than 100 pixels rms for the error symbols, or less than 10% of the display.

F.2 Task Instructions

The written instructions provided to participants are shown below. In addition to the written instructions, on the first day (training) participants were also given a demonstration of the task with all of the test conditions.

F.2.1 Day 1 Instructions

Perspective and Compensatory Displays Comparison: Part 1

Expected completion time: 5.5 hours

Thank you for agreeing to participate in this study. The objective of the study is to compare perspective displays (in which a view of the outside world is rendered) with compensatory displays (in which measurements such as position and velocity are explicitly presented). A total of six display conditions will be evaluated; two of the displays were present in the previous experiment.

You will be asked to perform a task using both perspective and compensatory displays. The task will be to maintain a fixed position despite wind disturbances. The vehicle you are controlling is not an airplane, or a helicopter, or any real vehicle. It hovers above the ground at a constant altitude, and you can make it move forward by moving the stick forward, and backward by moving the stick backward. The vehicle does not move up-down or side-to-side, nor does it roll, pitch, or yaw. The only motion it can do is fore-aft.

You will be given an opportunity to train on all of the display conditions. You will be given additional training time on the compensatory displays, since they were not present in the previous experiment in which you participated. First, you will receive eight one-minute training runs with each of the four compensatory displays. Next, you will receive five one-minute training runs with each of the six displays. Then you will complete five

one-minute data runs on each of the six displays. These data runs will be repeated two more times, for a total of fifteen data runs in each of the six conditions.

A score will be assigned to each run which is a combination of your position error and velocity. A smaller score is better. For training runs, your performance relative to your previous training scores will be shown. For data runs, your performance relative to other subjects data run scores (if available) will be shown. Training runs can be visually discriminated from data runs by the color of the ground plane or background. Training runs feature a brown ground plane or background; data runs feature a green ground plane or background.

During the initial training runs with the compensatory displays, you will be required to take a four minute break between conditions (after eight training runs). After that, at the end of every block of five runs, you will be required to take a two minute break. At the end of every 30 runs, you will be required to take five minute break. You are also encouraged to take breaks of whatever duration you wish between runs, in order to alleviate the discomfort which can occur from sitting in a fixed position for a prolonged period of time.

For a given type of display, use a consistent strategy. Once you have started the data runs (green ground plane/background), don't experiment with your strategy (for example, the aggressiveness of control movements).

F.2.2 Day 2 Instructions

Perspective and Compensatory Displays Comparison: Part 2

Expected completion time: 3.5 hours

Thank you for continuing your participation in this study.

The task is identical to the one performed in part one, but will require longer data run times. The task is to maintain a fixed position fixed despite wind disturbances. The vehicle you are controlling is not an airplane, or a helicopter, or any real vehicle. It hovers above the ground at a constant altitude, and you can make it move forward by moving the stick forward, and backward by moving the stick backward. The vehicle does not move up-down or side-to-side, nor does it roll, pitch, or yaw. The only motion it can do is fore-aft.

You will be performing four-minute data runs, as opposed to one-minute data runs. For each display condition, you will receive one one-minute training run, and two four-minute data runs. After completing this for all six display conditions, you will repeat this sequence. The purpose of the repetition is to allow averaging of data. A score will be assigned to each run which is a combination of your position error and velocity. A smaller score is better. For training runs, your performance relative to your previous training scores will be shown. For data runs, your performance relative to other subjects data run scores (if available) will be shown. Training runs can be visually discriminated from data runs by the color of the ground plane or background. Training runs feature a brown ground plane or background; data runs feature a green ground plane or background.

After each condition (one training and two data runs), you will be required to take a four minute break. After a total of 18 runs (between repetitions of the entire data set), you will be required to take a 20 minute break. You are also encouraged to take breaks as frequently as necessary to maintain performance on the task.

For a given type of display, use a consistent strategy. Once you have started the data runs (green ground plane or background), dont experiment with your strategy (for example, the aggressiveness of control movements).

F.3 Individual Model Parameter Summary

Some of the parameters presented in this section were derived from experimental data obtained during Experiment 2. The first two columns represent data taken with the Grid (G) and Line (L) perspective displays with the pitch disturbance present. The last six columns are the six displays evaluated in Experiment 3 without the pitch disturbance present.

Y_p model parameters K_p, ω_L, and fit quality index J_p are presented in Table F.1; the parameters τ, ω_N and ζ_N are shown in Table F.2. The crossover frequency ω_c and phase margin ϕ_m of Y_pY_c are in Table F.3.

	J_p							
	With θ		Without θ					
Obs.	G	L	G	L	C	CR	C*	CR*
1	17.9	36.6	47.9	56.3	70.6	48.0	85.9	226.3
2	18.5	55.8	117.1	65.2	37.9	59.4	25.3	14.1
3	11.4	14.3	39.2	33.5	121.0	44.8	55.8	23.4
4	39.6	6.5	15.9	34.3	14.6	11.7	25.6	38.9
5	48.2	33.6	90.8	55.8	121.8	72.6	77.5	57.6
6	45.7	7.4	40.3	29.4	32.4	29.5	27.3	24.3
	K_p							
	With θ		Without θ					
Obs.	G	L	G	L	C	CR	C*	CR*
1	2.29	2.23	2.40	2.16	2.39	2.68	2.47	2.44
2	2.12	2.13	2.32	2.24	2.06	2.34	2.27	2.22
3	1.69	1.54	2.08	1.98	2.09	2.11	2.13	2.00
4	2.35	2.16	2.41	2.41	2.18	2.36	2.38	2.36
5	2.21	1.68	2.29	2.37	2.27	2.52	2.34	2.36
6	1.21	1.63	1.71	1.62	1.83	1.80	1.86	1.69
	ω_L, rad/sec							
	With θ		Without θ					
Obs.	G	L	G	L	C	CR	C*	CR*
1	1.05	0.95	0.90	0.72	1.06	0.88	0.93	0.79
2	0.47	0.53	0.58	0.69	1.05	0.87	0.78	0.80
3	0.46	0.32	0.68	0.71	0.83	0.82	0.85	0.85
4	0.72	0.56	0.83	0.75	0.99	1.06	0.73	0.36
5	0.74	0.33	0.96	0.68	1.12	0.70	1.00	0.94
6	0.36	0.41	0.54	0.61	0.60	0.54	0.57	0.69

Table F.1: Y_p parameters K_p and ω_L, and model fit index J_p from Experiment 3.

	τ, sec							
	With θ		Without θ					
Obs.	G	L	G	L	C	CR	C*	CR*
1	0.21	0.22	0.21	0.22	0.21	0.21	0.21	0.19
2	0.24	0.22	0.24	0.22	0.24	0.22	0.25	0.22
3	0.25	0.24	0.24	0.24	0.24	0.22	0.24	0.22
4	0.22	0.24	0.22	0.25	0.22	0.21	0.24	0.24
5	0.21	0.24	0.24	0.22	0.22	0.19	0.19	0.18
6	0.24	0.22	0.22	0.22	0.21	0.21	0.21	0.19
	ω_N, rad/sec							
	With θ		Without θ					
Obs.	G	L	G	L	C	CR	C*	CR*
1	9.7	9.9	10.3	10.3	10.0	11.3	10.5	8.1
2	8.0	6.7	9.0	8.7	10.3	9.2	10.7	9.9
3	5.5	5.3	6.5	6.2	7.3	6.7	7.7	6.8
4	8.8	9.8	9.2	9.4	8.9	9.3	10.5	8.6
5	6.4	4.7	7.0	7.6	7.8	7.1	7.5	7.6
6	4.1	5.1	4.5	4.9	5.3	4.9	5.2	4.8
	ζ_N							
	With θ		Without θ					
Obs.	G	L	G	L	C	CR	C*	CR*
1	0.37	0.46	0.54	0.50	0.45	0.55	0.52	0.46
2	0.70	0.75	0.75	0.70	0.63	0.58	0.67	0.70
3	0.55	0.64	0.55	0.50	0.57	0.55	0.62	0.57
4	0.50	0.72	0.58	0.43	0.44	0.41	0.65	0.42
5	0.48	0.46	0.42	0.63	0.44	0.62	0.51	0.54
6	0.43	0.65	0.55	0.51	0.66	0.63	0.63	0.57

Table F.2: Y_p parameters τ, ω_N, and ζ_N from Experiment 3.

	ω_c (rad/sec)							
	With θ		Without θ					
Obs.	G	L	G	L	C	CR	C*	CR*
1	2.60	2.47	2.60	2.31	2.67	2.86	2.69	2.69
2	2.16	2.14	2.36	2.33	2.28	2.52	2.39	2.34
3	1.80	1.58	2.26	2.19	2.28	2.32	2.30	2.21
4	2.54	2.21	2.58	2.63	2.45	2.68	2.50	2.51
5	2.47	1.85	2.67	2.48	2.63	2.66	2.64	2.62
6	1.32	1.69	1.87	1.80	1.92	1.90	1.96	1.88
	ϕ_m (deg)							
	With θ		Without θ					
Obs.	G	L	G	L	C	CR	C*	CR*
1	28.1	27.3	27.1	33.8	25.3	25.1	26.2	27.7
2	30.8	25.2	25.1	25.8	22.2	23.4	24.0	26.1
3	33.4	41.2	23.1	24.6	21.5	21.2	20.5	22.8
4	27.9	31.0	23.3	25.3	25.7	25.3	25.4	36.5
5	24.2	37.2	17.0	21.9	18.1	20.4	20.8	23.3
6	48.1	35.6	26.7	30.5	25.9	26.6	26.7	26.4

Table F.3: Crossover frequency and phase margin of Y_pY_c from Experiment 3.

F.4 Individual Model Fit Plots

The model fits are shown in the following figures (Figures F.1 through F.48).

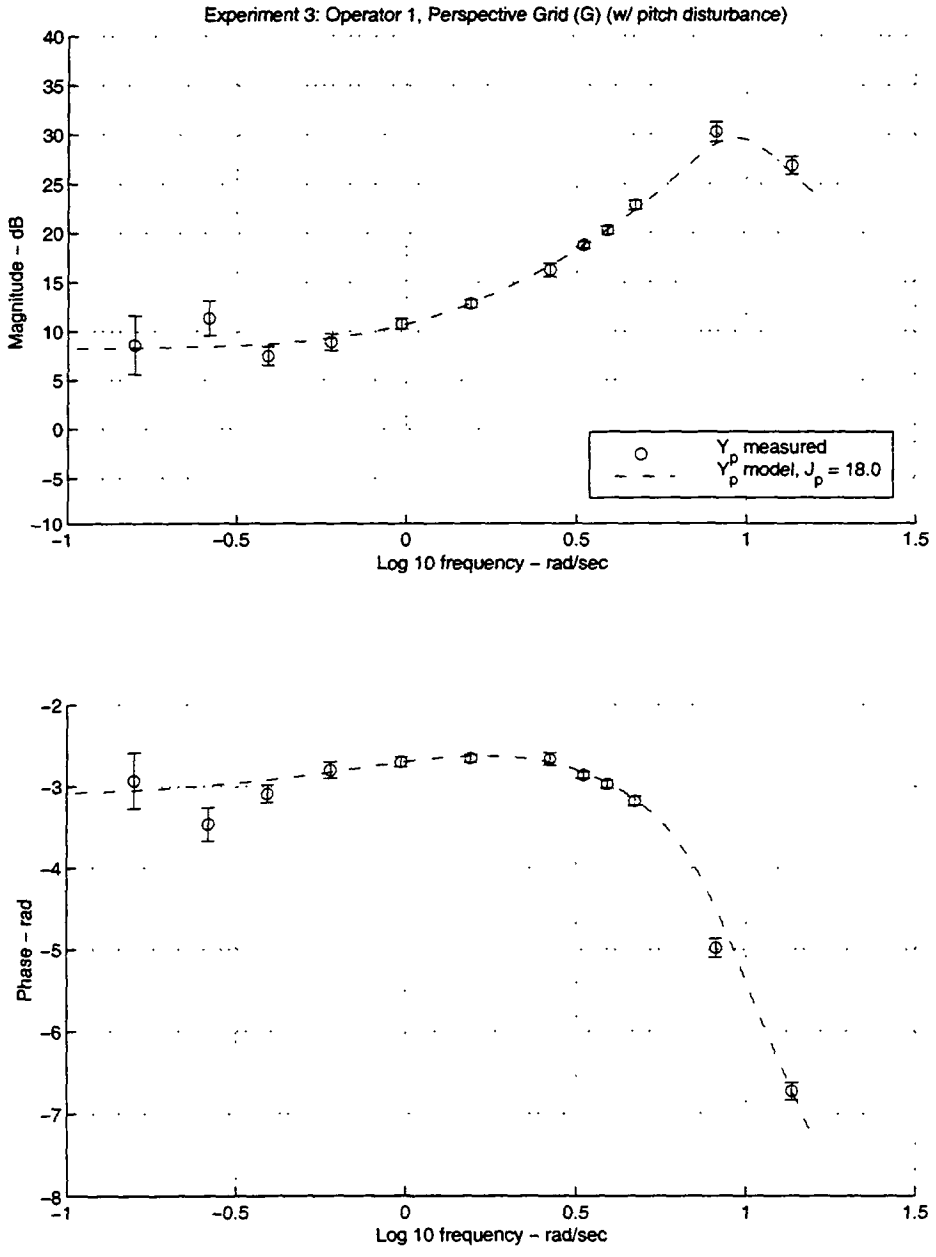

Figure F.1: Experiment 3 model fit results for Operator 1, Perspective Grid Display, with pitch disturbance. NOTE: the data presented in this plot was collected during Experiment 2. It is presented here for comparison purposes with Experiment 3.

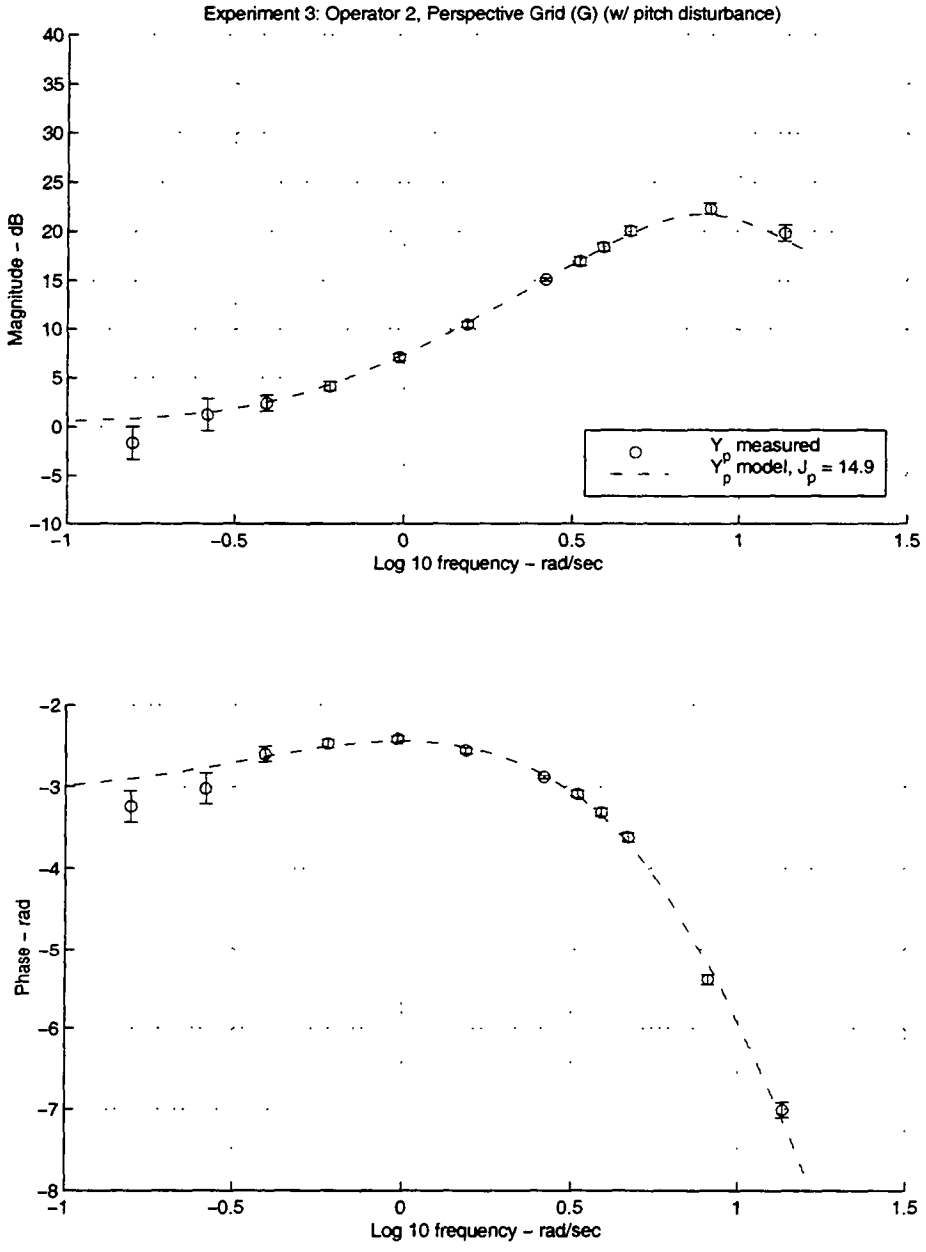

Figure F.2: Experiment 3 model fit results for Operator 2, Perspective Grid Display, with pitch disturbance. NOTE: the data presented in this plot was collected during Experiment 2. It is presented here to allow better direct comparison with Experiment 3 data.

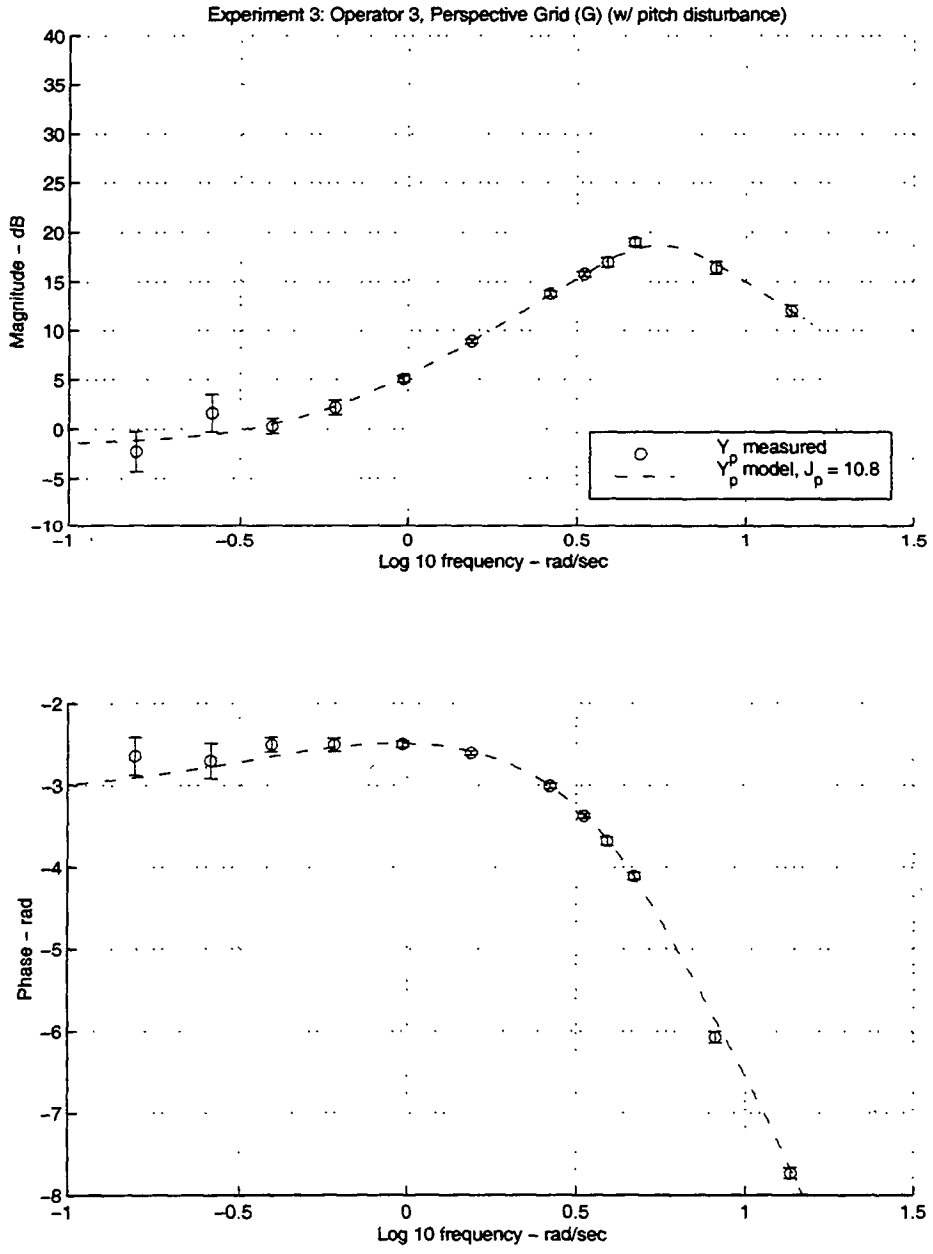

Figure F.3: Experiment 3 model fit results for Operator 3, Perspective Grid Display, with pitch disturbance. NOTE: the data presented in this plot was collected during Experiment 2. It is presented here to allow better direct comparison with Experiment 3 data.

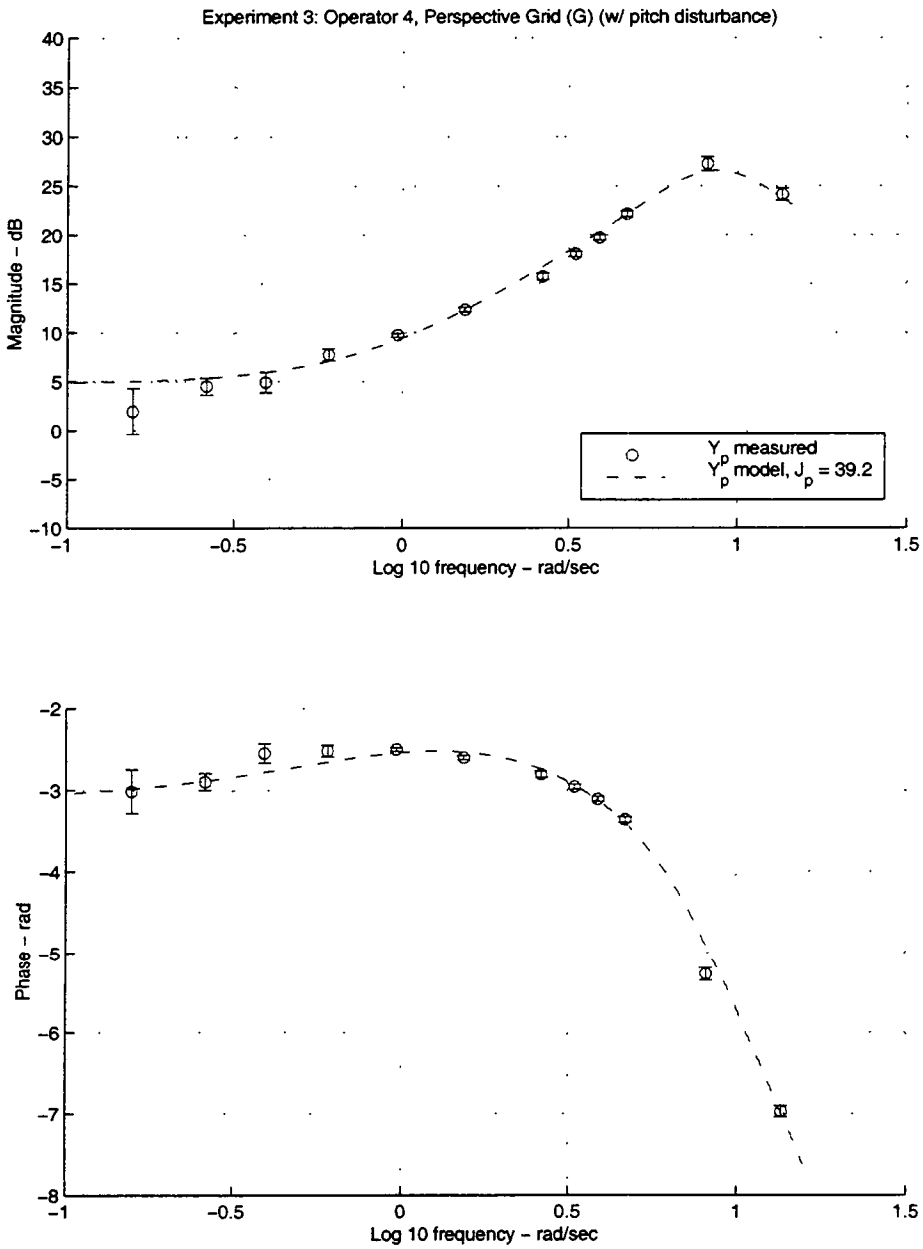

Figure F.4: Experiment 3 model fit results for Operator 4, Perspective Grid Display, with pitch disturbance. NOTE: the data presented in this plot was collected during Experiment 2. It is presented here to allow better direct comparison with Experiment 3 data.

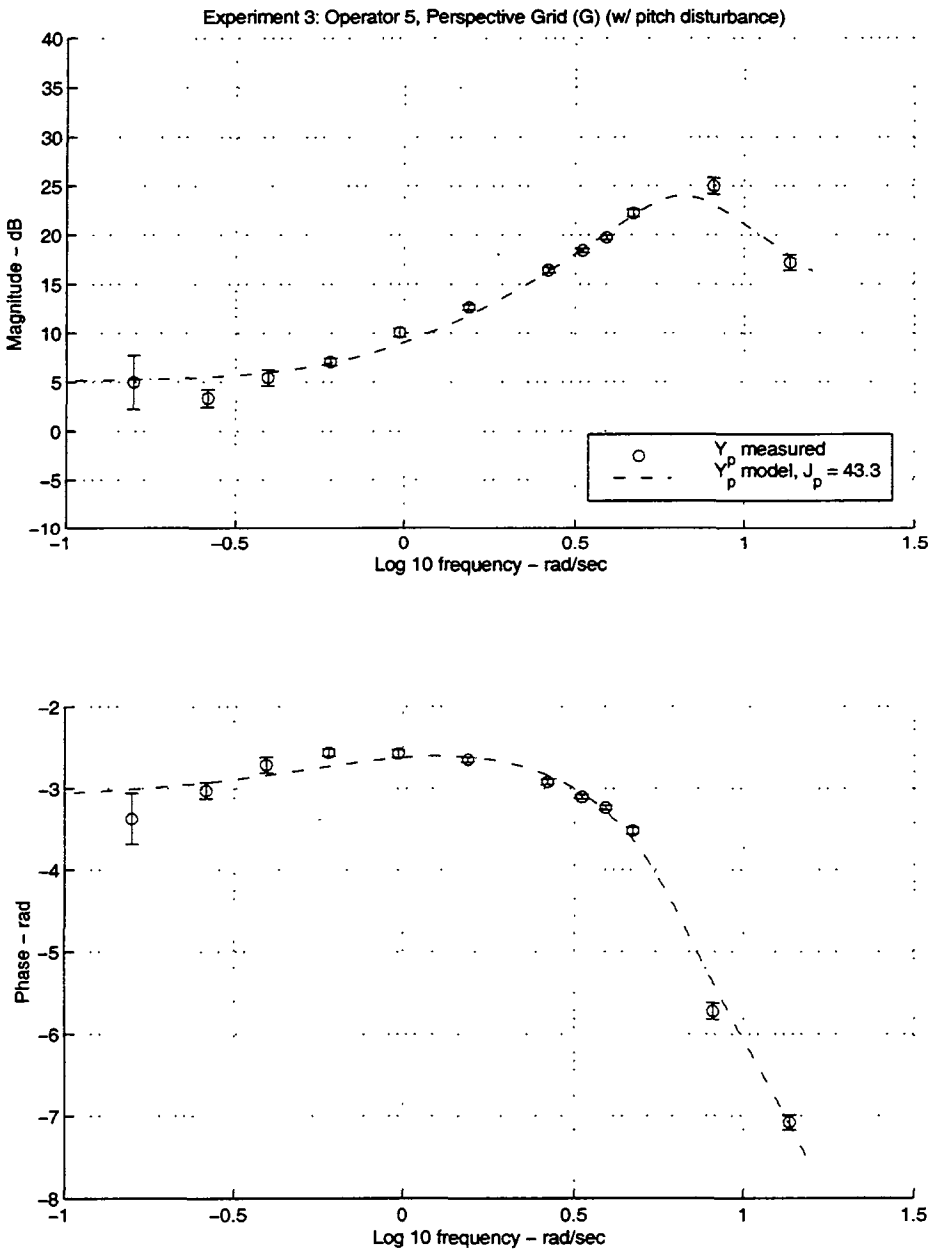

Figure F.5: Experiment 3 model fit results for Operator 5, Perspective Grid Display, with pitch disturbance. NOTE: the data presented in this plot was collected during Experiment 2. It is presented here to allow better direct comparison with Experiment 3 data.

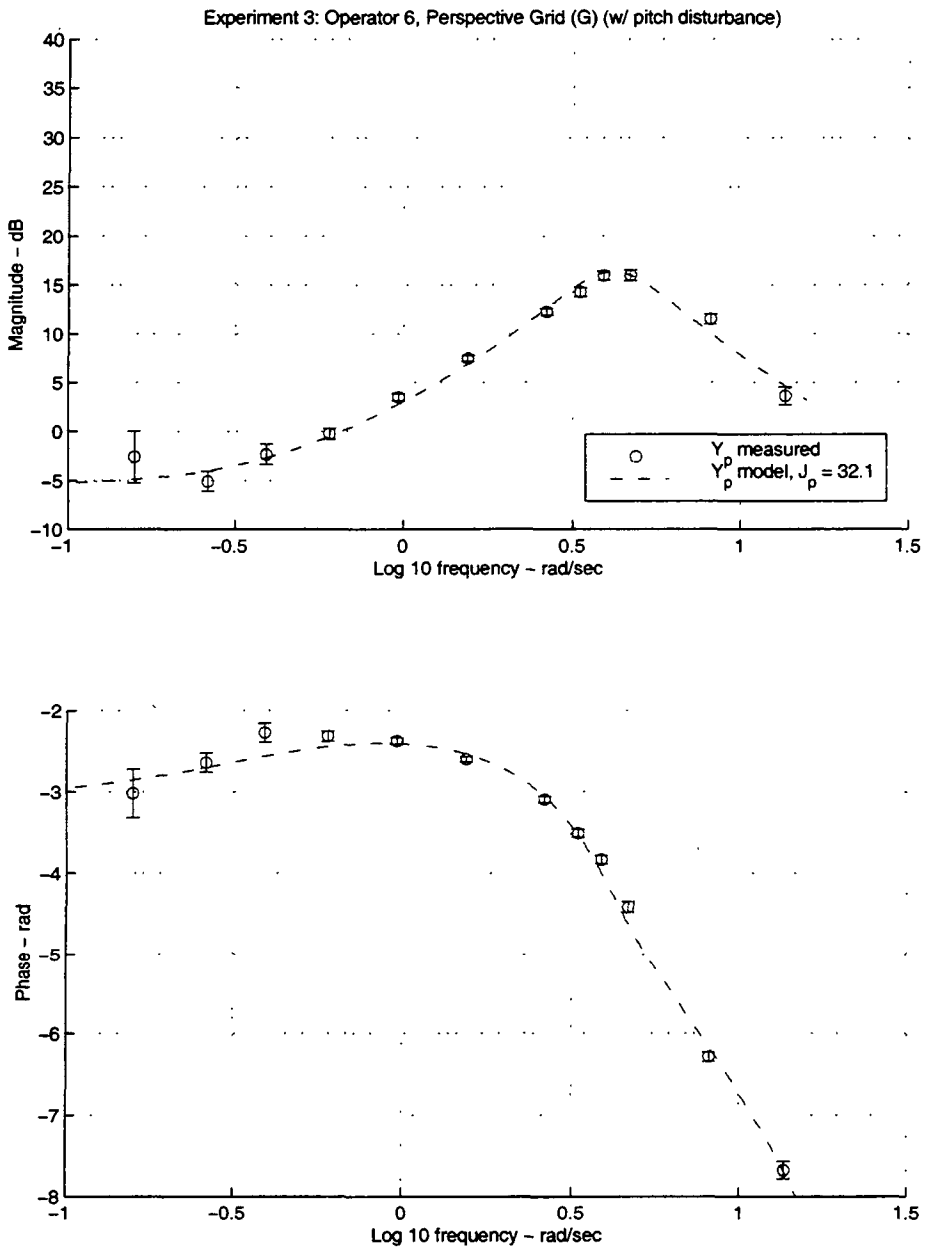

Figure F.6: Experiment 3 model fit results for Operator 6, Perspective Grid Display, with pitch disturbance. NOTE: the data presented in this plot was collected during Experiment 2. It is presented here to allow better direct comparison with Experiment 3 data.

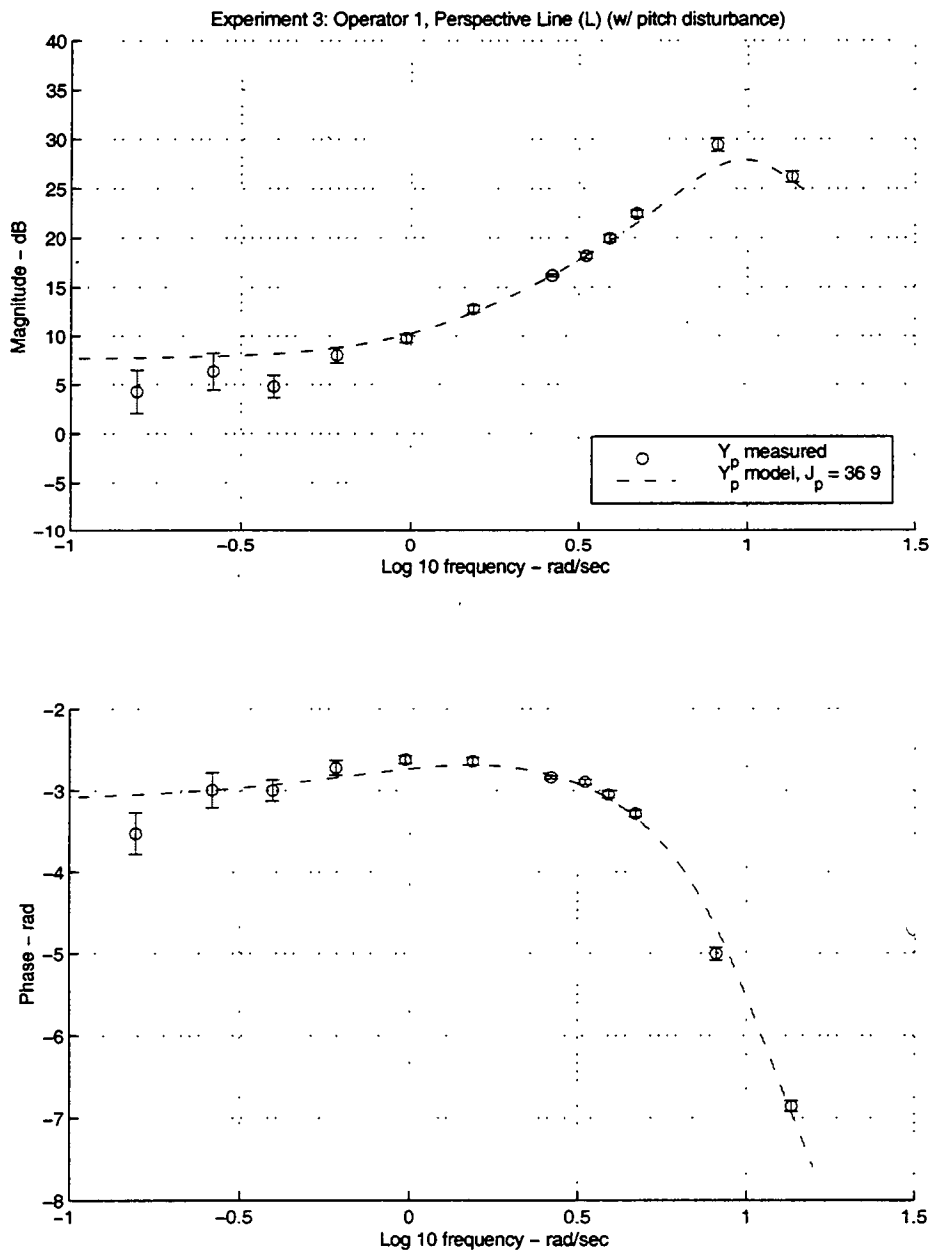

Figure F.7: Experiment 3 model fit results for Operator 1, Perspective Line Display, with pitch disturbance. NOTE: the data presented in this plot was collected during Experiment 2. It is presented here to allow better direct comparison with Experiment 3 data.

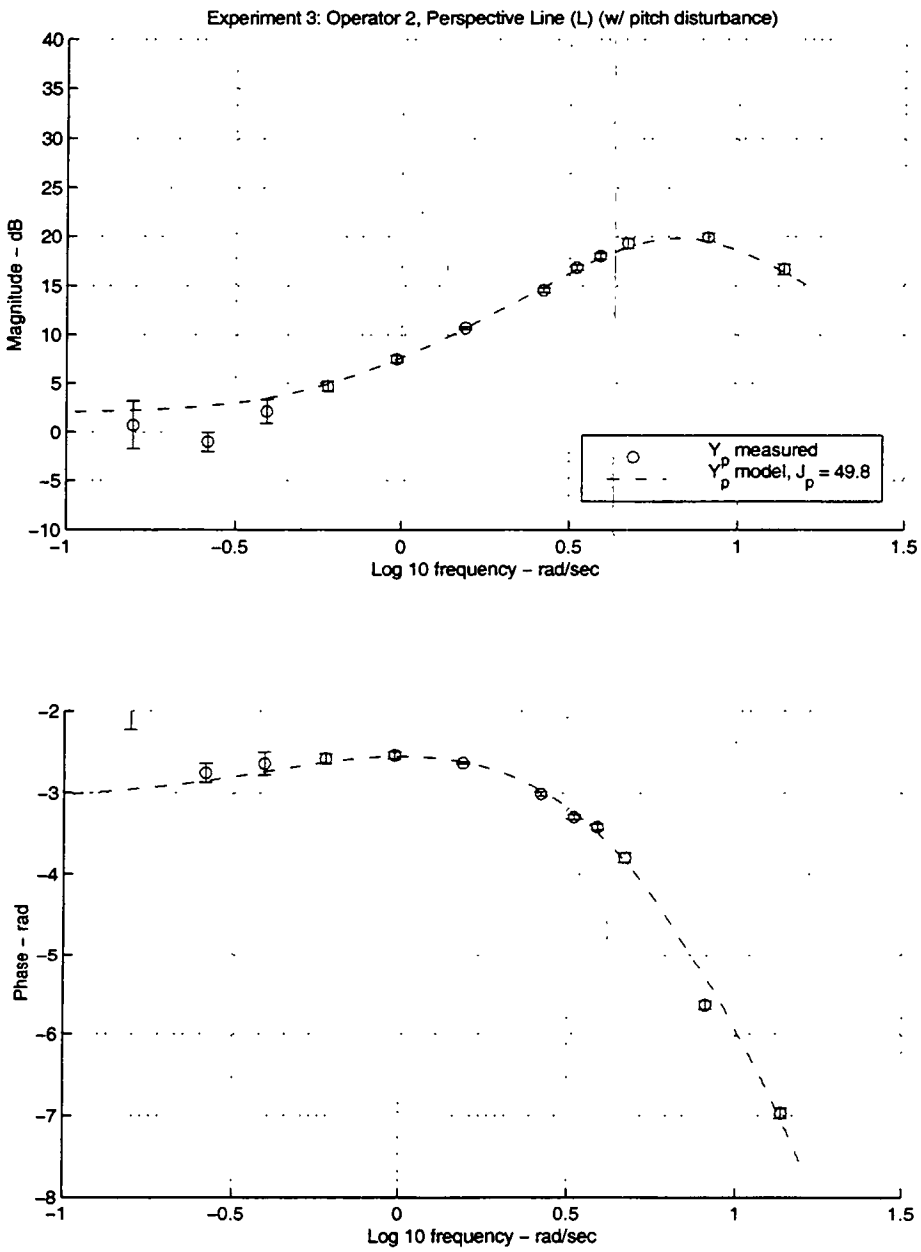

Figure F.8: Experiment 3 model fit results for Operator 2, Perspective Line Display, with pitch disturbance. NOTE: the data presented in this plot was collected during Experiment 2. It is presented here to allow better direct comparison with Experiment 3 data.

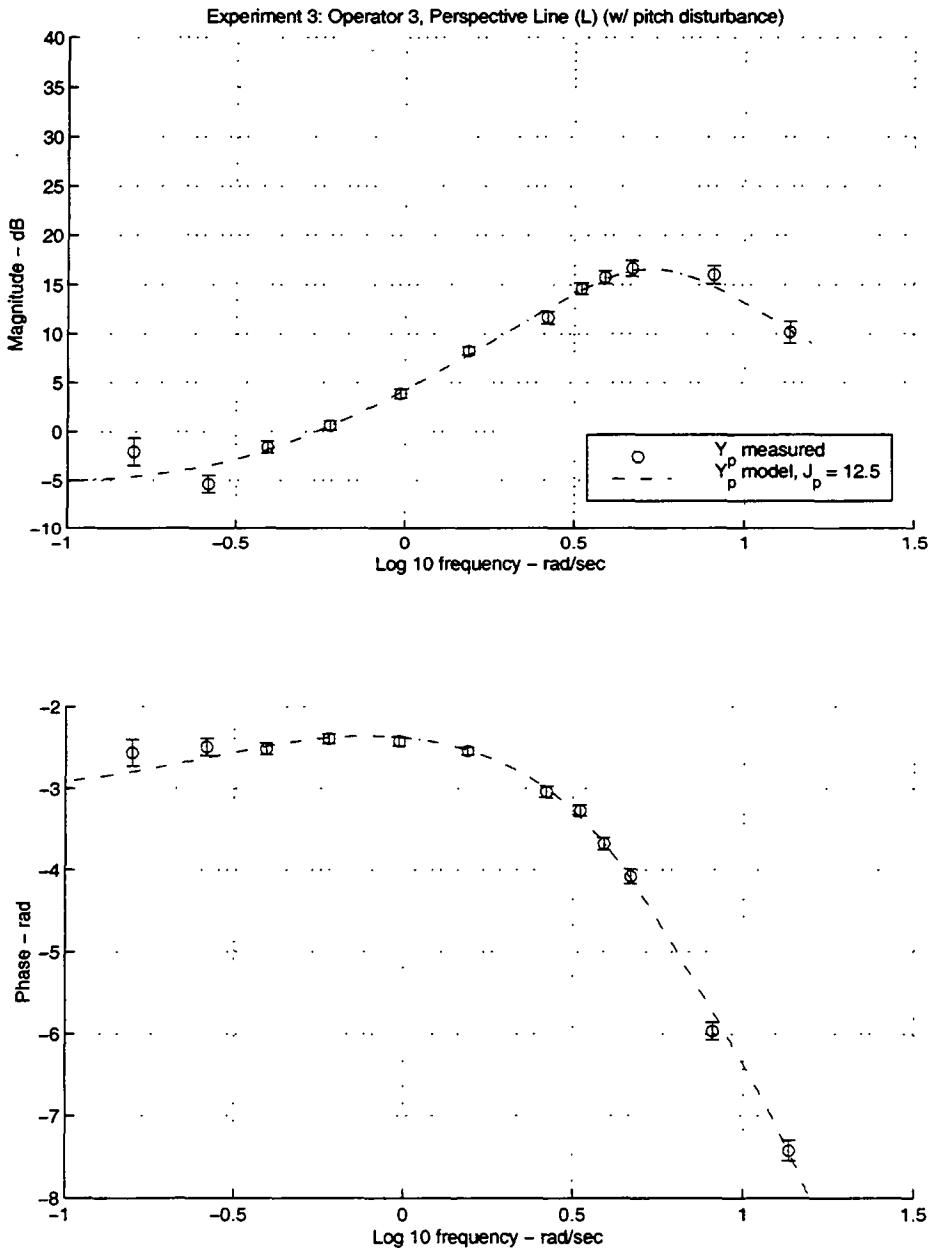

Figure F.9: Experiment 3 model fit results for Operator 3, Perspective Line Display, with pitch disturbance. NOTE: the data presented in this plot was collected during Experiment 2. It is presented here to allow better direct comparison with Experiment 3 data.

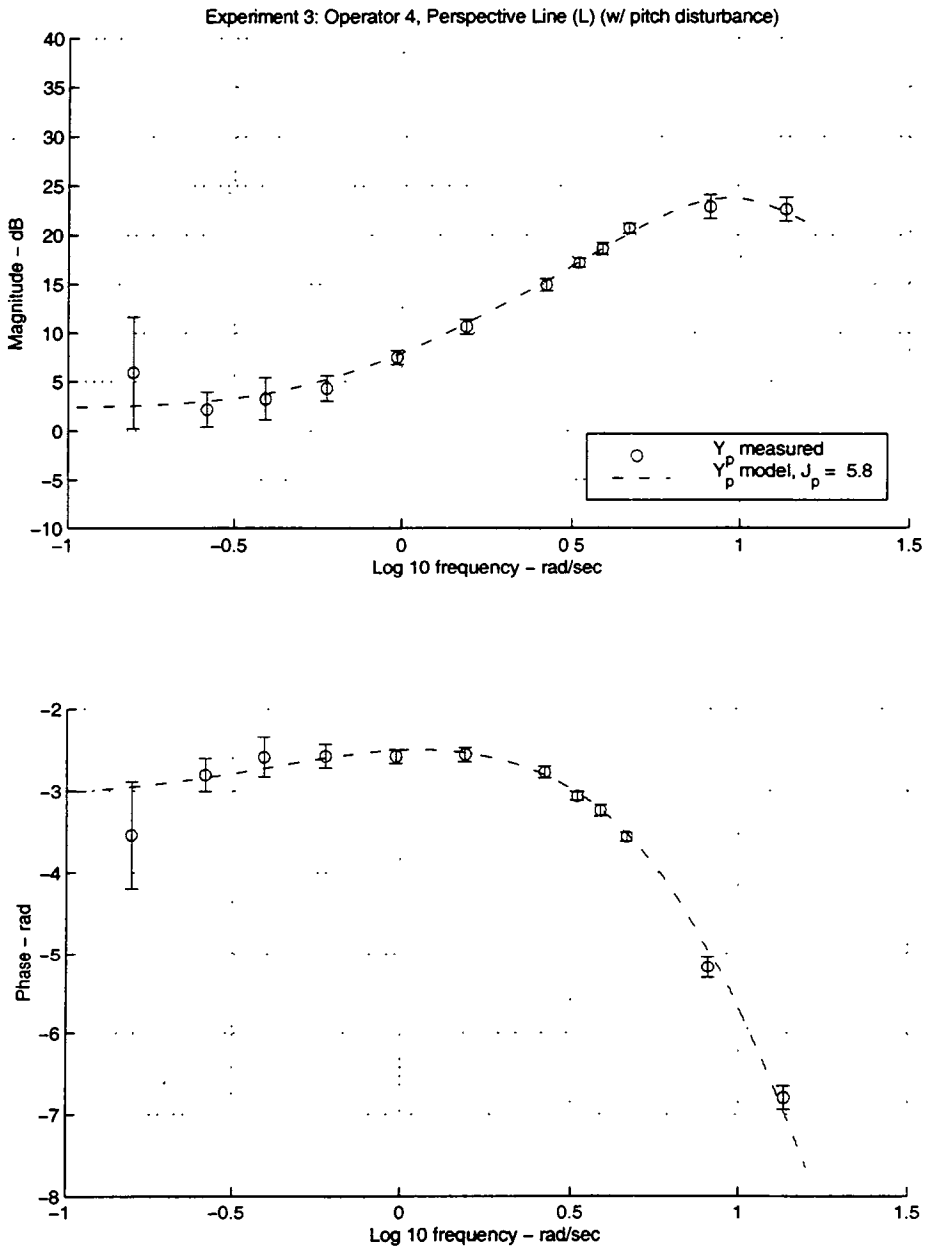

Figure F.10: Experiment 3 model fit results for Operator 4, Perspective Line Display, with pitch disturbance. NOTE: the data presented in this plot was collected during Experiment 2. It is presented here to allow better direct comparison with Experiment 3 data.

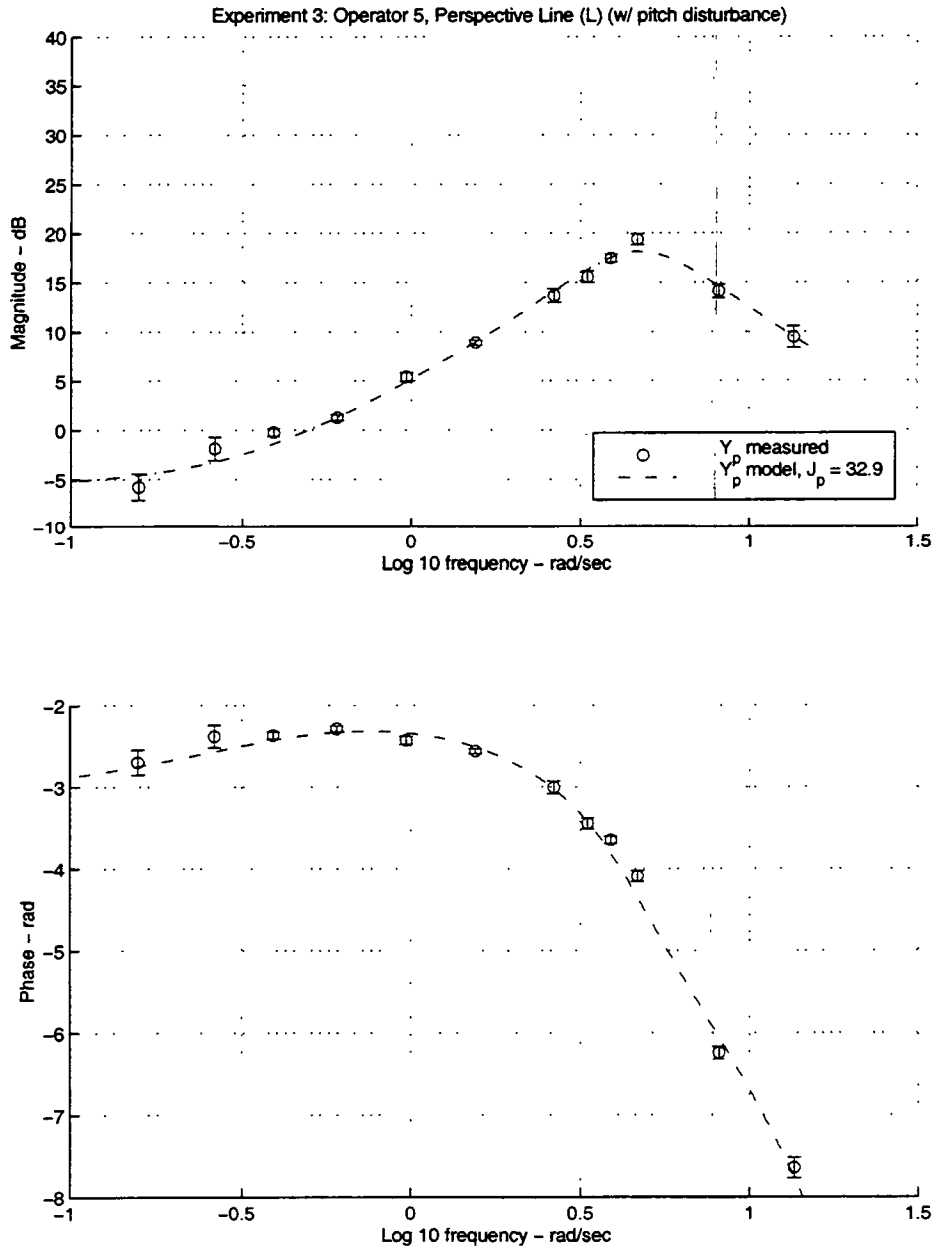

Figure F.11: Experiment 3 model fit results for Operator 5, Perspective Line Display, with pitch disturbance. NOTE: the data presented in this plot was collected during Experiment 2. It is presented here to allow better direct comparison with Experiment 3 data.

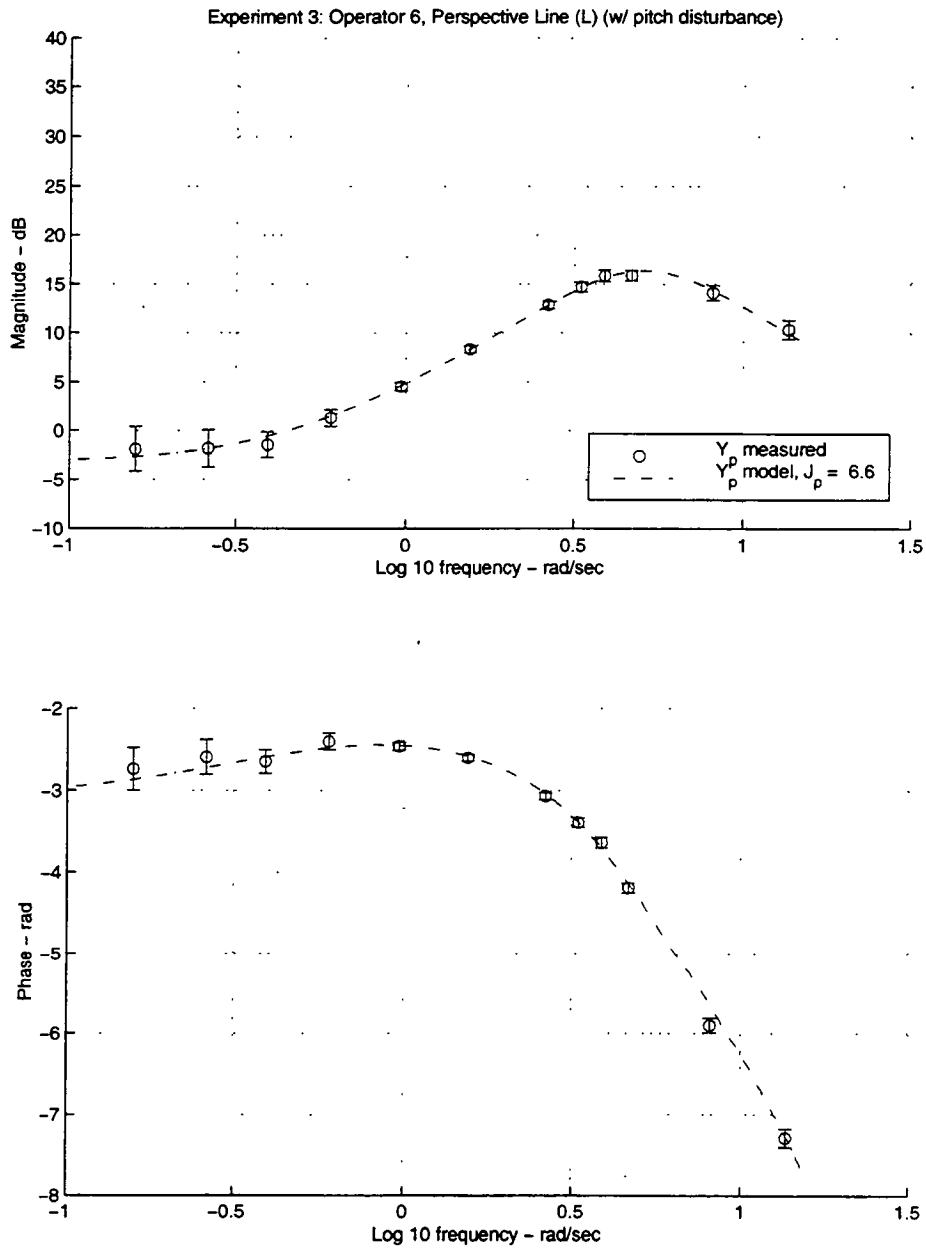

Figure F.12: Experiment 3 model fit results for Operator 6, Perspective Line Display, with pitch disturbance. NOTE: the data presented in this plot was collected during Experiment 2. It is presented here to allow better direct comparison with Experiment 3 data.

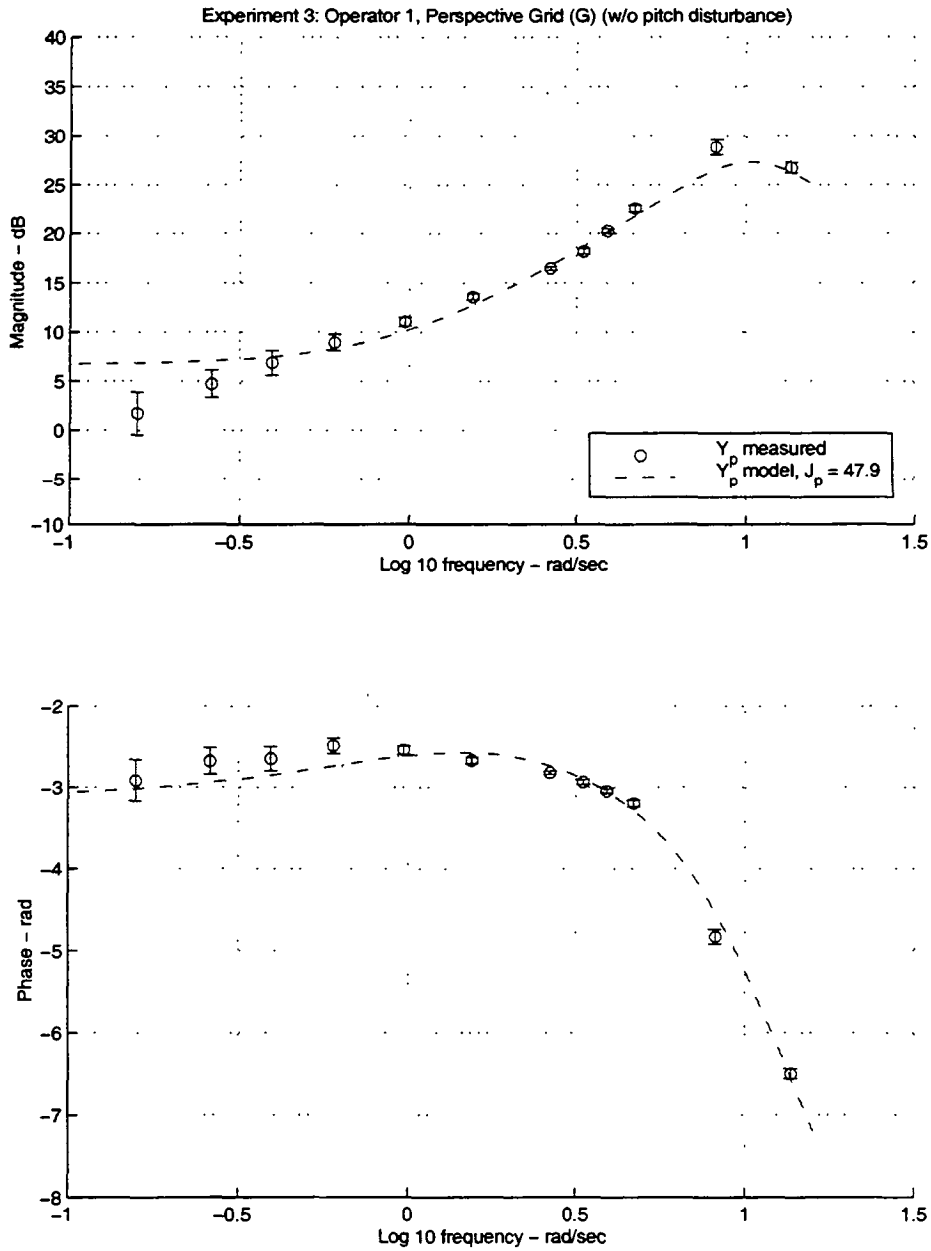

Figure F.13: Experiment 3 model fit results for Operator 1, Perspective Grid Display, with no pitch disturbance.

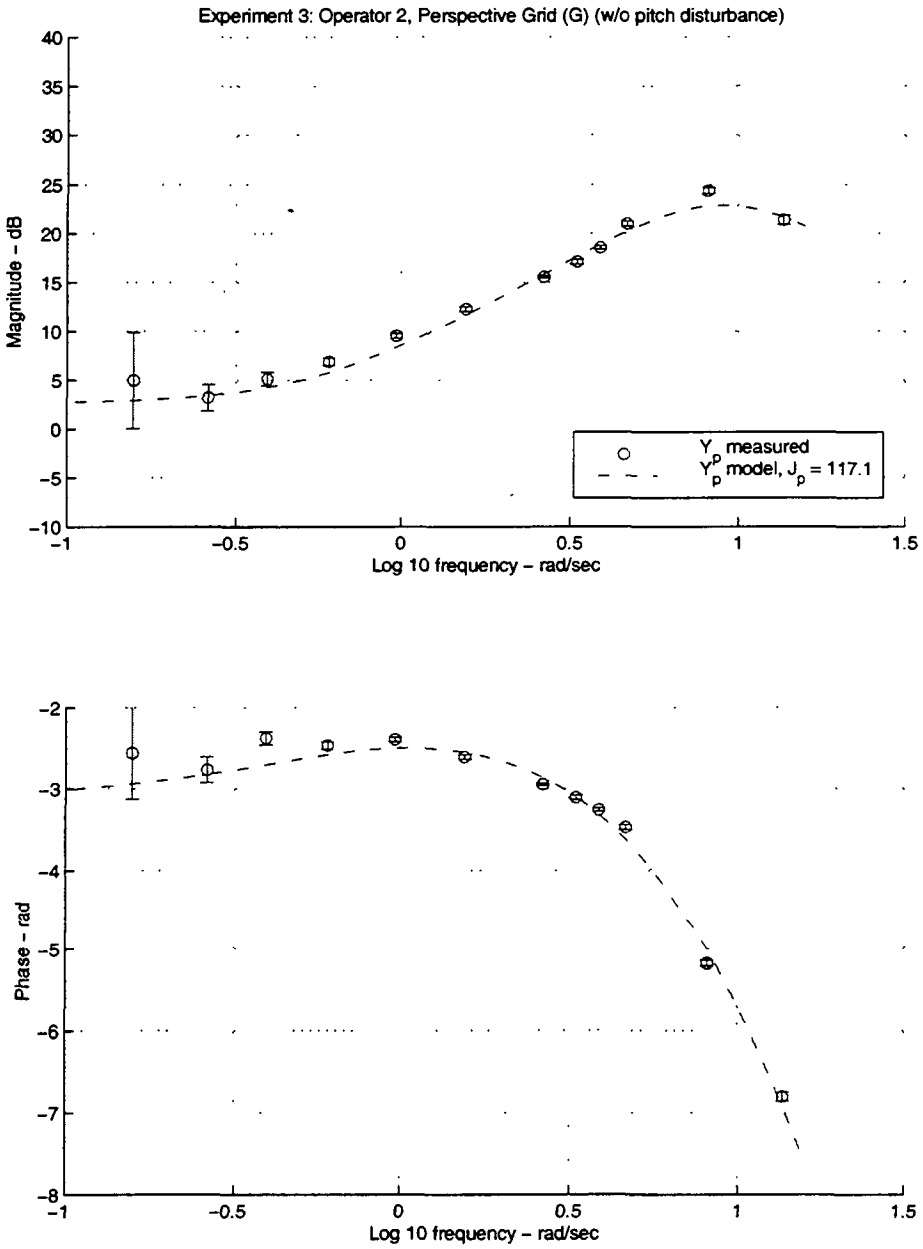

Figure F.14: Experiment 3 model fit results for Operator 2, Perspective Grid Display, with no pitch disturbance.

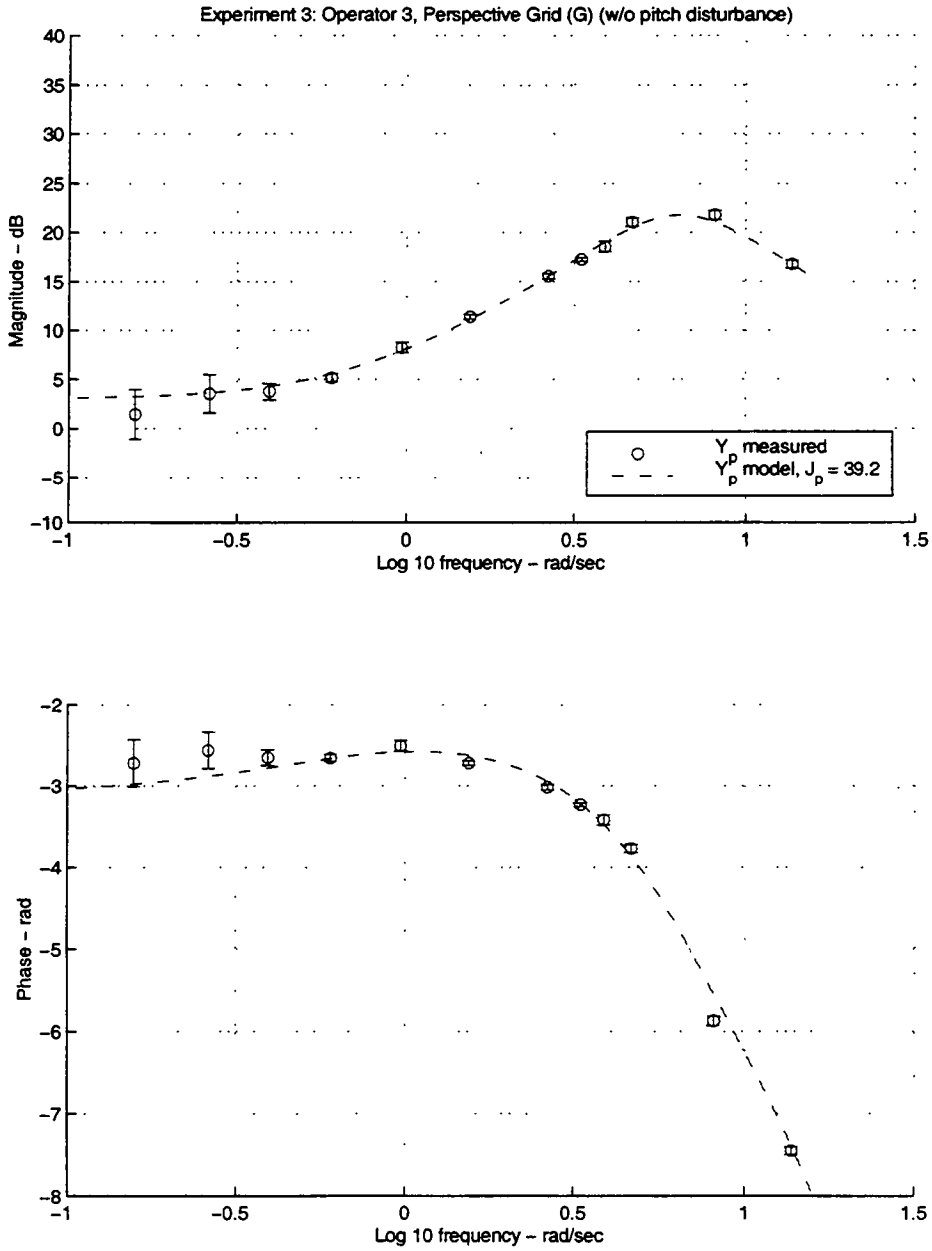

Figure F.15: Experiment 3 model fit results for Operator 3, Perspective Grid Display, with no pitch disturbance.

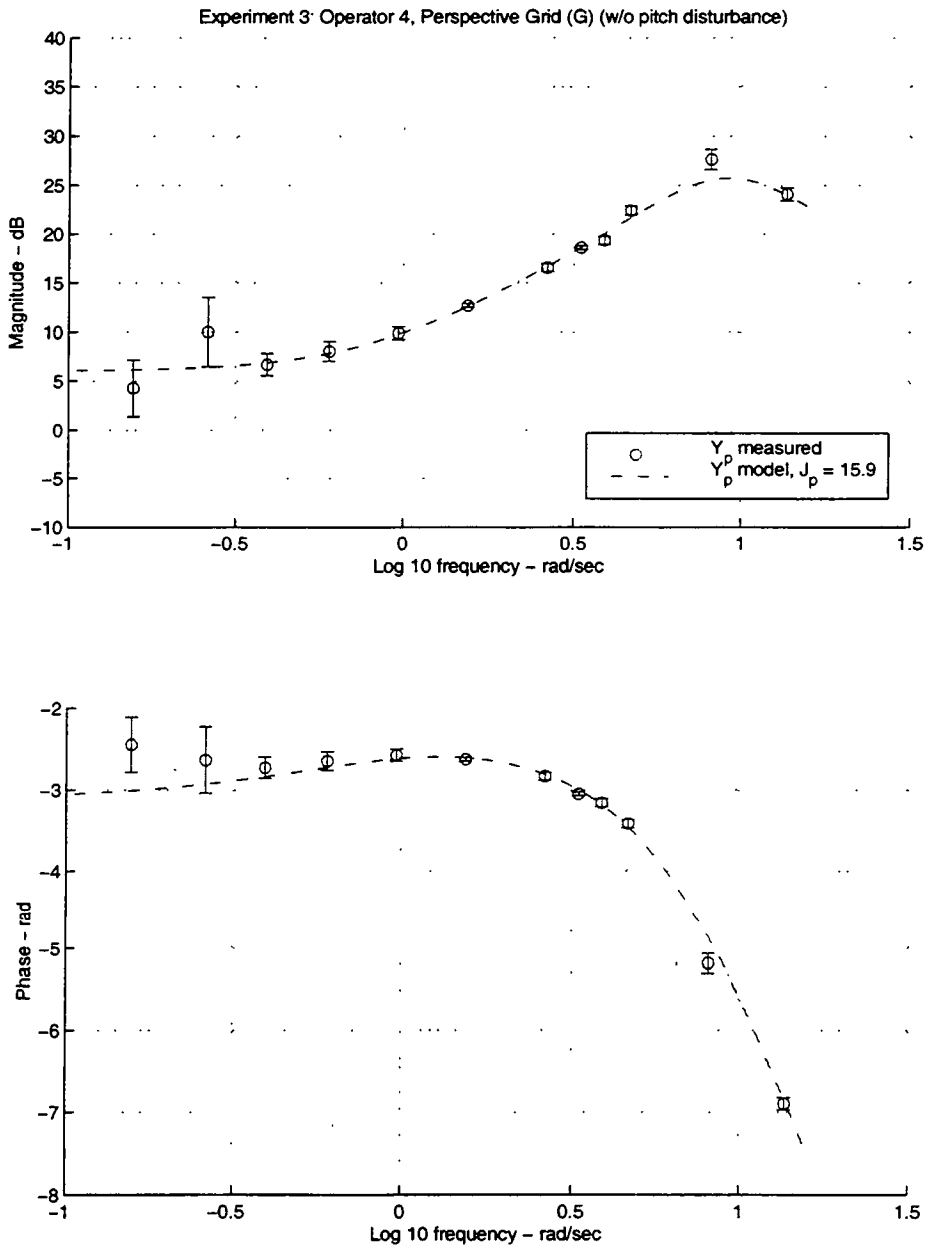

Figure F.16: Experiment 3 model fit results for Operator 4, Perspective Grid Display, with no pitch disturbance.

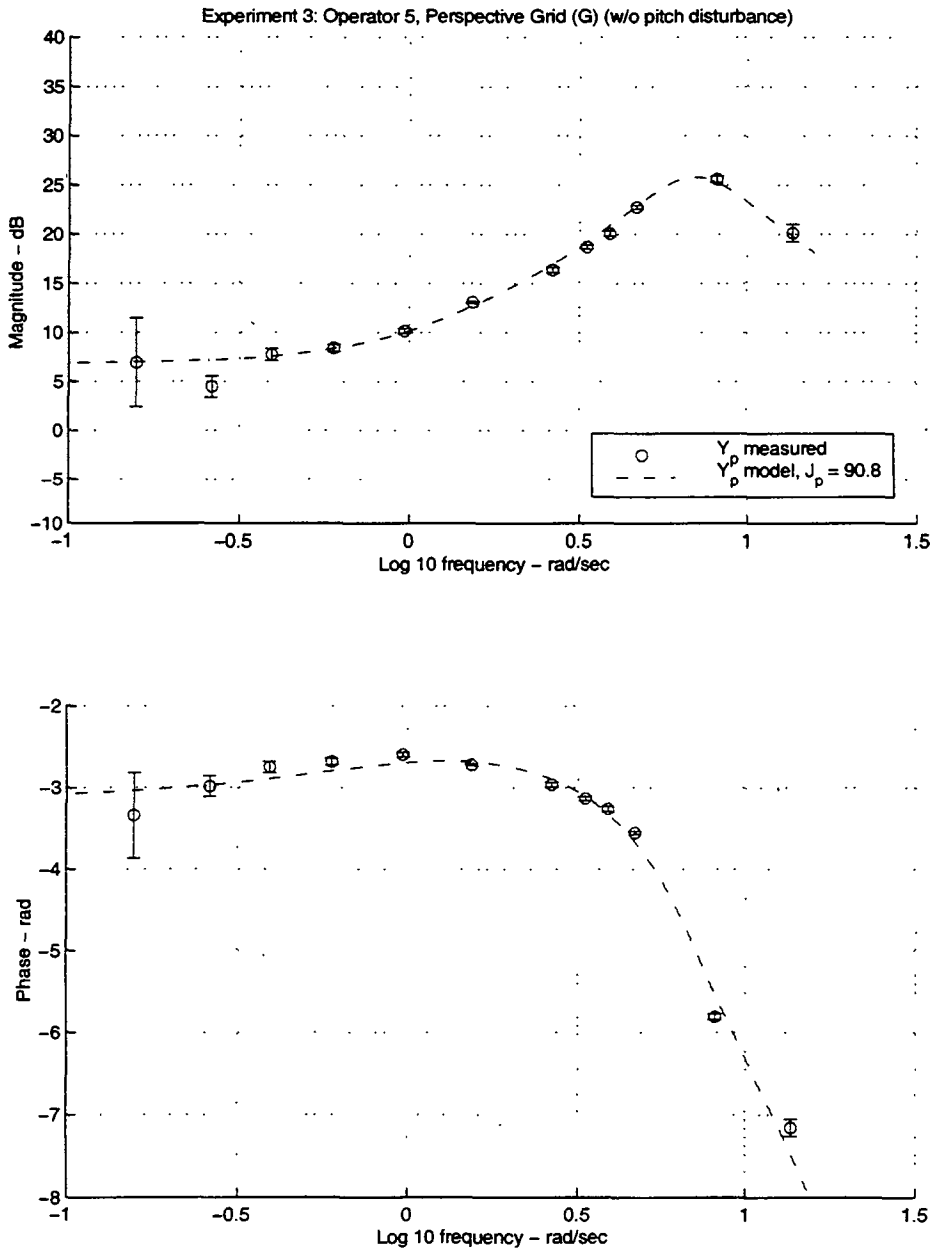

Figure F.17: Experiment 3 model fit results for Operator 5, Perspective Grid Display, with no pitch disturbance.

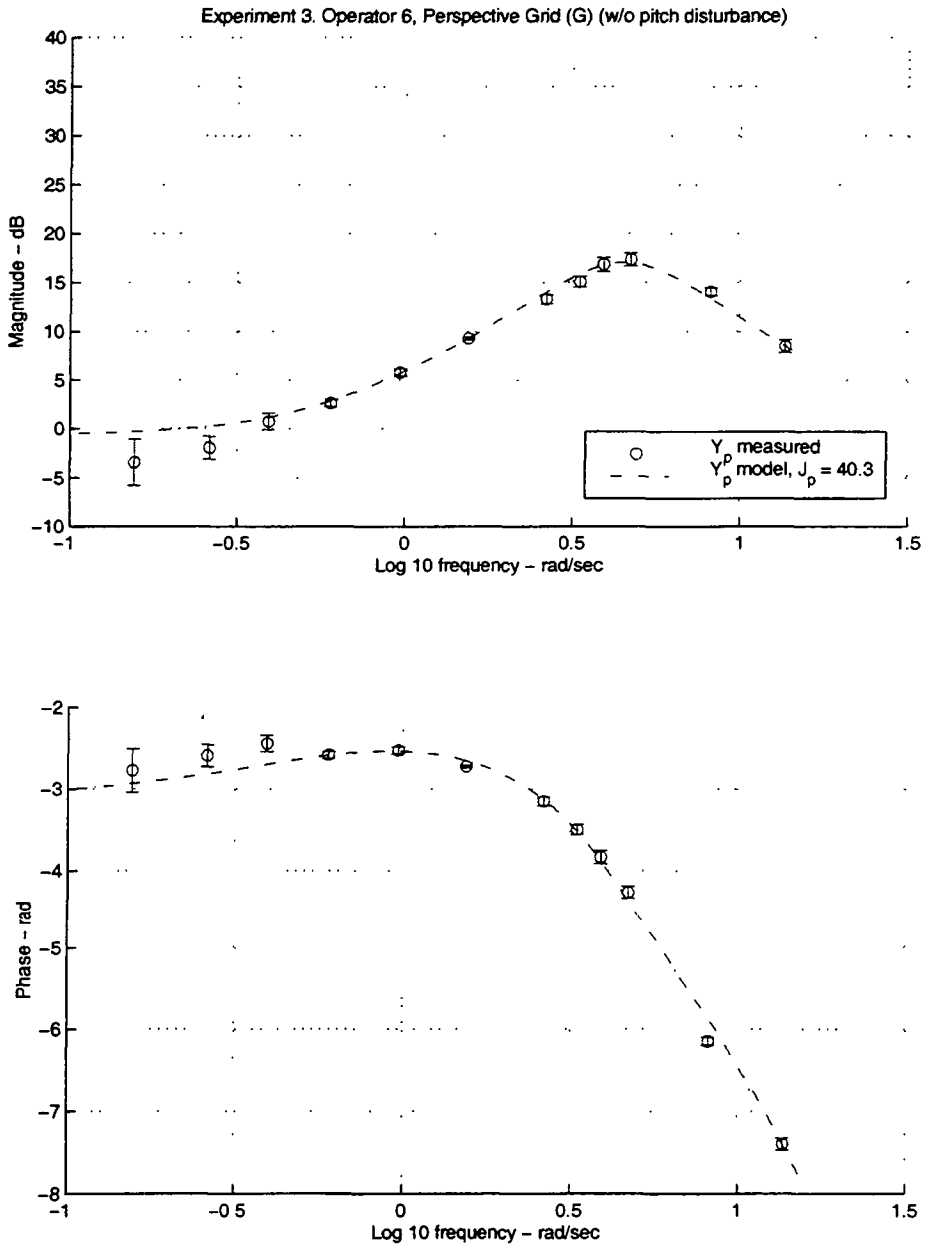

Figure F.18: Experiment 3 model fit results for Operator 6, Perspective Grid Display, with no pitch disturbance.

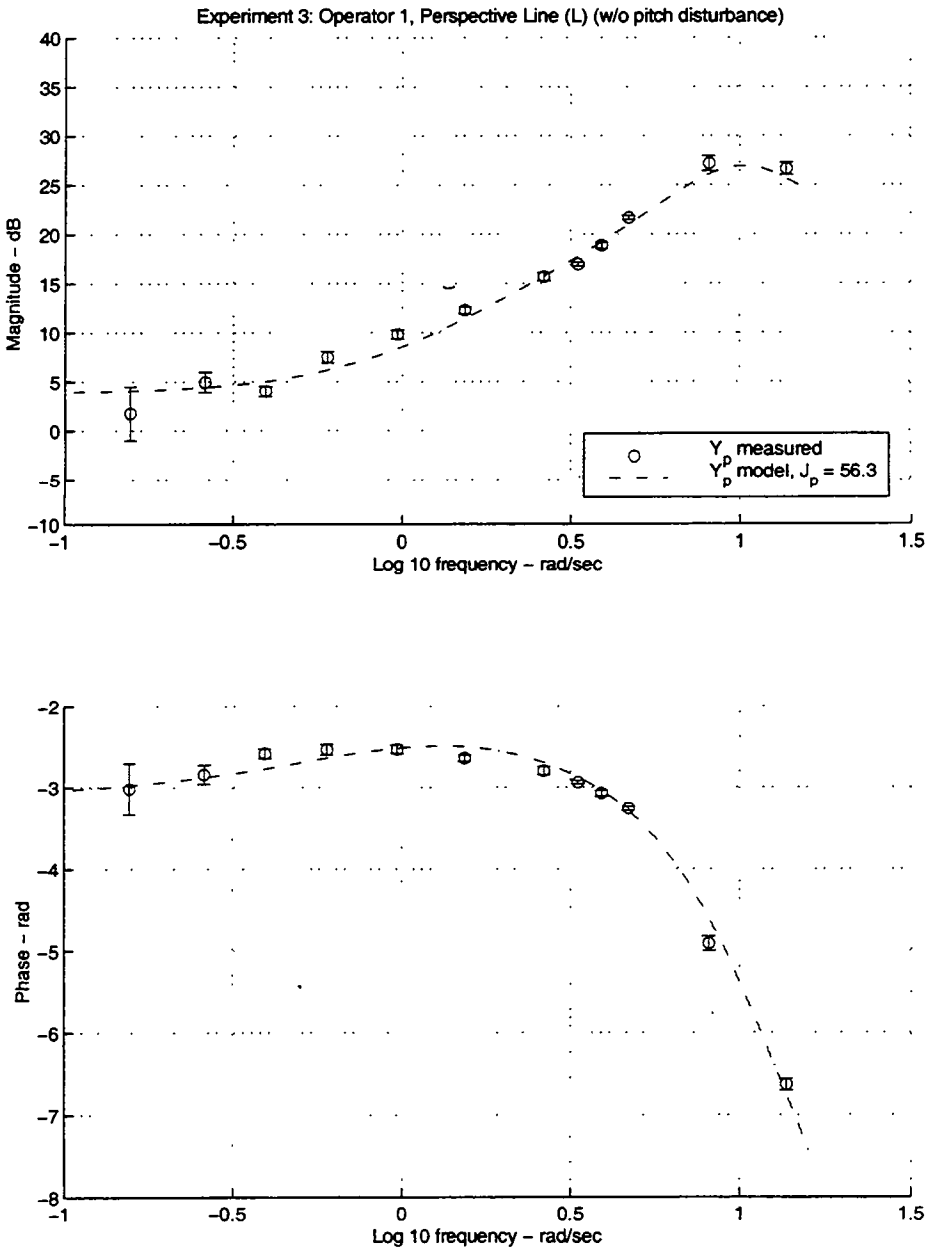

Figure F.19: Experiment 3 model fit results for Operator 1, Perspective Line Display, with no pitch disturbance.

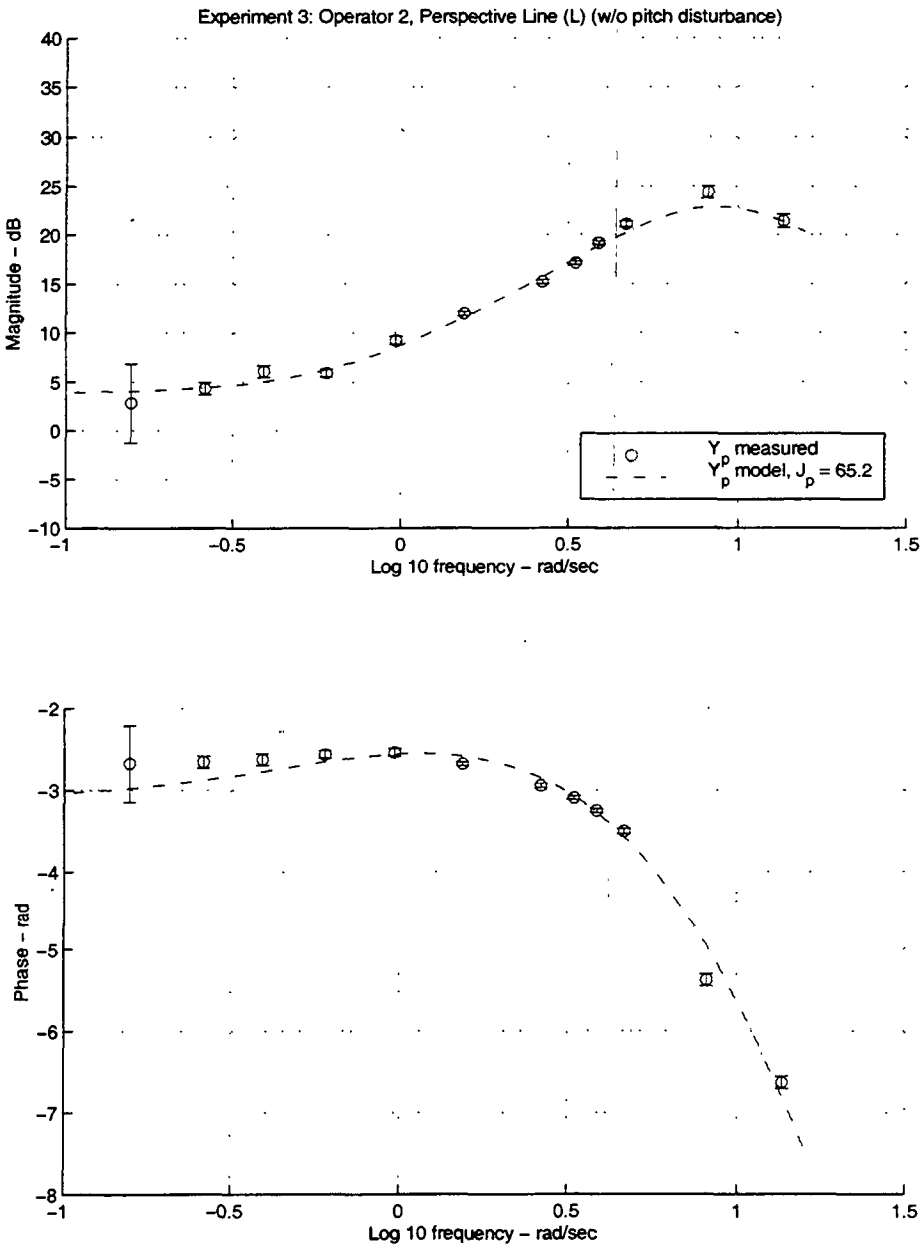

Figure F.20: Experiment 3 model fit results for Operator 2, Perspective Line Display, with no pitch disturbance.

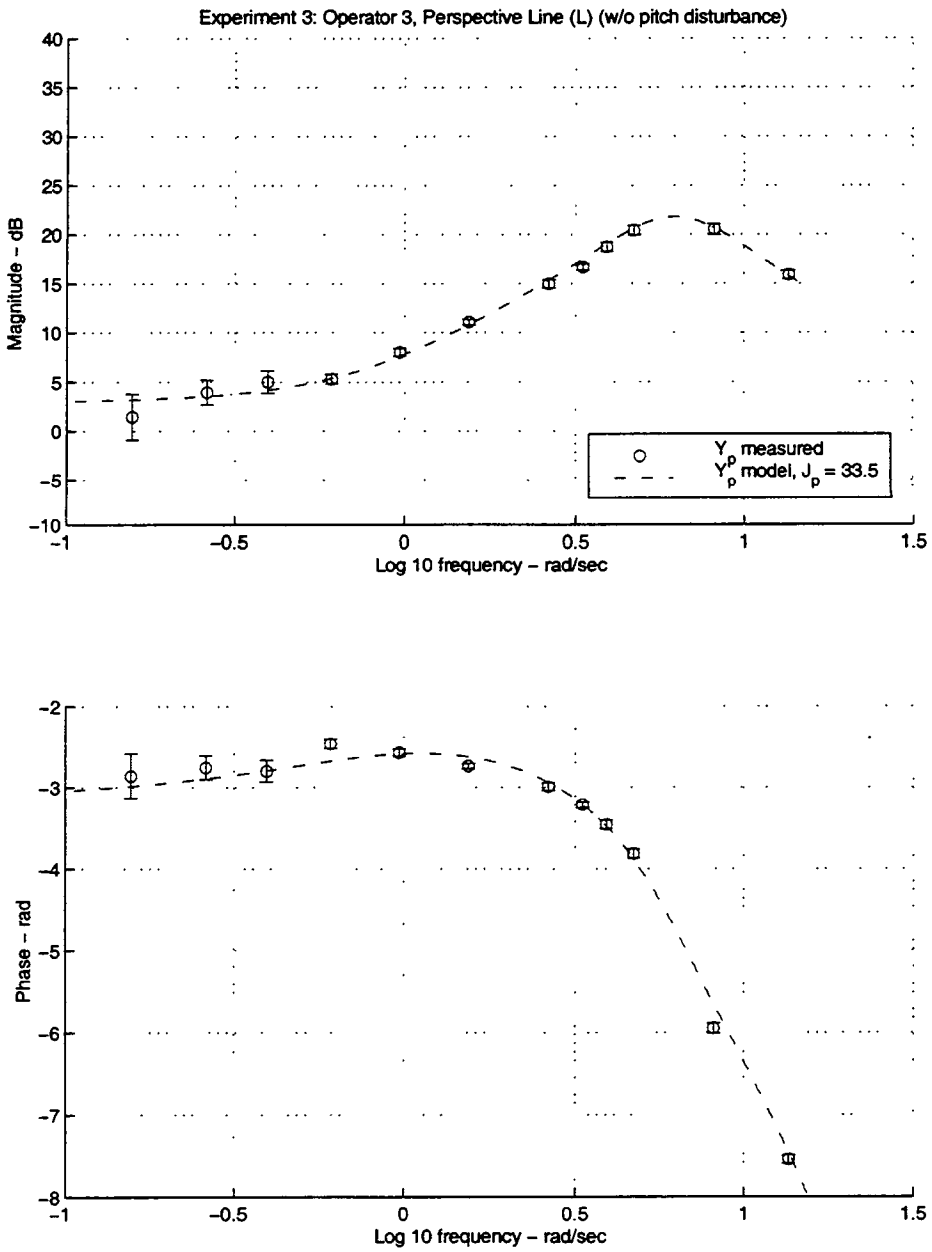

Figure F.21: Experiment 3 model fit results for Operator 3, Perspective Line Display, with no pitch disturbance.

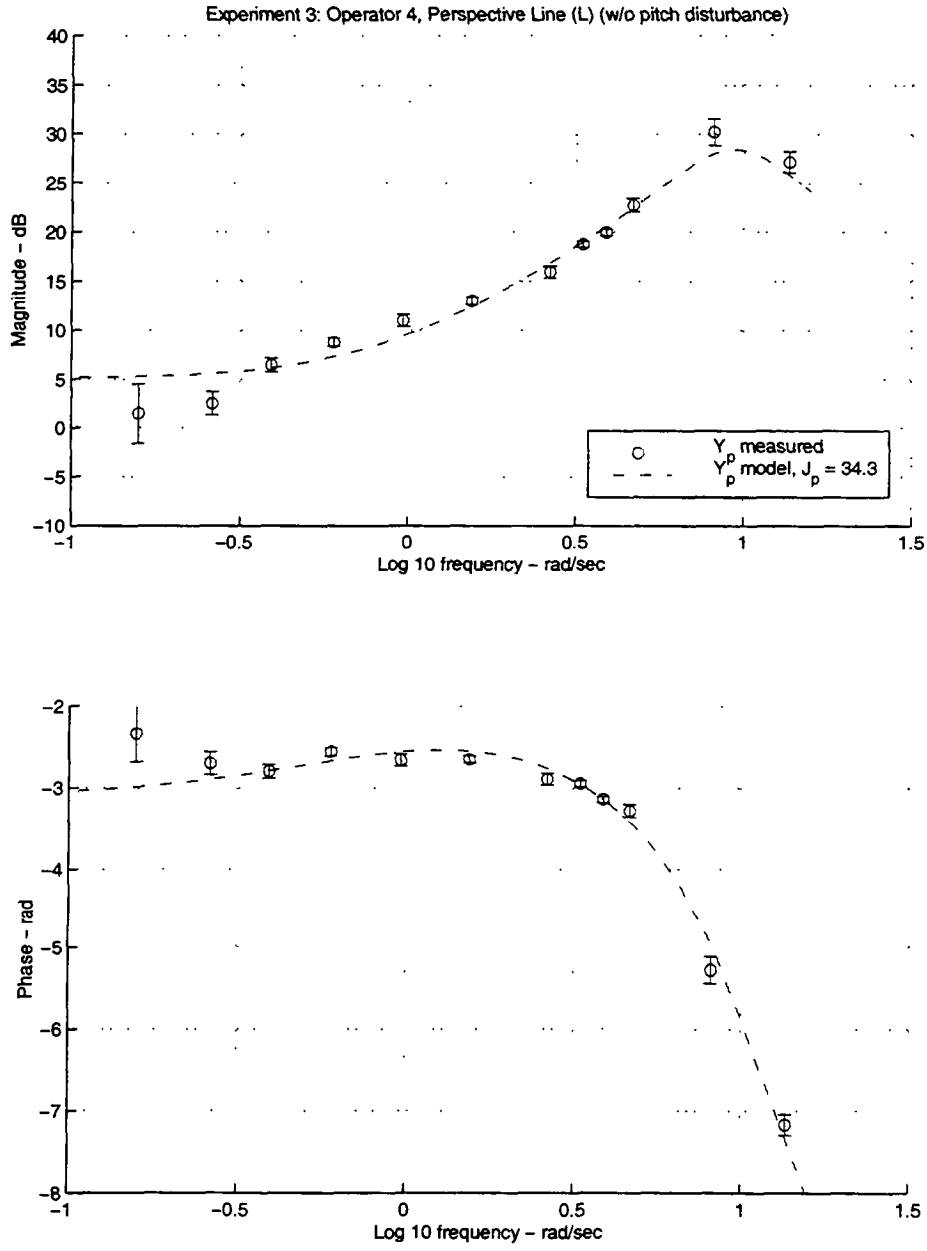

Figure F.22: Experiment 3 model fit results for Operator 4, Perspective Line Display, with no pitch disturbance.

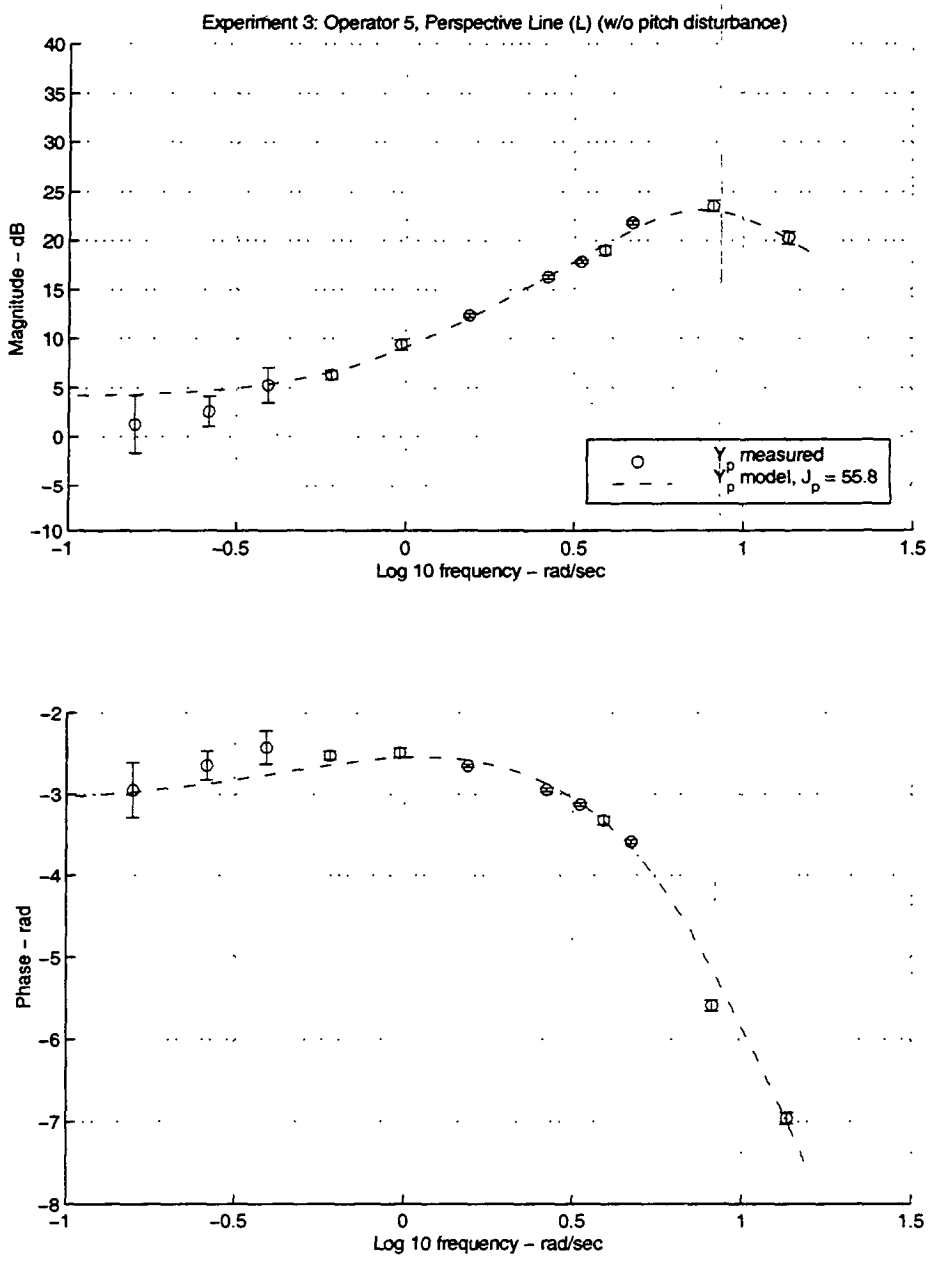

Figure F.23: Experiment 3 model fit results for Operator 5, Perspective Line Display, with no pitch disturbance.

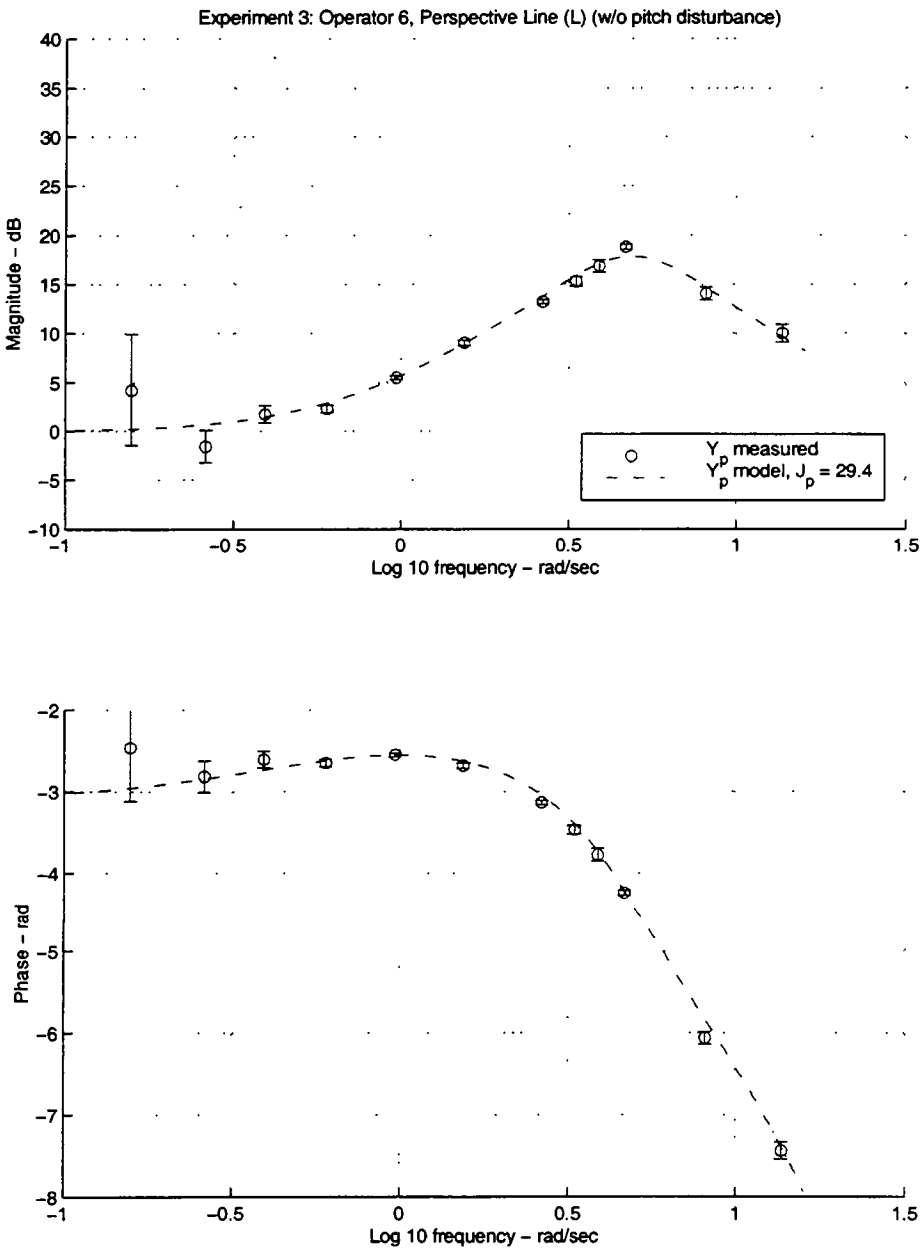

Figure F.24: Experiment 3 model fit results for Operator 6, Perspective Line Display, with no pitch disturbance.

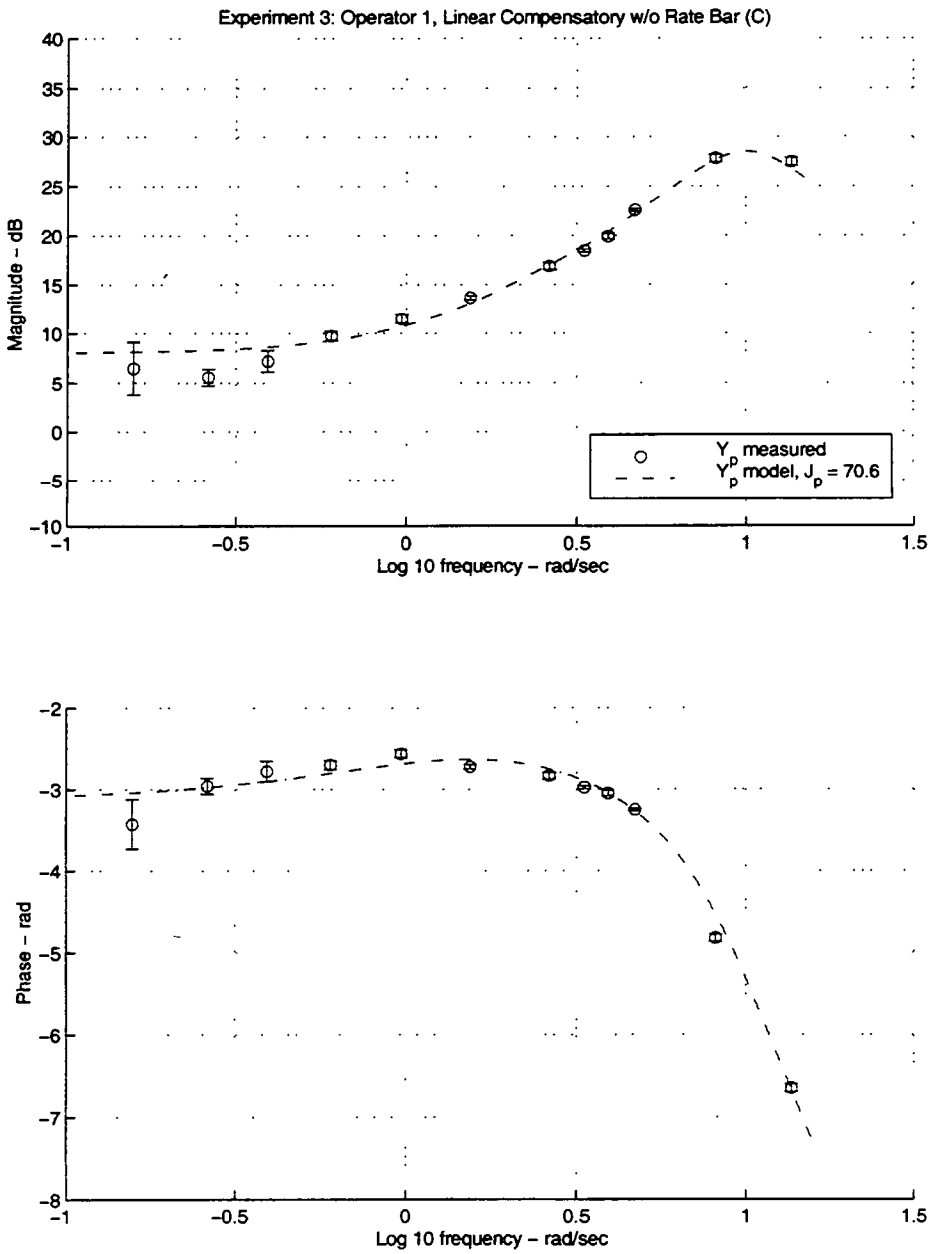

Figure F.25: Experiment 3 model fit results for Operator 1, Linear Compensatory Display, with no pitch disturbance.

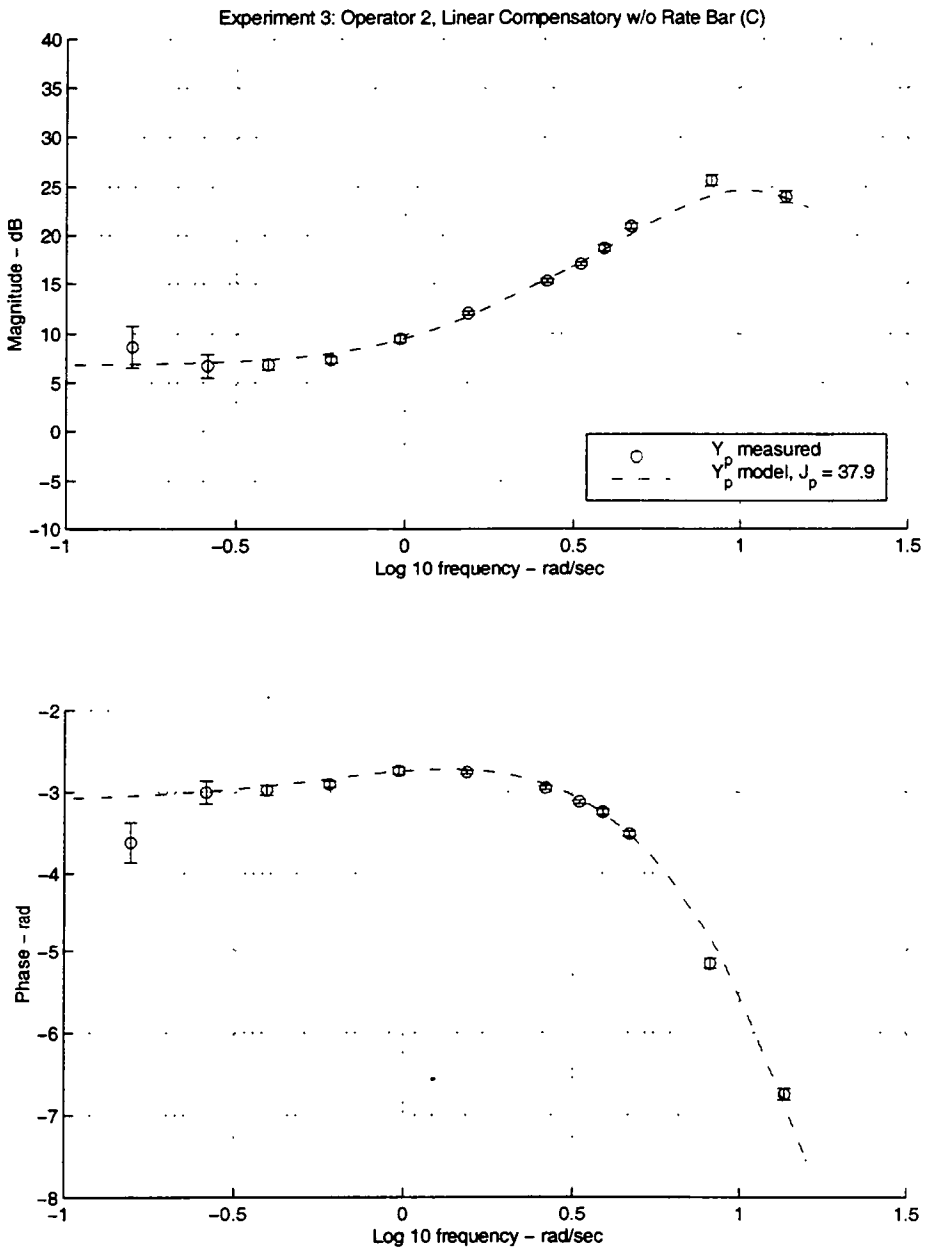

Figure F.26: Experiment 3 model fit results for Operator 2, Linear Compensatory Display, with no pitch disturbance.

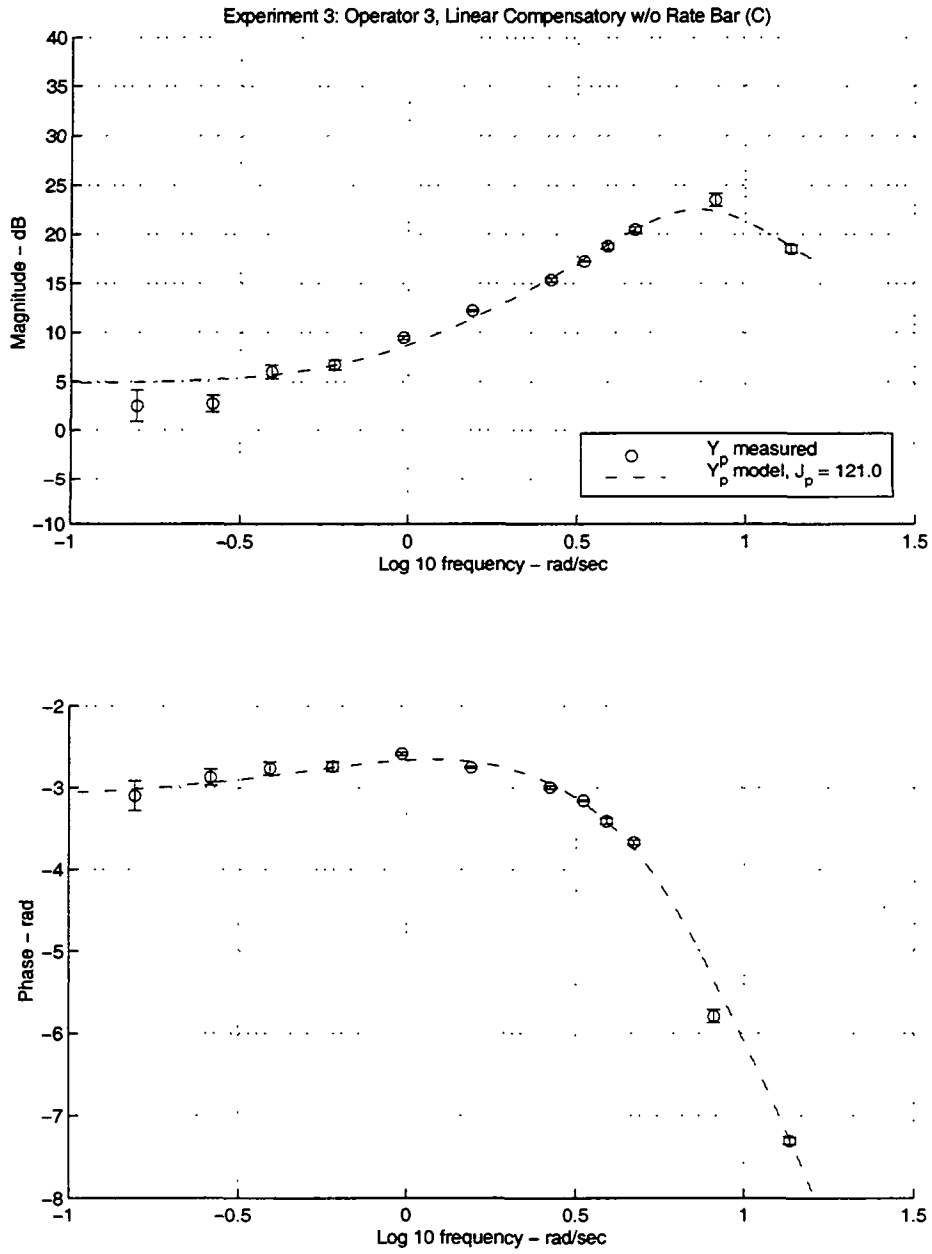

Figure F.27: Experiment 3 model fit results for Operator 3, Linear Compensatory Display, with no pitch disturbance.

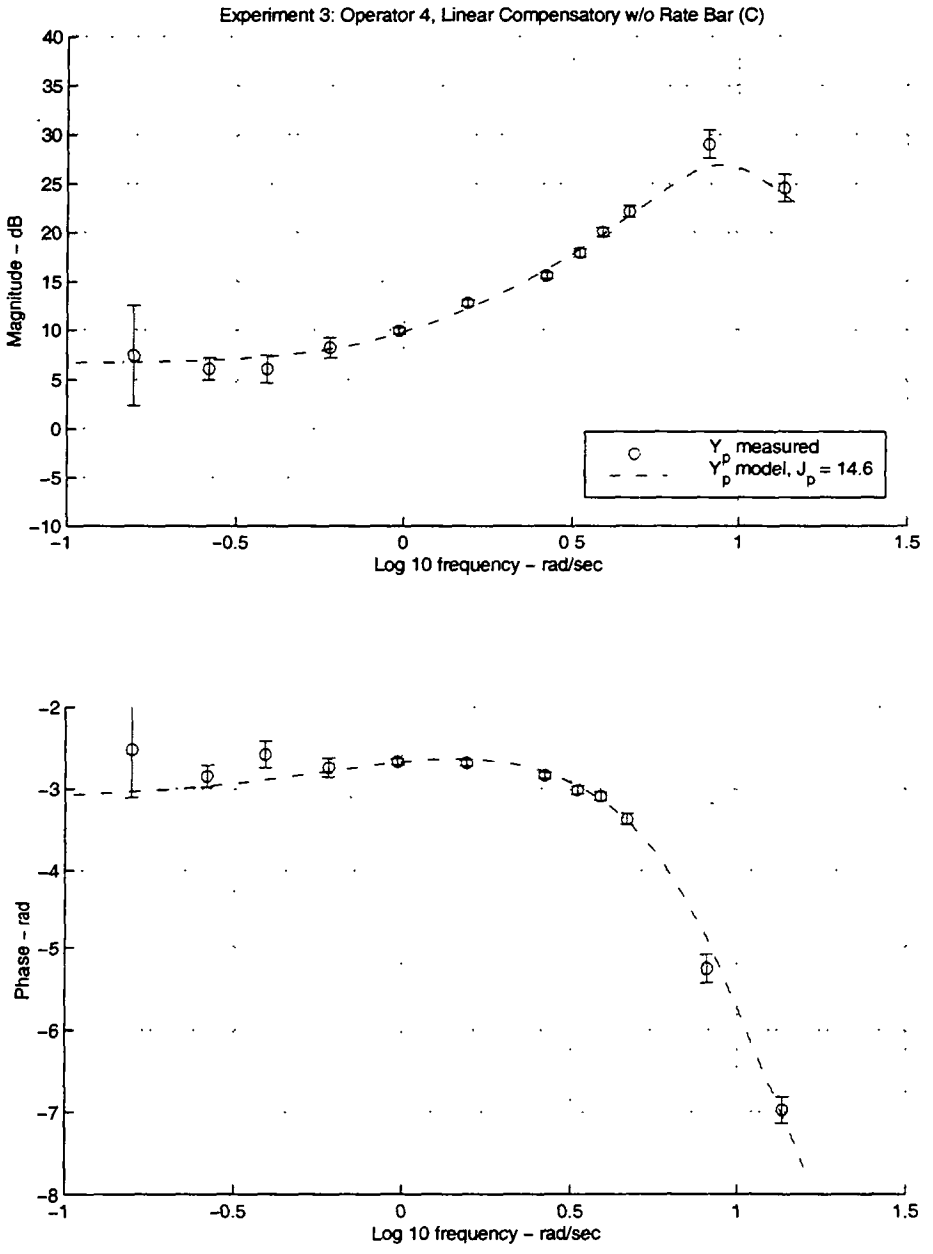

Figure F.28: Experiment 3 model fit results for Operator 4, Linear Compensatory Display, with no pitch disturbance.

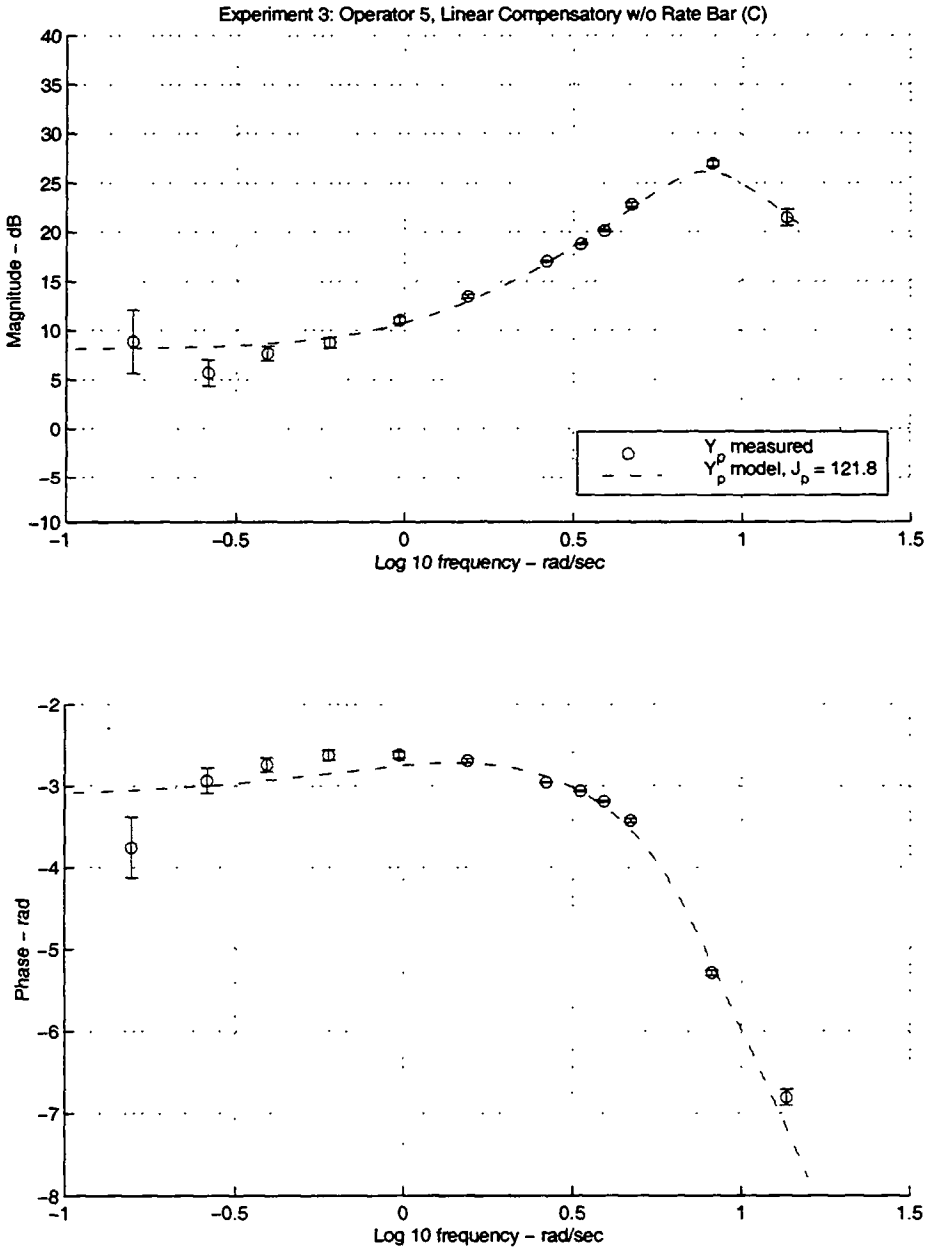

Figure F.29: Experiment 3 model fit results for Operator 5, Linear Compensatory Display, with no pitch disturbance.

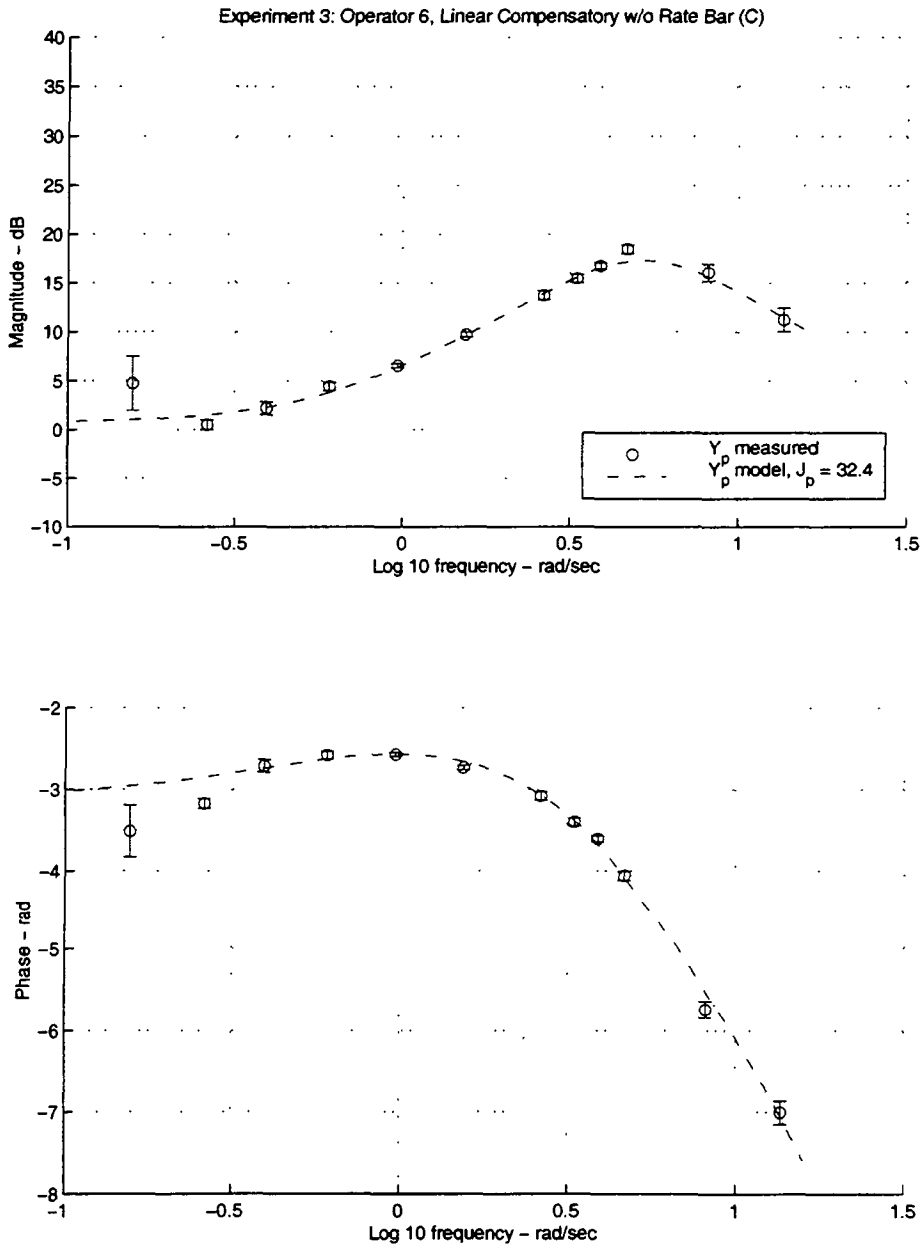

Figure F.30: Experiment 3 model fit results for Operator 6, Linear Compensatory Display, with no pitch disturbance.

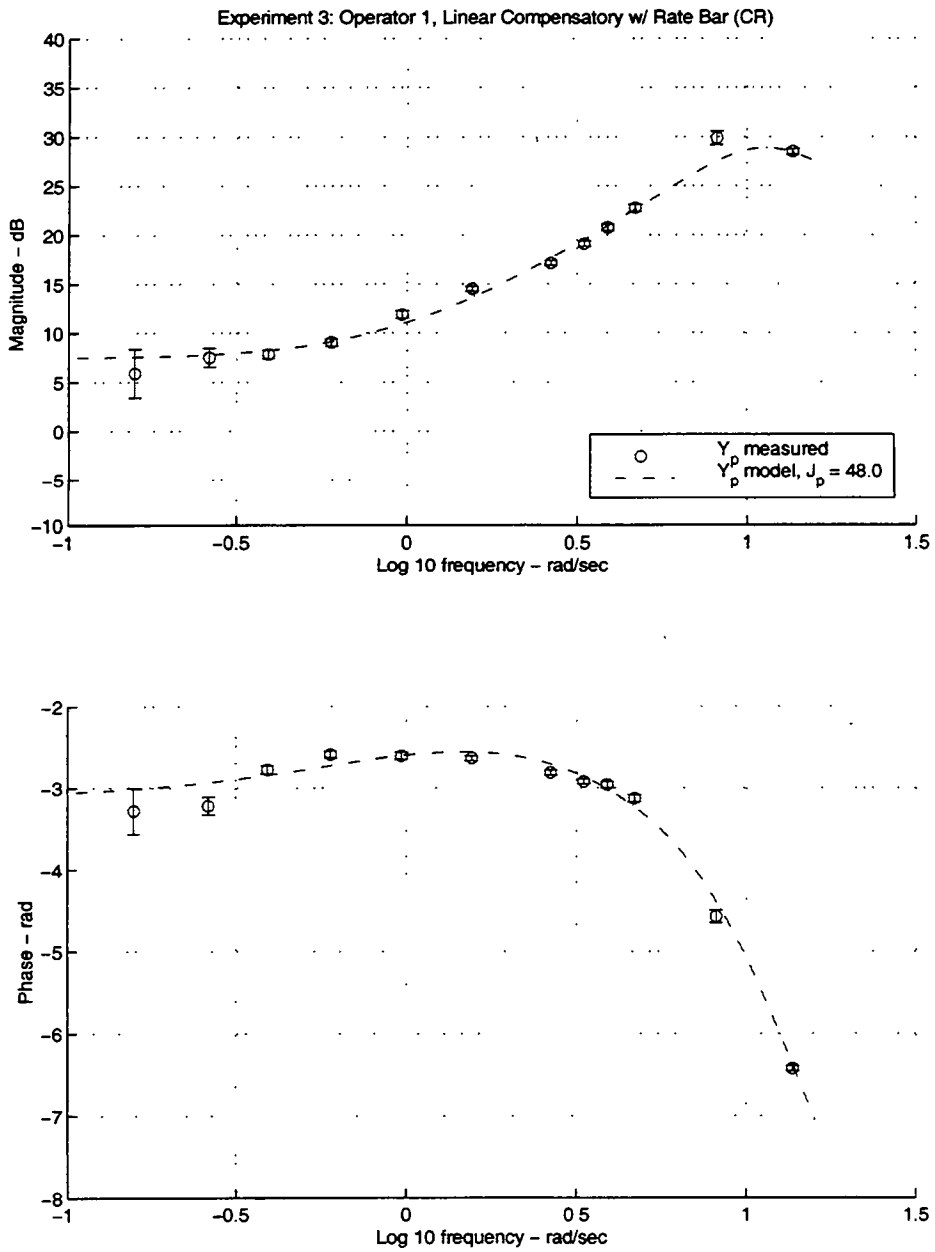

Figure F.31: Experiment 3 model fit results for Operator 1, Linear Compensatory w/Rate Bar Display, with no pitch disturbance.

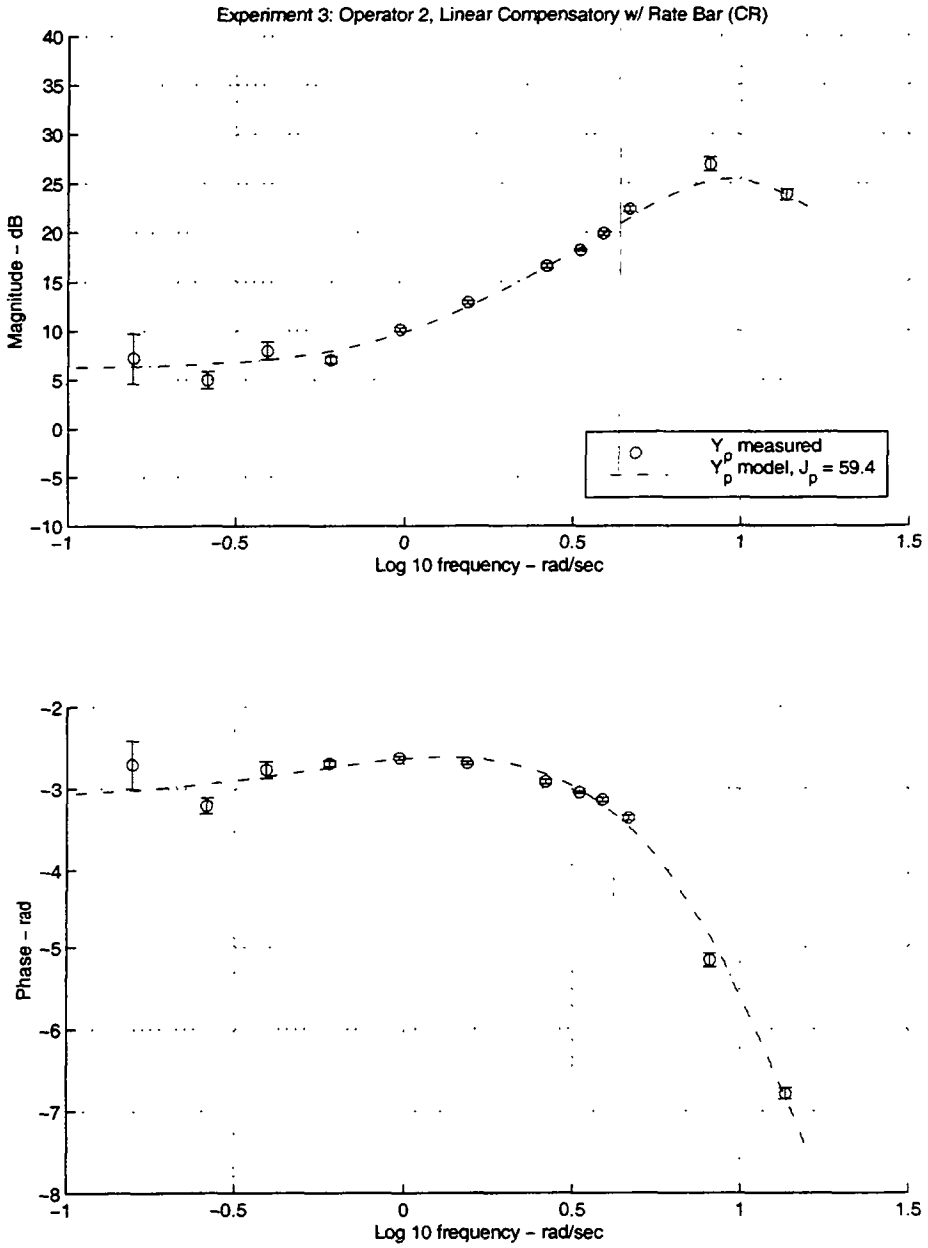

Figure F.32: Experiment 3 model fit results for Operator 2, Linear Compensatory w/Rate Bar Display, with no pitch disturbance.

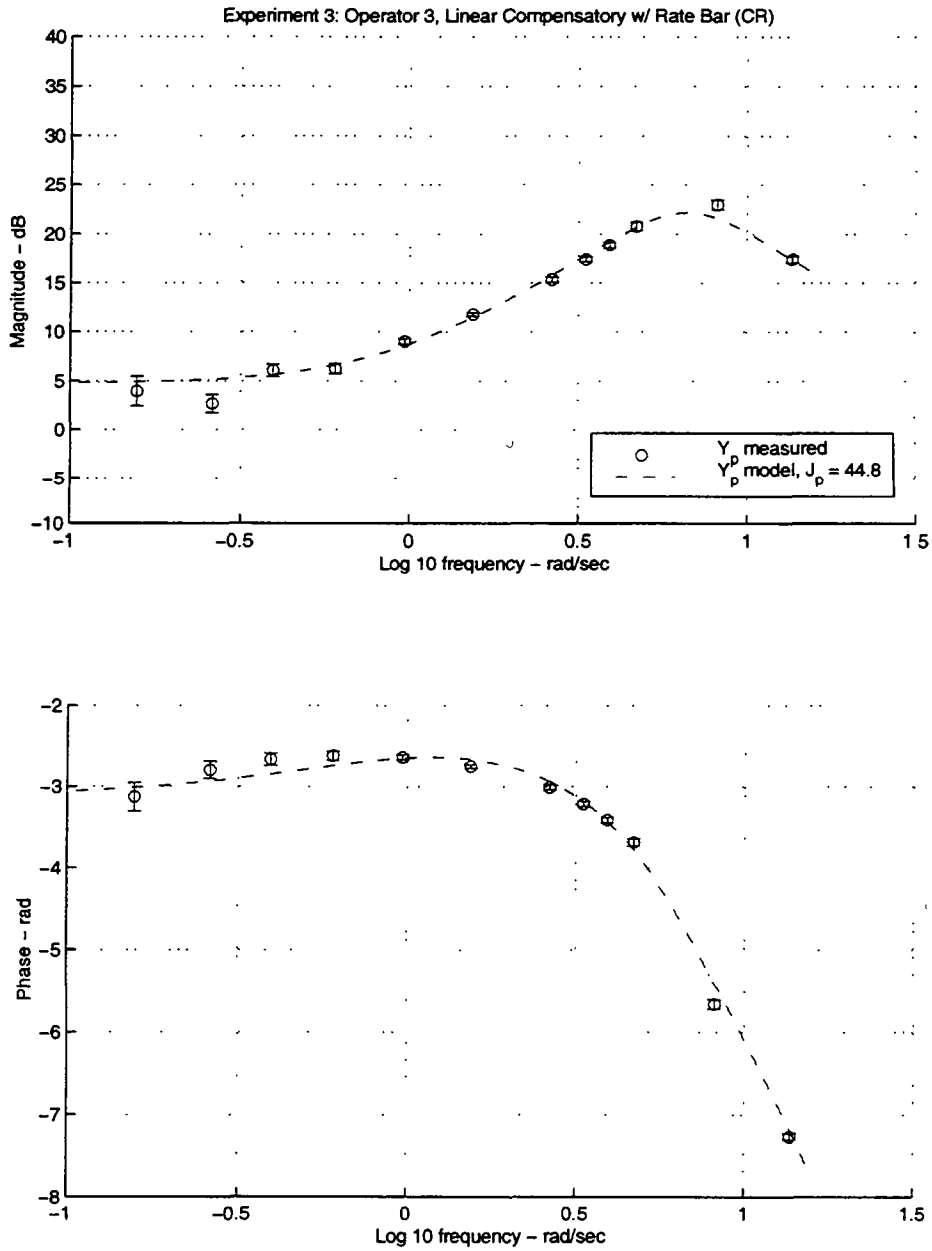

Figure F.33: Experiment 3 model fit results for Operator 3, Linear Compensatory w/Rate Bar Display, with no pitch disturbance.

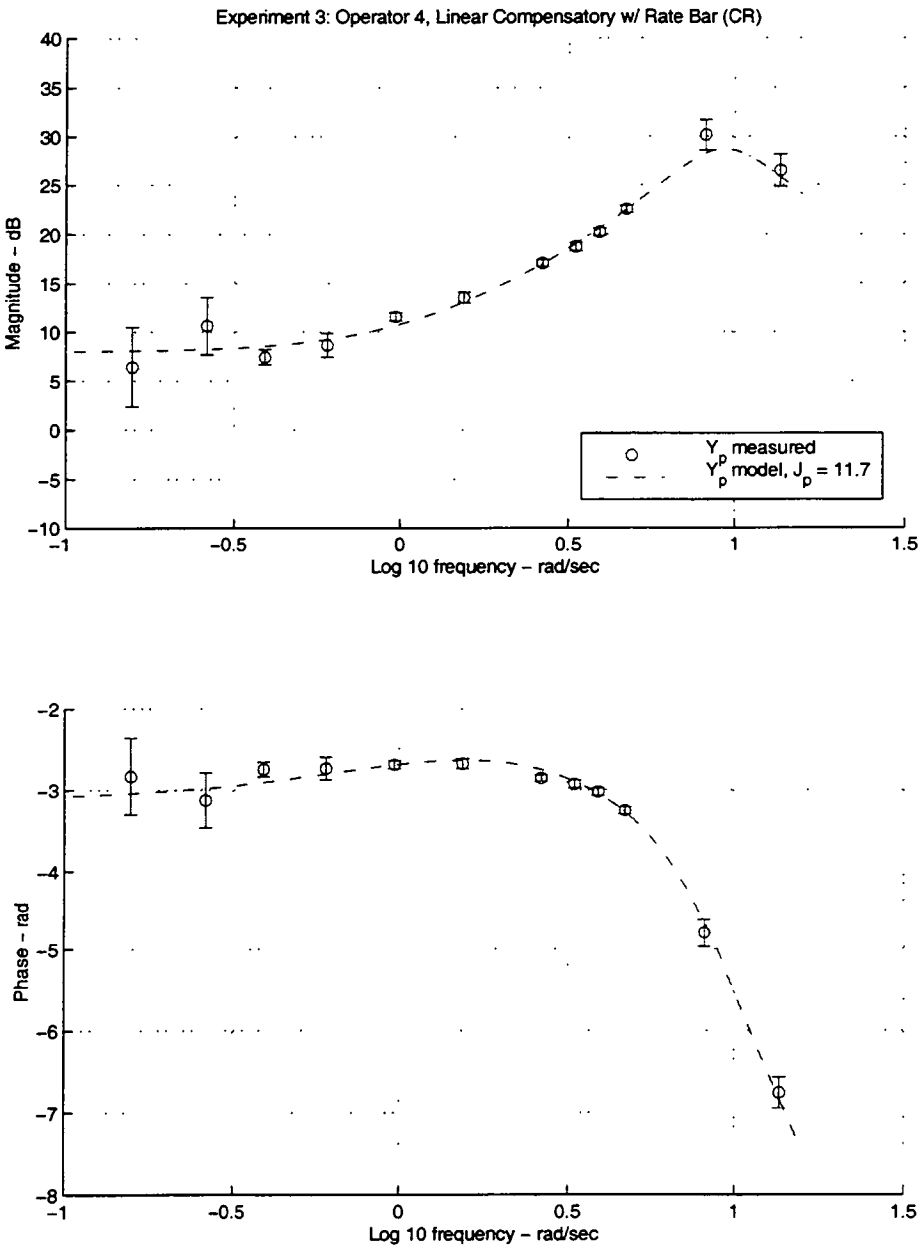

Figure F.34: Experiment 3 model fit results for Operator 4, Linear Compensatory w/Rate Bar Display, with no pitch disturbance.

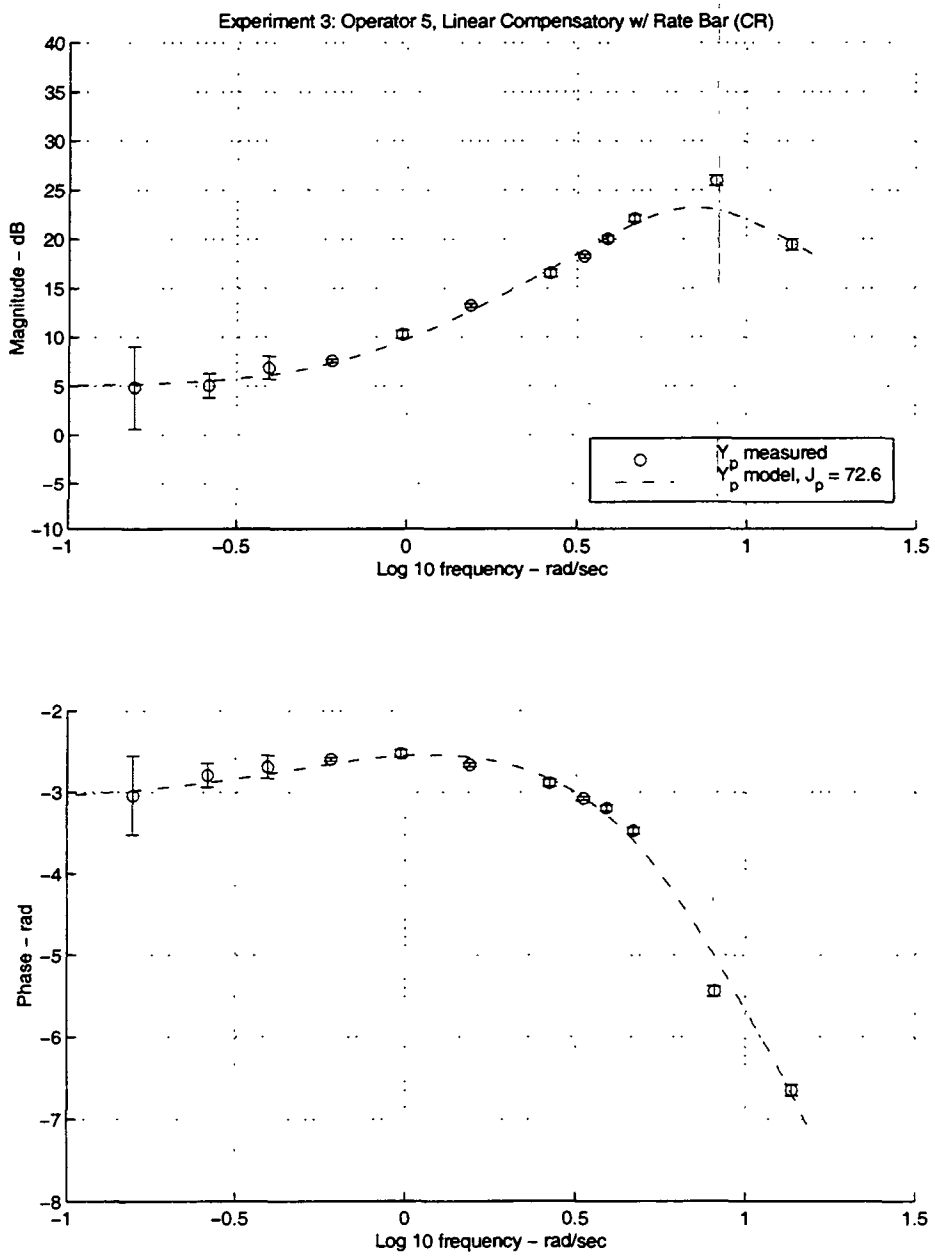

Figure F.35: Experiment 3 model fit results for Operator 5, Linear Compensatory w/Rate Bar Display, with no pitch disturbance.

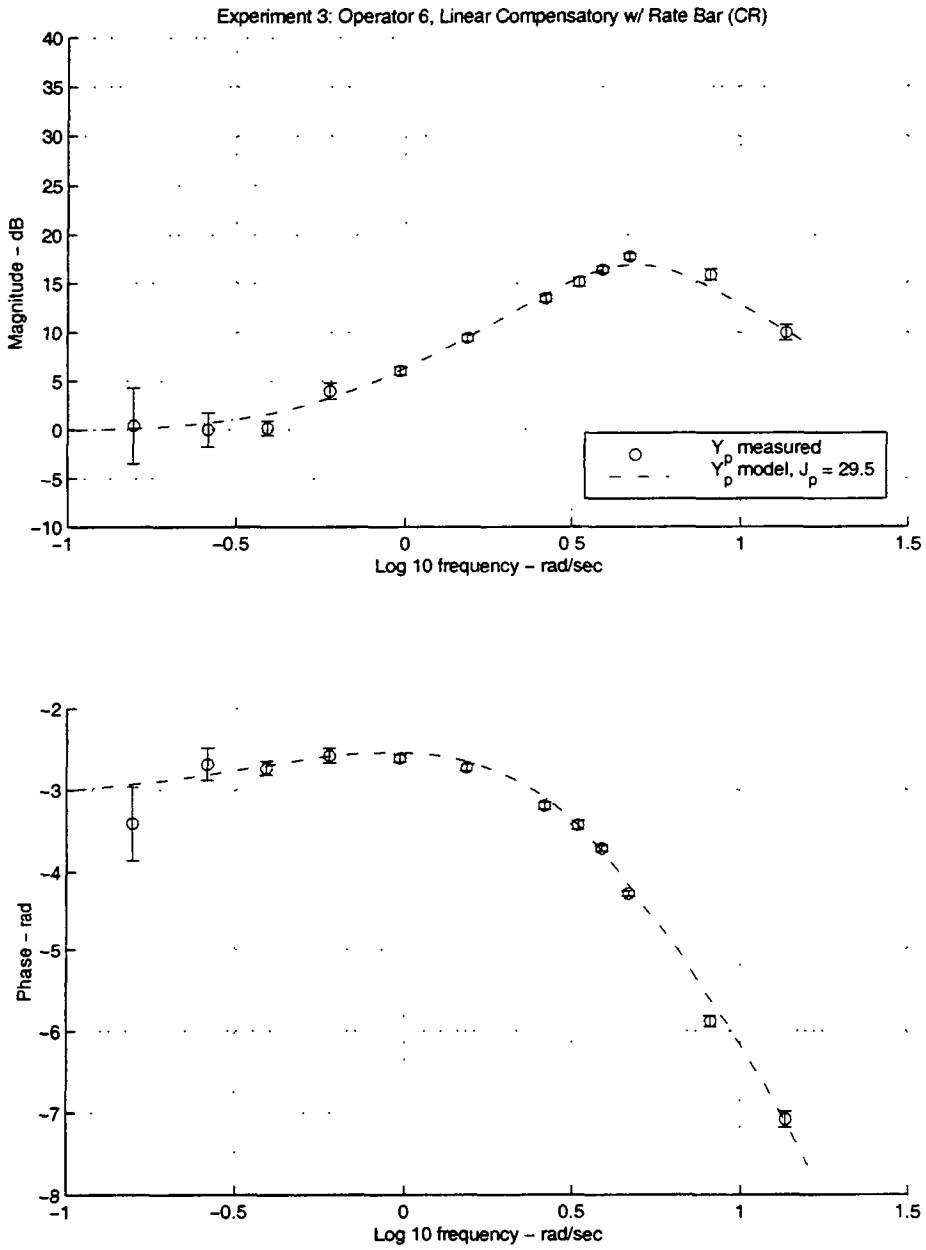

Figure F.36: Experiment 3 model fit results for Operator 6, Linear Compensatory w/Rate Bar Display, with no pitch disturbance.

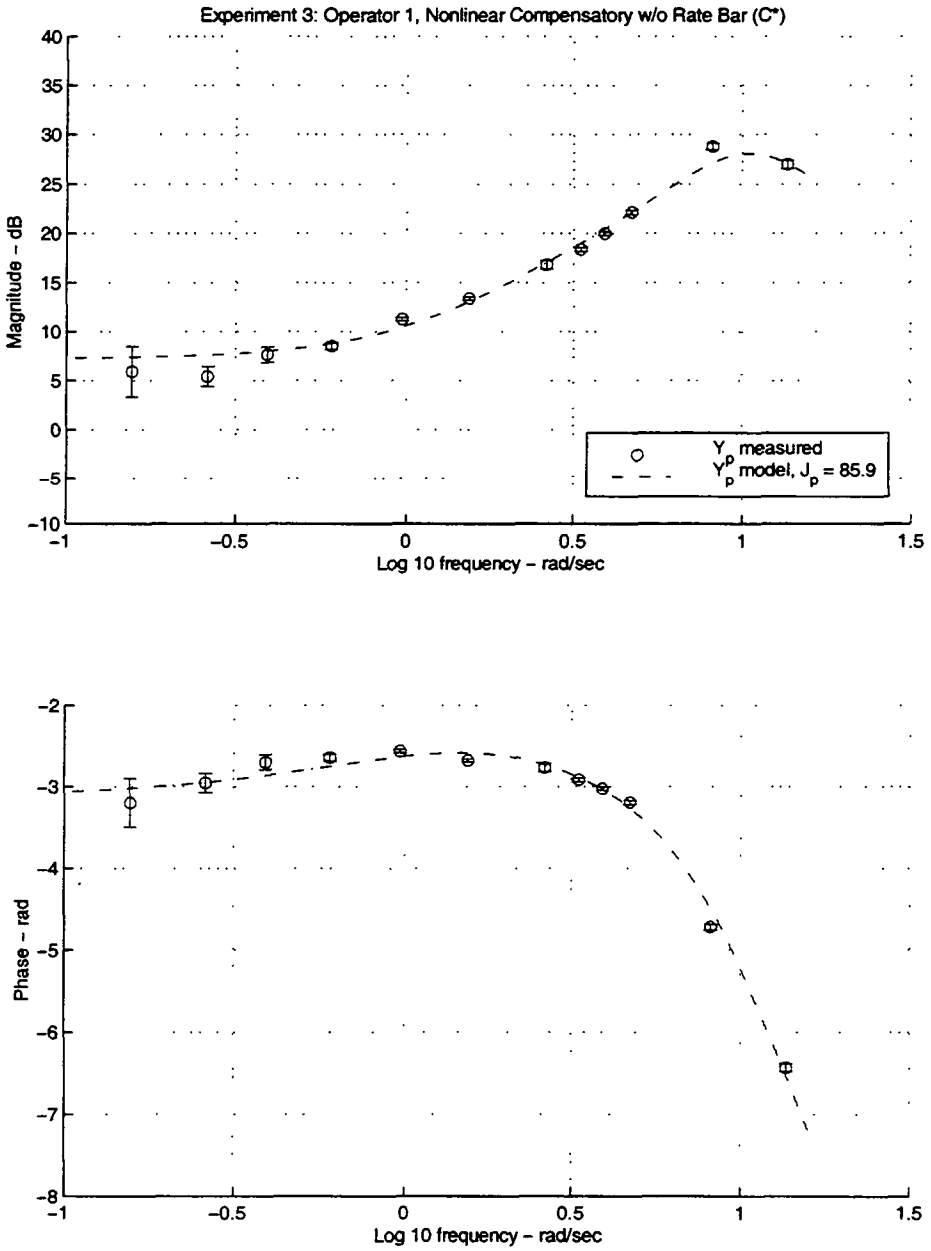

Figure F.37: Experiment 3 model fit results for Operator 1, Nonlinear Compensatory Display, with no pitch disturbance.

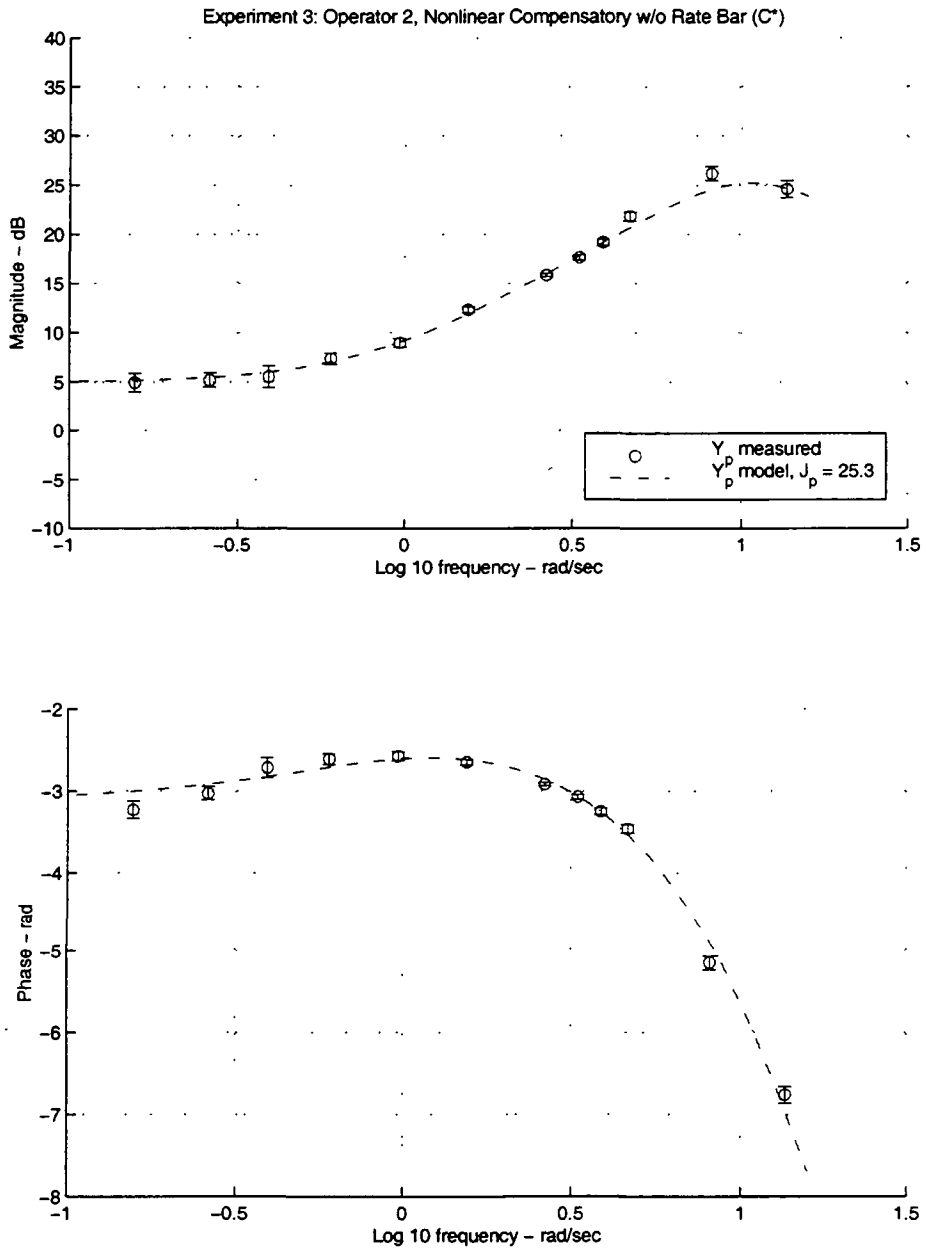

Figure F.38: Experiment 3 model fit results for Operator 2, Nonlinear Compensatory Display, with no pitch disturbance.

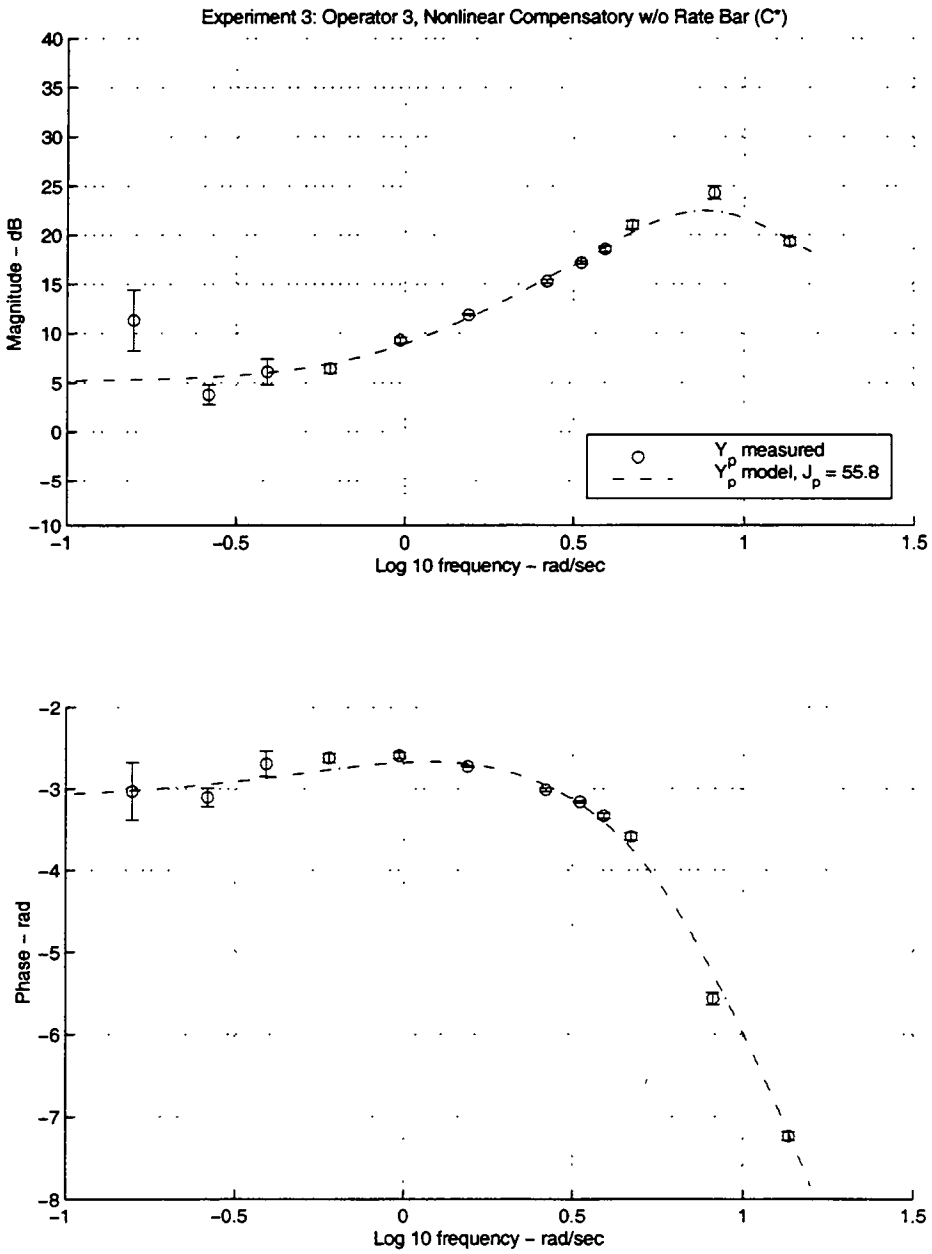

Figure F.39: Experiment 3 model fit results for Operator 3, Nonlinear Compensatory Display, with no pitch disturbance.

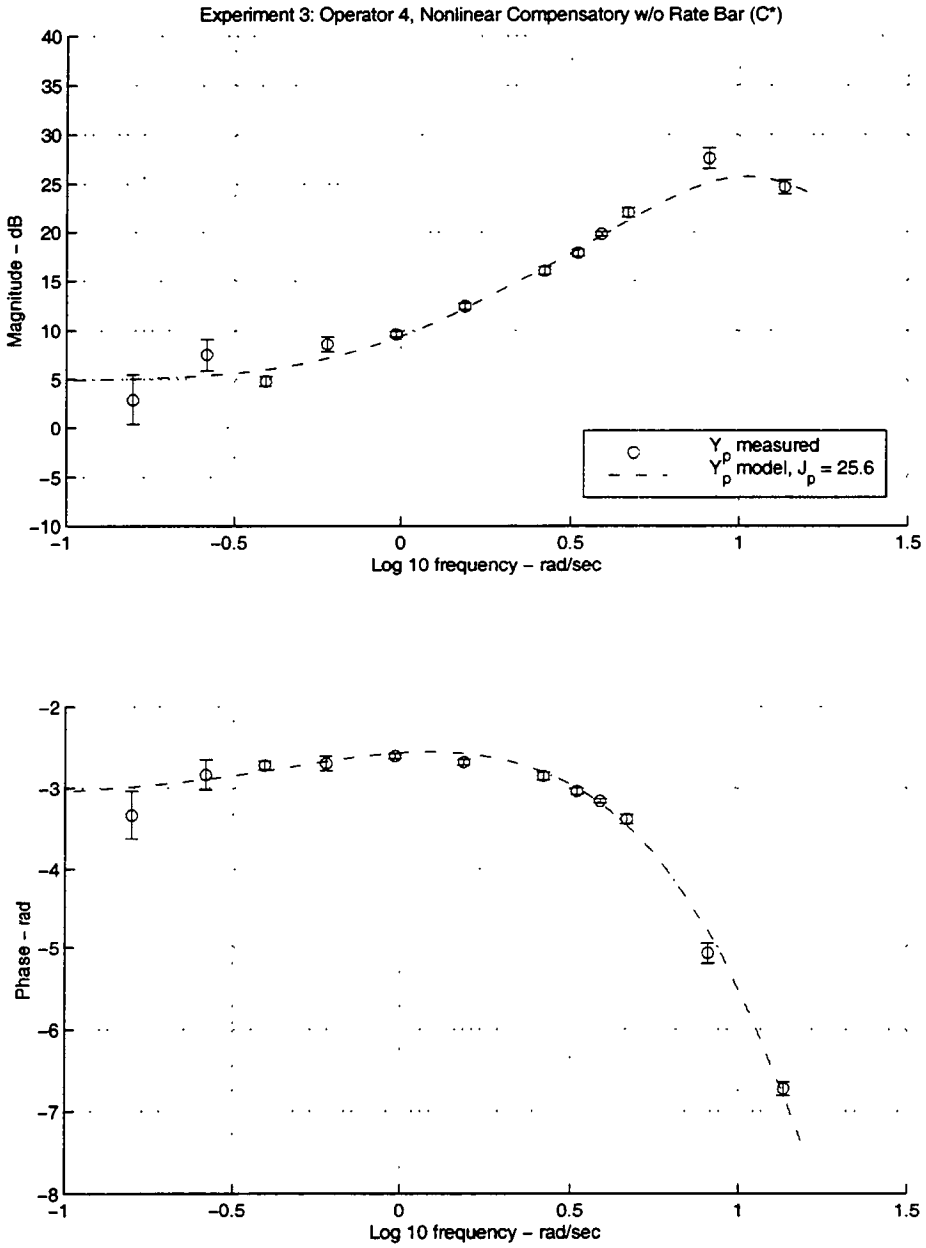

Figure F.40: Experiment 3 model fit results for Operator 4, Nonlinear Compensatory Display, with no pitch disturbance.

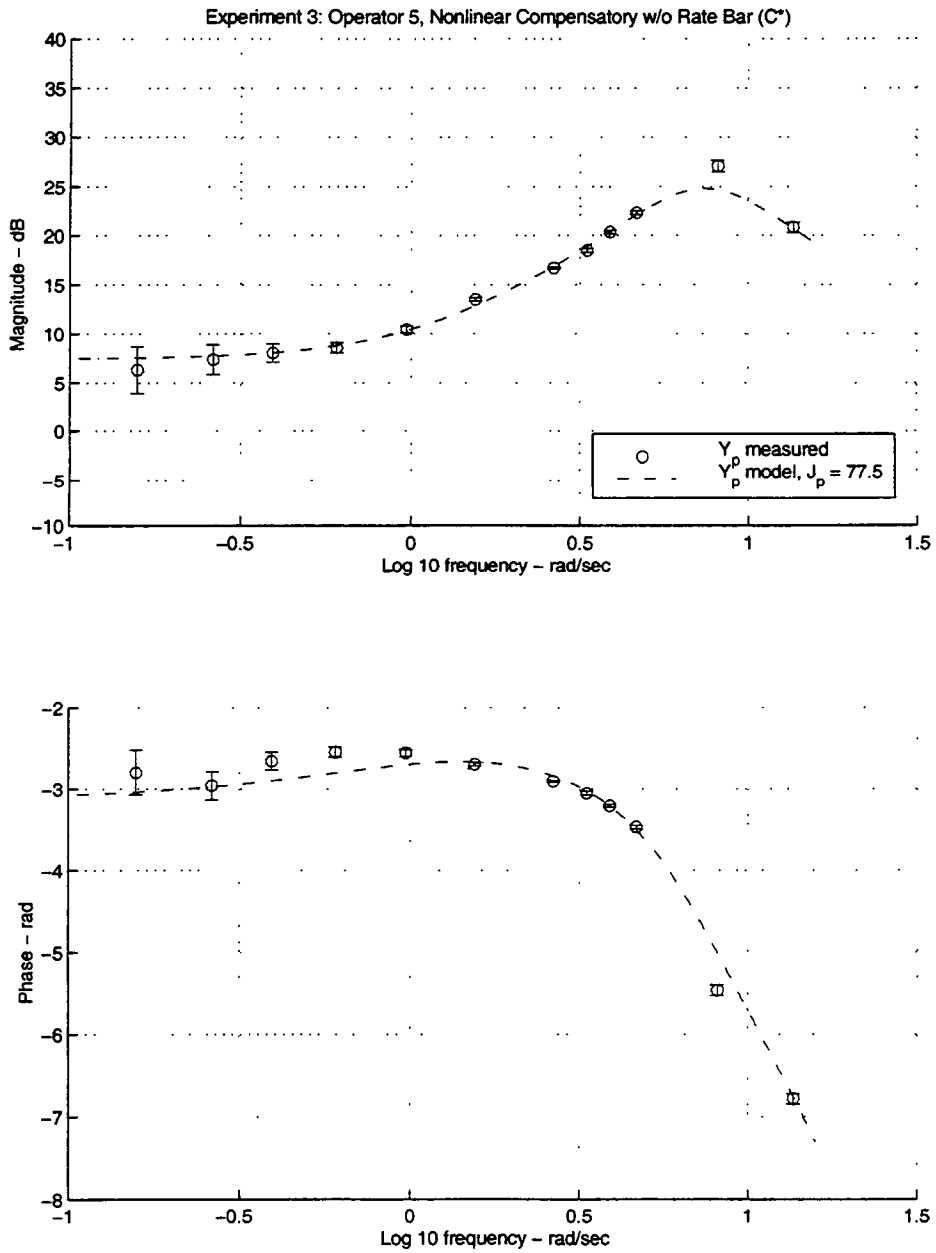

Figure F.41: Experiment 3 model fit results for Operator 5, Nonlinear Compensatory Display, with no pitch disturbance.

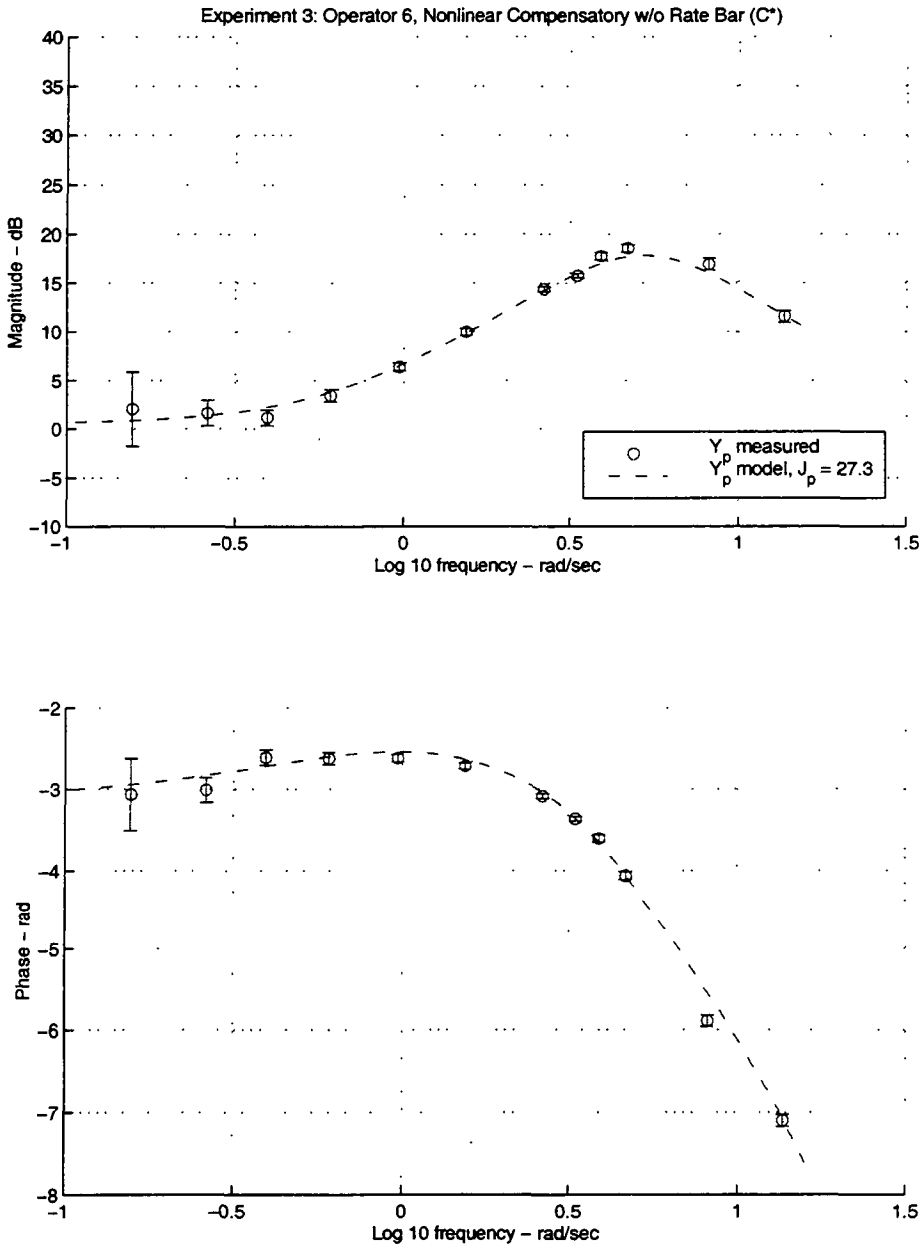

Figure F.42: Experiment 3 model fit results for Operator 6, Nonlinear Compensatory Display, with no pitch disturbance.

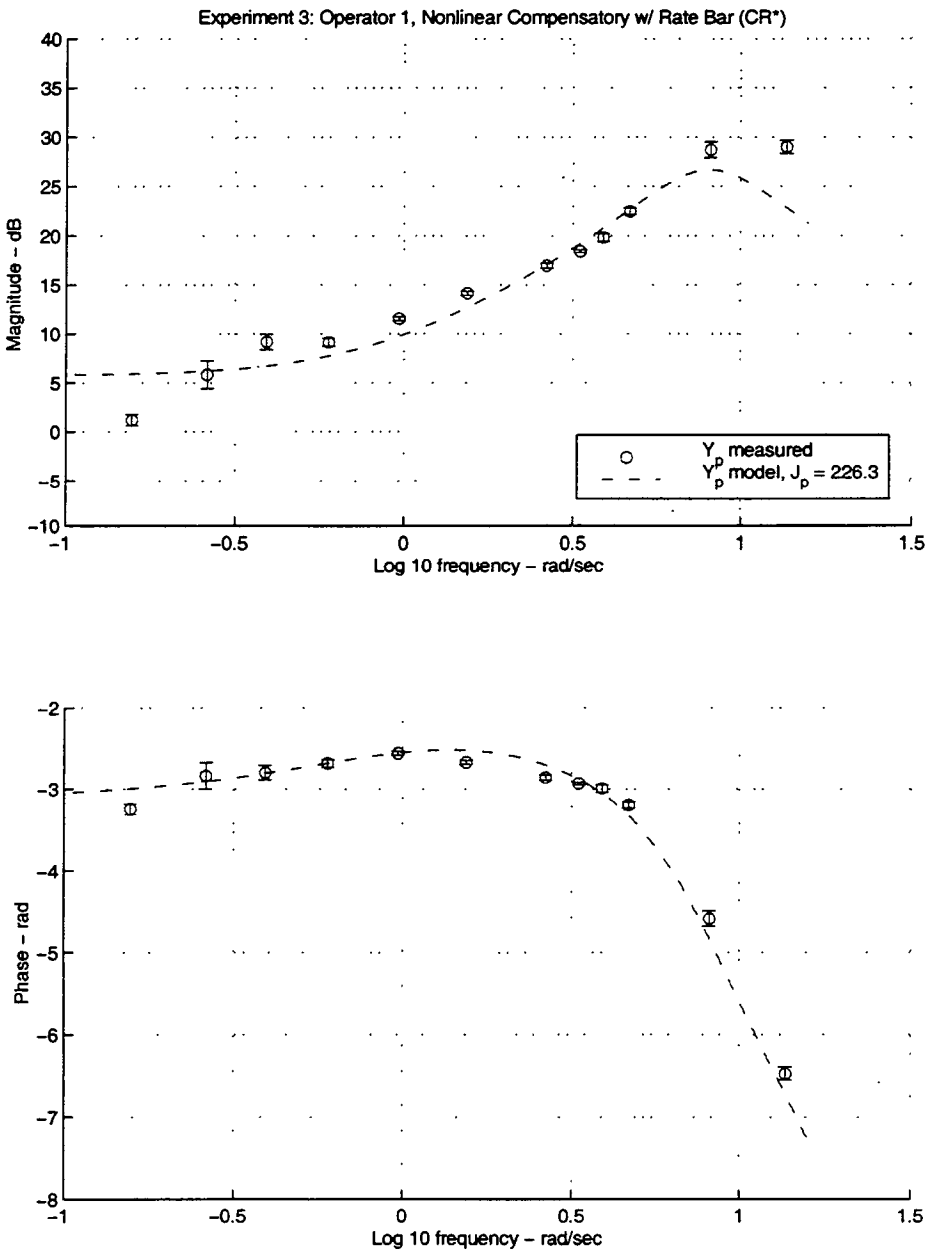

Figure F.43: Experiment 3 model fit results for Operator 1, Nonlinear Compensatory w/Rate Bar Display, with no pitch disturbance.

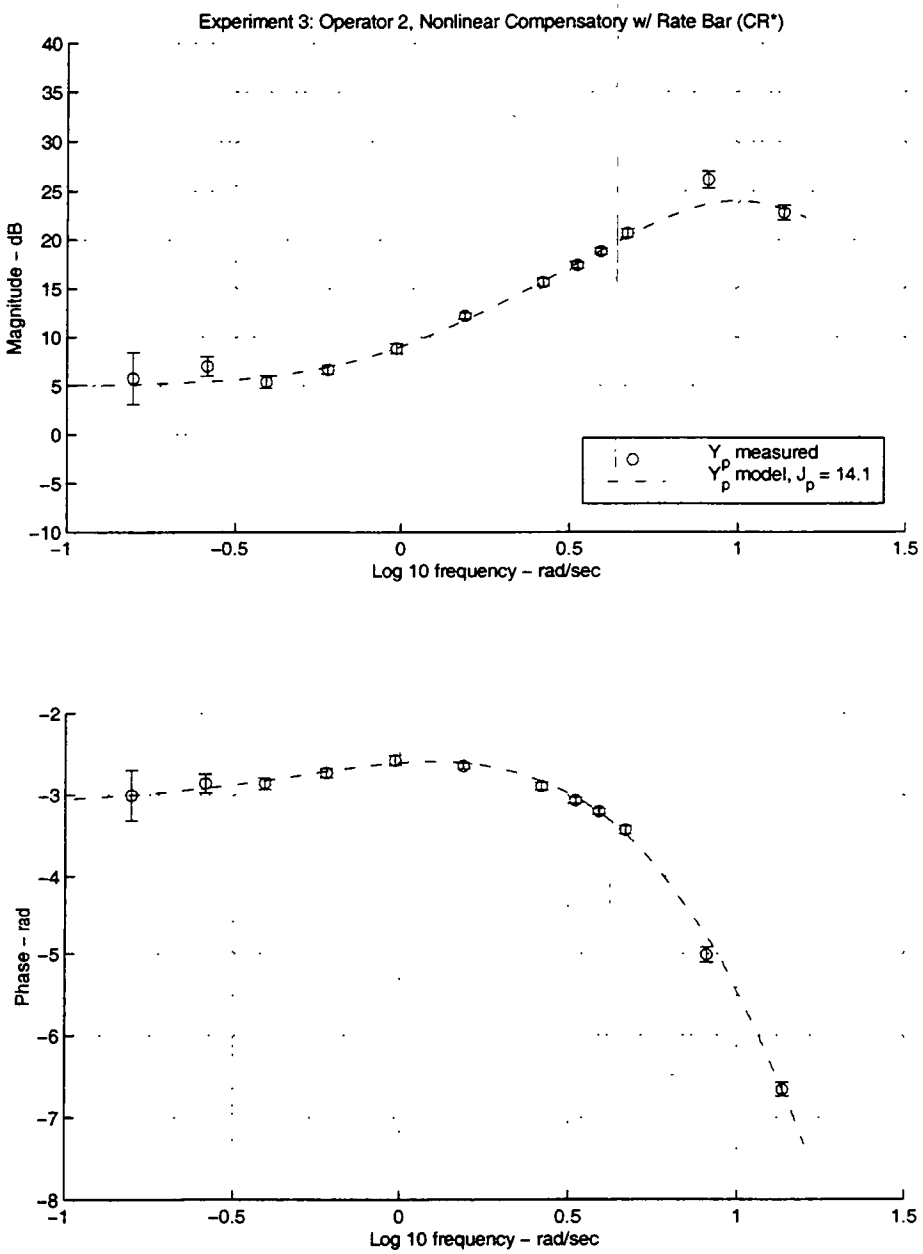

Figure F.44: Experiment 3 model fit results for Operator 2, Nonlinear Compensatory w/Rate Bar Display, with no pitch disturbance.

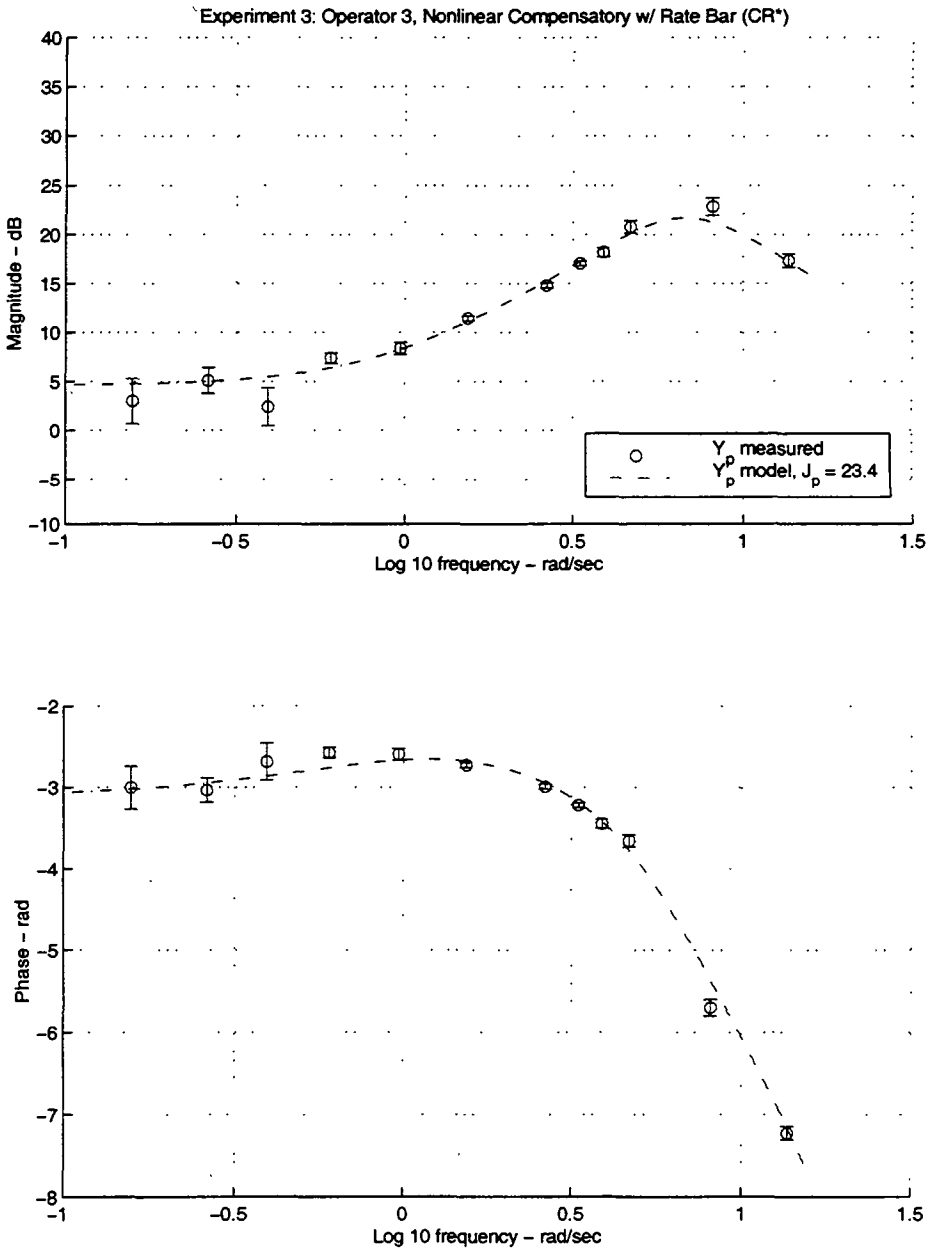

Figure F.45: Experiment 3 model fit results for Operator 3, Nonlinear Compensatory w/Rate Bar Display, with no pitch disturbance.

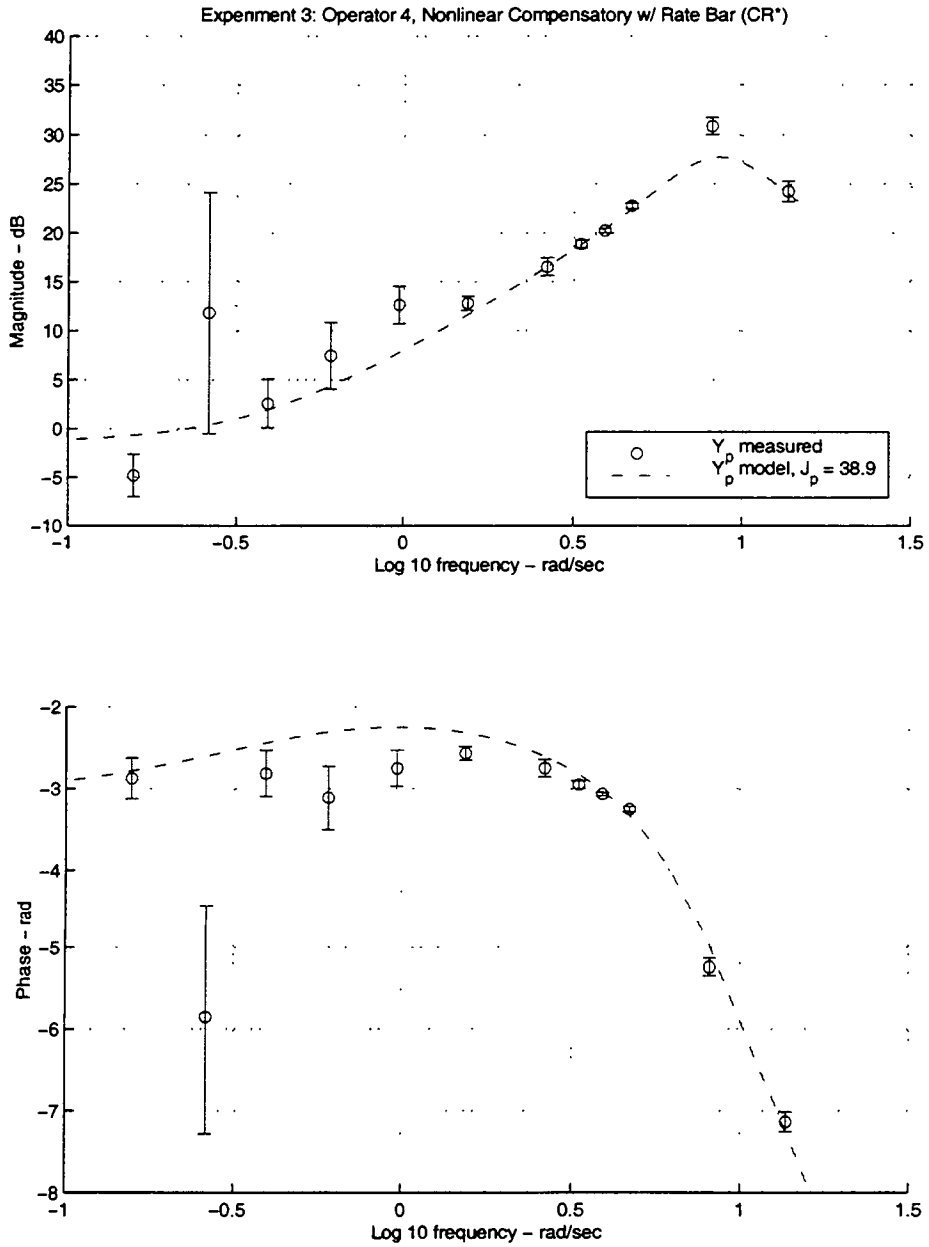

Figure F.46: Experiment 3 model fit results for Operator 4, Nonlinear Compensatory w/Rate Bar Display, with no pitch disturbance.

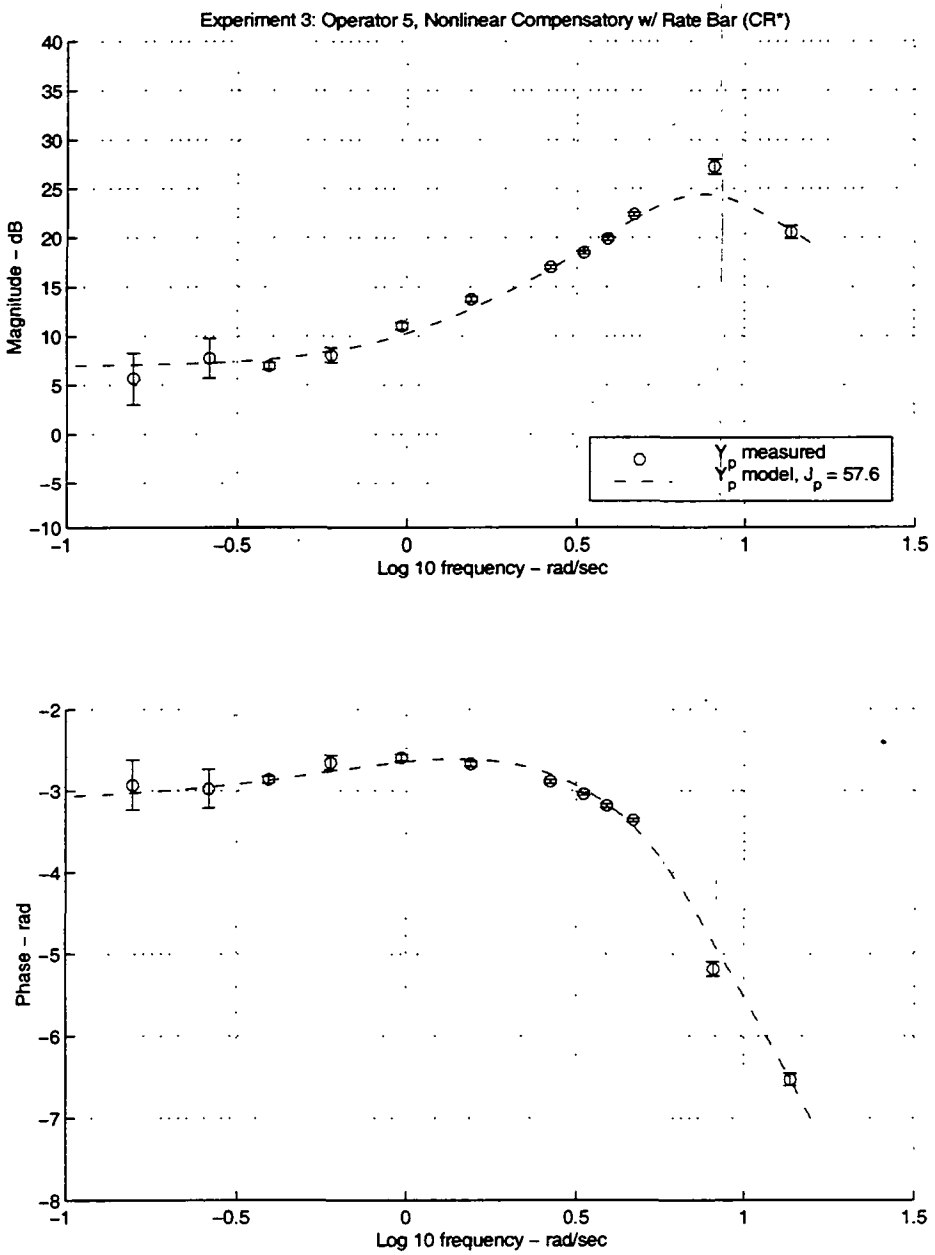

Figure F.47: Experiment 3 model fit results for Operator 5, Nonlinear Compensatory w/Rate Bar Display, with no pitch disturbance.

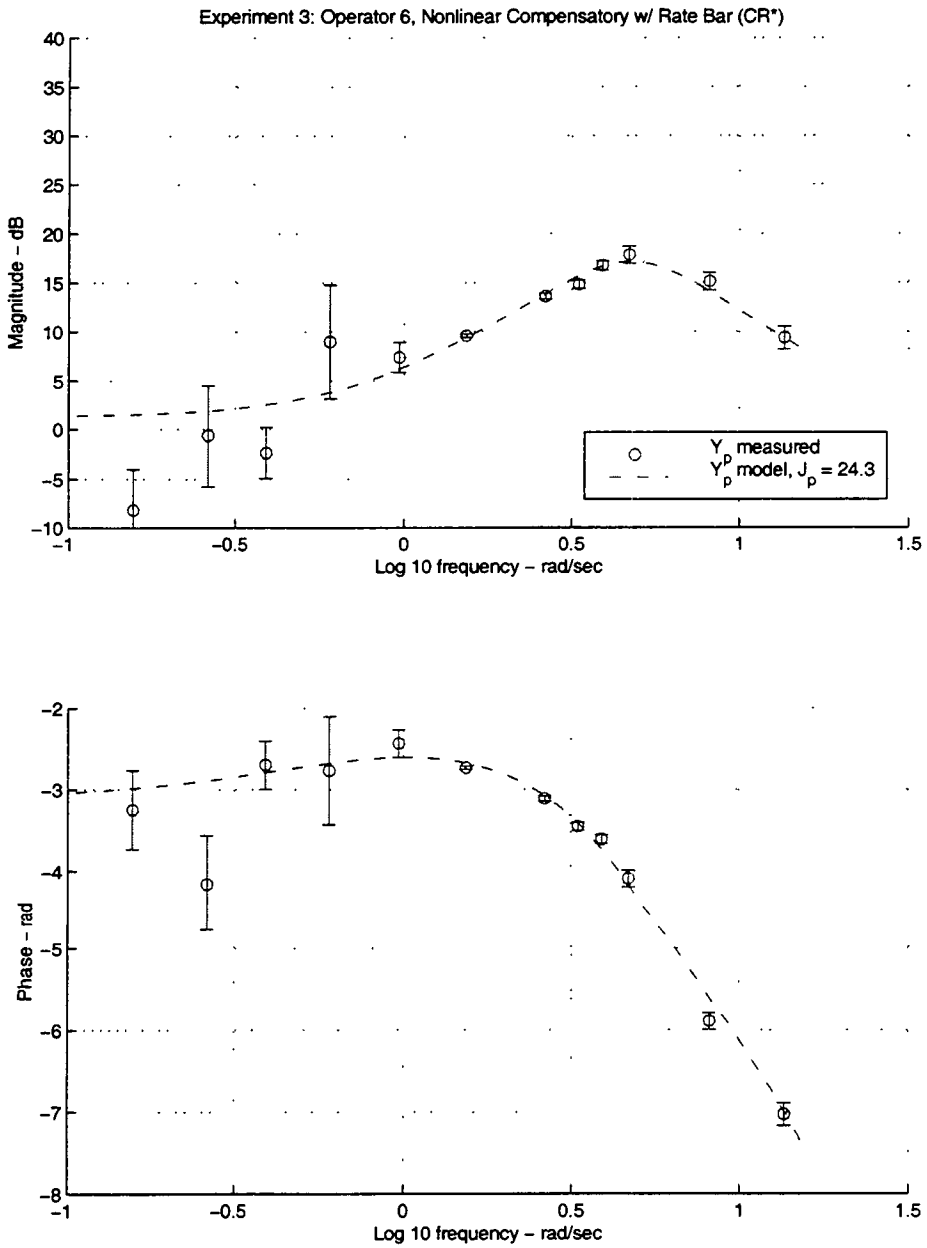

Figure F.48: Experiment 3 model fit results for Operator 6, Nonlinear Compensatory w/Rate Bar Display, with no pitch disturbance.

Bibliography

[1] Wickens, C. 1986. The effects of control dynamics on performance. In *Handbook of perception and human performance*, Vol. II of *Cognitive processes and performance*, edited by K. Boff, L. Kaufman, and J. Thomas. New York: John Wiley & Sons.

[2] Mulder, M. 1994. *Displays, perception and aircraft control: A survey of theory and modelling of pilot behaviour with spatial instruments.* Delft University of Technology Report LR-762.

[3] Hess, R. A. 1997. Feedback control models - manual control and tracking. In *Handbook of Human Factors and Ergonomics, Second Edition*, edited by G. Salvendy. New York:John Wiley & Sons.

[4] Sheridan, T. B. 1997. Supervisory Control. In *Handbook of Human Factors and Ergonomics, Second Edition*, edited by G. Salvendy. New York:John Wiley & Sons.

[5] Bruce, V., P. R. Green, and M. A. Georgeson. 1996. *Visual Perception: Physiology, Psychology, and Ecology.* East Sussex: Psychology Press.

[6] Warren, R., and A. Wertheim, eds. 1990. *Perception and control of self-motion.* Hillsdale: Lawrence Erlbaum Associates.

[7] Gibson, J. J., ed. 1947. *Motion picture testing and research.* Army Air Forces Aviation Psychology Program Research Reports, Report No. 7.

[8] Gibson, J. J. 1950. *The perception of the visual world.* Cambridge: The Riverside Press.

[9] Warren, R. 1982. *Optical transformation during movement: Review of the optical concomitants of egomotion.* AFOSR-TR-82-1028.

[10] Warren, R. and D. H. Owen. 1982. Functional optical invariants: A new methodology for aviation research. *Aviation, Space, & Environmental Medicine.* 53(10):977-83.

[11] Gibson, J. J. 1955. The optical expansion-pattern in aerial locomotion. *American Journal of Psychology.* 68:448-84.

[12] Gibson, J. J., P. Olum, and F. Rosenblatt. 1955. Parallax and perspective during aircraft landing. *American Journal of Psychology.* 68(3):372-85.

[13] Calvert, E. S. 1954. Visual judgements in motion. *Journal of the Institute of Navigation.* 7(3):233-50.

[14] Calvert, E. S. 1955. *Visual aids and their effect on landing success and safety.* Report of the Royal Aircraft Establishment. Report E. 1486.

[15] Havron, M. D. 1962. *Information available from natural cues during final approach and landing.* Human Sciences Research Inc, HSR-RR-62/3-MK-X.

[16] Naish, J. M. 1971. Control information in visual flight. In *Seventh Annual Conference on Manual Control,* Los Angeles. NASA SP-281. 167-76.

[17] Perrone, J. 1980. Slant underestimation: A model based on the size of the viewing aperture. *Perception.* 9:285-302.

[18] Perrone, J. 1982. Visual slant underestimation: a general model. *Perception.* 11:641-54.

[19] Perrone, J. 1983. *Visual slant misperception and the "black-hole" landing situation.* NASA TM 85866.

[20] Perrone, J. 1984. Visual slant misperception and the 'black-hole' landing situation. *Aviation, Space, and Environmental Medicine.* 55:1020-25.

[21] Galanis, G., A. Jennings, and P. Beckett. 1998. A mathematical model of glideslope perception in the visual approach to landing. *International Journal of Aviation Psychology.* 8(2):83-101.

[22] Owen, D. H. 1990. Perception & control of changes in self-motion: A functional approach to the study of information and skill. In *Perception & Control of Self-Motion*, edited by R. Warren and A. H. Wertheim. Hillsdale: Lawrence Erlbaum Associates.

[23] Johnson, W. W., P.S. Tsang, C. T. Bennett, and A. V. Phatak. 1987. The visual control of simulated altitude. In *Proceedings of the Fourth Symposium on Aviation Psychology.* Columbus. 216-22.

[24] Johnson, W. W., C. T. Bennett, K. O'Donnell and A. V. Phatak. 1988. Optical variables useful in the active control of altitude. In *23rd Annual Conference on Manual Control.* Cambridge.

[25] Flach, J. M., R. Warren, S. Garness, L. Kelly, and T. Stanard. 1997. Perception and control of altitude: Splay and depression angles. *Journal of Experimental Psychology: Human Perception and Performance.* 23(6):1-19.

[26] Johnson, W., and A. Phatak. 1989. Optical variables and control strategy used in a visual hover task. In *Proceedings of the IEEE International Conference on Systems, Man and Cybernetics.* Cambridge. 719-24.

[27] Tustin, A. 1947. The nature of the operator's response in manual control and its implication for controller design. *Journal of the IEE, 94* IIA(2).

[28] McRuer, D. T., D. Graham, E. Krendel, and W. Reisener, Jr. 1965. *Human Pilot Dynamics in Compensatory Systems.* Air Force Flight Dynamics Laboratory Technical Report: AFFDL-TR-65-15.

[29] Kleinman, D. L., S. Baron, and W. H. Levison. 1970. An optimal control model of human response, Part I. *Automatica.* 6(3):357-69.

[30] McRuer, D. T., and E. S. Krendel. 1974. *Mathematical Models of Human Pilot Behavior.* AGARD-AG-188.

[31] Baron, S., and J. Berliner. 1975. *MANMOD 1975: Human Internal Models and Scene Perception Models.* U.S. Army Missile Command RD-CR-76-3.

[32] Grunwald, A. J., and S. J. Merhav. 1974. *An analytical model for visual field control - a parametric study.* Israel Institute of Technology, Report TAE-217.

[33] Grunwald, A. J., and S. J. Merhav. 1976. Vehicular control by visual field cues – analytical model and experimental validation. *IEEE Transactions on Systems, Man and Cybernetics.* Volume 6, No. 12: pp 835-845

[34] Grunwald, A. J., and S. J. Merhav. 1978. Effectiveness of basic display augmentation in vehicular control by visual field cues. *IEEE Transactions on Systems, Man, and Cybernetics.* 8(9):679-90.

[35] Merhav, S. J., and A. J. Grunwald. 1978. Display augmentation in manual control of remotely piloted vehicles. *Journal of Aircraft.* 15(3):182-89.

[36] Wilckens, V. 1971. On the dependence of information display quality requirements upon human characteristics and "pilot/automatics"-relations. In *Seventh Annual Conference on Manual Control,* Los Angeles. NASA SP-281. 177-83.

[37] Barrows, A. K., K. W. Alter, P. Enge, B. W. Parkinson, and J. D. Powell. 1997. Operational experience with and improvements to a tunnel-in-the-sky display for light aircraft. In *Proceedings of ION GPS-97.* Kansas City.

[38] Theunissen, E. 1997. *Integrated design of a man-machine interface for 4-D navigation.* Ph.D. Thesis. Delft: Delft University Press.

[39] Grunwald, A. J., J. B. Robertson, and J. J. Hatfield. 1980. *Evaluation of a computer-generated perspective tunnel display for flight-path following.* NASA TP 1736.

[40] Grunwald, A. J., J. B. Robertson, and J. J. Hatfield. 1981. Experimental evaluation of a perspective tunnel display for three-dimensional helicopter approaches. *Journal of Guidance and Control.* 4(6):623-31.

[41] Grunwald, A. J. 1984. Tunnel display for four-dimensional fixed-wing aircraft approaches. *Journal of Guidance, Control, and Dynamics.* 7(3):369-77.

[42] Grunwald, A. J. 1996a. Improved tunnel display for curved trajectory following: experimental evaluation. *Journal of Guidance, Control, and Dynamics.* 19(2):378-84.

[43] Grunwald, A. J. 1996b. Improved tunnel display for curved trajectory following: control considerations. *Journal of Guidance, Control, and Dynamics.* 19(2):370-77.

[44] Negrin, M., A. J. Grunwald, and A. Rosen. 1991. Superimposed perspective visual cues for helicopter hovering above a moving ship deck. *Journal of Guidance.* 14(3):652-60.

[45] Grunwald, A. J., and S. Kohn. 1993. Flight-path estimation in passive low-altitude flight by visual cues. *Journal of Guidance, Control, and Dynamics.* 16(2):363-70.

[46] Grunwald, A. J., and S. Kohn. 1994. Visual field information in low-altitude visual flight by line-of-sight slaved helmet-mounted displays. *IEEE Transactions on Systems, Man, and Cybernetics.* 24(1):120-34.

[47] Wewerinke, P. H. 1978. *Visual scene perception process involved in the manual approach.* NLR TR 78130 U.

[48] Wewerinke, P. H. 1980a. Visual scene perception in manual control. Journal of Cybernetics and Information Science, ASC. 3:1-4.

[49] Wewerinke, P. H. 1980b. *The effect of visual information on the manual approach and landing.* NLR TR 80055 U.

[50] Baron, S., R. Lancraft, and G. L. Zacharias. 1980. *Pilot/vehicle model analysis of visual and motion cue requirements in flight simulation.* NASA CR-3312.

[51] Zacharias, G. L., and W. H. Levison. 1980. *Development of a model for the use of extra-cockpit visual cues.* BBN Report No. 4562. Cambridge: Bolt, Beranek, and Newman.

[52] Zacharias, G. L. 1982. *Flow-field cueing conditions for inferring observer self-motion.* BBN Report No. 5118. Cambridge: Bolt, Beranek and Newman.

[53] Zacharias, G. L., A.K. Caglayan and J.B. Sinacori. 1983. Model for visual flow-field cueing and self-motion estimation. In *Proceedings of the 1983 American Control Conference.* San Francisco. 1326-30.

[54] Zacharias, G. L. 1985a. Visual cueing model for terrain-following applications. *Journal of Guidance, Control, and Dynamics.* 8(2):201-7.

[55] Zacharias, G. L. 1985b. *Modelling the pilot's use of flight simulator visual cues in a terrain-following task.* Report No. R8505. Cambridge: Charles River Analytics.

[56] Zacharias, G. L. 1990. An estimation/control model of egomotion. In *Perception & Control of Self-Motion*, edited by R. Warren and A. H. Wertheim. Hillsdale: Lawrence Erlbaum Associates.

[57] Mulder, M. 1996. Modelling manual control of straight trajectories with a perspective flight-path display. In *Proceedings of the XVth European Annual Conference on Human Decision Making and Manual Control.*

[58] Schalkoff, R. J. 1989. *Digital image processing and computer vision.* New York: John Wiley & Sons.

[59] Greenwood, D. T. 1988. *Principles of dynamics.* Englewood Cliffs: Prentice-Hall.

[60] Sekuler, R., S. Anstis, O. Braddick, T. Brandt, J. A. Movshon, and G. Orban. 1990. The perception of motion. In *Visual Perception: The Neurophysiological Foundations*, edited by L. Spillmann and J. S. Werner. San Diego: Academic Press.

[61] Levison, W. H. 1980. *Measurement of Human Operator Response Behavior.* NASA CR-166038.

[62] Levison, W. H. 1986. Some computational techniques for estimating human operator describing functions. In *Proceedings of the Twenty-First Annual Conference on Manual Control.* NASA CP 2428.

[63] Eshow, M. M. 1992. Flight investigation of variations in rotorcraft control and display dynamics for hover. *Journal of Guidance, Control, and Dynamics.* 15(2):482-90.

[64] Hess, R. A. and B. D. McNally. 1986. Automation effects in a multiloop manual control system. *IEEE Transactions on Systems, Man, and Cybernetics.* 16(1):111-21.

[65] Hoh, R. H. and I. L. Ashkenas. 1981. Handling quality and display requirements for low speed and hover in reduced flight visibility. *Journal of the American Helicopter Society.* 26(1):19-28.

[66] Kaiser, M. K., M. J. Montegut, and D. R. Proffitt. 1995. Rotational and translational components of motion parallax: Observers' sensitivity and implications for 3-D computer graphics. *Journal of Experimental Psychology: Applied.* 1:321-31.

[67] Proffitt, D. R. and M. K. Kaiser. 1996. Hi-Lo stereo fusion. In *Visual Proceedings of SIGGRAPH'96.* 146.

[68] Nakayama, K. 1990. Properties of early motion processing: Implications for the sensing of egomotion. In *Perception & control of self-motion*, edited by R. Warren and A. H. Wertheim. Hillsdale: Lawrence Erlbaum Associates.

[69] Hoh, R. H. 1984. *Investigation of outside visual cues required for low speed and hover.* Systems Technology Inc. Technical Report No. 1213-1.

[70] Federal Aviation Administration Advisory Circular. 1994. *Heliport Design.* AC No.: 150/5390-2A.

[71] Lebacqz, J. V. 1978. *Survey of Helicopter Control/Display Investigations for Instrument Decelerating Approach.* NASA TM-78565.

[72] Graham, D. and McRuer, D. 1961. *Analysis of Nonlinear Control Systems.* New York: Dover Publications Inc.

[73] Hays, W. L. 1963. *Statistics for Psychologists.* New York: Holt, Rinehart and Winston.

[74] Hess, R. A. 1990. Identification of pilot-vehicle dynamics from simulation and flight test. In *Advances in aerospace systems dynamics and control systems*, edited by C. T. Leondes. Vol. 33 of *Control and dynamic systems: Advances in theory and applications.* San Diego: Academic Press.

[75] Franklin, G.F., J. D. Powell, and M. L. Workman. 1990. *Digital control of dynamic systems.* Reading: Addison-Wesley.

Report Documentation Page	Form Approved OMB No. 0704-0188

1. AGENCY USE ONLY *(Leave blank)*	2. REPORT DATE	3. REPORT TYPE AND DATES COVERED
	September 1999	Technical Memorandum

4. TITLE AND SUBTITLE	5. FUNDING NUMBERS
The Identification and Modeling of Visual Cue Usage in Manual Control Task Experiments	522-14
6. AUTHOR(S) Barbara Townsend Sweet	
7. PERFORMING ORGANIZATION NAME(S) AND ADDRESS(ES) NASA Ames Research Center Moffett Field, California 94035-1000	8. PERFORMING ORGANIATION REPORT NUMBER IH-004
9. SPONSORING/MONITORING AGENCY NAME(S) AND ADDRESS(ES) National Aeronautics and Space Administration	10. SPONSORING/MONITORING AGENCY REPORT NUMBER NASA/TM—1999-208798

11. SUPPLEMENTARY NOTES

Point of Contact: Barbara Townsend Sweet, M/S 262-2, Ames Research Center, Moffett Field, California 94035 (650) 604-0006

12A. DISTRIBUTION/AVAILABILITY STATEMENT	12B. DISTRIBUTION CODE
Subject Category: 54-04 Distribution: Public Availability: NASA CASI (301) 621-0390	

13. ABSTRACT *(Maximum 200 words)*

Many fields of endeavor require humans to conduct manual control tasks while viewing a perspective scene. Manual control refers to tasks in which continuous, or nearly continuous, control adjustments are required. Examples include flying an aircraft, driving a car, and riding a bicycle. Perspective scenes can arise through natural viewing of the world, simulation of a scene (as in flight simulators), or through imaging devices (such as the cameras on an unmanned aerospace vehicle).

Designers frequently have some degree of control over the content and characteristics of a perspective scene; airport designers can choose runway markings, vehicle designers can influence the size and shape of windows, as well as the location of the pilot, and simulator database designers can choose scene complexity and content. Little theoretical framework exists to help designers determine the answers to questions related to perspective scene content. An empirical approach is most commonly used to determine optimum perspective scene configurations.

The goal of the research effort described in this dissertation has been to provide a tool for modeling the characteristics of human operators conducting manual control tasks with perspective-scene viewing. This is done for the purpose of providing an algorithmic, as opposed to empirical, method for analyzing the effects of changing perspective scene content for closed-loop manual control tasks.

14. SUBJECT TERMS	15. NUMBER OF PAGES
Manual control, Visual cues, Perspective scene	336
	16. PRICE CODE A15

17. SECURITY CLASSIFICATION OF REPORT	18. SECURITY CLASSIFICATION OF THIS PAGE	19. SECURITY CLASSIFICATION OF ABSTRACT	20. LIMITATION OF ABSTRACT
Unclassified	Unclassified	Unclassified	Unlimited